U.S. DEPARTMENT OF ENERGY

Office of ENERGY EFFICIENCY & RENEWABLE ENERGY

Electrification

2021 Annual Progress Report

Vehicle Technologies Office

(This page intentionally left blank)

Disclaimer

Acronyms

A

AC	Alternating Current
ACC	Adaptive Cruise Control
accel	Acceleration
ACS	Advanced Combustion Systems
ACSforEVER	Advanced Climate Systems for EV Extended Range
AER	All-electric range
AFV	Alternative Fuel Vehicle
AMI	Advanced Metering Infrastructure
AMT	Automated Mechanical Transmission
ANL	Argonne National Laboratory
ANN	Artificial Neural Network
AOI	Areas of Interest
APEC	Asia Pacific Economic Council
APRF	Advanced Powertrain Research Facility
APT	Pressure Sensor
ASD	Aftermarket Safety Device
AVTA	Advanced Vehicle Testing Activity
AVTE	Advanced Vehicle Testing and Evaluation

B

BaSce	Baseline and Scenario
Batt	Battery
BEB	Battery Next-Generation Electric Transit Bus
BEC	Bussed Electrical Center
BEMS	Building Energy Management System
BET	Battery Electric Truck
BEV	Battery Electric Vehicle
BMW	Bayerische Motoren Werke AG
BSFC	Brake Specific Fuel Consumption
BTE	Brake Thermal Efficiency

C

CAC	Charge Air Cooler
CACC	Cooperative Adaptive Cruise Control
CAE	Computer-Aided Engineering
CAFE	Corporate Average Fuel Economy
CAN	Controller Area Network
CAV	Connected and automated vehicles
CARB	California Air Resources Board
CBD	Central Business District
CCS	Combined Charging System
CW, CCW	Clockwise, Counterclockwise

CD	Charge-Depleting
CERV	Conference on Electric Roads and Vehicles
CFD	Computational Fluid Dynamics
CFDC	Commercial Fleet Data Center
CFL	Combined Fluid Loop
CH4	Methane
CHTS	California Household Travel Survey
CIP	Common Integration Platform
Cm3	Cubic
CNG	Compressed Natural Gas
CO	Carbon monoxide
CO2	Carbon Dioxide
COMM	Commuter
Conv	Conventional Vehicle
COP	Coefficient of Performance
CPS	Cyber-Physical Security
CPSR	Constant Power Speed Ratio
CS	Charge Sustaining
Cs	Cold start
CV	Conventional vehicle

D

D3	Downloadable Dynamometer Database
DC	Direct current
DCFC	Direct Current Fast Charge
DCT	Dual-clutch transmission
decel	Deceleration
DER	Distributed energy resource
DFGM	Digital Flux Gate Magnetometer
DFMEA	Design of Failure Modes Analysis
DGE	Diesel Gallon Equivalent
DOE	U.S. Department of Energy
DOHC	Dual overhead cam
DS	Down speeding
DSM	Distributed Security Module
DSM	Diagnostic Security Module
DSP	Digital Signal Processor
DSRC	Dedicated Short Range Communications
dt	Change in time
dv	Change in velocity
Dyno	Dynamometer

E

EAVS	Electrically Assisted Variable Speed Supercharger
EC	European Commission
EDV	Electric Drive Vehicle

EDT	Electric Drive Technologies
EDX	Energy dispersive x-ray spectroscopy
EERE	Energy Efficiency and Renewable Energy
EGR	Exhaust Gas Recirculation
EG/W	Ethylene glycol/water
EOL	End of life
EPA	Environmental Protection Agency
ePATHS	Electrical PCM Assisted Thermal Heating System
EREV	Extended-Range Electric Vehicles
ESIF	Energy Systems Integration Facility
ESS	Energy Storage System
ETT	Electric Transportation Technologies
E-TREE	Electric Truck with Range Extending Engine
EUMD	End-Use Measurement Device
EV	Electric Vehicle
EV2G	Electric Vehicle-to-Grid
EVSE	Electric Vehicle Service Equipment
EXV	Electronic Expansion Valve

F

F	Force
FASTSim	Future Automotive Systems Technology Simulator
FC	Fuel cell
FC	Fast charge
FCons	Fuel consumption
FCTO	Fuel Cell Technologies Office
FE	Fuel Economy
FEA	Finite Element Analysis
FEX	Front-end Heat Exchanger
FHWA	Federal Highway Administration
FLNA	Frito-Lay North America
FM	Friction Modifier
FMEP	Friction Mean Effective Pressure
FOA	Funding Opportunity Announcement
FTIR	Fourier transform infrared spectroscopy
FTP	Federal Test Procedure
FWD	Four-wheel drive
FY	Fiscal year

G

g	gram
GB	Gigabyte
GCEDV	Grid Connected Electrical Drive Vehicles
GEM	Gas Emissions Model
GHG	Greenhouse Gas
GITT	Grid Interaction Tech Team

GMLC	Grid Modernization Lab Consortium
GnPs	graphene nanoplatelets
GO	Graphene Oxide
GPRA	Government Performance and Results Act
GPS	Global Positioning System
GREET	Greenhouse gases, Regulated Emissions, and Energy use in Transportation
GSF1	Generic Speed Form 1
GSU	Grid side unit
GUI	Graphic User Interface
GVW	Gross Vehicle Weight

H

h-APU	hybrid Auxiliary Power Unit
HATCI	Hyundai America Technical Center, Inc.
HC	Unburned hydrocarbons
HD	Heavy Duty
HEV	Hybrid-Electric Vehicle
H-GAC	Houston-Galveston Area Council
HHDDT	Heavy Heavy-Duty Diesel Truck
HHV	Hydraulic Hybrid Vehicle
HIL	Hardware-In-the-Loop
HP	Heat Pump
Hp	Horsepower
HTML	HyperText Markup Language
HV	High Voltage
HVAC	Heating Ventilating and Air Conditioning
HWFET	Highway Fuel Economy Test
HPMS	Highway Performance Monitoring System
HVTB	High Voltage Traction Battery
HWY	Highway Program or Highway Fuel Economy Test Cycle
HPC	High Performance Computing
HTR	Heater
Hz	Hertz

I

I	Inertia
IC	Internal Combustion
ICD	Interim Component Durability
ICDV	Internal Combustion Drive Vehicles
ICE	Internal Combustion Engine
ICTF	Intermodal Container Transfer Facility
ICU	Inverter-Charger Unit
IEB	Information Exchange Bus
IEC	International Electrotechnical Commission
IGBT	Insulated Gate Bipolar Transistors
IHX	Internal Heat Exchanger

INL	Idaho National Laboratory
INTEGRATE	Integrated Network Testbed for Energy Grid Research and Technology
IOT	Internet of Things
IR	Infrared Radiation
ISO	International Organization for Standardization
ITS	Intelligent Transportation Systems

J

JIT	Just-in-Time

K

kg	Kilogram
km	Kilometer
kW	Kilowatt
kWh	Kilowatt hour

L

L	litre
L1	Level 1 benchmark
L2	Level 2 benchmark
Lbf	Pounds force
LCC	Liquid-Cooled Condenser
LD	Light duty
LH	line haul
Li	Lithium
LIB	Lithium-ion battery
LLNL	Lawrence Livermore National Laboratory
LNG	Liquified natural gas
LTC	Lockport Technical Center
LV	Leading Vehicle

M

M	Mass
MBSE	Model Based System Engineering
MD	Medium Duty
mpg	Miles per gallon
MMTCE	Million Metric Tons of Carbon Equivalent
MIIT	Ministry of Industry and Information Technology
mi	Mile
MJ	Megajoules
MOSFET	Metal-Oxide Semiconductor Field-Effect Transistor
mph	Miles per hour
MPGe,	Miles per gallon equivalent, Miles per gallon gasoline equivalent
MTDC	Medium Truck Duty Cycle
MOVES	Motor Vehicle Emission Simulator
MRF	Moving Reference Frame
MURECP	Medium-Duty Urban Range Extended Connected Powertrain

MY	Model year
M2	Meters squared

N

NACFE	North American Council for Freight Efficiency
NDA	Non-Disclosure Agreement
NETL	National Energy Technology Laboratory
NHTS	National Household Travel Survey
NHTSA	National Highway Transportation Safety Administration
NM	Newton meters
NOx	Nitrogen oxides
NR	Natural Rubber
NRE	Non-Recurring Engineering
NREL	National Renewable Energy Laboratory
NRT	National Retail Trucking
NVH	Noise, vibration, and harshness
NVUSD	Napa Valley Unified School District
NYSERDA	New York State Energy Research Development Authority

O

OBC	On-board charger
OCBC	Orange County Bus Cycle
OEM	Original Equipment Manufacturer
OneSAF	One Semi-Automated Forces
ORNL	Oak Ridge National Laboratories

P

P	Active Power
PC	Polycarbonate
PCM	Phase-Change Material
PCU	Power Control Unit
PCU	Powertrain Control Unit
PEEM	Power Electronics and Electric Motor
PFC	Power factor correction
PFI	Port fuel injection
PGW	Pittsburgh Glass Works
PHEV	Plug-in Hybrid Electric Vehicle
PHEV##	Plug-in hybrid electric vehicle with ## miles of all-electric range
PI	Principal Investigator
PM	Permanent Magnet
PM	Particulate Matter
ppm	Parts per Million
PTC	Positive Temperature Coefficient (Electric Heater)
PTO	Power Take-Off
PVP	Polyvinylpyrrolidone
PWWMD	Public Works and Waste Management Department

λ	Power Factor
φ	Power Angle

Q

Q	Reactive power
QA	Quality assurance
QC	Quality control

R

R2	Coefficient of Determination
R/D	Receiver / Dryer
REV	New York State's Reforming the Energy Vision Initiative
REx	Range Extending Engine
rGO	reduced graphene oxide
RH	Relative Humidity
RMS	Root Mean Square
ROL	Ring-On-Liner
rpm	Revolutions Per Minute
RSU	Road Side Unit
RWDC	Real-World Drive-Cycle

S

S	Apparent power
SAE	Society of Automotive Engineers
SBR	Styrene-Butadiene Rubber
SC03	SC03 Supplemental Federal Test Procedure
SCAG	Southern California Association of Governments
SCAQMD	South Coast Air Quality Management District
SCIG	Southern California International Gateway
SCR	Silicon Controlled Rectifier
SCR	Selective Catalytic Reduction
SDO	Standards Definition Organizations
SI	Système International d'Unités
SI	Gasoline Spark Ignition
SNR	Sensor
SOC	State of Charge
SPL	Sound Pressure Level
SR	Speed Ratio
SS	Steady State
SPaT	Signal Phase and Timing
StAR	Storage-Assisted Recharging

T

T	Torque
TA	Technical Area
TA	Torque Assist
TC	Thermocouple

TE	Thermoelectric
TE	Transmission Error
TES	Thermal Energy Storage
TGA	thermogravimetric analysis
THC	Total hydrocarbon emissions
TIM	Thermal Interface Materials
TLRP	Thermal Load Reduction Package
TN	Testing Network
TOU	Time-Of-Use
TSDC	Transportation Secure Data Center
TSI	Turbocharged stratified injection
TUSD	Torrance Unified School District
TXVs	Thermal Expansion Valves

U

U.S. DRIVE	U.S. Driving Research and Innovation for Vehicle Efficiency and Energy Sustainability
UA	Transfer Coefficient
UC	Ultra-capacitor
UCR	University of California, Riverside
UDDS	Urban Dynamometer Driving Schedule
UN ECE	United Nations Economic Council for Europe
UPS	United Parcel Service
URL	Uniform Resource Locator
US06	Environmental Protection Agency US06 or Supplemental Federal Test Procedure
USABC	United States Advanced Battery Consortium
USCAR	U.S. Council for Automotive Research
Util	Battery capacity utilization

V

V	Voltage
V2G	Vehicle-to-Grid
VAr	Volt-Amp-reactive
VGI	Vehicle-Grid Integration
VGT	Variable Geometry Turbocharger
VIP	Vacuum Insulated Panels
VMT	Vehicle Miles Traveled
VS	Vehicle Systems
VSATT	Vehicle Systems Analysis Technical Team
VSI	Vehicle Systems Integration
VSST	Vehicle Systems Simulation and Testing
VTCab	Vehicle Thermal Cab Simulator
VTIF	Vehicle Testing and Integration Facility
VTO	Vehicle Technologies Office

W

dw	Change in Angle W

WCC	Water Cooled Condenser
WEC	World Endurance Championship
WEG	Water/Ethylene Glycol
Wh	Watt hour
WHR	Waste Heat Recovery
WPT	Wireless Power Transfer
WTW	Well-to-Wheels

X

XFC	Extreme Fast Charging
XPS	x-ray photoelectron spectroscopy

Z

ZECT	Zero-emissions cargo transport

Executive Summary

During fiscal year 2021 (FY 2021), the U.S. Department of Energy (DOE) Vehicle Technologies Office (VTO) funded early-stage research, development, demonstration, & deployment (RDD&D) projects that address Batteries and Electrification of the U.S. transportation sector. The VTO Electrification Sub-Program is composed of Electric Drive Technologies, and Grid Integration activities. The Electric Drive Technologies group conducts R&D projects that advance electric motors and power electronics technologies. The Grid and Charging Infrastructure group conducts R&D projects that advance grid modernization and electric vehicle charging technologies. This document presents a brief overview of the Electrification Sub-Program and progress reports for its R&D projects. Each of the progress reports provide a project overview and highlights of the technical results that were accomplished in fiscal year (FY) 2021.

Table of Contents

List of Figures

List of Tables

(This page intentionally left blank)

Vehicle Technologies Office Overview

Vehicles move our national economy. Annually, vehicles transport 12 billion tons of freight—more than $38 billion worth of goods each day[1]—and move people more than 3 trillion vehicle-miles.[2] Growing our economy requires transportation, and transportation requires energy. The transportation sector accounts for approximately 27% of total U.S. energy needs,[3] and the average U.S. household spends over 17% of its total family expenditures on transportation,[4] making it, as a percentage of spending, the most costly personal expenditure after housing. Transportation is critical to the overall economy, from the movement of goods to providing access to jobs, education, and healthcare.

The Vehicle Technologies Office (VTO) funds research, development, demonstration, and deployment (RDD&D) of new, efficient, and clean mobility options that are affordable for all Americans. VTO leverages the unique capabilities and world-class expertise of the National Laboratory system to develop new innovations in vehicle technologies, including advanced battery technologies (including automated and connected vehicles as well as innovations in efficiency-enhancing connected infrastructure); innovative powertrains to reduce greenhouse gas and criteria emissions from hard-to-decarbonize off-road, maritime, rail, and aviation sectors; and technology integration that helps demonstrate and deploy new technology at the community level. Across these technology areas and in partnership with industry, VTO has established aggressive technology targets to focus RDD&D efforts and ensure there are pathways for technology transfer of federally supported innovations into commercial applications.

VTO is uniquely positioned to accelerate sustainable transportation technologies due to strategic public-private research partnerships with industry (e.g., U.S. DRIVE, 21st Century Truck Partnership) that leverage relevant expertise. These partnerships prevent duplication of effort, focus DOE research on critical RDD&D barriers, and accelerate progress. VTO advances technologies that assure affordable, reliable mobility solutions for people and goods across all economic and social groups; enable and support competitiveness for industry and the economy/workforce; and address local air quality and use of water, land, and domestic resources.

Annual Progress Report

As shown in the organization chart (below), VTO is organized by technology area: Batteries & Electrification R&D, Materials Technology R&D, Advanced Engine & Fuel Technologies R&D, Energy Efficient Mobility Systems, and Technology Integration. Each year, VTO's technology areas prepare an Annual Progress Report (APR) that details progress and accomplishments during the fiscal year. VTO is pleased to submit this APR for Fiscal Year (FY) 2021. The APR presents descriptions of each active project in FY 2021, including funding, objectives, approach, results, and conclusions.

---

[1] U.S. Department of Transportation, Freight Analysis Framework Version 5.0 Data Tabulation Tool.
[2] U.S. Department of Transportation, March 2022 Traffic Volume Trends, Figure 1.
[3] U.S. Energy Information Administration. Monthly Energy Review, 2022, https://www.eia.gov/totalenergy/data/monthly/index.php.
[4] Davis, Stacy C., and Robert G. Boundy. Transportation Energy Data Book: Edition 39. Oak Ridge National Laboratory, 2020, https://doi.org/10.2172/1767864.

Organization Chart

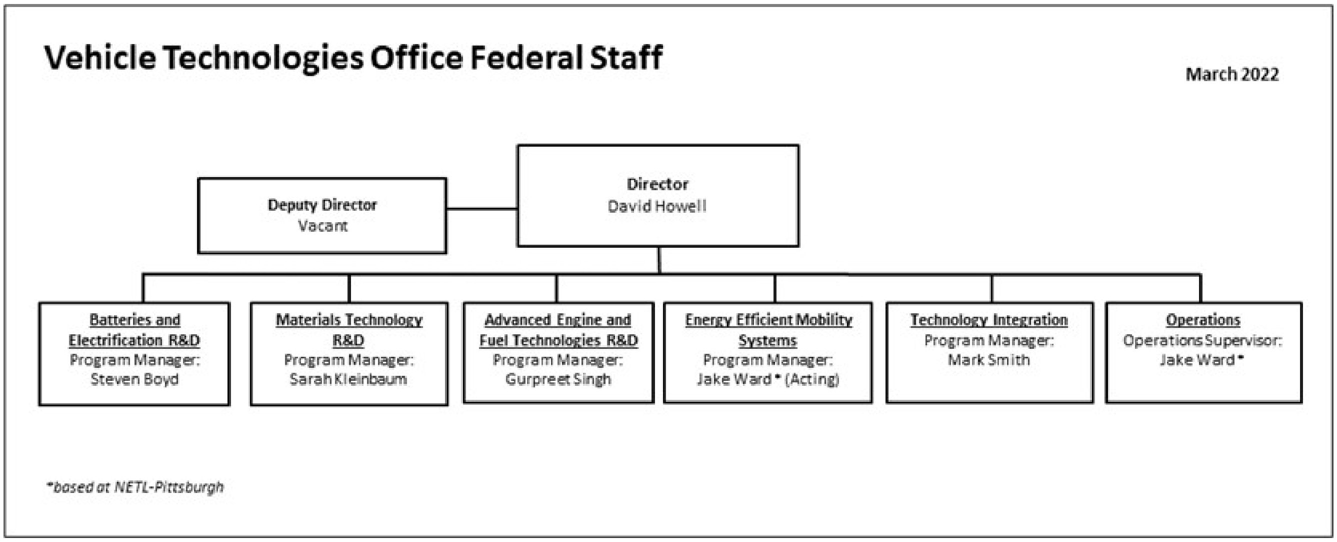

Electric Drive Technologies Program Overview

Introduction

The Electric Drive Technologies (EDT) program's mission is to conduct early-stage research and development on transportation electrification technologies that accelerate the development of cost-effective and compact electric traction drive systems that meet or exceed performance and reliability requirements of internal combustion engine (ICE)-based vehicles, thereby enabling electrification across all light-duty vehicle types.

Goals and Objectives

The goal of the EDT program is to develop an electric traction drive system at a cost of $6/kW for a 100-kW peak system by 2025. In addition, the program has a 2025 power density target of 33 kW/L for a 100-kW peak system. While achieving these targets will require transformational technology changes to current materials and processes, it is essential for enabling widespread electrification across all light-duty vehicle platforms.

Program Design and Execution

The EDT program provides support and guidance for many cutting-edge automotive technologies now under development. Researchers focus on developing revolutionary new power electronics (PE), electric motor (EM), and traction drive system (TDS) technologies that will leapfrog current on-the-road technologies. This will lead to lower cost and better efficiency in transforming battery energy to useful work. Research and development (R&D) is also aimed at achieving greater understanding of, and improvements in how the various components of tomorrow's automobiles will function as a unified system.

In supporting the development of advanced vehicle propulsion systems, the EDT program fosters the development of technologies that will significantly improve efficiency, costs, and fuel economy.

The EDT program directs early-stage research through a three-phase approach intended to

- Identify overall propulsion- and vehicle-related needs by analyzing programmatic goals and reviewing industry recommendations and requirements, and then develop and deliver the appropriate technical targets for systems, subsystems, and component R&D activities.
- Develop, test, and validate individual subsystems and components, including EMs and PE
- Estimate how well the components and subsystems work together in a vehicle environment or as a complete propulsion system and whether the efficiency and performance targets at the vehicle level have been achieved.

The research performed under this program addresses the technical and cost barriers that currently inhibit the introduction of advanced propulsion technologies into hybrid electric vehicles (HEVs), plug-in HEVs, battery electric vehicles (BEVs), and fuel cell powered automobiles that meet the DOE goals.

A key element in making these advanced vehicles practical is providing an affordable electric TDS. This will require attaining weight, volume, efficiency, and cost targets for the PE and EM subsystems of the TDS. Areas of development include:

- Novel traction motor designs that result in increased power density and lower cost

- Inverter technologies that incorporate advanced wide bandgap (WBG) semiconductor devices to achieve higher efficiency while accommodating higher-temperature environments and delivering higher reliability.
- Converter concepts that leverage higher-switching-frequency semiconductors, nanocomposite magnetics, higher-temperature capacitors, and novel packaging techniques that integrate more functionality into applications offering reduced size, weight, and cost.
- New onboard battery charging electronics that build from advances in converter architectures for decreased cost and size
- More compact and higher-performing thermal controls achieved through novel thermal materials and innovative packaging technologies
- Integrated motor-inverter TDS architectures that optimize the technical strengths of the underlying PE and electric machine subsystems.

VTO competitively awards funding through funding opportunity announcement (FOA) selections, and projects are fully funded through the duration of the project in the year that the funding is awarded. The future direction for direct-funded work at the National Laboratories is subject to change based on annual appropriations.

Electric Drive Technologies Lab Consortium

The multi-lab EDT Consortium will leverage U.S. research expertise and facilities at the national labs and universities to improve the power density of electric drives by 10X compared with the 2015 numbers while reducing the cost by 50% and doubling the lifetime miles within the next 5 years. The final objective of the consortium is to develop a 100-kW traction drive system that achieves a power density of 33 kW/L, has an operational life of 300,000 miles, and a cost of $6/kW. The system will be composed of a 100 kW/L inverter and a >20,000 rpm, 50 kW/L electric motor.

Research will be performed within the framework of a new research consortium consisting of a multi-disciplinary team that will plan, establish, conduct, and manage a portfolio of multi-lab and multi-university research efforts to advance the state-of-the-art in electric drive technologies.

The consortium is organized around three Keystone projects: (1) Power Electronics; (2) Electric Motors; and (3) Traction Drive System. The consortium will focus on early-stage research projects on advanced materials, high-density integration of dissimilar layers/materials, multifunctional subcomponents, and optimized and new thermal/electrical/magnetic architectures. New materials such as WBG semiconductors, soft magnetic materials, and ceramic dielectrics, merged using multi-objective co-optimization design techniques, will be utilized to achieve the program goals. Moreover, integration of components and subcomponents will further propel the research toward the goals of the consortium.

Consortium National Laboratory members include Ames Laboratory, The National Renewable Energy Laboratory (NREL), Oak Ridge National Laboratory (ORNL), and Sandia National Laboratories (SNL). University consortium partners include North Carolina State University, The University of Arkansas, Virginia Polytechnic Institute, University of Wisconsin-Madison, Georgia Institute of Technology, University of California-Berkeley, Illinois Institute of Technology (IIT), Purdue University, The State University of New York (SUNY), and The Ohio State University.

Grid and Infrastructure Program Overview

Introduction

The Grid and Charging Infrastructure (G&I) program's mission is to conduct early-stage research and development on transportation electrification technologies that enable reduced petroleum consumption by light, medium, and heavy-duty vehicles. The program identifies and enables the role of vehicles in the future electrical grid.

Charging of EVs at scale creates an unpredictable and stochastic load demand on the electric grid. Newer EVs being introduced in the market can charge at low and high rates based on the need and availability of charging infrastructure. Additionally, charging profiles for EVs manufactured by different Original Equipment Manufacturers (OEMs) vary significantly which complicates meeting the aggregated charging loads. This creates difficulty in the prediction of magnitude, location, and timing of charging loads and could potentially have a detrimental grid impact.

To enable successful deployment of EVs at scale, a holistic approach is required across the vehicle, charging infrastructure, and electric grid. Figure 1 presents the key components of charging ecosystems that create challenges to be addressed. This includes controls, high voltage power electronics, interoperability, wireless and other advanced high power charging (HPC) technologies, and integration and optimization with the grid and Distributed Energy Resources (DERs) such as stationary storage and photovoltaics.

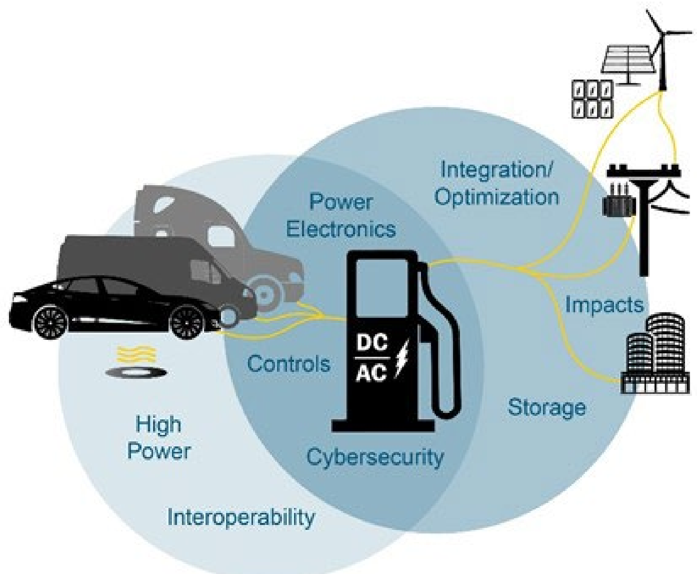

Figure 1 Key technologies and challenges addressed by the Grid and Infrastructure Program.

Hence, the effective control and optimization of the charging ecosystem is essential and is otherwise known as Smart Charge Management (SCM). SCM emphasizes the identification of pathways to reduce the potential grid impacts of EVs at scale, while providing enhanced value for EV/charging/grid systems including reduced costs and increased opportunities for grid services. If unmanaged, EVs at scale connecting to the grid would create numerous challenges for utilities, particularly at the distribution level, such as feeder voltage violations, system imbalances, flickers, equipment overloading, and large increases in daily peak loads. Interoperability and scalability, and high-speed communications and control are critical challenges facing SCM. Effective SCM will enable response to inappropriate energy management, malfunctioning equipment, and Cyber-Physical Security (CPS) breaches. SCM can also facilitate the provision of grid services from EV charging, including, but not limited to, peak load shaving, demand charge mitigation, voltage support, frequency regulation, and integration of renewable energy generation.

HPC of up to 400 kW for light-duty (LD) EVs, and 1+ MW for medium-duty (MD) and heavy-duty (HD) EVs, can enable greater vehicle utilization, extended range, and reduce recharging times. Technical advances are steadily being made with regards to HPC, but further progress is needed to facilitate the mass market adoption of EVs. Specific technical challenges include the requirement for intelligent design and integration with the grid and DERs, to mitigate ramp rates and surge power demands, lower system cost of ownership, and interoperability of HPC infrastructure with MD and HD EVs. Additionally, as the charging power levels steadily increase, new challenges are manifested in ensuring HPC is effectively integrated with the grid in an efficient, flexible, and secure manner. High voltage power electronics and materials with better thermal and electrical properties are key enabling technologies for advancing HPC. Furthermore, improvements in wireless charging are required including the development of novel coils, advanced field shaping techniques, and control strategies.

Rapidly increasing numbers of EVs with advanced communication functionalities and networked chargers, as well as the trend towards HPC, dramatically increase cyber related risks and consequences. Coordinated cyber-attacks on chargers/charging stations can lead to serious local and potentially broader grid disruptions such as wide-scale blackouts and/or brownouts. A comprehensive understanding of the threat environment, including risks and consequences therein, is needed to identify, minimize, and/or eliminate critical cyber-physical vulnerabilities. Advances are required in strategies, systems, and tools, including hardware/software for intrusion detection, threat mitigation and isolation, and charging system recovery.

Addressing the barriers above can only be done by conducting high risk projects that are beyond the suitable scope and developmental timeframes of industry. Furthermore, the transportation and utility sectors historically have not worked together, which complicates collaboration. A significant level of pre-competitive and vendor-neutral Research and Development (R&D) effort is needed to address the challenges associated with a safe and secure charging ecosystem for EVs at scale.

State of the Art

Electric Vehicle Charging

It is desirable to reduce EV refueling times to be competitive with conventional vehicle refueling times (e.g., 5-10 minutes for 400 miles of LD vehicle driving range). The table below lists the refueling characteristics of several types of installed commercial chargers and a conventional gasoline fueling pump. The technologies employed in the EV charging stations are shown in the figure below. It is important to note that the rate of energy transfer peaks early in the charging cycle and decreases as the battery pack approaches 100% state of charge (SOC). While the energy transfer rate is not constant during charging, given two chargers with different peak power ratings the charger with the higher peak power rating is potentially capable of minimizing EV charging times when compared to the EVSE with a lower maximum power rating. It is notable that the EV must be capable of accepting the higher power provided by the EVSE with the higher maximum power rating. To accomplish this capability some vehicle OEMs are increasing the operating voltage of the on-board battery pack and the maximum C-rate for charging battery cells. Currently Electrify America offers commercial charger solutions with peak power rating of 350 kW DC.[5] However, currently the maximum charge rate that is accepted by a LD vehicle is 262 kW DC (800V Porsche Taycan 2020). This LD vehicle can recharge from 0-80% SOC (~207 real-world miles of range) in 22 minutes using a 350 kW DC Fast Charger (CCS Charging Standard).[6]

Charging Standards

The two open fast charging standards on the market today CCS and CHAdeMO were both originally designed to work at 400V and have evolved to increase their peak charging power ratings.

The Combined Charging System (CCS) is an open, universal, and international charging system for electric vehicles based on international standards. It provides the solution for all charging requirements. The Combined Charging System is therefore ONE system for ALL. The CCS combines single-phase with fast 3-phase AC

[5] https://electrify-commercial.com/ 1/25/2021
[6] Source: https://www.zap-map.com/charge-points/porsche-taycan-charging-guide/. June 2021

charging using alternating current of maximum of 43 kW. It also provides very fast high-power DC charging (up to 450 kW) within a single system. Members are presently also working on a High-Power charging connector for commercial vehicles that can take multiple MW charging power. This extended High-Power charging will be used for specialty EV like busses, truck, etc. The CCS system includes the connector, the managing of control functions and the charging communication between electric vehicle and infrastructure.[7] The standard is backed by major European and U.S. OEMs and is positioned as the preferred option for a European network.

CHAdeMO was an initiative of Japanese car companies and was originally designed to charge at up to 50 kW at 400V.

The mid-term objective of XFC is to reduce LD charging time to approximately 10 minutes via a charge rate of approximately 350 to 400 kW. The long-term objective is to achieve charge rates of greater than 1 MW that will enable fast charging of both LD and Heavy Duty (HD) vehicles. The CHARIN connector standard is dedicated to achieving charge rates of up to 4 MW.

In addition to the conductive charging standards discussed above the wireless power transfer standard J2954 addresses charging of LD vehicles at peak rates of 22 kW and MD/HD vehicle charge rates of approximately 200 kW.

Currently Installed Charging Systems in the U.S

The characteristics of charging stations that are currently installed in the U.S. are provided in Table 1 and are shown in Figure 2.

Table 1 Light Duty Conventional and Electric Vehicle Refueling Characteristics

Type of Refueling	Gasoline	Level 1 110V (~1.4 kW)	Level 2 220V (~7.2 kW)	DC Fast Charger (50 kW, 150 kW, 350 kW)	Tesla V2 & V3 SuperChargers (145 kW,250 kW)
Range per Charge Time	400 miles /5 mins	3–5 miles /60 mins	25 miles /60 mins	50 kW: 150 miles /90 mins	250 kW:~360 miles[8] /60 mins
Time to Charge for 200 miles	<5 mins	37 hours	8 hours	50 kW: 2 hours	250 kW: 24 mins
Number of U.S. stations/connectors circa 2021[9]	153,000	42/312	39,915/85,615	4246/8430	1077/10,628

The summary of charge connector standards provided in the figure below includes the connector diagram, maximum output power, and applications for each of the connector standards.

[7] https://www.charinev.org/faq/ 1/25/2021.
[8] Source: Tesla Model 3 range, battery & charging, June 2021. https://www.drivingelectric.com/tesla/model-3/range
[9] Source: Alternative Fuels Data Center, National Renewable Energy Laboratory, June 2021. https://afdc.energy.gov

Diagram	Connector Standard	Maximum Output Power	Application Notes
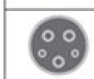	SAE J1772	19.2 kW AC	Used for Level 1 and Level 2 charging in North America. Commonly found on home, workplace, and public chargers.
	CCS	450 kW DC	Used for DC fast charging most vehicle models in North America. Generally installed at public chargers.
	CHAdeMO	400 kW DC	Used for DC fast charging select vehicles models in North America. Generally installed at public chargers.
	Tesla	22 kW AC 250 kW DC	Used for both AC and DC fast charging for Tesla models only.
	SAE J2954	22 kW light-duty, 200 kW heavy duty	Wireless power transfer. Standard for MD/HD vehicles is under development.
	SAE J3105	>1 MW	Automated connection device to charge MD/HD vehicles. Variants include pantograph up or down and pin-and-socket.
	CharIN Megawatt Charging System	4 MW	Conductive MW-level charging for MD/HD vehicles. Standard is under development.

Figure 2 Examples of EV Charging Stations and Connector Standards Sources: CEC [10,11,12,13,14,15,16]

[10] U.S. Department of Energy Alternative Fuels Data Center. "Developing Infrastructure to Charge Plug-In Electric Vehicles." https://afdc.energy.gov/fuels/electricity_infrastructure.html

[11] CharIn. 2020 "Mapping Standards for Low- and Zero-Emission Electric Heavy-Duty Vehicles," presentation. International Transportation Forum February 18-20, 2020 Workshop. https://www.itf-oecd.org/sites/default/files/docs/charging-infrastructure-standardisation-developments-bracklo.pdf.

[12] ChAdeMO. "Technology Overview." https://www.chademo.com/technology/technology-overview/.

[13] Tesla Motors. 2015. Form 10-K. Edgar Online. http://large.stanford.edu/courses/2015/ph240/romanowicz2/docs/tesla-annual.pdf

[14] Tesla Motors. 2019. "Introducing V3 Supercharging." https://www.tesla.com/blog/introducing-v3-supercharging.

[15] SAE. 2013. "Wireless Power Transfer of Heavy-Duty Plug-In Electric Vehicles and Positioning Communication J2954/2 Standard". https://www.sae.org/standards/content/j2954/2/.

[16] CharIn. 2020. "Mapping Standards for Low- and Zero-Emission Electric Heavy-Duty Vehicles," presentation. International Transportation Forum February 18-20, 2020 Workshop. https://www/itf-oecd.org/sites/default/files/docs/charging-infrstructure-standardisation-developments-bracklo.pdf.

Prototype Charging Systems

The research community has developed prototypes that charge at rates greater than 400 kW.

Light Duty Charging Station Prototype

Initiated in July 2016, the "Fast Charge" research project has received €7.8 million in funding from the German Federal Ministry of Transport and Digital Infrastructure. The implementation of the funding guidelines is being coordinated by the German National Organization Hydrogen and Fuel Cell Technology (NOW). The industrial consortium includes automotive manufacturers the BMW Group and Dr. Ing. h. c. F. Porsche AG, as well as operators Allego GmbH, Phoenix Contact E-Mobility GmbH (charging technology) and Siemens AG (electrical engineering)

The research consortium presented a prototype for a charging station with an output of up to 450 kW in Jettingen-Scheppach, located near the A8 motorway between Ulm and Augsburg. The new charging station is suitable for electric models of all brands with the European standard Type 2 variant of the widely used Combined Charging System (CCS) and is now available for use free of charge. A Porsche research vehicle with a net battery capacity of approximately 90 kWh achieved a charging capacity of over 400 kW on the new charging station, allowing for charging times of less than 3 minutes for the first 100 km range

Medium and Heavy-Duty Charging Station Prototype

Portland General Electric and Daimler Trucks North America are co-developing "Electric Island," a large public charging site for medium- and heavy-duty electric commercial vehicles expected to be the first of its kind in the United States. It is designed to support up to nine vehicle charging stations with charging levels of up to greater than one megawatt.[17]

Charging at Scale

The largest EV fast charging station in the U.S. opened in February 2020 in Pasadena, California. The station is comprised of 24 Tesla Superchargers and 20 of Tritium's DC fast chargers.[18]

There are several charging networks that have been initiated in the U.S.

- The Electrify America charging network currently has 635 installed charging stations and 125 charging stations that are 'coming soon'. The network currently has 2097 CCS, 635 CCS-CHAdeMO, and 118 Level 2 chargers.[19]
- The FordPass network will include more than 12,000 charging stations with a total of 35,000 plugs in the United States and some parts of Canada.[20]
- Tesla has 1077 public charging stations with about 10,628 plugs in the United States, according to the Alternative Fuels Data Center.

General Motors Co. is working with electric-vehicle charging operator EVgo Services to build a nationwide fast-charging infrastructure as the automaker prepares a major push into battery-powered models. The two companies will jointly invest in 2,750 fast chargers in cities and suburbs across the U.S. as GM moves to solve a chicken-and-egg problem that comes with selling EVs: A sparse network of chargers has turned off some potential buyers, but utilities and charging companies have been loath to expand the infrastructure until more plug-ins are on the road.[21]

---

[17] https://www.greenfleetmagazine.com/10131365/daimler-announces-electric-island-commercial-vehicle-charging-showcase?utm_source=feedburner&utm_medium=feed&utm_campaign=Feed%3A+GreenFleetMagazine-All+%28Green+Fleet+Magazine%29. December 1, 2020.

[18] https://cleantechnica.com/2020/02/17/largest-ev-fast-charging-station-in-the-us-opens-in-pasadena-california/

[19] Source: https://www.electrifyamerica.com/locate-charger/

[20] https://www.cnn.com/2019/10/17/cars/ford-electric-vehicle-charging-network/index.html

[21] https://www.ttnews.com/articles/gm-build-nationwide-ev-charging-network. July 31, 2020.

Goals and Objectives

Program Goal

The goal of the Grid and Infrastructure Program is to identify system pathways and conduct research to facilitate the development and harmonization of robust, interoperable, and cyber-secure electric vehicle charging and grid infrastructure that supports EVs at scale and incorporates advanced charging technologies, Distributed Energy Resources, and grid services

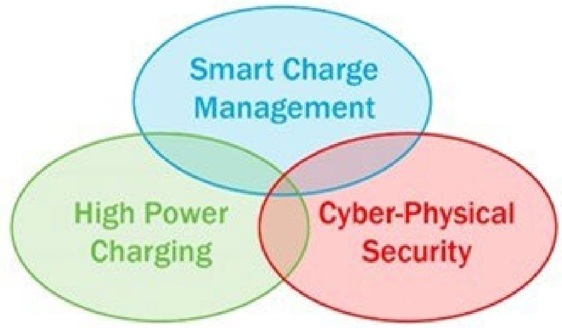

Figure 3 Strategic areas of the Grid and Infrastructure Program.

The G&I Program is focused on EVs, Electric Vehicle Supply Equipment (EVSE or chargers), and integration with the grid. The emphasis is upon foundational systems analyses; exploratory Research, Development, and Deployment (RD&D); and CPS; especially in critical areas that other stakeholders are not able to address. The three strategic areas addressed by the program are SCM, HPC, and CPS of charging infrastructure, as shown in Figure 3.

Each strategic area informs the others, providing a feedback mechanism to continuously refine and adjust program direction and focus. R&D activities span electrification of the LD, MD, and HD sectors of transportation. Additionally, given the cross-sectoral nature (vehicle, charging infrastructure, and the electric grid) of these activities, the program emphasizes close communication and coordination with other governmental and industry stakeholders, including Federal agencies, charger and vehicle OEMs, utilities, and charging network providers.

The G&I Program has established two targets for each of these strategic areas (SCM, HPC, and CPS) for the years 2023 and 2026. The strategic area targets directly support the long-term 2030 G&I Program targets, which are focused on resolving barriers and operationalizing solutions, in concert with transportation electrification stakeholders. All targets for 2023, 2026, and 2030 are listed below.

Year 2023

- SCM: Develop at least two viable smart charge management strategies and relevant tools to reduce the potential grid impacts of EVs at scale and enhance the value of EV charging systems by enabling grid services.
- HPC: Develop strategies and technologies for high power dynamic wireless charging and multi-port 1+ MW charging stations that enable vehicle charging through direct connection to medium voltage (≥ 12.47 kV) distribution.
- CPS: Develop a comprehensive threat model, prioritize high consequence events, and identify appropriate defense, detection, and mitigation strategies and tools for the EV charging ecosystem.

Year 2026

- SCM: Demonstrate and validate smart charge management strategies and relevant tools capable of controlling wide-scale utilization of high-power charging at 400 kW and above, while incorporating robust cyber-physical security methodologies.
- HPC: Demonstrate and validate viable high power dynamic wireless charging, and multi-port 1+ MW charging stations with direct connection to medium voltage distribution.

- CPS: Conduct wide-scale demonstrations to validate viable and robust cyber-physical security for the charging ecosystem in support of EVs at scale.

Year 2030

- Address technical barriers to the development and harmonization of a grid-integrated, robust, interoperable, and cyber-secure electric vehicle charging ecosystem that supports EVs at scale.

- Operationalize two technologies, tools or platforms that will enable interoperable, secure charging solutions that reduce costs for EV owners and fleets.

Program Design and Execution

The G&I Program carries out its mission by focusing its R&D investments on early stage, medium and long-term technology projects that are unlikely to be pursued by industry alone but have significant potential public benefit.

G&I R&D Functions

Smart Charge Management

Importance

The focus of SCM is to identify pathways to reduce the potential grid impacts of EVs at scale, while providing enhanced value for EV/charging/grid systems, including reduced costs and increased opportunities for grid services. If unmanaged, EVs at scale connecting to the grid would create numerous challenges for utilities, particularly at the distribution level. SCM techniques can be employed to intelligently control, and shift charging loads to mitigate this problem and facilitate the provision of advanced grid services from EV charging.

Specific challenges and barriers to SCM include determining the impact of controlled charging versus uncontrolled charging, identifying critical strategies, and enabling technologies, developing, and demonstrating SCM in integrated networks of building systems and DERs including stationary storage, and facilitating bi-directional power flow. Interoperability and scalability of SCM systems are needed to allow EVs from all OEMs to charge at EVSEs from multiple vendors to enable EVs at scale. High speed communication and controls with compatible device protocols and test tools for verification are required. SCM research is also needed to develop strategies and technologies for charging all EVs to enhance station resilience and mitigate potentially negative grid impacts. Finally, costs should be factored into the design of SCM hardware and grid upgrades so that they are minimized, while still providing the necessary charging service.

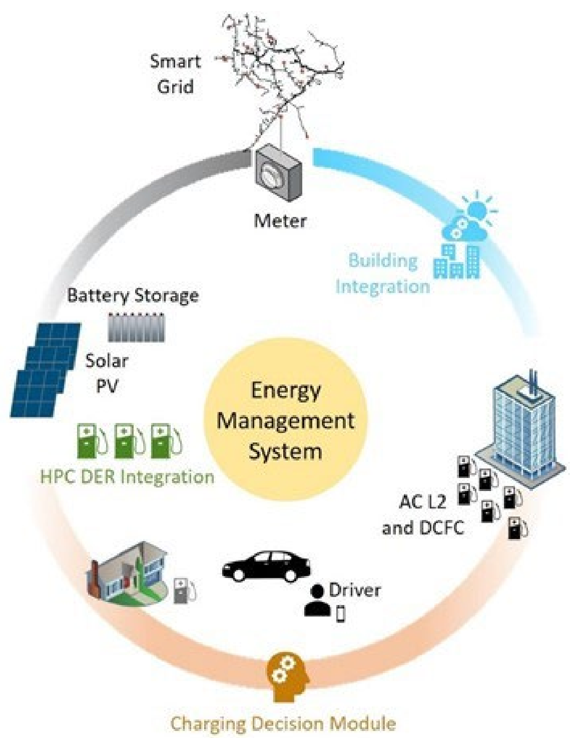

Figure 4 Key elements of Smart Charge Management.

VTO's current SCM R&D efforts

The G&I Program's SCM activities include systems analyses; research, development, and validation of critical enabling strategies and technologies; and demonstrations. Current projects have created tools and methodologies that form the building blocks for effective SCM. The DOE National Laboratories are focused on quantifying the effects of uncontrolled charging versus controlled charging, developing and evaluating the effectiveness of smart charge control strategies, and identifying required constraints and mechanisms to implement high-value charge control strategies.

In the fall of 2020, VTO launched utility-managed SCM projects that include research, development, and execution of a wide-scale demonstration that enables grid services from EVs and provides benefits to electricity grid operators, energy services providers, charging network operators, and EV owners. Figure 3 illustrates key elements of SCM including predictive charge decision making, controls, and integration of vehicle charging and distributed energy resources with buildings and the grid.

VTO R&D Outlook for Key Focus Areas

Building on the advances from current R&D efforts, future SCM activities target LD, MD, and HD EVs and fleets at charging stations, fleet depots, and travel centers. R&D is needed for real time detection and implementation of mitigation procedures when an EV charging station is acting out of the norm or has suffered a cyber breach. Likewise, for MD/HD EV fleet charging at depots and travel centers, the focus is to develop and demonstrate SCM strategies, systems, and tools to provide benefit to MD/HD fleets and owners, and to reduce potential grid impacts. To achieve effective SCM, a thorough understanding of HPC charge profiles, both conductive and inductive, is required for optimal integration of charging stations and the utility distribution grid. Another future thrust is to identify viable vehicle-to-everything (V2X) applications and requirements, and to subsequently develop and demonstrate technologies (on and off board) for low cost, interoperable, controllable, and bi-directional power flow. The following identifies specific targets for SCM for the years 2023 and 2026.

YEAR 2023

- Develop at least two viable smart charge management strategies and relevant tools to reduce the potential grid impacts of EVs at scale and enhance the value of EV charging systems by enabling grid services.

YEAR 2026

- Demonstrate and validate smart charge management strategies and relevant tools capable of controlling wide-scale utilization of high-power charging at 400 kW and above, while incorporating robust cyber-physical security methodologies.

High Power Charging

Importance

Successful deployment of HPC for LD (up to 400 kW) and MD/HD (1+ MW) EVs offers numerous benefits, including greater vehicle utilization, extended range, and recharging times comparable to refueling for conventional vehicles. However, HPC systems face multiple technical challenges and must be intelligently designed and integrated with the grid and DERs to mitigate ramp rates and surge power demands, lower system total cost of ownership, maximize the potential for grid services, and enable interoperability of HPC infrastructure with MD and HD EVs.

HPC exploratory R&D and analyses are needed to address issues associated with materials, power electronics, thermal management, and overall costs. Specific barriers exist with thermal loading of equipment and cables that enable service from the medium voltage grid and power transfer to the vehicle. Investigations are also needed into automated EVSE for HPC, especially above 400 kW charging levels. Advances in wireless charging are required, including the development of novel coils, advanced field shaping technologies, and mitigation of stray electric and magnetic fields.

Likewise, assessment and research are needed to understand the impacts of HPC on the grid, and unexpected grid events on HPC-enabled vehicles, and to help determine the appropriate response from EVs and EVSE. Clear understanding of both the impact of large numbers of HPC systems on distribution feeders and of methods to integrate and control stationary storage and other DERs, in support of HPC, are needed. Furthermore, identification and development of control strategies will be required to enable HPC stations to provide grid and building services.

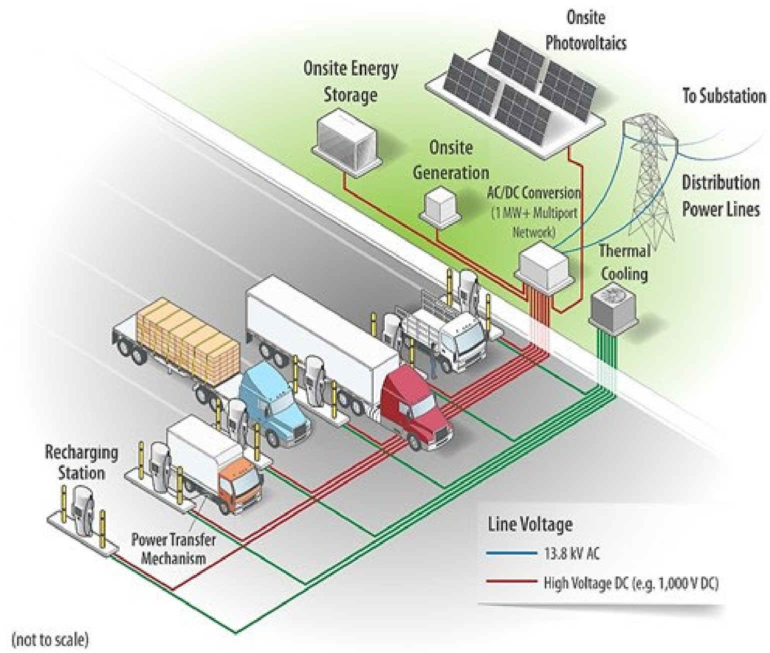

Figure 5 Conceptual configuration of an HPC station.

VTO's current HPC R&D efforts

The G&I Program supports RD&D of HPC in three areas: charging stations with multiple 400 kW EVSE for LD EVs, multi-MW charging stations for MD/HD EVs, and high-power static and dynamic wireless charging. For LD EVs, the focus is on developing and demonstrating charging stations with charging ports rated up to 400 kW and a total combined power rating that exceeds 1 MW. These stations will connect directly to medium voltage distribution networks and utilize stationary storage systems to minimize negative impacts on the grid. For MD/HD EVs, efforts are focused on developing strategies and technologies for 1+ MW multi-port chargers at fast charging travel plazas/truck stops and/or fleet depots. The G&I Program will conduct charging station utilization and load analysis, grid impacts and interconnection analysis, detailed power electronics component design, site and battery charge control, and charging connector design. Figure 5 provides a conceptual configuration of an HPC station for MD/HD EVs. High power static and dynamic wireless charging activities target establishing feasibility, overcoming technology gaps, and validating high power wireless charging with vehicle-level demonstrations. Efforts will analyze, design, build, and validate integrated high-power static and dynamic wireless charging systems that are viable for real world traffic conditions in the U.S.

VTO R&D Outlook for Key HPC Focus Areas

Future HPC activities target several areas including integration of dynamic wireless power transfer (dWPT) into roadways and development of innovative means to provide service to charging facilities. Deployment of dWPT into the roadway will require researching performance, field emissions, and power and control requirements, and addressing integration of the charging system. DC-as-a-Service (DCaaS) is an approach to provide direct current (DC) to charging stations that seamlessly integrates facility and EVSE loads, and DER. Research is needed to address DC isolation, metering, measurement, and protection. The following identifies specific HPC targets for 2023 and 2026.

YEAR 2023

- Develop strategies and technologies for high power dynamic wireless charging and multi-port 1+ MW charging stations that enable vehicle charging through direct connection to medium voltage (≥ 12.47 kV) distribution.

YEAR 2026

- Demonstrate and validate viable high power dynamic wireless charging, and multi-port 1+ MW charging stations with direct connection to medium voltage distribution.

Cyber-Physical Security

Importance

EVs and their connectivity with external systems have become increasingly complex. Apart from AC Level 1 chargers, EVSE have evolved rapidly to be networked and maintain a wide variety of communication functions. As communication networks for EVs, EVSE, and external systems increase, attack vectors and cyber-physical risks also increase for the charging infrastructure. Since EVSE at workplaces and public charging stations connect with many different EVs to provide charging services, it makes assuring CPS extremely difficult.

A major challenge posed by compromised charging infrastructure is the threat it poses to the electric grid. A localized cyber-physical attack on a set of EVSE/charging stations can lead to a sudden addition or reduction of loads that can cause local disruptions, brownouts, voltage imbalances, and undesirable power quality impacts. Large-scale, coordinated cyber-physical attacks on charging infrastructure supporting EVs at scale can also lead to wider grid disruptions, such as blackouts over large geographical areas. The lack of a comprehensive understanding of threats; disjointed implementation approaches; and limited best practices are major barriers to ensuring overall security of EVs, charging infrastructure, and the grid.

VTO's current CPS R&D efforts

Current CPS activities include research, development, and validation of technologies for real-time threat detection, mitigation, isolation, and restoration of charging infrastructure based on its physical signatures and performance. Activities at the National Laboratories include developing a comprehensive threat model, attack graphs, and technical risk assessment of the EV charging ecosystem, and prioritizing charging infrastructure high consequence events and mitigation strategies. Additional activities include penetration testing of 50 kW DC fast chargers and 400 kW HPC and developing recommendations for secure communications. VTO-funded projects led by industry, academia, and non-profit organizations are developing real-time detection, defense, and mitigation systems to protect EVs, charging infrastructure, and the grid. This includes hardened controllers, converters, and monitoring systems; a retrofittable and scalable open-source cybersecurity architecture; and game theory-based hardware and software to provide secure charging.

VTO R&D Outlook for Key CPS Focus Areas

Based on the assessments of risk and high consequence events, future activities will implement the best approaches to mitigate vulnerabilities and threats associated with the EV charging ecosystem. This effort will incorporate strategies, systems, and tools for secure charging, including hardware/software for cyber-physical intrusion detection, threat mitigation and isolation, and recovery. The most promising CPS countermeasures will be identified based on risk formulation (e.g., public key infrastructure, blockchain, moving target defense, and redundancy). Identified countermeasures that address the highest consequence events will be demonstrated and validated. The following identifies specific CPS targets for 2023 and 2026.

YEAR 2023

- Develop a comprehensive threat model, prioritize high consequence events, and identify appropriate defense, detection, and mitigation strategies and tools for the EV charging ecosystem.

YEAR 2026

- Conduct wide-scale demonstrations to validate viable and robust cyber-physical security for the charging ecosystem in support of EVs at scale.

EA2020 Vehicle Grid Integration

In FY21, the Energy Act of 2020 (Division Z of the Consolidate Appropriations Act, 2021 Public Law No. 116-260) directed the DOE Secretary to (a) Establish a research development, and demonstration program to advance the integration of electric vehicles, including plug-in hybrid electric vehicles, onto the electric grid, and (b) produce a 'Vehicles-To-Grid Integration Assessment Report' that presents the results of a study that examines the research, development, and demonstration opportunities, challenges, and standards needed for integrating electric vehicles onto the electric grid. The results and knowledge gained from all of the projects in the G&I portfolio were used in preparing the study requested by Congress and the report.

Bipartisan Infrastructure Law

The Bipartisan Infrastructure Law (BIL) was passed in 2021. The legislation will invest $7.5 billion to build out a national network of EV chargers in the United States. This is a critical step in the President's strategy to fight the climate crisis and it will create good U.S. manufacturing jobs. The legislation will provide funding for deployment of EV chargers along highway corridors to facilitate long-distance travel and within communities to provide convenient charging where people live, work, and shop. This investment will support the President's goal of building a nationwide network of 500,000 EV chargers to accelerate the adoption of EVs, reduce emissions, improve air quality, and create good-paying jobs across the country.

A Joint Office of Energy and Transportation has been established to support the implementation of the EV charging objectives of the BIL.

Information from the G&I projects is being fed to the Joint Office of Energy and Transportation and is being used to create requirements for the infrastructure funding established in the BIL.

EVs@Scale Consortium

In FY21 the Grid and Infrastructure program established the EVs@Scale Consortium to accelerate progress of EV Charging Infrastructure RD&D and engage stakeholders. It is an effort to streamline and coordinate Vehicle-Grid Integration activities across the national lab complex and increase the agility of the program to address rapidly evolving challenges and barriers to Vehicle-Grid Integration. The EVs@Scale Consortium includes the following national laboratories:

- Argonne National Laboratory
- Idaho National Laboratory
- National Renewable Energy Laboratory
- Oak Ridge National Laboratory
- Pacific Northwest National Laboratory
- Sandia National Laboratories.

The EVs@Scale organizes its activities within the following pillars:

1. Fuse: Vehicle-Grid Integration and Smart Charge Management
2. eChip: High Power Charging
3. Wireless Power Transfer
4. Cyber Security
5. Codes and Standards
6. Consortium Management.

Specific activities identified in the pillars above will be covered in future Annual Progress Reports.

Grid and Infrastructure Research Highlights

Accomplishments	Organization	Focus Area	Project Title
Designed a Novel High Power WPT device: The team worked on modeling, simulations, analysis, and design of the system power conversion stages and control systems and completed the design and simulations of the 300 kW inductive charging system. Since proposed concept is new, a relatively low-power, scaled-down version of the couplers were developed and tested to validate the concept and the operation. The prototype was tested with ~95% dc-to-dc efficiency with ~50 kW output.	ORNL	High Power Wireless Charging	High-Power Inductive Charging System Development and Integration for Mobility
Built and demonstrated zero emission capable electric truck technologies for drayage operations: As of 2019, all eleven electric trucks funded under this project were constructed with two trucks continuing demonstration efforts until March 2020. Overall, the trucks that have completed demonstration have proven successful in demonstrating their feasibility in various drayage operations and handling daily loads and many routine schedules. The trucks have generated significant interest from trucking companies, which helps to promote and to accelerate market adoption of electric truck technologies in cargo transport operations.	South Coast Air Quality Management District	Industry Awards	Zero Emission Drayage Trucks Demonstration (ZECT I)
65% Reduction in Fuel Consumption via Electrification: The Electric Truck with Range Extending Engine (ETREE) project team has developed an EV powertrain and related systems and completed J1526 fuel consumption testing that demonstrated 65% reduction in fuel consumption on a modified NREL80 cycle over a baseline vehicle. The test exceeded the project goal of 50% reduction in fuel consumption.	Cummins	Industry Awards	Cummins Electric Truck with Range-Extending Engine (ETREE)
McLaren built and tested a novel eAxle system, energy storage & range extender systems for installation and final calibration in four MD demonstration vehicles. There have been continued challenges to achieve the desired reliability for demonstration routes. The current system with the two-speed transmission feature will continue to be developed for demonstration in FY20.	McLaren Engineering	Industry Awards	Medium Duty Vehicle Powertrain Electrification and Demonstration

Accomplishments	Organization	Focus Area	Project Title
Delta designed and tested a high-efficiency, medium-voltage-input, solid-state-transformer-based 400-kW XFC for EVs achieving better than 96.5 percent efficiency. The XFC system consists of a Solid-State Transformer (SST), a Charge Controller (in power cabinet), a Charge Dispenser (A.K.A. User Unit) and an optional Energy Storage System (ESS). The test result shows that the SST module and the Buck module meet the specification. The integration of the series SST and Buck module is successful. The program objectives of FY19 were completely met.	Delta Electronics (Americas) Ltd)	Industry Awards – High Power Charging Enabling Technologies	High-Efficiency, Medium-Voltage-Input, Solid-State-Transformer-Based 400-kW/1000-V/400-A Extreme Fast Charger for Electric Vehicles
High Power Wireless System Development: The CALSTART project made significant progress in developing systems for high power and high-efficiency wireless charging of an electric medium duty delivery trucks. Team developed the resonant stage components and verified the resonant voltage gains that would optimize the power transfer between the ~750-800V primary dc bus voltage and the nominal 420V secondary. As of September 2019 the team was working on vehicle integrations and preparations to demonstrate the operation of the technology on the UPS research truck.	CALSTART, ORNL, UPS	Industry Awards- High Power Wireless Charging	Bidirectional Wireless Power Flow for Medium Duty Vehicle Grid Connectivity
Odyne progressed the development of a new class of PHEV Work Truck which will be modularized and customized to provide optimal ROI across multiple customers and applications. The work initially focused to demonstrate this technology as a Utility Work Truck variant. The project completed the final analytical drive optimization, selection of the primary path battery system. The project also built the prototype test chassis and ORNL Hardware-in-Loop (HIL) powertrain dynamometer test system fixturing and assembly.	Odyne Systems	Industry Awards	Development and Demonstration of Medium-Heavy Duty PHEV Work Trucks
NREL developed technology to mitigate demand charges via a charge management system integrating many different types of controllable loads for demand charge mitigation. The central controller only needs to add a list of MQTT message topics that are required for the new controllable loads and aggregate the forecasted energy needs of them into the optimization.	NREL	High Power Charging Enabling Technologies	Demand Charge Mitigation Technologies
WAVE developed a HP WPT System Requirements to develop and integrate a new 500 kW WXFC system into a Class 8 electric drayage truck developed by Cummins so that it can automatically and wirelessly charge at a high charging rate (c-rate) during their dwell times. The proposed wireless charger features a direct connection to the Medium Voltage (MV) 3-phase grid developed by Utah State University and Schneider Electric and the final prototype will be deployed at	WAVE, Utah State University, Schneider Electric, Total Transportation Services	Industry Awards-High Power Wireless Charging	High-Power Inductive Charging System Development and Integration for Mobility

Accomplishments	Organization	Focus Area	Project Title
Total Transportation Services Inc. (TTSI), which is a truck operator at the Port of Los Angeles (POLA).			
EPRI progressed V2G technology to improve the value of owning a Plug-in Electric Vehicle (PEV) in the form of an off-vehicle Smart Power Integrated Node (SPIN) system. SPIN enables increased renewable generation on the grid and providing Vehicle to Home type services in conjunction with on-vehicle and off-vehicle storage. A fully functional SPIN unit was delivered to NREL NTRC for acceptance testing of its operational modes. The project defined DC DER software and communications strategy—an industry first, that will inform both the IEC/ISO and SAE standards. The project defined a control and communications architecture for information exchange between the grid and SPIN as well as the SPIN and PEV. The project developed the SPIN master controller and integrated the IoTecha EVCC and SECC cards on Pacifica PHEV and SPIN. Setup of an End to end communications bench to verify system-level communications and control functions began. Off-board V2G functionality of the Pacifica PHEVs have been accomplished by refreshing the on-board V2G program. from the on-board V2G program have been refreshed to A battery test cycle has been defined and the battery has been provided by FCA to NREL where the test set up has been completed and the battery testing has commenced.	EPRI	Industry Awards-Vehicle-to-X (V2X)	Comprehensive Assessment of On- and Off-Board Vehicle-To-Grid Technology Performance and Impacts On Battery and The Grid (EPRI SPIN)
MUST began advancing the state of the art in EV charging by addressing the three key challenges of 1) battery charging algorithms for minimal damage during extreme fast charging, 2) medium-voltage power conversion for rapid, inexpensive deployment, and 3) grid compatibility to mitigate the impact of charging transients on the grid. The project produced preliminary results on sub-scale analysis, design, and construction that are to be completed in FY20 and scaled up in future years.	Missouri University of Science and Technology (MUST)	Industry Awards – High Power Charging Enabling Technologies	Enabling Extreme Fast Charging with Energy Storage

Accomplishments	Organization	Focus Area	Project Title
NCSU has made significant progress in all key aspects of the XFC station design. The team has selected the MV SST topology; completed the system-level control simulations, and has constructed a small proof-of-concept prototype to validate the system control. In addition, the team has made significant progress in designing the full-scale SST module and has identified a vendor for the DC/DC stage that will make up the DC node for the system. The team has made significant progress in developing the DC solid-state breaker and has completed a number of system-level protection coordination studies, which will drive the design of the DC distribution system. Finally, the team has selected the deployment site for the system and is making progress on completing the detailed engineering drawings for the system site.	North Carolina State University (NCSU)	Industry Awards – High Power Charging Enabling Technologies	Intelligent, Grid-Friendly, Modular Extreme Fast Charging System with Solid-State DC Protection
The EPRI led project team initiated development and validation of a system of PEV XFC equipment with a direct connection to the medium-voltage utility grid with a novel, modular, and interoperable approach. The objective of the project is to develop and demonstrate medium voltage SiC-based AC-DC conversion equipment and the DC to DC head unit for use in XFC equipment capable of simultaneously charging multiple light duty PEVs at rates of ≥350 kW and a combined power level of ≥1 MW while minimizing the impact on the grid and operational costs.	Electric Power Research Institute (EPRI), Eaton Corporation, NREL, Tritium, ANL	Industry Awards – High Power Charging Enabling Technologies	Direct Current Conversion Equipment Connected to the Medium-Voltage Grid for XFC Utilizing a Modular and Interoperable Architecture
Argonne collaborated with the European Union's JRC to uncover 'childhood diseases' in new XFC technology and inform the manufacturers accordingly. The project addressed identification and resolution of issues associated with a 200 kW XFC system. had a few technical issues early on, but when these issues were addressed by the manufacturer it was found to communicate according to the standards using an industry-standard interoperability test tool. The results showed the EVSE to be backward compatible with EVs below 50 kW charge levels. The DC communication analysis showed consistent messaging and timing. The results imply that integration of higher power charging stations in communication networks via OCPP should be accomplished with no more effort than lower power EVSE that communicate using OCPP.	ANL	High Power Charging Enabling Technologies	Fast Charging: Interoperability and Integration Technologies
INL developed XFC Technology Requirements: This project completed important preliminary research that is necessary for understanding the impact of fast charging on grid stability and identifying and mitigating cybersecurity vulnerabilities. A transient characteristic of a prototype commercial 350 kW XFC was discovered—namely ramp-down rate at the end of	INL	High Power Charging Enabling Technologies	Fast Charging: Grid Impacts and Cyber Security

Accomplishments	Organization	Focus Area	Project Title
charge events—that has the potential to impact grid stability.			
<u>ORNL identified technology targets to achieve an economically feasible dynamic wireless EV charging system applicable to LD vehicles and primary roadways.</u> The performance targets are: 1) Power transfer level for range extension: 150 kW – 235 kW 2) Efficiency: 90 % 3) Surface power density (SPD): 400 kW/m2 The project also analyzed a) Minimum roadway coverage solution for primary roadways for a LD vehicle, b) Current capabilities of SOA dynamic wireless systems, c) Performance of two candidate coil reference design as applied to 200 kW systems, and d) Derived a control-to-coil-current transfer function for a DWPT controller. <u>INL WPT EM-field Shaping and Shielding Solutions</u> Advanced magnetics 3-D finite element modeling tools were used to develop and analyze the EM field surrounding a 200-kW light-duty WPT system. The new EM-field shaping design uses innovated geometry of ferrite placement around the WPT to effectively shape the EM field therefore reducing the stray EM field surrounding the WPT system.	ORNL, INL, NREL	High Power Charging Enabling Technologies	High Power and Dynamic Wireless Charging for EVs
<u>Developed Grid-XFC Requirements to promote a reliable and resilient electric grid:</u> NREL quantified the effects of uncontrolled charging to understand how increased PEV adoption may negatively impact the grid. Progress considered the limitations of the grid and the impacts of PEV adoption. After acquiring distribution feeder data, the hosting capacity analysis displayed the grid's ability to serve larger loads, such as xFC. This analysis leads into uncontrolled charging simulations in which high levels of PEV adoption begin to create voltage and line loading violations throughout the feeder. These challenges make the case for controlled charging as a way to mitigate these problems. INL quantified the effects of uncontrolled charging to understand how increased PEV adoption may negatively impact the grid, and to analyzed the effectiveness of multiple control strategies in mitigating negative grid impacts introduced by PEVs at scale. High-fidelity charging models were integrated into Caldera to supplement existing control strategies	NREL, INL, SNL	High Power Charging Enabling Technologies	Smart Electric Vehicle Charging for a Reliable and Resilient Grid (RECHARGE)

Accomplishments	Organization	Focus Area	Project Title
developed in past projects. INL began work to develop new PEV charging control strategies.			
NREL Developed MultiPort 1+MW Charging Requirements -: The first year work of the project included -1) considered various use cases and travel patterns to develop / quantify expected vehicle loads at a multi-MW station, 2) analyzed and optimized charge port control and battery requirements in a multi-MW station, 3) developed a framework to analyze grid impacts of various multi-MW stations at the distribution level, 4) Analyzed and quantified connector and charging system electrical and thermal requirements. ANL Developed MultiPort 1+MW Charging Requirements: The work-in-progress CharIN HPCCV coupler specification covers MD/HD electric truck charging connections, with similar remaining requirements gaps in communication reliability, safety interlocks, cooling, and cord handling including robotic insertion/removal processes. A draft MW+ multiport charging requirements document was compiled. A concise digest was created to highlight the state of readiness of stake holders to plan deployment of MW+ multiport EV charging systems, including gaps in standards or data. ORNL assessed candidate 1+MW charging architectures: The three candidate architectures listed below were selected for in-depth study: 1) DC Coupled architecture: components are interconnected through a common 2kV DC bus 2) AC-Coupled architecture: components are interconnected through a common 480V, 60Hz AC bus 3) Medium Voltage(MV) Architecture: connects directly to the medium voltage distribution grid using a cascaded H-Bridge (CHB) converter Each of these approaches were investigated from the grid conversion and impact as well as the interaction with DERs and EV load converters. The MV topology using the CHB converter was selected as the most suitable.	NREL, ANL, ORNL	High Power Charging Enabling Technologies	Development of a Multiport 1+Megawatt Charging System for Medium- and Heavy-Duty Electric Vehicles
Developed charging infrastructure cyber threat prioritization system: Research efforts for this project were focused on trying to prevent high consequence manipulation and misuse of EV charging infrastructure. In order to effectively do so, researchers first conceptualized events that could be brought about by cyber manipulation to create a physically adverse effect on high-powered charging infrastructure, EVs, and/or the electric grid. Researchers then quantitatively scored the events using an impact severity scoring matrix and complexity multiplier. The high consequence events (HCEs) were scored and prioritized based upon this quantitative method. This prioritization ranking allows	INL	Cyber-Physical Security	Consequence-Driven Cybersecurity for High-Power Charging Infrastructure

Accomplishments	Organization	Focus Area	Project Title
researchers to focus their efforts on identifying and securing attack pathways enabling the most severe HCEs, then working to develop mitigation solutions to prevent and identify the cyber threats potentially leading to those HCEs.			
Began Developing EVSE Cyber-Physical Security Threat Models: There is no comprehensive EVSE cybersecurity approach and limited best practices have been adopted by the EV/EVSE industry. For this reason, there is an incomplete industry understanding of the attack surface, interconnected assets, and unsecured interfaces. Thus, comprehensive cybersecurity recommendations founded on sound research are necessary to secure EV charging infrastructure. This project is providing the automotive industry with a strong technical basis for securing this infrastructure by developing threat models, prioritizing technology gaps, and developing effective countermeasures. Specifically, the team is creating a cybersecurity threat model and performing a technical risk assessment of EVSE assets, so that automotive, charging, and utility stakeholders can better protect customers, vehicles, and power systems in the face of new cyber threats.	SNL, PNNL, ANL	Cyber-Physical Security	Securing Vehicle Charging Infrastructure
ANL progressed incorporating EVs and EVSE with ‘smart’ communication capabilities in the network at the Smart Energy Plaza; use cases have been demonstrated for controlled and emulated smart charging, EVs and EVSE have been acquired with high level language (i.e., smart) capability and the common integration platform, CIP.io, has been enhanced to enable charge scheduling using ISO 15118. However the GMLC use cases that depend on smart charging have not been demonstrated on schedule due to delays in overcoming the proprietary interfaces of the EVSE, The beta version of the Diagnostic Electric Vehicle Adapter (DEVA) was demonstrated on schedule.	ANL, INL	High Power Charging Enabling Technologies	Smart Vehicle-Grid Integration (Smart-VGI)
LLNL progressed development of a decentralized, collaborative algorithm that will enable local groups of charging station controllers to coordinate the load reduction responses required by the centralized grid command center, while meeting technological, policy, and contractual constraints imposed at the level of the smart charging stations and possibly at the level of the individual electric vehicles. The work developed charge management algorithms.	LLNL	Smart Charge Management	Scalable Electric Vehicle Smart Charging Using Collaborative Autonomy
The EPRI team developed the IGSRM tool. The EA tool and database provided a scalable architecture to develop new sub-systems, components, and cybersecurity risks and recommendations. The tool shall be used to develop a web-based IGSRM tool that reflect the reference cybersecurity architecture of a connected XFC ecosystem, recommended controls and their associated risk profiles. For the cybersecurity	EPRI	Cyber-Physical Security	Cybersecurity Platform and Certification Framework Development for eXtreme Fast Charging (XFC)

Accomplishments	Organization	Focus Area	Project Title
testing at the laboratories, The EPRI CSRL team focused on the EVSE charging infrastructure in fulfilment of its evaluation objectives. The NREL team completed laboratory testing of several cybersecurity aspects of the EV charging ecosystem using hardware, software emulation, and cloud interfaces.			

In this report the Grid and Infrastructure project reports that follow have been grouped into the chapter categories of Industry Awards (IA), High Power Charging (HPC) Enabling Technologies, Smart Charge Management (SCM), and Cyber-Physical Security (CPS). Many of the projects address multiple programs objectives. The Industry section describes projects that were awarded to commercial industry performers via DOE's Funding Opportunities Announcement (FOA) solicitation process. The HPC Enabling Technologies, SCM, and Cyber projects were awarded to National Laboratories via direct funding agreements.

Questions regarding the Grid and Infrastructure Program can be directed to the Technology Manager, Lee Slezak via email: lee.slezak@ee.doe.gov or telephone: (202) 586-2335

I Electric Drive Technologies

I.1 Electric Drive Technologies Research

I.1.1 Highly Integrated Power Module (Oak Ridge National Laboratory)

Emre Gurpinar, Principal Investigator
Oak Ridge National Laboratory
1 Bethel Valley Road
Oak Ridge, TN 37830
Email: gurpinare@ornl.gov

Susan Rogers, DOE Technology Development Manager
U.S. Department of Energy
Email: susan.rogers@ee.doe.gov

Start Date: October 1, 2020 End Date: September 30, 2021
Project Funding: $765,000 DOE Share: $765,000 Non-DOE Share: $0

Project Introduction

This project covers the design and development of next-generation wide-bandgap (WBG) power modules and associated components within the system. Various component challenges, such as substrates, integrated heat sinks, and automated design tools for power electronics to advance the power density, were addressed to reduce the footprint of the system and increase the level of integration.

Objectives

The overall objective of the project is to develop technologies for next-generation advanced integrated power electronic systems. These systems enable high power density and reliability to achieve the U.S. Department of Energy (DOE) Electrification (ELT) Program's 2025 technical targets: 100 kW/L, $2.70/kW, and 300,000 mi lifetime. Under the overall objective, two main streamlines were identified: (1) power module design and (2) automated design of power electronics.

Approach

The main approach is to increase the power density and reliability of power electronics to meet DOE ELT 2025 targets (100 kW/L, $2.70/kW, and 300,000 mi lifetime) by focusing on power module design and automated design of power electronics.

Substrates that offer better coefficient of thermal expansion matching among WBG devices and power module materials, improved heat extraction, and enhanced thermal and power cycling capability, allow increased power density and high reliability for WBG device-based power modules. Such substrates were investigated under the power module design streamline. Furthermore, multilayer substrates for enhanced electrical and thermal performance were evaluated. These solutions enabled reduced parasitic inductance in the system for optimum switching performance, reduced power module size, and direct attachment of high-performance heat sinks.

In Fiscal Year 2020, three main tasks were completed:

1. Design of the integrated silicon carbide power module based on thermally annealed pyrolytic graphite (TPG) embedded organic direct bonded copper (ODBC) substrate

2. Experimental characterization of the optimized heat sink based on multi-physics simulation and genetic algorithms (GAs)

3. Characterization of 1.2 kV, 13 mΩ silicon carbide metal-oxide-semiconductor field-effect transistors (MOSFETs) with different module layout and gate performance.

Results

1 Integrated Silicon Carbide Power Module Based on TPG Embedded ODBC Substrate, Integrated Gate Driver, and Heat Sink

In previous years, high thermal performance of the TPG-embedded substrates was validated in insulated metal substrates (IMSs). TPG embedding makes IMSs a viable option for high-power module design. However, the polymer dielectric used in IMS technology is rated only to 140°C and therefore is not suitable for high-temperature WBG-based power module designs. Alternatively, ODBC technology from DuPont provides high-temperature operation capability with integrated heat sink and gate driver via multilayer lamination availability. The TPG-embedded ODBC-based power module concept is shown in Figure I.1.1.1.

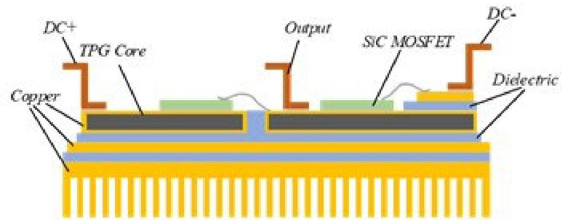

Figure I.1.1.1 TPG-embedded ODBC-based integrated power module concept.

The dielectric layer developed by DuPont can be used to laminate gold-plated copper, so it is suitable for lamination of the TPG-embedded copper cores used in the previous IMS design. Furthermore, the ODBC structure has flexible dielectric and metallization thickness. Therefore, the metallization and TPG core can be optimized to maximize heat spreading, and the dielectric thickness can be adjusted to comply with the breakdown voltage requirement of the power converter. In the three-layer structure shown in Figure I.1.1.1, the top layer is used for placing the dies and terminations, the middle layer is used for common mode shielding, and the bottom layer is used for the integrated heat sink. Additional layers above the top layer can be included for the gate driver and additional termination requirements. Based on this concept, finite element analysis (FEA)-based thermal analysis and optimization was conducted on the TPG-embedded ODBC substrate with three layers to find the optimum structure for a silicon carbide MOSFET-based power module. Two silicon carbide MOSFET dies were used in parallel for each switch position with 500 W/cm^2 heat flux across each die, 65°C surface temperature, and 15,000 W/(m^2·K) boundary condition at the bottom layer. Metallization, TPG thicknesses, and module width were studied for the parametric sweep analysis. The thermal analysis results for the maximum junction temperature of silicon carbide MOSFETs with respect to TPG thickness and module width are shown in Figure I.1.1.2. The results show that adequate TPG thickness; heat sink performance, modeled by heat transfer coefficient in this simulation; and module width enable the proposed structure to reach 500 W/cm^2 heat flux density for silicon carbide MOSFET. This value is 2.5–5 times higher than heat flux densities observed in Si insulated-gate bipolar transistor power module structures. The final module layout based on the thermal analysis is shown in Figure I.1.1.3. TPG was aligned underneath the silicon carbide MOSFETs to spread the generated heat across the module width and transfer it through the multilayer substrate structure. On the top surface, one side is dedicated to the gate driver placement, and the other side is dedicated to power terminals and power loop.

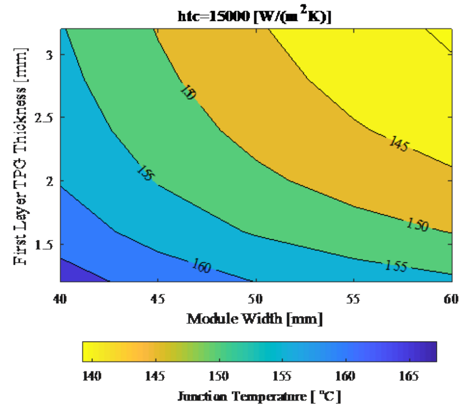

Figure I.1.1.2. Thermal analysis results for TPG-embedded ODBC power module.

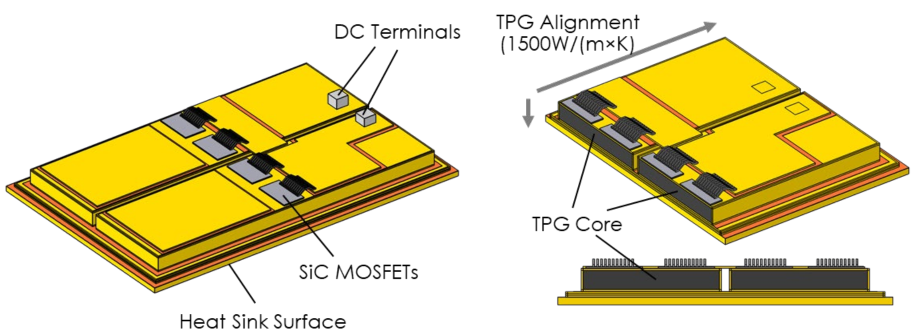

Figure I.1.1.3. Final module layout based on thermal analysis.

The next step in the substrate design process was development of a high-performance liquid-cooled heat sink design that can satisfy or exceed the boundary conditions used in the results shown in Figure I.1.1.2 to enable 500 W/cm^2 heat flux for silicon carbide MOSFETs and high power-density module design. This task used a GA-based multi-objective heat sink optimization tool, which was developed under this project. The design objectives included minimizing the power module volume and maximizing the heat transfer coefficient. Design constraints included 150°C maximum junction temperature, 2 kPa maximum pressure drop, 1.66 L/min flow rate, and 65°C coolant temperature. The design results for the heat sink with respect to heat transfer coefficient and volume are shown in Figure I.1.1.4. The proposed design approach generated heat sink designs that exceeded the thermal performance of the initial boundary conditions and minimized power module volume.

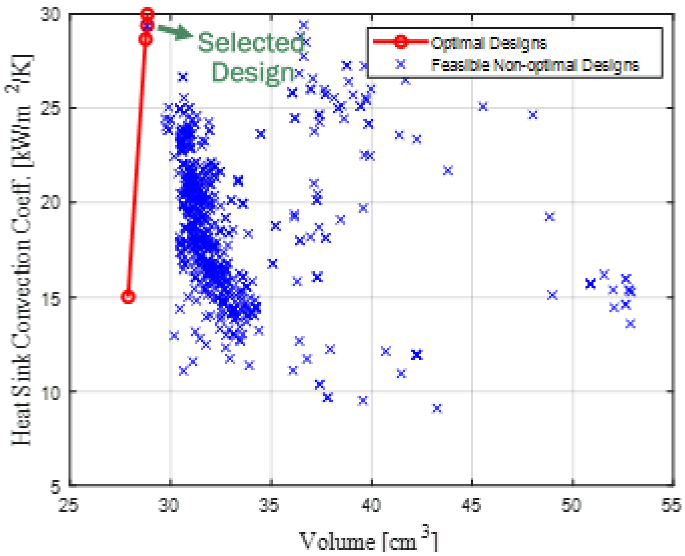

Figure I.1.1.4. Multi-objective optimization results for the heat sink design.

The cross section of the generated heat sink design, temperature profile, and pressure drop at rated operated conditions are shown in Figure I.1.1.5. The design achieves approximately 140°C junction temperature under worst-case operating conditions, and the flow across the heat sink is below the maximum limit.

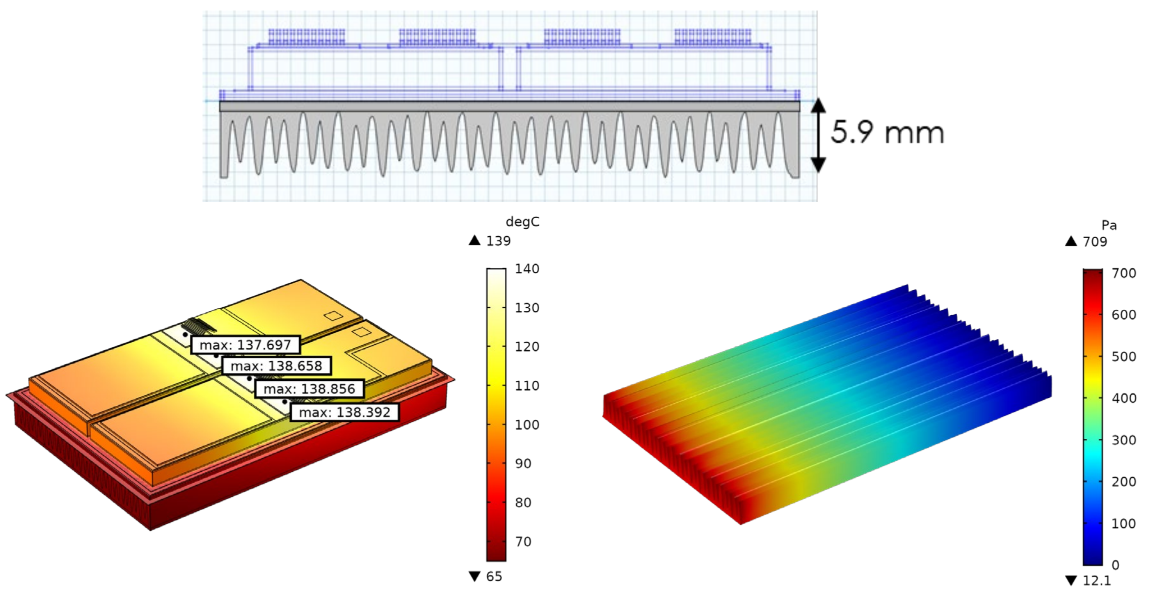

Figure I.1.1.5. (Top) Cross section of the selected heat sink design, (bottom left) temperature profile of power module, and (bottom right) pressure drop across heat sink with the selected heat sink design.

The final step of the module design process integrated the gate driver and power loop into the design and evaluated power loop layout performance using FEA. The integrated gate driver provides enhanced switching performance, with reduced parasitic inductance at the gate loop, and high current capability. These increased switching speeds require special attention to power-loop inductance to ensure clean switching and reduced switching losses. Therefore, a multilayer board that mimics the multilayer structure of the ODBC was designed and evaluated for the given power module layout. The final design of the gate driver and the simulated power loop stray inductance are shown in Figure I.1.1.6. The power loop inductance is less than 4 nH for frequencies greater than 1 MHz and therefore achieves low inductance layout.

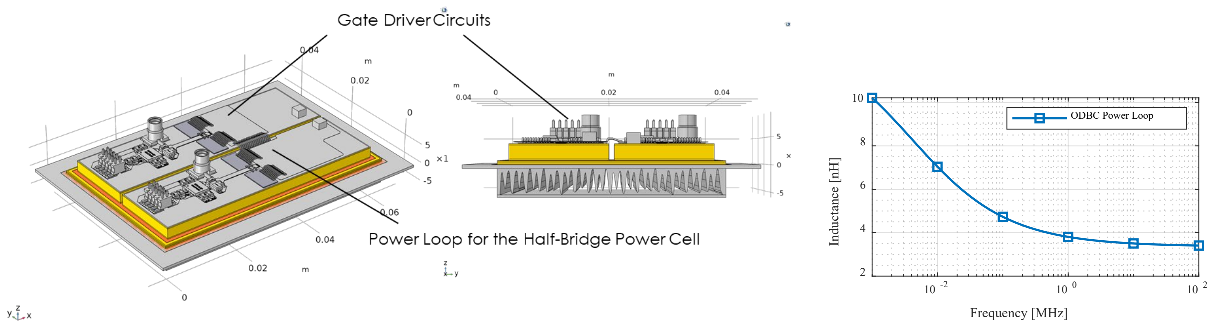

Figure I.1.1.6. (Left and middle) Gate driver and power loop design in the ODBC-based power module and (right) results for simulated power loop inductance.

2 Experimental Validation of AI-Optimized Heat Sinks

In this task, the liquid-cooled heat sinks generated by the GA optimization multi-physics tool were experimentally validated. Comparison of the prototype of the optimized heat sink with the pin fin-based heat sink used in the BMW i3 is shown in Figure I.1.1.7. The optimized design provides 50% volume reduction compared with conventional pin-fin design without penalizing the coolant pressure drop or module temperature profile. Furthermore, the optimized design achieves high thermal performance at increased flow rate conditions.

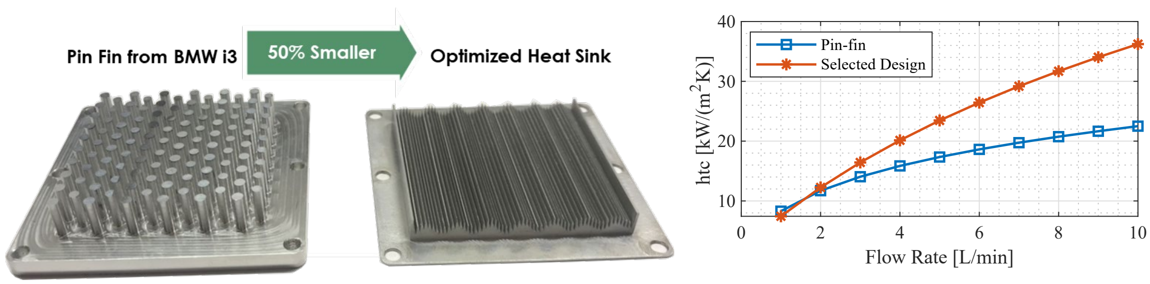

Figure I.1.1.7. (Left) Comparison of optimized heat sink with pin fin heat sink and (right) heat transfer coefficient comparison of optimized heat sink and pin fin with respect to flow rate.

For the experimental validation, the test setup (shown in Figure I.1.1.8) consisted of a direct bonded copper (DBC) structure with silicon carbide MOSFETs mounted on the optimized heat sink design shown in Figure I.1.1.7. The heat sink was machined on a manifold structure that seals the liquid coolant region, seals the enclosure with O-rings, and evenly distributes the coolant across the heat sink coolant region. The DBC was mounted to the heat sink using a thermal interface material and clamped using the high-temperature additively manufactured housing. One 900 V, 10 mΩ (CPM3-0900-0010A) silicon carbide MOSFET die per switch location was attached on the DBC with 50 µm thick 63/37 tin-lead solder. The DBC substrate used for the experimental validation in this study was formed by a 640 µm thick aluminum nitride ceramic insulator sandwiched between 300 µm thick copper planes. The thermal interface material used in this study was 1 mm thick with 5 W/(m·K) thermal conductivity.

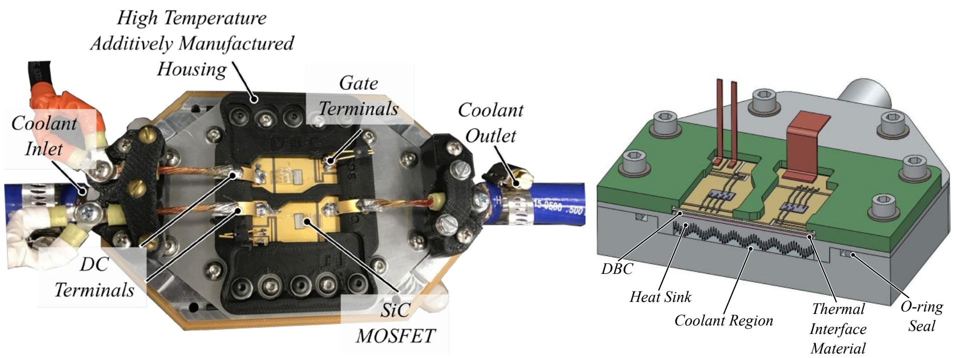

Figure I.1.1.8. (Right) CAD drawing of cross section of the experimental setup and (left) top view of experimental setup.

The comparison of simulation and experimental results (i.e., pressure drop and thermal resistance) for the optimized heat sink design are shown in Figure I.1.1.9. The experimental results are in good agreement with simulation results, and the optimized heat sink design is suitable for WBG-based module designs.

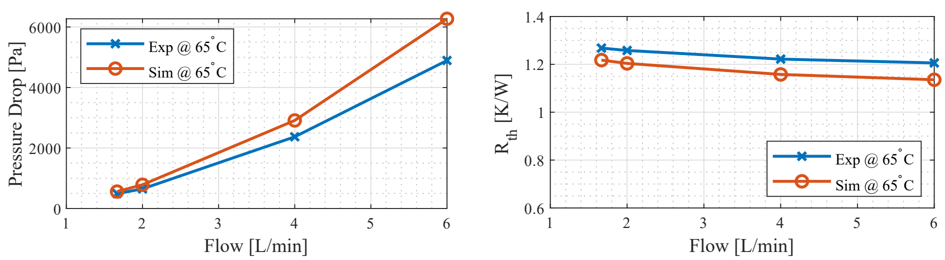

Figure I.1.1.9. (Left) Pressure drop and (right) thermal resistance comparisons of experimental and simulation results for optimized heat sink at 65°C coolant temperature.

3 Characterization of 1.2 kV, 13 mΩ Silicon Carbide MOSFETs with Different Module Layout and Gate Performance

Latest-generation 1.2 kV, 13 mΩ silicon carbide MOSFET dies were characterized under different operating conditions, such as power loop inductance, direct current-link voltage, load current, and gate resistance. The switching loss results were targeted to be used for thermal management and integrated inverter design in the Electric Drive Technologies Consortium. For this purpose, conventional DBC- and printed circuit board (PCB)-based samples were prototyped. The DBC-based solution has a horizontal power loop with relatively high inductance compared with the PCB-based solution in which a vertical power loop layout was employed to achieve low inductance. The PCB-based solution mimics the multilayer substrate layout targeted in the ODBC-based solution discussed in the previous sections. Figure I.1.1.10 shows photos of the DBC- and PCB-based silicon carbide MOSFET half-bridge prototypes.

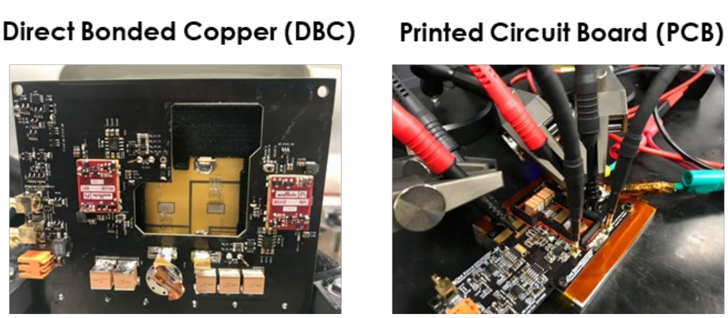

Figure I.1.1.10. (Left) DBC-based and (right) PCB-based half-bridge prototypes.

The turn-on and turn-off current and voltage waveforms of silicon carbide MOSFET with DBC- and PCB-based designs and different gate resistances are shown in Figure I.1.1.11. Using silicon carbide MOSFETs with the vertical layout, which provides low commutation loop inductance, results in 68% reduction in voltage overshoot during turn-off transient. Furthermore, it should be noted that the reduction in turn-off gate resistance does not change the switching speed of the device due to high internal gate resistance (6 Ω according to device datasheet CPM3-1200-0013A).

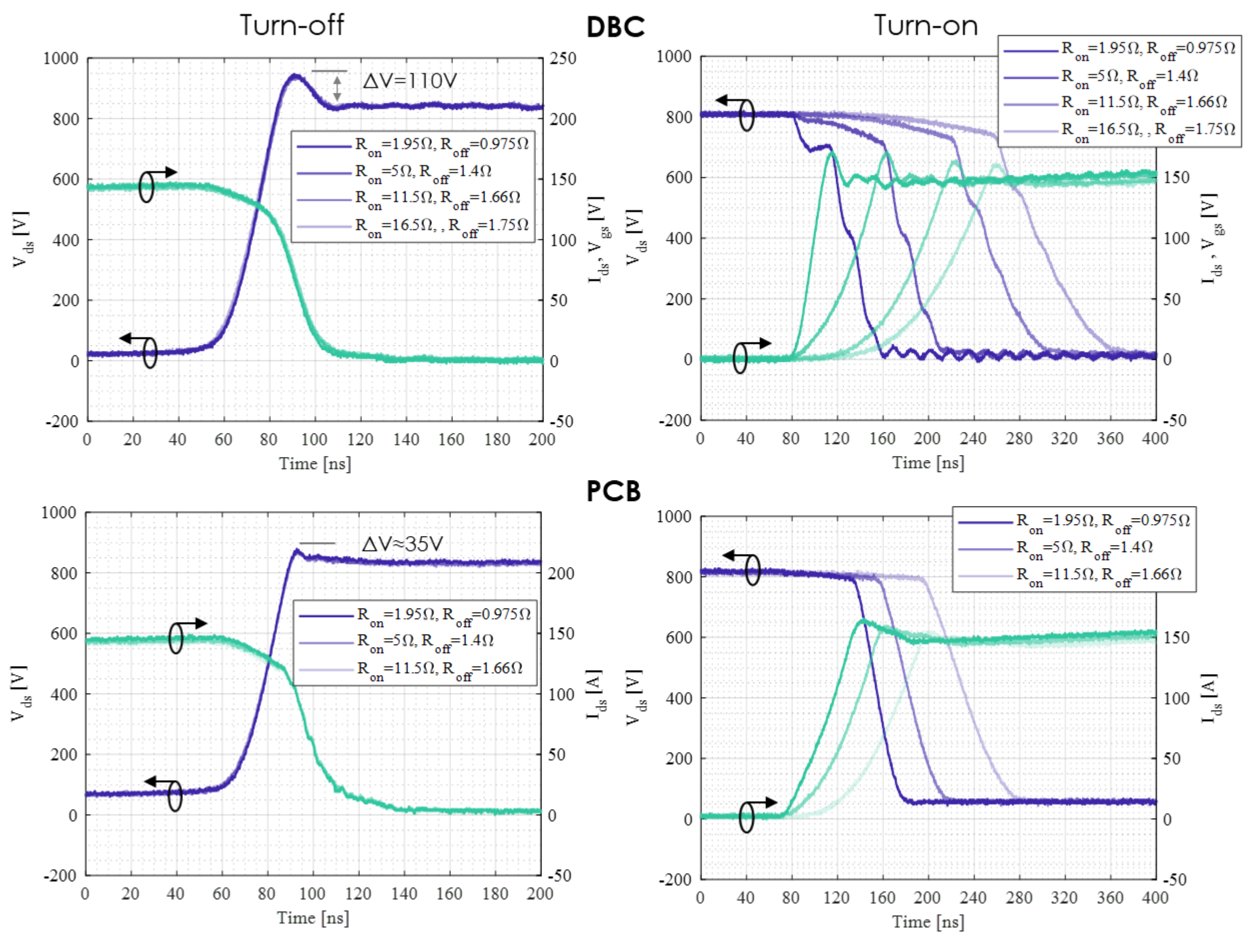

Figure I.1.1.11. Turn-off and turn-on switching transition waveforms for (top left, top right) DBC-based and (bottom left, bottom right) PCB-based silicon carbide MOSFET half-bridge circuits with different gate resistance conditions.

Conclusions

This report introduces new integrated multilayer substrate technology for next-generation advanced integrated power electronic systems enabling high power density and reliability to achieve DOE ELT 2025 technical targets (100 kW/L, $2.7/kW, and 300,000 mi lifetime). The thermal and electrical design of the ODBC-based substrate design was completed in this fiscal year. Furthermore, experimental characterization of the GA-optimized heat sink design was completed, and the performance of the proposed design and design tool was validated under a wide range of operating conditions. Finally, switching performance of latest-generation 1.2 kV silicon carbide MOSFETs were characterized under different operating conditions. The characterization results show that low inductance layout is crucial for WBG power electronics to achieve high switching speeds, low noise, and low overshoot across the power electronic system.

Key Publications

1. Gurpinar, E., S. Chowdhury, B. Ozpineci, and W. Fan. "Graphite Embedded High Performance Insulated Metal Substrate for Wide-Bandgap Power Modules." *IEEE Transactions on Power Electronics* 36, no. 1 (January 2021): 114–128. doi: 10.1109/TPEL.2020.3001528.

2. Sahu, R., E. Gurpinar, and B. Ozpineci. "Liquid-Cooled Heat Sink Optimization for Thermal Imbalance Mitigation in Wide-Bandgap Power Modules." *Journal of Electronic Packaging* 144, no. 2 (June 2022): 021103. https://doi.org/10.1115/1.4052068.

3. Husain, I., B. Ozpineci, M. Islam, E. Gurpinar, G. Su, W. Yu, S. Chowdhury, L. Xue, D. Rahman, and R. Sahu. "Electric Drive Technology Trends, Challenges, and Opportunities for Future Electric Vehicles." *Proceedings of the IEEE* 109, no. 6 (2021): 1039–1059. doi: 10.1109/JPROC.2020.3046112.

Acknowledgements

The principal investigator wishes to thank the project team members: Randy Wiles and Jon Wilkins for mechanical design support and Shajjad Chowdhury for characterization of the silicon carbide MOSFETs.

I.1.2 High-Voltage, High Power Density Traction Drive Inverter (Oak Ridge National Laboratory)

Gui-Jia Su, Principal Investigator
Oak Ridge National Laboratory
1 Bethel Valley Road
Oak Ridge, TN 37830
Email: sugj@ornl.gov

Susan Rogers, DOE Technology Development Manager
U.S. Department of Energy
Email: Susan.Rogers@ee.doe.gov

Start Date: October 1, 2020 End Date: September 30, 2021
Project Funding: $550,000 DOE Share: $550,000 Non-DOE Share: $0

Project Introduction

One of the barriers to meeting the U.S. Department of Energy (DOE) Electrification (ELT) Program's 2025 power electronics targets [1] is the direct current (DC) bus capacitor in the inverter. Using pulse-width modulation (PWM) schemes in the voltage source inverter to produce a desired set of alternating current (AC) voltages generates large ripple components in the DC-link current with root mean square (RMS) values greater than 60% of the motor RMS currents. The DC bus filter capacitor must absorb the ripple currents and suppress voltage transients; both are detrimental to the battery life and reliability of the semiconductor switches in the inverter. Available capacitors that can meet these requirements are costly and bulky: they make up one-fifth of the volume and cost of the inverter. Therefore, an urgent need exists to minimize this bulky component by significantly reducing the inverter ripple current. The goal for this project is to increase the power density of the traction drive power electronics system to meet DOE ELT 2025 targets (100 kW/L, $2.70/kW, and 300,000 mi lifetime) by focusing on power inverter architecture research and bus bar designs to reduce the needs for passive components.

Objectives

The overall objective of this project is to develop technologies for next-generation traction drive power electronics systems with an 8× increase in power density to achieve the DOE ELT 2025 power density target of 100 kW/L using novel traction drive inverter architecture, optimizing the bus bar design, and minimizing passive components. The objective for Fiscal Year 2021 was to design and build 100 kW inverter prototypes using technologies developed in the Electric Drive Technologies Consortium.

Approach

Three technical approaches were considered in this project. The first approach selected inverter architectures that can reduce the DC bus capacitor requirements. Multiphase inverters, segmented inverters, and open stator winding inverter drive configurations were evaluated. The second approach increased the inverter DC bus voltage to 800 V or higher. This increase took advantage of the inherently higher voltage ratings of silicon carbide switching devices, reduced the size of silicon carbide (SiC) dies (thus lowering the cost), and reduced phase and DC bus currents. The third approach optimized the designs for the inverter DC bus bars by employing embedded and distributed capacitors and direct cooling of the bus bars.

Results

The segmented inverter topology was selected due to its significantly reduced DC bus capacitance requirement. Figure I.1.2.1 shows a block diagram for the major components of a three-phase segmented inverter, and Table I.1.2.1 lists the inverter specifications. The inverter design optimized the SiC MOSFET power module packaging, heat sinks, gate drive, and current sensing. Wolfspeed SiC MOSFET dies (CPM3-

1200-0013A) were selected for the power modules. The SiC dies have the following ratings: 1,200 V and 102 A at 100°C with on-resistance 13 mΩ at 25°C or 21 mΩ at 175°C. Two designs for 100 kW segmented inverters were completed using the power modules developed by Electric Drive Technologies Consortium members Virginia Tech or the University of Arkansas.

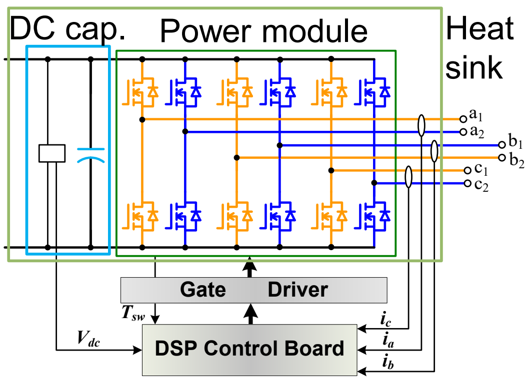

Figure I.1.2.1. Major components of three-phase segmented inverter.

Table I.1.2.1 Inverter Specifications

Vdc (V)	800	
Power (kW)	100	143 kVA at power factor 0.7
Efficiency (%)	98	
Coolant flow rate (L/min)	10	WEG, 50/50

Simulation studies were carried out using the commercial software package PLECS to determine the switch losses for the heat sink design. A PLECS loss model for the Wolfspeed SiC MOSFET was derived from the datasheets for the die and a packaged switch (CPM3-1200-0016A in TO-247-4L). Figure I.1.2.2 compares the conduction losses for MOSFET only, MOSFET with body diode, and body diode only in the third quadrant in (left top); MOSFET on-resistance, R_{dson}, in the first and third quadrants in (right); and switching losses in (left bottom) at different junction temperatures.

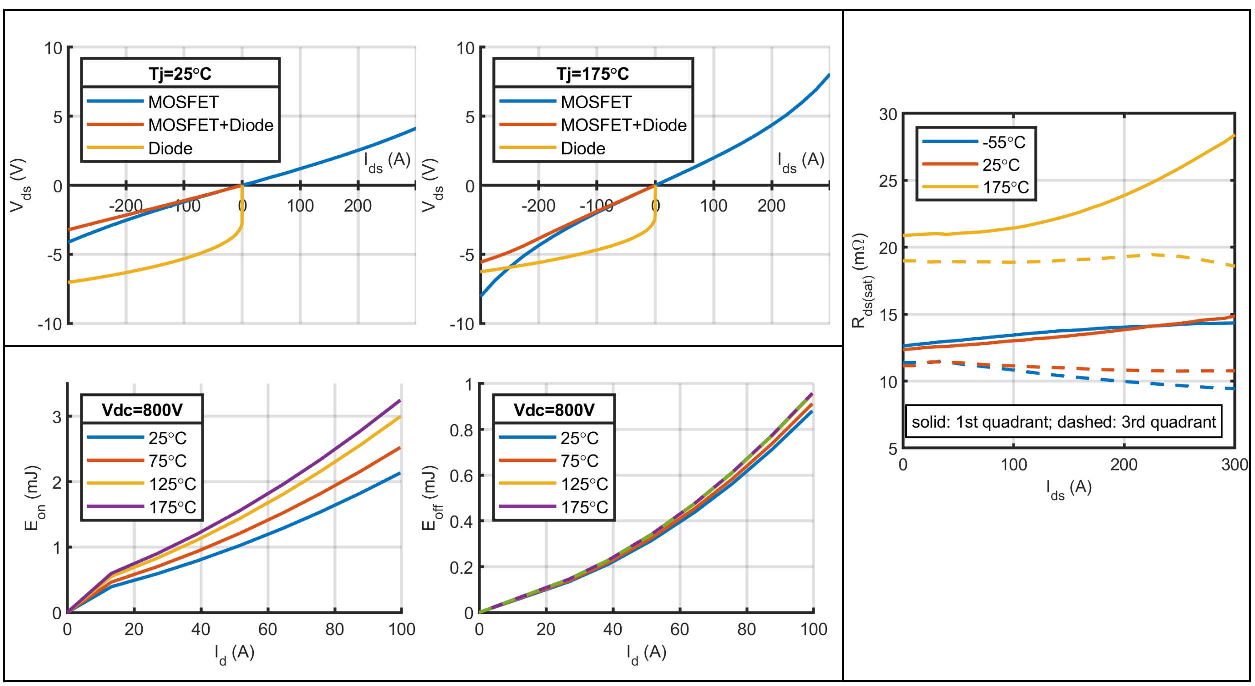

Figure I.1.2.2. Conduction loss model for the Wolfspeed SiC MOSFET die (CPM3-1200-0013A).

Figure I.1.2.3 compares the losses per switch in the segmented inverter at output power 100 kW, switching frequency 30 kHz, and power factors 0.6 and 0.7 with three different space vector PWMs (SVPWMs): (a) bus-clamped SVPWM with MOSFET only in the third quadrant, (b) bus-clamped SVPWM with MOSFET plus body diode in the third quadrant, and (c) symmetrical SVPWM with MOSFET plus body diode in the third quadrant. The results indicate (1) the bus-clamped SVPWM significantly reduces switching loss significantly compared with the symmetrical SVPWM and (2) the diode conduction in the third quadrant depends on power factor and switching scheme. Therefore, the bus-clamped SVPWM was adopted in the designs to enhance the inverter efficiency.

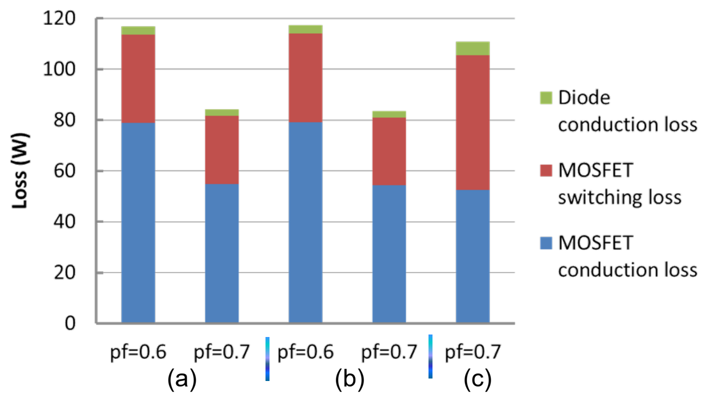

Figure I.1.2.3. Comparison of losses per switch at power factors 0.6 and 0.7 with three different SVPWMs.

Heat sinks for the Virginia Tech-designed double-side cooled power module were designed using Oak Ridge National Laboratory's (ORNL) genetic algorithm (GA)-based optimization tool in conjunction with the commercial finite element analysis (FEA) software package COMSOL Multiphysics. Figure I.1.2.4 shows Virginia Tech's phase-leg module, which employs two SiC dies, and plots the Pareto front and feasible designs for the GA-based heat sink design optimization. The optimization goal was to maximize the device-to-coolant convection coefficient and minimize the volume under the following conditions: 150 W loss in each chip (leading to a heat flux in each device of 474 W/cm^2), 65°C coolant inlet temperature, 1.67 L/m flow rate, <6.5°C coolant temperature rise at the outlet, <2 psi pressure drop, and <175°C maximum junction temperature. Figure I.1.2.5 shows optimal heat sink designs for the two configurations. Version 1 aligns the heat sink inlet/outlet with the power module gate leads and power tabs. Version 2 rotates the inlet/outlet 90°. Although the version 2 design has a 54% increase in volume compared with version 1, this increase does not interfere with electrical connections between the power modules and gate drives or between the modules and inverter DC inputs and AC outputs. Therefore, version 2 was selected for inverter prototype development. Figure I.1.2.6 shows FEA surface temperature for the version 2 heat sink design. The maximum junction temperatures for the two SiC dies were 153.3°C and 155.93°C, respectively. The pressure drop was 749.27 Pa, and the coolant outlet maximum temperatures were 74.89°C and 74.17°C, respectively.

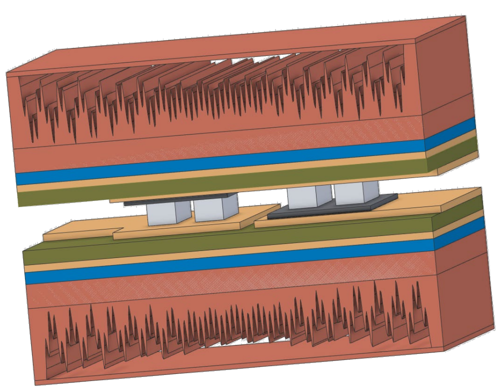

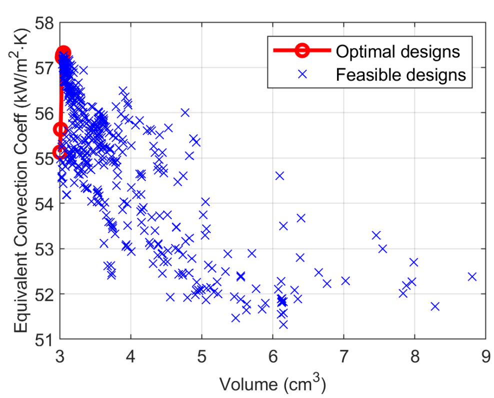

Figure I.1.2.4. (Left) Virginia Tech-designed double-side cooled power module and (right) feasible designs and Pareto-optimal front plot for the GA-based heat sink design optimization.

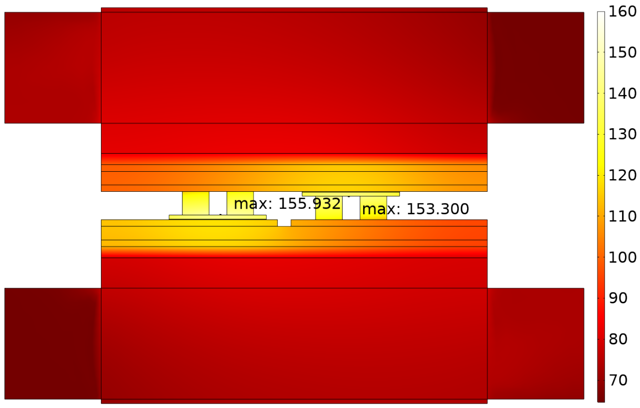

Figure I.1.2.5. FEA results for the version 2 heat sink design.

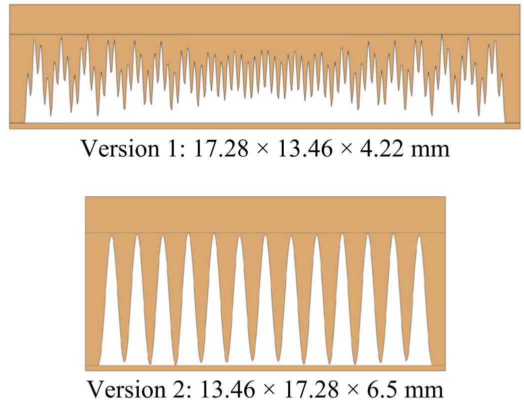

Figure I.1.2.6. Optimal heat sink designs.

A lumped thermal impedance model for the Virginia Tech-designed power module was derived using transient-response FEA simulations and incorporated in a PLECS thermal model (Figure I.1.2.7) to simulate the MOSFET junction temperature fluctuations in inverter operations. Figure I.1.2.8 plots simulation results for the symmetrical SVPWM (left) and bus-clamped SVPWM (right) and at output power 100 kW, switching frequency 30kHz, and power factor 0.7. The results indicate that the bus-clamped SVPWM gives more than 15°C reduction in maximum junction temperature compared with the symmetrical SVPWM.

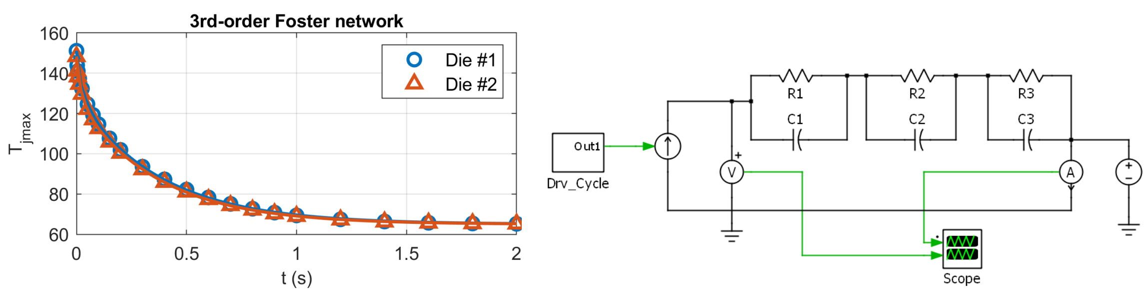

Figure I.1.2.7. PLECS thermal model.

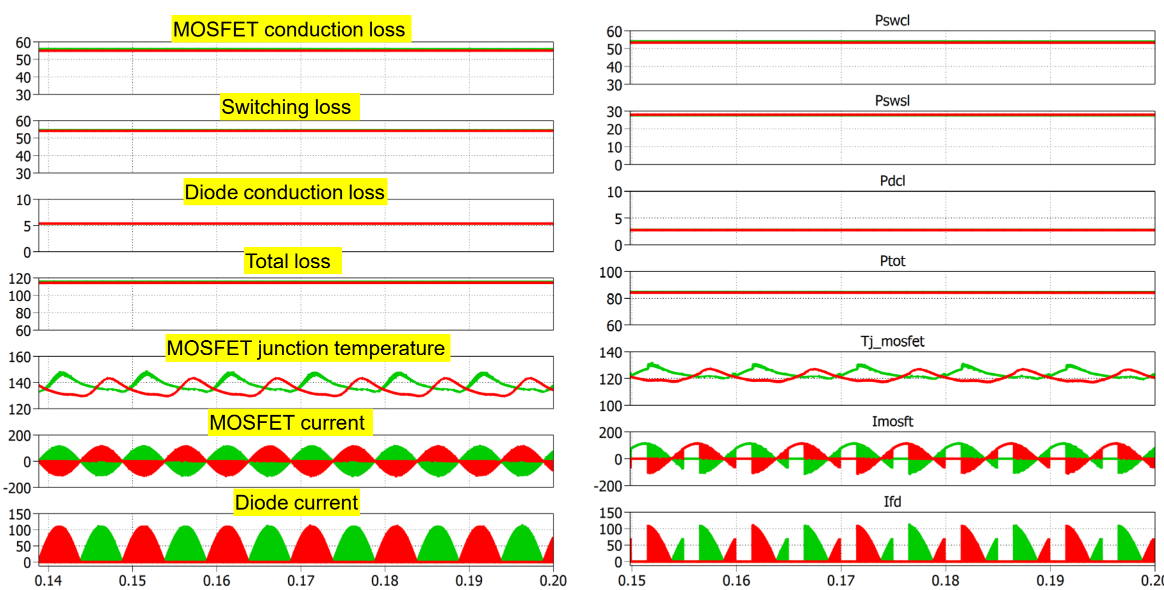

Figure I.1.2.8. Simulation results for MOSFET junction temperature fluctuations in inverter operations with (left) symmetrical SVPWM and (right) bus-clamped SVPWM.

Figure I.1.2.9 shows the inlet and outlet manifold design for ensuring an even flow distribution to the heat sinks. Figure I.1.2.10 shows a complete 100 kW inverter design using the Virginia Tech-designed phase leg modules. The TDK CeraLink capacitors were selected for the DC bus capacitor because of their high ripple current capability and operating temperature. The inverter design at a volume of 0.98 L is promising for meeting the power density (100 kW/L) and efficiency (97%) targets.

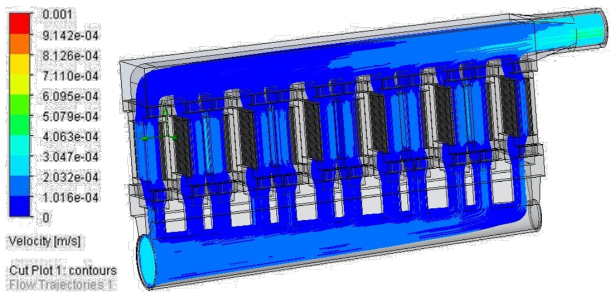

Figure I.1.2.9. Design for the inlet and outlet manifolds for ensuring an even flow distribution to the heat sinks.

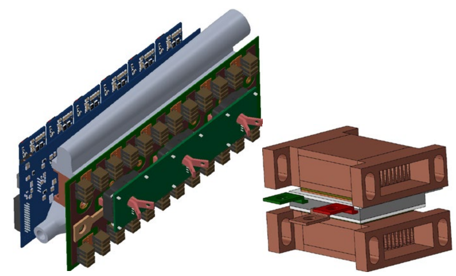

Figure I.1.2.10. Design for 100 kW segmented inverter using the Virginia Tech-designed power modules.

Heat sink design for the University of Arkansas-designed SiC power modules was completed using ORNL's GA-based optimization tool. The modules have two SiC dies in parallel for each switch and a total of four dies. Figure I.1.2.11(a) plots feasible designs and Pareto-optimal front for the heat sink designs. Four optimal candidates were selected for detailed FEA evaluations. Figure I.1.2.11(b) shows the maximum junction temperature of the four dies in the University of Arkansas-designed power module for the four heat sink designs. The results indicate the maximum junction temperature is lower than 152°C, and the pressure drop is below 356 Pa. The results also reveal that the #1 and #2 SiC dies have 5°C higher maximum junction temperature than the #3 and #4 SiC dies. A flow rate offset was introduced between the top and bottom heat sinks to balance the SiC temperatures, as shown in Figure I.1.2.12. The plot of maximum junction temperature vs. flow rate offset from FEA simulation results shows that the imbalance in maximum junction temperatures of the four SiC dies was corrected with a flow rate offset of 0.45.

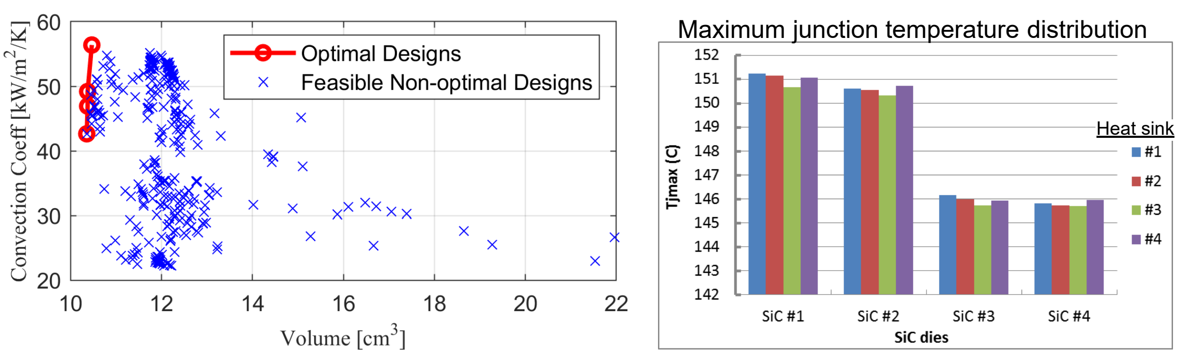

(a) (b)

Figure I.1.2.11. (a) Heat sink feasible designs and Pareto-optimal front plot for the GA-based optimization design for the UA power modules and (b) maximum junction temperature of the four SiC dies in the UA power module for the four optimal heat sink designs.

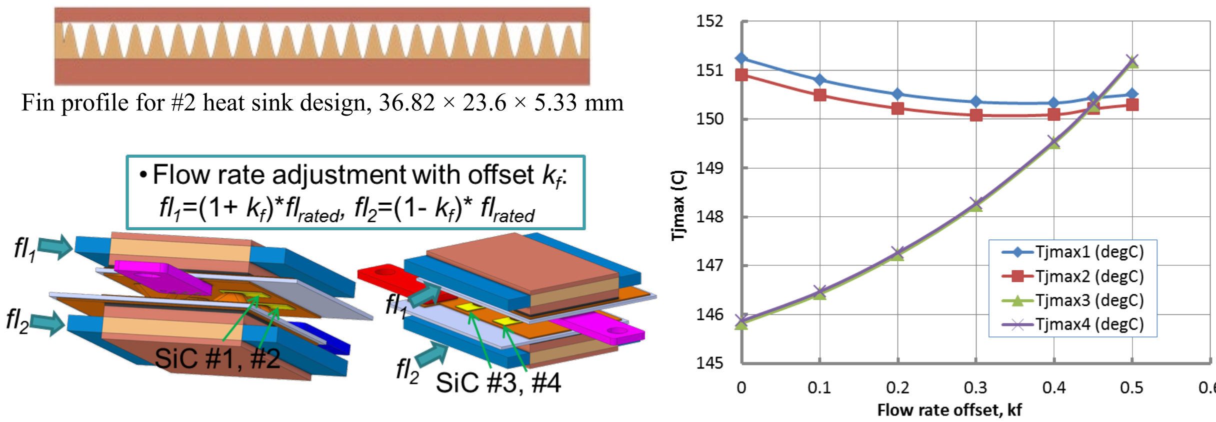

Figure I.1.2.12. Flow rate offset used for balancing the MOSFET junction temperatures for heat sink design #2.

A 100-kW inverter prototype based on the design using the Virginia Tech-designed power modules was fabricated. Figure I.1.2.13 shows photos of the 100-kW segmented inverter prototype components (left to right): power module, heat sink, gate drive side, and DC bus capacitor side of.

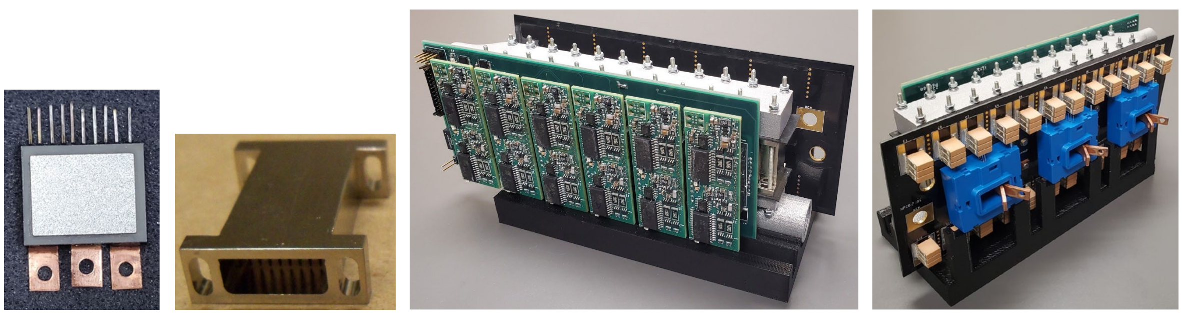

Figure I.1.2.13. Components of the 100 kW segmented inverter prototype using the Virginia Tech-designed power modules.

Conclusions

This report summarizes the design results for the 100-kW inverter using the segmented topology, double side cooled SiC MOSFET power modules, CeraLink capacitors, and mini-channel heat sinks optimized using GA tools to achieve high power density and reliability to meet the DOE ELT 2025 technical targets (100 kW/L, $2.7/kW, and 300,000 mi lifetime). The design using the Virginia Tech-designed SiC power modules is promising for achieving the program's power density target. A prototype based on this design was fabricated and will be evaluated experimentally in Fiscal Year 2022.

The designs discussed in this report used commercial-off-the-shelf current sensors, and future work will pursue integrating current sensing capabilities based on device parasitic voltage drop or giant magnetoresistance chips into the power modules.

Key Publications

1. Husain, I., B. Ozpineci, M. S. Islam, E. Gurpinar, G. Su, W. Yu, S. Chowdhury, L. Xue, D. Rahman, and R. Sahu. "Electric Drive Technology Trends, Challenges, and Opportunities for Future Electric Vehicles." *Proceedings of the IEEE* 109, no. 6 (2021): 1039–1059. doi: 10.1109/JPROC.2020.3046112.

2. Xue, L. L., G.-J. Su, and B. Ozpineci. 2021. "DC-Ripple-Energy Adaptive-Minimization (DREAM) Modulation Scheme for a High-Power Density Inverter." In *Proceedings of the 2021 IEEE Applied Power Electronics Conference and Exposition (APEC)*, June 14–17, 2021, pp. 186–191. doi: 10.1109/APEC42165.2021.9487324.

References

1. U.S. DRIVE Partnership. *Electrical and Electronics Technical Team Roadmap*. U.S. DRIVE, U.S. Department of Energy, October 2017. Available at https://www.energy.gov/sites/prod/files/2017/11/f39/EETT%20Roadmap%2010-27-17.pdf.

Acknowledgements

The principal investigator wishes to thank the ORNL team members: Raj Sahu, Emre Gurpinar, Lincoln Xue, Randy Wiles, and Jon Wilkins. The principal investigator also thanks the Virginia Tech team led by Prof. G. Q. Lu and the University of Arkansas team led by Prof. Alan Mantooth.

I.1.3 Non-Heavy Rare-Earth High-Speed Motors (Oak Ridge National Laboratory)

Tsarafidy Raminosoa, Principal Investigator
Oak Ridge National Laboratory
1 Bethel Valley Road
Oak Ridge, TN 37831
Email: raminosoat@ornl.gov

Mostak Mohammad, Principal Investigator
Oak Ridge National Laboratory
1 Bethel Valley Road
Oak Ridge, TN 37831
Email: mohammadm@ornl.gov

Susan Rogers, DOE Technology Development Manager
U.S. Department of Energy
Email: susan.rogers@ee.doe.gov

Start Date: October 1, 2020 End Date: September 30, 2021
Project Funding: $765,000 DOE Share: $765,000 Non-DOE Share: $0

Project Introduction

Global carbon dioxide emissions have steadily increased since 1900, with a sharp rise since 1945 [1], [2]. In the United States, the transportation sector is responsible for 28% of greenhouse gas emissions [3]. These observations have led to global environmental consciousness and tighter regulations of carbon dioxide emissions in several countries, resulting in the expansion of the electrification of passenger and commercial vehicles.

Most electric traction motors currently in production are permanent magnet (PM) synchronous motors, which have high torque and power density and excellent efficiency but use costly heavy rare-earth magnet material such as dysprosium. The price and supply of dysprosium have historically been unstable, leading to substantial progress in PM material technologies aimed at reducing or eliminating dysprosium (Dy) from PM synchronous motors. Dysprosium-free PM materials are now commercialized by major suppliers [4], [5], [6], which can help lower the cost of traction motors and accelerate the market penetration of electric vehicles. However, dysprosium-free PM materials have lower coercivity, so they are more prone to demagnetization than their conventional heavy rare-earth counterparts. Therefore, special attention should be paid to demagnetization when designing dysprosium-free PM motors.

This project developed a dysprosium-free PM outer rotor motor design enabling the integration of the drive and a shared cooling system between power electronics and motor.

Objectives

Project objectives include enabling the adoption of high-speed and high power density nonheavy rare-earth traction motors and analyzing the effect of new, advanced materials for nonheavy rare-earth electric motors. The tasks for Fiscal Year 2021 involved completing:

- A detailed design of a nonheavy rare-earth PM high-speed traction motor targeting the U.S. Department of Energy's (DOE) Electrification (ELT) Program's 2025 specifications [1] and enabling the integration of power electronics.
- A detailed design of an integrated shared cooling system between power electronics and motor.

Approach

To accomplish the project objectives, the team developed a 100-kW high-speed, high power density, nonheavy rare-earth traction motor to target the U.S. DRIVE (Driving Research and Innovation for Vehicle efficiency and Energy sustainability) specifications shown in Figure I.1.3.1. A dysprosium-free PM motor with an outer rotor configuration was designed to enable the integration of the drive and a shared cooling system between power electronics and motor. The electromagnetic, thermal, and mechanical feasibility of the design was verified. Because low-coercivity, dysprosium-free PMs were used, the robustness of the design against demagnetization was also confirmed. The current rating and direct current (DC)-link voltage were selected according to the power devices used in the drive. The design used a dual three-phase winding configuration powered by a dual three-phase segmented drive featuring interleaved switching to reduce the current ripple and thereby reduce the size of the DC-link capacitor [4].

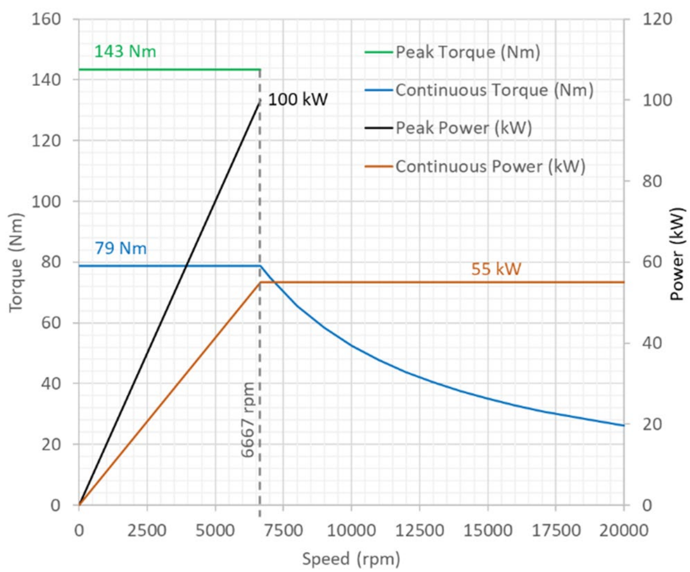

Peak power (kW)	100
Continuous power (kW)	55
Maximum speed (rpm)	≤20,000
Power factor	> 0.8
Maximum current (A)	600
Maximum efficiency (%)	> 97
Torque ripple (%)	5
Volume at 50 kW/L (L)	2
Mass at 5 kW/kg (kg)	20

Figure I.1.3.1. Summary of U.S. DRIVE specifications.

Results

An 18-slot/16-pole PM motor was designed under this project. The dimensions and materials used are shown in Figure I.1.3.2(a). Because the design used low-coercivity, nonheavy rare-earth PMs, a Halbach magnetization arrangement was selected to maximize the air-gap flux density and reinforce the resistance to demagnetization. Given the high operating frequency, especially at high speeds, the PMs were axially laminated with a lamination thickness of 2 mm to minimize eddy current losses. Furthermore, Litz wire was used in the winding to minimize alternating current (AC) losses. Figure I.1.3.2(b) shows the layout of Litz wire bundles within a stator slot. The electromagnetic loading under peak torque operation is shown in Figure I.1.3.3. The peak torque waveform is shown in Figure I.1.3.4. With an average torque of 169 N·m and only 1.3% ripple, the design met the peak power and torque quality requirements. Figure I.1.3.5 shows a sinusoidal line-to-line open-circuit voltage waveform at 20,000 rpm.

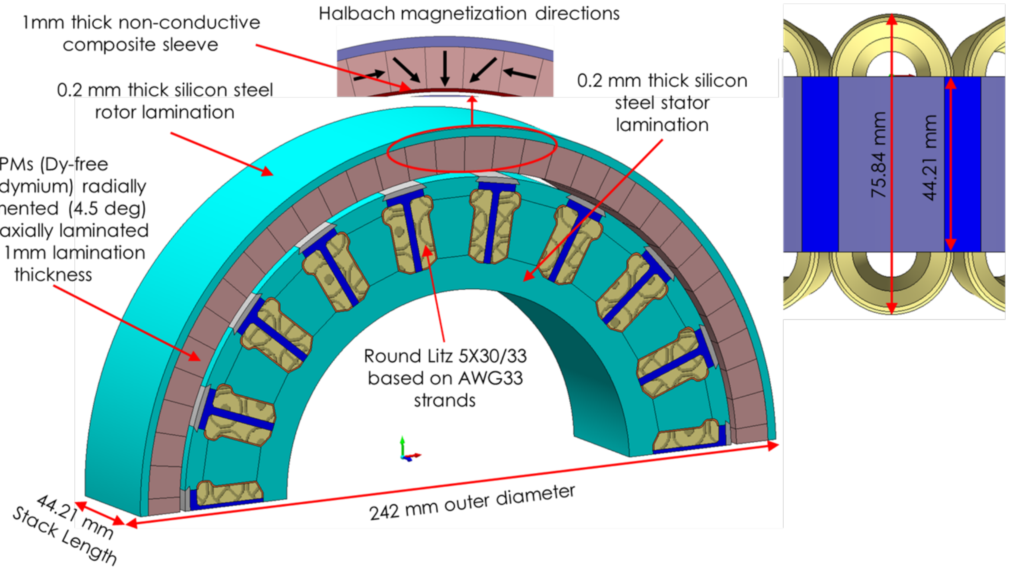

(a)

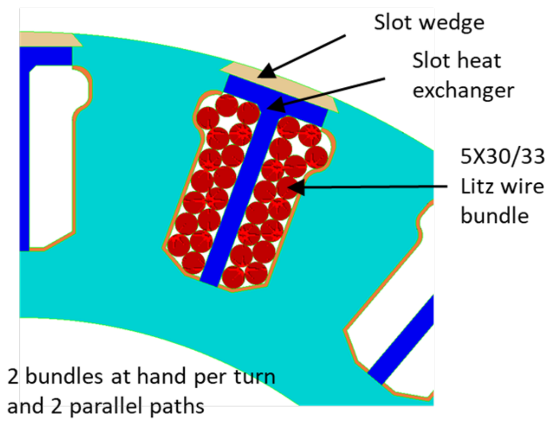

(b)

Figure I.1.3.2. PM traction motor design. (a) Materials and dimensions and (b) layout of Litz wire bundles within a stator slot.

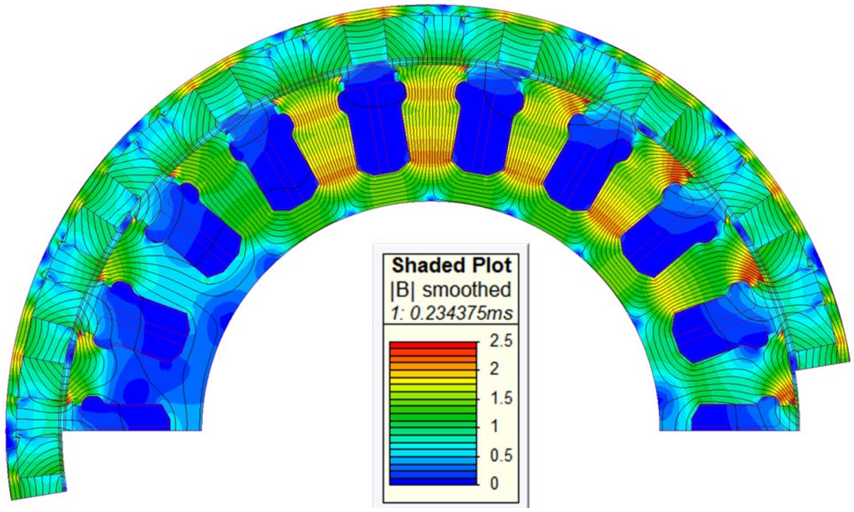

Figure I.1.3.3. Flux density map under peak torque operation.

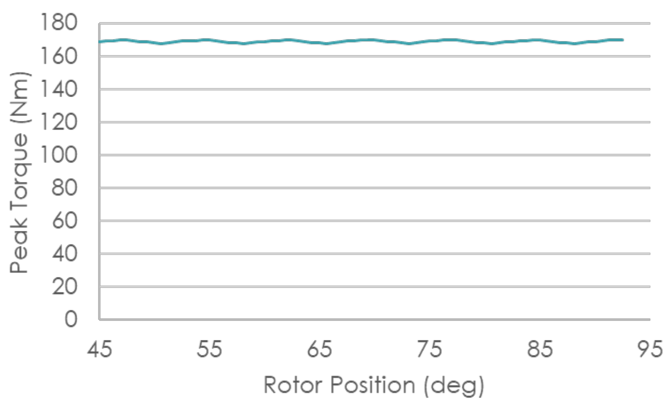

Figure I.1.3.4. Peak torque waveform.

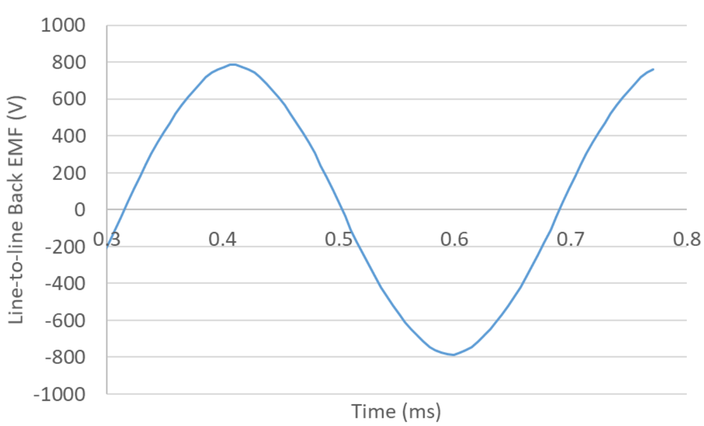

Figure I.1.3.5. Line-to-line open-circuit voltage waveform at 20,000 rpm.

To evaluate the design's resistance to demagnetization, an extreme scenario of transient three-phase short-circuit fault was simulated at 20,000 rpm using finite element analysis featuring dynamic nonlinear demagnetization modeling. The assumed temperature of the PMs was 150°C. The resulting reduction of the torque capability is shown in Figure I.1.3.6. Even if several subsequent faults were applied, the torque stabilized at 146 N·m and met the peak torque requirement. Therefore, the design was shown to be robust against demagnetization. The worst-case potential reduction in magnetization was introduced as a design margin. The calculated active volume was 2.48 L, including the end windings but excluding the stator inner space allocated to power electronics.

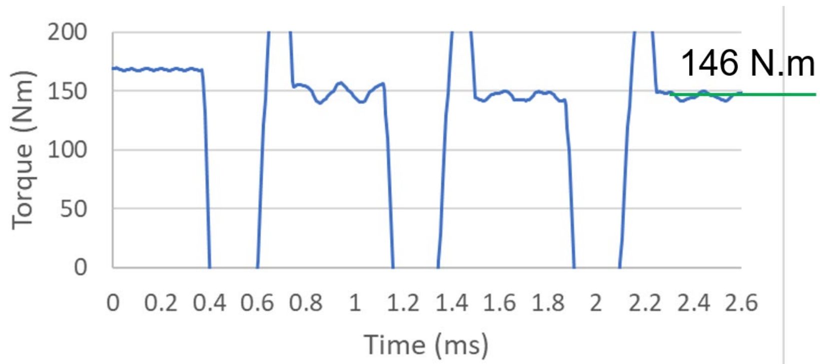

Figure I.1.3.6. Effect of successive three-phase short-circuit fault on peak torque capability.

The performance of the motor, including torque, power, efficiency, and power factor, is shown in Figure I.1.3.7. The figure shows that the design can provide the required continuous 55 kW power with a 12% design margin for the entire speed range while staying within the current and voltage limits. Furthermore, the efficiency specification was met, and the motor exhibited very good efficiency across the entire speed range (97.5% at base speed and 93.4% at top speed).

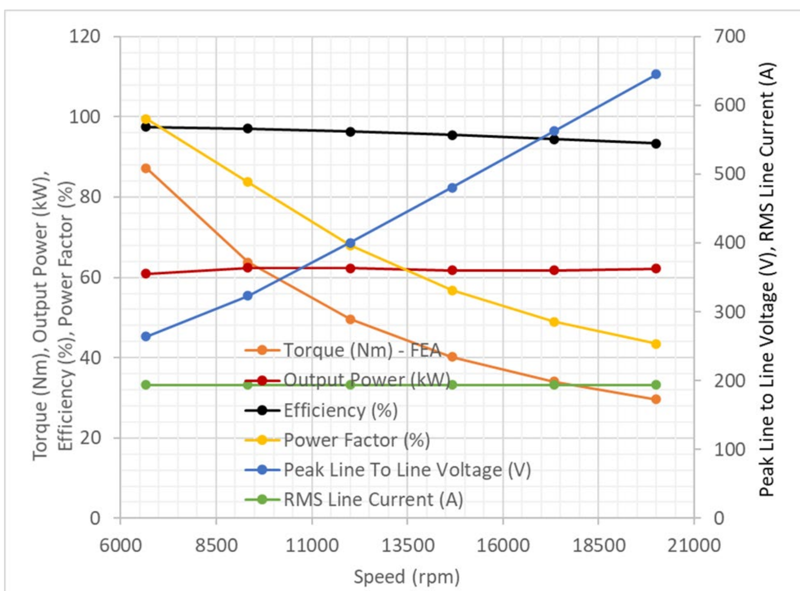

Figure I.1.3.7. Motor performance under 55 kW continuous operation.

The breakdown of the various electromagnetic loss components is shown in Figure I.1.3.8. As the speed increases, the losses are quickly dominated by iron loss. As a result, the 20,000-rpm operating point had the highest loss and the highest temperatures. This operating point was used for the thermal analysis.

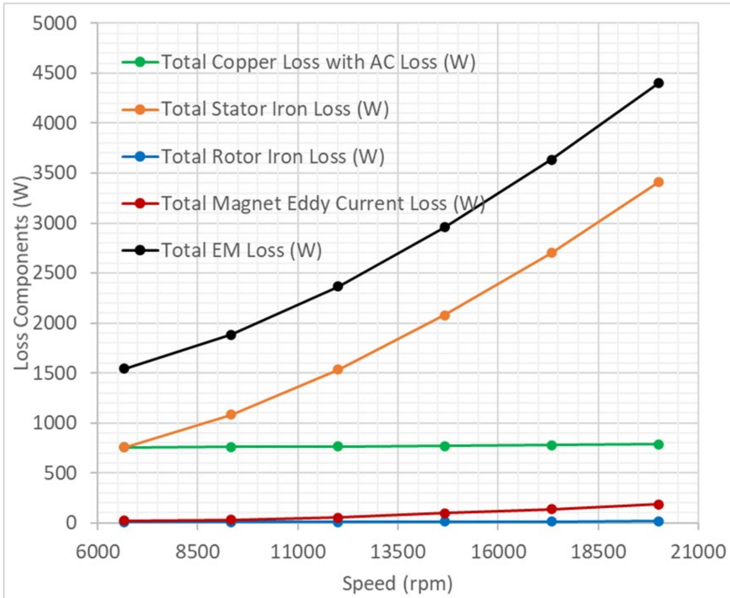

Figure I.1.3.8. Electromagnetic loss components for 55 kW operation with 0.2 mm thick silicon steel laminations.

A cross section of the mechanical assembly of the PM motor designed and tested in this project is shown in Figure I.1.3.9. The assembly was designed at the U.S. Department of Energy's Oak Ridge National Laboratory (ORNL) to enable the integration of the drive as well as a cooling system shared among the power electronics and the motor [9]. The loss distribution in the motor, including the AC losses in the winding and the eddy current losses in the magnets, was calculated and used as input to the thermal model. The thermal analysis and cooling system design were conducted by the National Renewable Energy Laboratory (NREL) [8].

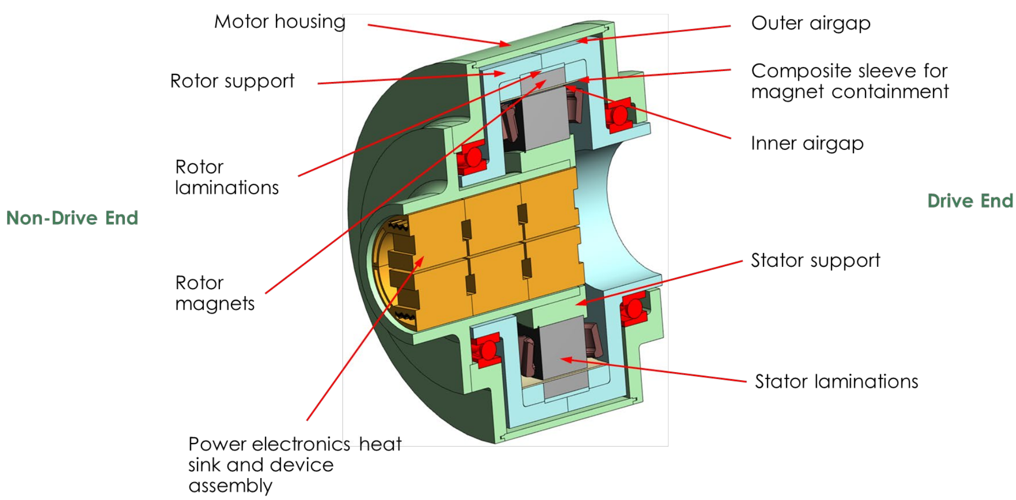

Figure I.1.3.9. Mechanical assembly of PM traction motor.

The windings were cooled by a 3D-printed ceramic heat exchanger similar to the one used by Sixel et al.[7]. The cooling system and temperature distribution at 55 kW and 20,000 rpm are shown in Figure I.1.3.10. The temperatures of the magnets and windings are nearly within the 150°C temperature limit. Furthermore, the segmentation and lamination of the PMs reduced the induced eddy currents so significantly that no active cooling was necessary to keep the magnet temperature below 150°C.

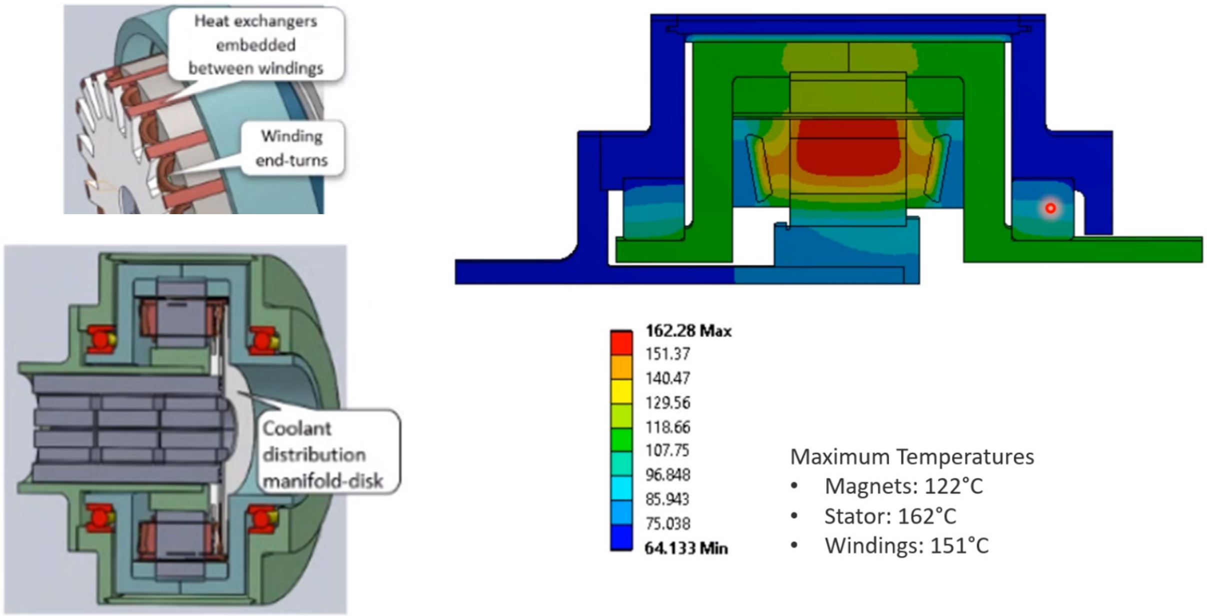

Figure I.1.3.10. (Left) Cross section and (right) temperature distribution of the cooling system.

Conclusions

A high-speed, high power density nonheavy rare-earth PM traction motor was designed to enable the integration of the drive and a shared cooling system between the motor and the power electronics. The design meets most of the DOE ELT targets, including the 100-kW peak and 55 kW continuous power, torque ripple, current, voltage, and efficiency requirements, and is robust against demagnetization even under worst-case scenarios. Future research will include validation of manufacturability via rapid prototyping and trial of subassemblies, construction of the integrated motor drive prototype, and experimental verification of the prototype's performance.

Key Publications

1. Raminosoa, T., R. Wiles, J. E. Cousineau, K. Bennion, and J. Wilkins. "A High-Speed High-Power-Density Non-Heavy Rare-Earth Permanent Magnet Traction Motor," In *Proceedings of the 2020 IEEE Energy Conversion Congress and Exposition (ECCE 2020)*, October 11, 2020.

2. Raminosoa, T., Pries, P., R. Wiles, and J. Wilkins., Rotary Transformer-Based Contactless Rotor Excitation System. Nonprovisional patent application based on US Provisional Application no. 63/023,525, May 2021.

References

1. U.S. DRIVE Partnership. *Electrical and Electronics Technical Team Roadmap*. U.S. DRIVE, U.S. Department of Energy, October 2017. Available at https://www.energy.gov/sites/prod/files/2017/11/f39/EETT%20Roadmap%2010-27-17.pdf.

2. TDK. *Neodymium Magnet: Dysprosium Free Type/Transverse Magnetic Field Molding Process.* Available at https://product.tdk.com/info/en/catalog/datasheets/magnet_neo_neorec45mhf_en.pdf.

3. Raminosoa, T., and T. Aytug. "Impact of Ultra-Conducting Winding on the Power Density and Performance of Non-Heavy Rare Earth Traction Motors." In *Proceedings of the 2019 IEEE International Electric Machines & Drives Conference (IEMDC)*, San Diego, CA, 2019, pp. 2107–2114. doi: 10.1109/IEMDC.2019.8785295.

4. Su, G., and L. Tang. “A Segmented Traction Drive System with a Small DC Bus Capacitor.” In *Proceedings of the 2012 IEEE Energy Conversion Congress and Exposition (ECCE)*, Raleigh, NC, 2012, pp. 2847–2853. doi: 10.1109/ECCE.2012.6342375.

5. New England Wire Technologies. *Litz Wire Technical Information*, 2003. Available at http://www.litzwire.com/nepdfs/Litz_Technical.pdf.

6. Ramonosoa, T., A. M. El-Refaie, D. Pan, K.-K. Huh, J. P. Alexander, K. Grace, S. Grubic, S. Galioto, P. B. Reddy, and X. Shen. “Reduced Rare-Earth Flux-Switching Machines for Traction Applications,” *IEEE Transactions on Industry Applications* 51, no. 4 (2015): 2959–2971. doi: 10.1109/TIA.2015.2397173.

7. Sixel, W., M. Liu, G. Nellis, and B. Sarlioglu. “Cooling of Windings in Electric Machines via 3D Printed Heat Exchanger.” In *Proceedings of the 2018 IEEE Energy Conversion Congress and Exposition (ECCE)*, Portland, OR, 2018, pp. 229–235. doi: 10.1109/ECCE.2018.8557845.

8. Bennion, K., “Electric Motor Thermal Management R&D”, National Renewable Energy Laboratory (NREL), Aug. 2019. Available: https://www.osti.gov/biblio/1559431

9. Chowdhury, S., “Integrated Electric Drive System (Keystone Project #3), Oak Ridge National Laboratory, June 2021. Available: https://www.energy.gov/sites/default/files/2021-06/elt221_chowdhury_2021_o_5-14_438pm_KF_TM.pdf

Acknowledgements

The principal investigator would like to thank ORNL’s Shajjad Chowdhury, Emre Gurpinar, Randy Wiles, and Jon Wilkins for the design of the integrated drive [9] and the mechanical assembly. The principal investigator would also like to thank NREL’s Emily Cousineau, Kevin Bennion, and Bidzina Kekelia for the thermal analysis and the design of the cooling system [8].

I.1.4 Integrated Electric Drive System (Oak Ridge National Laboratory)

Shajjad Chowdhury, Principal Investigator
Oak Ridge National Laboratory
1 Bethel Valley Road
Oak Ridge, TN 37932
Email: chowdhuryms@ornl.gov

Susan Rogers, DOE Technology Development Manager
U.S. Department of Energy
Email: susan.rogers@ee.doe.gov

Start Date: October 1, 2020 End Date: September 30, 2021
Project Funding: $420,000 DOE Share: $420,000 Non-DOE Share: $0

Project Introduction

The U.S. Department of Energy (DOE) recently announced technical targets for light-duty electric vehicles. DOE targets a power density of 33 kW/L for a 100-kW traction drive system by 2025 [1]. This target translates to an increase of a factor of 5.5 compared with the current state of the art. This project focuses on the tight integration of motor and inverter components to improve power density to achieve the target. Furthermore, this project optimizes the bulky direct current (DC)-link capacitor's volume and improves electrical performance and lifetime by identifying high energy density capacitor technologies and packaging techniques.

Objectives

This project's objective is to research technologies that will allow tight integration of the inverter with the motor resulting in a high power density integrated traction drive. Specific tasks for Fiscal Year 2021 included

- Identifying integration solutions for outer rotor motor to achieve the 2025 ELT targets,
- Estimating required inverter parameters for the designed traction motor and identified inverter cooling requirements, and
- Evaluating emerging capacitor technologies and identifying packaging techniques to optimize volume and electrical performance.

Approach

The approach to achieving project objectives included

- Finding possible integration methods for the outer rotor motor,
- Identifying and evaluating emerging capacitor technologies and selecting one for volume optimization, and
- Identifying ways to package capacitors to complement wide-bandgap devices.

Results

Internal Stator Mount Integration Technique

An integrated motor drive involves integrating all the components of an electric drive unit into a single casing, thereby reducing volume, cost, and installation complexity. A tightly integrated drive can increase power density by 10%–20% with a concomitant reduction of manufacturing and installation costs by 30%–40% [2]. Four different types of integration techniques are listed in the literature [3]. These integration techniques are introduced considering a traditional motor design in which the rotor is placed inside the stator. In the electric motor development project (Keystone 1), an outer rotor motor was designed to achieve high power density, as shown in Figure I.1.4.1(a). The designed outer rotor motor has a rotating part outside the motor and a complex mechanical structure; therefore, not all the traditional integration techniques can be utilized. The only two options are axial endplate mount and radial housing mount, but they may not suit tight integration. Therefore, a novel integration technique called internal stator mount integration was identified in which the inverter can be integrated inside the stator.

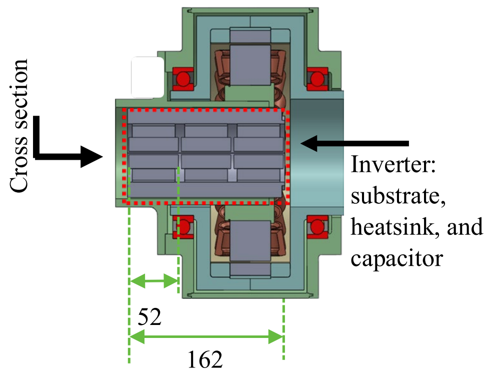

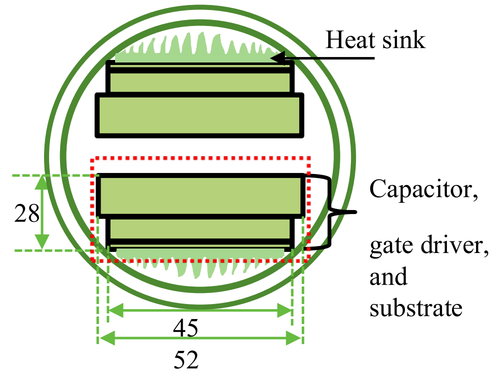

Figure I.1.4.1. (a) Internal stator mount integration technique for outer rotor motor showing the inverter dimensions and (b) inverter cross section showing the height and width of the inverter.

The outer rotor motor's dimensions were fixed based on the power electronic needs; therefore, the space for inverter integration was also fixed. The inverter was placed in the cylindrical hollow space inside the stator of the designed motor. A six-phase segmented inverter was selected for this project. Figure I.1.4.1(a) shows the placement of each phase leg with dimensions. A cross section of the cylindrical space is shown in Figure I.1.4.1(b); it shows that the inverter components' (i.e., substrate, gate driver, capacitor) heights must be less than 28 mm to fit inside the cylindrical space. This report presents the component sizing and selection to fit within this volume.

Motor Characteristics Identification

A steady-state motor model was developed to identify the electrical characteristics. The designed motor is a surface-mount permanent magnet motor with a base speed of 20,000 rpm, which means the motor does not go into the field weakening region ($i_d = 0$); therefore, the motor model can be developed using Eq. (1–6).

$$T_e = \frac{3}{2}\frac{P}{2} i_q \Psi_m \tag{1}$$

$$I = i_q = \frac{T_e}{\Psi_m}\frac{2}{3}\frac{2}{P} \tag{2}$$

$$V_d = i_d R \times L_d \frac{di_d}{dt} - \omega_e L_q i_q \tag{3}$$

$$V_q = i_q R \times L_q \frac{di_q}{dt} + \omega_e L_d i_d + \omega_e \Psi_m \tag{4}$$

$$V = \sqrt{(-\omega_e L_q i_q)^2 + (i_q R + \omega_e \Psi_m)^2} \tag{5}$$

$$\varphi = 90 - \cos^{-1}\left(\frac{V_d}{V}\right) \tag{6}$$

In the equations, T_e is electromagnetic torque, i_{dq} is stator d and q axis current, Ψ_m is the magnet flux, R is rotor resistance, L_{dq} is stator d and q axis inductance, I is the phase current amplitude, V is the phase voltage amplitude, ω_e is the rotor electrical speed, φ is the power factor angle, and P is the pole pair. A model was created using MATLAB, and various speeds and torque were input to identify the motor's response (i.e., phase current and power factor angle). The results are shown in Figure I.1.4.2. The results suggest that each phase leg of the inverter must be able to handle 225 A peak current with a power factor of 0.95. The results also provide voltage, current, and power factor values at different operating points. These values will be used to estimate capacitor current stress.

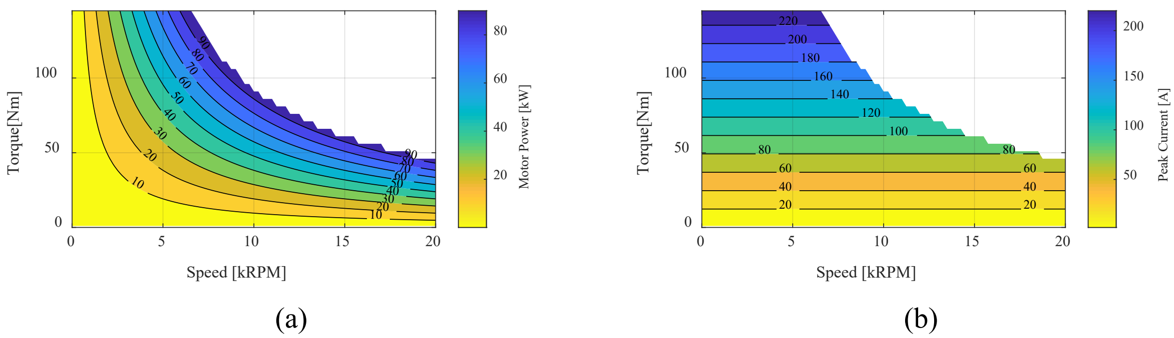

Figure I.1.4.2. (a) Torque-speed characteristics of the developed motor and (b) motor phase current for all operating conditions.

Capacitor Sizing, Characterization, and Packaging

DC bus capacitors occupy substantial space in an electric vehicle traction inverter, which limits the traction drive's volumetric power density. Typically, film capacitors are used; however, other capacitor technologies with higher energy densities can help reduce the overall size. Therefore, three commercial capacitor technologies were considered for use as DC bus capacitors: film, multilayer ceramic capacitor (MLCC), and lead lanthanum zirconate titanate (PLZT). The initial study proved that the ceramic-based capacitor has much higher energy density and current handling capacity per unit volume than the film capacitors [4]. Among the ceramic capacitor technologies, PLZT showed high-temperature operation and higher reliability owing to internal series-parallel connection [4]. The capacitance also demonstrated a negative temperature coefficient [4]. Therefore, the PLZT capacitor technology was selected for this project. Next, the capacitor bank was sized based on the motor currents shown in Figure I.1.4.2(b). The capacitor bank was sized taking into consideration segmented inverter topology that can help reduce the capacitor root mean square (RMS) current stress. Three different modulation techniques were evaluated: (1) carrier-based triangular modulation with 90° phase shift [5], (2) sawtooth with 180° phase shift [5], and (3) discontinuous space vector modulation [6]. The maximum RMS capacitor current is the same for all three modulation techniques and occurs at the knee curve at 100 kW power. The results suggest that the capacitor bank must be able to handle 120 A RMS current (Figure I.1.4.3(a)). The next step in capacitor sizing is to estimate the required capacitance to keep the voltage fluctuation within 5% of the rated voltage. This voltage fluctuation is inversely proportional to the frequency of the capacitor current; therefore, increasing the frequency will decrease the capacitance value for the given fluctuation voltage. A fast Fourier transform was performed over all three capacitor currents to identify the frequency components, as shown in Figure I.1.4.3(b). The triangular modulation technique introduced much higher frequency components; therefore, it required a smaller capacitance value for the same voltage oscillation.

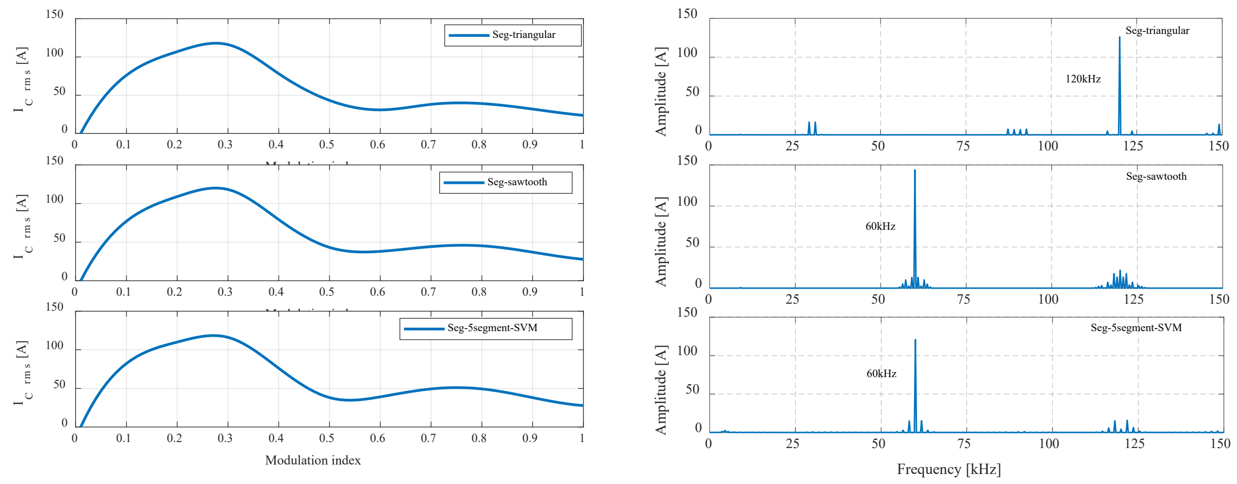

(a) (b)

Figure I.1.4.3. (a) Capacitor RMS current stress from various modulation schemes in segmented inverter showing that all modulation techniques introduce similar capacitor current and (b) frequency of the capacitor current for various modulation schemes showing that triangular modulation with 90° phase shift will introduce much higher frequency in the capacitor current.

A simulation-based approach identified the required capacitance value, where the capacitor current is integrated and then divided by the required voltage oscillation, which is 40 V (5% of 800 V bus) as shown in Eqs. (7–8).

$$i_c = C\frac{\Delta V}{\Delta t} \tag{7}$$

$$C = \frac{\int i_c}{\Delta V} \tag{8}$$

where i_c is the capacitor current, C is the capacitance, Δt is the switching time, and ΔV represents voltage oscillation. The capacitor bank's current conduction and capacitance requirements for different modulation schemes are tabulated in Table I.1.4.1. The results show that the capacitor bank must handle 120 A RMS current with only 15 µF capacitance for the triangular modulation technique and 25 µF for the sawtooth modulation technique. Although 15 µF is enough capacitance to keep the voltage oscillation within the limit, a 25 µF package was developed to evaluate all modulation techniques in a laboratory environment. The capacitor package was designed considering distributed capacitors in which each phase leg of a six-phase inverter will have its capacitor bank. Thus, a 4.2 µF (25 µF/6 phase leg) capacitor package was developed. To achieve the required capacitance value, 15 capacitors were paralleled in a circular printed circuit board (PCB) to achieve a symmetrical layout from the termination point. The symmetrical layout reduced layout inductance and mitigated the current and temperature imbalance that can be seen in traditional flat capacitor boards. The exploded diagram of the proposed circular capacitor package and the assembled capacitor package is shown in Figure I.1.4.4.

Table I.1.4.1. Capacitor Requirements for Various Modulation Techniques

Topology	Modulation	Maximum RMS current (A)	Frequency (kHz)	Required capacitance for 5% voltage ripple (µF)
Segmented	Triangular	113	120	15
	Sawtooth	115	60, 180	25
	Bus clamped	113	60	21

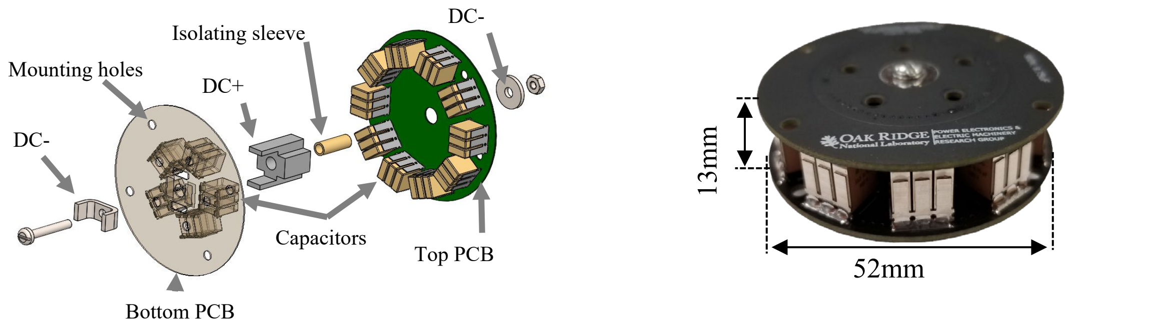

(a) (b)

Figure I.1.4.4. (a) Exploded diagram of the designed circular capacitor and (b) assembled circular capacitor package.

A laboratory test bed was set up to evaluate the designed capacitor’s electrical and thermal performance. The electrical characterization discussed in this section was conducted by connecting two similar capacitors or capacitor packages in series. One was connected to a DC source (for biasing purposes), and the other acted as a DC block. The voltage across the two series capacitors was zero; therefore, any network or component analyzers can be used for small signal analysis. A PCB was designed to characterize the capacitors. It contained two series capacitors, charging-discharging resistors, and a DC supply to vary the bias voltage from 0–800 V.

An environmental chamber was used to evaluate the parameters at various operating temperatures (−25°C–150°C). A network analyzer injected a small AC signal to measure the phase and impedance of the two series-connected capacitors. The results were postprocessed to identify the equivalent circuit parameters of a single capacitor package. The test results are plotted in Figure I.1.4.5. The capacitance of the PLZT capacitor increases with bias voltage up to 800 V, which is an antiferroelectric behavior. The capacitance value showed a different character when the operating temperature was varied; it increased when the temperature varied from −25°C – 75°C, then decreased beyond 75°C.

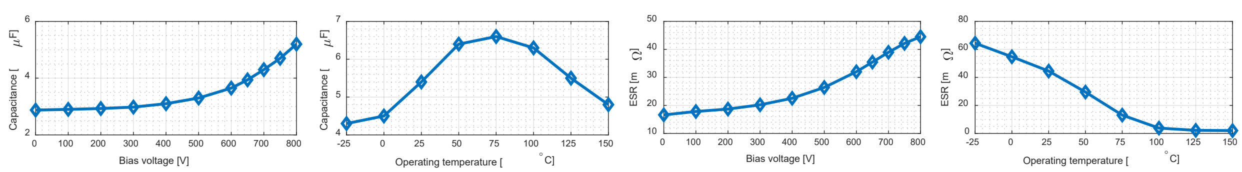

(a) (b) (c) (d)

Figure I.1.4.5. Circular capacitor’s electrical characteristics: (a) capacitance variation with bias voltage, (b) capacitance variation with operating temperature, (c) equivalent series resistance (ESR) variation with operating voltage, and (d) ESR variation with operating temperature.

This capacitance behavior with temperature ensures current balancing among the parallel capacitor branches and avoids thermal runaway. Another challenge with PLZT capacitors is the increment in equivalent series resistance (ESR) with bias voltage (Figure I.1.4.6(c)), which is much higher than the similarly sized film or ceramic capacitors [4]. The ESR reduces drastically with operating temperature and reaches a steady state at around 100°C (Figure I.1.4.5(d)), suggesting that this type of capacitor will perform best if operated at more than 100°C.

After detailed electrical characterization, the developed capacitor package’s thermal performance was evaluated. The performance of the capacitor was assessed by injecting a high-frequency triangular current. A gallium nitride-based half-bridge power module was used as a synchronous buck converter to transfer energy between the input and output capacitor bank, as shown in Figure I.1.4.6(a). An inductor was used in series with the test capacitor, and the inductance value was varied to keep the RMS current constant at 40 A at different operating frequencies; results at 60 kHz are shown in Figure I.1.4.6(b). According to the datasheet, these capacitor packages will handle more than 100 A current at 85 kHz. Nevertheless, in this case, the maximum RMS current is limited to 40 A to keep the gallium nitride device temperature below 130°C. All the assembled capacitor packages were painted black, and a thermal camera captured the results at the various switching frequencies. Images captured by the thermal camera for traditional flat and circular designs are shown in Figure I.1.4.7. The images show the asymmetric temperature distribution of flat capacitor boards and point to the fact that the connector is cooling down the capacitors close to the terminations. This phenomenon can also be seen in an actual inverter system in which the bus bar may be at a lower temperature than the capacitor board and will act as a heat sink for some capacitors.

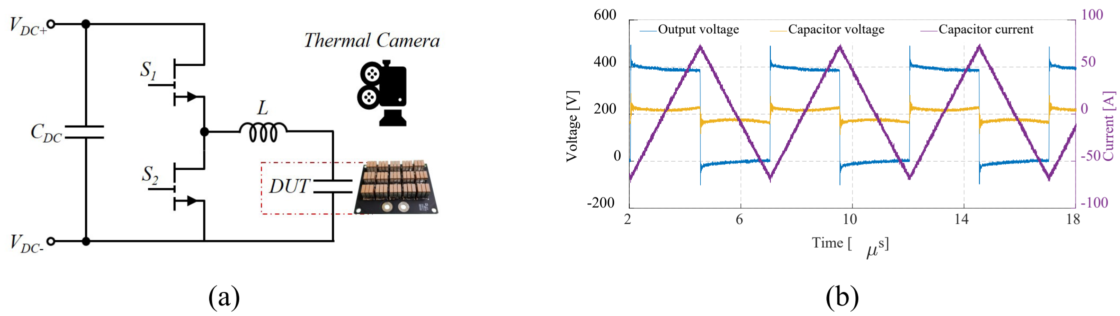

Figure I.1.4.6. (a) Thermal evaluation setup using gallium nitride-based half-bridge synchronous buck converter for triangular current injection and (b) injected current waveform with output and capacitor voltage.

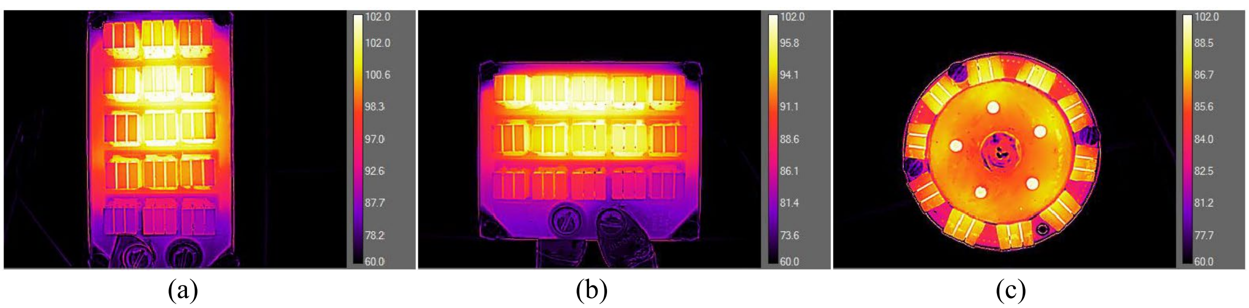

Figure I.1.4.7. Thermal camera images showing packaged capacitors temperature distribution (°C): (a) asymmetric temperature distribution of the 3 × 5 flat capacitor board at 60 kHz, (b) asymmetric temperature distribution of the 5 × 3 flat capacitor board at 60 kHz, and (c) symmetric temperature distribution of the circular capacitor board at 60 kHz.

Asymmetrical temperature distribution will decrease the operating lifetime of the flat capacitor board. However, the circular capacitor board shows a more symmetrical temperature distribution within the inner and outer circle capacitors. Two reasons for the temperature difference between the inner and outer circle are (1) the top PCB covers the inner capacitor circle; therefore, the heat generated in the inner circle is trapped, and (2) the inner circle has a lower copper trace area, which can be easily modified to decrease the temperature difference.

The capacitor packages' maximum, minimum, and average temperatures are shown in Figure I.1.4.8 and are compared in Figure I.1.4.9. Temperatures shown in these figures are the average temperature measured from the top surface of the capacitor. First, the individual capacitor's average surface temperature was measured to identify the minimum and maximum temperature. Then the total average was calculated based on the average temperature of all 15 parallel capacitors. Bottom capacitors were exposed in the circular capacitor board for thermal measurement; therefore, aforementioned averaging method was used. The capacitors soldered to the top boards were buried inside; therefore, small holes were created to take the thermal measurement from the bottom surface of the capacitor. The results listed in Table I.1.4.2 show that the circular capacitor has a lower temperature difference among the parallel capacitor branches, and the temperature variation with frequency is minimal compared to traditional flat designs. The results suggest that the symmetrical distribution of discrete capacitors improves electrical performance by improving layout inductance and symmetrical thermal distribution, thus improving the overall inverters' performance and lifetime.

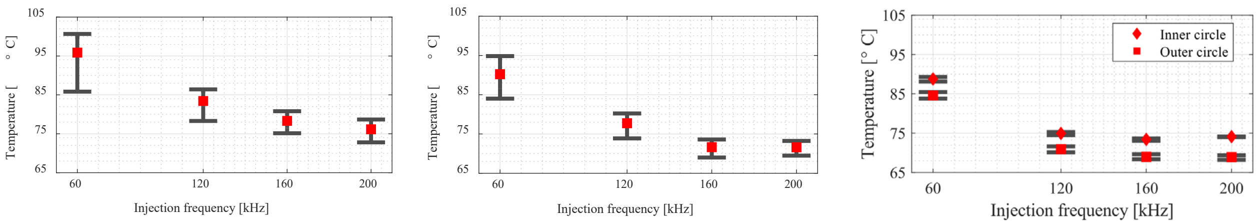

(a) (b) (c)

Figure I.1.4.8. (a) Capacitor temperature for 3 × 5 flat capacitor board at various injection frequencies, (b) capacitor temperature for 5 × 3 flat capacitor board at various injection frequencies, and (c) capacitor temperature for proposed circular capacitor board at various injection frequencies.

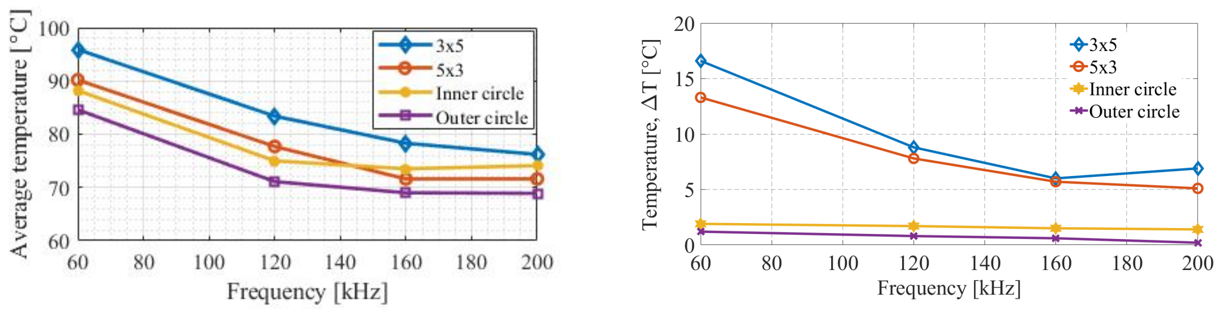

(a) (b)

Figure I.1.4.9. (a) Average temperature variation for different packages and (b) temperature variation among the parallel capacitor branches for different packages.

Table I.1.4.2. Designed circular capacitor parameters

Parameters	Values	Comments
Volume	0.028 L	Total 0.168 L
Capacitance	4.2–6 µF	100 kHz
Required current	20 A	Segmented inverter
ESR	2.73 mΩ	100 kHz, 100°C
ESL-circular	3 nH	10 MHz
ESL-flat-3 × 5	4.9 nH	10 MHz
ESL-flat-5 × 3	5.3 nH	10 MHz
Temperature difference, ΔT	1.8°C	Almost invariant with frequency

Conclusions

This report identifies the dimensions inside the outer rotor motor to evaluate the size and shape restriction for inverter components. The challenge posed by the integration was to miniaturize inverter components (i.e., heat sink, substrate, capacitors) without sacrificing performance. This project investigated capacitors, where three capacitor technologies: film, MLCC, and PLZT were evaluated for power density and performance. Previous results suggested that PLZT may yield the best solution in terms of power density and thermoelectrical performance.

The capacitor bank was sized based on the designed motor, and a new symmetrical (i.e., circular) capacitor package was proposed to improve electrical and thermal performance. Two test beds were set up to evaluate the electrical and thermal performance. The results showed that the designed circular package has 40% less layout inductance and 80% lower change in temperature among parallel capacitor branches at 120 kHz compared with traditional flat capacitor boards. The results show that ceramic capacitors with segmented inverter topology can decrease the capacitor volume by 70%. Moreover, advanced capacitor packaging techniques can improve electrical and thermal performance, which leads to increased lifetime.

Key Publications

1. Husain, I., B. Ozpineci, M.S. Islam, E. Gurpinar, G. Su, W. Yu, S. Chowdhury, L. Xue, D. Rahman, and R. Sahu. "Electric Drive Technology Trends, Challenges, and Opportunities for Future Electric Vehicles." *Proceedings of the IEEE* 109, no. 6 (2021): 1039–1059. doi: 10.1109/JPROC.2020.3046112.

2. Cousineau, J., K. Bennion, S. Narumanchi, S. Chowdhury, and B. Kekelia. "Comparison of Thermal Management Approaches for Integrated Traction Drives in Electric Vehicles: Preprint." United States. Available at https://www.osti.gov/servlets/purl/1710139.

3. Chowdhury, S., B. Ozpineci, E. Gurpinar, and R. Sahu. High-Performance Capacitor Packaging for Next Generation Power Electronics. IP: 202004713, accepted for provisional patent application [05/18/2021].

4. Chowdhury, S., Raminosoa, T., Ozpineci, B., Wiles, R.H., Gurpinar, E., Su, G.J., Pries, J.L. Highly Integrated Electric Drive with Outer Rotor Motor. IP: 201904474 accepted for provisional patent application [05/24/2021].

References

1. U.S. DRIVE Partnership. *Electrical and Electronics Technical Team Roadmap*. U.S. DRIVE, U.S. Department of Energy, October 2017. Available at https://www.energy.gov/sites/prod/files/2017/11/f39/EETT%20Roadmap%2010-27-17.pdf.

2. Throne, D., F. Martinez, R. Maguire, and D. Arens. *Integrated Motor/Drive Technology with Rockwell Connectivity*, November 2021 Available at http://www.cmafh.com/enewsletter/PDFs/IntegratedMotorDrives.pdf.

3. Chowdhury, S., E. Gurpinar, G. Su, T. Raminosoa, T. A. Burress, and B. Ozpineci. "Enabling Technologies for Compact Integrated Electric Drives for Automotive Traction Applications." In *Proceedings of the 2019 IEEE Transportation Electrification Conference and Expo (ITEC)*, Detroit, MI, 2019, pp. 1–8. doi: 10.1109/ITEC.2019.8790594.

4. Chowdhury, S., E. Gurpinar, and B. Ozpineci. "High-Energy Density Capacitors for Electric Vehicle Traction Inverters." In *Proceedings of the 2020 IEEE Transportation Electrification Conference & Expo (ITEC)*, Chicago, IL, 2020, pp. 644–650. doi: 10.1109/ITEC48692.2020.9161588.

5. Su, G., and L. Tang. "A Segmented Traction Drive System with a Small DC Bus Capacitor." In *Proceedings of the 2012 IEEE Energy Conversion Congress and Exposition (ECCE)*, Raleigh, NC, 2012, pp. 2847–2853. doi: 10.1109/ECCE.2012.6342375.

6. Su, G. "High-Voltage, High-Power Density Traction Drive Inverter." Presented in DOE annual merit review, October 17, 2021. Available at https://www.energy.gov/sites/default/files/2021-06/elt209_su_2021_o_5-14_246pm_KS_TM.pdf.

Acknowledgements

The principal investigator wishes to thank project team members: Emre Gurpinar, Raj Sahu, Gui-Jia Su, Tsarafidy Raminosoa, and Jon Wilkins of Oak Ridge National Laboratory for their contributions and Bidzina Kekelia of National Renewable Energy Laboratory for collaboration.

I.1.5 Power Electronics Thermal Management (National Renewable Energy Laboratory)

Gilbert Moreno, Principal Investigator
National Renewable Energy Laboratory
15013 Denver West Parkway
Golden, CO 80401
Email: gilbert.moreno@nrel.gov

Susan Rogers, DOE Technology Development Manager
U.S. Department of Energy
Email: susan.rogers@ee.doe.gov

Start Date: October 1, 2019 End Date: September 30, 2024
Project Funding: $350,000 DOE share: $350,000 Non-DOE share: $0

Project Introduction

The 2017 *Electrical and Electronics Technical Team Roadmap* [1] proposes aggressive research and development targets aimed at improving power electronics technology to enable the mass-market penetration of electric-drive vehicles. Achieving these aggressive targets will require a decrease in cost (year 2025 cost target: $2.70/kW) and an increase in power density (year 2025 power density target: 100 kW/L) as compared with current on-road technology. Replacing traditional silicon device-based components with more efficient and higher-temperature wide-bandgap (WBG) semiconductor device-based components will enable increased power density. However, meeting the power density target will also require innovative thermal management solutions to increase the heat fluxes dissipated and allow for compact electronics packaging.

This project conducts research to develop new power electronics thermal management technologies to increase power density, enable high WBG temperature operation, and decrease cost. The performance (e.g., thermal resistance, pumping power) of the power electronics cooling technologies developed in this project are compared to the performance of current, on-road technology. One of the main challenges to achieving high power densities is associated with packaging high-temperature (up to 250°C) WBG devices near lower-temperature-rated components (e.g., electrical boards and capacitors).

Objectives

The primary project objective is to develop novel thermal management technologies to enable achieving the 100-kW/L power density target. Additional project objectives are to:

- Develop cooling solutions that enable high-heat-flux, high-temperature WBG operation and low-temperature, low-cost capacitors.
- Decrease cost by proposing low-cost cooling technologies that enable decreasing the number of semiconductor devices and use automotive-qualified fluids (e.g., water-ethylene glycol [WEG], automatic transmission fluid [ATF]).

Approach

A dielectric fluid, single-phase heat-transfer cooling concept is proposed for cooling automotive power electronics. Dielectric fluids have poor thermal properties compared with WEG, but they enable a redesign of the power module to eliminate thermal bottlenecks (i.e., dielectric ceramic) within the package. Jet impingement configurations are used to augment the fluid’s convective cooling and counterbalance the fluid’s poor properties. The single-phase dielectric fluids proposed are synthetic hydrocarbons (oils), have properties similar to ATFs, are relatively inexpensive, and are environmentally friendly (e.g., global warming potential <1). This proposed cooling concept may enable the use of new driveline fluids (ATF-like fluids) that are tailored for these power electronics cooling applications. Single- and double-side-cooled dielectric fluid concepts are designed via modeling, and their performance was predicted and compared to current, on-road technology. Experiments were conducted and used to validate model predictions under different operating conditions (e.g., different fluid flow rates, types, and temperatures).

Results

In prior work, a single-side-cooled dielectric fluid cooling system was designed through computational fluid dynamics (CFD) modeling using Alpha 6 as the coolant [2], [3]. The dielectric fluid system uses dielectric-fluid slot jets impinging on finned surfaces and is predicted to provide a high thermal performance (specific thermal resistance [R''_{th} = 22 mm^2·K/W]) and require a low pumping power (0.2 W). This year, experiments were conducted with a single-side cooling prototype to measure its performance with two fluids (dielectric fluid AmpCool-100 [AC-100] and ATF [Ford Mercon LV]), and the results were compared to model predictions. Two double-side-cooled, dielectric fluid concepts were also designed via modeling. The experimental results for the single-side concept and model predictions for the double-side-cooled concept are provided in the following sections.

Experimental Validation (Single-Side-Cooled Concept)

A prototype of the single-side-cooled dielectric fluid concept was fabricated and its performance was measured. The single-side-cooled concept was designed to cool 12 devices (three-phase inverter scale) and dissipate 2.2 kW of heat (estimated heat load for a 100-kW WBG inverter). The fluid manifold was composed of three parts—two manifold enclosure components and one jet manifold. The manifold enclosure was computer numerical control (CNC)-machined out of polyether ether ketone (PEEK) and the jet manifold was 3D-printed out of polycarbonate. An injection molding fabrication process may be used for mass manufacturing of the fluid manifold components. The cold plate fins were fabricated by Wieland using their MicroCool fabrication process. The fabricated finned heat spreader has fins that are slightly curved and has 15 fins, compared with the 16-fin design used in the CFD modeling. Twelve resistive heaters were used to simulate heat from 5×5-mm silicon carbide (SiC) metal-oxide-semiconductor field-effect transistors (MOSFETs). Figure I.1.5.1Figure I.1.5.3 shows computer-aided design (CAD) drawings for all the components including the finned heat spreaders, heating block, and fluid manifold components. Pictures of the fabricated components are provided in Figure I.1.5.2.

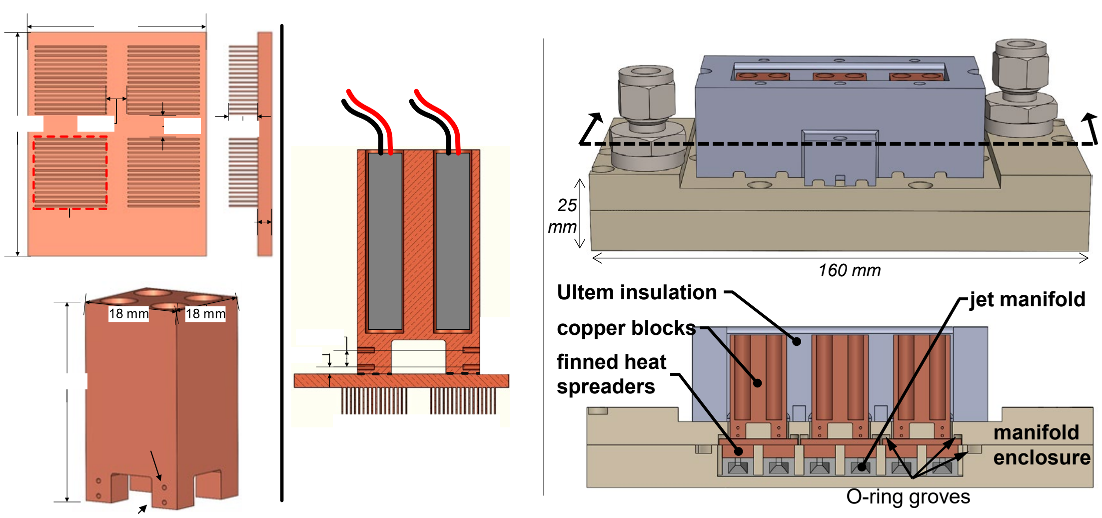

Figure I.1.5.1 CAD drawings of the finned heat spreader and copper heated block (left) and the entire single-side-cooled thermal management system (right)

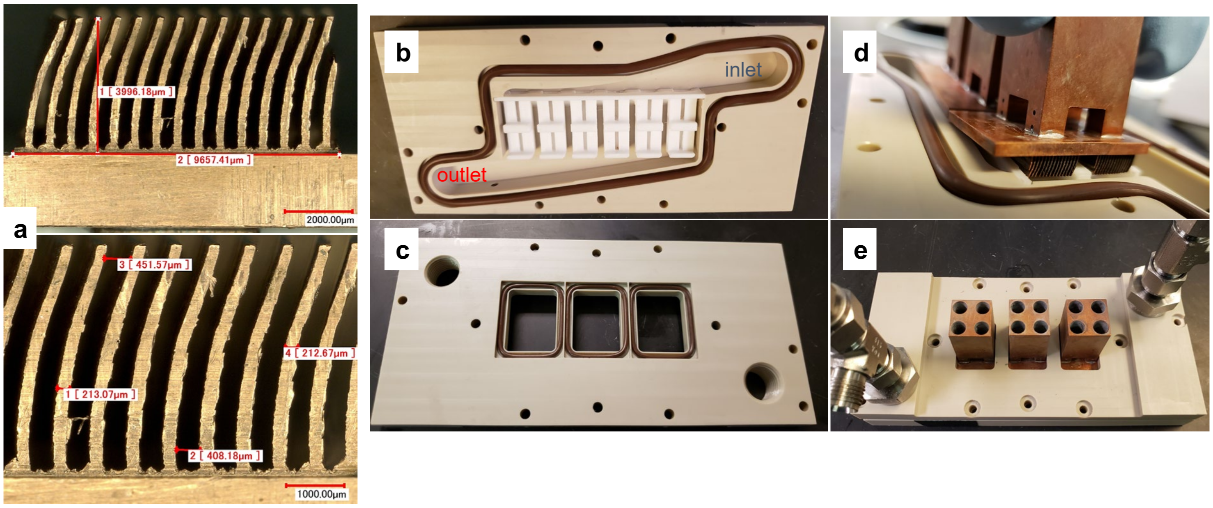

Figure I.1.5.2 Images of the fins (a) and dielectric fluid distribution system: fluid manifold components (b, c), heat spreader with copper block (d), and fully assembled system (e)

Figure I.1.5.3 shows the dielectric fluid loop that was used to measure the performance of the dielectric fluid cooling concept. The loop includes a fluid reservoir with internal heating coil, speed-controlled gear pump, filter, gear flow meter, air-cooled heat exchanger, and test sample (i.e., dielectric fluid cooling prototype). The reservoir is first filled with about 1 liter of dielectric fluid, and the fluid is heated to the desired set point using a chiller/heater circulator and internal (to the reservoir) heating coil. The speed-controlled gear pump is then used to circulate fluid through the test sample, and its speed is adjusted to achieve the desired flow rate. A LabVIEW program controls a data acquisition system and power supply to conduct the experiments. More information on the design of the dielectric fluid concept and fluid loop can be found in prior year-end reports [2–3]. Experiments were then conducted to measure the heat exchanger thermal resistance versus pumping power of the dielectric fluid concept for the two fluids at different fluid flow rates and temperatures.

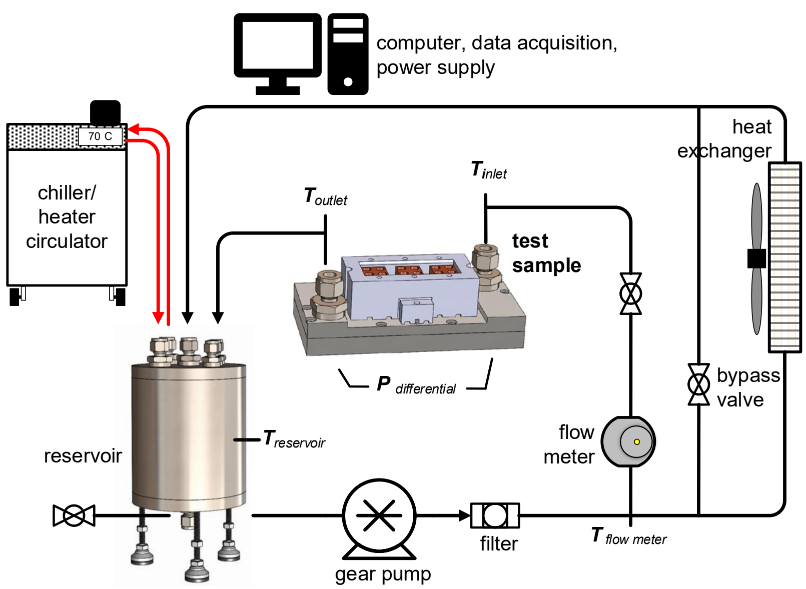

Figure I.1.5.3 Schematic of the dielectric fluid loop. Temperature (T) and pressure (P) sensor locations are indicated in the schematic

The heat exchanger case-to-fluid thermal resistance ($R''_{th,\, case\text{-}fluid}$) was measured and defined per Equation 1:

$$R''_{th,\, case-fluid} = \frac{Area\,(\overline{T_{case}} - T_{fluid})}{Heat_{per\ device}} \qquad (1)$$

where *Area* is the 5×5-mm area of the heat source (equal to the SiC devices being simulated), $\overline{T_{case}}$ is the average temperature at the heat spreader base, T_{fluid} is the fluid inlet temperature, and $Heat_{per\ device}$ is the heat dissipated per heater. These experiments measured the thermal performance of the heat exchanger (heat exchanger base to fluid) and not the junction-to-fluid resistance because actual devices were not used in these experiments.

Figure I.1.5.4 plots the thermal resistance (Eq. 1) versus the pumping power, defined as the product of the volumetric flow rate and the total (inlet to outlet) pressure drop for AC-100 and ATF. Measurements were taken at different fluid flow rates (1–4 L/min) and fluid temperatures (30°C and 70°C). The experimental results and associated 95% confidence interval error bars are provided alongside the CFD model predictions. Overall, there is a good match in the thermal resistance versus pumping power trend between experiments and model predictions. The maximum thermal resistance deviation between experiments and model is about 10% (experiments ≤ 10% higher than model predictions). More discrepancy (~14%) between model and experiments is observed in the pumping power for ATF at the highest flow rate. The difference between experimental and modeling results are partially associated with lower total fin area (~8% lower) for the fabricated heat spreader compared with the model (e.g., the fabricated heat spreaders had 15 fins compared with the 16 fins used in the model).

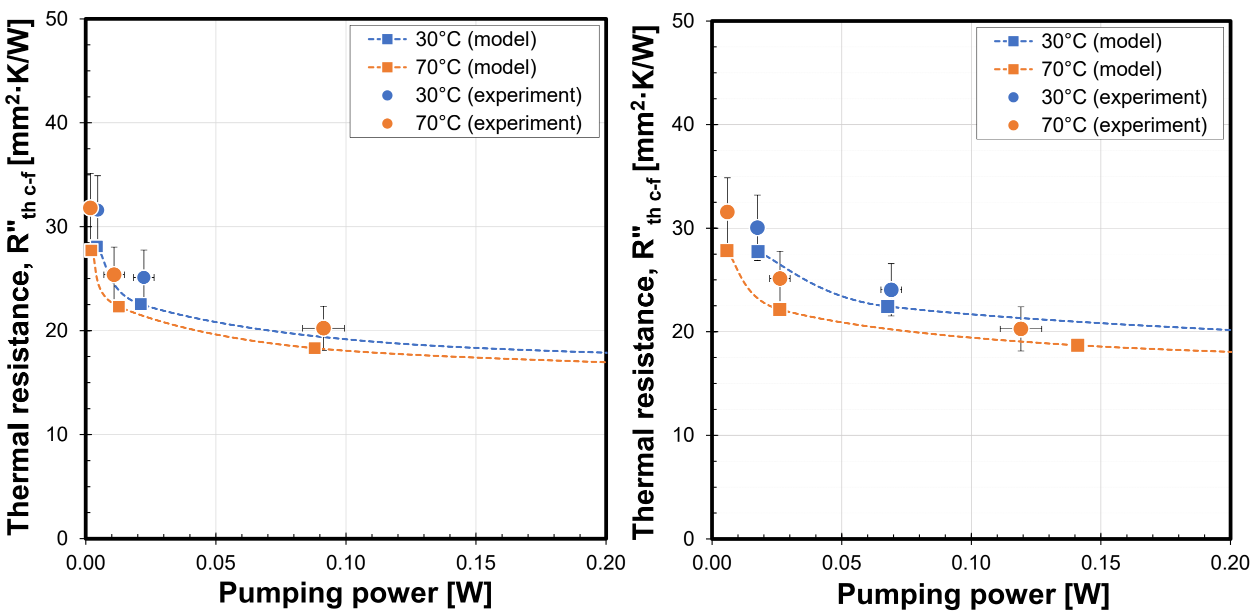

Figure I.1.5.4 Experimental and modeling results for AC-100 (left) and ATF (right)

Figure I.1.5.5 compares the experimentally measured performance of AC-100, ATF, and Alpha 6. Alpha 6 results were taken from the 2020 year-end report [3]. The results show that all fluids provide about the same thermal resistance value when compared at the same flow rate. However, AC-100 consistently provides the lowest pumping power due to its lower viscosity compared with the other two fluids. The lower pumping power (i.e., pressure drop) of AC-100 makes it a good candidate for power electronics cooling applications. ATF and Alpha 6 provide similar performance (thermal resistance and pumping power) because they have similar viscosity versus temperatures characteristics.

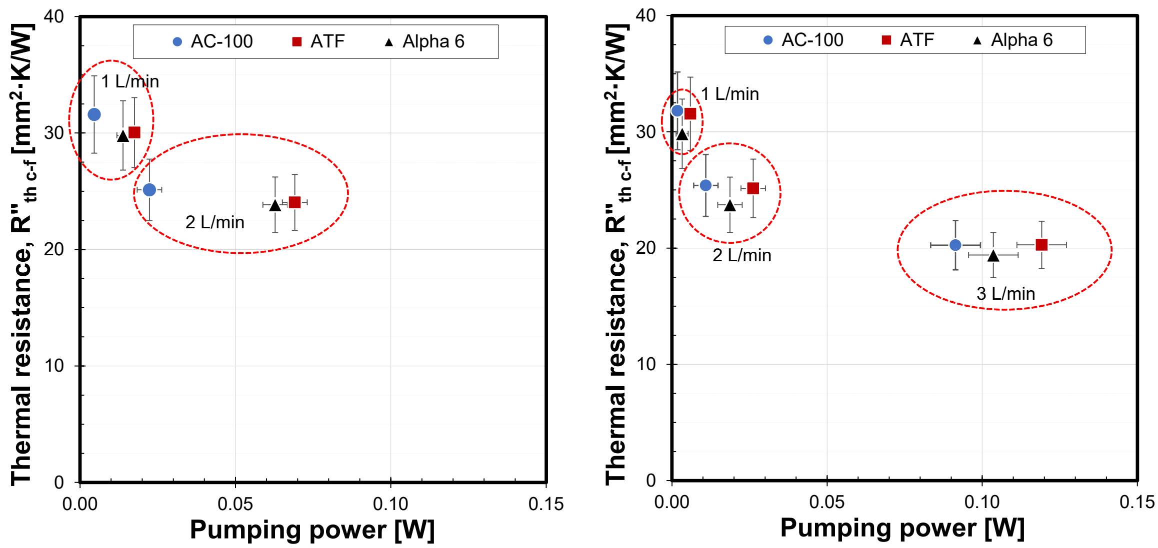

Figure I.1.5.5 Comparisons of the experimentally measured thermal resistance versus pumping power values for the three fluids—30 °C results (left) and 70 °C results (right). The dashed red circles group the results according to the flow rate

Double-Side, Dielectric Fluid Cooling Concept

Parallel-flow and a series-flow concept were designed to cool the top and bottom sides of the modules (Figure I.1.5.6) [4]. These double-side-cooled concepts use dielectric fluid slot jets impinging on finned heat spreaders bonded to both sides of the semiconductor devices. The cooling concept was designed to cool 12 SiC devices with two devices per switch position. The parallel flow configuration equally divides the total flow rate between the 24 slot jets (12 on top side and 12 on bottom side) to provide both sides with the same low-temperature fluid. The series-flow configuration sequentially flows fluid through each side of the module and requires lower flow rates compared to the parallel flow configuration. Both double-side-cooled concepts use the same fin design used for the single-side-cooled concept.

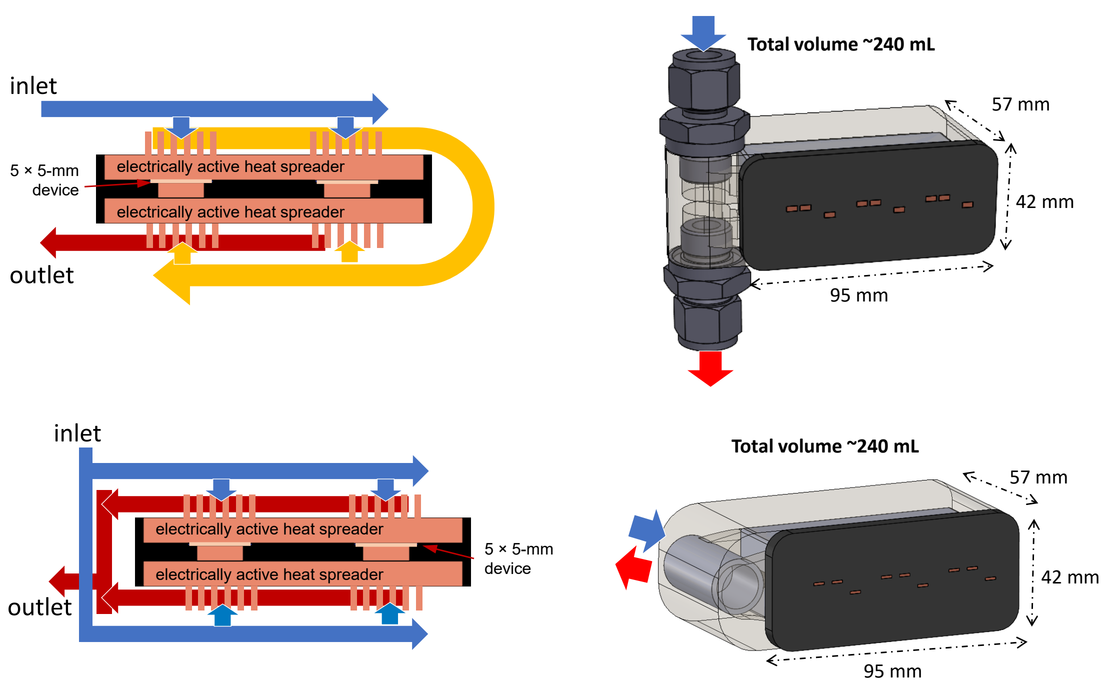

Figure I.1.5.6 Schematics and 3D CAD drawings of the series-flow (top) and parallel-flow (bottom) double-side-cooled, dielectric fluid concepts

Detailed modeling was initially conducted with the series-flow concept because preliminary analyses indicated that the series-flow configuration could provide a slightly lower thermal resistance than the parallel configuration when compared at the same pumping power. The CFD-computed velocity streamlines and temperature contours for the series-flow concept at 4-L/min total flow rate, AC-100 fluid, 70°C inlet temperature, and 2.2 kW of total heat dissipation are shown in Figure I.1.5.7. The average slot jet velocities are 0.3 m/s and the total pressure drop from the inlet to the outlet is computed to be a relatively low 0.6 psi. The maximum junction temperatures are predicted to be ~156°C at 716-W/cm^2 device heat flux to provide a junction-to-fluid thermal resistance of 12 mm^2-K/W. The double-side concept reduces temperatures by ~64°C compared to the single-side concept at 716-W/cm^2 device heat flux and operates below the 175°C temperature limit typical of today's SiC power modules.

Table I.1.5.1 provides the performance metrics for the single- and double-side dielectric fluid cooling concepts and compares them to the 2015 BMW i3 performance. The heat flux is computed assuming 175°C maximum junction temperature and 70°C inlet fluid temperatures. The results shown in Table I.1.5.1 are computed assuming 175°C maximum junction temperature whereas the results in Figure I.1.5.7 are computed at 156°C maximum junction temperature (716 W/cm^2 heat flux). As shown, both dielectric fluid concepts outperform the 2015 BMW i3 and provide lower thermal resistance and pumping power within a smaller volume. The double-side-cooled concept is predicted to lower the thermal resistance and pumping power by ~75% and ~80%, respectively, compared to the 2015 BMW i3 and allow for a device heat flux >800 W/cm^2 at $T_{j,\,maximum}$ = 175°C.

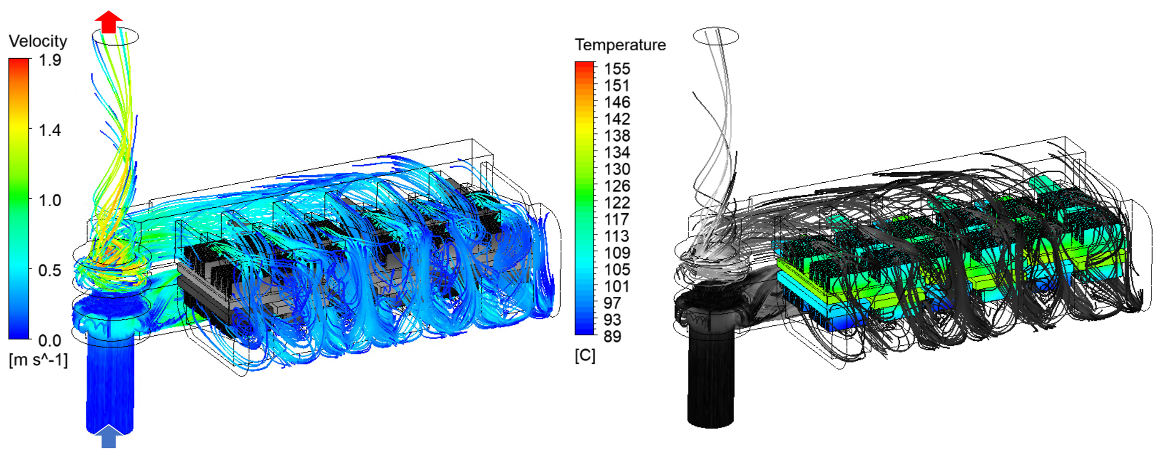

Figure I.1.5.7 CFD-computed velocity streamlines (left) and temperatures (right) for the double-side-cooled, dielectric fluid series-flow design

Table I.1.5.1 Performance Metrics for the Two Dielectric Fluid Concepts; Reference Data Are Provided for the 2015 BMW i3 for Comparison

System	Thermal resistance (junction-to-fluid)	Flow rate	Pressure drop	T_j maximum	Device heat flux (Assuming T_{inlet} = 70°C)	Total volume (power modules and cold plate)
	mm²·K/W	*L/min*	*Psi [kPa]*	*°C*	*W/cm²*	*mL*
2015 BMW i3, (WEG cooled)	49	10	1.4 [9.6]	175	214	900
Single-side cooled dielectric fluid	**20**	**4.1**	**0.2 [1.4]**	**175**	**525**	**120**
Double-side cooled dielectric fluid	**12**	**4.1**	**0.6 [4]**	**175**	**875**	**240**

Conclusions and Future Work

The project's major conclusions are summarized below:

- Experiments were conducted to measure the heat exchanger performance using AC-100 dielectric fluid and ATF at various fluid flow rates and temperatures. The experimental results were in good agreement with model predictions.
- Experimental results show that the three fluids evaluated (Alpha 6, AC-100, ATF) provide approximately the same heat exchanger thermal resistance when compared at the same flow rate. However, the pressure drop (pumping power) does vary between fluids due to differences in viscosity. AC-100 consistently provides the lowest pumping power due to its relatively low viscosity.
- Parallel-flow and series-flow double-side-cooled, dielectric fluid concepts were designed. The series-flow concept is predicted to allow for T j, maximum = 156°C at heat flux of 716 W/cm2, resulting in a junction-to-fluid thermal resistance of 12 mm2-K/W. The total pressure drop for the series flow concept was estimated to be a relatively low 0.6 psi.
- The results presented in this report demonstrate the thermal performance advantages of redesigning the power module to eliminate the ceramic material and reduce the package conduction resistance. Moreover, the use of more aggressive cooling strategies like jet impingement can be used to enhance convective heat transfer coefficients and offset the poor fluid properties associated with most dielectric fluids. The dielectric fluids may also enable efficient cooling of the bus bars to decrease capacitor and gate driver temperatures.

Future Work

- We will evaluate the long-term reliability of the dielectric fluids under simulated operating conditions.
- We will fabricate a SiC module (current work used resistance heaters to simulate the SiC devices) that uses a dielectric fluid cooling solution and conduct experiments to measure the junction-to-fluid thermal resistance.
- We will co-optimize the thermal and thermomechanical performance of the double-side-cooled, dielectric fluid concept to further improve performance.

Key Publications and Patent Applications

1. Moreno, G. 2020. "Power Electronics Thermal Management." In *Electrification: 2020 Annual Progress Report*, U.S. Department of Energy Office of Energy Efficiency and Renewable Energy Vehicle Technologies Office, Washington, D.C.
2. Moreno, G., et al. 2021. "Electric-Drive Vehicle Power Electronics Thermal Management: Current Status, Challenges, and Future Directions." *ASME Journal of Electronic Packaging*, 144 (1): 011004.
3. Moreno, G., et al. 2021. "Jet Impingement Manifolds for Cooling Power Electronics Modules." US20210212242A1, filed October 29, 2019.

References

1. U.S. DRIVE. 2017. *Electrical and Electronics Technical Team Roadmap: October 2017*. U.S. Department of Energy Office of Energy Efficiency and Renewable Energy Vehicle Technologies Office, Washington, D.C.
2. Moreno, G. 2019. "Power Electronics Thermal Management." In *Electrification: 2019 Annual Progress Report*, U.S. Department of Energy Office of Energy Efficiency and Renewable Energy

Vehicle Technologies Office, Washington, D.C. https://www.energy.gov/sites/prod/files/2020/06/f76/VTO_2019_APR_ELECTRIFICATION_FINAL_compliant_.pdf.

3. Moreno, G. 2020. "Power Electronics Thermal Management." In *Electrification: 2020 Annual Progress Report*, U.S. Department of Energy Office of Energy Efficiency and Renewable Energy Vehicle Technologies Office, Washington, D.C. https://www1.eere.energy.gov/vehiclesandfuels/downloads/VTO_2020_APR_ELECTRIFICATION_COMPILED_REPORT_July%2014%20compliant_.pdf

4. Moreno, G., Narumanchi, S., Bennion K., Kotecha, R., Paret, R., and Xuhui, F. 2021. "Jet Impingement Manifolds for Cooling Power Electronics Modules." US20210212242A1, filed October 29, 2019, and published July 8, 2021.

Acknowledgments

The significant contributions of Xuhui Feng, Ramchandra Kotecha, Sreekant Narumanchi, and Jeff Tomerlin are acknowledged. A portion of the research was performed using computational resources sponsored by the U.S. Department of Energy's Office of Energy Efficiency and Renewable Energy located at the National Renewable Energy Laboratory.

I.1.6 Magnetics for Ultra-High Speed Transformative Electric Motor (Ames Laboratory)

Iver Anderson, Principal Investigator
Ames Laboratory (USDOE), Iowa State University
222 Metals Development, Iowa State University
Ames, IA 50011
Email: andersoni@ameslab.gov

Matthew Kramer, Principal Investigator
Ames Laboratory (USDOE), Iowa State University
125 Metals Development, Iowa State University
Ames, IA 50011
Email: mjkramer@ameslab.gov

Jun Cui, Principal Investigator
Ames Laboratory (USDOE), Iowa State University
106 Wilhelm, Iowa State University
Ames, IA 50011
Email: cuijun@ameslab.gov

Susan A. Rogers, DOE Technology Development Manager
U.S. Department of Energy
Email: susan.rogers@ee.doe.gov

Start Date: March 1, 2019 End Date: September 30, 2023
Project Funding: $600,000 DOE share: $600,000 Non-DOE share: $0

Project Introduction

This project is part of the multi-lab Electric Drive Systems Consortium that will leverage U.S. research expertise and facilities at the national labs and universities to improve the power density of electric drives by 10x compared with the 2015 numbers while reducing the cost by 50% and doubling the lifetime miles within the next 5 years. The project is organized around three Keystones: (1) Power Electronics; (2) Electric Motors; and (3) Traction Drive System. The research activities at Ames support the Electric Motors Keystone 2 project.

The DOE 2025 target on electric motor power density is 50 kW/L. Such an aggressive target limits the choices for permanent magnets (PM) to the most powerful Nd-Fe-B based magnets, whose magnetic properties are strongly temperature dependent. Better thermal stability is achieved currently by adding significant amounts of Co and Dy [1], both with increased cost. Unfortunately, Dy is extremely scarce and highly localized in supply. The U.S. Department of Energy (DOE) highlighted Dy as the single most critical strategic metal not only in the U.S., but world-wide. According to the USGS Minerals Commodities Summaries, the average price of Dy_2O_3 jumped from $295/kg in 2010 to $1410/kg in 2011, then retreated to $179/kg in 2018. Since then, Dy_2O_3 price has been steadily increasing, $239 in 2019, $258 in 2021, and expected to reach $290 in 2022 [2]. With foreseeable large increase in the number of electrical vehicles and their dependence on permanent magnet traction motors, the supply risk for Nd, Pr and Dy is expected to remain at high level with their projected demand to more than double by 2030 [3]. Strategies to mitigate the RE materials criticality issues include increasing and diversifying the supply and reducing demand. While several mines outside of China—in Australia, Vietnam and the US—have opened and have begun production of RE elements, the most desired “heavy” RE (HRE) elements, in particular, Dy and Tb, remain low in supply because none of these newly opened mines are rich in heavy RE reserves. To reduce the demand for heavy RE elements, alternative magnet technologies that eliminate or use much less Dy have to be developed, where Dy is used now for maintaining Nd-Fe-B's coercivity at high temperature [4]. In 2020, Ames Lab researchers have demonstrated that significantly reducing the grain size of a Nd-Fe-B magnet will improve its coercivity, making it possible to use a microstructure engineering grain-refinement approach to replace the chemistry approach, i.e., a Dy addition. However, fine-grain magnet requires ultra-fine feedstock powders (<2 μm), which are much more sensitive to degradation when exposed to oxygen. To manufacture fine grain magnet from ultra-fine powders, the manufacturing process must be modified with additional controls of oxygen. Alternatively, one can passivate the powder and reduce its oxygen sensitivity to that of normal powders (3-5 μm). We plan to focus on developing a novel passivation technology that can enable the mass production of fine-grain magnet using ultra-fine Nd-Fe-B powders.

One viable approach to drastically increase motor power density is to increase motor speed. Although not specified by the DOE 2025 target, 90% efficiency is a key operational limit for electric motors because less efficient motors consume more power (including power for extra motor cooling), impose extra load on the vehicle battery, and diminish the impact of increasing power density. To maintain such high efficiency at high speed, the magnetic materials, especially soft magnetic cores, need to exhibit exceptionally high electrical resistivity in order to minimize otherwise substantially higher loss caused by increased eddy current heating. These tight constraints on materials are further tightened by the 2025 cost target of $3.3/kW, which disqualifies most of the existing advanced soft magnetic materials (e.g., amorphous and nanocrystalline) from meeting these requirements. It appears that one of the barriers for meeting the DOE 2025 targets of 50 kW/L power density is the lack of cost-effective soft magnetic materials that can run at high frequency without excessive eddy current heating. 6.5% Si steel has been demonstrated as a cost effective (from raw materials perspective) advanced soft magnetic materials suitable for high-speed motor application. Previously, Ames researchers have successfully addressed the brittleness problem associated with the high silicon content. However, the developed solution is based on planar flow casting process that requires heavy capital investment. We plan to lower the requirement on the processing equipment by enabling direct use of melt-spun wires, which are much simpler to manufacture than wide thin sheets.

Objectives

This project will develop the PM and SM materials and their processes for high-speed traction drive motors. For PM materials, the objective is to enable fine grain RE permanent magnet free of heavy rare earth elements by developing ultra-fine powder passivation technology. For SM materials, the objective is to lower the application cost of the 6.5% Si steel by developing the novel wire-bundle near-net-shape stator concept that can use be cost-effective melt-spun wires.

Approach

Grain size reduction is a viable approach for eliminating or reducing critical heavy RE (HRE) elements usage in the magnets for PM motors while maintaining their high temperature performance. It is possible to push the coercivity to beyond 20 kOe with ultrafine grains. With such high coercivity at room temperature, even with the typical rate of coercivity decay with increasing temperature (-0.6%/K) [1], there will still be enough coercivity at the 450 K, where the high-speed motor may operate. The challenge for the ultrafine grain approach is to develop feedstock powders with particle size near 1 μm; and more importantly, to keep the grain size near 2 μm during sintering to full density. This also requires development of alternative particle surface passivation methods and extreme care in handing powders to restrict oxidation. In FY20, Ames Lab successfully demonstrated the fine-grain magnet concept. In FY21, Ames Lab carried out investigations of industrially viable processing methods to passivate feedstock powders with particle size (< 3 μm) and demonstrated the effectiveness of NF_3 gas on passivating Nd-Fe-B at elevated temperature. In FY22, Ames Lab will focus on optimizing the passivation process and the bulk magnet fabrication process using the passivated ultrafine powders.

Melt-spinning is a viable approach for enabling 6.5% Si steel for high power density motor applications, in spite of its higher cost than traditional methods for producing common 3.2% Si steel. It has been established that the electromagnetic properties of 6.5% Si steel are superior to that of commonly-used 3.2% Si steel [6], except that the 6.5% Si steel is brittle and cannot be readily mass-produced using the cost-effective slab-casting and cold-rolling method. Ames Lab has showed that 6.5% Si steel becomes ductile after rapid quenching from high temperature [7]. Melt-spinning is traditionally used for manufacturing amorphous and nanocrystalline materials where rapid cooling rate is essential for preventing grain growth. One of the shortcomings of the current industrial planer flow casting is the limited throughput due to the difficulty in making a wide ribbon with smooth surfaces, which requires a thin and steady feeding of molten steel over a wide wheel width. The width ribbon can be manufactured is about 220 mm wide. In comparison, narrow ribbon (or a thin wire) doesn't need control of smooth surface. In theory, one can place many small nozzles in parallel and simultaneously melt-spun steel wires, thereby dramatically increases the productivity. In FY21, Ames lab has completed investigations of melt-spinning related process parameters and developed near-net-shape fabrication concepts for the stator core designed by ORNL using melt-spun wires. Various shape melt-spun 6.5%Si ribbon bundle samples have been made, including rectangular prism and toroid shapes. Optimum melt-spinning parameters and heat treatment conditions were determined. We have also been working closely with our motor collaborators to further refine the stator model for wire bundle implementation, which sets off our FY22 motorette demonstration work. To improve the packing densities and allow for post-assembly annealing, we will pursue the formation of thermally formed oxides for electrical insulation and high-temperature binders for 6.5%Si in FY22.

Permanent magnet traction motors are the most compact and efficient electric drive motors. Their optimization is a fine balance between the properties and topology of SM and PM components and the demagnetization fields. Clearly, a new motor topology with complex flux patterns that can take full advantage of new PM and SM materials is needed. The Ames team will continue to work with ORNL, NREL, and SNL to demonstrate the newly developed magnetics in an electric motor.

Results

Task 1: Develop fine grain RE permanent magnet with high coercivity at high temperature

Ames researchers are developing an in-situ NF_3 coating for passivating ultra-fine Nd-Fe-B powders. Ames have demonstrated the proof of process using high-energy SPEX mill to produce new fresh particle surfaces which are exposed to NF_3 at elevated temperatures and promote a fluorination reaction to form a RE fluoride coating, and thus passivating the fine powders. Ames researchers can control the extent of the passivation by controlling the time-temperature-gas content in the reaction vessel based on the chemical reaction: $2NF_3 + 2RE = 2REF_3 + N_2$. Passivated powders were tested in a TGA with temperature ramping from RT to 300 0176C (dry air). Figure I.1.6.1a shows the non-passivated powder experienced a sudden weight-gain at 260°C due to oxidization, while the weight gain for the passivated powder is gradual and relatively slow. Figure I.1.6.1b shows the non-passivated powder gain weight faster than the passivated powder during isothermal holds at 150 and 200°C in the TGA.

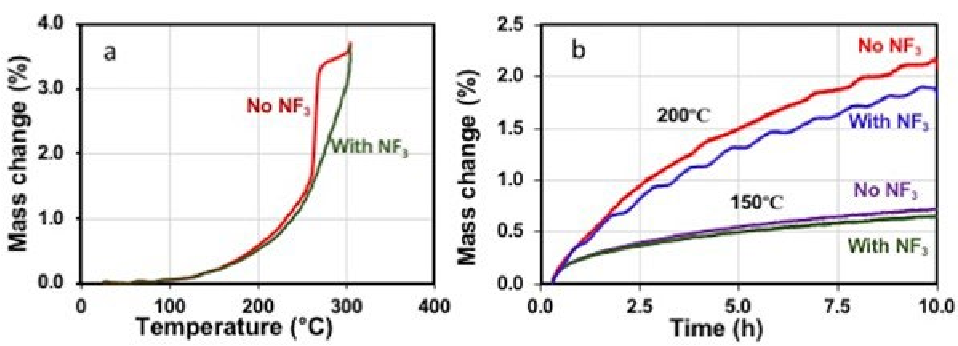

Figure I.1.6.1 TGA curves of passivated and non-passivated powders in dry air. a) ramping temperature from RT to 300°C (10 0176°C/min); b) isothermal holding temperature at 150 and 200°C for 10 hrs.

Our initial work used commercial Dy-free Nd-Fe-B alloy powders which we ball milled conventionally (in liquid cyclo-hexane, without NF_3) up to 11h, causing average particle size to decrease to 2.1 µm, but average grain size of resulting sintered magnets grew to 3.8 µm, due to grain growth from high temperature sintering (1080C). Intrinsic coercivity H_{cj} and maximum energy product $(BH)_{max}$ of these ultrafine grained magnets was 12.7 kOe and 43.6 MGOe. While our new work with high energy milling has further refined feedstock powder size, reduction of sintering temperature also is needed to suppress grain growth in magnets and fully exploit ultrafine grain benefits on magnetics. Thus, an extrinsic transient liquid phase (TLP) sintering aid addition (5wt.%) of Pr-30.2at.%Cu (442°C eutectic), was studied for consolidation at a series of reduced sintering temperatures, down to 1045C. This significantly raised the Hci to 15.6 kOe, benefitting presumably from suppression of grain growth, but reduced the energy product to 35.8 MGOe (Figure I.1.6.2a) because of a reduction in saturation magnetization from the reduced magnet volume that was occupied by the TLP. However, when another 1045°C sintered sample with the TLP addition also was annealed at 480°C, 5h (Figure I.1.6.2b), coercivity rose further to 17.0 kOe without a decrease in MGOe. This promising result was presumably from increased grain defect "smoothing" by penetration of residual liquid TLP further into the magnet microstructure. These improved magnetic properties will be correlated with microstructural analysis to verify these benefits.

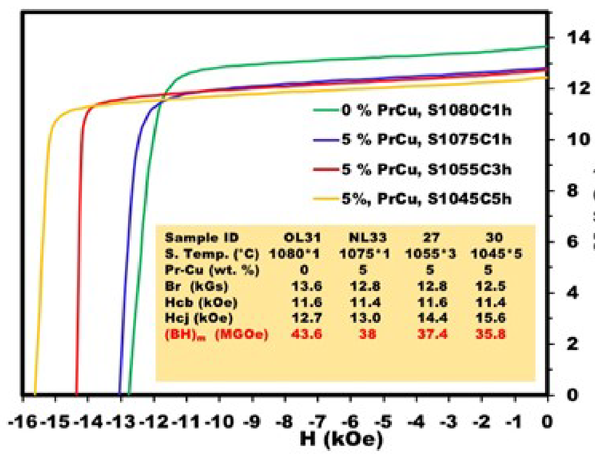

(a)

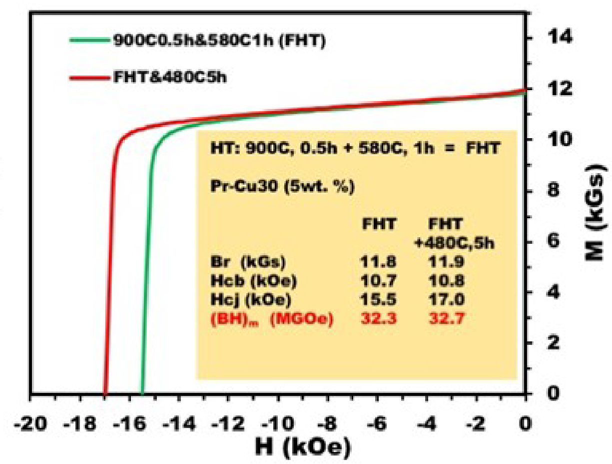

(b)

Figure I.1.6.2 Summary of results on hysteresis graph results on; a) effect of TLP and sintering temperatures on coercivity, and b) effect of 480°C anneal with TLP on coercivity (sample sintered at 1045°C, 5h).

Task 2: Development of cost-effective manufacturing process for high performance soft magnetic materials in thin sheet form

Previous research showed that the planar flow casting method is a suitable manufacturing method for mass production of ductile thin sheets of 6.5% Si steel for motor applications. Such method has been used for producing amorphous and nanocrystalline materials that are ideal for stationary transformer and power electronic applications due their brittleness as the result of nano scale grain size. Most nanocrystalline materials are brittle because grain boundaries' effect in pinning dislocation movement. The melting point of 6.5% Si steel is 1475 0176°C, about 400–600 0176°C higher than those of the amorphous or nanocrystalline metals. Such high processing temperature impose excessive thermal load on the melt spinning system, making it difficult to control nozzle to wheel distance, which in turn, making it difficult to produce wide and smooth ribbons. In FY20, after successfully produced 20 mm wide 6.5% Si steel ribbon, Ames researchers concluded that the capital cost of the wide ribbon approach might be too high for the industry to adopt. An innovative approach is needed to cost-effectively produce rapidly solidified 6.5% Si steel.

In FY21, Ames researchers creatively solved problem with the wire-bundle approach, which only needs ribbon as narrow as 1 mm. These wires can be made with much smaller and cheaper equipment. Moreover, the wire bundle concept enables constant magnetic flux density distribution within the soft magnetic materials. This is superior to the traditional laminate approach where the flux density distribution is non-uniform and only part of the magnetic material is fully utilized. In FY21, various melt-spinning process parameters and heat treatment were investigated for the selection of narrow ribbons with a desired combination of mechanical and magnetic properties. Table I.1.6.1 shows magnetic properties of the ribbons subjected to various processing conditions and compared it to the baseline materials (i.e., the currently widely used 3.2% Si steel). It shows the as-spun 6.5% Si wire bundles have superior magnetic properties than 3.2% Si silicon, and a high-temperature annealing plus aging treatment can further improve its iron losses at various excitation frequencies. Building on the established processing, actual size 6.5% Si U-shape bundle motorette will be built and sent to testing by NREL and ORNL in FY22. Ames researchers will work on spot welding technique to join the ribbons and on thermal processes to grow natural oxide for insulating purpose.

Table I.1.6.1 Magnetic Properties of 3.2% Sheet Sample and Ribbon Bundle Samples of 6.5% with Different Process Parameters

Sample	Wheel speed	Nozzle wheel gap	Thickness ribbon	Thickness sample	Heat treatment status	Hc	DC,μMax @ B max = 1T	DC coreloss @ B max = 1T	B8	B25	B50	W10/60	W10/400	W5/1k	W2/5k	W1/10k
	m/s	mm	mm	mm		A/m	/	J/m^3	Tesla	Tesla	Tesla	W/kg	W/kg	W/kg	W/kg	W/kg
Fe-3.2Si sheet	n/a	n/a	0.35	0.35	GOSi-Steel	9.3	12690	34.84	1.74	1.88	1.94	0.85	16.9	21	56.1	52.9
Fe-6.5Si ribbon	20	10	0.025	0.33	AS+CR	159.9	1032	650.1	0.66	0.95	N/M	N/M	36.7	30.7	33.2	17.6
Fe-6.5Si ribbon	20	10	0.025	0.49	AS+CR+AN	43.4	3849	187.4	1.16	1.31	1.43	1.5	11.1	8.8	11.8	7.3
Fe-6.5Si ribbon	20	10	0.025	0.3	AS+CR+AN+AGE	43.1	4921	189.8	1.15	1.29	1.41	1.47	11.0	8.1	12.2	7
Fe-6.5Si ribbon	10	10	0.07	0.5	AS	62.6	3295	241.6	1.16	1.37	1.49	1.93	14.0	11.5	14.9	8.5
Fe-6.5Si ribbon	10	10	0.07	0.35	AS+AN	35.0	4424	144.8	1.17	1.33	1.45	1.19	**9.4**	**8.1**	**13.2**	**9.5**
Fe-6.5Si ribbon	10	1	0.07	0.4	AS+AN	31.4	4572	135.3	1.19	1.33	1.45	1.1	**9.0**	**7.6**	**12.8**	**9.3**
Fe-6.5Si ribbon	7	1	0.09	0.7	AS+AN	26.9	5376	120.0	1.19	1.33	1.46	1.0	**8.9**	**8.1**	**15.5**	**12.2**
Fe-3.2Si ribbon	10	1	0.07	0.43	AS+AN	70.0	1805	253.9	0.98	1.36	1.53	2.0	**16.0**	**14.3**	**19.1**	**12.3**
Fe-6.5Si-0.9Al	20	1		0.47	AS+AN	50.3	3377	238.5	1.02	1.19	1.30	1.90	**13.7**	**10.0**	**12.7**	**7.7**

GOSi-Steel: Grain oriented silicon steel; W10/60: loss as B = 1T, f = 60Hz; B8: flux density at H = 800 A/m.
AS: 20 m/s as spun; CR: cold roll (30.5% reduction); AN: 1100°C 2h annealing; AGE: 650°C ordering aging; N/M: not measured.

Conclusions

In FY21, the Ames team has been working on development of permanent and soft magnetic materials for the next generation of high power density drive motors. These two efforts were aimed at improving coercivity of PM without HRE elements for motor rotors through grain size refinement and at reducing eddy current losses in motor cores by enabling highly resistive 6.5% Si steel to be cost effectively produced, both with methods that can be scaled for manufacturing. A passivation technique was developed and demonstrated to handle ultrafine Nd-Fe-B powders. A novel wire-bundle concept was demonstrated for making near-net-shape stators from narrow Fe-6.5Si melt spun ribbons.

Key Publications

1. Tang, W., Ouyang, G., Cui, B., Wang, J., Dennis, K.W., Kramer, M.J., Anderson, I. E. and Cui, J., 2021. Magnetic and mechanical properties of grain-refined Dy-free Nd-Fe-B sintered magnets. Journal of Magnetism and Magnetic Materials, 521, p.167533.

2. Ouyang, G., Macziewski, C.R., Jensen, B., Ma, T., Choudhary, R., Dennis, K., Zhou, L., Paudyal, D., Anderson, I., Kramer, M.J. and Cui, J., 2020. Effects of Solidification Cooling Rates on Microstructures and Physical Properties of Fe-6.5% Si Alloys. Acta Materialia, p.116575.

3. Ouyang, G., Jensen, B., Tang, W., Schlagel, J., Hilliard, B., Pan, C., Cui, B., Dennis, K., Jiles, D., Monson, T. and Anderson, I., 2020. Near Net Shape Fabrication of Anisotropic Fe-6.5% Si Soft Magnetic Materials. Acta Materialia. 201, p.209–216.

4. Ouyang, G., Jensen, B., Macziewski, C.R., Ma, T., Meng, F., Lin, Q., Zhou, L., Kramer, M. and Cui, J., 2019. Characterization of ordering in Fe-6.5% Si alloy using X-ray, TEM, and magnetic TGA methods. Materials Characterization, 158, p.109973.

References

1. Liu, S., and G. E. Kuhl. Development of New High Temperature and High-Performance Permanent Magnet Materials. No. UDR-TR-2000-00092. DAYTON UNIV OH RESEARCH INST, 2000.
2. M. Garside, Global price forecast of rare earth oxides 2019–2025, Statista, 2020.
3. Castilloux, R., Rare Earth Magnet Market Outlook to 2030, Adamas Intelligence.
4. Nothnagel, P., K-H. Müller, D. Eckert, and A. Handstein. "The influence of particle size on the coercivity of sintered NdFeB magnets." Journal of magnetism and magnetic materials 101, no. 1-3 (1991): 379–381.
5. Bance, Simon, et al. "Grain-size dependent demagnetizing factors in permanent magnets." Journal of Applied Physics 116.23 (2014): 233903.
6. K. Hono and H. Sepehri-Amin, "Strategy for high-coercivity Nd-Fe-B magnets," Scripta Materialia, vol. 67, no. 6, pp. 530–535, Sep. 2012, doi: 10.1016/j.scriptamat.2012.06.038.
7. W. Tang, G. Ouyang, B. Cui, J. Wang, K.W. Dennis, M.J. Kramer, I.E. Anderson, J. Cui, "Magnetic and mechanical properties of grain-refined Dy-free Nd-Fe-B sintered magnets," Journal of Magnetism and Magnetic Materials 521 (2021) 167533.
8. Ouyang, Gaoyuan, et al. "Review of Fe-6.5 wt% Si high silicon steel—A promising soft magnetic material for sub-kHz application." Journal of Magnetism and Magnetic Materials 481 (2019): 234–250.
9. Ouyang, Gaoyuan, et al. "Characterization of ordering in Fe-6.5% Si alloy using X-ray, TEM, and magnetic TGA methods." Materials Characterization 158 (2019): 109973.

I.1.7 Advanced Packaging Designs – Reliability and Prognostics (National Renewable Energy Laboratory)

Douglas DeVoto, Principal Investigator
National Renewable Energy Laboratory (NREL)
15013 Denver West Parkway
Golden, CO 80401
Email: douglas.devoto@nrel.gov

Susan Rogers, DOE Technology Development Manager
U.S. Department of Energy
Email: susan.rogers@ee.doe.gov

Start Date: October 1, 2018 End Date: September 30, 2024
Project Funding (FY 21): $175,000 DOE share: $175,000 Non-DOE share: $0

Project Introduction

The U.S. Department of Energy's Office of Energy Efficiency and Renewable Energy Vehicle Technologies Office and the Electrical and Electronics Technical Team have proposed aggressive research and development targets [1] aimed at improving power electronics technology to enable the mass-market penetration of electric-drive vehicles. Achieving these aggressive power electronics targets will require a decrease in cost (year 2025 cost target: $2.70/kW) and an increase in power density (year 2025 power density target: 100 kW/L) as compared with current, on-road technology. Replacing traditional silicon device-based components with more efficient and higher-temperature wide-bandgap semiconductor device-based components will enable increasing the power density. However, meeting the power density target will also require innovative packaging and thermal management solutions to increase the heat fluxes dissipated, and allow for compact electronics packaging.

Decreasing the thermal resistance pathway in power electronics packages is a primary objective for maximizing the performance of wide-bandgap devices. This can be accomplished by either replacing package layers with new materials that enable greater thermal, electrical, and reliability performance, or eliminating layers and components through new packaging designs. Safe and robust operation of the power electronics requires electrical isolation of the high-voltage circuitry within the power electronics module. For example, typical power electronics modules use a ceramic material within the package for electrical isolation and wire bonds for electrical connections.

Objectives

The primary deliverable for this project will be to construct a power electronics package utilizing an organic, electrically insulating substrate material with a direct chip-to-chip interconnect technology and demonstrate superior thermal performance and greater reliability under thermal cycling, thermal aging, vibration, power cycling, and electrical high-potential evaluation over traditional packages. This will be accomplished through the following tasks:

- *Design optimization of a power electronics package.* A multiphysics optimization process will incorporate the electrically insulating substrate alternative into a novel power electronics package. Electrical, thermal, and mechanical constraints will be balanced through this optimization.
- *Prototype construction and evaluation.* Example power electronics packages based on an electrically insulating substrate alternative with devices joined by quilt packaging (QP) will be developed. A multiphysics modeling evaluation of the sample geometries will determine thermal and

thermomechanical performance, while a reliability assessment will measure electrical performance during accelerated tests.

Approach

The project aim is to develop a power-dense, reliable, and cost-effective 3D power electronics package enabled by an alternative electrical isolation material: an organic direct bond copper (ODBC) substrate. This material provides equivalent electrical isolation to current technologies while providing high thermomechanical reliability at high device junction temperatures, as well as enabling higher power densities. In addition, eliminating design constraints associated with traditional ceramic substrates reduces device-to-coolant thermal resistance, simplifies package design, and offers more design flexibility. This package design will eliminate component layers in a new, low-cost, simplified manufacturing process for a packaging design that will allow for higher power densities and reliability. Additionally, the new circuit board structure will transport heat out of encapsulated component areas within a 3D structure. This work is being performed in collaboration with Oak Ridge National Laboratory (ORNL) and DuPont.

QP is a chip-to-chip interconnect technology that incorporates conductive metal “nodules” on the sides of the chips. The technology has been commercialized by Indiana Integrated Circuits, LLC (IIC) from research originating at the University of Notre Dame [2]. IIC designed QP test chips for NREL in FY 2019 to evaluate the electrical and reliability characteristics of the interconnect technology as a replacement for traditional wire bond interconnects. Design work with IIC also involved collaboration with ORNL.

Results

Power Electronics Module Design with Organic Insulating Substrate

Traditional ceramic substrates perform three functions in a power module assembly: a thermal management path from the switching devices to the heatsink or cold plate, electrical connections between the devices and external busbars, and electrical isolation of the thermal management components. Direct bond copper (DBC) substrates with an aluminum oxide (Al_2O_3) ceramic were conventionally selected for power modules due to their adequate performance in electrical isolation, thermal management, and reliability. A thin Cu oxide layer on the Cu foils is used to bond the metallization layers to the ceramic in an oxygen-rich environment at a eutectic point of 1,066°C. The process temperature must be carefully controlled, as the melting point of Cu is 1,085°C. Foils are symmetrically bonded to both sides of the ceramic to prevent cracking or warping during cooling to room temperature [3]. Alternative ceramic materials have aimed to improve performance over Al_2O_3 substrates by increasing bending strength, fracture toughness, thermal conductivity, dielectric strength, or more closely matching their coefficient of thermal expansion (CTE) to Si or wide-bandgap devices. Zirconia-toughened alumina (ZTA) substrates add a percentage of zirconium oxide (ZrO_2) to Al_2O_3 prior to sintering to improve the ceramic’s bending strength. ZTA substrates typically have a lower thermal conductivity than Al_2O_3 substrates but can compensate for this by using a thinner ceramic layer due to their enhanced mechanical properties [4]. Aluminum nitride (AlN) ceramics have been selected for their higher thermal conductivity and low CTE that is closely aligned with semiconductor devices. AlN is bonded to Al metallization layers through a direct bond aluminum (DBA) brazing process using an Al-Si alloy film that exhibits a eutectic phase at 577°C [5]. Further package CTE alignment with DBA substrates can be obtained by selecting aluminum silicon carbide (AlSiC) baseplates. AlN substrates can also be bonded with Cu metallization layers through the DBC process or by active metal brazing (AMB). AMB commonly bonds AlN or silicon nitride (Si_3N_4) to Cu with a brazing material under an inert gas or vacuum environment. The higher fracture toughness of Si_3N_4 and ZTA ceramics has allowed for thicker Cu metallization layers and higher device operating temperatures, but metallization layers have typically not exceeded thicknesses of 1.0 mm. Substrate reliability studies have shown that the lifetime of substrates significantly decreases as metallization layer thickness increases from modeling [6] and experimental [7] results.

Previous work has outlined the thermal performance and reliability of the ODBC substrate [8],[9] and shown that the thermal resistance of an ODBC substrate is comparable to ceramic-based substrates. Reliability experiments have shown no concerns with thicker (>1.0 mm) Cu metallization layers under thermal cycling conditions. Efforts to synthesize ODBC substrates were the primary focus of work this year. While bonding criteria for ODBC substrates requires pressure and temperature parameters analogous to sintered Ag bonding, etching the topside metallization requires a new process. After a DBC substrate is bonded, a photoresist film coats the topside metallization layer and is patterned with a mask and ultraviolet light. After development and baking of the photoresist, chemical etchant removes Cu not covered by the photoresist, followed by removal of the remaining photoresist [10]. The process steps for chemically etching Cu are shown in Figure I.1.7.1.

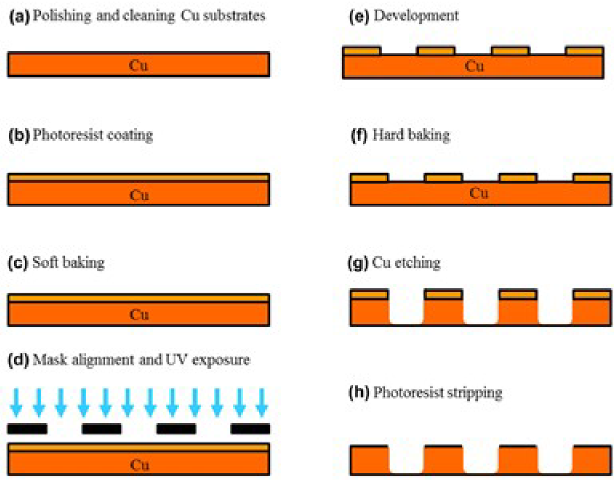

Figure I.1.7.1 Cu etching process 10

Traditional chemical etching requires increasing spacing between electrical conductors as the metallization layer thickness increases due to lateral etching below the photoresist mask. The minimum recommended width spacing is 0.8 mm for a 0.6-mm-thick DBC and 1.2 mm for a 0.8-mm-thick AMB substrate [11], as illustrated in Figure I.1.7.2. This prevents fine features from being etched in thick metallization layers and limits power module designs.

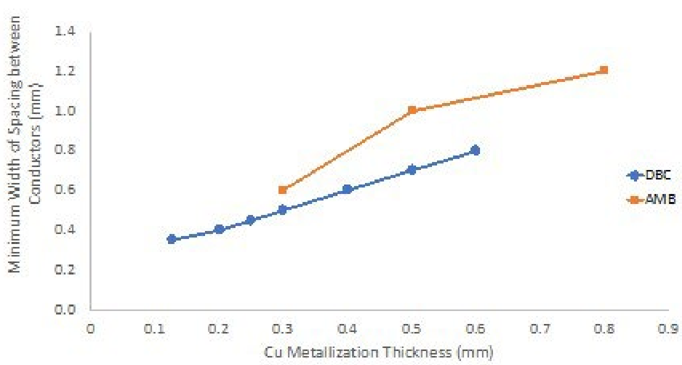

Figure I.1.7.2 Minimum width of spacing between conductors based on metallization thickness [11]

Thick-film printing is the process of directly screen-printing a Cu paste onto a ceramic substrate and then drying and firing the paste at approximately 950°C in an inert N_2 environment. While the number of steps is simplified over a chemical etch process and fine features can be printed, one print can only create up to a 60-µm-thick layer after firing, requiring at least five printing processes to achieve a 300-µm metallization layer. The current carrying capacity of thick-film printing is reduced 10% compared to a DBC metallization of the same thickness due to lower porosity within the Cu [12]. However, the lower porosity and the ability to step down layers at the perimeter of Cu features allows for strain relief that extends the lifetime of the substrate under thermal cycling conditions [13].

Instead of chemical etching or thick-film processes, a mechanical etching process was used to fabricate ODBC substrates. A computer numerical control (CNC) router first partially machines the bottom face of the topside metallization layer, as shown in Figure I.1.7.3, step 1. This step is required as later attempts to machine electrical features would damage the polyimide electrical insulating layer. The Cu and polyimide layers are stacked and then bonded under pressure and temperature in an oven (steps 2 and 3). A mirrored pattern of the CNC machining process in step 1 is completed to remove the remaining Cu material (step 4) to create the final electrical pattern.

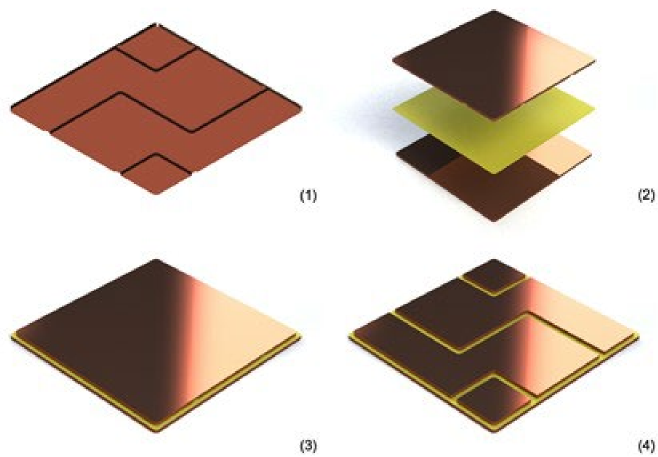

Figure I.1.7.3 ODBC assembly process

An example of a substrate undergoing mechanical etching in a CNC machine and a finished prototype sample with 1.0-mm-thick Cu metallization layers is shown in Figure I.1.7.4.

Figure I.1.7.4 CNC machining process (left) and a prototype ODBC substrate (right)

Electrical evaluation of the prototype ODBC substrate with a high potential tester found the dielectric layer withstood up to 1.5 kV DC with no resulting breakdown. This value will be higher when the edges are sealed with encapsulant.

The ODBC substrate's increased top metallization layer thickness could potentially cause premature failure within the die-attach layer due to CTE mismatch and higher strain levels. To alleviate this concern, a thermomechanical analysis of the device-attach solder layer was completed in FY 2020 and found that strain energy density values of a solder die attach slightly increased with thicker metallization layers. Using the same package geometry as the thermomechanical model, devices were sintered to metallization layers whose thicknesses varied from 0.5 mm to 9.4 mm. The samples were thermally cycled between -40°C and 150°C in a benchtop oven. The samples are shown in Figure I.1.7.5.

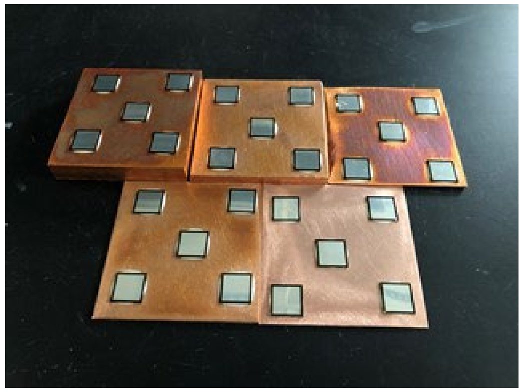

Figure I.1.7.5 ODBC thermomechanical modeling results

Preliminary nondestructive evaluations show no difference in die attach reliability due to metallization thickness variations, but 2,000 thermal cycles will be completed before die shear tests are performed. Any trends between die-attach failure and metallization thickness will then be identified.

Direct Chip-to-Chip Electrical Connection Within a Power Electronics Module

Experimental samples were previously designed in collaboration with IIC and ORNL in FY 2019, and a design of experiments was established based on previous QP experience to optimize the size and shape of the connecting nodules. Six samples were delivered to NREL and three separate accelerated tests—sinusoidal vibration, mechanical shock, and thermal cycling—were conducted in FY 2020. The QP assemblies were mounted to DuPont ODBC substrates with a die-attach solder for ease of handling during evaluation. The complete sample package of two die joined by QP and mounted on the ODBC substrate is shown in Figure I.1.7.6.

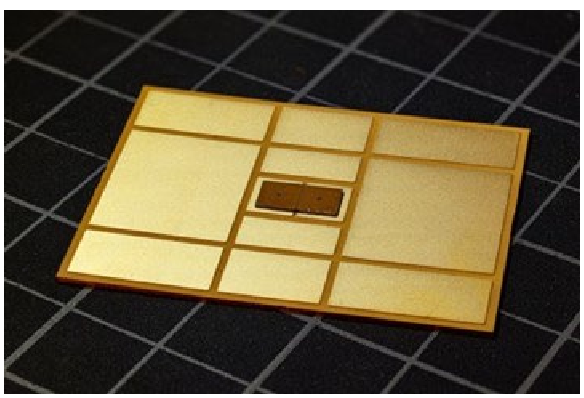

Figure I.1.7.6 Evaluation sample

Degradation of the QP nodules was monitored by electrical resistance measurements across the nodule connections with a Hioki RM3544 Resistance Meter before and during accelerated tests, but it was difficult to select an optimal nodule geometry from the measurements. Observed cracking in the QP nodules was initiated by a torsional stress caused by the tilting of one of the dies. Further analysis attributed this to a weak die-attach solder layer that allowed movement of the die after several hundred thermal cycles. A thermomechanical model of the QP geometries was developed to quantify the impact of nodule shapes and sizes under vibration conditions independent of die-attach strength. The QP nodule geometries used in the modeling analysis are summarized in Table I.1.7.1.

Table I.1.7.1 Quilt Packaging Modeling Geometry Summary

Nodule Shape	Nodule Width (µm)
Rectangle	100
Rectangle	300
Rectangle	700
Triangle	100
Triangle	300
Triangle	700

Each nodule geometry consisted of two devices joined together that were then mounted onto an ODBC substrate, replicating the physical samples in geometry and material properties, as shown in Figure I.1.7.7.

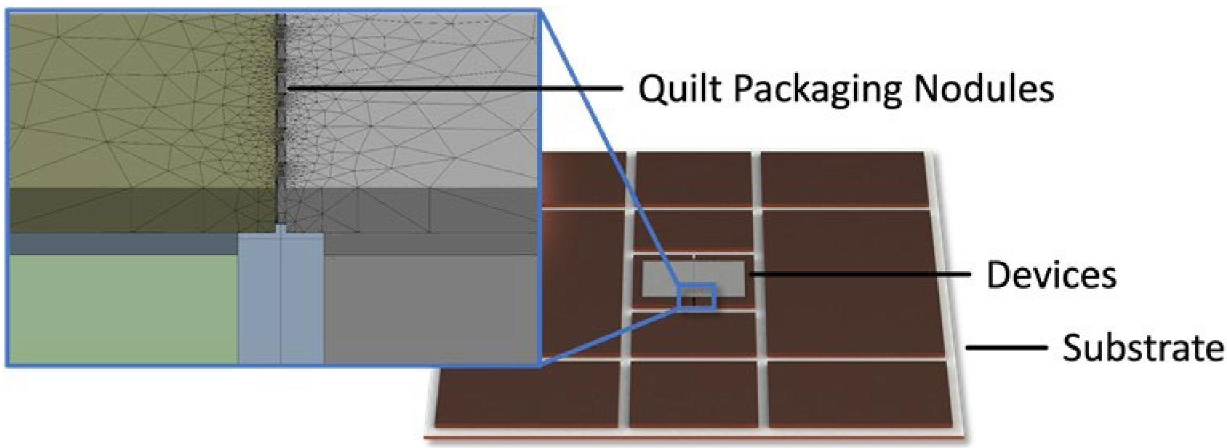

Figure I.1.7.7 Model package geometry

The outer perimeter of the substrate was defined as a fixed support, and a sinusoidal sweep from 0 Hz to 20,000 Hz at 20-g acceleration was repeated for x, y, and z axes. The acceleration magnitude and frequency range were both larger than the experimental IEC 60068-2-6 sinusoidal vibration profile [14], as concerns for the strength of the weak die-attach solder were not present in the model. The total deformation and equivalent stress results were reviewed for each geometry in each axis orientation, for a total of 18 harmonic response models. Their results are summarized in Figure I.1.7.8 and Figure I.1.7.9.

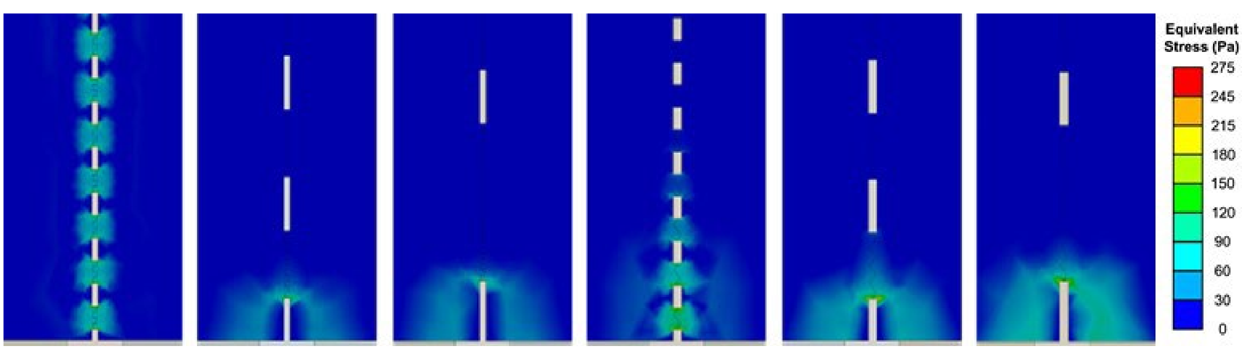

Figure I.1.7.8 Equivalent stress (Pa) for each QP geometry (rectangular 100, 300, and 700 µm; triangular 100, 300, and 700 µm) in the z-axis package geometry

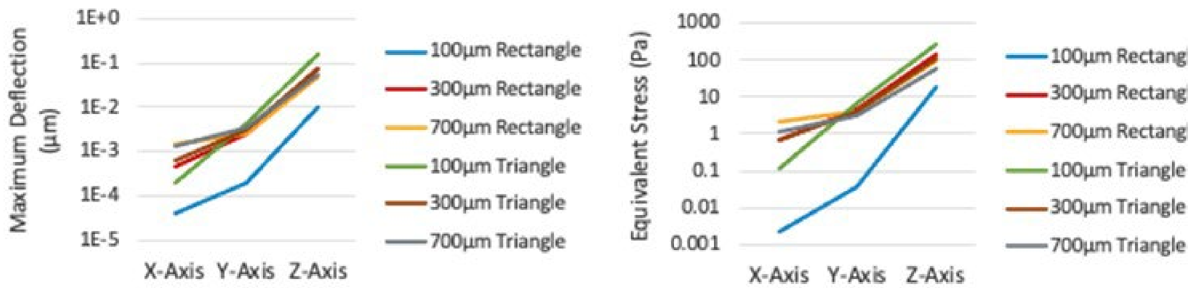

Figure I.1.7.9 Maximum deflection (µm) and equivalent stress (Pa) for each QP geometry

Modeling results indicate that the rectangular nodule shape with a nodule width of 100 µm is the best QP design to minimize deflection and stress under vibration conditions. This can be attributed to several factors. The contact area of the rectangular shapes is greater than the triangular shapes, and stress concentrations are more evenly distributed across nodules when nodule widths are smaller. Recommendations for optimal QP geometries and improving the strength of the die attach in future samples has been conveyed to IIC for production of additional samples in FY 2022. After additional experimental and modeling milestones are met, the goal of an assembled half-bridge module in collaboration with ORNL, IIC, and DuPont will be evaluated.

Conclusions

The project aim is to develop a power-dense, reliable, and cost-effective 3D power electronics package enabled by an alternative electrical isolation material and electrical interconnect method. The project accomplishments for FY 2021 are summarized below:

- Prototype substrates utilizing organic electrically insulating materials have been fabricated that validate a new packaging process. The ability to bond thick Cu metallization layers (1–1.5 mm) using the new process improves heat spreading directly below devices and lowers their junction temperatures. The substrate's dielectric layer was stressed to 1.5 kV DC with no resulting breakdown. ODBC substrates will be integrated into power module prototypes in FY 2022.

- Harmonic response models identified optimized QP nodule geometries under sinusoidal sweep vibration profiles. Modeling results are serving as guidance for the next round of samples that will be fabricated by IIC in FY 2022.

Key Publications

1. DeVoto, D. 2021. "Advanced Packaging Designs – Reliability and Prognostics (NREL)." In *Electrification: 2020 Annual Progress Report*, Washington, D.C.: U.S. DOE EERE VTO, 57–64.

2. Gurpinar, E., Sahu, R., Ozpineci, B., and DeVoto, D. 2020. "Analysis and Optimization of a Multi-Layer Integrated Organic Substrate for High Current GaN HEMT-Based Power Module." *2020 IEEE Workshop on Wide Bandgap Power Devices and Applications in Asia (WiPDA Asia)*, Japan, September 2020.

References

1. U.S. DRIVE. 2017. *Electrical and Electronics Technical Team Roadmap*. Washington, D.C.: U.S. DRIVE. https://www.energy.gov/eere/vehicles/downloads/us-drive-electrical-and-electronics-technical-team-roadmap.

2. Lu, T., Ortega, C., Kulick, J., Bernstein, G. H., Ardisson, S., and Engelhardt, R. 2016. "Rapid SOC prototyping utilizing quilt packaging technology for modular functional IC partitioning." *2016 International Symposium on Rapid System Prototyping (RSP)*, Pittsburgh, PA, 2016, 1–7. doi: 10.1145/2990299.2990313.

3. Miric, A., and Dietrich, P. 2015. "Inorganic Substrates for Power Electronics Applications." *Heraeus Deutschland.*

4. Park, J., Kim, M., and Roth, A. "Improved thermal cycling reliability of ZTA (Zirconia Toughened Alumina) DBC substrates by manipulating metallization properties." *CIPS 2014; 8th International Conference on Integrated Power Electronics Systems*, 2014, pp. 1–9.

5. Lin, H. T., Wereszczak, A. A., and Waters, S. 2013. "Low-Cost Direct Bonded Aluminum (DBA) Substrates." *2013 DOE VTO Annual Merit Review*, Washington, D.C., May 2013.

6. Xu, L., Zhou, Y., and Liu, S. 2013. "DBC substrate in Si- and SiC-based power electronics modules: Design, fabrication and failure analysis." *2013 IEEE 63rd Electronic Components and Technology Conference*, 2013, pp. 1341–1345, doi: 10.1109/ECTC.2013.6575747.

7. Dupont, L., Khatir, Z., Lefebvre, S., and Bontemps, S. 2006. "Effects of metallization thickness of ceramic substrates on the reliability of power assemblies under high temperature cycling." *Microelectronics Reliability*, 46 (9–11), pp. 1766–1771, https://doi.org/10.1016/J.MICROREL.2006.07.057.

8. DeVoto, D. 2020. "Advanced Packaging Designs – Reliability and Prognostics (NREL)." In *Electrification: 2019 Annual Progress Report*, Washington, D.C.: U.S. DOE EERE VTO, 95–101, doi:10.2172/1637435.

9. DeVoto, D. 2021. "Advanced Packaging Designs – Reliability and Prognostics (NREL)." In *Electrification: 2020 Annual Progress Report*, Washington, D.C.: U.S. DOE EERE VTO, 57–64.

10. Chen, Y.L., Wu, J., and Lee, C.C. 2018. "Solid-state bonding of silicon chips to copper substrates with graded circular micro-trenches." *J Mater Sci: Mater Electron* 29, 10037–10043, https://doi.org/10.1007/s10854-018-9047-7.

11. Rogers Corporation. 2021. "curamik® Ceramic Substrates Technical Data Sheet." 2021. https://rogerscorp.com/-/media/project/rogerscorp/documents/advanced-electronics-solutions/english/data-sheets/technical-data-sheet-curamik-ceramic-substrates.pdf.

12. Blank, T., Leyrer, B., Maurer, T., Meisser, M., Bruns, M., and Weber, M. 2014. "Copper thick-film substrates for power electronic applications." *Proceedings of the 5th Electronics System-integration Technology Conference (ESTC)*, 1–6.

13. Wei, V., Huang, M., Lai R., and Persons, R. 2014. "A comparison study for metalized ceramic substrate technologies: For high power module applications." *2014 9th International Microsystems, Packaging, Assembly and Circuits Technology Conference (IMPACT)*, 2014, pp. 141–145, doi: 10.1109/IMPACT.2014.7048425.

14. International Electrotechnical Commission. 2007. *IEC 60068-2-6:2007: Environmental Testing – Part 2–6: Tests – Test Fc: Vibration (Sinusoidal).* Geneva, Switzerland: International Electrotechnical Commission.

Acknowledgments

The significant contributions of Joshua Major and Paul Paret are acknowledged.

I.1.8 Electric Motor Thermal Management (National Renewable Energy Laboratory)

Kevin Bennion, Principal Investigator
National Renewable Energy Laboratory
15013 Denver West Parkway
Golden, CO 80401
Email: kevin.bennion@nrel.gov

Susan Rogers, DOE Technology Development Manager
U.S. Department of Energy
Email: susan.rogers@ee.doe.gov

Start Date: October 1, 2018 End Date: September 30, 2024
Project Funding (FY 21): $250,000 DOE share: $250,000 Non-DOE share: $0

Project Introduction

This project is part of a multi-lab consortium including multiple universities, the National Renewable Energy Laboratory (NREL), Oak Ridge National Laboratory (ORNL), Sandia National Laboratories (SNL), and Ames Laboratory. The project and consortium leverage research expertise and facilities at the national labs, universities, and industry to significantly increase electric drive power density and reliability while simultaneously reducing cost. The consortium is organized around three Keystone projects: (1) Power Electronics, (2) Electric Motors, and (3) Traction Drive System. The Electric Motors Keystone project at NREL focuses primarily on improvements (reductions) in the passive thermal resistance of the electric motor and improved active fluid-based cooling technologies to increase power density, in line with the most recent research priorities outlined in the U.S. DRIVE *Electrical and Electronics Technical Team (EETT) Roadmap* [1].

In the area of electric drive motors, the EETT roadmap highlights the importance of reducing the thermal resistance of the motor packaging stack-up to increase power density. The roadmap also mentions that the thermal conductivity of the materials within the motor influence the amount of material necessary to generate the required mechanical power. The roadmap emphasizes research areas with a focus on material physics-based models, improved materials, and thermally conductive epoxy and fillers. In addition, it highlights a research gap in that the material performance characterization techniques are not well known or identified in the literature.

Heat transfer and thermal management are critical to electric motors because—as mentioned in the EETT roadmap—thermal constraints place limitations on how electric motors ultimately perform. The thermal management of electric motors for vehicles is complex because of the multiple heat transfer paths within the motor, the variation in heat due to motor operating conditions, and the multiple material interfaces through which heat must pass through to be removed. For these reasons, "heat transfer is as important as electromagnetic and mechanical design" [2] for solving research challenges to improve the electric motor power density, cost, and reliability, as outlined by the EETT roadmap.

Objectives

Research under this project will be performed within the framework of a research consortium consisting of a multidisciplinary team that will plan, establish, conduct, and manage a portfolio of multi-lab and multi-university research efforts to advance the state of the art in electric drive technologies. The final objective of the consortium is to develop a 100-kW traction drive system that achieves a power density of 33 kW/L, has an operational life of 300,000 miles, and a cost of $6/kW. The system will be composed of a 100-kW/L inverter and a >20,000-rpm, 50-kW/L electric motor. Building on the research experience and capabilities within each laboratory, the multi-lab consortium will focus on achieving research objectives within three Keystone projects: (1) Power Electronics, (2) Electric Motors, and (3) Traction Drive System.

For the Electric Motors Keystone project, key consortium objectives will focus on research on motor technology gaps to enable increased power density and reliability, supporting research pathways in power electronics technologies. As power electronics technologies develop to enable higher operating temperatures, higher system voltages, and higher switching frequencies, motor technologies will also be necessary to realize the electric drive system benefits. Key consortium motor research pathways include motor material improvements (electrical, magnetic, and thermal), higher motor operating speeds, and higher system voltages. NREL research will provide motor researchers—within and outside the consortium—with the data and models to enable motor innovations and the use of novel materials and designs. The work supports broad demand for data, analytical methods, and experimental techniques to improve and better understand motor thermal management. It also combines unique capabilities, facilities, and expertise in addition to the data, analysis methods, and experimental techniques to improve and better understand heat transfer within electric motors to meet the demands of electric drive vehicles. NREL's focus in fiscal year (FY) 2021 included:

- Developing models, simulation tools, and experimental prototypes in support of consortium team members for quantifying thermal performance and heat transfer technologies to support motor development efforts.
- Utilizing NREL's thermal characterization setup for measuring thermal resistance of high-thermal-resistance materials and interfaces in support of the consortium team members.

Approach

The ability to remove heat from an electric motor depends on the passive-stack heat transfer within the motor and the convective cooling heat transfer of the selected cooling technology. In addition, as new materials are developed, it is important to characterize temperature-dependent material properties and thermal interface properties. Characterization of new materials enables motor designers to evaluate the potential performance trade-offs of new materials for motor applications. For this reason, the approach for the research project splits the efforts between two primary areas. The first focus area for NREL during FY 2021 utilized experimental facilities at NREL to measure new motor materials at elevated temperatures in collaboration with consortium members. The second focus area involved providing motor system thermal analysis for electric motor research efforts performed within the consortium.

Material and Interface Thermal and Mechanical Characterization

NREL provided support to measure high-thermal-resistance materials at elevated temperatures in collaboration with SNL. The experimental setup is shown in Figure I.1.8.1. The left image shows the experimental setup within the environmental chamber to enable measurements at elevated temperatures. The right image shows the experiment with the material sample provided by SNL. The work during FY 2021 with SNL focused on mechanical and thermal measurements of new motor materials developed by SNL.

Figure I.1.8.1 Constructed experimental hardware inside environmental chamber (Source: Emily Cousineau, NREL)

Motor System Thermal Analysis

The research performed in the motor system thermal analysis area focused on working with three consortium collaborators—University of Wisconsin–Madison, Georgia Institute of Technology (Georgia Tech), and ORNL. The collaboration with the University of Wisconsin focused on NREL providing technical support, thermal data, and material information to support the University of Wisconsin-led integrated cooling for motor and power electronics. The collaborations with Georgia Tech and ORNL are described in more detail below.

Collaborations with Georgia Tech involved research efforts for advanced convective heat transfer technologies for electric machines at Georgia Tech. NREL provided technical support, motor geometry information, thermal modeling results, and experimental data to support evaluations of advanced cooling concepts. NREL also provided access to NREL laboratories to a Georgia Tech student to perform experimental work. A portion of the collaborative work led by Georgia Tech was summarized in a paper presented at the 2020 International Technical Conference and Exhibition on Packaging and Integration of Electronic and Photonic Microsystems (InterPACK 2020). A journal publication has also been prepared and submitted for review. Experiments for the developed end-winding cooler were fabricated and conducted at NREL (Figure I.1.8.2). The left image shows the assembled experiment for the end-winding cooler and the right image provides an exploded drawing of the end-winding cooler. The U-shaped end-winding cooler was 3D-printed at NREL from a high-temperature plastic (ULTEM 9085). A silicone compound with a thermal conductivity of 3.5 W/m-K was placed between the motor end-winding and the end-winding cooler to improve the thermal contact.

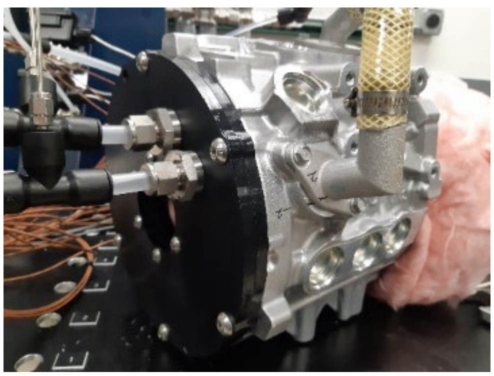

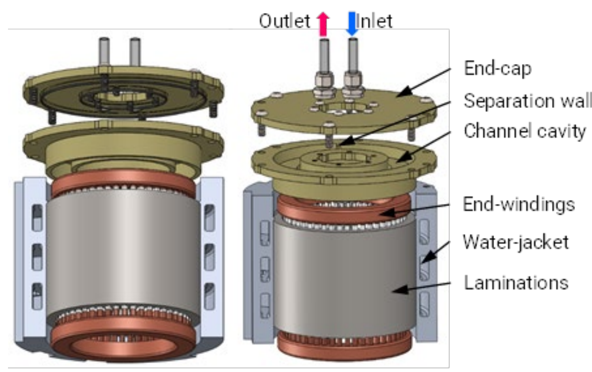

Figure I.1.8.2 Collaboration with Georgia Tech to support research for advanced convective heat transfer technologies for electric machines. (Left) Fabricated end-winding cooling installed at NREL for experimental evaluation. (Right) End-winding cooling heat exchanger construction drawing. (Source: Sebastien Sequeira, Georgia Tech and NREL)

The collaboration with ORNL supported motor thermal analysis and thermal design of advanced machine designs led by ORNL. The collaboration between NREL and ORNL is summarized in Figure I.1.8.3. ORNL led the overall iterative electric machine design process with an emphasis on the electromagnetic and mechanical assembly design. NREL, in collaboration with ORNL, performed the thermal analysis and cooling design. A summary of the initial work is summarized in an ORNL-led paper presented at the 2020 IEEE Energy Conversion Congress and Exposition (ECCE). During FY 2021, NREL focused on refining the motor slot heat exchanger shown in Figure I.1.8.4.

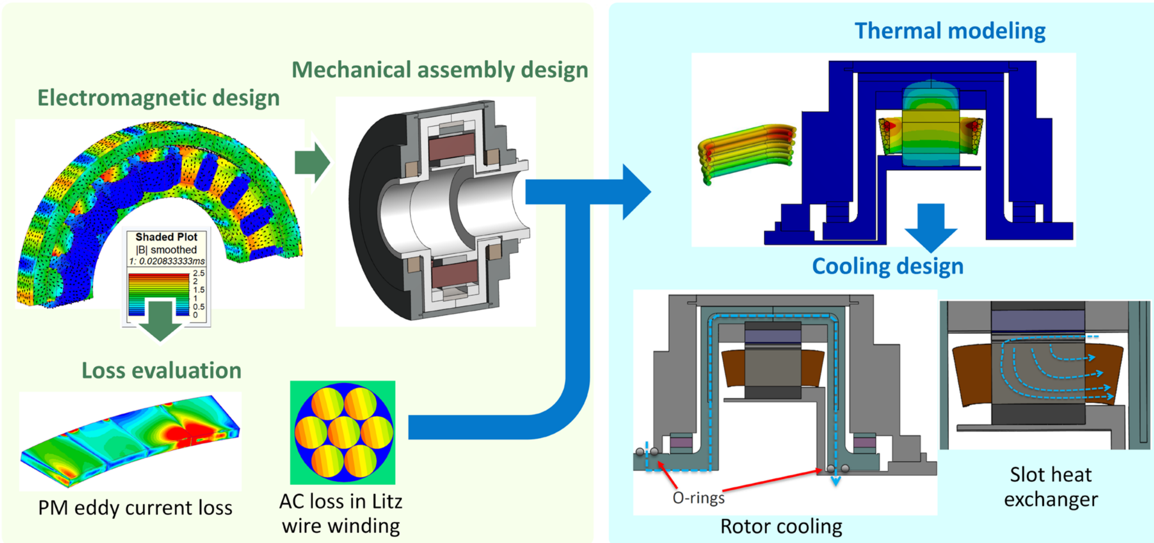

PM: Permanent Magnet, AC: Alternating Current

Figure I.1.8.3 ORNL and NREL motor analysis approach

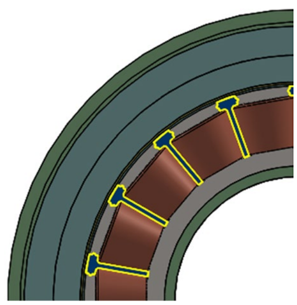

Figure I.1.8.4 Illustration of down selected concept for placing cooling channels within the stator slot between the coil windings and stator tooth tips (Source: Emily Cousineau, NREL)

Results

The following sections summarize the results for both the thermal resistance experimental work for material thermal characterization and the consortium team member motor system thermal analysis collaborations.

Material and Interface Thermal and Mechanical Characterization

NREL developed and utilized experimental methods to measure high-thermal-resistance materials at elevated temperatures in collaboration with SNL. During FY 2021, NREL characterized the thermal conductivity versus temperature of multiple materials, as shown in Figure I.1.8.5. The measurements demonstrated that the iron-nitride-filled samples show a factor of 7.5 higher thermal conductivity at 45°C as compared to the unfilled base epoxy samples.

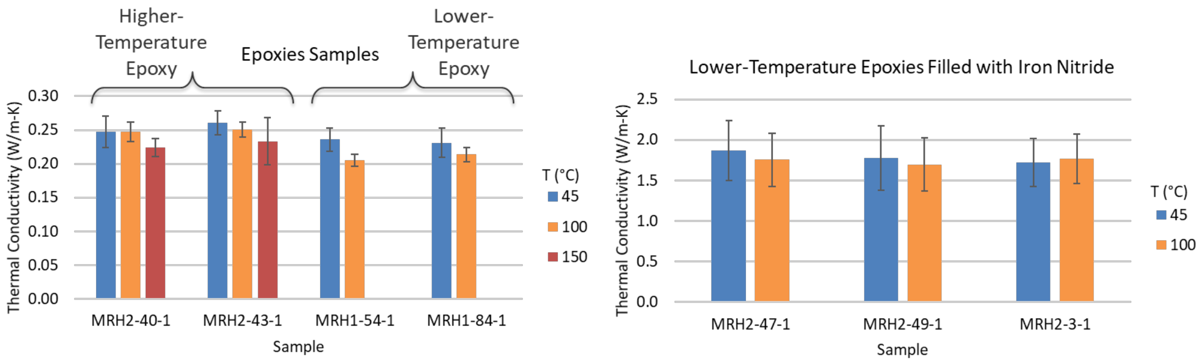

Figure I.1.8.5 Experimental results performed at NREL with SNL-developed materials showing about a 7.5 factor of improvement in thermal conductivity at 45 °C relative to unfilled base epoxy samples: unfilled epoxy samples (left) and filled epoxy samples (right). The error bars represent the 95th percentile measurement uncertainty.

Motor System Thermal Analysis

Figure I.1.8.6 provides a summary of the experimental data collected on the motor subcomponent (motorette) developed in collaboration with Georgia Tech. The left image highlights temperature measurement locations around the motor end-winding. The thermal image was used to verify the temperature uniformity around the stator winding when selecting temperature measurement locations. The right image plots the percent decrease in temperature due to the end-winding cooler (C) relative to the baseline motor water jacket (WJ). The flow rate within the end-winding cooler and water jacket is also called out in the plot legend. The results show that the end-winding cooler has a significant impact in reducing the end-winding temperature. The error bars in the plot represent the measurement uncertainty.

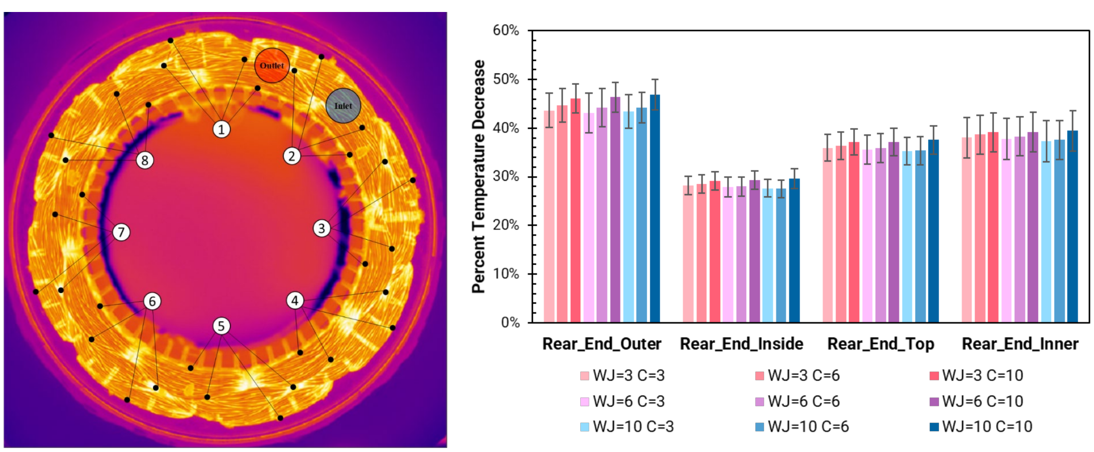

Figure I.1.8.6 Collaboration with Georgia Tech to support research for advanced convective heat transfer technologies for electric machines showing end-winding temperature measurement locations (left), and the percent decrease in temperature relative to baseline stator cooling jacket at each flow rate (L/min) in the stator water jacket (WJ) and the end-winding cooler (C) (right).

The work supporting the ORNL-led motor research efforts focused on an outer-rotor motor configuration as shown in Figure I.1.8.3. The motor design went through multiple design iterations during FY 2021. The iterative design approach investigated multiple design configurations to facilitate integration with the in-process inverter. NREL led the thermal analysis aspects of the motor design, and Figure I.1.8.7 highlights two significant accomplishments during FY 2021. The left plot provides the simulated maximum winding temperature versus the in-slot heat exchanger convective heat transfer coefficient. The analysis shows an in-slot heat transfer coefficient of 3,000 W/m²-K or greater is required to maintain the steady-state winding temperature within the 150°C winding temperature target. Computational fluid dynamics work performed during FY 2021 confirmed the preliminary heat exchanger design meets the heat transfer convective heat transfer coefficient target. The right image of Figure I.1.8.7 shows the motor's transient response for a peak-power operating condition. The analysis shows the motor is capable of operating for the required 30 seconds before reaching the winding thermal limit of 150°C.

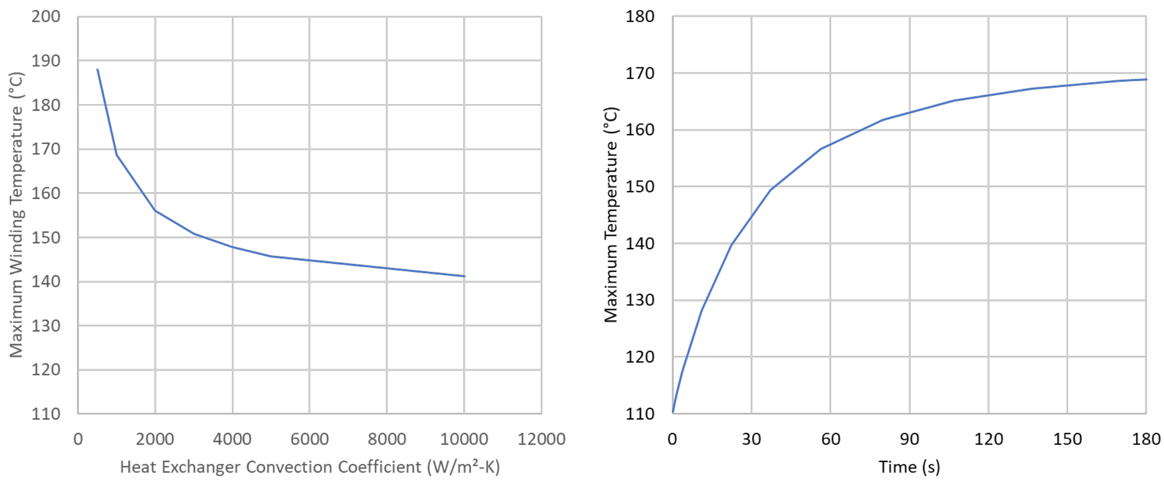

Figure I.1.8.7 Steady-state maximum winding temperature at maximum speed operating point showing that an approximate heat transfer coefficient within the heat exchanger of 3,000 W/m^2-K meets target temperature of 150°C (left). Transient temperature response at peak power operating point showing ability to operate over 30 seconds before reaching 150°C temperature limit (right).

Conclusions

During FY 2021, NREL efforts focused on supporting collaborations with external research partners within the Electric Drive Technologies research consortium. The primary collaborations described in this report include the ones with Georgia Institute of Technology, ORNL, and SNL. Efforts with Georgia Institute of Technology involved advanced convective heat transfer technologies for electric machines. The work led to a conference publication (InterPACK 2020)—highlighted in the Key Publications. A journal manuscript was also prepared and submitted for review during FY 2021. The collaborative experimental work at NREL provided access to the NREL laboratory for a student to experimentally demonstrate the thermal performance benefits of the end-winding cooler concept. The collaboration with ORNL supported efforts led by ORNL to develop a high-speed, non-heavy-rare-earth outer-rotor motor. NREL supported the ORNL effort by leading the thermal analysis and design of advanced machines. The work resulted in identifying a thermal management approach to meet the aggressive motor performance objectives. A summary of the motor research was published and presented at the 2020 ECCE conference. The thermal modeling and analysis work performed by NREL during FY 2021 confirmed the ability to meet the steady-state and transient peak-power operating requirements. Finally, collaborations with SNL utilized an experimental apparatus developed at NREL to measure high-thermal-resistance materials at elevated temperatures. The work during FY 2021 focused on thermal conductivity measurements of the SNL-provided material samples for motor applications.

Key Publications

1. Bennion, K. 2021. "Electric Motor Thermal Management R&D." 2021 DOE VTO Annual Merit Review, Washington D.C., June 2020.

2. T. Raminosoa, R. Wiles, J. E. Cousineau, K. Bennion, and J. Wilkins, "A High-Speed High-Power-Density Non-Heavy Rare-Earth Permanent Magnet Traction Motor," in 2020 IEEE Energy Conversion Congress and Exposition (ECCE), Oct. 2020.

3. S. Sequeira et al., “Validation and Parametric Investigations Using a Lumped Thermal Parameter Model of an Internal Permanent Magnet Motor,” Proceedings of the ASME 2020 International Technical Conference and Exhibition on Packaging and Integration of Electronic and Photonic Microsystems, Oct. 2020.

4. X. Feng, E. Cousineau, K. Bennion, G. Moreno, B. Kekelia, and S. Narumanchi, “Experimental and numerical study of heat transfer characteristics of single-phase free-surface fan jet impingement with automatic transmission fluid,” *International Journal of Heat and Mass Transfer*, vol. 166, Feb. 2021.

References

1. U.S. DRIVE. 2017. *Electrical and Electronics Technical Team Roadmap: October 2017*. Washington, D.C.: U.S. Department of Energy Office of Energy Efficiency and Renewable Energy Vehicle Technologies Office. https://www.energy.gov/sites/prod/files/2017/11/f39/EETT%20Roadmap%2010-27-17.pdf.

2. J.R. Hendershot and T.J.E. Miller. 1994. *Design of Brushless Permanent-Magnet Motors*. (Oxford, UK: Magna Physics Publishing).

Acknowledgments

The significant contributions from Emily Cousineau, Doug DeVoto, Xuhui Feng, Bidzina Kekelia, Joshua Major, Sreekant Narumanchi, and Jeff Tomerlin (NREL) to the project are acknowledged. The following support and collaborations are also acknowledged: Tsarafidy Raminosoa, Mostak Mohammad, and Randy Wiles (ORNL); Todd Monson (SNL); and Sebastien Sequeira, Yogendra Joshi, and Satish Kumar (Georgia Institute of Technology).

I.1.9 Power Electronics: Vertical GaN Device Development (Sandia National Laboratories)

Andrew Binder, Principal Investigator
Sandia National Laboratories
P.O. Box 5800, MS 1086
Albuquerque, NM 87185
Email: abinder@sandia.gov

Susan Rogers, DOE Technology Development Manager
U.S. Department of Energy
Email: susan.rogers@ee.doe.gov

Start Date: October 1, 2018 End Date: September 30, 2023
Project Funding: $800,000 DOE share: $800,000 Non-DOE share: $0

Project Introduction

This project is part of a multi-lab consortium that leverages U.S. research expertise and facilities at national labs and universities to significantly advance electric drive power density and reliability, while simultaneously reducing cost. The final objective of the consortium is to develop a 100-kW traction drive system that achieves 33 kW/L, has an operational life of 300,000 miles, and a cost of less than $6/kW. One element of the system is a 100-kW inverter with a power density of 100 kW/L and a cost of $2.7/kW. New materials such as wide-bandgap semiconductors, soft magnetic materials, and ceramic dielectrics, integrated using multi-objective co-optimization design techniques, will be utilized to achieve these program goals. This project focuses on a subset of the power electronics work within the consortium, specifically the design, fabrication, and evaluation of vertical GaN power devices suitable for automotive applications.

Objectives

Gallium Nitride (GaN) is a promising wide-bandgap (WBG) semiconductor material that could enable higher-performance power electronic devices than traditional Silicon (Si) or even its WBG counterpart, Silicon Carbide (SiC). This is based on the increased critical electric field of GaN, which would enable lower-resistance devices with the same hold-off voltage as devices fabricated from the other materials. This is a key performance metric for power devices. Laterally-oriented, High Electron Mobility Transistors (HEMTs) based on AlGaN and GaN materials are common in high-frequency applications and are being established in lower-voltage power switching applications (approximately 600 V and below). However, with the emerging commercial maturation of GaN substrates, traditional vertically-oriented device structures (such as are common in Si and SiC) can now be realized in GaN, with several promising demonstrations of high-voltage pn diodes and vertical transistors appearing in the literature [1], [2], [3]. While GaN pn diodes may be of interest, the ~3 V turn-on voltage, determined mainly by the bandgap of the material, discourages their use in some power-switching circuits due to the loss of power conversion efficiency resulting from this high turn-on voltage. Instead, more promising candidates for these power conversion systems, including automotive inverters, are GaN Schottky barrier diodes (SBDs) and Junction Barrier Schottky (JBS) diodes, shown in Figure I.1.9.1 (a), which have turn on voltages of ~1 V as determined by the Schottky barrier height of the metal to the semiconductor material, rather than the semiconductor bandgap.

Similarly, vertically-oriented GaN transistors promise high-performance as power electronic devices if several key growth and fabrication challenges are overcome for the GaN material system. Interestingly, several different types of vertical GaN transistors have been demonstrated including Metal Oxide Semiconductor Field-Effect Transistors (MOSFETs) in the trench configuration (T-MOSFET, shown in Figure I.1.9.1 b), the double-well (D-MOSFET) configuration (shown in Figure I.1.9.1 c), and the Current Aperture Vertical Electron Transistor (CAVET) configuration [4], [5], [6]. Each of these device topologies has benefits and challenges associated with fabrication and performance, but the MOSFET designs show the most promise for power switching applications and are being investigated during this effort. With the MOSFET device designs, challenges exist in making the semiconductor/insulator (or oxide) interface due to the lack of a good native oxide for GaN (Si and SiC both have native oxides). In addition, selective-area doping control, which is needed to form lateral pn junctions, cannot be easily achieved in GaN. Current state-of-the-art GaN devices use techniques such as ion implantation with special anneal processes (high-pressure and high-temperature) [7] or epitaxial regrowth [8] to realize selective-area doping control. Both techniques are relatively immature in GaN, and their behavior needs to be studied and techniques need to be developed to control these processes for eventual use in power systems for electric vehicles.

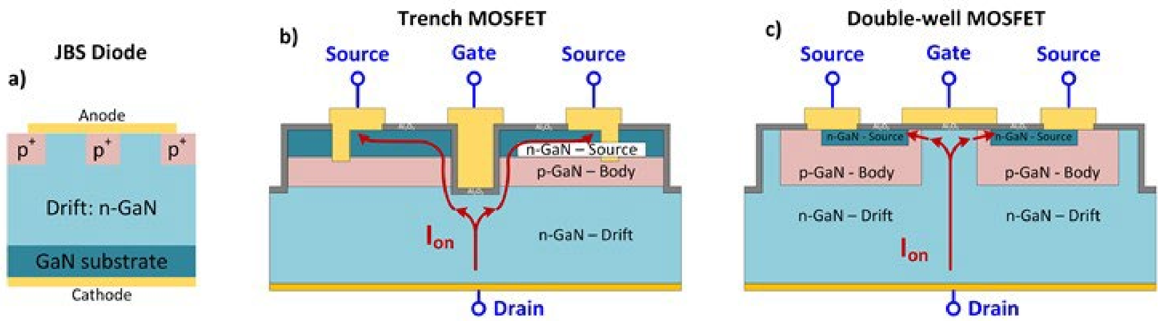

Figure I.1.9.1 (a) Schematic drawing of JBS diode, (b) schematic drawing of Trench MOSFET, and (c) schematic drawing of a Double-well MOSFET.

The first year of this effort focused on the development of simulation and modeling capabilities to help drive the designs of future GaN diodes and transistors. In parallel, epitaxial growth and fabrication processes were initiated toward realizing and demonstrating these devices. The second year of this effort has focused on fabrication and a first-generation demonstration of these devices. With demonstrators for both the JBS and trench MOSFET complete, the third year of the program (this year) focused on improving the baseline performance. This year's focus included iterating to improve passivation quality, tackling challenges related to etch-and-regrowth, and improving off-state characteristics for both the JBS and MOSFET devices. In the future, once devices of sufficient performance are achieved these will be further characterized in a performance and reliability test-bed (created under a different project within the consortium) to evaluate their suitability for electric drive applications, especially regarding their ability to meet the DOE consortium targets. Also, with increasing maturity, the devices can be shared with the consortium partners, who will evaluate them in electric drive systems and provide feedback to us for further improvement in their performance for power electronics.

Approach

The focus of this past year has been on improving baseline performance for both the JBS and MOSFET device. In many cases, challenges faced by both devices can more easily be addressed through cycles of learning on a simpler device. For instance, the pn diode platform can be used to benchmark passivation quality and to evaluate edge termination effectiveness, a simple Schottky Barrier diode can be used to understand the influence of etch damage and etch-damage recovery procedures on n-type GaN, and the MOSCAP can be used to evaluate gate dielectric performance on m-plane GaN. Experiments on these three devices were heavily leveraged in the past year to improve device performance for the JBS and MOSFET platforms. Examples of the three devices are shown in Figure I.1.9.2..

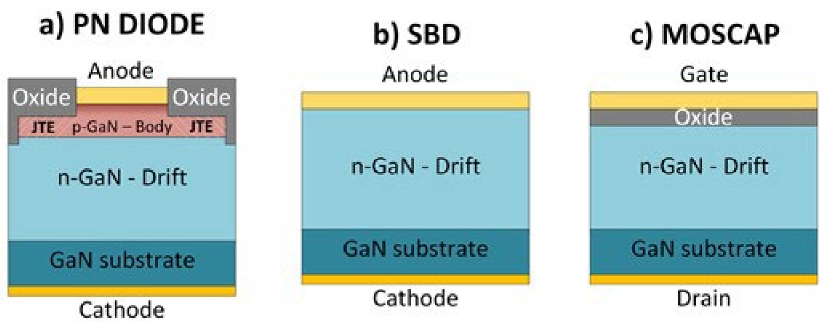

Figure I.1.9.2 Studies on these three devices, the pn diode, the Schottky Barrier diode, and the MOSCAP lends insight into improving performance for the JBS and MOSFET devices.

Results

Vertical GaN PN Diodes

Previous results from the JBS demonstrator indicated that issues with the etch-and-regrowth process and issues with the passivation process contributed substantially to the leakage current in reverse bias. To address the issues related to the passivation we conducted a set of passivation experiments on the pn diode platform. Although the passivation serves many roles when examining device reliability, our initial metric is to create a passivation that does not contribute a substantial leakage current to the device. In order to assess the quality of the passivation, and the impact to reverse leakage current, it is necessary first to establish a known-good pn diode process. To do this we took the JBS process and eliminated the steps related to etch-and-regrowth which then yields a pn diode rather than a JBS diode. This baseline pn diode structure is depicted in Figure I.1.9.3 a and is comprised of a single-zone step etched JTE and a 1-2kV drift epi design. From this simplified process we have been able to consistently demonstrate noise-floor level reverse leakage characteristics for unpassivated pn diodes across multiple device lots (see the black curves in Figure I.1.9.3 b & c). This demonstrates the effectiveness of our edge termination scheme, and our ability to make quality high-voltage, low reverse-leakage pn diodes.

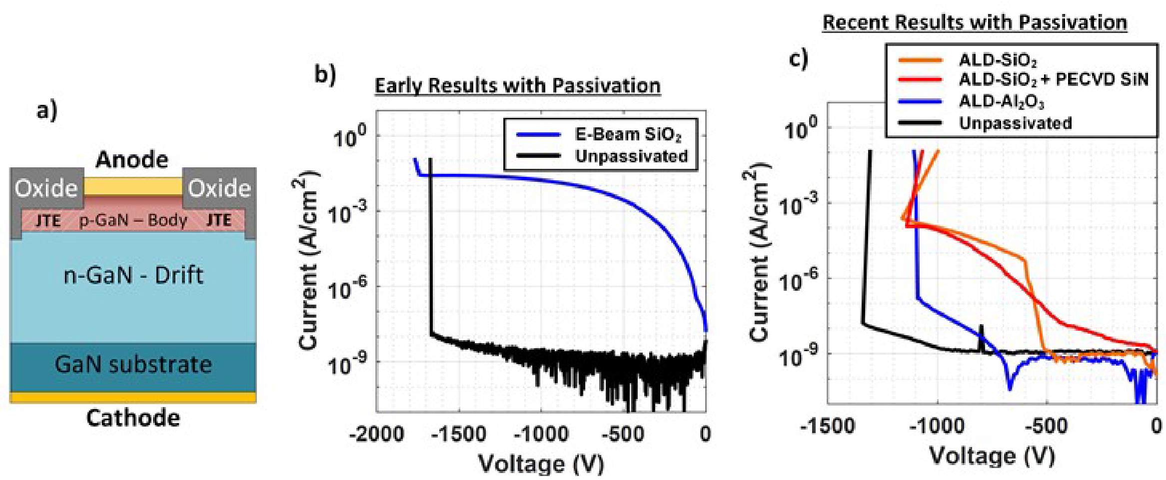

Figure I.1.9.3 Sandia's recent progress for GaN passivations. Using a pn diode (a) to test passivated and unpassivated devices (b) showing how poor passivation can result in substantial leakage currents. Recent passivation results for atomic layer deposited films (c) look promising for realizing low leakage pn diodes. Note, all devices are tested under flourinert during high voltage testing.

Using this platform, various passivation films have been evaluated in regard to the impact on reverse IV performance. Our early experiments with an electron-beam deposited SiO_2 film (500 nm thick) showed a substantial increase in reverse-leakage current compared to our baseline unpassivated devices on a sister-wafer

(Figure I.1.9.3 b). This serves as an example of how a poor passivation process can have a dramatic impact on diode performance. Our recent work with thermal atomic layer deposited films (Figure I.1.9.3 c) shows that the ALD-Al_2O_3 film (100 nm thick) has noise-floor level leakage current in reverse out to a few hundred volts before breakdown. The results presented in Figure I.1.9.3 c are each from separate quarter-wafer pieces from the same wafer. Some doping variations are expected across the wafer, so absolute breakdown results are also expected to shift from one quarter to another.

We are working to establish a bi-layer passivation process to create a substantially thick passivation film. Our prime candidate at this time is a bi-layer ALD-Al_2O_3 (100 nm) + PECVD-SiN (thickness TBD) film. Previous experience at Sandia with PECVD films on GaN demonstrated considerably high leakage currents under high reverse bias which may be the result of unwanted plasma damage to the surface from the PECVD process. This drives the desire to have an intermediate dielectric layer between the GaN surface and the substantially thick PECVD film. Once a baseline passivation process can be established (one that does not add significantly to reverse leakage), more work should be undertaken regarding long term reliability of these films, especially related to stress from high humidity and high temperature.

Passivation induced leakage current was a major contributor to the leakage current seen in the JBS devices [9] and the ability to make quality passivated pn diodes is a step in the right direction towards making low leakage JBS devices.

Vertical GaN Schottky Barrier Diodes

The impact of etch-induced-damage on the n-type Schottky contact can be more easily quantified by evaluating a Schottky Barrier diode (SBD) rather than experimenting directly on the JBS diode. The etch-and-regrowth process and subsequent etch-back steps are critical pieces in the JBS process flow and solving the challenges involved in these processes is the most difficult piece of making a GaN JBS diode. We have made great progress in this past year towards developing an etch-damage-recovery process for improving the performance of Schottky contacts on etched n-type GaN. The baseline structure for evaluating the impact of etch-damage and recovery techniques is a simple SBD structure as represented in Figure I.1.9.4 a. With this structure we can demonstrate a baseline undamaged SBD with near noise floor level reverse leakage current out to -100 V bias. In contrast, the etch damaged device shows a large initial leakage current near the zero-bias point, and a larger leakage slope leading to an increase in leakage current of five orders of magnitude by the -100 V bias point. This is a great example of just how much etch-damage can influence the diode characteristics. To remedy this problem, we are evaluating several etch-damage-recovery techniques that show promise for recovering the noise floor out to -20 or -40 V bias and can reduce the leakage at -100 V by two orders of magnitude compared to the untreated (etch-damaged) sample. These results are presented in Figure I.1.9.4 b.

The ability to recover an etch-damaged surface is a major step towards making low leakage etched-and-regrown JBS devices. In this next year we plan to study the impact of our recovery techniques on etched-and-regrown pn diodes, and we also will be testing these techniques on the full JBS device. Further information on the state of the JBS progress can be found in Ref. [9].

Vertical GaN MOSCAPs

In the past year we have demonstrated a 1st generation process for vertical GaN trench MOSFETs, and our goal is to improve on that baseline by reducing the off-state leakage current and increasing the blocking voltage limit. The three major aspects we are concerned with are improving the passivation quality to reduce passivation related leakage current, improving the gate trench etch and etch-damage removal processes, and improving the quality of the gate dielectric and the dielectric/semiconductor interface. The first two items we have already discussed (improving passivation and improving etch-damage-removal processes), the last item we will address here.

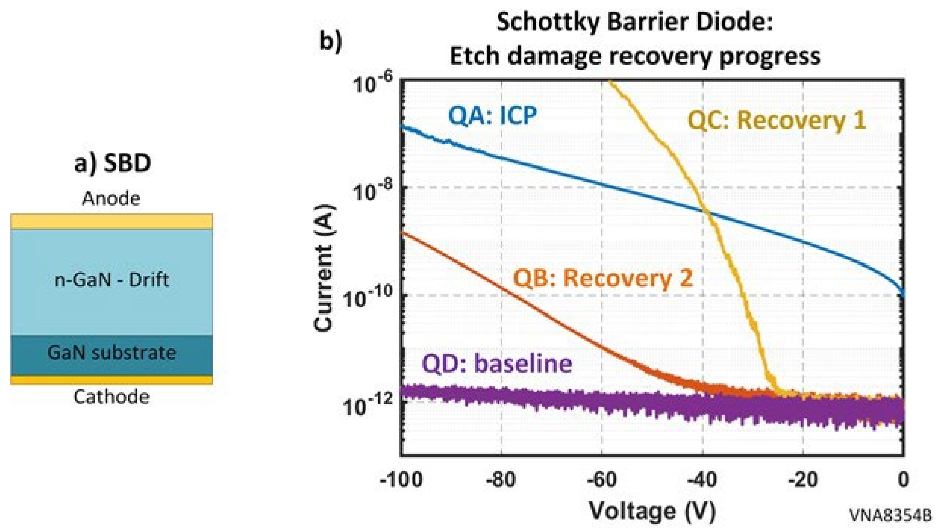

Figure I.1.9.4 Sandia's progress towards developing an etch-damage-recovery process for treating ICP-etch-damaged n-type GaN. The SBD baseline structure (a) consists of a shadow-mask evaporated Pd/Au Schottky contact on n-type GaN. The baseline device (QD) has no etch damage, the other three samples are etch-damaged with QB and QC having different etch-damage-recovery processes prior to metallization. Results of the experiment (b) show good progress towards developing an etch-damage-recovery process that can recover the noise floor and reduce leakage current at higher voltages.

Improving the gate dielectric is a complex process with a lot of knobs to turn. Our most promising gate dielectrics have been atomic layer deposited (ALD) films. Films deposited by ALD are generally very high quality making this a favorable method for depositing non-native oxides. In this past year we have focused primarily on developing ALD-SiO_2 and ALD-Al_2O_3 films for use as the MOSFET gate dielectric. These films have also shown good success in operating as the first layer in a bi-layer passivation used on pn diodes as we discussed earlier in this report (see Figure I.1.9.3). Substantial progress has been made especially for improving the leakage characteristics and dielectric strength of our ALD-SiO_2 film by adding a high temperature post deposition anneal. Leakage performance comparing the first-generation film to the second-generation film with a post deposition anneal are shown in Figure I.1.9.5a.

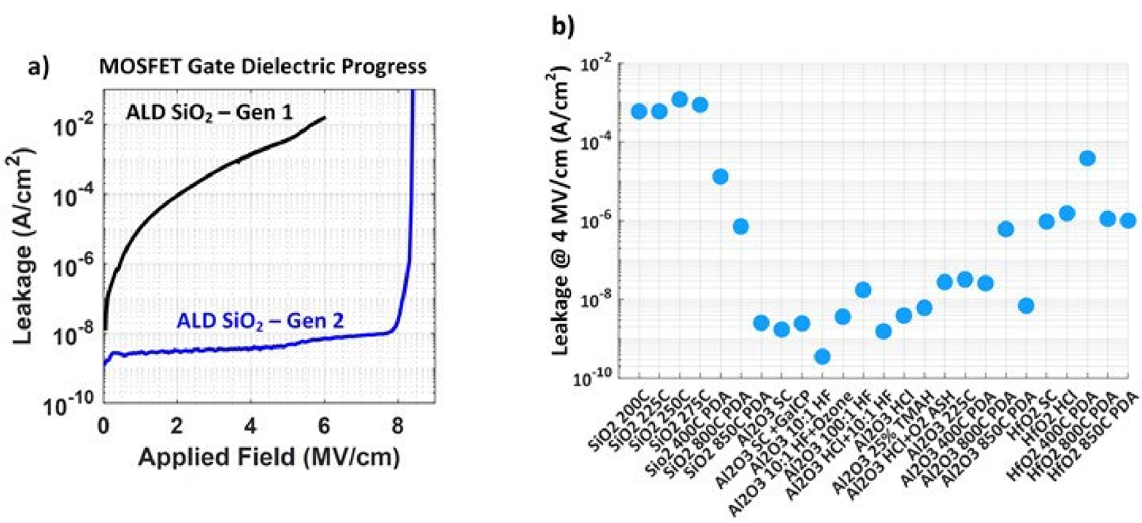

Figure I.1.9.5 Examples of our recent progress on GaN dielectrics showing (a) the improvement made from our first-generation SiO_2 process to the second-generation film, and (b) the static leakage performance of a large variety of different thin-film processes and surface treatment techniques for establishing a successful gate dielectric process on GaN.

The relationship between the dielectric and semiconductor interface plays a critical role in the dynamic behavior of a MOS device, and therefore the conditioning of the interface prior to depositing the dielectric needs special care. We have conducted a large survey of surface treatment options and performed experiments to assess the impact of surface treatments on both static and dynamic performance of MOSCAPs. A summary of some of the static characteristics can be found briefly in Figure I.1.9.5.b. More details on our GaN dielectric study can be found in Ref. [10].

Conclusions

GaN offers the promise of power electronic devices with performance that exceeds conventional Si and even SiC-based devices. This is due to its advantageous material properties, chiefly its higher breakdown electric field. Due to the increased maturity of GaN substrates, vertical GaN devices showing promising performance are being demonstrated and are being considered for insertion into power conversion applications. This project has focused on the design, simulation, and fabrication processes needed to build vertical GaN diodes and transistors for use in electric drive traction systems. Following the successful demonstration of a JBS device and a trench MOSFET in the past year, this year's work has focused on improving the baseline performance of these devices. Substantial progress has been made developing an improved passivation process, developing etch-damage-removal processes, and improving our gate dielectric process. The improved passivation process as well as the new etch-damage-removal techniques look promising for reducing the leakage current on the JBS device. In the next year we plan to continue to improve our baseline performance and we are pushing closer towards test-bed evaluation of some of our devices. The progress on passivation in this past year should enable us to start packaging devices in the near future for better collaboration with the circuits and systems team.

Key Publications

1. T. Binder et al., "Etched and Regrown Vertical GaN Junction Barrier Schottky Diodes," in The 8th Workshop on Wide Bandgap Power Devices and Applications (WiPDA 2021), 2021.

2. E. Glaser, A. T. Binder, L. Yates, A. A. Allerman, D. F. Feezell, and R. J. Kaplar, "Analysis of ALD Dielectric Leakage in Bulk GaN MOS Devices," in The 8th Workshop on Wide Bandgap Power Devices and Applications (WiPDA 2021), 2021.

3. L. Yates, A. Binder, J. Dickerson, G. Pickrell, and R. Kaplar, "Electro-thermal Simulation and Performance Comparison of 1.2 kV, 10 A Vertical GaN MOSFETs," Rio Grande Symposium on Advanced Materials, Albuquerque, NM (September 2019).

References

1. I. C. Kizilyalli, A. P. Edwards, O. Aktas, T. Prunty, and D. J. I. T. o. E. D. Bour, "Vertical power pn diodes based on bulk GaN," vol. 62, no. 2, pp. 414–422, 2014.

2. A. Armstrong et al., "High voltage and high current density vertical GaN power diodes," vol. 52, no. 13, pp. 1170–1171, 2016.

3. H. Ohta, K. Hayashi, F. Horikiri, M. Yoshino, T. Nakamura, and T. J. J. J. o. A. P. Mishima, "5.0 kV breakdown-voltage vertical GaN p–n junction diodes," vol. 57, no. 4S, p. 04FG09, 2018.

4. T. Oka, Y. Ueno, T. Ina, and K. J. A. P. E. Hasegawa, "Vertical GaN-based trench metal oxide semiconductor field-effect transistors on a free-standing GaN substrate with blocking voltage of 1.6 kV," vol. 7, no. 2, p. 021002, 2014.

5. H. Otake, S. Egami, H. Ohta, Y. Nanishi, and H. Takasu, "GaN-Based Trench Gate Metal Oxide Semiconductor Field Effect Transistors with Over 100 cm2/(V s) Channel Mobility," Japanese Journal of Applied Physics, vol. 46, no. 25-28, p. L599, 2007.

6. S. Chowdhury, M. H. Wong, B. L. Swenson, and U. K. J. I. E. D. L. Mishra, "CAVET on bulk GaN substrates achieved with MBE-regrown AlGaN/GaN layers to suppress dispersion," vol. 33, no. 1, pp. 41–43, 2011.

7. T. Anderson et al., "Activation of Mg implanted in GaN by multicycle rapid thermal annealing," vol. 50, no. 3, pp. 197–198, 2014.

8. G. Pickrell et al., "Regrown Vertical GaN p–n Diodes with Low Reverse Leakage Current," vol. 48, no. 5, pp. 3311-3316, 2019.

9. A. T. Binder et al., "Etched and Regrown Vertical GaN Junction Barrier Schottky Diodes," in The 8th Workshop on Wide Bandgap Power Devices and Applications (WiPDA 2021), 2021.

10. C. E. Glaser, A. T. Binder, L. Yates, A. A. Allerman, D. F. Feezell, and R. J. Kaplar, "Analysis of ALD Dielectric Leakage in Bulk GaN MOS Devices," in The 8th Workshop on Wide Bandgap Power Devices and Applications (WiPDA 2021), 2021.

Acknowledgements

This work is supported by the DOE Office of Energy Efficiency and Renewable Energy, Vehicle Technologies Office. Sandia National Laboratories is a multi-mission laboratory managed and operated by National Technology and Engineering Solutions of Sandia, LLC., a wholly owned subsidiary of Honeywell International, Inc., for the U.S. Department of Energy's National Nuclear Security Administration under contract DE-NA0003525. The views expressed in the article do not necessarily represent the views of the U.S. Department of Energy or the United States Government.

I.1.10 High-Reliability Ceramic Capacitors to Enable Extreme Power Density Improvements (Sandia National Laboratories)

Jack Flicker, Principal Investigator
Sandia National Laboratories
P.O. Box 5800, MS 1033
Albuquerque, NM 87123
Email: jdflick@sandia.gov

Susan Rogers, DOE Technology Development Manager
U.S. Department of Energy
Email: susan.rogers@ee.doe.gov

Start Date: October 1, 2018 End Date: September 20, 2024
Project Funding: $70,000 DOE share: $70,000 Non-DOE share: $0

Project Introduction

A detailed Genetic Algorithm (GA) topology optimization [1] for the vehicle Electric Traction Drive (EDT) synchronous boost converter and inverter is being carried out. Candidate designs from pareto frontiers have been identified for SiC and GaN based semiconductor switches that achieve large power densities. However, these optimal designs are enabled only through the use of high energy density multilayer ceramic capacitors (MLCCs) in a large, distributed architecture of many (~250) small value MLCCs. Use of these distributed small MLCC capacitors on a DC bus enables significant gains in system power density, but due to the increased component count has a detrimental effect on system-level mean time to failure (MTTF). To achieve system-level power density and cost requirements while still meeting reliability targets, it will be necessary to significantly increase MTTF of base-metal electrode MLCCs. For these devices, the primary failure mechanism at high voltage and high temperature is low insulation resistance and shorting caused by electromigration of defects in the dielectric layer. Oxygen vacancies, a natural defect which occurs during firing of the capacitors in reducing atmospheres to enable base-metal electrodes (Ni), migrate under the applied electric field and gather at the cathode. This decreases the Schottky barrier height at the metal-dielectric interface causing leakage and, eventually, shorting. Minimization of this failure mechanism is paramount for increasing MTTF.

Objectives

The objective of this research is to investigate ways to extend MTTF through system level control instead of from a material science approach. Decades of R&D have gone into minimizing oxygen vacancies, preventing their diffusion via the addition of migration barriers (i.e., grain boundaries), binding dopants to pin them in place, etc. This vast amount of research and development has resulted in the current state of base-metal electrode MLCCs with significantly increased lifetimes. However, further increases in lifetime are difficult to achieve compositionally/microstructurally, and other solutions may be necessary on a device level. This work investigates that approach.

Approach

Instead of addressing performance/reliability through material composition and microstructure, we take an innovative approach to prevent oxygen vacancies from reaching the cathode by applying a reverse bias periodically (*i.e.,* an AC waveform) to push the oxygen vacancies back to their original positions. This approach may be difficult to implement on a circuit level, but if successful may allow for unique circuit designs based on much longer lifetime high-density MLCC capacitors.

Results

To understand the role of AC waveforms on ceramic capacitor lifetime under accelerated testing, initial tests were completed on individual piece-parts of modest voltage (6.3 V X7R automotive grade MLCCs).

Capacitors were evaluated at 10x rated voltage and 255°C. These aggressive acceleration conditions were necessary due to the inability of the initial measurement setup to measure samples in parallel. Therefore, a high acceleration condition was necessary to evaluate multiple samples in series. As shown in Figure I.1.10.1, the samples run under DC bias (orange) failed in ~20 hrs for this accelerated condition, and the distribution of failure of the initial parts is quite tight. Afterwards, AC square waves of ±10x V_{rated} were applied at different frequencies to capacitors with the same lot/date code. As shown in Figure I.1.10.1, the lifetime of the capacitors increased significantly with increasing lifetime as a function of frequency. The increase is nonlinear with frequency, with higher frequencies showing diminishing returns. These initial results were exciting, but to fully explore the Temperature/Voltage/Frequency space a larger throughput of capacitors is necessary due to the long time period necessary for testing, especially if more realistic acceleration conditions are to be evaluated.

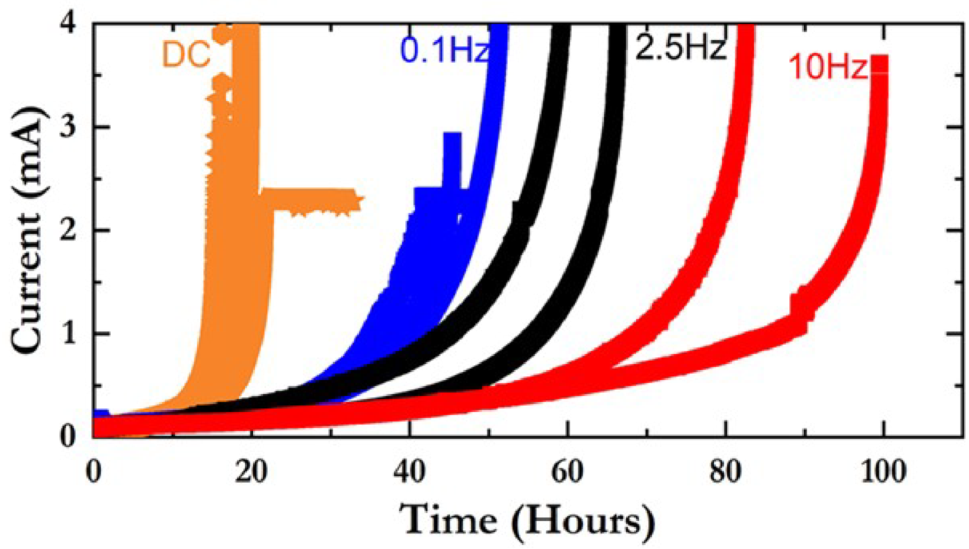

Figure I.1.10.1 Change in Lifetime of MLCCs under different AC Loads. 6.3V X7R capacitor, 10x Vr, 255C.

A system to simultaneously evaluate 40 capacitors under AC conditions with temperature control was fabricated using a custom heating stage, multiple relays, and an H-bridge. This scale-up allows for much quicker measurements than previously possible, as well as Weibull statistics to be performed. This is important due to the propensity for X7R MLCC capacitors to contain infant mortality (Weibull β<1) and early-wear-out (Weibull β ~1.5) failures in conjunction with wear-out (Weibull β~5–10). The unit contains a power/voltage bus that delivers the high voltage for accelerated degradation, and a low-voltage measurement bus to which capacitors can be switched to allow for any two-terminal device measurement, most importantly insulation resistance. The capacitor can then be returned to the high voltage bus to continue degradation.

The system is LabVIEW controlled, can supply up to 600 V to DUTs, and reaches temperatures of 300°C. Heating is performed via heater cartridges encased in an alumina block, which acts both as the heater and electrical shielding. High temperature pogo pins are used to push brass rods through quartz isolation tubes for contact, and the aluminum block is grounded for guarding purposes. DUTs can be disabled individually via relays once they have failed (either via leakage degradation or short) so that the test is not interrupted. The H-bridge can be used to provide fast signal switching, limited in frequency only by the power supply current and the capacitive load. Frequencies of ~0.1-10 Hz are expected to be common in our accelerated testing, but the period of switching in a decelerated fashion will be much slower in an ideal circuit—days, weeks, months, or (hopefully) years.

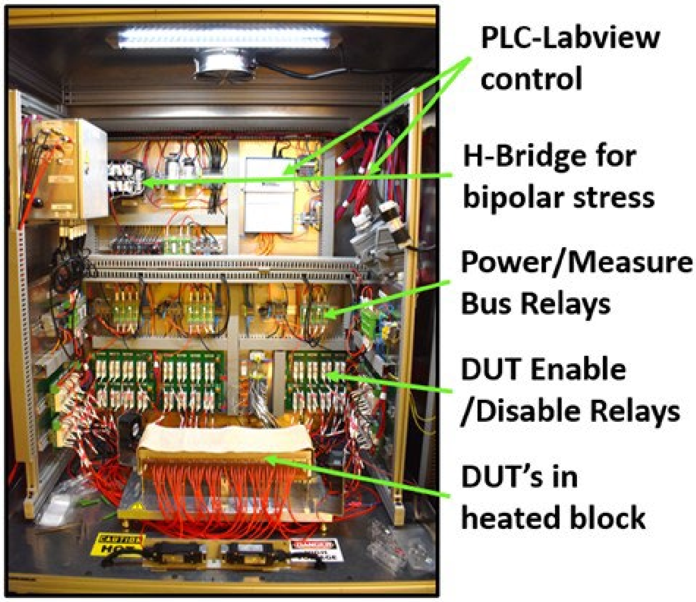

Figure I.1.10.2 Image of high voltage AC highly accelerated lifetime system with cutout showing CAD drawing of the pogo-pin setup.

The system is operational, and initial measurements on this system occurred this FY and will continue for the course of the project.

Initial testing results from the end of FY21 are shown in Figure I.1.10.3 on a Weibull plot. Samples in this initial scale-up study were an automotive grade 100 V X7R 0805 1 μF MLCC. Voltage acceleration was not utilized for initial testing (test voltage of 100 V). A temperature of 200°C during testing gave a lifetime which was reasonable for the measurements (~2 days). Capacitors from the same lot/date code were then measured under 1 Hz and 5 Hz bipolar square wave waveforms.

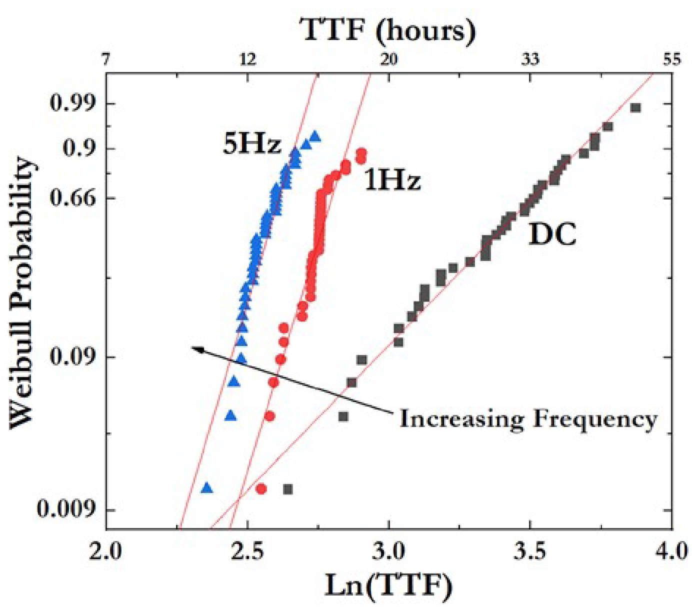

Figure I.1.10.3 Change in Time to Failure for 100 V 1 mF 0805 X7R capacitors as a function of frequency. Measurement occurred at 100 V and 200 C. A clear decrease in lifetime with increased frequency is seen, in opposition to initial results.

As can be seen, these test results show a distinctly different trend than the initial test results. Namely, the increased frequency of voltage application resulted in *lower* lifetimes instead of *longer* lifetimes. This difference is not currently understood, but a hypothesis can be made and tested in future work. The difference between initial and scaled-up results may be due to changes in failure mechanisms due to different acceleration conditions. Higher electric fields (note: 100 V parts at 1x V_{rated} have a higher internal electric field than 6.3 V parts at 10x V_{rated}) may promote increased electrostrictive action in the parts, resulting in microcracking and field concentration, and therefore quicker failure. Internal electric field strength, the electrostrictive response of the dielectric layers, temperature (above or below the Curie and Burns temperatures), humidity, case size, and more may affect the ability to accelerate oxygen vacancy migration. Further research is required to investigate the effects of these parameters. For now, a tentative model of two frequency dependences is found, as schematically shown in Figure I.1.10.4.

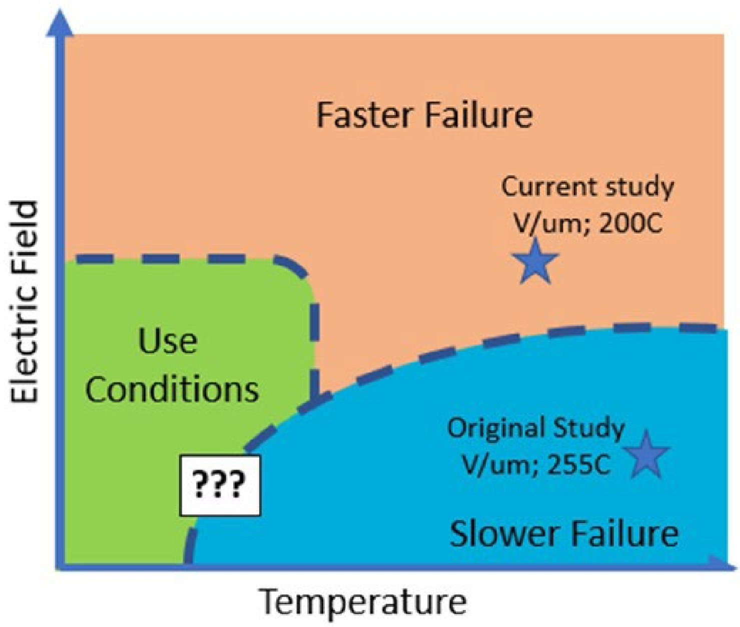

Figure I.1.10.4 Schematic representation of current results showing change in frequency-dependent time to failure as a function of acceleration conditions. The differentiation between these two conditions, and the behavior at use conditions, is unknown.

Future work will include expanding this study to multiple other acceleration conditions on similar parts and understanding the lifetime dependence and failure mechanism under AC conditions in different regimes. Failure analysis on some parts will be performed to help aid in this work.

Conclusions

AC square wave application during accelerated testing has been found to both increase and decrease lifetime under different testing conditions. The root cause for these different behaviors is currently unknown but could be due to oxygen vacancy migration under AC conditions and electrostrictive strain based microcracking, respectively. Further research is required to understand this phenomenon.

References

1. "Co-Optimization of Boost Converter Reliability and Volumetric Power Density Using Genetic Algorithm," 2020 IEEE Energy Conversion Congress and Exposition (ECCE). Detroit, MI. October 2020.

Acknowledgements

Jon Bock led the technical work on capacitors, and Will Bachman helped to fabricate the AC HALT test system. This work is supported by the DOE Office of Energy Efficiency and Renewable Energy, Vehicle Technologies Office. Sandia National Laboratories is a multi-mission laboratory managed and operated by National Technology and Engineering Solutions of Sandia, LLC., a wholly owned subsidiary of Honeywell International, Inc., for the U.S. Department of Energy's National Nuclear Security Administration under contract DE-NA0003525. The views expressed in the article do not necessarily represent the views of the U.S. Department of Energy or the United States Government.

I.1.11 Bottom-Up Soft Magnetic Composites (Sandia National Laboratories)

Todd Monson, Principal Investigator
Sandia National Laboratories
P.O. Box 5800, MS 1415
Albuquerque, NM 87185
Email: tmonson@sandia.gov

Susan Rogers, DOE Technology Development Manager
U.S. Department of Energy
Email: susan.rogers@ee.doe.gov

Start Date: October 1, 2018 End Date: September 30, 2023
Project Funding: $125,000 DOE share: $125,000 Non-DOE share: $0

Project Introduction

In order to meet 2025 goals for enhanced peak power (100 kW), specific power (50 kW/L), and reduced cost (3.3 $/kW) in a motor that can operate at ≥ 20,000 rpm, improved soft magnetic materials must be developed. Better performing soft magnetic materials will also enable electric motors without rare earth elements. In fact, replacement of permanent magnets with soft magnetic materials was highlighted in the Electrical and Electronics Technical Team (EETT) Roadmap [1] as a R&D pathway for meeting 2025 targets. Eddy current losses in conventional soft magnetic materials, such as silicon steel, begin to significantly impact motor efficiency as rotational speed is increased. Soft magnetic composites (SMCs), which combine magnetic particles with an insulating matrix to boost electrical resistivity (ρ) and decrease eddy current losses, even at higher operating frequencies (or rotational speeds), are an attractive solution. Today, SMCs are being fabricated with values of ρ ranging between 10^{-3} to 10^{-1} µohm·m [2], which is significantly higher than 3% silicon steel (~0.5 µohm·m) [3]. The isotropic nature of SMCs is ideally suited for motors with 3D flux paths, such as axial flux motors. Additionally, the manufacturing cost of SMCs is low, and they are highly amenable to advanced manufacturing and net-shaping into complex geometries, which further reduces manufacturing costs. There is still significant room for advancement in SMCs, and therefore additional improvements in electrical machine performance. For example, despite the inclusion of a non-magnetic insulating material, the electrical resistivities of SMCs are still far below that of soft ferrites ($10 - 10^8$ µohm·m).

We are developing SMCs from the bottom up, with a final objective of creating composites with high magnetic material loading (and therefore high magnetization) while increasing the value of ρ several orders of magnitude over current state-of-the-art SMCs. To accomplish our goals, we are starting with particles of γ’-Fe_4N, which have a saturation magnetic polarization (J_s) of 1.89 T, or slightly greater than Si steel [4] and a ρ of ~ 2 µohm·m [5]. In our bottom-up approach we begin by coating the magnetic particles with a diamine, which chemically reacts directly with epoxide terminated monomers to form a cross-linked epoxy composite. This “matrix-free” approach to composite formation will not suffer from the same nanoparticle aggregation and phase separation effects commonly observed in most nanocomposites [6]. Furthermore, it should ensure better separation between magnetic particles and significantly reduce or eliminate inter-particle eddy currents. A precedent already exists for the use of epoxies in electrical machine construction [7], [8]. Additionally, it is possible to design epoxy systems with glass transition temperatures (T_g) well in excess of the target maximum motor operating temperature of 150°C [9] as was documented in last year’s annual progress report. Furthermore, composites have been successfully demonstrated in high-speed motors [10] and even flywheels rotating at speeds up to 60,000 rpm [11].

Objectives

The project objective is to develop high-magnetization, low-loss iron-nitride-based soft magnetic composites for electrical machines. These new SMCs will enable low eddy current losses and therefore highly efficient motor operation at rotational speeds up to 20,000 rpm. Additionally, iron nitride and epoxy composites will be capable of operating at temperatures of 150°C or greater over a lifetime of 300,000 miles or 15 years.

Approach

A high-level overview of our approach is:

1. Convert commercially available mixed-phase iron nitride powder to nearly phase-pure γ'-Fe_4N
2. Coat iron nitride particles with diamine molecules (part A of epoxy chemistry)
3. Combine surface functionalized particles with epoxide terminated monomers (part B of epoxy chemistry)
4. Fabricate SMC parts by adding mixture from #3 into a hot-pressing die
5. Evaluate and test the fabricated SMC part
6. Optimize SMC magnetic volume loading, magnetic properties, and physical properties.

Results

1. Development of a lab scale hot pressing setup

In order to progress beyond the 65 vol.% Fe_4N achieved in our iron nitride/epoxy composites during FY 2020, we needed to move beyond curing our SMC samples in a mold and begin using a hot press for part fabrication. For this reason, we built a lab scale hot pressing setup. An image of the hot-pressing setup is displayed in Figure I.1.11.1. A zoomed in image of the die, thermocouple, and heating band inside of the press can be seen in Figure I.1.11.2. The specific components of our hot-pressing setup are as follows: A 20-ton E-Z press (P/N 0012-6306) from International Crystal Laboratories (ICL); a CSI32R-C24 Benchtop Temperature Controller from Omega; an R-type (Pt 13% Rh/Pt, P13R-020-12) thermocouple, also from Omega; heating bands of various sizes from TempCo which are rated for 120V AC. The heating bands are constructed of mica insulated steel on the inner surface and stainless steel on the outer surface. The die for producing cylindrical test samples was a 3/8" ID stainless steel die from Carver. When fabricating toroids, a toroidal die from Electrodes, Inc. machined out of I-82 graphite was used. The ID of the pressed toroids was 6 mm, and their OD was 9 mm.

Figure I.1.11.1 Lab scale hot pressing setup used for SMC part fabrication.

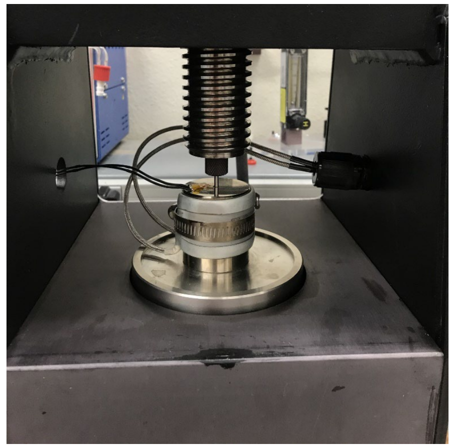

Figure I.1.11.2 Close up image of a die for hot pressing SMC samples. A heating band surrounds the die, and the temperature is monitored with a thermocouple.

Prior to sample fabrication, control over the temperature inside the die was evaluated. As can be seen in Figure I.1.11.3, the temperature inside the die routinely stabilizes within 10°C of the temperature set point.

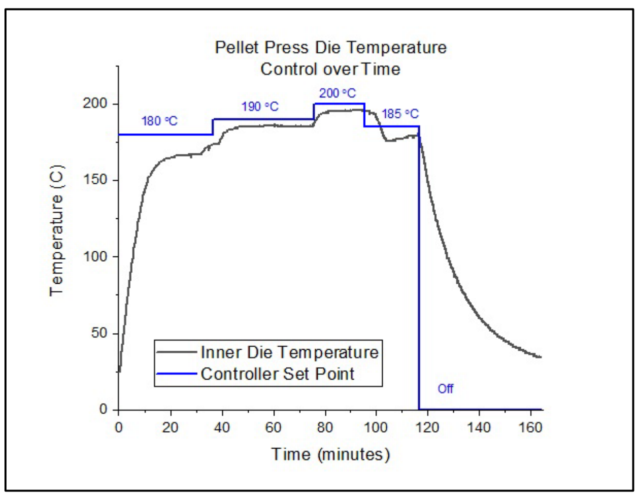

Figure I.1.11.3 Temperature inside the hot-pressing die in relation to the temperature set point.

2. Iron nitride/epoxy composite fabrication via hot pressing

Iron nitride-based SMCs were constructed using our new hot-pressing setup. The processing parameters were optimized such that Fe_4N loadings ≥ 70 vol.% could be achieved. Prior to adding the uncured iron nitride/epoxy mixture, the die was coated with boron nitride (BN) spray to serve as a release agent. A SMC with 71.4 vol.% Fe_4N was achieved using a pressure of 500 MPa and a temperature of 180°C. The sample was pressed for 18 hours (overnight) and allowed to cool for 2 hours before removing from the die. The sample can be seen in Figure I.1.11.4.

Figure I.1.11.4 Iron nitride-based SMC containing 71.4 vol.% Fe_4N. In the images located in the center and right-hand side, the sample has been cut using a diamond saw prior to insertion in a magnetometer.

The sample's magnetic properties were characterized using a vibrating sample magnetometer (VSM) from Quantum Design. The magnetic hysteresis curve is plotted in Figure I.1.11.5. The sample achieved a saturation magnetization (M_s) of 144 Am^2/kg. As a comparison, bulk iron has a M_s of 217 Am^2/kg. When converted to saturation magnetic polarization (J_s) the SMC has a J_s of 0.96 T. This is nearly double that of soft ferrites ($J_s \sim 0.5$ T), and half the value of Si steel ($J_s = 1.87$ T). This puts iron nitride/epoxy SMCs in good standing amongst other insulating soft magnetic materials. Further increases in both M_s and J_s can be expected as the volume loading of iron nitride is increased further through additional process and material improvements.

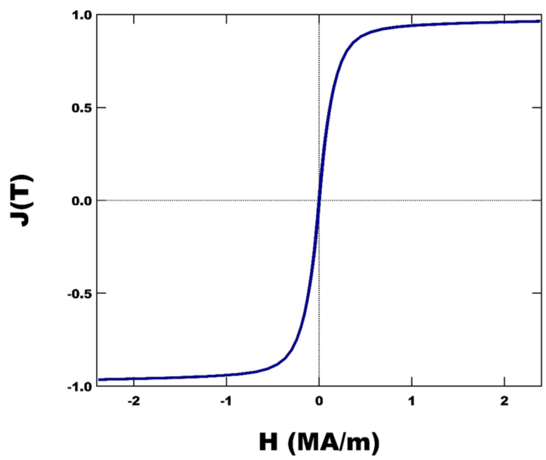

Figure I.1.11.5 Magnetic hysteresis curve (plotted as J vs. H) for an iron nitride-based SMC containing 71.4 vol.% Fe_4N.

3. Thermal Characterization of iron nitride/epoxy SMCs

To ensure our magnetic composites are well designed for electric motor operation, it is also important to characterize, and perhaps even tune, the thermal conductivity of the samples. Additionally, understanding the thermal conductivity of our composite samples will be important for the consortium members attempting to integrate our bottom-up SMCs into their motor designs. Sandia has partnered with EDTC consortium member NREL to complete thermal conductivity measurements of our epoxy-based composites. NREL's thermal characterization setup requires 2" x 2" square samples no more than 2 mm thick. There is also a requirement that the square faces be flat and co-planar for high quality data to be collected. A photograph of NREL's thermal characterization apparatus is displayed in Figure I.1.11.6

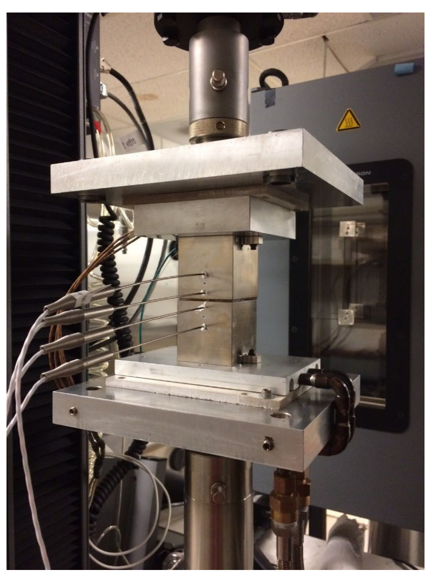

Figure I.1.11.6 Apparatus at NREL for bulk and thermal resistance measurement.

Both neat epoxy and Fe_4N/epoxy samples with 60 vol.% iron nitride loading were prepared. Uncured samples were added to a 3D printed mold and cured at temperature. Cured samples were polished to ensure the square faces were both smooth and co-planar with one another. Figure I.1.11.7 displays a 2” x 2” 60 vol.% Fe_4N in epoxy sample shipped to NREL for thermal characterization.

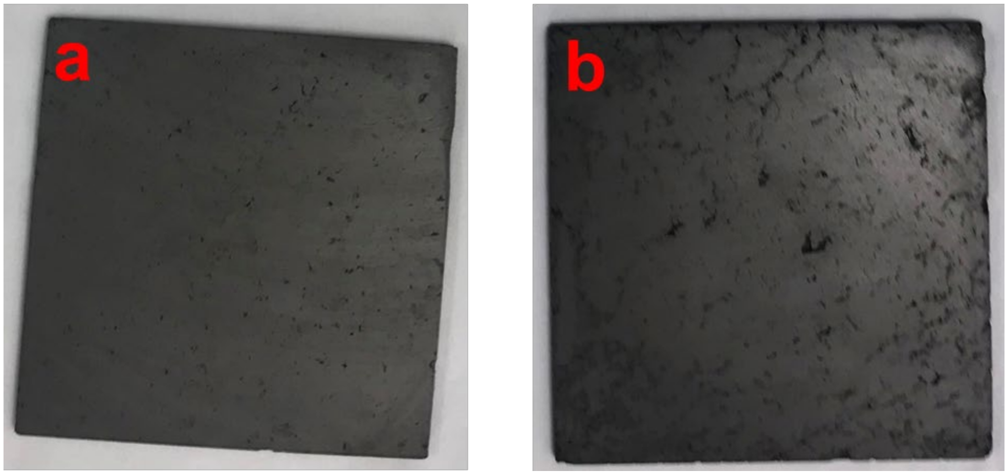

Figure I.1.11.7 Front and back of a 2” x 2” 60 vol.% Fe_4N in epoxy sample shipped to NREL for thermal characterization.

Thermal conductivity data collected at NREL for neat epoxy samples at three different temperatures (45°C, 100°C, and 150°C) are shown in Figure I.1.11.8. Figure I.1.11.9 contains the data for the 60 vol.% Fe_4N/epoxy composites. Neat epoxy samples averaged a thermal conductivity of 0.24 W/m·K and iron nitride filled epoxy samples averaged 1.8 W/m·K.

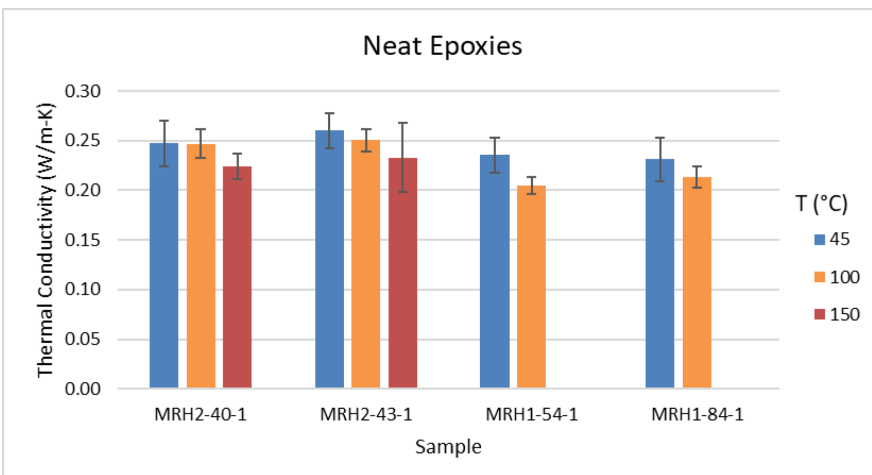

Figure I.1.11.8 Thermal conductivity results for neat epoxy samples collected at three different temperatures.

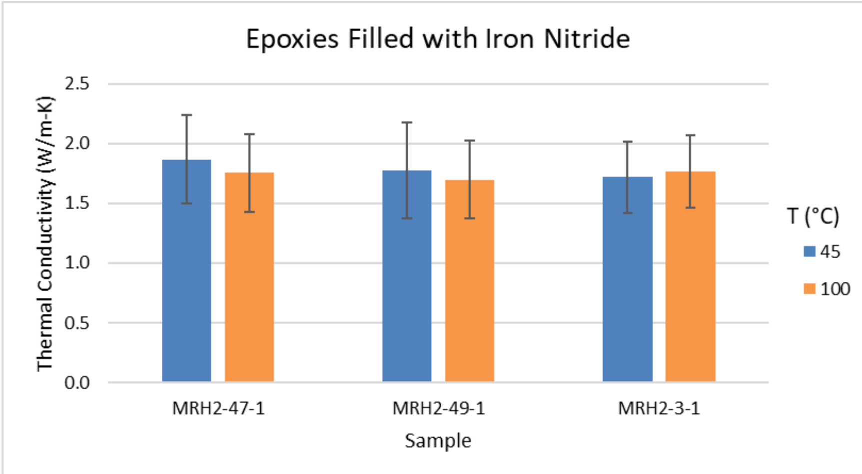

Figure I.1.11.9 Thermal conductivity results collected at both 45 °C and 100 °C for epoxy composites containing 60 vol.% Fe_4N.

Conclusions

During FY21, significant progress was made in the fabrication and characterization of iron nitride (γ'-Fe_4N) based magnetic composites for electric motors. The reader should keep in mind that these materials also show substantial promise as inductor cores for electric drive power electronics. A lab based hot pressing setup was constructed and used to produce Fe_4N based SMCs with an iron nitride vol.% loading > 70 %. The J_s of these samples was nearly 1 T, which is double that of the leading state-of-the-art insulating soft magnetic material (ferrite). Additionally, further increases in J_s for Fe_4N based SMCs are imminent. Samples were fabricated for thermal conductivity measurements by consortium member NREL and the thermal conductivity for 60 vol.% Fe_4N in epoxy composites was higher than expected (1.8 W/m·K). This higher thermal conductivity could prove helpful in the cooling of electric motors constructed with Fe_4N based SMCs. Future work will focus continuing to increase magnetic material volume loading and enhance magnetic performance in both electric motor and motor drive applications. Additionally, during FY 2021 we will continue to collaborate with EDTC consortium NREL and investigate the mechanical strength of Fe_4N/epoxy composites.

Key Publications

1. T.C. Monson, B. Zheng, R. Delaney, C. Pearce, Y. Zhou, S. Atcitty, E. Lavernia, Synthesis and Behavior of Bulk Iron Nitride Soft Magnets via High Pressure Spark Plasma Sintering. *Journal of Materials Research*, (2021). DOI: 10.1557/s43578-021-00379-z.

2. G. Ouyang, B. Jensen, W. Tang, J. Schlagel, C. Pan, B. Cui, K. Dennis, D. Jiles, T.C. Monson, I. Anderson, M.J. Kramer, and J. Cui, Near Net Shape Fabrication of Anisotropic Fe-6.5%Si Soft Magnetic Materials. *Acta Materialia* **201**, 209–216 (2020). DOI: 10.1016/j.actamat.2020.09.084.

References

1. US Drive, "Electrical and Electronics Technical Team Roadmap," Partnership Plan, Roadmaps, and Other Documents 2017.

2. H. Shokrollahi and K. Janghorban, "Soft magnetic composite materials (SMCs)," Journal of Materials Processing Technology, vol. 189, no. 1–3, pp. 1–12, 2007, doi: 10.1016/j.jmatprotec.2007.02.034.

3. J. S. Corporation. Super CoreTM Electrical steel sheets for high-frequency application. (2017). JFE Steel Corporation. [Online]. Available: http://www.jfe-steel.co.jp/en/products/electrical/catalog/f1e-002.pdf

4. J. M. D. Coey, Magnetism and Magnetic Materials. New York: Cambridge University Press, 2010.

5. T. C. Monson et al., “Soft Magnetic Multilayered FeSiCrB–Fe4N Metallic Glass Composites Fabricated by Spark Plasma Sintering,” IEEE Magnetics Letters, vol. 10, pp. 1–5, 2019, doi: 10.1109/LMAG.2019.2906832.

6. M. Qu et al., “Magneto-photo-acoustic imaging,” Biomed. Opt. Express, vol. 2, no. 2, pp. 385–396, 2011/02/01 2011, doi: 10.1364/BOE.2.000385.

7. M. Magazine. https://magneticsmag.com/new-structural-adhesive-from-delo-for-magnet-bonding-has-high-temperature-stability/ (accessed).

8. Crosslinktech. http://www.crosslinktech.com/products-by-application/featured-electric-motor-products.html (accessed).

9. M. Bond. https://www.masterbond.com/techtips/how-optimizing-glass-transition-temperature-tg (accessed).

10. A. Schoppa and P. Delarbre, “Soft Magnetic Powder Composites and Potential Applications in Modern Electric Machines and Devices,” IEEE Transactions on Magnetics, vol. 50, no. 4, pp. 1–4, 2014, doi: 10.1109/TMAG.2013.2290135.

11. P. Mason, K. Atallah, and D. Howe, Hard and soft magnetic composites in high-speed flywheels. 1999.

Acknowledgements

This work is supported by the DOE Office of Energy Efficiency and Renewable Energy, Vehicle Technologies Office. Sandia National Laboratories is a multi-mission laboratory managed and operated by National Technology and Engineering Solutions of Sandia, LLC., a wholly owned subsidiary of Honeywell International, Inc., for the U.S. Department of Energy’s National Nuclear Security Administration under contract DE-NA0003525. The views expressed in the article do not necessarily represent the views of the U.S. Department of Energy or the United States Government. We wish to thank Melinda Hoyt, Charles Pearce, Emily Johnson, and Tyler Stevens for their fabrication of magnetic composites; Robert Delaney and Charles Pearce for their assistance with magnetic characterization; and Mark Rodriguez for his help with X-ray diffraction data collection and analysis. We would also like to acknowledge key collaborators within the electric drive systems consortium: Kevin Bennion (NREL), Emily Cousineau (NREL), Iver Anderson (Ames Lab), Jun Cui (Ames Lab), and Matt Kramer (Ames Lab).

I.1.12 Component Modeling, Co-Optimization, and Trade-Space Evaluation (Sandia National Laboratories)

Jason Neely, Principal Investigator
Sandia National Laboratories
P.O. Box 5800, MS 1152
Albuquerque, NM 87185
Email: jneely@sandia.gov

Susan Rogers, DOE Technology Development Manager
U.S. Department of Energy
Email: susan.rogers@ee.doe.gov

Start Date: October 1, 2018 End Date: September 30, 2023
Project Funding: $300,000 DOE share: $300,000 Non-DOE share: 0

Project Introduction

This project is intended to support the development of new traction drive systems that meet the targets of 100 kW/L for power electronics and 50 kW/L for electric machines with reliable operation to 300,000 miles. To meet these goals, new designs must be identified that make use of state-of-the-art and next-generation electronic materials and design methods. Designs must exploit synergies between components, for example converters designed for high-frequency switching using wide band gap devices and ceramic capacitors. This project includes: (1) a survey of available technologies; (2) the development of design tools that consider the converter volume and performance; (3) exercising the design software to evaluate performance gaps and predict the impact of certain technologies and design approaches, i.e., GaN semiconductors, ceramic capacitors, and select topologies; and (4) building and testing hardware prototypes to validate models and concepts. Early instantiations of the design tools enable co-optimization of the power module and passive elements and provide some design guidance; later instantiations will enable the co-optimization of inverter and machine. Prototype testing begins with evaluation of simpler conversion topologies (i.e., the half-bridge boost converter) and progresses with fabrication of prototype inverter drives.

Objectives

For FY21, objectives included

- Investigate the feasibility of using nano-composite materials to realize a distributed EMI filter
- Investigate the use of 3D printed ceramics to improve thermal management
- Continue to Generate high-fidelity dimensional and electrical models for principal power electronic components within a novel inverter design
- Co-Optimize inverter design with machine model for power density, reliability, and efficiency
- Select a candidate inverter design from the Pareto-Optimal front, build, and test it.

Approach

The R&D approach employed by the team includes four strategies for generating design guidance and optimal designs, listed in order of increased fidelity and resources:

1. ***Empirical and First-Principles Analysis***: This uses first-principles knowledge, such as physical models, as well as comparative designs to inform the design.

2. ***High-Fidelity Modeling and Analysis***: This uses higher-order models that consider the component equivalent circuits, dimensions, reliability calculations, etc.

3. ***Global Co-Optimization***: With the definition of one or more performance metrics, components are simulated together, and their performance is measured and compared.

4. ***Hardware Iteration***: Using optimal designs identified in software, hardware exemplars are built and evaluated; 3 and 4 are iterated to create the best results.

In FY21, the project included elements of all four strategies, applied with different weight to the five objectives. Empirical analysis and modeling were applied to evaluate the feasibility of realizing a distributed filter using nanocomposite and to investigate the use of 3D printed ceramics for improving thermal management. Project efforts also continued to improve the fidelity of component models, developing the optimization software into a tool to identify designs in the Power Density-MTBF trade-space, using this software also to predict converter performance for SiC vs GaN and film vs ceramic capacitors, and building a power converter prototype to validate models. Hardware iteration also continued with inverter fabrication and test.

Based on the optimization results attained for an inverter drive in FY20, the principal contributors to inverter volume remained to be the thermal management components (i.e., the cold plate) and the AC EMI filter that connected the inverter drive to the motor. In particular, the optimization had selected for designs with 5 or more phases (i.e., multi-phase designs), ceramic capacitors, and higher-frequency switching. This primarily reduced the dc link capacitor size, but the greater number of phases increased the footprint of the devices and increased the number of EMI filter elements (i.e., more inductor cores). Thus, in FY21, the team investigated two approaches to mitigate filter and thermal management component size.

To address the filter size, the feasibility of using nano-composite materials to realize a distributed EMI filter was investigated. Specifically, the nanocomposite material, when evaluated as a bulk material, is insulating and has a magnetic permeability of $\mu_r \sim 5–10$; based on the spacing of nanoparticles and the permittivity of the epoxy, the material should have a permittivity of $\varepsilon_r \sim 5–10$. If the conductor spacing, geometry, and length are such that the distributed capacitance and inductance between conductors are sufficient, then EMI filtering can be accomplished in the AC bus (estimated to be approx. 10 cm long) if a nanocomposite encapsulant is used for the insulation. In FY21, the team investigated the feasibility of this approach using COMSOL multi-physics simulations.

To address the thermal management size, the team investigated the use of 3D printed ceramic components that could be used to realize a “surround cooling” capability that could be simpler and potentially more effective than double-sided cooling. In FY21, the team obtained samples of 3D printed material from Lithoz, performed flash diffusivity measurements to determine key parameters, and evaluated the efficacy of different geometries on managing heat using COMSOL Multi-physics simulations.

For the optimization work, the team continued to use the Genetic Optimization System Engineering Tool (GOSET) developed by Purdue University [1]. This MATLAB®-based software package consists of several scripts for implementing and solving a genetic algorithm optimization problem. The genetic algorithm is a probabilistic method for optimizing multi-input systems with non-convex solution spaces using the principles of genetics and a user-defined fitness function. GOSET allows for multiple fitness functions to be co-optimized into a Pareto front. To set up the optimization, the circuit schematic and physical layout were partially defined, and the dimensions of and between components, thicknesses of insulators, lengths of conductors, choice of SiC or GaN, number of phases, etc. were formulated and linked to the schematic definition in order to compute a volume and evaluate the circuit/system performance using a dynamic simulation. As described in the previous report, to evaluate system reliability, component mean time between failure (MTBF) quantities were also computed for SiC MOSFETS and capacitors using MIL-HDBK-217F calculations [2].

In FY21, the team worked to validate the simulation models used for optimization using test results from the boost converter built in FY20. The team also worked to increase the fidelity of component models developed for inductors, capacitors, switches, and heatsinks. Revised models were extended to the development of a 10-kW peak, 5.5 kW continuous multi-phase inverter. A set of inverter designs in the power density-MTBF design space were identified using GOSET, and a candidate design was selected and built.

Results

Feasibility Study of Distributed Filter

To investigate whether distributed inductance and capacitance might be sufficient to accomplish low-pass filtering and allow for the elimination of lumped-element inductors and capacitors, detailed COMSOL simulations were performed initially on a 2-conductor example. These assumed a 20 cm length, a flat rectangular copper conductor, and an insulating medium with $\mu_r = 10$ and $\varepsilon_r = 10$. Simulations were done on 2D and 3D cases. See illustration of 2D simulation results in Figure I.1.12.1 and illustration of 3D results in Figure I.1.12.2.

For this configuration, simulations identified potential for $L \sim 1.8$ µH/m and $C \sim 588$ pF/m. For these values and a candidate bus cable length of 20 cm, the cut-off frequency was estimated to be $f_c \sim 24.5$ MHz. This is well above the switching frequency of the converter (100s of kHz) and would thus be insufficient for filtering ripple. In addition, even for EMI filtering, if one were to assume a transition time of 100 nsec (T_{on} or T_{off}), one would need a filter cutoff well below 3.5 MHz. Thus, the team has concluded that this approach is not likely to work as proposed. The team will next consider the potential of using distributed inductance (to eliminate the inductor core) combined with lumped capacitor elements.

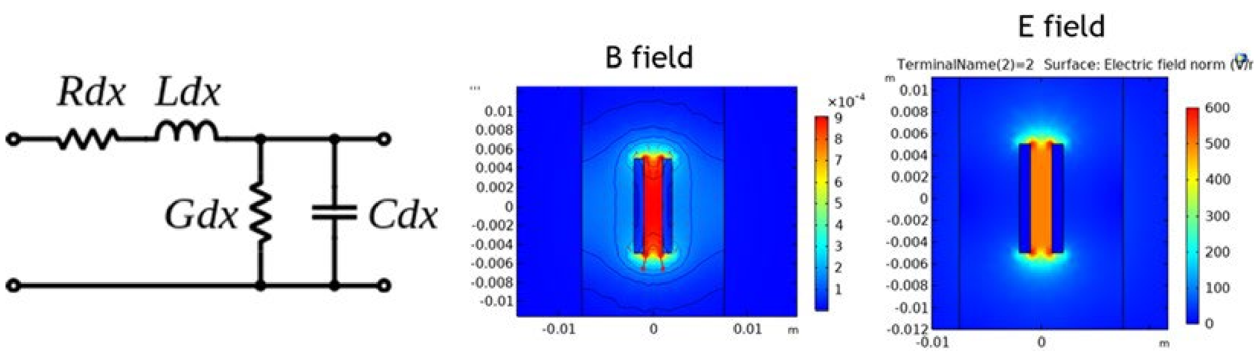

Figure I.1.12.1 (Left) Simplified Schematic of distributed inductance and capacitance (center) B-field simulations in COMSOL and (right) E-field simulations in COMSOL

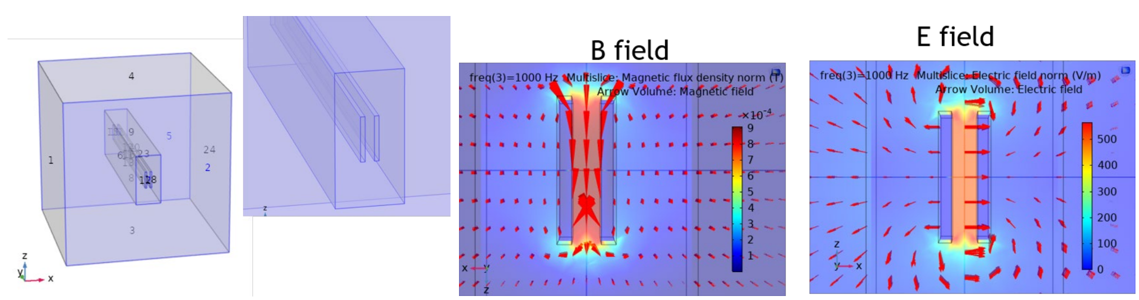

Figure I.1.12.2 (Left) 3D rendering of 2-conductor configuration (right) illustration of B-field and E-field lines in 3D

Investigation of 3D printed ceramics to improve thermal management

To improve thermal management, either to reduce the volume of thermal management components, or to reduce junction temperatures for a given volume, a new approach was investigated for the removing heat from the semiconductor devices. Specifically, 3D printed Al_2O_3 ceramic components can be used to surround and even encase electronic components with significant thermal loads. With this approach, a cold plate would still be used, but the ceramic components would route heat away from the top of devices down to the cold plate. This accomplishes double-sided cooling but avoids the complexity of contemporary assemblies. These components can have high resolution features ~100 µm and thus tightly fit around components and potentially include additional features, such as fins. To investigate this approach, samples were acquired from Lithoz and tested using flash diffusivity measurements. Printed Al_2O_3 ceramics measured thermal conductivities ranged from: 33.5 to 38.7 W/m-K and demonstrated a linear correlation with density. See Figure I.1.12.3.

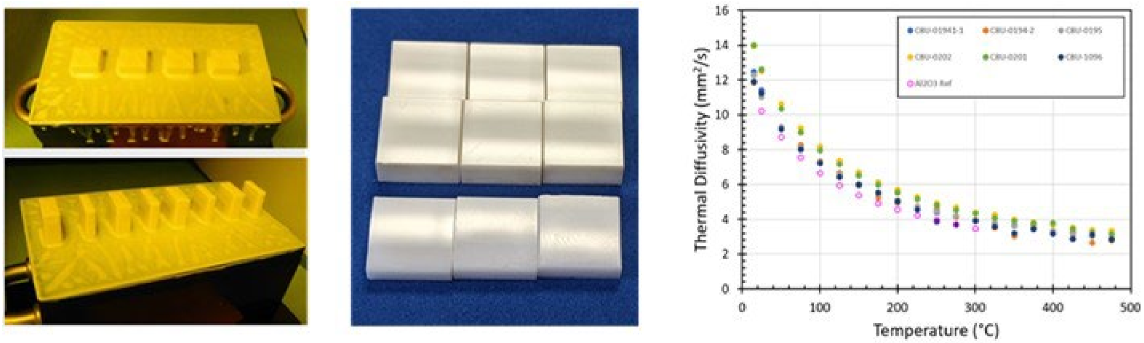

Figure I.1.12.3 (Left) As printed Al_2O_3 samples (center) sintered and polished samples and (right) measured thermal diffusivity as a function of temperature

These parameters were then used to inform COMSOL simulations to evaluate three design cases. Case 1 is the baseline case with a 2x2 mm^2 die bonded to a substrate and dissipating 10 W. Case 2 adds a ceramic structure around the device and encapsulates with a thermal epoxy. Case 3 fully encases the device and adds fins to the topside to enhance cooling. This preliminary modeling study showed a potential 11% and 29% reduction in temperature rise for Case 2 and Case 3 respectively, compared to the baseline. See Figure I.1.12.4 for an illustration of the three cases and a plot of simulated temperature rises.

The results of this simulation study are very promising, and the team plans to continue this work in FY22, including the fabrication and test of candidate Al_2O_3 ceramic components.

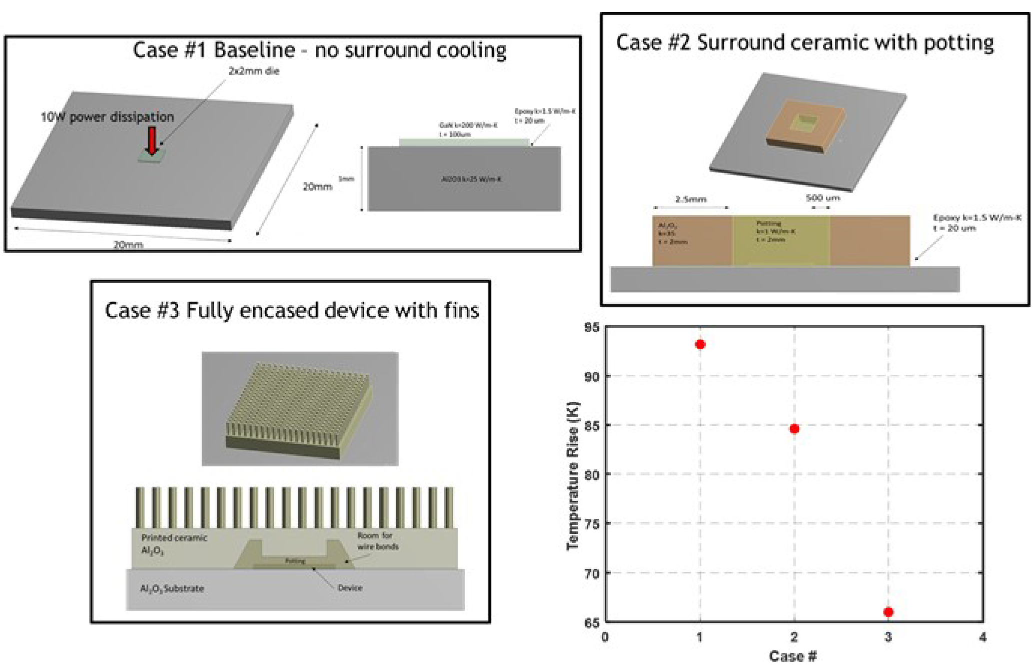

Figure I.1.12.4 Illustrates three design cases and the simulated temperature rise of the device junction for each

Optimization of Inverter Drive Volumetric Power Density, Efficiency, and MTBF

The team used GOSET to identify a set of designs for 10 kW peak, 5.5 kW continuous that were optimized in the efficiency-power density design space. This is an extension of the work in FY20 [3],[4]. A candidate design with 5 phases and a potential power density of 42.3 kW/L and 95.6% efficiency (at full voltage and steady-state power) was identified, and a prototype was designed. See Figure I.1.12.5. Therein, it is noted that the cold plate and AC filter inductors still dominate the size of the prototype. The prototype was built and tested. Thus far, the optimized inverter prototype has been tested up to 400 V with a demonstrated ~98% efficiency. Experimental voltage and current waveforms have also been validated against the simulation model at these voltage and power levels. The test setup, inverter photo and select waveforms are shown in Figure I.1.12.6. Evaluation of the prototype is ongoing.

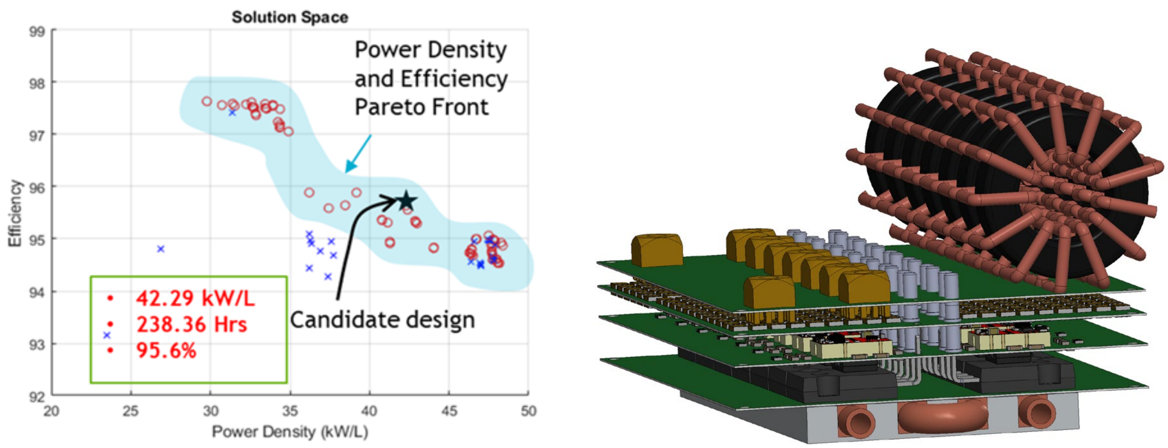

Figure I.1.12.5 (Left) Pareto Optimal Front with Candidate design indicated and (Right) 3D illustration of candidate design

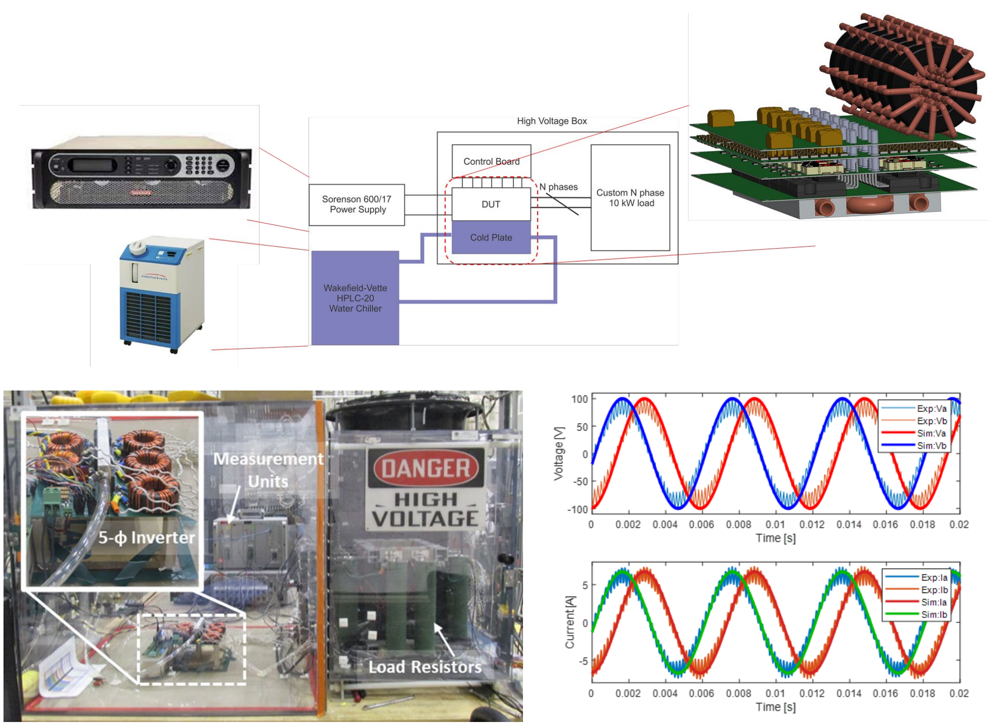

Figure I.1.12.6 (Top) Experimental setup (bottom Left) Prototype 5-phase Inverter in protective enclosure and (bottom right) simulated and measured waveforms

Finally, to support a more comprehensive optimization and prototype selection going forward, the optimization configuration was changed to enable co-optimization across three objectives: Power density, MTBF, and conversion Efficiency and to display the Pareto Optimal front as a surface. See Figure I.1.12.7. This approach is expected to better illustrate the tradespace and to provide better design choices going forward.

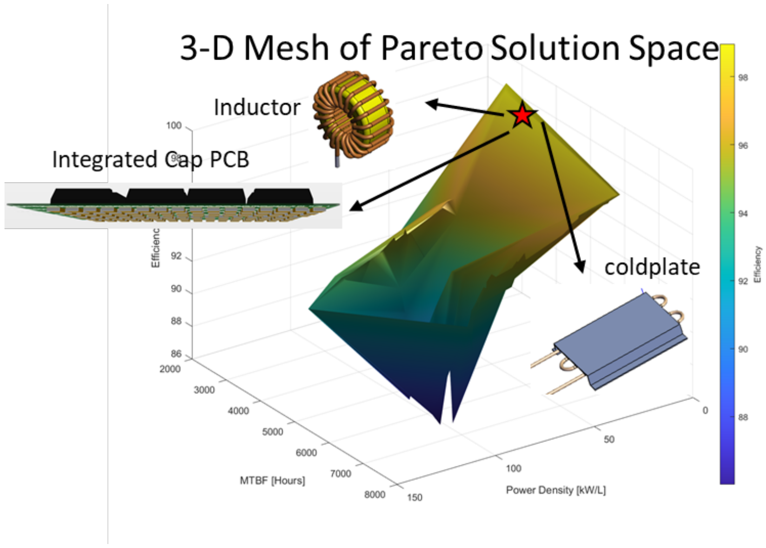

Figure I.1.12.7 3D Pareto-Optimal Surface (3 objectives) for Power Density, MTBF, and Efficiency

Conclusions

This project is focused on developing improved designs for future traction drive systems through the combined use of WBG devices, ceramic capacitors, high-frequency switching, and multi-phase designs that enable considerable improvements in power density. Designs are developed with the help of tools developed to perform multi-objective optimizations on electric drive designs. Unlike previous work, these include optimizations that consider component reliability, herein computed as mean time between failure (MTBF). In FY21, the project team continued the development and use of an optimization tool based on GOSET [1] to co-optimize converter power density, efficiency, and mean time between failures (MTBF) in a 10-kW peak, 5.5 kW continuous multi-phase inverter. A pareto optimal front was first generated in the efficiency-power density design space, an inverter design was selected, built, and tested to validate time-domain performance predictions. The project team later modified the optimization software to co-optimize across three objectives that include efficiency, power density, and MTBF. The team also investigated new approaches to reduce the size of the AC filter using distributed inductance and capacitance, but this scheme seems unlikely to yield a large benefit. The team also investigated the use of 3D printed Al_2O_3 ceramic components to aid in thermal management; the results of this work are very promising. Future work will refine the design tools and extend their use to optimize the inverter designs across the three design objectives, and to co-optimize the inverter and machine designs. The team will also continue the investigation of 3D printed Al_2O_3 ceramic components for thermal management.

Key Publications / Presentations

1. J. Neely, G. Pickrell, J. Flicker, L. Rashkin, R. Kaplar, “The Case for Vertical Gallium Nitride Devices in Electric Vehicle Drives,” *2020 IEEE Applied Power Electronics Conference* (APEC2020), Industry Session: Vehicle Electrification II.

2. L. Gill, J. C. Neely, L. J. Rashkin, J. D. Flicker and R. J. Kaplar, “Co-Optimization of Boost Converter Reliability and Volumetric Power Density Using Genetic Algorithm,” *2020 IEEE Energy Conversion Congress and Exposition (ECCE)*, Detroit, MI, USA, 2020, pp. 5302–5309, doi: 10.1109/ECCE44975.2020.9235716.

3. L. Rashkin, J. Neely, L. Gill, J. Flicker and R. Darbali-Zamora, "Optimal Power Module Design for High Power Density Traction Drive System," *2020 IEEE Transportation Electrification Conference & Expo (ITEC)*, Chicago, IL, USA, 2020, pp. 134–138, doi: 10.1109/ITEC48692.2020.9161703.

References

1. S. D. Sudhoff, GOSET: Genetic Optimization System Engineering Tool: For Use with MATLAB®, version 2.6, January 1, 2014.

2. *Military Handbook: Reliability prediction of electronic equipment*, 1991. Available: https://snebulos.mit.edu/projects/reference/MIL-STD/MIL-HDBK-217F-Notice2.pdf

3. L. Gill, J. C. Neely, L. J. Rashkin, J. D. Flicker and R. J. Kaplar, "Co-Optimization of Boost Converter Reliability and Volumetric Power Density Using Genetic Algorithm," *2020 IEEE Energy Conversion Congress and Exposition (ECCE)*, Detroit, MI, USA, 2020, pp. 5302–5309, doi: 10.1109/ECCE44975.2020.9235716.

4. L. Rashkin, J. Neely, L. Gill, J. Flicker and R. Darbali-Zamora, "Optimal Power Module Design for High Power Density Traction Drive System," *2020 IEEE Transportation Electrification Conference & Expo (ITEC)*, Chicago, IL, USA, 2020, pp. 134–138, doi: 10.1109/ITEC48692.2020.9161703.

Acknowledgements

This work is supported by the DOE Office of Energy Efficiency and Renewable Energy, Vehicle Technologies Office. Sandia National Laboratories is a multi-mission laboratory managed and operated by National Technology and Engineering Solutions of Sandia, LLC., a wholly owned subsidiary of Honeywell International, Inc., for the U.S. Department of Energy's National Nuclear Security Administration under contract DE-NA0003525. The views expressed in the article do not necessarily represent the views of the U.S. Department of Energy or the United States Government.

I.1.13 Integrated Traction Drive Thermal Management (National Renewable Energy Laboratory)

Bidzina Kekelia, Principal Investigator
National Renewable Energy Laboratory
15013 Denver West Parkway
Golden, CO 80401
Email: bidzina.kekelia@nrel.gov

Susan A. Rogers, DOE Technology Development Manager
U.S. Department of Energy
Email: susan.rogers@ee.doe.gov

Start Date: October 1, 2018 End Date: September 30, 2024
Project Funding (FY 21): $250,000 DOE share: $250,000 Non-DOE share: $0

Project Introduction

To enable the mass-market penetration of electric-drive vehicles and meet consumer electric vehicle performance expectations, the U.S. DRIVE 2017 *Electrical and Electronics Technical Team Roadmap* [1] proposes aggressive research and development targets aimed at reducing cost and increasing electric traction-drive system power density to 33 kW/L by 2025. The target includes high-voltage power electronics and a single traction-drive electric motor. Achieving this level of system power density requires integration of the inverter and the electric motor into a single traction module. However, this approach also requires innovative thermal management solutions to provide adequate cooling to more densely packed electrical components and keep their operating temperatures within optimal range.

Objectives

The main objectives of this project are to:

- Research and evaluate motor-integrated power electronics topologies and thermal management solutions for electric traction drives.
- Identify candidate driveline fluids suitable for direct cooling of traction-drive components and high-voltage power electronics.
- Characterize selected driveline fluids by measuring convective cooling and, if appropriate and feasible, electrical properties.
- Provide support to other collaborating researcher teams of the Electric Drive Technologies Consortium in thermal management aspects for their integrated drive concepts.

Approach

Building on previous years of research of most efficient heat removal from integrated traction-drive components and modeling of various cooling strategies, several scenarios were selected for comparative analysis. The results, outlining benefits and drawbacks of each approach, were summarized in a conference publication [2] and a popular online magazine article, which was accepted for publication for a Spring 2022 issue [3].

Support activities in thermal management component design and thermal modeling for integrated traction drives of Oak Ridge National Laboratory (ORNL) and University of Wisconsin research teams are continuing. An initial design for ORNL's outer-rotor motor thermal management system is presented in the Results section. Collaboration with the University of Wisconsin team is also successfully progressing, and early design of their integrated drive is presented in the Results section.

Results

Modeling Integration Concepts and Comparative Analysis of Cooling Approaches

In comparative analysis, three main integration approaches were identified for electric traction drives:

1. Power electronics enclosure attached to an electric motor case, eliminating the wire harness, but with separate (often sequential) cooling loops.
2. Power electronics radially integrated onto the electric motor case with a shared cooling loop.
3. Power electronics axially integrated onto the front/back of the electric motor case with potentially a single fluid cooling solution (circulating water-ethylene glycol or using automatic transmission fluid [ATF] jet impingement).

All three integration approaches yield volumetric and weight savings compared to the traditional traction system solutions. Based on the above integration approaches, several cooling scenarios were analyzed—including combination of water-ethylene glycol flow in internal channels of cooling jacket and ATF jet impingement on stator winding end-turns and power electronics. The modeled and reviewed integration cases show that with careful design and selection of the appropriate cooling techniques, sufficient cooling can be achieved both for the electric motor and the power electronics with a single, compact thermal management solution. Tight integration of power electronics into the electric motor enables volume, mass, and cost savings on their enclosures, interconnections, cooling systems, and overall number of required parts, making the electric vehicle propulsion system lighter and more efficient as a result.

Jet Impingement Cooling

Experimental convective heat transfer characterization of jet impingement cooling with ATF was not carried out during fiscal year (FY) 2021. The plan is to modify the existing experimental fluid loop or build a small, dedicated fluid loop bench for characterization of jet impingement cooling and continue work in FY 2022.

Instead, FY 2021 proved to be interesting in terms of research collaboration with other groups involved with ATF jet impingement cooling of electric traction drives. IFP Energies Nouvelles (IFPEN)—a French public research, innovation, and training organization in the fields of energy, transport, and the environment [4]—reached out to the Advanced Power Electronics and Electric Machines (APEEM) group at the National Renewable Energy Laboratory (NREL) and expressed an interest in further modeling of NREL's ATF jet impingement experimental characterization results. Of particular interest was temperature-dependent enhancement of heat transfer coefficients of ATF jet impingement cooling. Preliminary results of IFPEN's modeling study were recently shared with the APEEM group, which showed good agreement with NREL's experimental results (increase in heat transfer coefficients with increased temperature). Coauthoring a joint manuscript with IFPEN is planned. In addition, the APEEM group was invited to deliver a keynote presentation at the Large-Eddy Simulation for Energy Conversion in electric and combustion Engines (LES4ECE) virtual conference organized by IFPEN [5].

Supporting ORNL's Outer-Rotor Integrated Motor Design

Thermal management system design for ORNL's outer-rotor integrated drive (Figure I.1.13.1) is ongoing. Application of nontraditional materials (ceramics, thermally enhanced resins) and manufacturing processes (3D printing) is being explored for key thermal management system components.

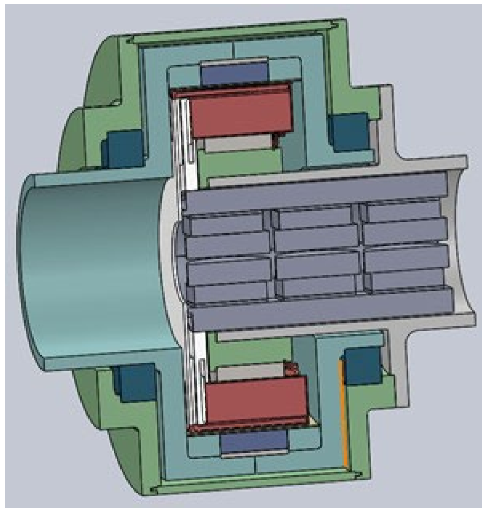

Figure I.1.13.1 ORNL's outer-rotor motor with integrated inverter in the central cavity (Figure courtesy of Bidzina Kekelia, NREL)

Manufacturing of the second iteration of the distribution manifold disk with attached phase-separator heat exchangers shown in Figure I.1.13.2 from ceramics proved to be challenging due to its large diameter.

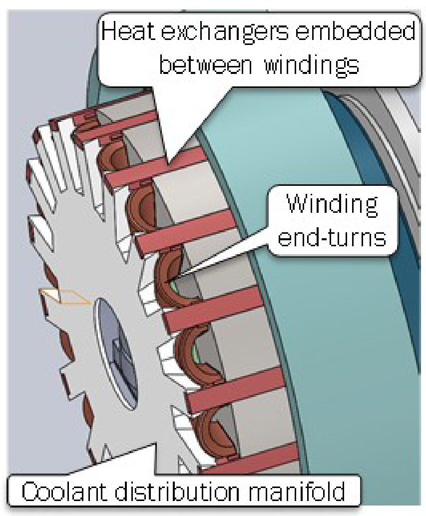

Figure I.1.13.2 The second iteration of the design of cooling system components: fluid distribution manifold disk is shown in white (Figure courtesy of Bidzina Kekelia, NREL)

Thus, it was decided to reconfigure the phase-separator heat exchangers with coolant inlet-outlet turned by 90° (Figure I.1.13.3) and redesign the distribution manifold disk with smaller effective diameter (to be completed in FY 2022).

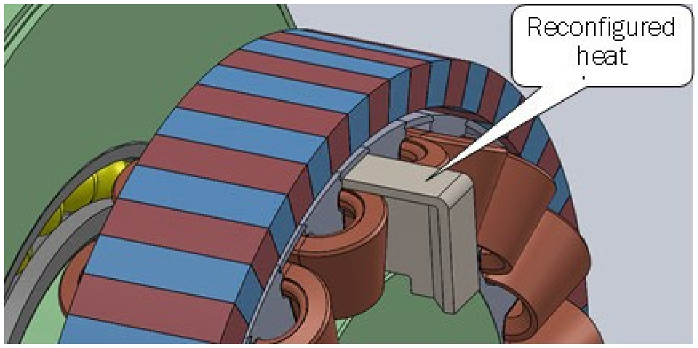

Figure I.1.13.3 The redesigned phase-separator heat exchanger with 90° reoriented coolant inlet-outlet (Figure courtesy of Bidzina Kekelia, NREL)

Further work on design, manufacturing, and performance evaluation of select key components and subassemblies of ORNL's integrated traction-drive thermal management system employing novel materials and methods is planned in FY 2022, namely 3D printing with ceramic and thermally enhanced polymers/resins of phase-separator heat exchangers and coolant distribution manifold.

Supporting University of Wisconsin's Integrated Motor Design Team

The NREL team is participating in regular weekly (general design emphasis) and biweekly (thermal management emphasis) meetings with University of Wisconsin team and advising on various aspects of thermal modeling in commercial finite element analysis (FEA) and computational fluid dynamics (CFD) software and material/interface selection for key components of the integrated drive. The current design stage of the drive is illustrated in Figure I.1.13.4.

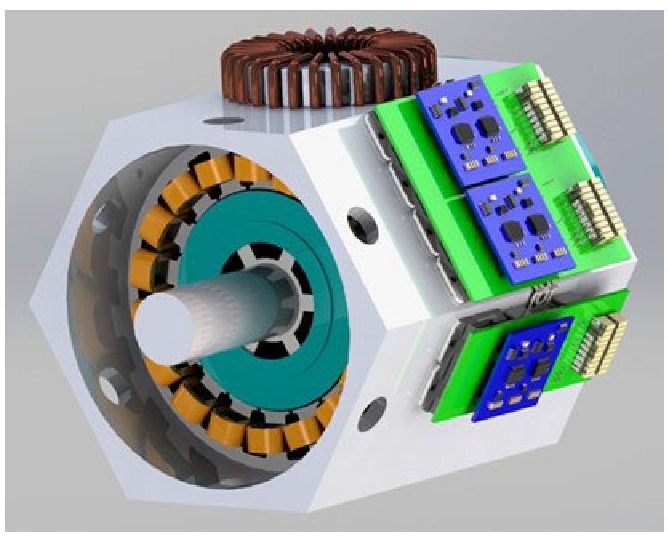

Figure I.1.13.4 Design progress in University of Wisconsin's integrated traction drive (Figure courtesy of the University of Wisconsin)

Conclusions

The project accomplishments and conclusions for FY 2021 are summarized as follows:

- Based on previous research and comparative thermal analysis of selected cooling approaches for the integrated electric drives, it was shown that with careful design and selection of the appropriate cooling techniques, sufficient cooling can be achieved both for the electric motor and the power electronics with a single, compact thermal management solution.

- Thermal modeling study results were summarized in a conference paper and online magazine (see Key Publications).
- A research collaboration on jet impingement cooling techniques for electric traction drives was initiated with IFP Energies Nouvelles—a French public research, innovation, and training organization in the fields of energy, transport, and the environment.
- Application of novel materials (ceramics, thermally enhanced resins) and manufacturing processes (3D printing) for key integrated drive thermal management system components was proposed. Further design, modeling, and experimental evaluation of these components and/or subsystems is planned by the NREL team in FY 2022.

Key Publications

1. Kekelia, B, Cousineau, JE, Bennion, K, Narumanchi, S, and Chowdhury, S. “Comparison of Thermal Management Approaches for Integrated Traction Drives in Electric Vehicles.” *Proceedings of the ASME 2020 International Technical Conference and Exhibition on Packaging and Integration of Electronic and Photonic Microsystems*. Virtual, Online. October 27–29, 2020. V001T01A001. ASME. https://doi.org/10.1115/IPACK2020-2524
2. Kekelia, B, and Narumanchi, S. “Thermal Management of Integrated Traction Drives in Electric Vehicles.” *Electronics Cooling* (accepted for publication, Spring 2022 issue).

References

1. U.S. DRIVE. 2017. *Electrical and Electronics Technical Team Roadmap.* Washington, D.C.: U.S. Department of Energy Office of Energy Efficiency and Renewable Energy Vehicle Technologies Office. https://www.energy.gov/sites/prod/files/2017/11/f39/EETT%20Roadmap%2010-27-17.pdf.
2. Kekelia, B, Cousineau, JE, Bennion, K, Narumanchi, S, & Chowdhury, S. “Comparison of Thermal Management Approaches for Integrated Traction Drives in Electric Vehicles.” *Proceedings of the ASME 2020 International Technical Conference and Exhibition on Packaging and Integration of Electronic and Photonic Microsystems*. Virtual, Online. October 27–29, 2020. V001T01A001. ASME. https://doi.org/10.1115/IPACK2020-2524
3. Kekelia, B, & Narumanchi, S. “Thermal Management of Integrated Traction Drives in Electric Vehicles.” *Electronics Cooling* (accepted for publication, Spring 2022 issue).
4. IFP Energies Nouvelles. “Research and Innovation for the Energy Transition and Sustainable Mobility.” https://www.ifpenergiesnouvelles.com
5. IFP Energies Nouvelles. “LES4ECE virtual conference: LES for Energy Conversion in electric and combustion Engines.” https://www.les4ece.com/en

Acknowledgements

The author would like to acknowledge the significant contributions of Kevin Bennion and Emily Cousineau from NREL. Valuable input and technical data from Shajjad Chowdhury, Tsarafidy Raminosoa, and Randy Wiles from ORNL are also appreciated.

I.1.14 Power Electronics Materials and Bonded Interfaces – Reliability and Lifetime (National Renewable Energy Laboratory)

Paul Paret, Principal Investigator
National Renewable Energy Laboratory (NREL)
15013 Denver West Parkway
Golden, CO 80401
Email: paul.paret@nrel.gov

Susan A. Rogers, DOE Technology Development Manager
U.S. Department of Energy
Email: susan.rogers@ee.doe.gov

Start Date: October 1, 2018 End Date: September 30, 2024
Project Funding(FY 21): $175,000 DOE share: $175,000 Non-DOE share: $0

Project Introduction

Robust and reliable power electronics packaging technologies are critical for the safe operation of wide-bandgap devices such as silicon carbide and gallium nitride, particularly at high temperatures. The unique characteristics of wide-bandgap devices that prove to be challenging for their packaging are high switching speed (dV/dt and di/dt), high operation temperature, and high electric field. The cost and power-density targets for these packages or modules only increase the challenges associated with their design and development. Material selection and component design within a package play a key role in determining its reliability and lifetime under high-temperature operating conditions. Advanced packaging layouts, such as 3D packaging, planar interconnects, and direct-lead bonding, are considered by researchers and engineers to minimize loop parasitics and reduce the junction-to-coolant thermal resistance. Materials in the right combination need to be properly integrated to address the inherent coefficient of thermal expansion and stiffness mismatch issues within packaging.

For a traditional silicon device-based power electronics package, bonded interfaces (i.e., die-attach and substrate-attach) are prone to failure under environmental loading conditions such as thermal cycling and power cycling. The reliability of the package is dictated—to a significant extent—by the ability of these interface materials to withstand the stress imposed on them under long-term exposure to high temperatures and thermal gradients. While the maximum operating temperature of Si devices is around 150°C, the 200°C–250°C desired operating temperature range of wide-bandgap devices places a more stringent requirement on the reliability and lifetime of the bonded interfaces. Solders such as SAC305 and 63Sn37Pb are not suitable for operation at these extreme temperatures. Among the high-temperature-compatible bonded interfaces, sintered silver and transient liquid-phase bonded materials are regarded as strong candidates; however, their reliability and failure mechanisms at high temperatures need to be investigated.

This report describes research at the National Renewable Energy Laboratory (NREL) in assessing the reliability and lifetime prediction model development of sintered silver and the copper-aluminum (Cu-Al) transient-bonded interface material. In collaboration with Virginia Tech (VT), samples with sintered silver as the bonded material were fabricated and subjected to accelerated thermal cycling. High-lead solder samples were also fabricated at NREL for comparison with sintered silver results. In addition, a lifetime prediction model for sintered silver was developed by correlating crack growth rates obtained from experiments and strain energy density per cycle results computed through finite element modeling. Along with sintered silver, collaborative efforts between NREL and Georgia Tech on the fabrication and thermal cycling of Cu-Al bonded interface samples are discussed.

Objectives

The major objectives of this project are to:

- Evaluate the reliability of sintered silver by subjecting coefficient of thermal expansion (CTE)-mismatched coupons—with sintered silver as the bonded interface material—to accelerated thermal cycling. Crack propagation or any other failure mechanisms that originate and evolve under thermal cycling will be periodically monitored through scanning acoustic microscopy imaging.
- Develop thermomechanical models to obtain theoretical parameters such as von Mises stress, strain-energy density, and J-integral, and formulate a lifetime prediction model based on these modeling outputs and experimental data.
- Synthesize Cu-Al bond samples with less than 5% void fraction and subject these samples to accelerated thermal cycling.

Approach

Sintered Silver

In previous years of this project, sintered silver samples were fabricated at VT using two different synthesis profiles. One was purely a pressureless sintering approach, while a small amount of sintering pressure in the range of 3–10 MPa was attempted in the other profile. The pressureless sintering profile never resulted in good quality joints, whereas joints with less than 3% void fraction were obtained in almost all the pressure-sintered samples. In all cases, the sample configuration consisted of a Cu disk bonded to an Invar disk with sintered silver as the bonded material, as shown in Figure I.1.14.1. The diameter and thickness of these disks are 25.4 mm (1 inch) and 2 mm, respectively. With this configuration, samples with three different bond diameters (22 mm, 16 mm, and 10 mm) were fabricated and then subjected to a thermal cycle from -40°C to 200°C. Scanning acoustic microscope (C-SAM) images of the samples obtained after 50 cycles revealed a large amount of degradation in the sintered silver joint layer. A combination of adhesive and cohesive crack propagation was observed in the cross-sectional images of these samples. Thermomechanical modeling to study the degradation behavior of sintered silver joints under thermal cycling was also developed.

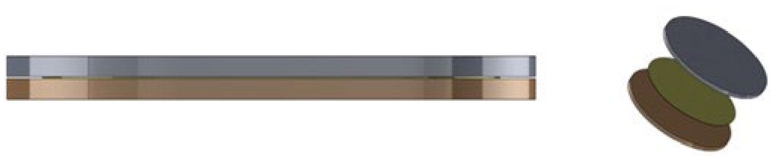

Figure I.1.14.1 Circular coupons (Φ25.4 mm) for reliability evaluation; Cu (bottom) bonded to Invar (top) using sintered silver or high-lead solder (95Pb5Sn)

In fiscal year (FY) 2021, samples with high-lead solder (95Pb5Sn) as the bonded material and a disk thickness of 1 mm were subjected to thermal cycling to obtain reference data. The joint diameter was kept at 25.4 mm. Similar samples with sintered silver were also fabricated; however, these samples delaminated after just 10 thermal cycles. We included these thinner samples in the project to study the impact of sample thickness on the reliability of the bonded material. Additionally, a lifetime prediction model for sintered silver was formulated by correlating the crack growth rates obtained from experiments and the strain energy density per cycle results computed through modeling. This lifetime prediction model encompasses the thermomechanical behavior of sintered silver at 200°C.

Cu-Al Transient Liquid-Phase Bond

A transient liquid-phase bond was developed at Georgia Tech using a Cu-Al eutectic, which can be used as a bonded material in high-temperature power electronics applications. To create this bond, Cu and Al foils are joined in a specific bulk ratio and heated above their eutectic point, but below the melting temperature of the constituent metals. Although this material has demonstrated potential for high reliability under certain specific configurations in other projects, its reliability—when used for bonding in CTE-mismatched samples under a thermal cycle of -40°C to 200°C—needs to be evaluated. To this end, attempts were made at Georgia Tech in FY 2020 to improve the bond quality of Cu-Al samples in which the alloy was bonded between AlN (0.63-mm-thick) and AlSiC (3-mm-thick) coupons. The size of these coupons was 25.4 mm × 25.4 mm (1 inch × 1 inch). Initial characterization of these samples was conducted at NREL through C-SAM imaging and thermal resistance measurements using an ASTM thermal interface material (TIM) stand. A schematic of the sample and a picture of the TIM stand are shown in Figure I.1.14.2. Thermal cycling from -40°C to 200°C was also conducted on the samples.

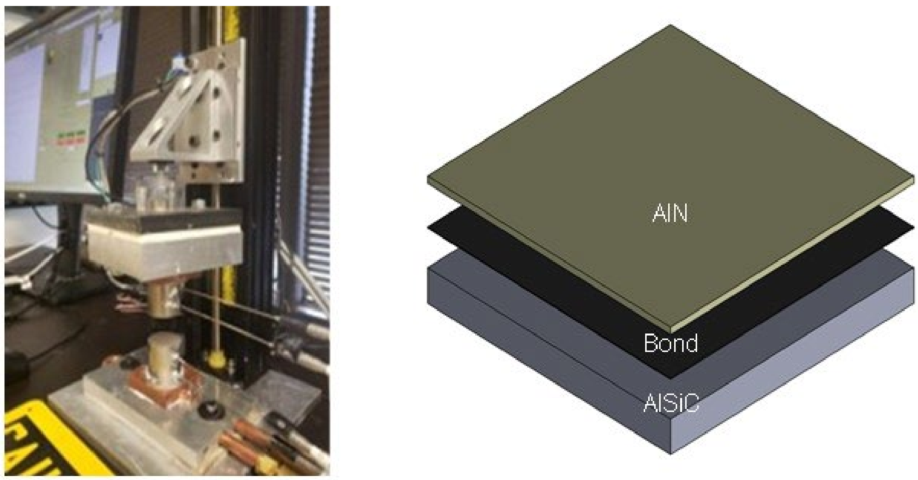

Figure I.1.14.2 ASTM TIM stand (left) and sample configuration for the reliability evaluation of the Cu-Al bond (right)

Results

Sintered Silver

Figure I.1.14.3 shows the C-SAM images of sintered silver and 95Pb5Sn solder joints before and after 50 cycles of thermal cycling from -40°C to 200°C. Although the pre-cycling images of sintered silver were presented in the previous reports, they are included here for comparison with solder joints. The white patches on the images before cycling likely indicate the presence of voids or represent poor bonding quality. An observation of the C-SAM images after 50 cycles reveals the significant increase in the white regions within the bond due to the formation of cracks. Crack formation is evident at both the Cu side and Invar side of the bond layer in all samples.

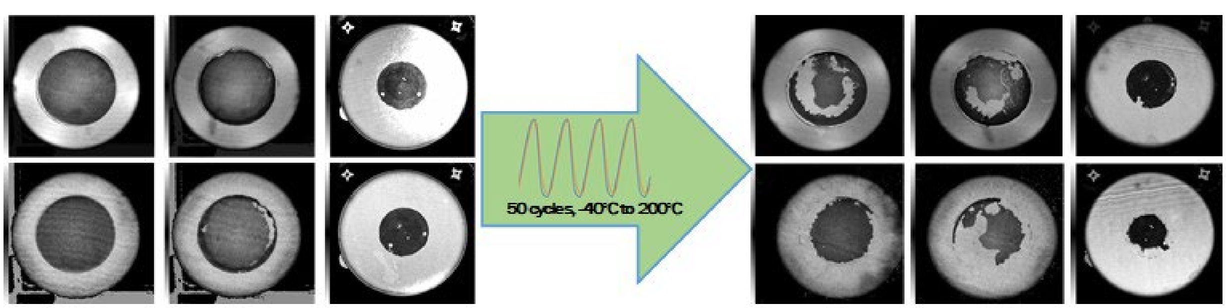

Figure I.1.14.3 C-SAM images of sintered silver and 95Pb5Sn solder joints before cycling (left) and after 50 thermal cycles (right); Cu-side images (top) and Invar-side images (bottom); within each figure, 3 MPa sintered silver is at the left, 10 MPa sintered silver is at the center, and 95Pb5Sn solder joint is at the right.

Figure I.1.14.4 shows a comparison of the crack growth rates between solder and the 3-MPa sintered silver samples. Here, the 25.4-mm-diameter solder samples are compared with the 22-mm sintered silver samples.

Although it is hard to accurately estimate the crack growth in sintered silver in the initial stages of thermal cycling due to the lower frequency of measurements, it can be observed that solder exhibited a significantly lower initial crack propagation rate in the 25.4-mm case. Also, despite the 10-mm solder samples reaching the failure criterion of 20% crack growth in just 20 cycles, the crack growth rate thereafter slows down toward the later stages of thermal cycling. Based on these experimental observations, we can conclude that under a large CTE-mismatch configuration subjected to a thermal cycling profile of -40°C to 200°C with high ramp rates, solder demonstrates a higher reliability potential than sintered silver for large-area attachment applications.

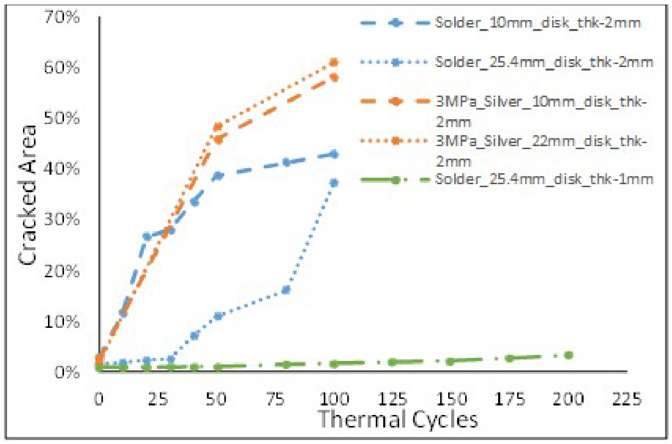

Figure I.1.14.4 Crack growth comparison between solder and sintered silver samples

To investigate the impact of outer coupon thickness on the reliability of the bond material, we fabricated additional samples with 1-mm-thick Cu and Invar disks and subjected them to thermal cycling. In these samples, we kept the bond diameter at 25.4 mm for both sintered silver and solder joints. The objective here was to study the thermomechanical behavior of the bond materials under the same CTE-mismatch configuration but with a lower sample stiffness. Similar to the 2-mm-thick configuration, these samples were characterized using C-SAM images before the start of thermal cycling and at every 10-cycle interval. In this experiment, the initial void fraction was measured at around 2.5% and 1% for sintered silver and solder samples, respectively. Under thermal cycling, the sintered silver samples completely delaminated after just 10 cycles, whereas the amount of cracking in the solder samples was measured at around 3% even after 200 cycles, as shown by the green dash-dotted line in Figure I.1.14.4. In general, a thinner outer or adjacent disk should improve the reliability of the bond, as it allows for more compliance and a resulting reduction in the stress imparted on the joint. This trend was clearly observed for the solder samples with their significantly lower crack growth rate, but the total delamination of sintered silver samples after just 10 cycles likely indicates a poor initial bond strength stemming from either the nonuniform flatness of the outer disks or minor variations in the synthesis process.

To understand the failure mechanisms that occurred in sintered silver and solder joints under thermal cycling, we obtained and analyzed cross-sectional optical microscope images of a few samples. Figure I.1.14.5 shows the optical cross-sectional image of a solder bond (top) and the scanning electron microscope (SEM) image of a sintered silver sample. In sintered silver samples, we found the overall failure mechanism to be a combination of adhesive and cohesive fracture, with adhesive fracture being predominant in general. In some cases, cohesive cracks took the form of a short, near-vertical path, whereas in a few other cases, we observed extended cohesive cracking along the longitudinal direction of the bond. Cohesive cracking alone was not observed in any of the samples, and in most cases, they primarily acted as a connecting path between the adhesive cracks at both interfaces. The crack likely originated in the adhesive mode at either the Cu side or the Invar side and migrated to the other end through the bond, driven by the nature of pore distribution in the sintered silver material. Ion milling was conducted on the cross-sectioned samples prior to the SEM imaging process. A careful analysis of SEM images reveals the presence of minor cohesive cracks between small voids within the bond region. Also, the formation of these minor cracks seems to be independent of the major adhesive cracks occurring at the interface. The bond regions between the voids could be under a larger stress concentration compared to the remaining sections, thus leading to the formation of thin cracks.

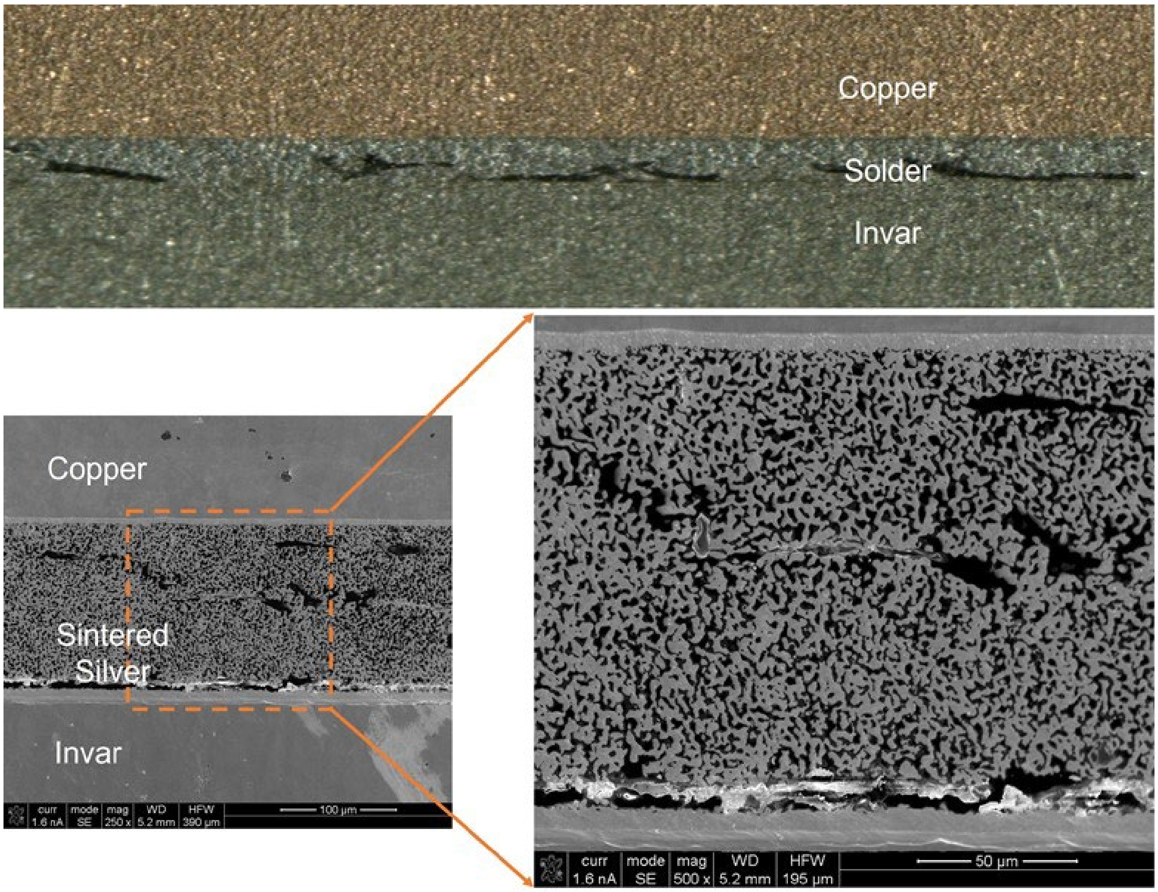

Figure I.1.14.5 Cross-sectional images of solder (top) and sintered silver (bottom) bonds

The observation of adhesive cracking in sintered silver samples in this study is similar to the results obtained by Knoerr, Kraft, and Schletz [1], but cohesive cracking was the main failure mechanism in nano-silver samples subjected to thermal cycling experiments by Siow and Chua [2]. In the case of solder bonds, a similar failure mechanism—a combination of adhesive and cohesive fracture—was observed, but the crack initially followed a meandering trajectory and then extended on as an adhesive fracture. The cracks occurred mostly at and in the vicinity of the solder-Invar interface.

In addition to experimental results, we computed strain energy density per cycle values at the sintered silver and solder interfaces through thermomechanical modeling, and the results were presented in the FY 2020 report. An agreement between the modeling and experimental results of sintered silver samples allows us to formulate a lifetime prediction model by correlating the strain energy density per cycle with the crack growth rate, as shown in Figure I.1.14.6. In this graph, the crack growth measurements of the 3-MPa sintered silver samples with different bond diameters at the 50-cycle interval were converted to crack growth rates and are expressed in percentage of the cracked area over the number of thermal cycles. We selected the 50-cycle mark because all samples were recorded to have reached the failure criterion by then. A simple power-law model, similar to a Paris' law equation, was used to define the correlation that serves as the lifetime prediction model. From Figure I.1.14.6, the lifetime prediction model is:

$$\frac{dA}{dN} = 0.76\,\Delta W^{0.431} \tag{1}$$

Here, $\frac{dA}{dN}$ denotes crack growth rate and ΔW represents the volume-averaged strain energy density per cycle.

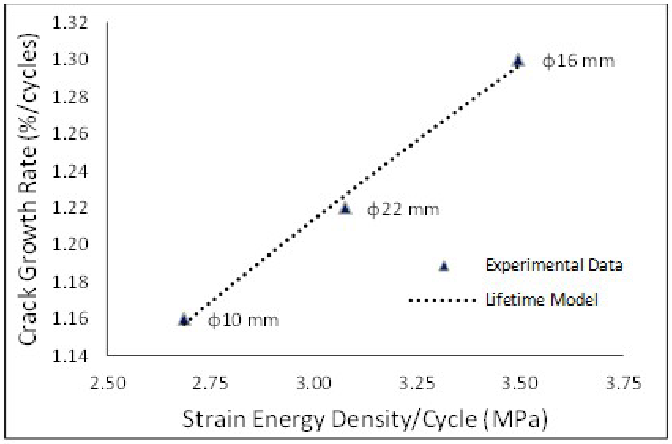

Figure I.1.14.6 Lifetime prediction model of sintered silver

Although lifetime models of sintered silver exist in the literature, the model in Equation 1 encompasses the thermomechanical behavior of sintered silver as a large-area attachment at a high temperature of 200°C, which, to the authors' knowledge, has not been covered prior to this study. It must be noted that this lifetime model is based on average values of crack growth rates recorded for sintered silver samples of different bond diameters, but no solid conclusions as to which bond diameter performed the best can be derived based on the experimental results alone. Also, the coefficients in the model depend on the bond region selected for volume-averaging the strain energy density results. As a 2-mm-wide outer annular region of the bond was selected in this study, practitioners of the lifetime model in Equation 1 must be sure to select a similar geometrical region in their respective designs to obtain lifetime results with improved accuracy. Additionally, the crack growth rates obtained as outputs using Equation 1 can be converted to cycles-to-failure predictions, with failure defined as a certain percentage of crack growth by area. Apart from the typical drawbacks of an empirical approach to develop lifetime models, a restriction of the model in Equation 1 is that it is completely based on sintered silver samples fabricated under 3 MPa of sintering pressure. Hence, application of this model to cases other than 3 MPa may result in less accurate predictions.

Cu-Al Transient Liquid-Phase Bond

In FY 2021, samples with Cu-Al as the bond between 0.63-mm-thick AlN and 3-mm-thick AlSiC coupons were bonded at Georgia Tech and sent to NREL for reliability evaluation. Similar to the sintered silver samples, the initial characterization of these samples was conducted through C-SAM images. Additionally, overall thermal resistance of the samples was measured using the ASTM TIM stand. C-SAM images of these samples fabricated in FY 2020 revealed a significant presence of voids indicating a poor bond quality. This year, different variations were attempted in the fabrication process; however, the defect fraction was still not within the acceptable range of less than 5% of the entire bonding area.

Figure I.1.14.7 shows the C-SAM images of the Cu-Al joints before thermal cycling. Large patches of white regions can be observed in these images, which denote the presence of voids. A total of 15 samples were subjected to high-temperature thermal cycling from -40°C to 200°C.

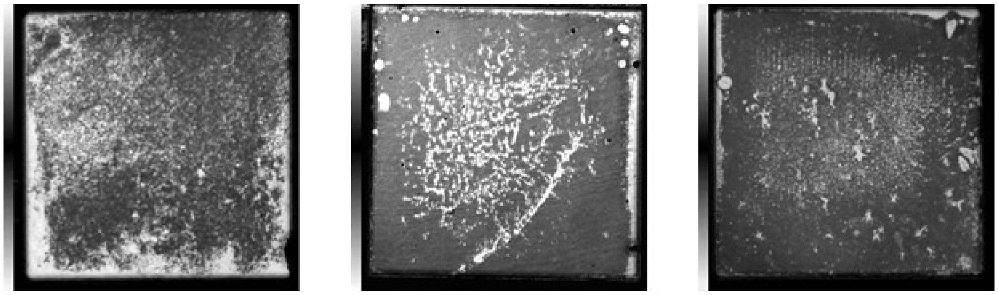

Figure I.1.14.7 C-SAM images of Cu-Al bonds in different samples

The variation in thermal resistance and defect fraction of the Cu-Al samples under thermal cycling is shown in Figure I.1.14.8. These graphs show that the defect growth rate was minimal in most of the samples, which can be attributed to the low coefficient of thermal expansion mismatch between AlN and AlSiC. Also, a direct correlation between the thermal resistance values and defect fractions could not be observed due to variations in their trends under thermal cycling. For example, a lower thermal resistance was measured for sample 7 at 50 cycles than sample 8, but this trend did not match with the defect fractions of these samples. As a next step, the uncertainty of thermal resistance measurements will be quantified and a comparison between these two reliability performance indicators will be made after several thermal cycles.

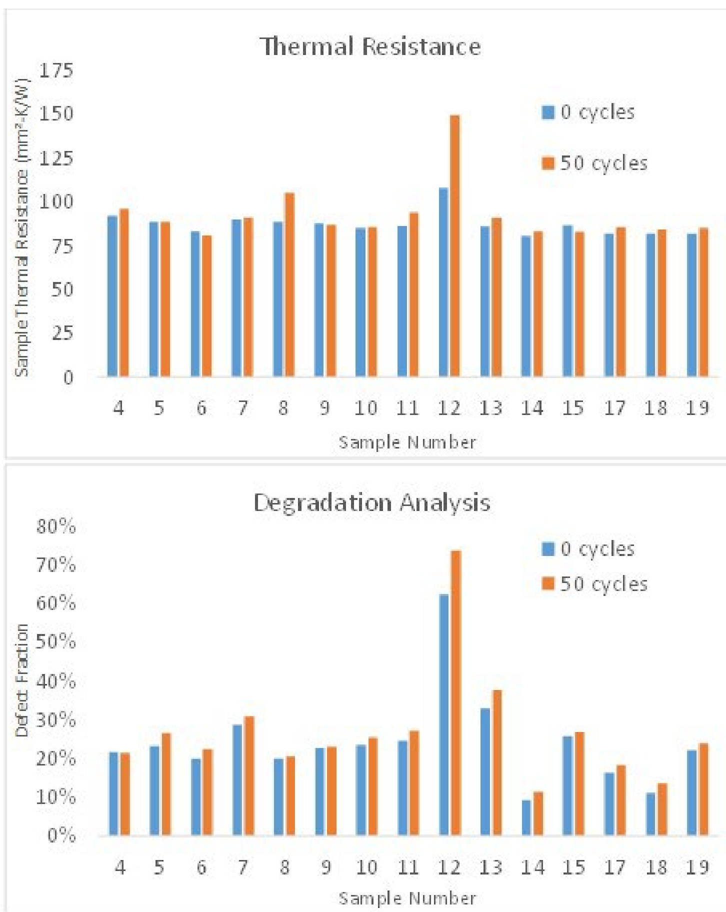

Figure I.1.14.8 Overall sample thermal resistance measurements (top) and defect fraction (bottom) before and after 50 thermal cycles

Conclusions

Power electronics packaging for safe operation of wide-bandgap devices at high temperatures is a challenging research goal. This project focuses on the reliability evaluation and lifetime prediction of bonded materials to determine their applicability in high-temperature packaging. The bonded materials of interest are sintered silver and a transient liquid-phase Cu-Al bond.

A lifetime prediction model was developed for sintered silver with inputs from thermal cycling experiments and thermomechanical modeling. This lifetime model will be an important tool for power electronics engineers in the design process of packages for high-temperature operation. In our experiments, solder joints performed slightly better than sintered silver, although the crack growth rate was very high for both materials under thermal cycling.

Additional synthesis variations are required to achieve superior bonding quality with the Cu-Al samples. Initial characterization followed by thermal cycling was conducted on a few samples. The minimal defect growth observed under thermal cycling can be mainly attributed to the low coefficient of thermal expansion mismatch between AlN and AlSiC coupons in the sample. Future efforts will be focused on improving the bond quality and continuing the thermal cycling experiments on these samples.

Key Publications

1. P. Paret. 2021. "Performance and Reliability of Bonded Interfaces for High-Temperature Packaging." In *Electrification: 2020 Annual Progress Report*, Washington, D.C.: U.S. Department of Energy Office of Energy Efficiency and Renewable Energy Vehicle Technologies Office.

2. P. Paret. 2021. "Power Electronics Materials and Bonded Interfaces – Reliability and Lifetime." *DOE VTO Annual Merit Review*, Washington, D.C., June 2021.

3. P. Paret, J. Major, D. DeVoto, S. Narumanchi, C. Ding, and G.Q. Lu, "Reliability and Lifetime Prediction Model of Sintered Silver under High-Temperature Cycling," *IEEE Journal of Emerging and Selected Topics in Power Electronics,* DOI**:** 10.1109/JESTPE.2021.3121195.

References

1. M. Knoerr, S. Kraft, and A. Schletz, "Reliability assessment of sintered nano-silver die attachment for power semiconductors," in 2010 12th Electronics Packaging Technology Conference, Dec. 2010: 56–61, doi: 10.1109/EPTC.2010.5702605.

2. K. S. Siow and S. T. Chua, "Thermal Cycling of Sintered Silver (Ag) Joint as Die-Attach Material," JOM 71, no. 9 (Sept. 2019): 3066–3075, doi: 10.1007/s11837-019-03461-4.

Acknowledgments

The contributions of Joshua Major and Douglas DeVoto in conducting several reliability evaluation experiments are acknowledged. The author also would like to thank Chao Ding and G.-Q. Lu at VT, and Chidinma Imediegwu and Samuel Graham at Georgia Tech for their valuable technical inputs and help with sample synthesis.

I.1.15 Rugged WBG Devices and Advanced Electric Machines for High Power Density Automotive Electric Drives (North Carolina State University) – Part I

Victor Veliadis, Principal Investigator
North Carolina State University
930 Campus Shore Drive, Suite 200
Raleigh, NC 27606
Email: jvveliad@ncsu.edu

Iqbal Husain, Principal Investigator
North Carolina State University
930 Campus Shore Drive, Suite 200
Raleigh, NC 27606
Email: ihusain2@ncsu.edu

Susan A. Rogers, DOE Technology Development Manager
U.S. Department of Energy
Email: susan.rogers@ee.doe.gov

Start Date: April 1, 2019 End Date: March 30, 2024
Project Funding: $300,000 DOE share: $300,000 Non-DOE share: $0

Project Introduction

DOE EDT 2025 has set an ambitious target for traction electric motors. The targets are to increase power density (kW/L), and to reduce cost ($/kW) using Heavy Rare Earth (HRE) free permanent magnets. The targets for power density, efficiency, and cost are 50 kW/L, 97%, and 3.3 $/kW, respectively. The research approach adopted by North Carolina State University is to meet or exceed these targets by 2025 through design innovations, new manufacturing processes, and innovations in materials and thermal management. So far, two motor designs namely- Space-shifted dual three phase (SS-DTP) IPMSM with novel segmented V-shaped magnets (Design II), and Slotless Halbach outer rotor PMSM with winding embedded liquid cooling (WELC) (Design III), have been down selected from several designs and also shown to be most promising in achieving the specified targets. The SS-DTP IPMSM shown in Figure I.1.15.1 was chosen for its high power density, high efficiency, fault tolerant capabilities and the established industry acceptance of its rotor structure amongst electric traction motors in commercial electric vehicles. Meanwhile, the choice of the Slotless-Halbach design shown in Figure I.1.15.2 is due to its lightweight structure and high efficiency; these machines are extremely compact, completely HRE-free, and can be operated at very high speeds. However, the low thermal mass and high electrical loading results in thermal management issues. To tackle this challenge, innovations in liquid cooling design and materials need to be further explored.

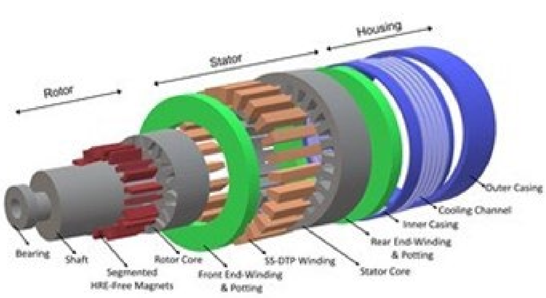

Figure I.1.15.1 Structure of the SS-DTP IPMSM

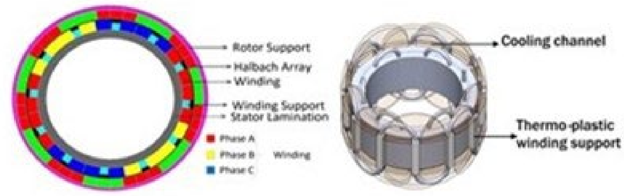

Figure I.1.15.2 Structure of the Slotless halbach PMSM with WELC

Objectives

The overall objective of this project portion is to design, evaluate and verify the performance of a high-speed electric machine optimized for high power density (kW/L) and ultra-high efficiency with HRE-free magnets.

In the past year, the electric machines research team has down-selected the two designs above for further analysis and development with the following objectives:

- Design II: To perform a comprehensive 3D demagnetization check on the HRE-free magnets under extreme conditions; to investigate the mechanical and structural integrity of the rotor at very high operating speeds; to characterize the motor; and to conduct a cost-performance survey of different core materials.
- Design III: To design, fabricate, test and verify the viability of the proposed winding embedded liquid cooling technology on a 10 kW scaled machine prototype.

Approach

Design II

First, a comprehensive 3D finite element (FE) model of the machine was used to verify the torque output capabilities, demagnetization performance and structural integrity at extreme operating conditions. Next, a high fidelity nonlinear dynamic model was also developed to quickly predict its behavior and establish its different torque components. Finally, the cost of production of the stator and rotor with two candidate core materials- Hiperco50 and HF-10 were obtained from their commercial suppliers and their respective performances were evaluated.

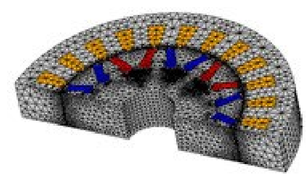

Figure I.1.15.3 FEA model of the SS-DTP IPMSM

Design III

A scaled down 10 kW prototype of the Slotless-Halbach outer rotor PMSM has been designed and is being fabricated and tested to demonstrate the effectiveness of the WELC concept. In order to achieve very high power density and meet the low-cost target requirements, some key enabling technologies include:

- The novel Winding Embedded Liquid Cooling (WELC) strategy used to achieve a slot current density of up to 33 A/mm2.
- Custom injection molded thermally conducting plastic (Coolpoly D5506) winding supports with integrated cooling channel shown in Figure I.1.15.4
- Cobalt-free HF-10 laminations used in stator to achieve a low cost without sacrificing performance as iron losses are inherently low.
- HRE-free magnets arranged in a three-segment Halbach array.

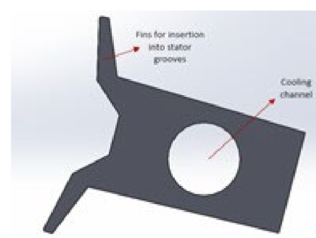

Figure I.1.15.4 Winding support in with integrated cooling channel

Results

Design II

The results of the 3D demagnetization analysis in Figure I.1.15.5 confirm that the segmented HRE-free magnets are indeed safe from permanent demagnetization when exposed negative fields at high temperatures. The minimum magnet flux density, 0.34T is higher than the knee of the demagnetization curve, 0.2T at temperatures below 120˚C. The results of the 3D structural stress test at 20,000 rev/min in Figure I.1.15.6 shows that the maximum stress (249 Mpa) in the machine is sufficiently lower than the yield strength of the core material (400 MPa) and that the deformation is far lesser than the physical air gap length. The dynamic modelling work was used to generate nonlinear maps of flux linkages, apparent inductances, and incremental inductances from which the magnet and reluctance torque components were derived. Figure I.1.15.7 show that total torque results from the nonlinear model closely match that obtained from FE analysis. Finally, a survey of the cost-performance benefits of the use of Hiperco 50 and/or HF-10 material for the stator and rotor core was conducted under four case studies. The results show that the Hiperco 50 remained the best option for meeting both the power density and output torque targets set by the consortium. The summary of this analysis is given in Table I.1.15.1.

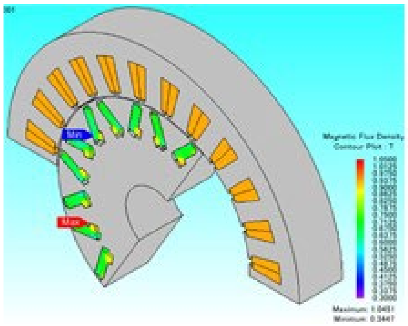

Figure I.1.15.5 Demagnetization performance under sudden three phase short circuit.

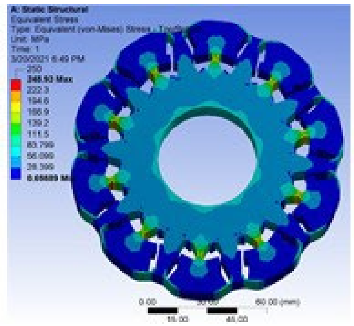

Figure I.1.15.6 Mechanical stress results at rotor speed of 20,000 rev/min.

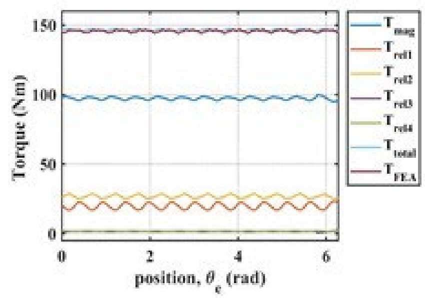

Figure I.1.15.7 Torque separation analysis at rated load condition

Table I.1.15.1 Cost-Performance Analysis of Two Core Materials

	Case I	Case II	Case III	Case IV
Core Material				
Stator	Hiperco 50	HF-10	HF-10	HF-10
Rotor	Hiperco 50	HF-10	Hiperco 50	HF-10
Electromagnetic Performance				
Peak Torque (Nm)	145	132	115	110
Power Density (kW/L)	50.0	46.3	40.3	38.6
Cost ($ per-unit)				
Stator	1.00	1.00	0.24	0.24
Rotor	0.75	0.30	0.75	0.30

The winding supports with embedded cooling channels were injection molded from thermally conducting Coolpoly D5506 plastic which has a thermal conductivity of 9.6 W/mK. The lamination was fabricated from HF-10 non-grain-oriented steel as the slotless machine does not have highly saturated laminated teeth, where most of the iron losses occur in a slotted machine. Therefore, the use of a high saturation flux density steel, such as Hiperco 50, is not justified in this design due to the high cost associated with this material. The injection molded winding supports are designed with lateral fins which fit into grooves cut into the lamination for a stable mechanical and thermal contact. PVC tubing connects the winding supports and provides a path for coolant to flow between winding supports. The coolant used is a 50/50 mixture of ethylene glycol and water. The windings are composed of 65 turns of AWG 20 wire per coil and two coils per slot.

Design III

The design of the scaled prototype was carried out using Altair Flux 2D electromagnetic FEA tool and the output parameters obtained from FEA simulation are listed in Table I.1.15.2. The scaled down prototype has a rated power of 10.8 kW at 6670 rpm, which corresponds to a rated torque of 15.5 Nm as seen in Figure I.1.15.8.

Table I.1.15.2 Parameters of scaled down, 10.8 kW version of Design III

Parameters	Value
Output Torque (Nm)	15.5
Base Speed (rpm)	6670
RMS Phase Current (A)	28
Current Density (A/mm^2)	33
Output Power (kW)	10.8
Core Loss (W)	15
DC Copper Loss (W)	274
Magnet Loss (W)	59
Efficiency (%)	96
Power Density (kW/L)	28.2

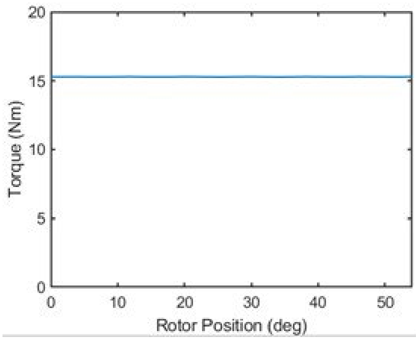

Figure I.1.15.8 Torque Profile of the Design III scaled-down prototype

Figure I.1.15.9 Top view of scaled down prototype of design III showing laminations and winding support

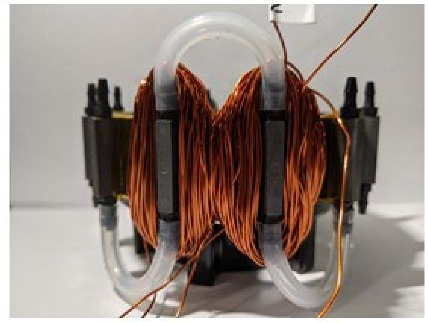

Figure I.1.15.10 Prototype stator showing windings and cooling channels

The assembled prototype, shown in Figure I.1.15.9 and Figure I.1.15.10 has been tested at a current of 4A and a flow rate of 0.5 l/min. From preliminary testing, it was seen that even at this low flow rate, WELC results in a substantial improvement in the thermal performance of the slotless machine. The steady state temperature rise, as seen from Figure I.1.15.11 shows a 40 % improvement with winding embedded liquid cooling compared to without any cooling. CFD simulations in Ansys Fluent show that a continuous current of 12 A and peak current of 18 A is possible using WELC, but these operating conditions are yet to be tested and will be presented in future reports. Apart from the prototyping efforts, demagnetization analysis has also been performed for Design III. The worst-case operating condition is simulated by supplying the rated motor current along the negative d-axis. From Figure I.1.15.12, it can be seen that the flux density in all three of the magnet segments under a pole are above the knee point of the NEOREC45MHF Dysprosium-free NdFeB magnets at 120° C (0.2 T). Therefore, they would not undergo irreversible demagnetization even at rated current and maximum rotor temperature.

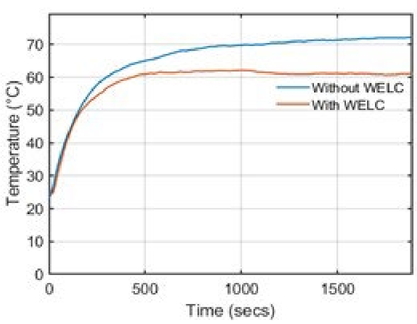

Figure I.1.15.11 Temperature rise in end windings of the Design III prototype

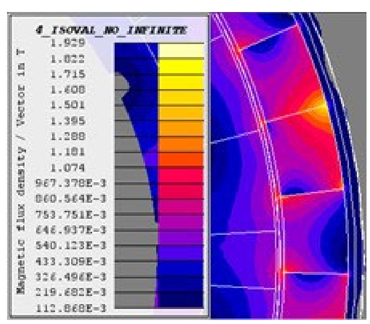

Figure I.1.15.12 Flux densities in design III at peak operating current

Figure I.1.15.13 WELC prototype thermal test set-up

Conclusions

In conclusion, the results of the 3D FE analysis of the SS-DTP IPMSM (Design II) confirm that the proposed design is safe from the effects of negative fields at high temperatures and remains structurally intact at very high speeds. The results of the cost-performance survey show that although the Hiperco 50 remained the best option for achieving the DOE targets in this design, the overall cost is only slightly higher than alternative options.

Furthermore, a scaled-down prototype of slotless Halbach outer rotor PMSM (Design III) has been designed and is being fabricated and tested using the setup shown in Figure I.1.15.13 to evaluate the novel WELC concept. The results from initial thermal testing has been very promising and also consistent with CFD simulations. The overall cooling strategy will therefore enable the achievement of electrical loading as high as 33 A/mm^2 in Design III, allowing it to satisfy the target power density requirements. Demagnetization analysis also shows that the HRE-free magnets used in the Halbach array are safe from demagnetization under worst case operating conditions.

Key Publications

1. Md Sariful Islam, Iqbal Husain, Ritvik Chattopadhyay, and Gregory D. Buckner, "Three-Dimensional Air-gap Electric Machines Employing Winding Embedded Liquid Cooling", US 17/482,645.
2. M.S. Islam, S. Agoro, R. Chattopadhyay and I. Husain, "Heavy Rare Earth Free High Power Density Traction Machine for Electric Vehicles", 2021 *IEEE International Electric Machines & Drives Conference (IEMDC)* (pp. 1–8).
3. R. Chattopadhyay, M.S. Islam, R. Mikail, and I. Husain, " Partial Discharge Analysis and Insulation Design of High Speed Slotless Machine for Aerospace Applications", 2021 *IEEE Energy Conversion Congress & Expo,* Vancouver, BC.

I.1.16 Rugged WBG Devices and Advanced Electric Machines for High Power Density Automotive Electric Drives (North Carolina State University) – Part II

Victor Veliadis, Principal Investigator
North Carolina State University
930 Campus Shore Drive, Suite 200
Raleigh, NC 27606
Email: jvveliad@ncsu.edu

Subhashish Bhattacherya, Principal Investigator
North Carolina State University
930 Campus Shore Drive, Suite 200
Raleigh, NC 27606
Email: sbhatta4@ncsu.edu

Susan A. Rogers, DOE Technology Development Manager
U.S. Department of Energy
Email: susan.rogers@ee.doe.gov

Start Date: April 1, 2019 End Date: March 30, 2024
Project Funding: $300,000 DOE share: $300,000 Non-DOE share: $0

Project Introduction

The DOE has set aggressive targets for 2025 to meet consumer performance expectations from electric vehicles (EVs). The DOE 2025 targets aim towards achieving a traction drive in the range of 100 kW. The high voltage power electronics' cost and power density targets are $2.6/kW and 100 kW/L, respectively. Wide bandgap (WBG) devices have widely gained attention for the traction inverter because of their ability to operate at high switching frequency and produce extremely low losses. The project's objective is to characterize the ruggedness of WBG devices and modules and explore new designs for automotive electric applications. The project particularly focuses on ruggedness evaluation, short circuit performance, gate driver designs, and novel traction inverter designs based on GaN devices. The prior work had characterized several commercially available GaN devices through double pulse test, short circuit test, safe operating area (SOA) determination, and power cycling test. Additionally, a methodology for comprehensive loss evaluation of traction inverter under more realistic conditions using urban and highway drive cycle models was presented. The present report focuses on the design and evaluation of gate driver and short circuit protection for GaN devices operating at high dv/dt and di/dt conditions. The report also presents design details of a prototype GaN-based three-level active neutral point clamped (3L-ANPC) traction inverter for 800V DC bus voltage. The design challenges that have been addressed include power layout structure, thermal and gate driver design for parallel devices in operation.

Objectives

- Short Circuit Protection
- Design of GaN-based 3L-ANPC converter.

Approach

1. Short Circuit Protection

One of the significant drawbacks of commercially available GaN devices is small short-circuit time. Several GaN devices were evaluated in BP1, and a summary of their short-circuit performance is shown in Table I.1.16.1.

Table I.1.16.1 Short Circuit Time of Different GaN Devices

Manufacturer	Rating	Short circuit current (A)	Short circuit time (ns)
A	650V, 60A (25°C)	300	640 (at 400V)
B	600V, 31A (25°C)	140	40(at 400V)
C	650V, 46.5A (25°C)	533	74(at 400V)

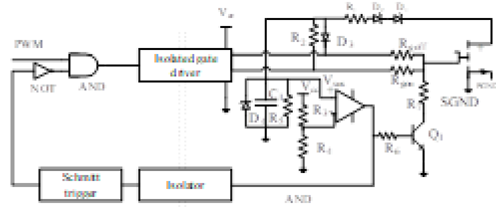

Figure I.1.16.1 Schematic representation of designed short circuit protection.

A short circuit protection circuit was designed and evaluated for the safe operation of the device from manufacturer A. The designed circuit logic is shown in Figure I.1.16.1. The key challenge here is the selection of components. The OPAMP, MOSFET, and the isolator can have a delay in the 100ns range. The components are carefully selected to reduce the delay in device turn-off. The achieved short circuit detection time is about 200ns.

2. Design of GaN-based 3L-ANPC converter

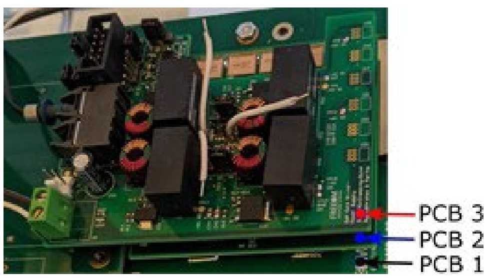

Figure I.1.16.2 Image showing assembled half-bridge power block (PCB 1 + PCB 2 + PCB 3) in 3L-ANPC.

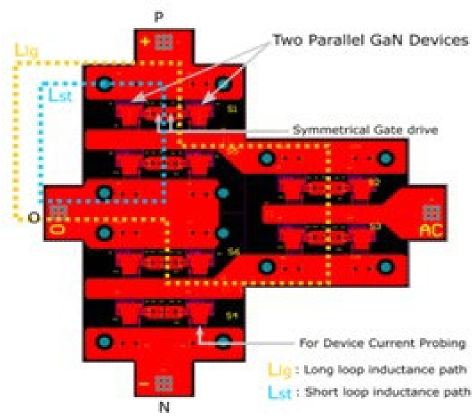

Figure I.1.16.3 PCB layout design of 3L-ANPC phase leg highlighting the long loop and short loop inductaces.

A GaN-based three-level active neutral point clamped (3L-ANPC) phase leg was designed with two parallel GaN devices as shown in Figure I.1.16.3. Each 3L-ANPC phase leg was designed with three symmetrical half-bridge power blocks. The phase leg assembly consists of three PCBs stacked together, shown in Figure I.1.16.2. The devices used to realize each active switch of 3L-ANPC are two parallel-connected bottom-cooled 650V, 60A GaN HEMTs. A single-layer insulated metal core substrate (IMS) PCB with 125µm dielectric material of thermal conductivity 3W/mK is used for PCB-1. PCB 2 contains the gate drive totem pole stage for the top and bottom device of the half-bridge power block. Additionally, PCB 2 also includes the decoupling capacitors for the power commutation loop. PCB1 and PCB 2 together form a vertical flux cancellation path for minimizing the power loop inductance. PCB 3 generates the bipolar gate drive bias voltage of +6V and -4V. PCB 3 also generates the deadband between the top and bottom device gate signal. The designed gate drive stages ensure gate and power loop symmetry for parallel devices, minimization of gate and power loop inductance. Two critical challenges addressed through design include efficient heat extraction from devices and minimizing power and gate loop inductances for faster switching.

Results

1. Short Circuit Protection

The experimental test results of short circuit test are presented. The short circuit test is performed at different voltage levels. It is observed that the short circuit detection time decreases with the increase in voltage level. Figure I.1.16.4 shows test result at 400V with short circuit detection 200ns. As observed from the results in Figure I.1.16.4, the designed protection circuit ensures a noise-free fast detection and safe turn-off of GaN device under short circuit event.

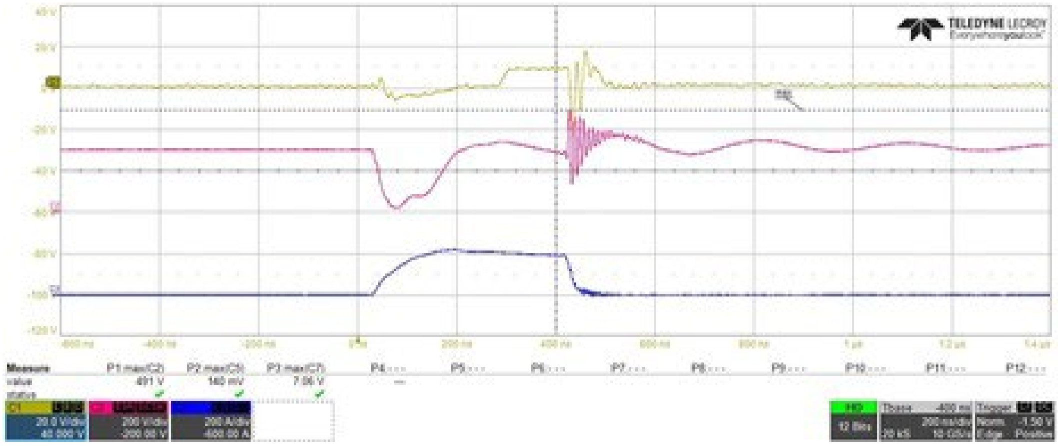

Figure I.1.16.4 Short circuit detection at 300 V. Ch1: Fault signal(20V/div), Ch2: V_{ds} (200V/div), Ch3: I_d(200A/div)

2. *Double Pulse Test Results of Half-Bridge Power Block with Integrated Gate Drive Stages*

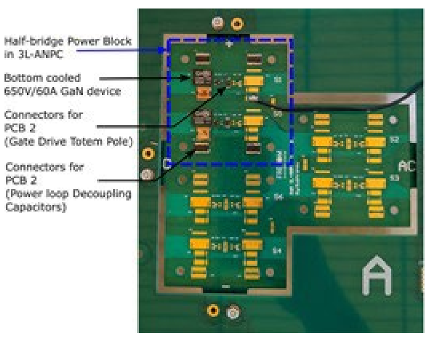

Figure I.1.16.5 Image showing PCB 1 – IMS PCB for 3L-ANPC. The half-bridge power block evaluated in this report is highlighted.

The designed prototype 3L-ANPC converter is currently being evaluated. Initial test results of an assembled half-bridge power block in the 3L-ANPC is presented here.

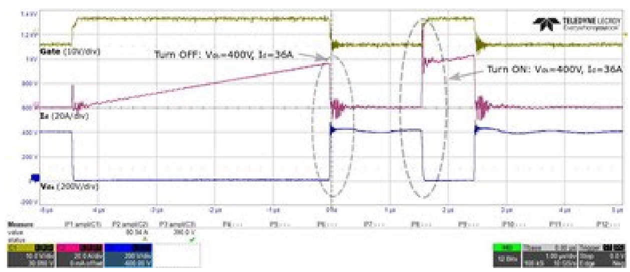

Figure I.1.16.8 Double pulse test results of GaN-based half-bridge power block at V_{ds} = 400V and I_d = 36A.

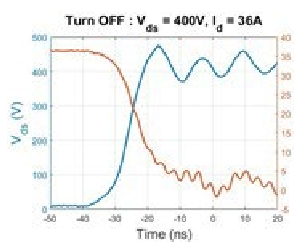

Figure I.1.16.7 Highlighted turn off operation from DPT result in Figure I.1.16.6.

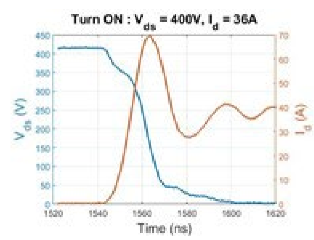

Figure I.1.16.6 Highlighted turn on operation from DPT result in Figure I.1.16.6.

Table I.1.16.2 Double Pulse Test details

Turn OFF	Turn ON
Rg = 5Ω (+ 1Ω + 1Ω distributed gate and source resistances) Measured di/dt = 1.7A/ns Measured dv/dt = 31.1V/ns Measured Energy Loss = 121.7μJ	Rg = 10Ω (+ 1Ω + 1Ω distributed gate and source resistances) Measured di/dt = 3.9A/ns Measured dv/dt = 13.5V/ns Measured Energy Loss = 248.4 μJ

The evaluated half-bridge power block of the designed 3L-ANPC stage is shown in Figure I.1.16.5. The double pulse test results are presented in Figure I.1.16.8 – Figure I.1.16.6 for test conditions given in Table I.1.16.2.

Conclusion

In conclusion, short circuit protection and a gate driver circuit for GaN devices have been designed and evaluated. The design details of a prototype GaN-based traction inverter for operating at 800V DC voltage have been presented. The designed protection circuit ensures detection of a short circuit event and safe turn-off of GaN device in 200ns time for a 400V operating voltage. Initial test results towards the evaluation of the prototype traction inverter have been presented. A double pulse test has been used to evaluate the half-bridge power block in 3L-ANPC with integrated gate drive stages. The test results confirm the robust performance of the designed gate driver under fast switching transients.

Key Publications

1. S. Satpathy, S. Bhattacharya and V. Veliadis, “Comprehensive Loss Analysis of Two-level and Three-Level Inverter for Electric Vehicle Using Drive Cycle Models,” *IECON 2020 The 46th Annual Conference of the IEEE Industrial Electronics Society*, 2020, pp. 2017–2024, doi: 10.1109/IECON43393. 2020. 9254520.

2. P. P. Das, S. Bhattacharya and V. Veliadis, “Control of Parallel Connected Interleaved Neutral Point Clamped Inverters for Electric Vehicle Drives,” *IECON 2020 The 46th Annual Conference of the IEEE Industrial Electronics Society*, 2020, pp. 1309–1316, doi: 10.1109/IECON43393.2020.9254462.

3. S. Satpathy, P. P. Das and S. Bhattacharya, “Study of Switching Transients based on dv/dt and di/dt for a GaN-based Two-Level Pole,” *2021 IEEE 12th Energy Conversion Congress & Exposition – Asia (ECCE-Asia)*, 2021, pp. 19–25, doi: 10.1109/ECCE-Asia49820.2021.9479426.

4. P.P. Das, S. Satpathy, S. Bhattacharya and V. Veliadis, “Paralleing of Four 650V/60A GaN HEMTs for High Power Traction Drive Applications”, Final paper submitted in ECCE 2021.

I.1.17 Cost Effective Rare-Earth-Free Flux Doubling, Torque Doubling, 8X Power Density Traction Motor with Near-Zero Open-Circuit Back- Electromotive Force (EMF) and No Cogging Torque (University of North Carolina at Charlotte)

James Gafford, Principal Investigator
University of North Carolina at Charlotte
9201 University City Boulevard
Charlotte, NC 28223
Email: jgafford@uncc.edu

Susan Rogers, DOE Technology Development Manager
U.S. Department of Energy
Email: Susan.rogers@ee.doe.gov

Start Date: October 1, 2019 End Date: March 31, 2022
Project Funding (FY 21): $270,638 DOE share: $210,638 Non-DOE share: $60,000

Project Introduction

This project proposes to develop a high power density, high speed traction motor architecture called QMag, driven by a high power density motor drive inverter using silicon carbide semiconductor devices. This new architecture will achieve the efficiency and power density targets by means of innovative winding and rotor structures, high bandwidth controls, and advanced thermal management solutions. The project team will pursue the goals of the project systematically, through Finite Element Analysis for machine design, through simulation and co-simulation techniques for power electronics and controls evaluation, by using design principles for prototyping, and finally laboratory testing and evaluation. If this project successfully achieves and demonstrates the DOE targets for power density, cost, and reliability, the technology has the potential to become a core enabler of the flagship higher power product portfolio in commercial traction businesses, which has so far been confined to DC, induction, Brush Less DC (BLDC), Permanent Magnet AC (PMAC), and reluctance machines.

Objectives

The U.S. DRIVE Electrical & Electronics Technical Team Roadmap (2017) [1] identified key challenges and R&D targets for Electric Traction Drive Systems in the year 2025 including: (1) cost reduction—achieving cost parity with ICE drivetrains at $6/kW for 100 kW peak power rating; (2) power density improvement—addressing packaging challenges and achieving a motor power density of 50 kW/litre and power electronics density of 100 kW/litre, and an overall system figure of 33 kW/litre; (3) reliability improvement up to 300,000 miles (distance) or 15 years (lifetime); (4) reduction of reliance on rare-earths, with NdFeB -free/reduced, Dy-free/reduced designs. In order to achieve these targets, this project proposes to develop and demonstrate a novel 125 kW motor architecture and SiC converter based electric traction drive system that can achieve 8X power density at half cost and 2X useful life, while applying the QMag principle to power conversion and motor design and advanced cooling. The project activities will focus on:

- Feasibility evaluation, practical implementation and scaling of QMag principle
- Design and implementation of power converter and motor drive system
- Design and implementation of advanced cooling system
- Overall system (motor + power converter) optimization for traction applications and testing

Approach

Traction motor: This project proposes to use the QMag topology to design the traction motor, which is based on the QMag technology, alternatively termed as the Parallel Path Magnetic Technology [2]:

- The QMag topology features permanent magnets placed in magnetically attracting manner (circumferentially vs radially) and inter-dispersed with control winding coils, enabling greater flexibility in flux path shaping, as shown in Figure I.1.17.1
- The castellated rotor has no interior or surface magnets, offering high-speed operation, reliability, and high power density to achieve DOE targets
- Direct winding cooling techniques boost current density capability, hence the torque performance.

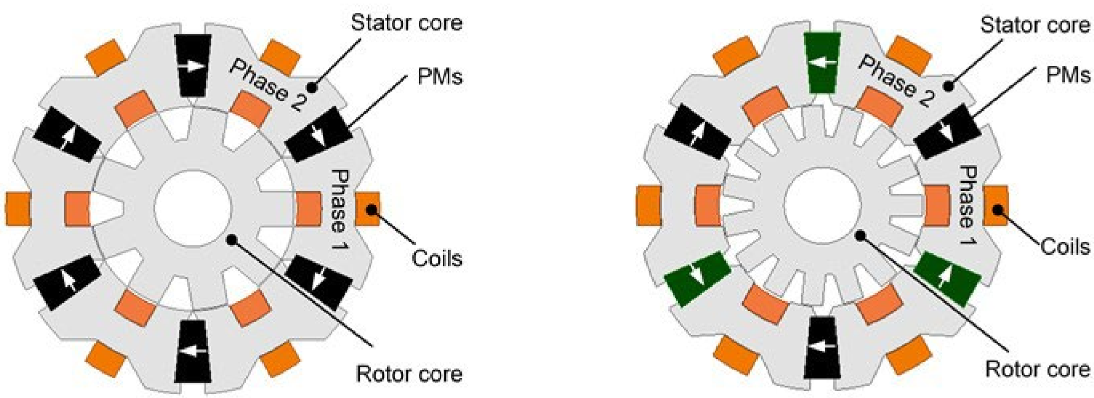

(a) (b)

Figure I.1.17.1 QMag topology illustration, (a) type-C (all magnets are magnetized in the same direction), (b) type-A (adjacent magnets are magnetized in opposite directions to concentrate flux).

Motor drive inverter

This project will develop a motor drive inverter using half-bridge silicon carbide (SiC) modules. The inverter will operate at switching frequencies, thereby low distortion output current and reduced torque ripple. SiC power modules optimized for reduced conduction losses will be utilized, in order to handle high current drive requirements by the QMag motor. The switching frequency of the inverter will be optimized for all operating power ranges, high power quality, power density, and efficiency. Thermal management of the semiconductor devices will be achieved through liquid cooling, with a water-ethylene glycol mix being the coolant.

Integration of traction motor and drive inverter

The traction motor and drive inverter are being designed concurrently, with frequent coordination of operating conditions and performance specifications. Finite Element Analysis platforms (Ansys) are being used to design, optimize, and validate the traction motor; power electronic simulation platforms (Powersim, Matlab) are used to design the drive inverter—the integrated traction system will be validated using co-simulation methods. The prototypes of traction motor and inverter drive will be integrated and tested on a dynamometer testbed.

Results

A survey of state-of-the-art designs for existing products and reported research studies was conducted in order to establish a basis of comparison for the electric machine performance and characteristics. The results provide the research team with a benchmark for evaluation of the QMag motor design under development and for substantiating relative merits and capabilities in terms of high power density, high speed operation, simplified modular manufacturability, improved cooling, etc.

Parametric models for a number of motor topologies were developed following the principle of operation of QMag motors. Based on a parametric electromagnetic finite element analysis (FEA) model for the QMag topology with Gramme-type windings illustrated in Figure I.1.17.2 with 10 independent geometric and control variables, a large-scale design optimization was performed. The objective was to maximize the power density with a 50 kW/L target, efficiency, and power factor, assuming an equivalent electric loading, i.e., the product of current density and slot fill factor, equal to 9.75A/mm^2 can be achieved by the cooling design and advanced winding technology.

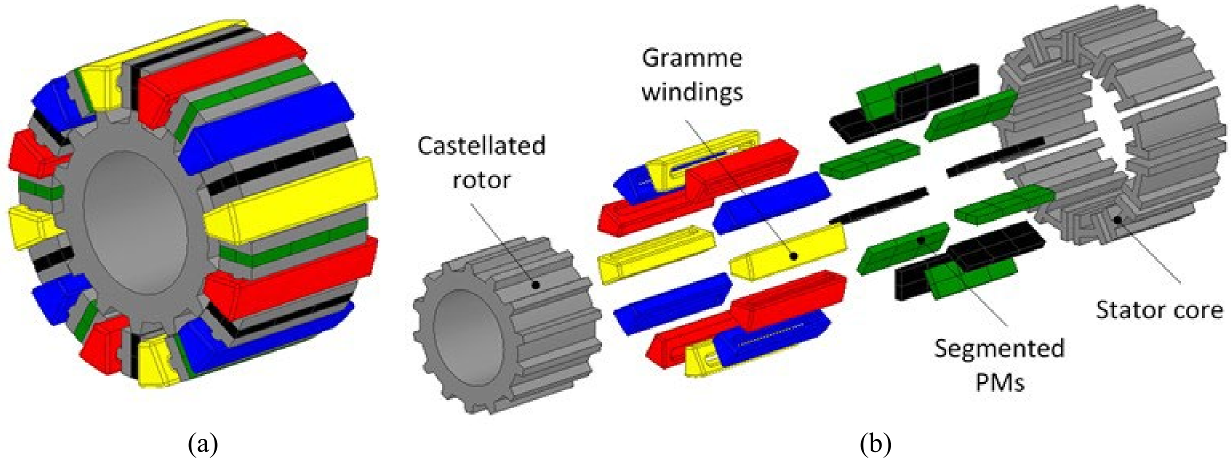

Figure I.1.17.2 One implementation of the QMag technology, (a) assembled view, (b) exploded view.

Multiple design generations of the adopted heuristic optimization yielded a satisfactory Pareto front. A number of candidate designs were identified, with estimated power density capable of meeting DOE targets, as shown in Figure I.1.17.3. The torque-speed and efficiency maps have also been calculated based on 2D electromagnetic FEA, showing that the optimally designed motor can operate with constant power 125 kW at up to 3X the base speed 12,500r/min.

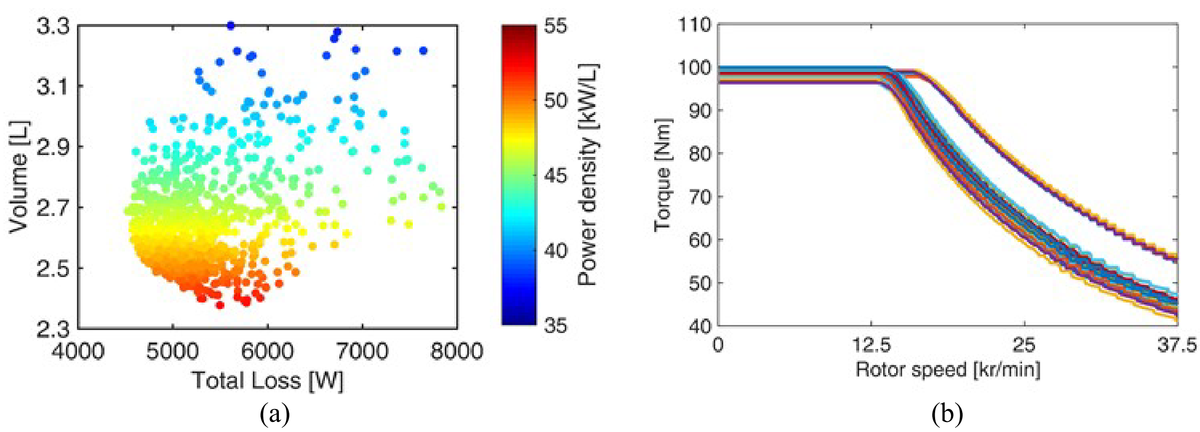

Figure I.1.17.3 Large-scale design optimization of one implementation of the QMag technology. (a) Designs evaluated by FEA, (b) Torque-speed envelops of all the Pareto front designs in (a).

A systematic comparative study between two QMag motor topologies was also carried out based on multi-objective design optimizations, one with 10 rotor protrusions (10-P) and the other 14 rotor protrusions (14-P), as shown in Figure I.1.17.4. The three concurrent objectives were to maximize the power density, minimize the total loss, and maximize the power factor. The computational results show that, optimal 14-P designs can achieve similar fundamental power factors as optimal 10-P designs. There are trade-offs between 10-P and 14-P designs in terms of the power density and total loss.

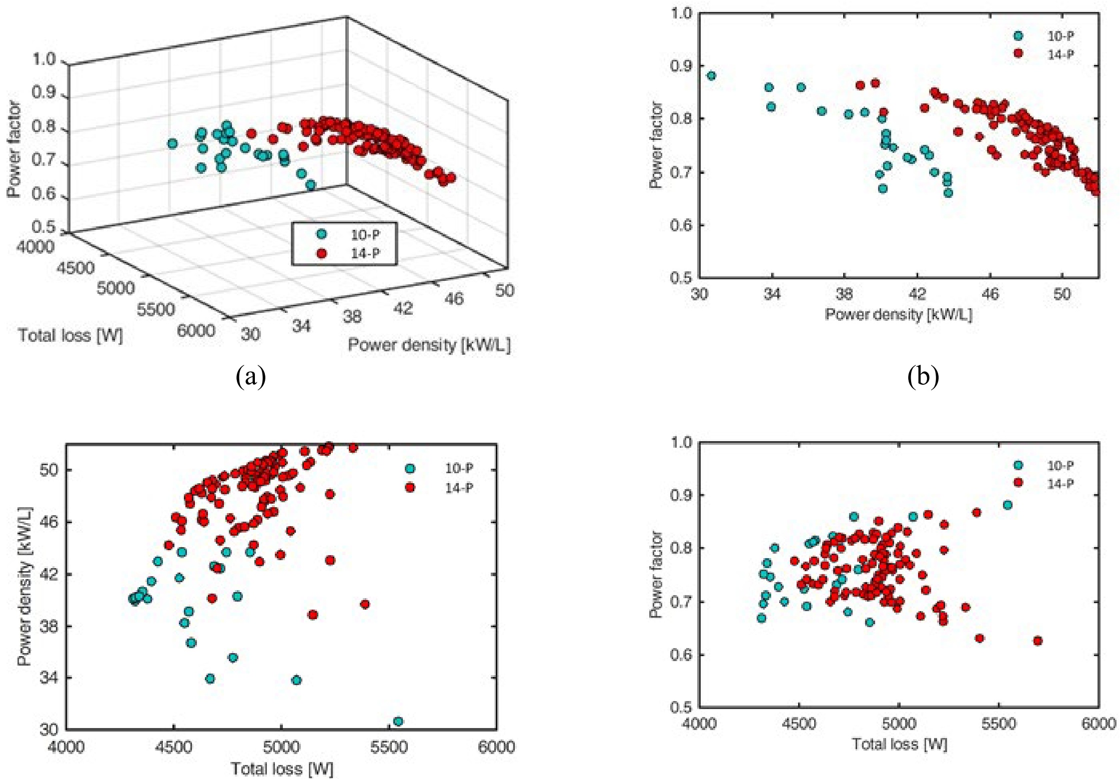

(a) (b)

(c) (d)

Figure I.1.17.4 Systematic comparison of two QMag motors with 10-P and 14-P, respectively. (a) 3D view of Pareto fronts, (b) projection in the power density-power factor plane, (c) projection in the total loss-power density plane, (d) projection in the total loss-power factor plane.

Advanced winding and cooling technologies for EV traction motors was surveyed, which served as the basis for the proposed winding manufacturing and cooling design of QMag motors. A concept design has been proposed using two stator cooling jackets, with the stator core, windings, and rotor immersed in oil or water coolants, in order to mitigate the heating effects of the large specific losses, which are typically high for high power density electric machines.

To validate the proposed very high power density motor and the adopted design optimization approaches, as well as to identify the potential challenges in manufacturing and testing to achieve the final goal of 50 kW/L, a 28hp open frame lab prototype (OFLP) motor rated at 40Nm and 5,000r/min was fabricated, as shown in Figure I.1.17.5. The experimental testing was conducted to measure the OC back-electromotive force (EMF) for a single phase with 4 coils connected in series, as plotted in Figure I.1.17.7 (a), showing good agreement between the experimental measurements and 2D FEA calculations. A back emf test was performed up to 3,500 rpm (limited by prime mover ratings). Observed stator line-line voltage at 3,500 rpm shown, with highly sinusoidal waveform of fundamental frequency 583 Hz, has been shown in the Figure I.1.17.7. (b).

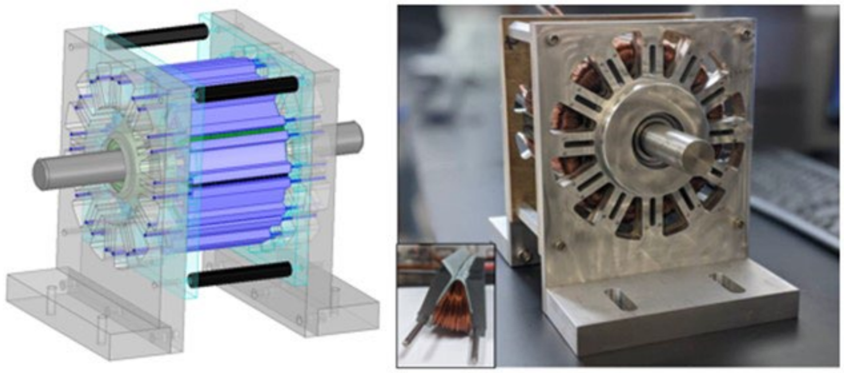

Figure I.1.17.5 The CAD drawing and photo of the full assembly for the open frame lab prototype motor. Dowel pins were used in the laminated stator segments. PMs were segmented in both radial and axial directions to reduce the PM eddy current losses. All the coil terminals have been brought out for detailed testing purpose. One phase coil wound on modular core segment as shown in inset image.

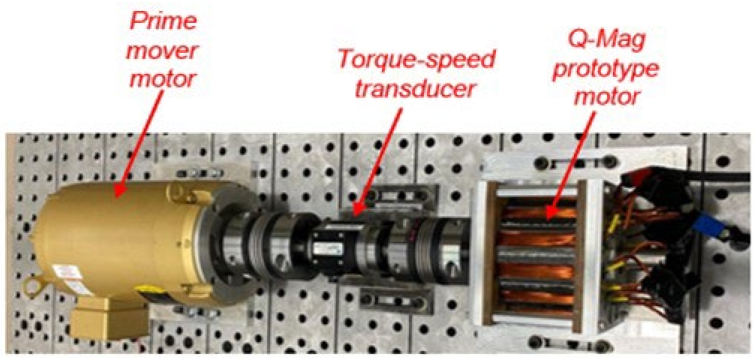

Figure I.1.17.6 Back emf test setup of OFLP motor winding in star connection topology.

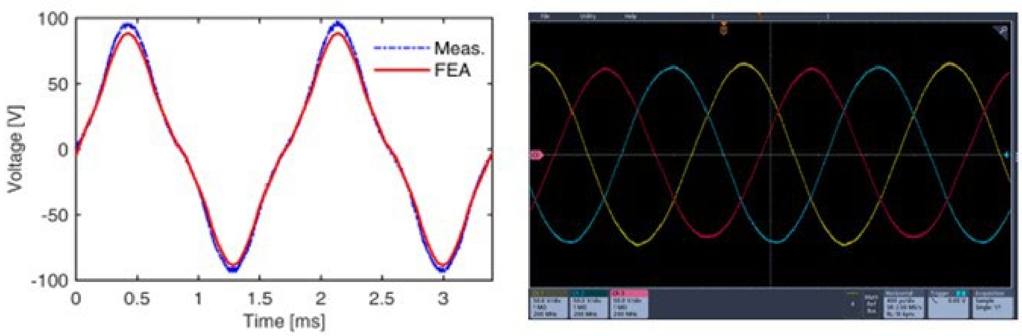

(a) (b)

Figure I.1.17.7 a) Simulated and experimental open-circuit back EMF for phase-A open ended winding. (b) Experimental open-circuit back EMF for phase-A, B, and C in star connection topology.

A locked rotor test setup was designed and fabricated by the project team, consisting of an indexing head and a locking block. The rotor position was moved in 1° (mechanical) increments, over a total span of 36° as shown in Figure I.1.17.8. Motor stator phases B & C were connected to a common terminal and in series with phase A. DC current was injected up to 500 A. Torque performance up to 90 Nm measured, compared to 96 Nm in simulation results, with the difference potentially explained by material tolerances, deviation in physical properties between simulation components and real-world materials, and lack of liquid cooling (further analysis is in progress).

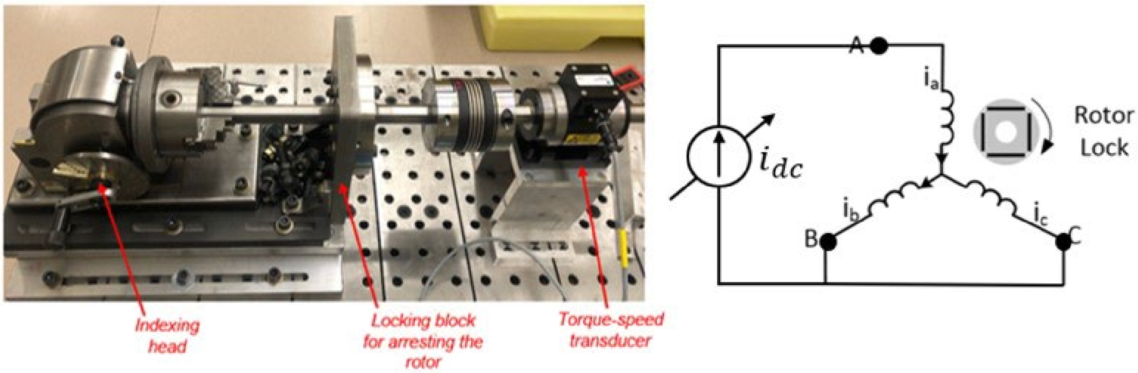

Figure I.1.17.8 Locked rotor test setup and a simplified equivalent circuit diagram.

The static torques at different rotor positions were also measured when the phase-A winding was connected in series with the parallel of phase-B and phase-C windings. Each phase has 4 coils connected in series. It is shown that, within the expectation, the measured static torque has the same trend as the 2D FEA as seen in Figure I.1.17.9. The deviation is approximately 10% and can be explained by the backlash of the locking device, especially at the high torque region, the temperature rise, the inaccuracies of material properties, etc. The OFLP motor achieves a power density of 8.4kW/L at 5,000r/min with an open housing for air cooling at a current density of 9.75A/mm2. The reduced power density is attributed to the low copper slot fill of 0.41 achieved by hand wound wired coils, the reduced speed due to the limitations of current testing facilities, and the reduced current density to prevent overheating with the air cooling. The 50 kW/L target is anticipated to be achieved by improving the copper slot fill to 0.7–0.8 by advanced winding technologies, for example, the additively manufactured coils [3], and increasing the current density to produce higher torque enabled by the advanced cooling technologies, such as the one presented in [4], and operate the motor at the designed rated speed of 12,500r/min. In the meantime, reducing the losses, mainly the core losses, by reducing the number of rotor protrusions and therefore the fundamental driving frequency is underway to simplify the cooling design. Reducing the fundamental frequency will also benefit the control system and reduce the switching frequency.

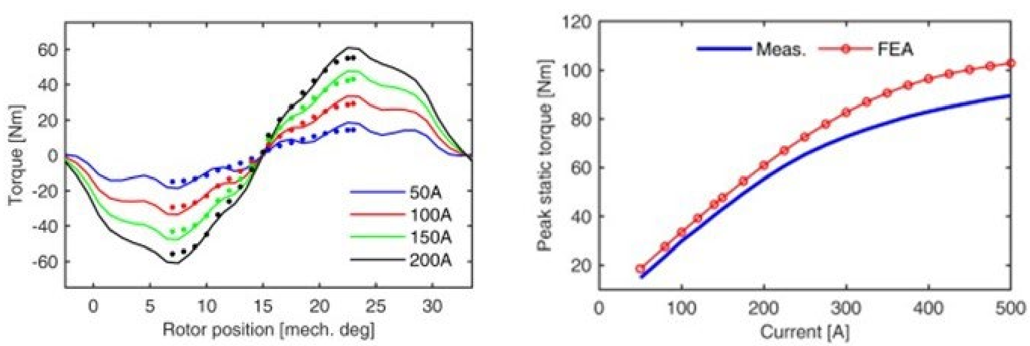

(a) (b)

Figure I.1.17.9 (a) Testing results of torque measured static torque versus rotor positions (continuous lines—FEA results, dots—experimental measurements). (b) Testing and simulation results of peak torque versus different current values.

The OFLP motor has been designed to operate at a current of 135A peak to deliver a torque of 41Nm at a rated speed of 5000RPM (523.5rad/s). System in the loop simulation has been performed employing a linear or lumped parameter model of the permanent magnet-based motors in the PSIM. Closed-loop speed and torque control of the system in the loop of a linear model of the OFLP motor have been performed during budget periods I & II. The precise behavior of the OFLP motor could be replicated in the simulation platform by considering the effect of saturation and spatial harmonics [5]. JMAG has been used to create a high-fidelity nonlinear model of the OFLP motor. The high-fidelity nonlinear model of the OFLP motor has been imported into the PSIM simulation platform. System in the loop simulation has been performed on a high-fidelity model of the OFLP motor. A workflow has been proposed to generate a code to implement speed and torque control algorithms employing JMAG, PSIM, and Typhoon HIL [6] as shown in Figure I.1.17.10. (a).

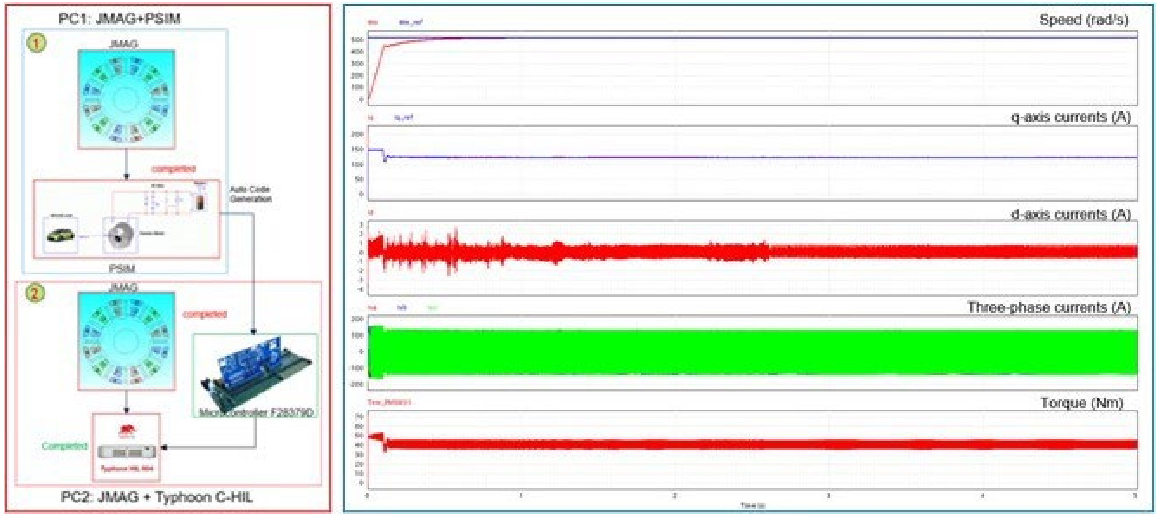

(a) (b)

Figure I.1.17.10 (a) Workflow of implementation of the control algorithms considering a high-fidelity model of prototype of the Q-MAG motor drive system. (b) Discrete domain simulation results of the prototype of the Q-MAG motor drive system consists of speed (rad/s), synchronous frame reference currents (A), three phase currents (A) and load torque (Nm).

System in the loop simulation model of the OFLP motor drive system is in continuous domain. The simulation model has been reconfigured into a discrete domain to replicate a precise model of the hardware setup of the traction motor drive system employing a high-performance TI microcontroller F28379D. The discrete PSIM simulation model of the Q-MAG motor prototype consists of an analog to digital (ADC) port, Texas Instruments digital motor control (TI-DMC) blocks, PWM ports, and an encoder. The three-phase currents, speed, and torque signals have been sampled at appropriate employing zero-order hold operation. Feedback currents have been signals conditioned to match the ADC input requirements of the microcontroller F28379D.

The feedback signals have been digitalized and transformed into synchronous reference frames using TI DMC blocks. Speed controller has been configured to generate a reference current proportional to the load torque of the motor. The reference currents have been compared with the feedback currents to implement current controller algorithms to generate respective d-axis and q-axis voltages. The voltages have been normalized and sinusoidal pulse width modulation has been performed to generate switching pulses with an appropriate deadtime. Average torque of 41Nm, 135A peak at a rated speed of 523.5 rad/s or 5000 RPM have been observed in the discrete domain simulations as shown in the Figure I.1.17.10. (b). The results are a close match to the specifications of the OFLP of the Q-Mag motor. A code has been generated and deployed into the microcontroller F28379D. Validation of the code employing Typhoon controller hardware in the loop (C-HIL) system and hardware implementation of the OFLP motor drive system are in progress.

Conclusions

The proposed Q-Mag architecture based electric drivetrain system under development promises to meet DOE EETT targets power density improvement, cost reduction, and magnetics utilization. Motors based on Q-Mag technology have been analyzed through large-scale design optimization studies and shown to be feasible candidates for traction applications with a maximized power density of over 50 kW/litre, and additional merits of high-speed operation capability, a wide speed range of 3X base speed, simplified modular manufacturability, improved cooling, etc. The proposed motor has numerous advantages for high power density designs, such as the high-speed operation capability, better cooling design, compact winding structure, modularized manufacturing of the stator, and an inherent wide speed range with a constant power speed ratio of at least 3:1. Appropriate combinations of stator PMs, stator windings, and rotor protrusions are required to produce high torque. The electromagnetic performance tradeoffs mainly lie between the power density and efficiency, and large-scale design optimizations are required to achieve the optimal designs in the sense of multiple objectives. Advanced winding technologies that can substantially increase the copper slot fill and cooling techniques that can effectively dissipate the heat generated by losses in the stator are two enabling technologies to achieve the 50 kW/L target for the proposed topology. The design and simulation of high-fidelity nonlinear model of motor drive system consists of SiC inverter, control algorithm development show the rated operating point of OLFP motor, and preliminary designs show that power densities at 100 – 150 kW/litre for the inverter, also meeting DOE targets. The project team is currently undertaking the validation of control algorithm employing Typhoon controller hardware in loop (C-HIL), hardware implementation of OFLP motor drive system, and design of thermal management system.

Key Publications

1. P. Han et al., “Design Optimization of a Very High power density Motor with a Reluctance Rotor and a Modular Stator Having PMs and Toroidal Windings,” 2021 IEEE Energy Conversion Congress and Exposition (ECCE), 2021, pp. 4424–4430, doi: 10.1109/ECCE47101.2021.9595129.

2. C. S. Goli, M. Manjrekar, S. Essakiappan, P. Sahu and N. Shah, “Landscaping and Review of Traction Motors for Electric Vehicle Applications,” 2021 IEEE Transportation Electrification Conference & Expo (ITEC), 2021, pp. 162–168, doi: 10.1109/ITEC51675.2021.9490129.

3. C. S. Goli, S. Essakiappan, P. Sahu, M. Manjrekar and N. Shah, “Review of Recent Trends in Design of Traction Inverters for Electric Vehicle Applications,” 2021 IEEE 12th International Symposium on Power Electronics for Distributed Generation Systems (PEDG), 2021, pp. 1–6, doi: 10.1109/PEDG51384.2021.9494164.

References

1. U.S. DRIVE Electrical and Electronics Technical Team Roadmap, October 2017

2. Charles J. Flynn, “Parallel Magnetic Circuit Motor”, US Patent US 2011/0089775A1

3. N. Simpson, C. Tighe, and P. Mellor, “Design of high-performance shaped profile windings for additive manufacture,” in IEEE Energy Convers. Congr. Expo. (ECCE), 2019, pp. 761–768.

4. S. A. Semidey and J. R. Mayor, “Experimentation of an electric machine technology demonstrator incorporating direct winding heat exchangers,” IEEE Trans. Ind. Electron., vol. 61, no. 10, pp. 5771–5778, 2014.

5. “Motor Control Development Tools Work with JMAG,” JMAG Users Conference Proceedings, Feb 2021.

6. “Ultra-High-Fidelity Hardware in the Loop (HIL) Simulation for EV Motor Drives with Seamless integration with JMAG-RT,” JMAG Users Conference Proceedings, Feb 2021.

Acknowledgements

Contributions to the project were made by the following team members: Mr. Joe Flynn, Dr. Peng Han, Mr. Chandra Sekhar Goli, Mr. Nakul Shah, Mr. Rohan Gosalia, Dr. Dan Ionel, Dr. Somasundaram Essakiappan, Dr. Madhav Manjrekar, and Dr. Prasanth Kumar Sahu. The project team wishes to thank Mr. John Tabacchi, DOE NETL Program Officer.

I.1.18 Integrated Motor and Drive for Traction Application (University of Wisconsin-Madison)

Bulent Sarlioglu, Principal Investigator
University of Wisconsin – Madison
1415 Engineering Drive
Madison, WI 53706
Email: sarlioglu@wisc.edu

Susan Rogers, DOE Technology Development Manager
U.S. Department of Energy
Email: susan.rogers@ee.doe.gov

Start Date: April 1, 2019 End Date: April 1, 2024
Project Funding: $300,000 DOE share: $300,000 Non-DOE share: $0

Project Introduction

The objective of the project is to research, design, develop, and test a high-performance traction motor and a high-efficiency traction inverter, and then to combine them into a state-of-the-art integrated motor drive (IMD) that requires only a single housing for use in vehicle applications.

The new IMD system will significantly increase the motor and inverter power density values to meet the aggressive DOE targets while simultaneously reducing their cost. The high-power-density, reduced-cost prototype IMD will become a valuable source of technical data that can be used by automakers and their suppliers to improve the performance of future EV traction drive systems.

Objectives

This project has two separate sets of performance targets for the power electronics and motor presented together in Table I.1.18.1.

Table I.1.18.1 Power Electronics and Motor Requirements

Power Electronics Requirement	
Parameter	**Measure**
Cost ($/kW)	≤ 2.7
Peak Power Density (kW/L)	≥ 100
System Peak Power Rating (kW)	100
Electic Motor Requirement	
Parameter	**Measure**
Cost ($/kW)	≤ 3.3
Peak Power Density (kW/L)	≥ 50
System Peak Power Rating (kW)	100

Approach

This project began with an evaluation of several types of electric motors and inverters that are candidates for future land-based vehicle traction applications. The evaluation results led to selection of the surface permanent magnet (SPM) machine and current-source inverter (CSI) as the most desirable machine and inverter technologies for the new integrated motor drive (IMD) that now is being developed into a working state-of-the-art prototype unit during the remainder of the project.

During Budget Period #1, a literature review was carried out that set the stage for trade-off studies to evaluate several alternative motors and inverters that were candidates for adoption in the target integrated motor drive system. The motor configurations as well as the power inverter topologies were compared, leading to selection of the SPM machine and CSI as the most promising motor/inverter technologies for further development.

During Budget Period #2 a preliminary SPM motor electromagnetic design and CSI electrical design have been carried out. A bench-top version of the CSI has been designed and fabricated to verify key IMD concepts and to reduce technical risks. In addition, preliminary thermal and mechanical designs of the motor and inverter were developed, including their physical integration into an IMD configuration.

During Budget Period #3 (still under way at the time of this writing), the prototype IMD design is being finalized in preparation for fabrication. The final prototype machine and inverter designs will be reviewed individually and in combination prior to initiating construction. A dynamometer test-stand will be designed, including instrumentation for testing the motor and power inverter.

During Budget Period #4, the prototype motor and power inverter will first be tested individually. Integration of the motor and power electronics into the same IMD enclosure will be carried out. Initial tests will then be conducted to demonstrate the functionality of the prototype IMD unit.

During Budget Period #5, the combined prototype IMD system will be tested. The IMD performance will be measured and documented to verify the ability of the prototype IMD unit to meet its performance targets.

Results

IMD concept development

A motor and an inverter with the controller are the key elements of an IMD, as shown in Figure I.1.18.1. By eliminating the bulky high voltage ac cables and terminals used to connect the inverter to a motor, the total volume and cost of the motor drive system can be significantly reduced [1],[2],[3]. Therefore, the IMD configuration is favored in the traction motor drive system, where minimizing volume and cost are paramount. Based on the results of the preliminary design review during BP#2, we carried out a more detailed design of the integrated motor drive (IMD). The power electronics components, including the dc/dc converter, dc-link inductor and CSI, are radially mounted on the hexagonal surfaces of the machine housing and share the same water-cooling jacket with the stator of the machine. The CSI printed circuit board (PCB) is split into two boards, and the power modules are directly mounted on the surface of the hexagonal housing under the CSI PCBs, as shown in Figure I.1.18.1. The spiral channel for water jacket is used to cool both the power electronics and machine stator.

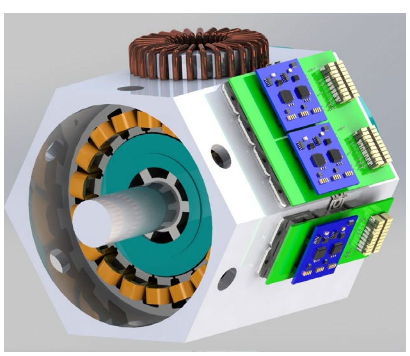

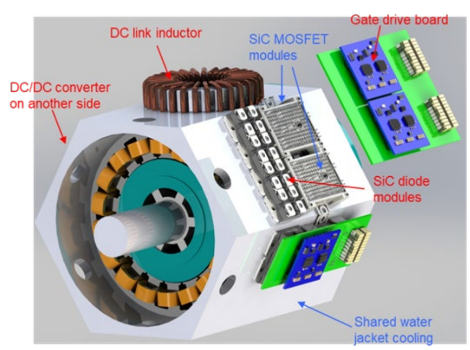

Figure I.1.18.1 Conceptual configuration of radially mounted IMD with shared water jacket cooling and hexagonal housing

CSI double pulse test

To estimate the power electronics losses and efficiency, it is necessary to measure the power device characteristics. The double-pulse test (DPT) is a well-known method to characterize the power devices and power modules. This method allows the evaluation of transient performance metrics such as the turn-on/turn-off switching losses and the rise/fall time at different voltage and current levels. It is important to note that the switching characteristics of such devices are not only dependent on its internal structure but also on the external circuit to which it is connected, including its physical layout. Hence, the conventional DPT circuit configuration designed for a conventional VSI is not suitable for a CSI [4]. The proposed CSI-based double-pulse test circuit and its control signals are shown in Figure I.1.18.2.

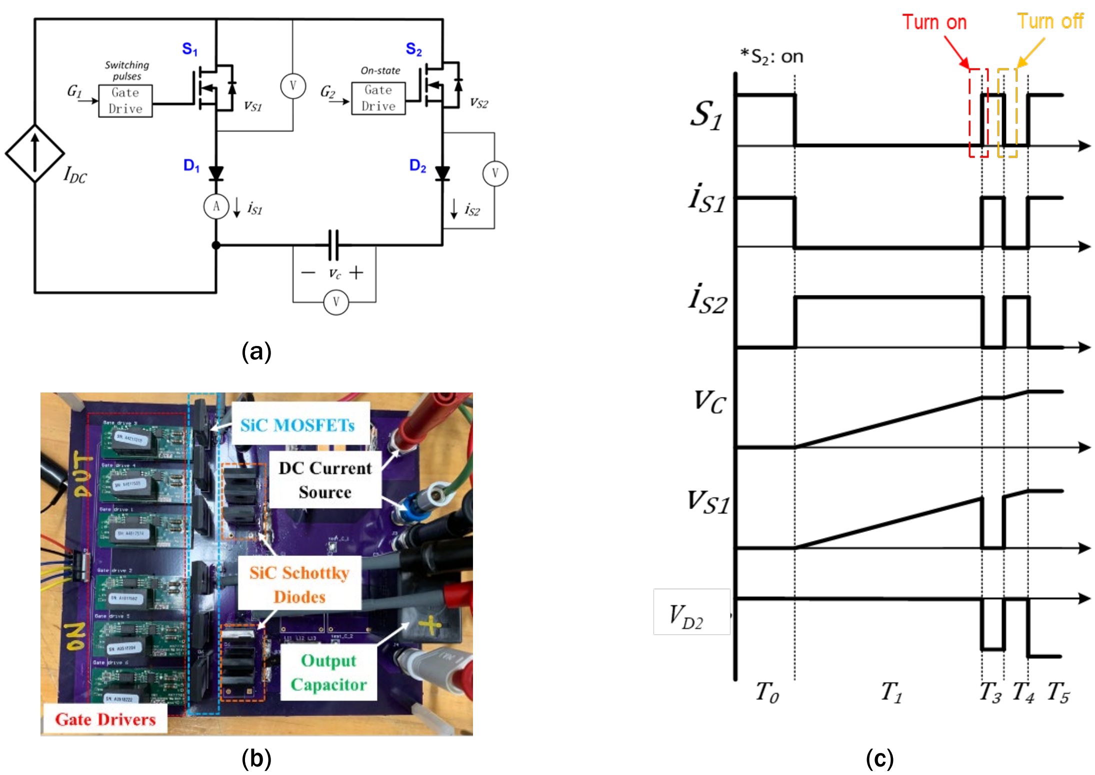

Figure I.1.18.2 (a) CSI DPT circuit; (b) CSI DPT prototype for power devices characterization; (c) CSI DPT signals [1]

A CSI DPT circuit has been developed to measure the switching characteristics of the SiC MOSFET and SiC Schottky diodes selected for use in the CSI. At this stage in the project, a single CSI switch included 3 paralleled discrete SiC MOSFETs (C3M0016120K from CREE) and 3 paralleled SiC Schottky diodes (GC50MPS12-247 from GeneSiC) in series with the MOSFETs to handle the current required for this 55-kW motor drive system, as shown in Figure I.1.18.2 (a). More recently, attention has been focused on SiC power modules instead of the discrete power switches used for the DPT tests described here.

The turn-on and turn-off switching waveforms of the SiC MOSFET S_{c1} with a 20 Ω turn-on resistance in the gate drive are shown in Figure I.1.18.3 (a) and (b). It can be observed that the measured current rise time of the SiC MOSFET is 61.6 ns, and the measured current fall time is 39.6 ns at the 15 A, 280 V operating point. The current and voltage oscillations during the SiC MOSFET turn-on and turn-off transient are caused by the parasitic inductance of the film capacitor and the PCB conductor traces between switches S_{c1} to S_{c3}. The measured turn-on energy is 0.0743 mJ, and the turn-off energy is 0.0389 mJ. Even though the turn-on peak power loss is smaller than the turn-off peak power, the turn-on energy is larger because of the longer turn-on time. The on-state resistance of the SiC MOSFET and SiC Schottky diode, and the diode forward voltage were measured at the same 15 A test condition, as shown in Table I.1.18.2. Closer examination has shown that the oscillatory voltage transients during both transition events contribute little to the measured turn-on and turn-off energy values.

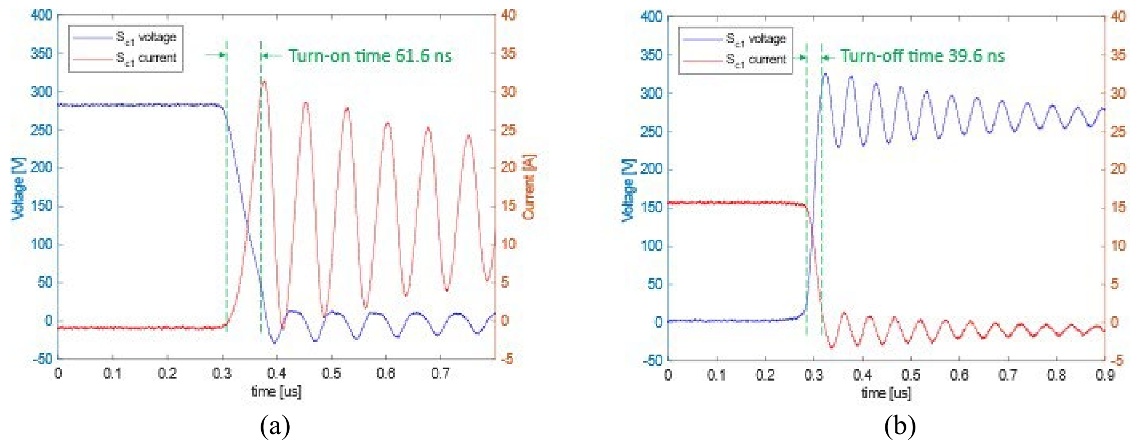

Figure I.1.18.3 (a) Measured SiC MOSFET turn-on waveform; (b) Measured SiC MOSFET turn-off waveform

Table I.1.18.2 Measured On-state Resistances and Forward Voltage of SiC MOSFET and Schottky Diode at 15 A using DPT Circuit

	On-state resistance [mΩ]	Built-in voltage drop [V]
SiC MOSFET	19.7	-
SiC Schottky diode	17.5	0.866

The estimated CSI loss and efficiency based on the CSI DPT measurement results and the CSI loss model are shown in Table I.1.18.3. Those estimates are based on the rated steady-state operating point of 55 kW. The dc-link voltage is 650V, the dc-link current is 115A, and the switching frequency of the CSI is 50 kHz. The conduction and switching losses for the SiC MOSFETs and SiC Schottky diodes are extrapolated to 120°C from the measured temperatures. The results in this table indicate that the estimated loss of CSI is 1096.6 W, and the efficiency of the CSI is 98.04% at the rated 55 kW operating point.

Table I.1.18.3 Total CSI Loss Estimation based on CSI DPT Results at 55 kw Operating Point

	Parameter	Loss (W)
CSI	MOSFET switching loss	177.0
	MOSFET conduction loss	200.8
	Diode conduction loss	306.8
	Inductor loss	412
	Total CSI loss	**1096.6**
	Efficiency	**98.04%**

Bench-top prototype inverter

The CSI-based motor drive including the front-end dc/dc converter is shown in Figure I.1.18.4. This dc/dc converter is responsible for converting the battery voltage source into a regulated current that is delivered to the dc link of the CSI.

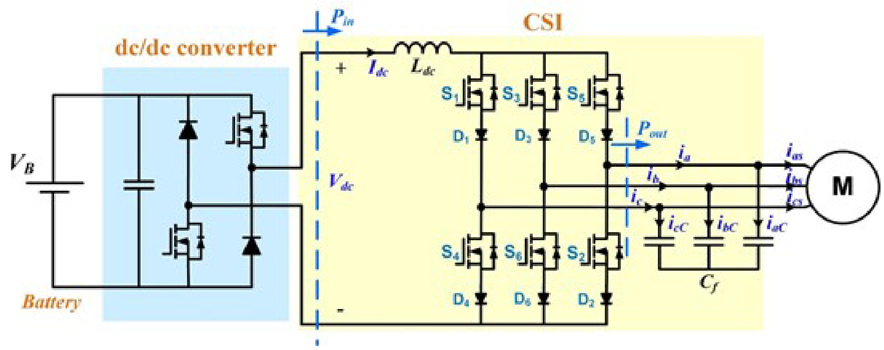

Figure I.1.18.4 Baseline CSI-based motor drive system for traction application

The bench-top prototype CSI was fabricated and tested with a high power RL load to verify the function of the system. Figure I.1.18.5 shows the preliminary experimental platform for CSI operation. For this preliminary test, the CSI is directly connected to a commercial power source configured to behave as a current source.

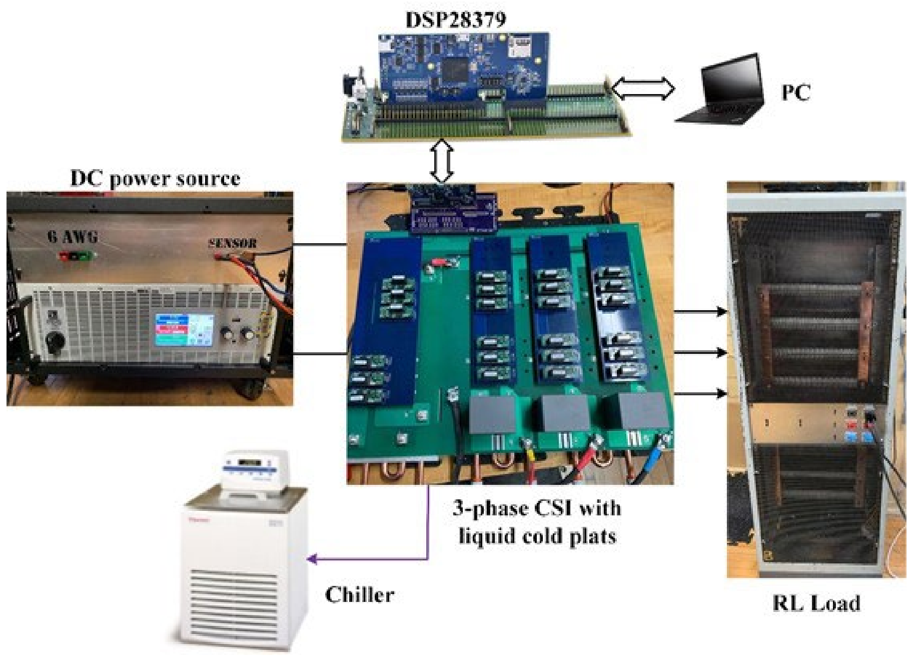

Figure I.1.18.5 Block diagram of the key testbed component

The fabricated CSI benchtop has been tested with a three-phase RL load, and the CSI's line-to-line voltage/phase currents have been compared to the simulation results. The CSI is controlled using a DSP TMS320F28379D controller board. Since the simulation assumes idealized switching transient, the line-to-line voltage obtained from the simulation is almost ideal sinusoid compared to the measured waveform from the experiment, as shown in Figure I.1.18.6. As shown in Figure I.1.18.6 (a), the measured voltage has larger ripple compared to the simulation results. The CSI's phase currents have also been measured experimentally and are compared to the simulation results, as shown in Figure I.1.18.7. The second-order LC filter formed by the CSI's output ac filter C and load inductance L sufficiently attenuates the high-frequency current components. Thus, the measured phase current is almost identical to that obtained from the simulation, as shown in Figure I.1.18.7. To reduce the switching oscillation caused by the parasitic inductance and parasitic capacitance in the current commutation loop, an alternative approach using SiC MOSFET and diode modules in place of the discrete devices is being aggressively investigated, with promising early results.

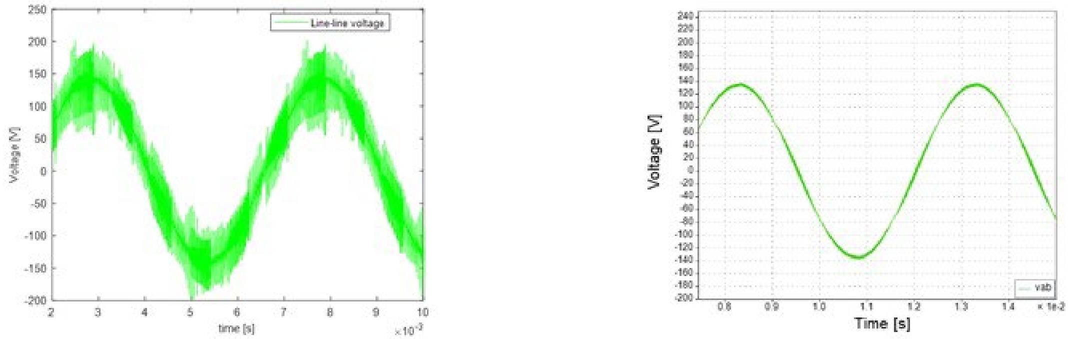

(a) Experimental result (b) Simulation result

Figure I.1.18.6 Measured and simulated line-to-line voltage comparison of CSI benchtop with RL load

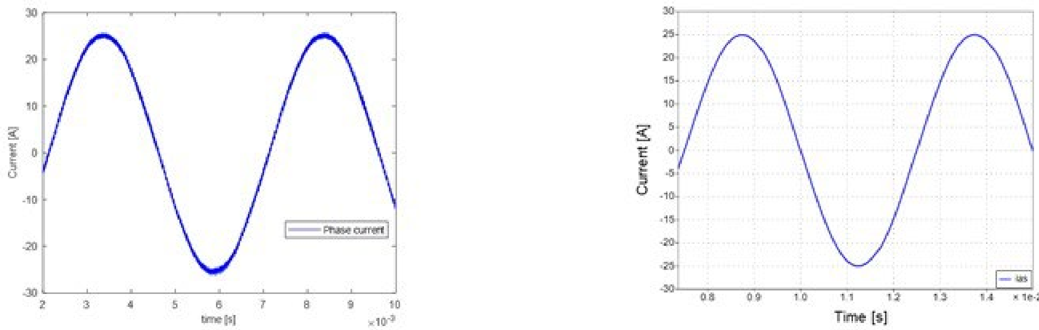

(a) Experimental result (b) Simulation result

Figure I.1.18.7 Measured and simulated phase current comparison of CSI benchtop with RL load.

Design of a CSI-excited SPM machine with CPSR of 3

Based on the design requirements, the maximum speed of the machine is 20,000 rpm, while the constant power speed ratio (CPSR) is set to a value of 3. The resulting corner speed is 6,667 rpm. Since the peak power is 100 kW and continuous power is 55 kW, the corresponding steady-state and peak torque values are 143.2 Nm and 78.8 Nm. The power density for 100 kW power output is designed to reach 50 kW/L, and no heavy rare-earth material is being used in the neodymium-iron magnets.

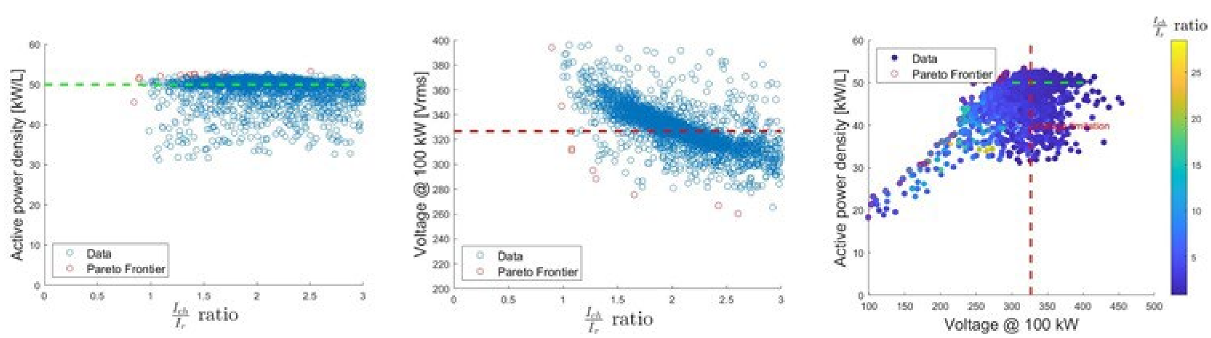

(a) (b) (c)

Figure I.1.18.8 Optimization results from the genetic algorithm; (a) active power density vs. Ich/Ir (b) motor L-N rms voltage at 100 kW vs. Ich/Ir (c) motor L-N rms voltage at 100 kW vs. active power density with the color of the design data points indicating the value of Ich/Ir.

This machine is designed and optimized by applying a genetic algorithm. This algorithm reflects the process of natural selection in which the most promising designs are selected for reproduction to produce offspring in the next generation. Figure I.1.18.8 shows the optimization results. Over 7,000 candidate designs have been evaluated over 90 generations. Figure I.1.18.8 (a) shows the relationship between active power density and the ratio of characteristic current (I_{ch}) to the rated current (I_r). Achieving a I_{ch}/I_r ratio equal to 1 indicates the optimal flux-weakening capability. Figure I.1.18.8 (b) shows the relationship between voltage at 100 kW and the ratio of characteristic current (I_{ch}) to the rated current (I_r). The purpose of this plot is to find the design that can meet voltage limitation of the devices. The motor maximum line-to-neutral voltage limit (326 Vrms) shown in Figure I.1.18.8 (b) is equivalent to 800 V_{pk} line-to-line voltage applied to the 1.2 kV SiC MOSFET. This provides a 50% safety factor for the 1.2 kV SiC MOSFET devices at the 100-kW operating point.

Figure I.1.18.8 (c) is the combination of (a) and (b) with the best candidates appearing in the upper left quadrant of the two orthogonal dashed lines. The Pareto front is shown by the red outlined circles in Figure I.1.18.8 (c) which indicates that the optimization process can successfully meet the active power density requirement. However, the majority of designs that meet the power density requirement have a ratio I_{ch} and I_r over 1.5, and very few of them have ratios close to 1. Optimal flux weakening capability is achieved with the ratio I_{ch} / I_r equal to 1, signifying that here is a tradeoff between active power density and I_{ch} / I_r ratio.

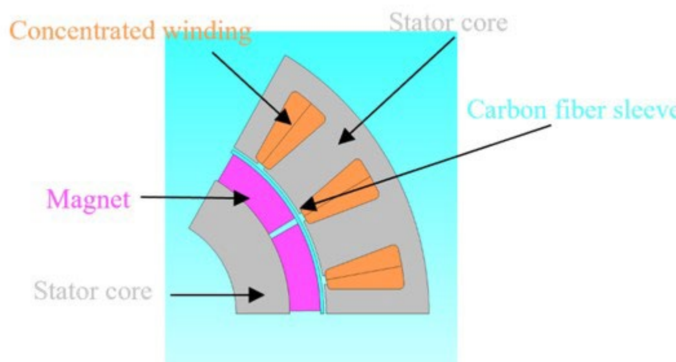

Figure I.1.18.9 Cross-section view of the optimized CSI-excited machine

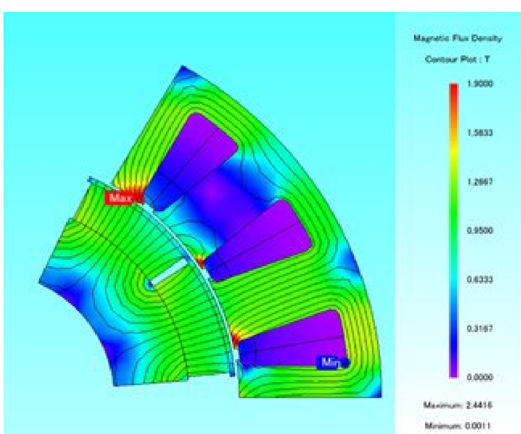

Figure I.1.18.10 Predicted flux density distribution for rated 55 kW, 6,667 rpm operation

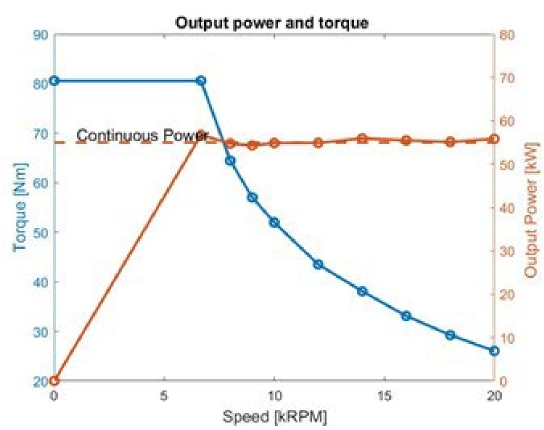

Figure I.1.18.11 Calculated torque-vs-speed envelope curve and power-vs-speed envelope of the proposed machine with a CPSR of 3.

A cross-section view of the selected machine from this optimization process is shown in Figure I.1.18.9 which identifies its concentrated windings, stator and rotor cores, permanent magnets, and carbon fiber sleeve. Figure I.1.18.10 shows the flux density distribution of the machine at the rated 55 kW, 6,667 rpm operating point. Figure I.1.18.11 shows the calculated torque-vs-speed envelope curve and power-vs-speed envelope curve of the proposed machine with a CPSR of 3. This machine can achieve a corner speed of 6,667 rpm and a maximum speed of 20,000 rpm by using flux weakening.

Conclusions

This report has provided a summary of key findings developed to date during the third year of the project. A conceptual configuration of the radially-mounted integrated motor drive designed with a shared water jacket cooling and hexagonal housing has been developed. The characteristics of the SiC MOSFET and in-series SiC Schottky diode initially selected for the 55 kW (cont.) CSI have been measured using the CSI DPT technique. The estimated efficiency of the 55 kW CSI based on the CSI DPT measurement results is 98.04% for rated continuous power delivery. The benchtop CSI was tested with a three-phase RL load. The measured line-to-line voltage and phase current waveforms of the benchtop CSI have been compared with the simulated waveform results, demonstrating very close agreement.

A CSI-driven SPM machine with a CPSR of 3 has been designed and evaluated. The maximum speed of this machine is 20,000 rpm, and the corner speed is 6,667 rpm with a CPSR of 3. The proposed machine is capable of delivering 100 kW peak power and 55 kW continuous power. Genetic optimization has been used to optimize the machine's power density while meeting all of the machine's torque-speed requirements and operating within the voltage limits set by the power switch devices used in the inverter. Structural analysis has been performed to calculate the thickness of the carbon fiber sleeve to safely retain the magnets at all speeds up to 20,000 rpm.

Key Publications

1. F. Chen, S. Lee, R. A. Torres, T. M. Jahns, and B. Sarlioglu, "Performance evaluation and loss modeling of WBG devices based on a novel double-pulse test method for current source inverter," in *Proc. IEEE Transportation Electrification Conference & Expo (ITEC)*, 2021, pp. 219–224.

2. W. Feng, H. Ding, S. Lee, F. Chen, T. Jahns, and B. Sarlioglu, " "Design of high power density 100 kW surface permanent magnet machine with no heavy rare earth material using current source inverter for traction application," in *Proc. IEEE Transportation Electrification Conference & Expo (ITEC)*, 2021, pp. 1–6.

3. F. Chen, S. Lee, T. M. Jahns, and B. Sarlioglu, "Comprehensive efficiency analysis of current source inverter based on CSI-type double pulse test and genetic algorithm," in *Proc. IEEE Energy Conversion Congress & Expo. (ECCE)*, 2021.

References

1. T. M. Jahns and H. Dai, "The past, present, and future of power electronics integration technology in motor drives," in *CPSS Transactions on Power Electronics and Applications*, vol. 2, no. 3, pp. 197–216, Sept. 2017.

2. J. Wang, Y. Li, and Y. Han, "Integrated modular motor drive design with GaN power FETs," in *IEEE Transactions on Industry Applications*, vol. 51, no. 4, pp. 3198-3207, July–Aug. 2015.

3. G. Su, L. Tang, C. Ayers, and R. Wiles, "An inverter packaging scheme for an integrated segmented traction drive system," in *Proc. IEEE Energy Conversion Congress and Exposition*, Denver, CO, 2013, pp. 2799–2804.

4. F. Chen, S. Lee, R. A. Torres, T. M. Jahns and B. Sarlioglu, "Performance evaluation and loss modeling of WBG devices based on a novel double-pulse test method for current source inverter," in *Proc. IEEE Transportation Electrification Conference & Expo (ITEC)*, 2021, pp. 219–224.

Acknowledgements

The project team would like to acknowledge the research members we collaborated with from Ames Lab, Oak Ridge National Lab, and National Renewable Energy Lab.

I.1.19 Multi-Objective Design Optimization of 100 kW Non-Rare-Earth or Reduced-Rare Earth Machines (Purdue University)

Scott Sudhoff, Principal Investigator
Purdue University
1285 Northwestern Avenue
West Lafayette, IN 47906
Email: sudhoff@purdue.edu

Steve Pekarek, Co-Principal Investigator
Purdue University
1285 Northwestern Avenue
West Lafayette, IN 47906
Email: spekarek@purdue.edu

Susan Rogers, DOE Technology Development Manager
U.S. Department of Energy
Email: susan.rogers@ee.doe.gov

Start Date: May 15, 2021 End Date: May 14, 2022
Project Funding: $300,000 DOE share: $300,000 Non-DOE share: $0

Project Introduction

The goal of this project is to reduce the size, weight, cost, and losses associated with rotating electric machinery and its associated power electronics for electric and hybrid vehicle applications. In particular, the goal of this effort is to facilitate electric machinery that will meet the requirements set forth in the U.S. DRIVE Electrical and Electronics Technical Team Roadmap of October 2017. This document calls for an electric machine with a peak power of 100 kW, a continuous rated power of 55 kW, a peak speed of less than 20,000 rpm, a volume of no more than 2 liters, a mass of less than 20 kg, and a useful life of 15 years or 300,000 miles of vehicle service. This will be achieved through a combination of (i) new materials, (ii) new electric machine topologies, (iii) advances in power electronics, and (iv) superior design through the use of formal and rigorous multi-objective optimization-based design built on advanced analysis techniques. This effort is being conducted by a large consortium comprised of national laboratories (Sandia National Laboratories, Oak Ridge National Laboratories, Ames Laboratory, and the National Renewable Energy Laboratory) and universities (Virginia Tech, Georgia Tech, SUNY, Arkansas, Ohio State, IIT, Purdue, University of Wisconsin – Madison, University of California Berkeley, and North Carolina State). Purdue's role focuses on (ii) and (iv).

Objectives

The objective of this effort is to explore the use of new materials and develop new design paradigms to enable unprecedented propulsion motor power densities at a reduced cost. In order to achieve this objective, Purdue's goals will be to investigate new machine topologies, such as the homopolar ac machine, and to develop new improved design codes which (*i*) incorporate high switching frequency performance analysis, (*ii*) thermal performance, (*iii*) high-speed rotor structural analysis, and (*iv*) advanced magnetic analysis techniques into its existing design paradigm based on rigorous multi-objective optimization in order to take best advantage of new materials and machine topologies developed by Purdue and other team members. An additional objective will be to build and test a prototype machine whose design is based on the enhanced design paradigm developed under this effort.

Approach

In order to achieve the objectives described in the previous section, Task 3.1 is the focus of the third year of the program. The SOPO for the third year of this effort and the subsequent tasks are summarized below.

Table I.1.19.1 Statement of project objectives and four main sub-tasks for the third year of this effort.

Milestone	Type	Description	Status	Completion Date
(D)HAM, PMAC machine comparison	Technical	The Pareto optimal fronts of HAM and PMAC machines will be compared by the end of BP3: Q1	Complete	June 31, 2021
ICPM code complete	Technical	Design code for an ICPM including structural and thermal analysis will be complete by BP3: Q2	Complete	September 30, 2021
Asymmetric Reluctance Machine (ARM) code complete	Technical	Design code for an Asymmetric Reluctance Machine structural and thermal analysis will be complete by BP3: Q3	In Progress	N/A
Comprehensive machine evaluation	Go/No Go	At the end of BP3: Q4, all machines considered will have been compared in terms of their Pareto optimal fronts.	In Progress	N/A

There are four main sub-tasks to this year's effort. The first concerns a novel machine invented at Purdue, now referred to as the DHAM for Dual rotor Homopolar AC Machine. This machine shows considerable promise. A patent for this device was formally filed in November 2021. The machine can be shown to yield high power density, even using ferrite magnets. The second concerns the ICPM, or Inert Core Permanent Magnet machine. This machine attempts to minimize mass by avoiding the use of a steel core. The third subtask focuses on the ARM, or Asymmetrical Reluctance Machine. In this machine, torque density is increased in one direction by sacrificing it in another. This particular device has no PM usage. The final subtask will be to compare all of the machine variants just considered (and others) and make a recommendation for future exploration. This is a concluding task for the year.

Results

In this section, results will be presented for the Dual Rotor Homopolar AC Machine (DHAM), Inert Core Permanent Magnet Machine (ICPM), and Asymmetrical Reluctance Machine (ARM).

Dual Rotor Homopolar AC Machine

The Dual Rotor Homopolar AC Machine (DHAM) is a novel rotating electric machine which can operate either as a motor or as a generator. It has a dual rotor topology and utilizes both a radial and axial flux paths. Figure I.1.19.1**.** illustrates a field-wound version of the machine; Figure I.1.19.2 depicts a permanent magnet version of the machine.

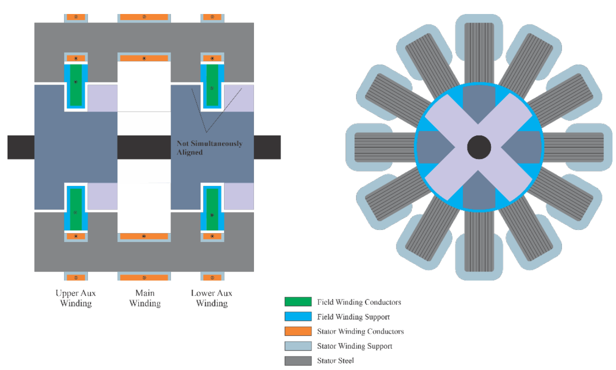

Figure I.1.19.1 DHAM with field windings.

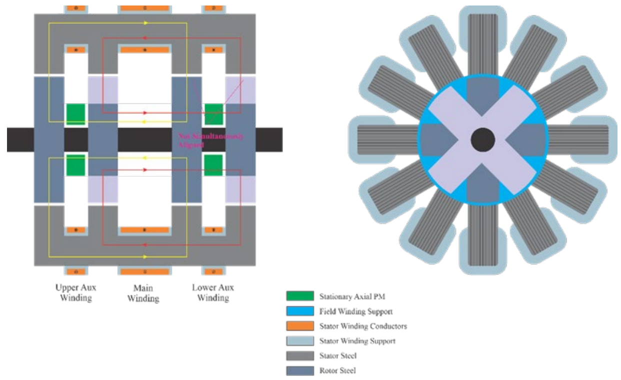

Figure I.1.19.2 DHAM with permanent magnets.

The power transfer to the machine is through the main windings of the machine which are polyphase. Nominally, a three-phase system is employed for the main windings, although any number of phases greater than one could be used. The voltage and current waveforms associated with the main windings are nominally sinusoidal, and the torque produced by the machine is nominally constant. Unlike other homopolar machines, the flux through the main winding does not have a dc bias leading to better material utilization.

The auxiliary windings of the machine (upper and lower), are connected together in parallel as the voltage across the two windings is essentially identical, and the required currents are opposite. Thus, as a whole, little or no excitation of the auxiliary winding is required. The role of the auxiliary winding is to distribute the flux in the desired fashion.

Attractive features of this machine are as follows: (i) **the field winding (or permanent magnets) can be stationary**. This facilitates cooling, electrical connections to the field, and eliminates mechanical stresses in high-speed machines. This feature also facilitates the use of superconducting field windings, if desired. For low-speed machines, the magnets can be placed on the rotor and allowed to rotate, if desired. Here there is still an advantage in that the magnets are at a smaller radius than the teeth and thus experience less force, and are more easily structurally wrapped than in traditional machines since flux is not crossing a radial airgap in this region; (ii) **the rotor itself is nominally lossless**, which also facilitates high speed applications, (iii) **the stator structure is inherently segmented**, facilitating manufacturing, as well as facilitating the construction of large machines; (iv) **the stator is easy to wind**. This facilitates high winding packing factor helping to reduce the size of the machine and improve thermal transfer, (iv) the **machine has a wide (theoretically infinite) constant power speed range**. This may make it ideal for applications such as flywheel energy storage; (vi) **space within the machine is available for the inverter**.

A design model of the DHAM machine was created to explore its capability and used in the context of a multi-objective optimization. This optimization was based on the machine requirements shown in Figure I.1.19.3. The requirements were based on the ORNL led machine group within the VTO consortium. The requirements are based on 100 kW peak power, 55 kW continuous power, 20,000 rpm maximum speed, and a 3-1 constant power speed range.

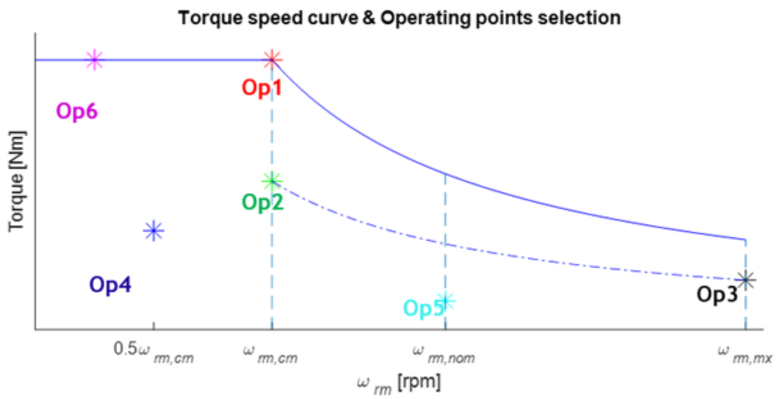

α_{CPSR}	3
$P_{\mathrm{mx},pk}$(kW)	100
$P_{\mathrm{mx},ct}$(kW)	55
$P_{\mathrm{nom},ct}$(kW)	27.5
$\omega_{rm,mx}$ (rpm)	20,000
$\omega_{rm,crn}$ (rpm)	$\omega_{rm,mx}/\alpha_{CPSR}$
$\omega_{rm,nom}$ (rpm)	$\sqrt{\omega_{rm,crn}\omega_{rm,mx}}$

	Op1	Op2	Op3	Op4	Op5	Op6
Speed	$\omega_{rm,crn}$	$\omega_{rm,crn}$	$\omega_{rm,mx}$	$\omega_{rm,crn}/2$	$\omega_{rm,nom}$	$\omega_{rm,crn}/4$
Power	$P_{\mathrm{mx},pk}$	$P_{\mathrm{mx},ct}$	$P_{\mathrm{mx},ct}$	$P_{\mathrm{mx},ct}/3$	$P_{\mathrm{mx},ct}/3$	$P_{\mathrm{mx,pk}}/4$
Weight	5%	15%	5%	20%	40%	15%

Figure I.1.19.3 Performance requirements.

The anticipated performance of the machine relative to a standard surface mounted permanent magnet ac machine (PMAC) is shown in Figure I.1.19.4. The optimization metrics were system efficiency and size (geometric mean of volume and mass), but machine efficiency and volumetric torque density are shown in Figure I.1.19.4 so as to focus on electric machine performance metrics.

As illustrated, two types of machines are considered, each with three variants. The two machine types are the PMAC machine and the DHAM. The variants are designs based on inexpensive AlNiCo magnets, inexpensive ferrite magnets, and rare-earth magnets. Within each variant, clearly the poorest machines were those with AlNiCo; ferrite the next best, and rare-earth being the best. Perhaps this is not surprising. However, for this study, it can be seen that, for example, the ferrite based DHAM dominated the rare-earth PMAC.

Cross sectional diagrams of a 20 kW/L ferrite magnet based DHAM are shown in Figure I.1.19.5. A feature of the DHAM is that the stator assemblies can be built with two sizes (referred to as short and tall teeth) in order to increase power density. Cross sections of the machine through both of these sized teeth are shown in Figure I.1.19.5. Observe there is an empty volume in the center of the machine. The intent is that this space will be used by the power electronics.

The operation of the DHAM is somewhat involved. This is fully described in the last quarterly report (BP3, Q2). It should be noted that the main windings of the machine are a three-phase balanced set with ideally sinusoidal voltages and currents. The auxiliary windings do not require excitation. The machine can be built in versions with a field winding, a stationary permanent magnet, or a rotating permanent magnet.

Work has begun to validate the design model against a 3D FEA. Thus far, the comparison between the design model and the 3D FEA has proven encouraging. As previously mentioned, a patent application has been filed.

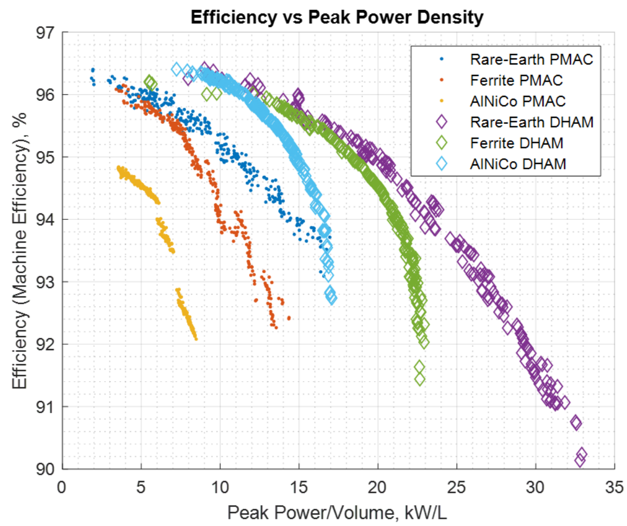

Figure I.1.19.4 DHAM performance.

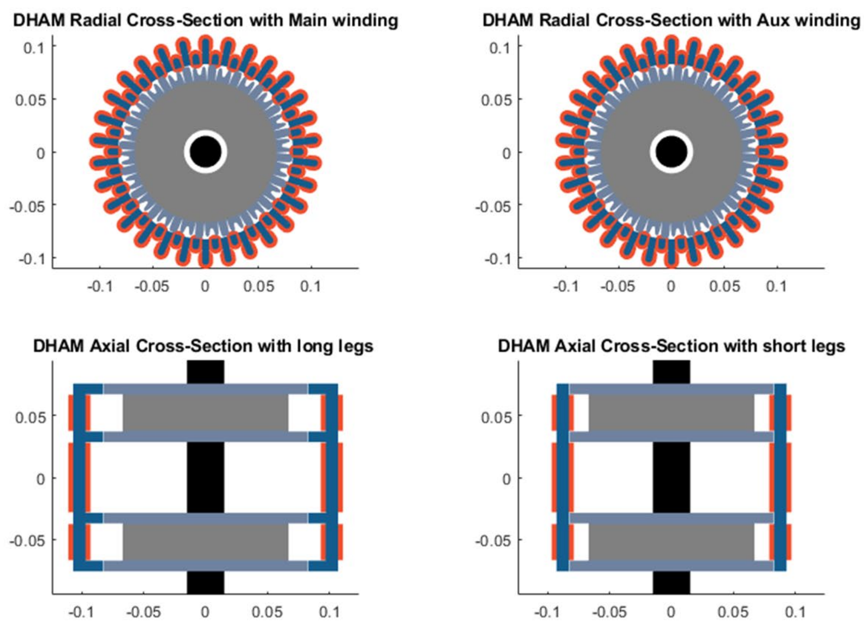

Figure I.1.19.5 20 kW/L ferrite based DHAM.

Inert Core Permanent Magnet Machine (ICPM)

Over the course of the year, the team developed the topology of an inert core permanent magnet machine (ICM), a variant of which is shown in Figure I.1.19.6. As shown, the stator consists of conductors placed within a traditional stator-type structure. In the figure, the lines in the stator region represent places for stator teeth, which has been assumed to be made magnetically inert (i.e., plastic), in which case the machine has no iron and only uses stator conductors and permanent magnets to tailor the flux paths necessary for torque production. The rotor has poles that are positioned within and outside of the stator. The inner and outer rotor sections each contain permanent-magnet-based poles that are configured as Halbach arrays and are arranged to establish flux in a radial direction across the airgaps. These arrays are arranged so that no rotor steel is needed to establish the flux path within the rotor. The promising aspects of this topology are the potential to reduce steel cost and mass, the potential to use non-rare-earth magnets, and the fact there are two stator/rotor interactions that yield torque, potentially increasing the machine torque density. Although there is PM material in this topology, a goal will be to consider non-rare-earth magnets in much of the array segments.

A design toolbox for the evaluation of the ICPM has been developed that enables the user to perform multi-objective optimization of the machine subject to the performance requirements shown in Figure I.1.19.3. As part of the design toolbox, the design variables include the height, depth, and material for each section as well as the stator winding arrangement. Due to the presence of time-varying fields within the stator slots, the conductors are assumed to be made of Litz-wire, whose minimum gauge of individual strands, can also be specified. The toolbox includes a Method of Moments (MoM) algorithm to evaluate the electromagnetic behavior of the machine and a thermal equivalent circuit to evaluate the temperatures throughout the machine. The thermal equivalent circuit has been validated using a commercial finite element design code.

Design studies have been initiated for the ICPM to evaluate its potential. Specifically, a population-based design was initiated with the performance specifications of the effort set as constraints of the optimization. The performance metrics included minimizing machine mass and minimizing system (machine + inverter) loss. Thermal constraints were imposed so that the maximum temperature within the windings was less than 400K at all potential steady-state operating points. A second population-based design was performed in which the thermal model was decoupled and a current density limit of 20 A/mm^2 was imposed at all steady-state operating points as a proxy to keep temperature low. A comparison between the pareto optimal fronts of the ICM with and without the thermal model are shown in Figure I.1.19.7. From the fronts, one can observe that the impact of the thermal constraints is significant. Specifically, the front of the machine that includes a thermal model drastically shifts towards the right, indicating that the machine becomes larger in mass to maintain thermal stability. This is somewhat expected since replacing the stator iron with a plastic material has a disadvantage in that it adds a significant resistive path for the heat to be dissipated from the windings. To avoid this, the machine optimization selects machine geometries with reduced conductor loss, which increases the cross section required of the conductors. A potentially positive characteristic of the machine is viewed when considering the front without the thermal constraint included, but with the current density of 20 A/mm^2. There one can observe that the overall system mass is quite low. Indeed, it has been found to beat that of a traditional PMAC machine with a similar current density constraint. Based upon these results there is presently an effort to further enhance the design toolbox to include active cooling. Specifically, we are developing means to place the conductors within cooling channels to enable higher current densities. As an alternative we are also evaluating the use of thermal plastics for the stator with relatively high conductivity for use in removing excess heat.

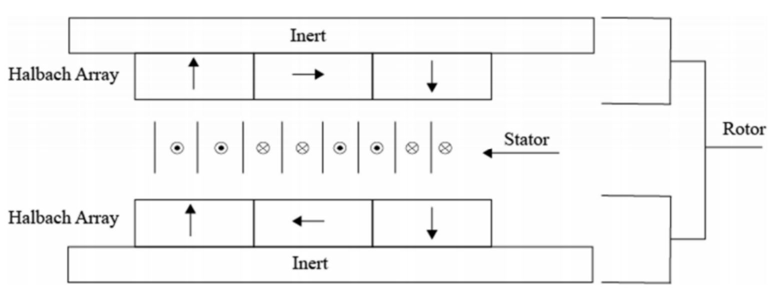

Figure I.1.19.6 Inert core permanent magnet machine

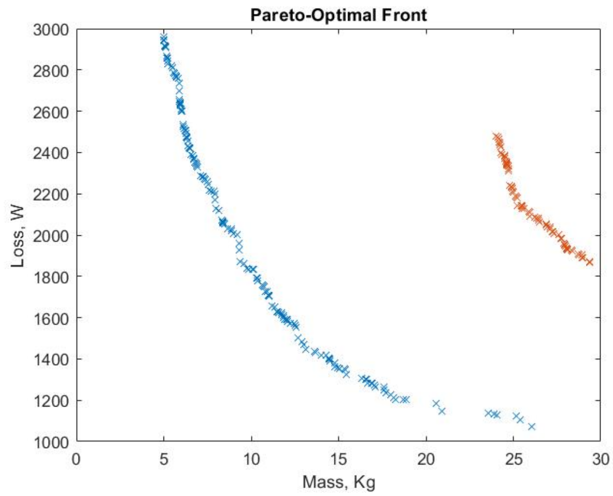

Figure I.1.19.7 Pareto-optimal front comparison of ICPM with/without thermal constraints

Asymmetric Reluctance Machine

Over the past year, another focus has been on the development of a MoM-based model to enable the design of rotationally asymmetric reluctance machines (ARM) [1]. A cross-sectional view of a single pole of an ARM is shown in Figure I.1.19.8. The ARM is a potentially cost-effective machine topology due to the fact that it does not have permanent magnets. In addition, it is relatively straightforward to manufacture. To evaluate its potential, an MoM based model of the ARM has been developed that enables the multi-objective design of the machine, with the pole dimensions and asymmetric aspect ratios shown in Figure I.1.19.8 included as genes. For the MoM modeling of this machine, a challenge is that it is likely to operate in a region of magnetic saturation, which requires volume meshing and an iterative approach to solve. The volume meshing/iterative solver capabilities were incorporated into the machine model. Initial design runs using the toolbox have been performed. As an example, to validate the toolbox, a design run was initiated for a 3 kW, 3000 rpm machine that matched that presented in [1]. For this run, to match the optimization from [1], the MoM was set to solve linear magnetics and the flux density constraints in the iron were consistent with that used in [1]. The Pareto-optimal front shown in [1] is shown together with that obtained from the MoM toolbox in Figure I.1.19.9. The results provide confidence that the toolbox is able to calculate the performance of the ARM in optimization studies. Indeed, runs have been initiated for the DOE driving cycle. A thermal model that utilizes thermal equivalent circuits is presently being developed and will be coupled to the MoM model to support coupled thermal/electromagnetic evaluation.

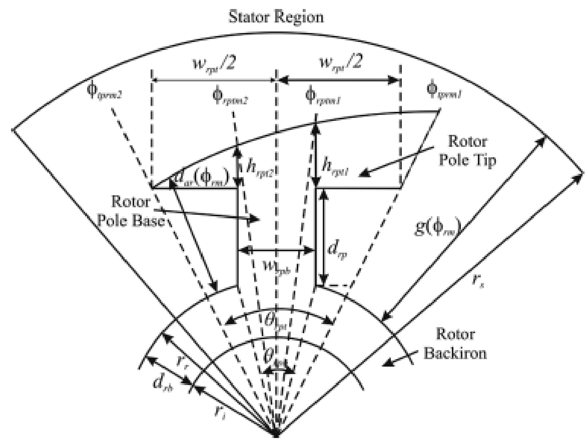

Figure I.1.19.8 Cross-Section of an ARM.

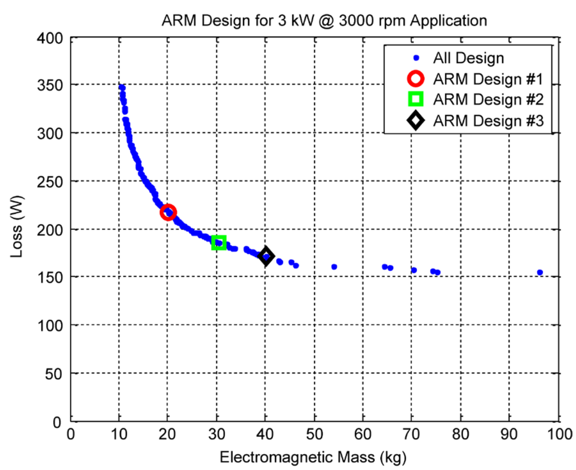

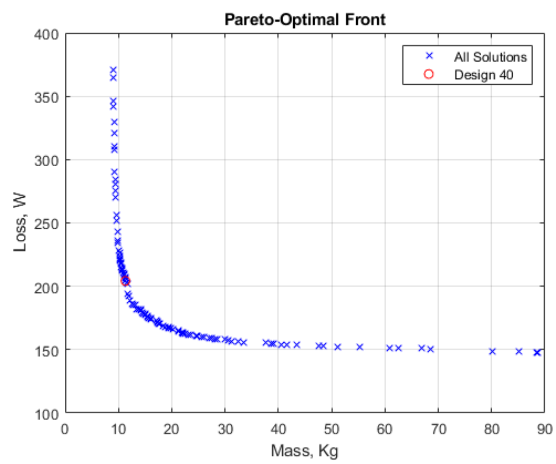

Figure I.1.19.9 Pareto-Optimal Fronts from [1] (left) and MoM-Toolbox (right).

Conclusions

At this point in BP3, it would seem the both the DHAM and ICPM hold promise. In particular, the DHAM shows the ability to exhibit high power density with low-performance. A patent application has been filed. The ICPM hold promise as a means of reducing machine mass.

Key Publications

1. Scott Sudhoff, Jiazhou Zhong, Steve Pekarek, “Dual Rotor Homopolar AC Machine,” nonprovisional patent application submitted to U.S. patent office in November 2021. Attorney docket number PRF-69245-02.

References

1. C. A. Harianto and S. D. Sudhoff, “A Rotationally Asymmetric Reluctance Machine with Improved Torque Density,” in *IEEE Transactions on Energy Conversion*, vol. 28, no. 1, pp. 62–75, March 2013.

Acknowledgements

Although Purdue is collaborating with the entire consortium, the relationship with Sandia National Laboratories has been particularly helpful. Thus, the help and contributions by Jason Neely, Lee Rashkin, Todd Monson, and Vipin Gupta are particularly recognized.

I.1.20 Cost competitive, High-performance, Highly Reliable Power Devices on SiC (SUNY Polytechnic Institute)

Woongje Sung, Principal Investigator
Research Foundation for SUNY Polytechnic Institute
257 Fuller Road
Albany, NY 12203
Email: wsung@sunypoly.edu

Susan Rogers, DOE Technology Development Manager
U.S. Department of Energy
Email: susan.rogers@ee.doe.gov

Start Date: April 16, 2019 End Date: April 15, 2024
Project Funding (FY21): $333,000 DOE share: $300,000 Non-DOE share: $33,000

Project Introduction

The primary objective of this project is to ensure that the next-generation of wide-bandgap devices have sufficient performance, reliability, and price to achieve the system-level DOE goals. In this project, we will develop 1200V SiC MOSFETs that are superior to Silicon counterpart (IGBT) in all aspects, such as cost, performance, and reliability. To accomplish the goal, many different variations in device/process design will be pursued and the proposed device will be fabricated at a production-grade cleanroom facility.

Objectives (BP2)

- Cost competitive
- High-performance (BV=1600 V, Ron,sp=5 mΩ-cm2, Vth=2 V)
- High reliability (Short Circuit SOA of >2µs).

Approach

Over the 5 years of the entire project span, this project aims to develop cost competitive, high performance, and highly reliable SiC MOSFETs to assist the team to achieve system level DOE goal.

Cost

A dramatic reduction in chip price can be achieved by conducting ion implantations at room temperature (RT). The process flow will be significantly simplified by RT implants. Appropriate analyses due to RT implants will be conducted. An innovative approach for the gate oxide formation will further reduce the chip size, and thus, chip price. Unipolar diode integration within the MOSFET structure will be demonstrated.

Performance

Cell optimization will be carried out using 2-D simulation, such as reducing cell pitch and optimization of the JFET region. Various edge termination structures, such as FFRs, RA-JTE, and Hybrid-JTE will be designed. Process split, such as gate oxide using ALD, self-alignment channel, and channeling implant to form deep junction will be conducted.

Reliability

Short-circuit and avalanche characteristics will be evaluated by mixed-mode device simulations. Process splits such as p-well implant and thin gate oxide will be carried out.

Results

In the second year of this project, SUNY Polytechnic Institute has fabricated SiC MOSFETs with many different design variations. The third group of fabricated devices (Lot 3, 1st lot in BP2) satisfies all the static performance targets.

1. Lot 1 Characterization for packaged device

Figure I.1.20.1 shows the reliability and ruggedness characteristics of the fabricated 1.2 kV MOSFETs in Lot 1. The typical switching turn-on and turn-off waveforms at V_{dc} of 800 V are shown in Figure I.1.20.1 (a) and (b), respectively. The double test with R_g of 20 Ω was conducted to measure switching characteristics. The normal switching behaviors were achieved. Figure I.1.20.1 (c) shows short-circuit waveforms at V_{ds} of 800 V and V_{gs} of 20 V. Short-circuit withstand time (SCWT) of 2 µs was accomplished. The improvement of short-circuit characteristics was implemented in Lot 3 using a deep Pwell structure. Figure I.1.20.1 (d) and (e) show positive (V_{gs} of 20 V) and negative (V_{gs} of -10 V) bias temperature instability, respectively. The relatively large V_{th} shift occurs due to the utilization of deposited gate oxide. In order to minimize V_{th} shift during BTI measurement, thermal gate oxide was used in Lot 2. The body diode degradation of the fabricated MOSFETs is shown in Figure I.1.20.1 (f). There is no degradation of MOSFETs at the stress of 5 A. The harsh condition (e.g., high drain current and high temperatures) will be applied to observe the body diode degradation. The unclamped inductive switching (UIS) waveforms of the fabricated SiC MOSFETs from Lot 1 are shown in Figure I.1.20.1 (g). The test was conducted at Vdc of 100 V and L of 11 mH. Avalanche energy of 665 mJ, which is reasonable value in the ~30 A 1.2kV MOSFETs, is achieved.

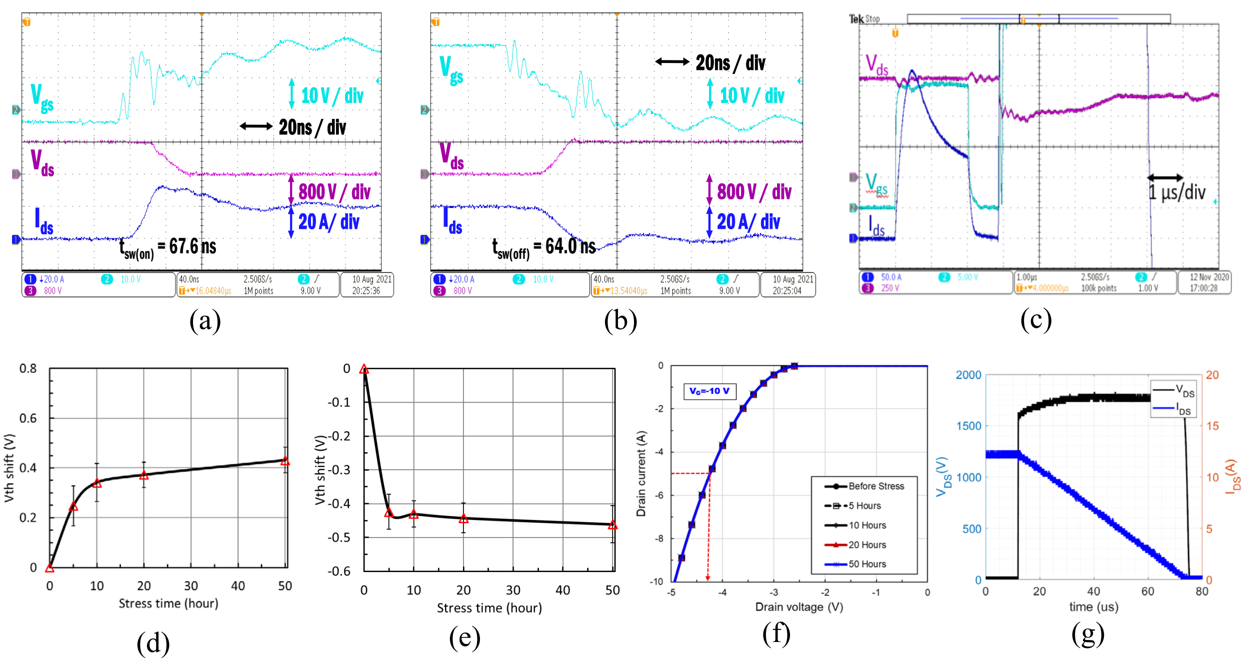

Figure I.1.20.1 (a) switching turn-on waveforms, (b) switching turn-off waveforms, (c) short-circuit waveforms, (d) PBTI, (e) NBTI, (f) body diode degradation, and (g) UIS waveforms of the fabricated SiC MOSFETs

2. Lot 2 Characterization

Table I.1.20.1 shows the wafer splits for 2nd lot. 4 different JFET doping concentrations were used to optimize the JFET region in terms of specific on-resistance ($R_{on,sp}$), breakdown voltage (BV), and short-circuit (SC) capability. Approximately 100 devices (Figure I.1.20.2 (a)) from Lot 2 were packaged to investigate the reliability and ruggedness.

Table I.1.20.1 Summary of wafer split for Lot 2.

	Doping in JFET region
Wafer1	3×10^{16} cm^{-3}
Wafer2, 3	5×10^{16} cm^{-3}
Wafer4, 5	7×10^{16} cm^{-3}
Wafer6	9×10^{16} cm^{-3}

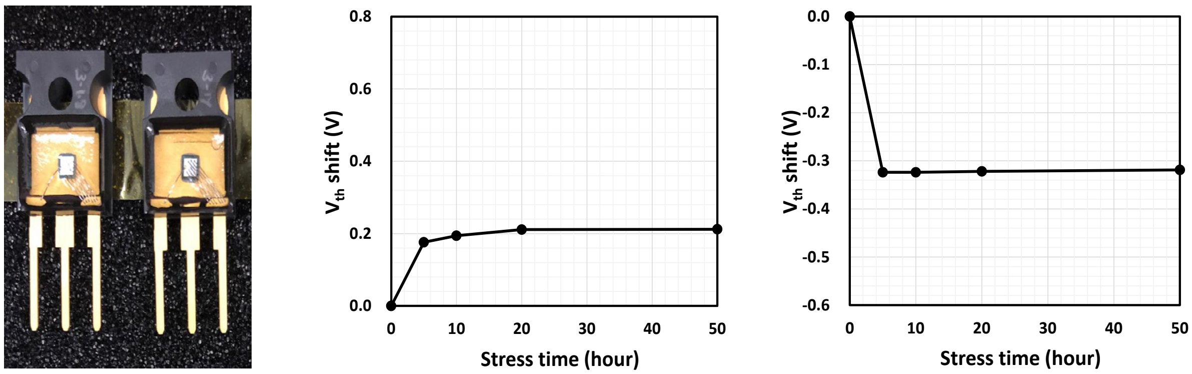

(a) (b) (c)

Figure I.1.20.2 (a) Image of the packaged devices from Lot2. (b) PBTI, and (c) NBTI of the fabricated MOSFETs.

Figure I.1.20.2 (b) and (c) show positive (V_{gs} of 20 V) and negative (V_{gs} of -10 V) bias temperature instability, respectively. Both of the PBTI and NBTI from Lot 2 were improved when compared to Lot 1. This is because thermal gate oxide was used in Lot 2. The higher quality of thermal gate oxide results in the improvement of BTI characteristics. The remaining reliability and ruggedness tests for Lot2 will be conducted at OSU.

3. Lot 3 characterization

Figure I.1.20.3 (a) shows the conventional structure of a 1200V MOSFET. The drift layer was designed to be 10 µm thick with a doping of 8×10^{15} cm^{-3} to achieve a breakdown voltage of around 1700V with a parallel-plane PN junction. The on-resistance can be reduced by reducing cell pitch, increasing channel mobility, and optimizing the JFET region. The cell pitch was largely reduced by putting the P+ source in the orthogonal direction, intermittently. An accumulation channel was designed for higher channel mobility. For lower $R_{on,sp}$ and higher BV, JFET width and doping concentration were optimized using 2-D device simulations [1]. Figure I.1.20.3 (b) shows the novel structure of a 1200V MOSFET. The extended P-well was formed using channeling implant, which is a novel implantation technique to implement a deep junction. The deep P-well structure can improve the static characteristics and reliability. Before the fabrication of the MOSFETs using channeling implantation, SIMS was conducted to confirm the channeling effect of the Al implantation. The implant profiles for the P-well of the conventional and novel MOSFETs are shown in Figure I.1.20.3 (c). The depth of channeling implant offers approximately 2.5 times deeper implant than that of the random implants using similar energy of Aluminum.

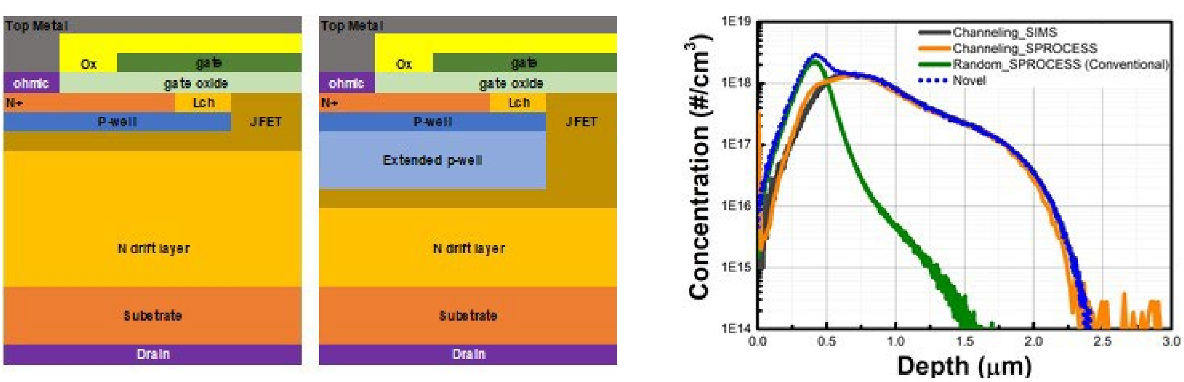

(a) (b) (c)

Figure I.1.20.3 Cross-sectional view of (a) conventional 1.2kV 4H-SiC MOSFETs and (b) novel 1.2kV 4H-SiC MOSFETs. (c) Implant profiles for conventional and proposed P-wells based on SIMS and SPROCESS [2]. The novel P-well is composed of conventional random implant as well as channeling implant.

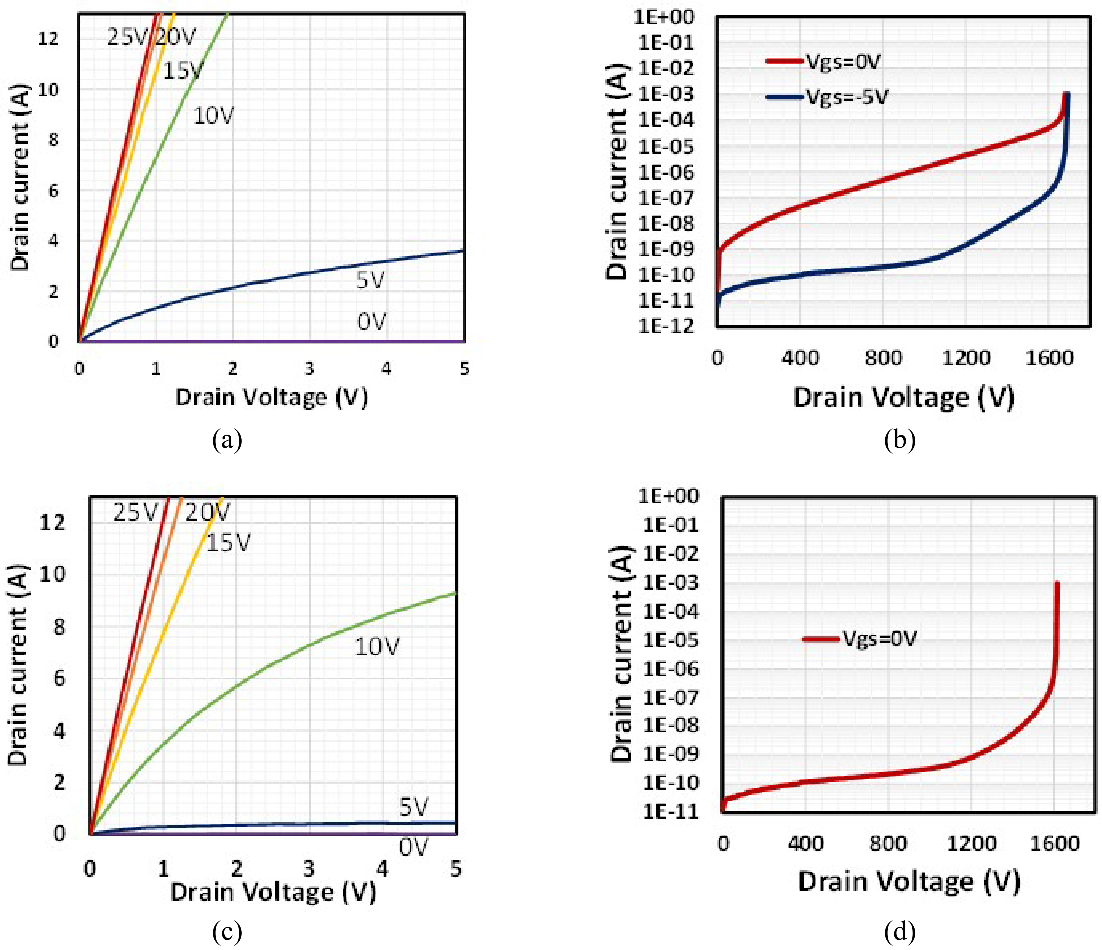

Figure I.1.20.4 (a) the output characteristics and (b) blocking behaviors of the conventional MOSFETs (WF#6, Lot 3). (c) the output characteristics and (d) blocking behaviors of the proposed MOSFETs (WF#10, Lot 3).

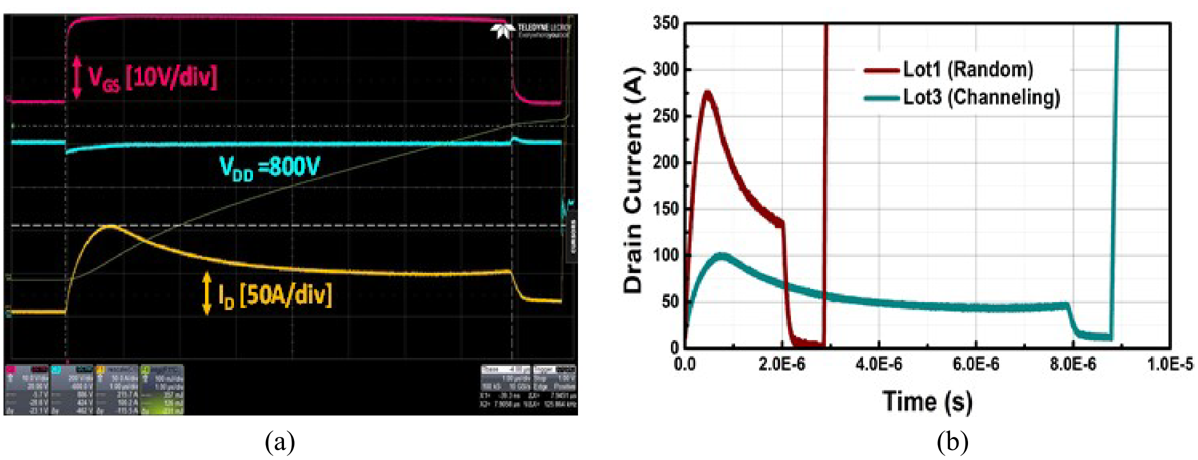

Figure I.1.20.5 (a) Short-circuit waveforms of the MOSFETs with the deep P-well using channeling implantation. The MOSFETs with the deep P-well achieved SCWT of 8 μs. (b) Drain currents of the MOSFETs from Lot 1 (random implants) and Lot 3 (channeling implants) under SC conditions. The approximately 4 times longer SCWT was achieved in the MOSFETs from Lot 3.

Figure I.1.20.4 (a) and (c) show the output characteristics of the conventional and novel MOSFETs, respectively. Slightly better conduction behaviors are achieved from the conventional MOSFETs as the proposed MOSFETs have relatively high JFET resistance due to the deeper P-well region. However, the novel MOSFETs provide extremely low leakage current during the blocking behaviors at V_{gs} of 0 V as shown in Figure I.1.20.4 (b) and (d). Although the deeper P-well has the higher $R_{on,sp}$, the leakage current was significantly reduced as shown in Figure I.1.20.4 This is because the deeper P-well contributes to the increase in the channel potential, suppressing the leakage current from the channel. Moreover, the reliability and short-circuit characteristics are improved when using the deeper P-well. Figure I.1.20.5 (a) shows the short-circuit waveforms of the novel MOSFETs using channeling implantation. The measurement for short-circuit was conducted under the following conditions: R_g of 20 Ω, V_{gs} of 20 V, and V_{ds} of 800 V. Figure I.1.20.5 (b) shows the drain current of the MOSFETs from Lot 1 and Lot 3 under SC condition. The measured MOSFETs in Figure I.1.20.5 (b) have almost identical $R_{on,sp}$. Compared to conventional MOSFETs from Lot 1, the maximum drain current decreases by ~2.7 times, when using the novel structure from Lot 3 due to deeper P-well, resulting in the reduction in junction temperatures in the SiC MOSFET. This low junction temperature contributes to the improvement of SC ruggedness, which is ~4 times longer than the conventional MOSFET structure; the novel MOSFETs achieved a SCWT of 8 µs. The trade-off relationship between $R_{on,sp}$ and SCWT was significantly improved by the novel structure with a deep P-well. A novel approach to improve SCWT with no impact on $R_{on,sp}$ enables the decrease of the saturation current under high drain bias. The remaining reliability and ruggedness tests will be conducted at OSU.

Table I.1.20.2 Summary of wafer split and static characteristics (Lot 3)

	Implant type	JFET doping concentration	P-well implant depth (doping)	Solderable metal	Ron,sp (mohm-cm^2) (V_{gs}=20V)	BV (V)
Wf1	Random	5×10^{16} cm^{-3}	~0.7 µm (2×10^{18})	X	3.98	1667
Wf2	Random	5×10^{16} cm^{-3}	~0.8 µm (2×10^{19})	X	9.3 (Vgs=35V)	1682
Wf3	Random	5×10^{16} cm^{-3}	~1.0 µm (2×10^{18})	X	5.02	1657
Wf4	Random	5×10^{16} cm^{-3}	~1.0 µm (2×10^{18})	O	4.57	1654
Wf5	Random + channeling	5×10^{16} cm^{-3}	~1.8 µm (2×10^{18})	X	4.43	1569
Wf6	Random	8×10^{16} cm^{-3}	~0.7 µm (2×10^{18})	X	3.63	1679
Wf7	Random	8×10^{16} cm^{-3}	~0.8 µm (2×10^{19})	X	9.18 (Vgs=35V)	1681
Wf8	Random	8×10^{16} cm^{-3}	~0.8 µm (2×10^{19})	O	9.12 (Vgs=35V)	1684
Wf9	Random	8×10^{16} cm^{-3}	~1.0 µm (2×10^{18})	X	4.69	1658
Wf10	Random + channeling	8×10^{16} cm^{-3}	~1.8 µm (2×10^{18})	X	4.12	1615
Wf11	Random + channeling	8×10^{16} cm^{-3}	~1.8 µm (2×10^{18})	O	4.04	1589
Wf12	SIMS analysis for channeling implantation					

Table I.1.20.2 summarizes the wafer split and static characteristics of the nominal device from Lot 3. Different JFET doping concentrations and P-well depths were investigated. Solderable metal for the front side was also applied to examine the double-sided cooling package. The high JFET doping provides the reduction in $R_{on,sp}$.

For WF#2, 7 and 8, which have the high doping concentration in the P-well, very high $R_{on,sp}$ was obtained even with high gate voltages were applied. The high doping concentration of the P-well makes the strong inversion channel mode, resulting in the higher V_{th} and lower channel mobility. The on-wafer measurements for the devices from Lot 3 were completed. The MOSFETs and JBSFETs from WF#10 were diced and packaged. OSU is presently measuring the packaged devices in terms of the reliability and ruggedness. The remaining wafers (#1, 3, 4, 5, 6, 9, 11) were diced, and they are in the package process. After packaging, OSU will also measure the reliability and ruggedness test. Furthermore, OSU will fabricate inverter using nominal devices of WF#10.

4. Device design and fabrication of Lot 4

For high-temperature operation (~250°), different channel types (accumulation and inversion mode channel), and deep P-well were designed. Also, thinner gate oxide (25nm) was applied to reduce the operating gate voltage

and improve the short-circuit characteristics. The mask for Lot 4 includes 17 different devices, which are a PiN diode, a JBS diode, and various MOSFETs, JBSFETs, and HEXFETs. In order to operate MOSFETs at high-temperature (~250°C), MOSFETs with long channel length and narrow JFET width were included. There are 13 photolithography process steps, including 6 implant processes. Fabrication for Lot 4 will be completed in early December 2021.

5. Device design and fabrication of Lot 5

For further improvement of the trade-off relationship between $R_{on,sp}$ and SCWT, the optimization of the channeling implantation was conducted. Moreover, the current spreading layer (CSL) and accumulation channel were optimized to improve the static characteristics. The mask for Lot 5 includes 16 different devices, which are a PiN diode, a JBS diode, and various MOSFETs, JBSFETs, and HEXFETs. MOSFETs with different channel lengths and JFET widths were included. There are 11 photolithography process steps, including 5 implant processes. Fabrication for Lot 5 started in early October 2021.

Conclusions

This year, SUNY Poly has focused on improving the trade-off relationship between $R_{on,sp}$ and SCWT. Lot 3 has been successfully completed and shows promising static performances and short-circuit characteristics. Moreover, other reliability and ruggedness tests were successfully conducted and demonstrated in Lots 1 and 2. Many different variations in both device designs and process conditions were examined through Lots 1, 2, and 3. Lessons learned from Lots 1, 2, and 3 have been reflected in the design of Lot 5 and Lot 6 (1^{st} and 2^{nd} lots for BP3). The remaining reliability and ruggedness tests for Lot 2 and 3 will be conducted at OSU. The fabrication for Lot 4 and 5 will be completed in early December 2021 and early March 2022.

Key Publications

1. Dongyoung Kim, Nick Yun, Junchong Fan, Susanna Yu, Adam J Morgan, Minseok Kang, Seung Yup Jang, Woongje Sung, and Anant K. Agarwal, "A Static, Switching, Short-circuit Characteristics of 1.2 kV 4H-SiC MOSFETs: Comparison between Linear and (Bridged) Hexagonal Topology," Presented in *the 8th IEEE Workshop on Wide Bandgap Power Devices and Applications (WiPDA 2021)*

2. Dongyoung Kim, Nick Yun, Seung Yup Jang, Adam J. Morgan, and Woongje Sung, "An Inclusive Structural Analysis on the Design of 1.2kV 4H-SiC Planar MOSFETs," *Journal of the Electron Devices Society*, vol. 9, pp. 804–812, Sep. 2021. DOI: 10.1109/JEDS.2021.3109605

3. Dongyoung Kim, and Woongje Sung, "Improved Short-circuit Ruggedness for 1.2kV 4H-SiC MOSFET using a Deep P-well implemented by Channeling Implantation," in *IEEE Electron Device Letters*, DOI: 10.1109/LED.2021.3123289.

References

1. Woongje Sung, Kijeong Han, B. J. Baliga, "Optimization of the JFET region of 1.2kV SiC MOSFETs for improved high frequency figure of merit (HF-FOM)," 2017 IEEE 5th Workshop on Wide Bandgap Power Devices and Applications (WiPDA)

2. Synopsys Inc., SentaurusTM Process User Guide, ver. K-2015.06, June 2015.

Acknowledgements

SUNY would like to thank SiCamore Semi, Bend, OR for the fabrication of the devices. We acknowledge that the channeling implantations for the proposed devices in lot 3 were conducted by NISSIN ION EQUIPMENT CO.,LTD., Kyoto, Japan.

I.1.21 Cost competitive, High-performance, Highly Reliable Power Devices on GaN (SUNY Polytechnic Institute)

Shadi Shahedipour-Sandvik, Principal Investigator
SUNY Polytechnic Institute
257 Fuller Road
Albany, NY 12203
Email: sshahedipour-sandvik@sunypoly.edu

Susan Rogers, DOE Technology Development Manager
U.S. Department of Energy
Email: susan.rogers@ee.doe.gov

Start Date: April 16, 2019 End Date: April 15, 2024
Project Funding (FY21): $333,000 DOE share: $300,000 Non-DOE share: $33,000

Project Introduction

The primary objective of this project is to demonstrate highly reliable wide bandgap AlGaN/GaN HEMT power devices in comparison to HEMT on foreign substrate. In this project, we will demonstrate AlGaN/GaN HEMT power devices with greater performance and reliability. To accomplish this goal, growth conditions and processing will be optimized for HEMT devices on foreign substrates as well as on resistive bulk GaN to reduce the effect of structural defects in the bulk and at interfaces. Additionally, we investigate the processing of gate dielectric materials to improve the performance and reliability of HEMT devices.

Objectives

- AlGaN/GaN growth on foreign substrates (sapphire, Si)
- AlGaN/GaN growth on GaN substrate
- HEMT material optimization.

Approach

Improvement of Off-State Leakage in AlGaN/GaN HEMTs

The main objective of our project is to offer deeper understanding of the impact of dislocation defects/substrate on AlGaN/GaN HEMT performance. However, to do so, having a high quality HEMT structure itself is important so that the contributing factors to performance can be distinguished. A poor quality AlGaN/GaN HEMT will mask the impact of substrate.

Much of our previous work has focused on optimizing the fabrication process to increase ION/IOFF ratio by decreasing IOFF, however, material optimization is also essential for low IOFF. In order to decrease IOFF, minimizing the background impurity concentrations in the channel layer is critical. The growth pressure of the GaN channel and the AlGaN barrier layers are generally the same in order to keep ramping and discontinuity between layers to a minimum. In our case, that is at 100 Torr.

One of the most common intentional impurities in MOCVD GaN is carbon. It is well known that increasing growth pressure decreases [1]. However, by increasing the pressure of the channel layer, an additional discontinuity in the growth conditions of GaN and AlGaN is introduced. In order to mitigate impurity incorporation and interface roughness, both of which are detrimental to 2DEG mobility, three different ramping schemes were investigated between the GaN and AlGaN layers: (1) Direct ramp from 300 Torr GaN growth condition to 100 Torr AlGaN growth condition, (2) AlN interlayer added between 300 Torr GaN and

100 Torr AlGaN layers, and (3) thin 100 Torr GaN transition layer between 300 Torr GaN and 100 Torr AlGaN.

Results

Improvement of Off-State Leakage in AlGaN/GaN HEMTs

On-wafer Hall effect measurements for the three HEMT growths described above are compared to a "standard" HEMT growth with 100 Torr GaN channel layer in Table I.1.21.1. All HEMT growths with 300 Torr channel layer have lower mobilities than the HEMT with 100 Torr channel layer. Nevertheless, the most critical-to-quality metric is the I_{ON}/I_{OFF} ratio of fabricated devices.

Table I.1.21.1 Mobility and Carrier Concentration Values for HEMT Growth Conditions Investigated

	100 Torr uGaN (standard recipe)	300 Torr uGaN with direct ramp	AlN Interlayer	100 Torr GaN Transition Layer
Mobility (cm^2/V-s)	1100	947	836	996
Density ($\times 10^{13}$ cm^{-2})	1.84	2.68	3.19	2.61

Devices fabricated from these experiments showed high leakage and very little gate control. High leakage was measured between nominally isolated device area. We believe this is in large part due to issues with fabrication while issues with growths may also exist. We plan to repeat these growth and fabricate new devices.

References

1. N. A. Fichtenbaum, T. E. Mates, S. Keller, S. P. DenBaars, and U. K. Mishra, "Impurity incorporation in heteroepitaxial N-face and Ga-face GaN films grown by metalorganic chemical vapor deposition," J. Cryst. Growth, vol. 310, no. 6, pp. 1124–1131, 2008, doi: 10.1016/j.jcrysgro.2007.12.051.

Acknowledgements

B. McEwen, E. Rocco, K. Hogan, and V. Meyers, substantially contributed to the work presented here.

I.1.22 Design, Optimization, and Control of a 100 kW Electric Traction Motor Meeting or Exceeding DOE 2025 Targets (Illinois Institute of Technology)

Ian P. Brown, Principal Investigator
Illinois Institute of Technology
3301 South Dearborn Street
Chicago, IL 60616
Email: ibrown1@iit.edu

Susan Rogers, DOE Technology Development Manager
U.S. Department of Energy
Email: Susan.Rogers@ee.doe.gov

Start Date: April 1, 2021 End Date: March 30, 2022
Project Funding: $342,962 DOE share: $300,000 Non-DOE share: $42,962

Project Introduction

The Illinois Institute of Technology (IIT) is a member of the Department of Energy Electric Drives Technologies (EDT) Consortium. IIT's role in the consortium focuses on developing electric traction motors for electric vehicles with 8x the power density and half the cost of state-of-the art traction motors.

Objectives

The overall objective of the electric motor portion of the Electric Drives Technology consortium is to research, develop, and test electric motors for use in electric vehicles capable of the specifications in Table I.1.22.1. Reduced scale physical prototypes and full-scale design studies are planned at regular intervals to ensure progress towards the targets.

Table I.1.22.1 EDT Consortium Motor Targets

Parameter	Target Value
Peak Power Rating (kW)	100
Power Density (kW/l)	≥ 50
Cost ($/kW)	≤ 3.3

Approach

To meet the electric traction motor power density and cost targets of Table I.1.22.1, a number of approaches are being pursued simultaneously throughout the course of this project which address all of the major volumetric power density influences. Many of the approaches are synergistic and complementary with the approaches being taken by partner Electric Drive Technology Consortium member national laboratories and universities. Specific areas of focus during this past budget period include the following.

- Multiphysics design for increased power density through maximum utilization of active materials.
    - Topological optimization techniques to distribute materials in an optimal manner without a geometric template subject to magnetic and structural objectives and constraints.
    - Combined topology and dimensional/shape optimization techniques to leverage the strengths of both techniques.
    - Improved dimensional optimization techniques which simultaneously address electromagnetic, thermal, and structural design in a computationally efficient manner through metamodeling.

- Developing high slot fill windings for increased current loadings or efficiency. Potential options that have been investigated include low proximity loss bar/hairpin windings, cast windings, and die compressed windings.
- Investigation of aggressive cooling strategies and optimization/calibration of spray cooling models.
- Apply new technologies, concepts, materials, and learnings from the Illinois Institute of Technology research group and other Electric Drives Technology Consortium members in prototype electric traction motors.

Results

Magneto-Structural Combined Dimensional and Topology Optimization Using a PM Function Interpolation

Electric machine optimization is usually carried out by varying dimensional parameters of a geometric template which defines the machine's shape or geometry. Because the geometric features and dimensions of the template are not truly independent, the range over which the dimensional variables can vary must be restricted to avoid unfeasible geometries. Also, it is difficult to know a priori what small features to incorporate into the template to reduce torque ripple and stress concentrations. Topology optimization offers an interesting alternative where material is distributed in free-form manner in the design domain.

In a past annual report, a magneto-structural combined dimensional and topology optimization technique was described that used mesh deformation to allow block or rectangular shape permanent magnets (PMs) to change position or size in the rotor design domain while topology optimization of the surrounding iron takes place [1]. Using this technique, the mesh may become overly distorted if a dimensional optimization variable changes over a large range. In this budget year, a new approach has been developed that does not require mesh deformation.

Instead, the block/rectangular PM shape is expressed as a smoothed Heaviside rectangular function whose output represents the presence or absence of PM material and is projected or interpolated into the design domain mesh, Figure I.1.22.1. The position, size, and rotational angle of the projected PM are controlled by a dimensional variable expressed through the PM function. An example of the projection of the PM function into the rotor mesh for two flat bar and one v-configuration is shown in Figure I.1.22.2.

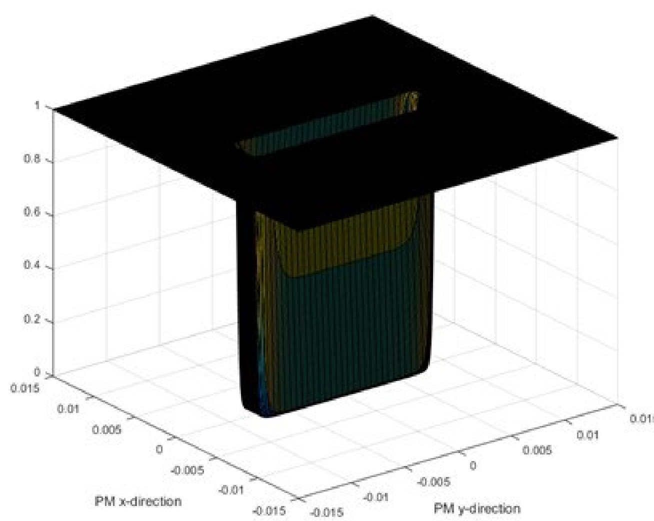

Figure I.1.22.1 Example smoothed Heaviside rectangular PM function where a zero indicates the presence of PM and 1 the absence of PM.

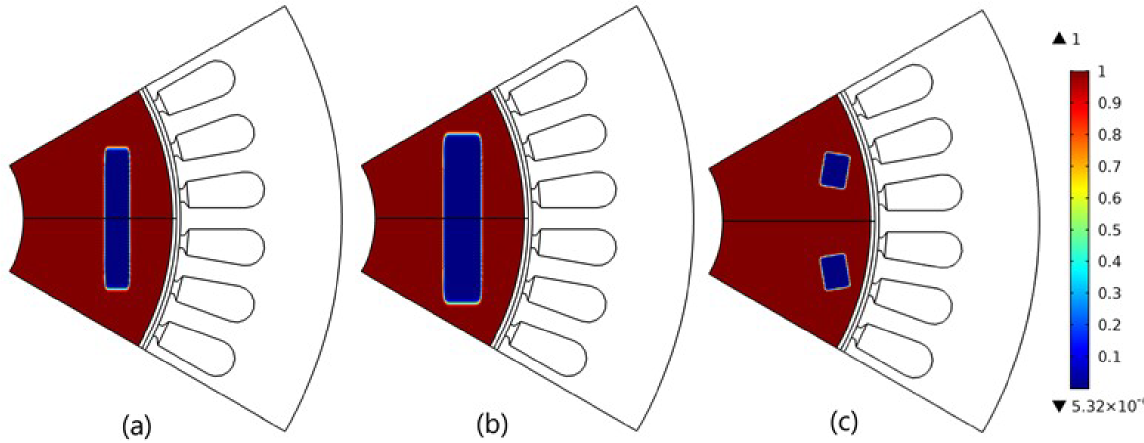

Figure I.1.22.2 Example initial PM function projections into the rotor design domain: (a) initial PM magnet function, (b) increased PM size, (c) two small PMs in a v-configuration.

The dimensional PM controls, along with the electrical steel normalized density control variables, are combined into a single combined dimensional and topology optimization problem which can be solved using nonlinear programming techniques such as the globally convergent method of moving asymptotes (GCMMA). Three example combined dimensional and topology optimizations using the proposed technique to maximize the average torque subject to constraints on the torque ripple, Von Mises stress, and compliance are shown in Figure I.1.22.3. Three cases with different PM dimensional variables are shown. In the first, only the PM radial position is variable (left). In the second, the PM radial position and size are variables (center). The third PM configuration has two PMs arranged in a v-shape with their radial position, size, and V angle as dimensional variables (right). The resulting iron and PM distributions are shown in Figure I.1.22.3. Iron is represented by red, air by blue, and PM by light green.

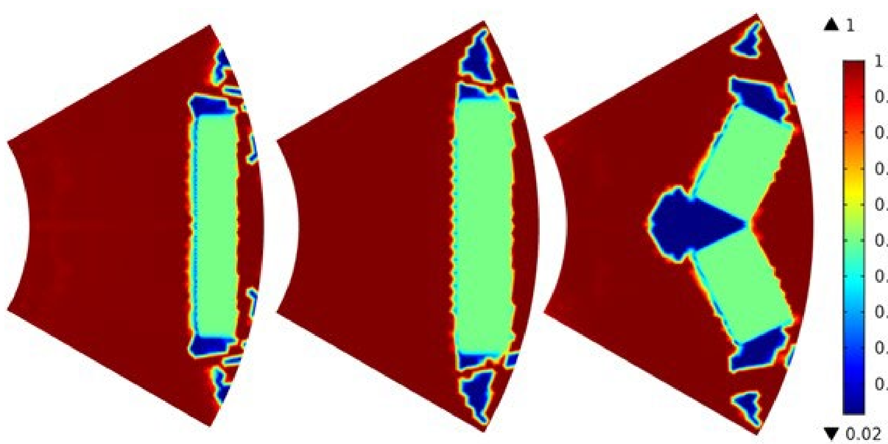

Figure I.1.22.3 Example problem optimization results where the materials distributed are permanent magnet (light green), electrical steel (red), and air (blue).

While the PM function projection approach avoids having to deform the mesh, there is no longer a distinct geometric boundary between the PM and the surrounding iron or air. To accurately model the centrifugal forces in the system, an equivalent pressure to that caused by the magnet is imposed on the iron elements nearest to the magnets in the radial direction, Figure I.1.22.4. The mass and Young's modulus of the PM is then set to zero for the structural FEA simulation. Constraints maybe placed on the maximum Von Mises stress and the global compliance of the design domain. Stress and displacement distributions for the three examples are shown in Figure I.1.22.5 and Figure I.1.22.6 respectively. The stresses and displacements remain below the imposed limits.

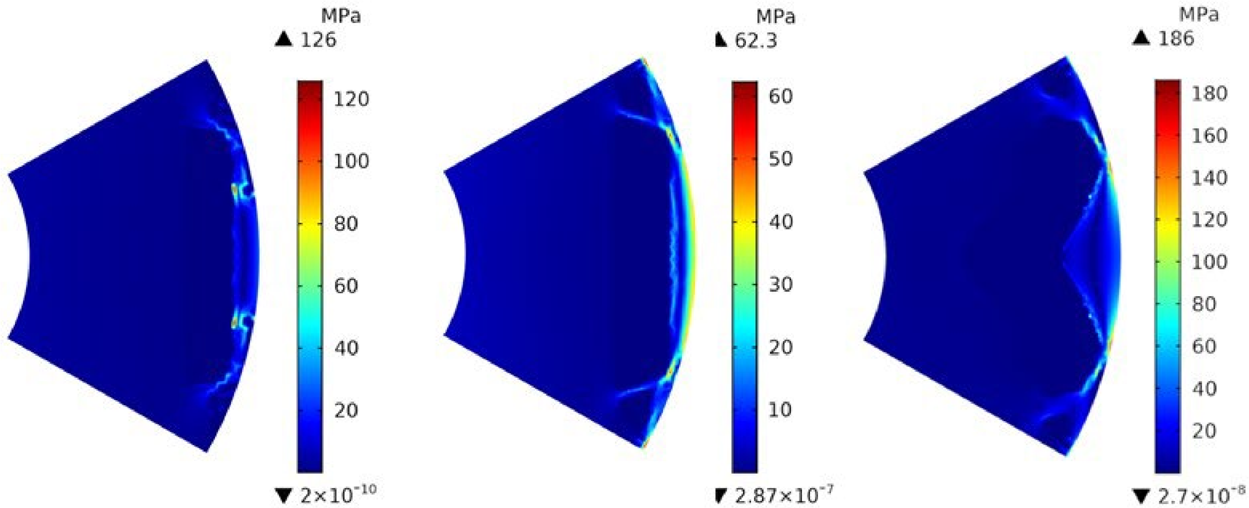

Figure I.1.22.4 Example optimization results' equivalent permanent magnet contact centripetal load mimicked as a pressure load on the nearest radial iron elements (red).

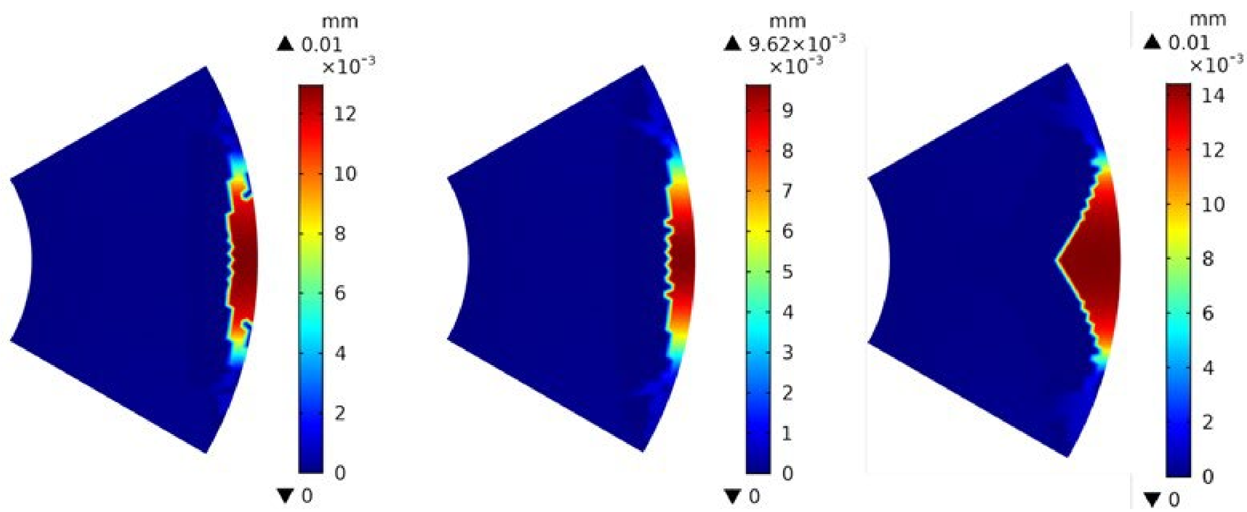

Figure I.1.22.5 Example optimization results' Von Mises stress distributions.

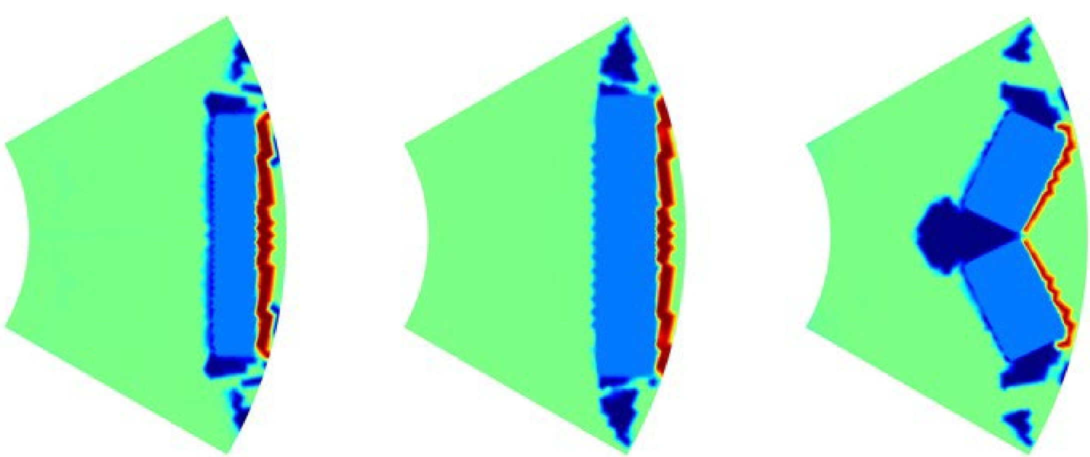

Figure I.1.22.6 Example optimization results' displacement distributions.

Cycle Metamodeling Based Optimization

A geometric template based, electric machine design optimization tool has also been developed which allows for optimization of the electric machine efficiency over a drive cycle subject to constraints such as torque capability, voltage limits, current densities, torque ripple, and mechanical stress. The drive cycle is represented by a number of load or operating points that can be defined by the user or potentially derived from a clustering algorithm. If the number of load points is large direct optimization of the design becomes computationally infeasible even with multiple designs being evaluated in parallel. Instead, a metamodeling-based approach is used. A sensitivity study is first carried out sampling the design space to create a representative meta-model. The optimization process then uses the meta-model to evaluate thousands of potential designs. Optimum designs or a sampling of Pareto front designs are then verified using a full analysis. This approach significantly reduces the computational expense. The process chain for the sensitivity analysis, metamodel creation, optimization and validation is shown in Figure I.1.22.7. Other analysis including demagnetization checks and electromagnetic tooth force analysis for noise vibration and harshness have also been developed such that they can be incorporated into the metamodeling process.

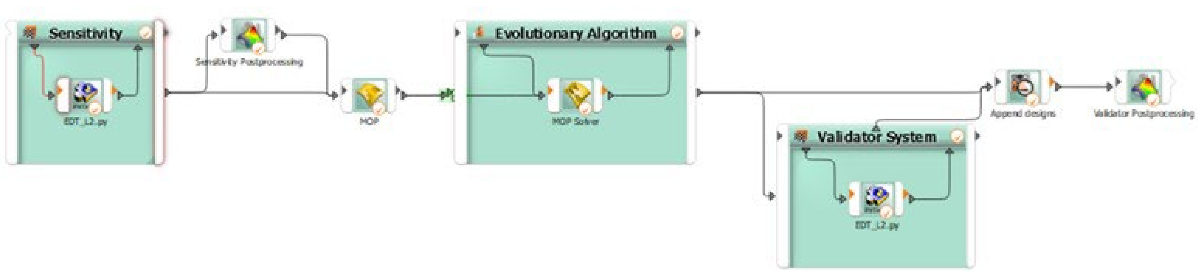

Figure I.1.22.7 Example metamodeling-based design optimization process chain.

Cast and Additively Manufactured Windings

Investigations into high slot fill cast and additively manufactured windings and their cooling were initiated during this budget period. Trial coils suitable for a fractional slot concentrated winding machine were manufactured. A lost wax casting process, potentially compatible with high volume manufacturing, was utilized to produce a trial copper coil and partial coils only consisting of end turns and heat transfer blocks. An additively manufactured trial coil was also produced using atomic diffusion additive manufacturing (ADAM) but found to not meet required dimensional and surface finish tolerances. The trial cast copper coil is shown in Figure I.1.22.8 before insulation and compression. As cast, the coil turns are not insulated from one another. A polyimide insulating process is being developed including the investigation of surface preparations and additives to reduce the surface tension after dipping the coil in the polyimide solution to prevent pooling. Polyimide insulation offers very high temperature capability and dielectric strength. An example copper sample coupon with a polyimide coating is shown in Figure I.1.22.9. Work on the polyimide coating process is ongoing. Additional additive manufacturing methods to produce coils including binder jets are also being investigated.

Figure I.1.22.8 Sample cast copper coil for high slot fill, fractional slot concentrated winding before insulation and compression.

Figure I.1.22.9 Representative copper test coupon for polyimide dip coating process.

Spray Cooling Jet Optimization

A test rig for the measurement of heat extraction through spray cooling of the end turns has been constructed. Cast end turn samples have been designed and manufactured to be swappable with a cartridge heating system capable of producing high losses compatible with high current density windings, Figure I.1.22.10. The test rig also allows for spray nozzles and flow rates to be easily changed. The goal is to optimize the heat extraction from cast copper coils for a future prototype. The same test rig will also be used for optimizing the heat transfer from the end turns of the form wound prototype stator currently under construction and described later in this report.

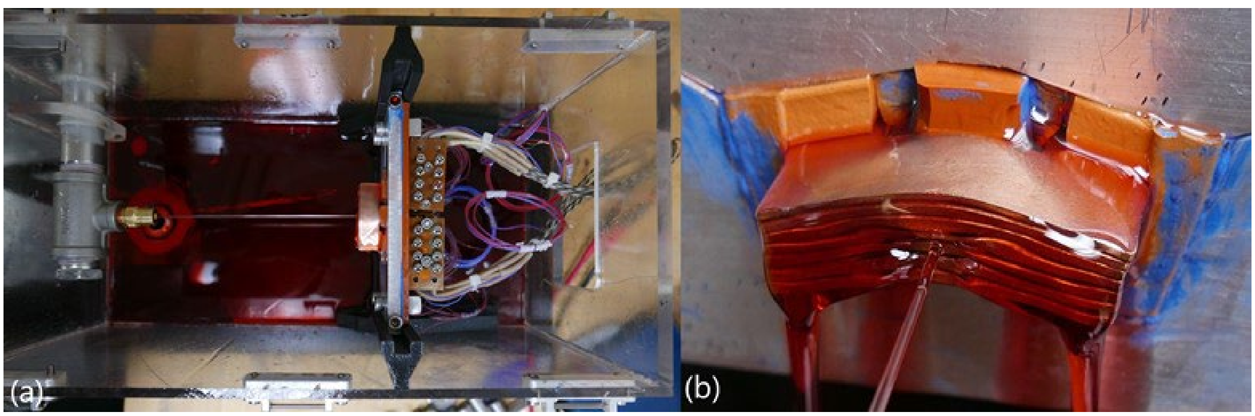

Figure I.1.22.10 Flexible spray cooling test rig (a) and cast copper end turn sample mounted in it (b). A variable heat flux is supplied by cartridge heaters and the flow velocity, spray distance, and nozzle are controllable.

High Power Density Interior Permanent Magnet Synchronous Machine Prototype

A high performance interior permanent magnet synchronous machine (IPMSM) prototype has been designed using the metamodeling-based optimization method presented earlier in this report. The intent of this particular prototype is to research how detailed state-of-the-art optimization and existing manufacturing methods can approach the power density goal of 50 kW/l. The output power target for this prototype is 100 kW at a base speed of 6,600 RPM with an active stator volume of 2 liters. Outputs considered during the optimization included the weighted efficiency over six operating points in an anticipated drive cycle, average torque, terminal voltage, stator current density, maximum rotor stress, and torque ripple. The down-selected machine is shown in Figure I.1.22.11. The rotor design was further refined to reduce stress concentrations and insert magnet retention and assembly features. A high stator slot fill is critical for reaching the required ampere-turns and keeping the stator current density to levels that are feasible to cool. Hairpin windings offer high slot fills but are very difficult to prototype in an academic setting. Instead, form windings inserted through open slots were used instead. Trial form wound stator coils have been prototyped using a custom form winding machine, Figure I.1.22.12. A housing and shaft system has also been designed for the prototype, with both automatic transmission fluid (ATF) spray cooling of the end turns, and a water ethylene glycol (WEG) cooling jacket is incorporated into the stator housing, Figure I.1.22.13.

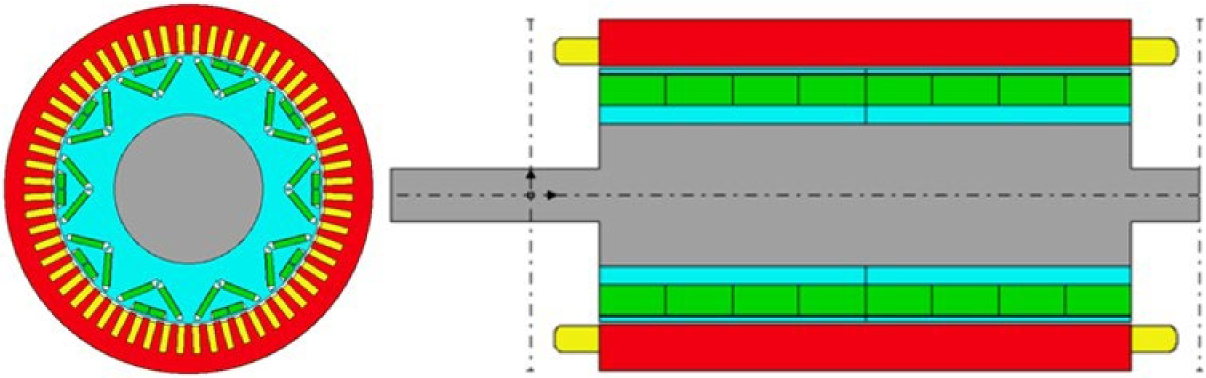

Figure I.1.22.11 Radial (left) and axial (right) cross-sections of the optimized prototype IPMSM.

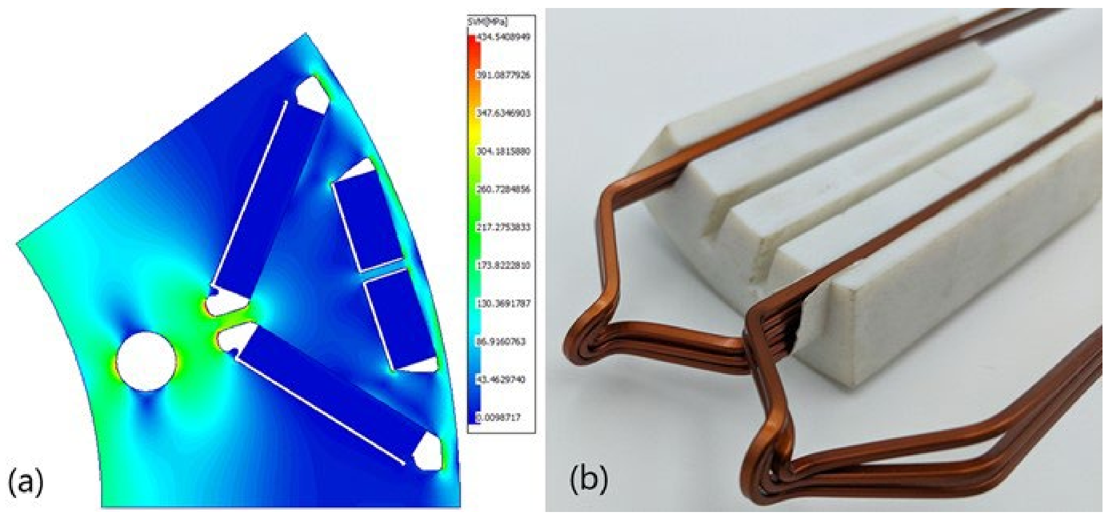

Figure I.1.22.12 Rotor design with stress reduction, magnet insertion, and assembly features added (a), and trial high slot fill form winding (b).

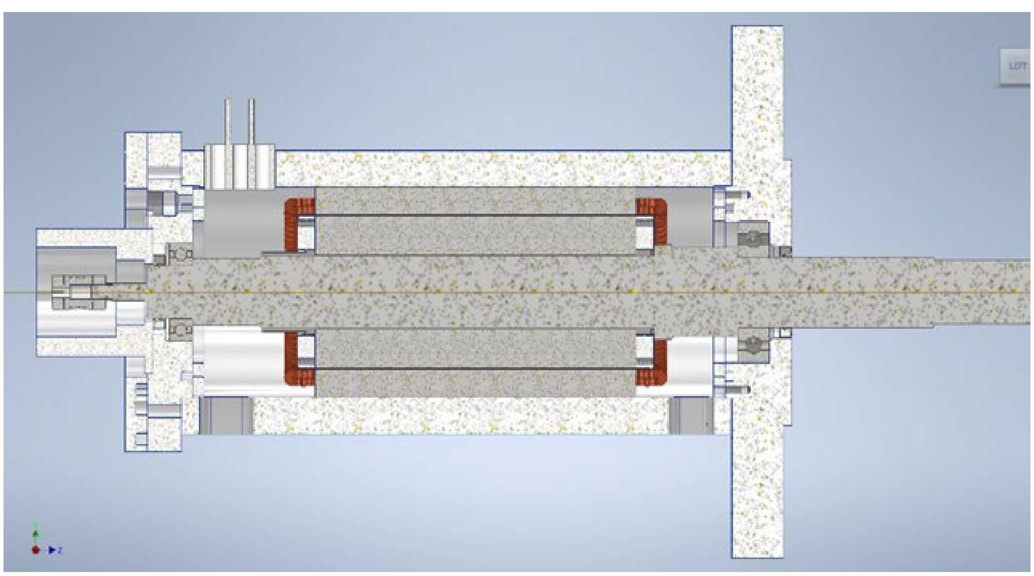

Figure I.1.22.13 Prototype motor assembly including shaft, housing, and resolver. The housing incorporates both a WEG cooling jacket and ATF spray cooling features in the end plates.

Conclusions

In this budget period a combined dimensional and topology optimization technique for the design of IPMSM rotors has been developed which uses a function projection instead of mesh deformation. This technique allows optimal material distribution while still ensuring manufacturable PMs. A metamodeling based dimensional optimization technique was also developed to maximize the efficiency over a drive cycle subject to constraints. This technique was used to design a high power density IPMSM prototype. High slot fill windings and their cooling was also a focus of research during this budget period. Cast copper windings were prototyped and a test setup for optimizing their spray cooling was constructed.

Key Publications

1. F. Guo, I.P. Brown, "Combined Dimensional and Topology Optimization of Interior Permanent Magnet Synchronous Machine Rotors Using a Permanent Magnet Function Interpolation Method," 2021 IEEE Energy Conversion Congress and Exposition, Vancouver, CA, 2021.

2. N. Tang, I.P. Brown, "Comparison of Candidate Designs and Performance Optimization for an Electric Traction Motor Targeting 50 kW/L Power Density," 2021 Energy Conversion Congress and Exposition, Vancouver, CA, 2021.

3. N. Krause, A. Di Gioia, I. P. Brown, "Multi-Core Microcontroller Hardware in the Loop System for Electric Machine Control," 2021 Energy Conversion Congress and Exposition, Vancouver, CA 2021.

References

1. F. Guo, I.P. Brown, "Magneto-Structural Combined Dimensional and Topology Optimization of Interior Permanent Magnet Synchronous Machine Rotors," 2020 IEEE Energy Conversion Congress and Exposition, Detroit, MI, 2020.

I.1.23 Device- and System-Level Thermal Packaging for Electric-Drive Technologies (Georgia Institute Of Technology)

Yogendra Joshi, Principal Investigator
Georgia Institute of Technology
771 Ferst Drive, Atlanta, GA 30332
Email: yogendra.joshi@me.gatech.edu

Samuel Graham, Co-PI
Georgia Institute of Technology
801 Ferst Drive, Atlanta, GA 30332
Email: sgraham@gatech.edu

Satish Kumar, Co-PI
Georgia Institute of Technology
771 Ferst Drive, Atlanta, GA 30332
Email: satish.kumar@me.gatech.edu

Susan Rogers, DOE Technology Development Manager
U.S. Department of Energy
Email: susan.rogers@ee.doe.gov

Start Date: April 1, 2019 End Date: April 1, 2023
Project Funding: $1,500,000 DOE share: $1,500,000 Non-DOE share: $0

Project Introduction

This project aims to research, develop, and test Electric Traction Drive System Technology for use in vehicle applications capable of meeting the targets set by the Department of Energy Vehicle Technologies Office. The project is categorized into three major thrusts: Bonding interfaces for packaging, Thermal management of electric vehicles (EVs) power inverters, and electric motor thermal management.

A transient liquid phase bonding technique is being developed to directly bond dielectric substrates with AlSiC heatsinks for use in power electronic packages. AlSiC has been demonstrated to improve the lifetime of the packages by at least 16 times and overall significant performance enhancements can be achieved by eliminating duplicate layers in commercially available direct bonded copper (DBC) and integrating a streamlined substrate to cold plate assembly. Fabricated samples are found to have good interfacial adhesion, low void composition and resistance to applied shear stresses.

For thermal management of electric vehicles, vapor chambers (VC) for high heat fluxes were investigated. The vapor chamber consisted of a 40 mm x 40 mm x 0.85 mm structure, with the wicking structure fabricated using sintered 200-micron copper particles. Arc welding was used for sealing the VC. Simulations of a representative power module were performed with suggestions on how to improve thermomechanical reliability and thermal performance. Flow boiling in microchannels was numerically examined to compare the alternative geometries (constricted inlet, diverging, and auxiliary jetting) with a baseline straight microchannel. Performance quantification showed results consistent with literature, with void fraction visualization lending additional insight into bubble dynamics. Embedded cooling tests were performed for heat fluxes up to 1 kW/cm^2.

As water jackets in current electric vehicles undercool the end-windings, a new cooling design for end-winding cooling was fabricated and tested. A cap for the end-windings was printed and placed on the end-windings, which were filled in with silicone sealant. The Nissan Leaf electric motor was used as the testbed for this configuration. The physical testing used a 50/50 mixture of water ethylene glycol and took place at the

National Renewable Energy Laboratory's facilities. Augmenting the Leaf's cooling with the end-winding thermal management setup decreased end-winding external temperatures by 35% or more. Subsequently, a CFD model was used to calculate heat transfer coefficients which was used for calibration of end-winding thermal resistances. The lumped parameter thermal network was then updated with an end-winding channel equivalent resistor network. Additional work has been performed in numerical replication of prior results by NREL.

Objectives

- Investigate the capability of the transient liquid phase (TLP) bond system in bonding Al coupons as in commercial DBA substrates to a low coefficient of thermal expansion (CTE) AlSiC cold plate as a packaging alternative.
- Examine and identify Cu-Al intermetallic compounds formed during TLP bonding and identify their effects on material properties.
- Develop an approach for multi-physics modeling for SiC and GaN packaging systems.
- Demonstrate compact modeling-based co-design and optimization framework for power inverter
- Establish single-phase cold plate design with integrated vapor chamber (VC) for operation at 1 kW/cm2 and 200°C device temperature
- Numerical modeling of alternative microchannel geometries
- Demonstrate ability to dissipate 1 kW/cm2 through embedded cooling technologies
- Design and demonstrate end-winding cooling solution on a representative EV motor
- Update LPTN network to include calibrated thermal resistances of the tested end-winding cooling configuration

Approach

Bonding interface for packaging

In order to understand of the capabilities of the Cu-Al eutectic transient liquid phase bonding system, the technique was modified and applied to bonding Al metal to AlSiC cold plates. The procedure, which includes the use of Al and Cu foils between the interacting layers, is similar to the process for bonding AlN to AlSiC discussed previously by Pahinkar et al. The starting concentration of Al in the bond layer was reduced (from three to one 50um Al foil) to account for the increase in Al content in the top layer coupon. The original Cu thickness was maintained at 25 µm.

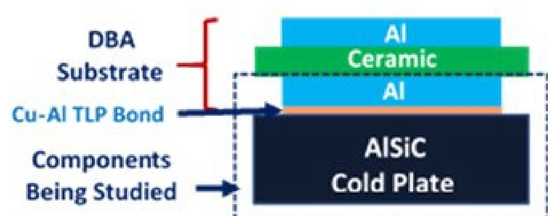

Figure I.1.23.1 Bonding stack for Al – AlSiC layers

To study the intermetallic phases formed between TLP bonded power electronic material layers, an analysis of the crystalline structure via X-ray diffraction was conducted. X-ray diffraction (XRD) is a nondestructive method to analyze material properties such as the composition, structure, and texture of crystalline samples. A material crystal is bombarded with X-rays of a certain wavelength, at particular incident angles to produce reflected X-rays. When the wavelengths of the scattered X-rays interfere constructively, a diffracted beam of X-rays will leave the crystal at an angle equal to that of the incident beam. The general relationship between the wavelength of the incident X-rays, angle of incidence and crystal lattice spacing is known as Bragg's Law, and expressed as $n \cdot \lambda = 2d \cdot \sin\Theta$ where n is the integer order of interference, λ is the wavelength, d the lattice spacing, and Θ is the Bragg angle.

A Malvern PANalytical Empyrean X-ray Diffraction platform with a copper anode was used for the XRD analysis. Identification of Cu-Al intermetallic phases was executed by matching the resulting patterns to the built-in Joint Committee on Powder Diffraction Standards (JCPDS) database software on the machine and these results were further compared with those of EDS. A phase diagram of the Cu-Al system identifies possible intermetallic compounds which may be formed between copper and aluminum at different concentrations and temperatures.

X-ray diffraction analyses were conducted along the interfaces of all the samples to identify the compounds present. In each case, an XRD experiment was first performed on the AlSiC (bottom) surface and then on the top surface of AlN, Cu or Al to determine a standard reference pattern for each of the aforementioned elements and compounds. This was done to enable identification and elimination of known compounds. Next, XRD tests along the cross-sectioned surfaces of the various sample combinations were conducted. Intermetallic phases were determined by first identifying the standard peaks from the XRD patterns. Since the interface region being investigated consists of a small surface area, (approximately 50x25 um), to increase the intensity of the measured XRD patterns, the diffraction experiment was performed slowly over a 12-hour period for each sample, with the detector rotating through an angle of approximately 15° per hour in the Bragg-Brentano geometry.

Thermal management of electric vehicles (EVs) power inverters

We investigated an integrated vapor chamber (VC), with cold plate for high heat flux power devices of 1 kW/cm^2 and up to 200°C junction temperature. The VC assembly is shown in Figure I.1.23.2. The heat source is an insulated gate bipolar transistor. The VC's dimensions are of 40 mm x 40 mm x .85 mm thickness. The VC employs a customized wick structure fabricated by sintering copper particles of 200 um. A condenser with posts for structural integrity is employed. The evaporator and condenser are sealed using gas-tungsten arc edge welding then charged with de-ionized water. A rectangular cold plate acts as the VC condenser. To gather baseline data, a commercial vapor chamber of 90 mm x 90 mm x 1.5 mm thickness and a metal foam wick of 10% void fraction is used in the stack assembly. The thermal characterization of the VC is ongoing. The results will be compared and discussed with the baseline results. A simplified conduction-based model is also developed to predict the thermal performance of the integrated assembly.

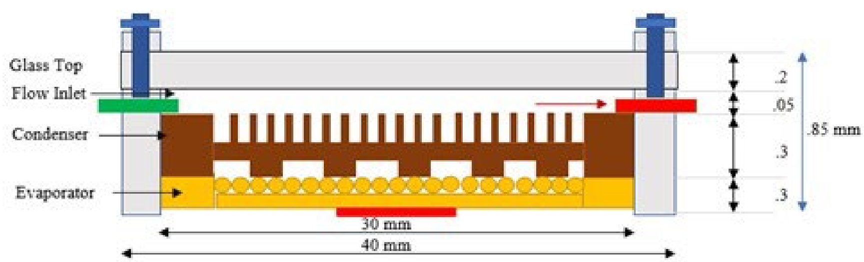

Figure I.1.23.2 Schematic of integrated vapor chamber for thermal packaging of high-power devices

We also developed an approach for performing multi-physics modeling on a full-scale power inverter. A compact modeling-based co-design and optimization framework is demonstrated to investigate the optimal performance of packaging. Figure I.1.23.3 (a) shows the CAD of a BMW i3 power module. Each sub module consists of eight silicon insulated gate bipolar transistors (IGBTs) and diodes. Total power dissipation of the transistors and diodes at the inverter level is 920W. Ethylene-glycol and water is used as a coolant at 85°C.

The simulations and thermal-mechanical co-optimization is performed on a single sub-module shown in Figure I.1.23.2.

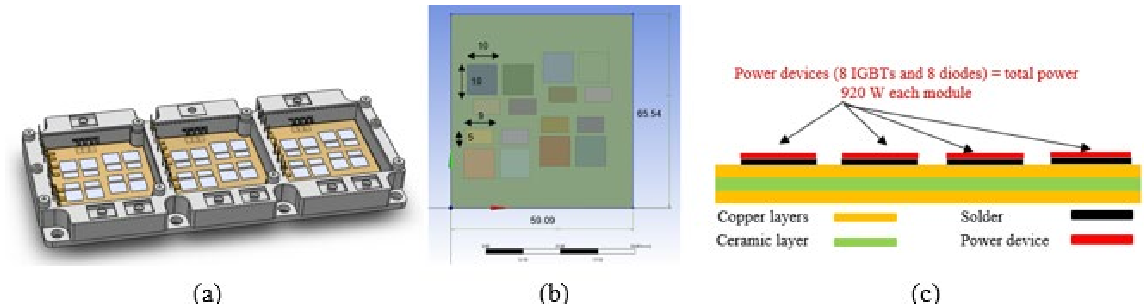

Figure I.1.23.3 The CAD drawing of BMW i3 power module. (b) The simulation domain (top view) of the power module (c) The side view of the power module.

A coupled thermal-mechanical co-optimization approach is adopted to identify the optimal configuration of the sub-module. The design parameters with constraints, material properties and boundary conditions are tabulated in Table I.1.23.1.

Table I.1.23.1 Design Parameters for the Modeling (II) Material Properties of the Components for the Thermal Analysis (III) Boundary Conditions for Thermal-Mechanical Simulations

Table I Design Parameters

ID	Design Parameters	Initial value	Lower bound	Upper bound
P1	DBC length	59.09	59	75
P2	DBC width	65.54	65	80
P3	Top copper layer thickness	0.3	0.3	1.0
P4	Bottom copper thickness	0.3	0.3	1.0
P5	Ceramic layer thickness	0.3	0.3	1.0
P6	Igbt bottom - left	9.87	8	12
P7	Igbt top - left	18.65	16	20
P8	Igbt bottom - right	13.92	12	16
P9	Igbt top - right	14.60	12	16
P10	Igbt pitch	2.0	2.0	5.0
P11	Diode pitch	3.0	3.0	6.0
Output Parameter				
P12	Maximum junction temperature and Thermomechanical stress	*All the dimensions are in mm*		

Table II Material Properties

Material Property	Copper	Ceramic	Silicon	Solder
Density (kg/m³)	8,960	3,780	2,330	7,350
Thermal Conductivity (W/m-K)	390	25	124	250
Specific Heat (J/kg. K)	385	880	750	230

Table III Boundary Conditions

Boundary Conditions	Values
Total power input	920 W
Volumetric heat generation	Igbt (each) – 1.0e+10 W/m³, diode (each) – 3.3e+9 W/m³
Coolant temperature	80 °C
Film coefficient at the back side of copper layer	10,000 W/m²-K

For the microchannel flow boiling modeling, CFD/HT analyses using a three-dimensional (3D) volume of fluid (VOF) model coupled with a phase-change model for the interfacial heat and mass transfer were performed for multiple microchannel configurations (constricted inlet, expanding, and auxiliary jetting microchannels). A benchmark case of a rectangular microchannel was examined to quantify baseline thermohydraulic performance. Results demonstrated slight to significant thermal performance improvements for all cases, and significant pressure benefits for the expanding and jetting cases, consistent with experimental results in literature. Bubble dynamics and visualization for the baseline and alternative configurations are provided to give insight into their underlying physics, and the differences in performance were investigated and compared with available literature.

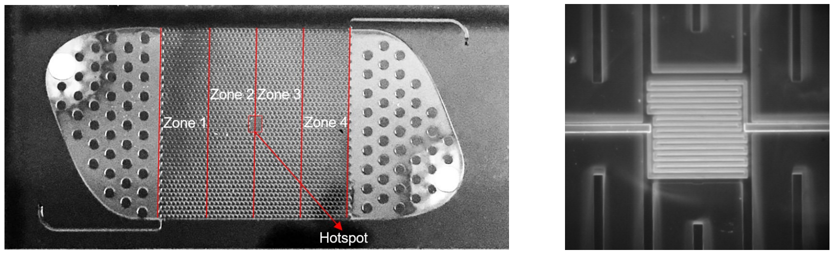

Figure I.1.23.4 Embedded cooling test vehicle with pin fins (left) and hotspot heater (right) shown

A silicon test device with pin fins etched into the substrate on one side and platinum heaters deposited onto the other was fabricated for dissipating high heat fluxes using embedded cooling in power devices. The dielectric HFE 7200 was used to test the silicon devices in a closed flow loop with single phase flows. Sufficient sub-cooling was used to not see boiling flows despite the relatively low boiling point of 78°C at atmospheric pressure.

Electric motor thermal management

An end-winding channel cooling system for the Nissan Leaf was proposed and fabricated. Sealing was done with temperature-cured silicone sealant for the end-windings, after which a 3D printed channel system was designed and printed. The end-winding cooling was used in conjunction with the motor's water jacket. CFD models calculated the heat transfer coefficient inside the end-winding cooling solution at several inlet velocities. An equivalent resistance network for the end-winding cooling solution was developed using experimental data for model calibration. This allowed for a validated LPTN model with calculated channel resistances, including potting material thickness and contact resistance effects.

Results

Bonded interfaces

Following a series of experiments, the Al coupons were successfully bonded to AlSiC plates using the Cu-Al TLP technique. To assess the composition and quality of the bond layer, the samples were cross-sectioned using wire electrical discharge machining (EDM) and polished to 0.05um using Silicon Carbide grit discs and Aluminum Oxide solution. Scanning Electron Microscope (SEM) imaging and Energy-dispersive X-ray spectroscopy (EDX) were conducted on cross-sectioned samples to examine the interface and microstructure of the resulting bond (Figure I.1.23.5).

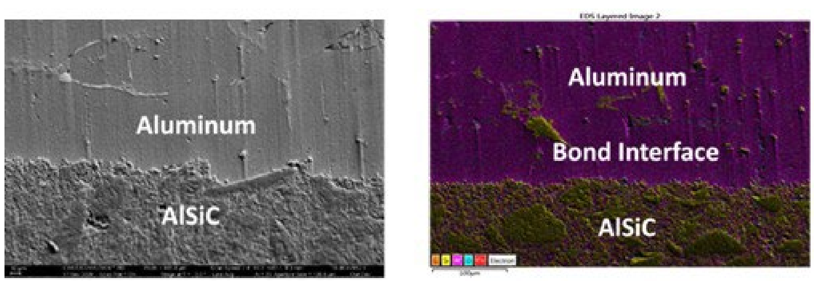

Figure I.1.23.5 SEM and EDS image results

C-SAM imaging revealed the Al-AlSiC bond interface to have low void composition which is corroborated by the SEM image of the cross-sectioned sample showing no bond line defects. The Al-AlSiC assembly stack differs from the AlN-AlSiC samples in that the later has an observable bond layer with a thickness of about 100 um on average. In the case of Al-AlSiC, the bond is marked by a distinct interface between the Al metal and the AlSiC matrix. This signifies that the Cu in the bond from the 25-um foil completely diffuses through the Al metal and into the Al-356 in the AlSiC coupon, bonding the two without forming a significant intermetallic phase. This conclusion is corroborated by the EDS line graph below.

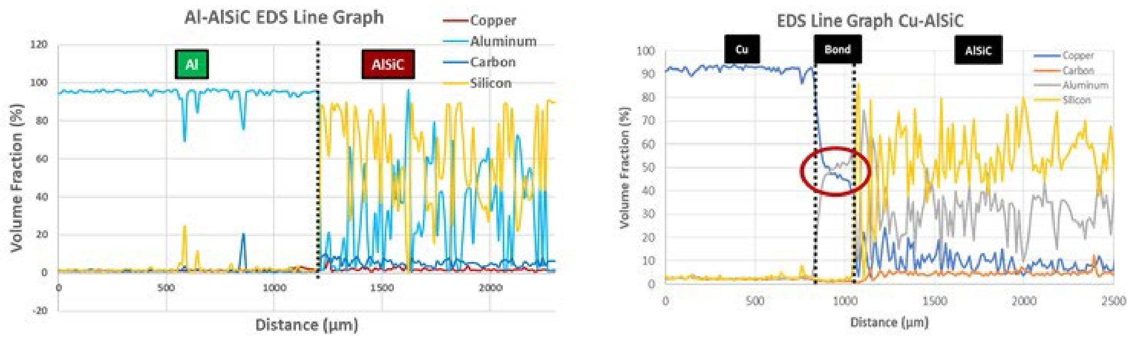

Figure I.1.23.6 EDS line graph through Al-AlSiC bond and Cu-AlSiC bond which shows near 50:50 Cu:Al ratio

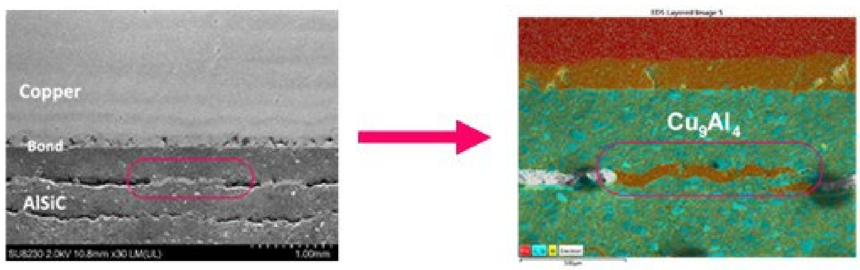

Figure I.1.23.7 Sub layer cracks in Cu-AlSiC sample identified as Cu9Al4 via XRD and EDS

Thermal Management of Electric Vehicle (EV) power inverters

The results of the thermo-mechanical simulations are shown in Figure I.1.23.8. The maximum junction temperature for the steady-state condition is found to be 144.43°C on the IGBT areas with an HTC of 10 kW/m^2-K. The convective boundary condition is applied on the back side of the copper surface with a coolant temperature of 80°C. The effect of coolant can be seen at the edge of the DBC layers. The maximum stress is found to be 229 MPa at the edges of the power devices on the top layer of the copper layer as shown in Figure I.1.23.8(b) that can be related to the high thermal stress. Due to thermal spreading between the layers, the stress in the other two layers is low. The Von-Mises stress is further reduced in the ceramic layer. This is due to the fact that the ceramic has different material property that provides more spreading and stability to the structure.

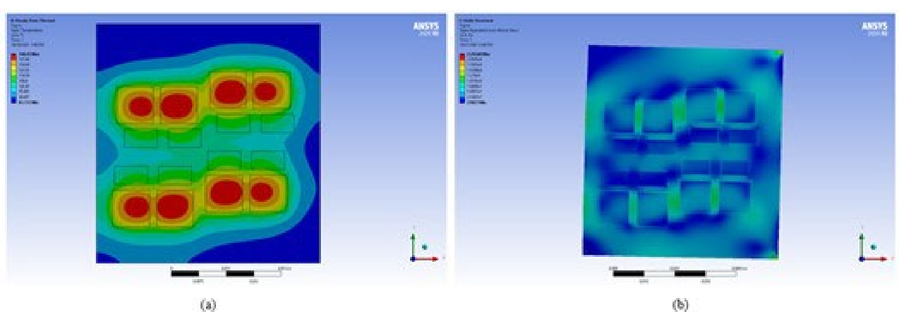

Figure I.1.23.8 (a) Temperature (°C) contours on the top copper layer (b) Von-Mises stress (in Pa) distribution on the top copper layer

The objective functions for the thermo-mechanical co-optimization are the junction temperature and Von-Mises stress. The simulations are performed for three combinations of reduced-order models. Multi-objective genetic algorithm is used to find the Pareto optimal solutions. The average root-mean-square error (in %) are 8.62, 10.82 and 9.23 for the Box-Behnken + Second Order Polynomial, Box-Behnken + Kriging, and LHC + Second Order Polynomial, respectively. Using the optimized parameters, the final junction temperature is found to be 121.5°C, which is reduced by 15.7 % with respect to the initial design. Consequently, the thermal stress values for the top copper layer, ceramic layer and bottom copper layer are reduced by 6.9%, 74.9%, and 79.5%, respectively. The surface area is increased by 15%. The optimized copper layer thickness for the top copper layer and the bottom copper layer is 1.0 mm. The top copper layer thickness is increased by 233.3%, which has benefits in improving the thermal-mechanical performance of the power module. Similarly, the optimized ceramic layer thickness is found to be 0.3 mm. The footprint values are also optimized, and the percentage change are also observed in this study.

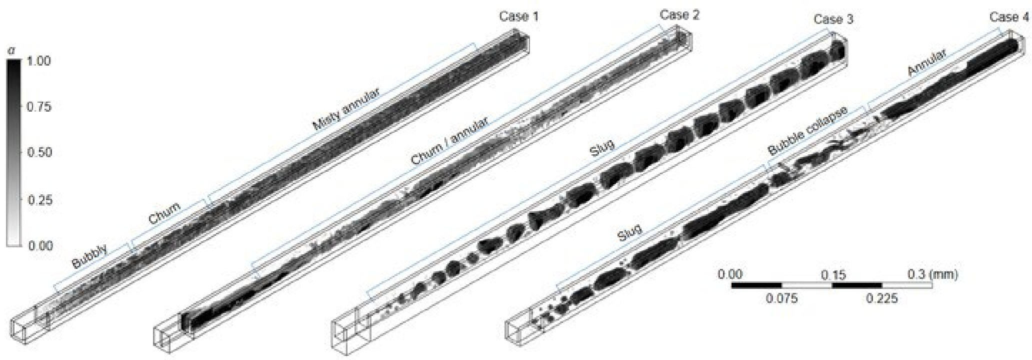

Figure I.1.23.9 Volume renderings of void fractions for (a) baseline rectangular (b) constricted inlet (c) diverging (d) auxiliary jetting microchannels

Four different microchannel geometries were simulated with the volume of fluid method for interface generation and the Lee model for energy and mass transfer resulting from phase transfer. Comparison with the flow regime maps of Harirchian and Garimella showed good agreement for all of the cases. Additionally, their performance can be seen in Table I.1.23.2. A journal paper discussing further results for bubble visualization and the mechanics behind performance differences was published in *Physics of Fluids* (included in Key Publications).

Table I.1.23.2 Values of h_{tp} and ΔP for each Microchannel Case

Case	h_{tp} (kW·m^{-2}·K^{-1})	ΔP (kPa)
1	49.5	19.3
2	51.1	25.3
3	61.5	8.21
4	54.8	14.9

Using a silicon microgap cooler enhanced with pin fins for embedded cooling of power electronics devices showed the ability to dissipate in excess of 1 kW/cm^2. Below the test device schematic is shown, with the hotspot heater highlighted. HFE 7200 was used with a flow rate of 150 mL/min inlet temperature of 10°C, corresponding to subcooling of 68°C to enforce single-phase flow. The right of the same figure shows the change in temperature with increasing hotspot heat fluxes.

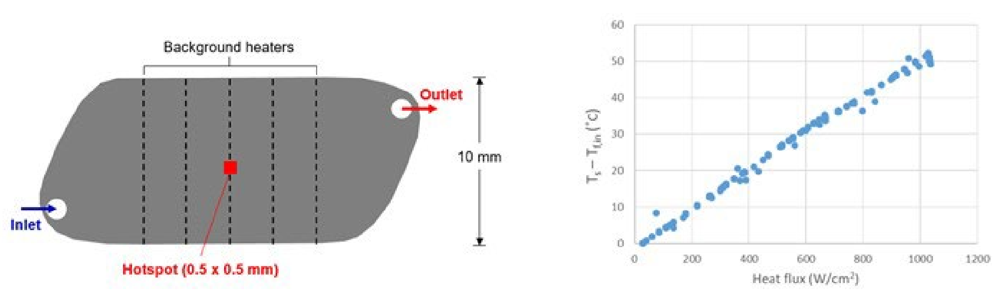

Figure I.1.23.10 Silicon microgap test vehicle schematic with heaters shown (left) and heater ΔT (right) at constant flow rate

Electric Motor Thermal Management

Figure I.1.23.11 shows a CAD cross-sectional view of the final assembly of the Nissan Leaf motor with end-winding channel cooling. The right shows the results with water jacket cooling (in gray) versus water jacket cooling augmented with end-winding cooling. When the end-winding cooling is not used, the difference between different end-winding location temperatures is small. When the end-winding cooling is used, the internal temperatures are the highest as expected.

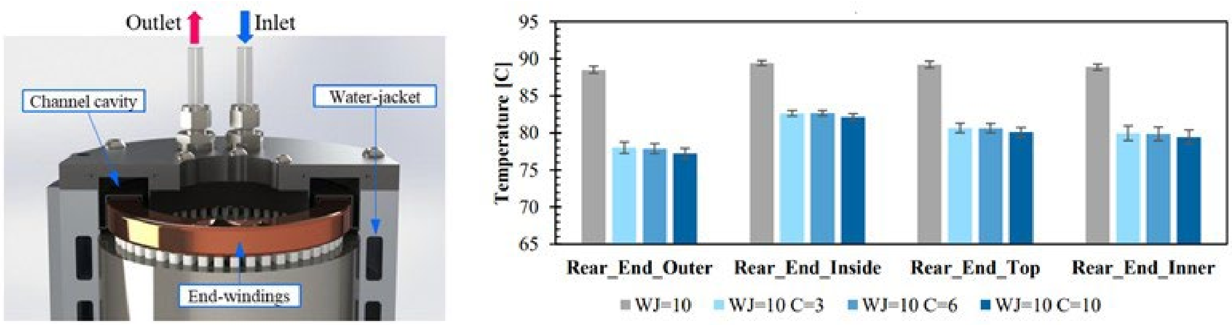

Figure I.1.23.11 Cross-sectional view of the final assembly of the end-winding channel and the Nissan Leaf motor (left) Mean end-winding temperature on the outer, inside, top and inner surfaces with water jacket flow rate 10 L/min and end-winding flow rate C

CFD simulations were used to calculate the heat transfer coefficient from the end-winding cooling channel. After finding this value, the remaining resistances (from contact resistances and potting) were calibrated using an optimization script in Python with the Sequential Least Square Quadratic Programming optimization algorithm. The calibrated lumped parameter thermal network (LPTN) gave a maximum temperature difference of 1.06°C with the experimental results. The end-winding LPTN can be seen in Figure I.1.23.12.

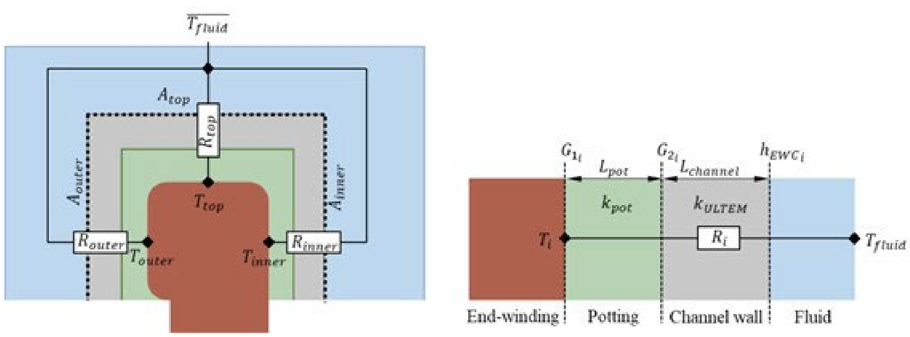

Figure I.1.23.12 End-winding thermal resistance network with zoomed in view

Conclusions

- Comparing XRD results of AlN-, Cu- and Al-AlSiC with C-SAM, EDS and SEM images, it was observed that bonded samples with higher intermetallic compound content such as in Cu-AlSiC exhibited higher rates of defects upon cooling. The IMC interface boundary increases resistance to plastic deformation—leading to increased hardness and brittle cracks. Maintaining initial Cu-Al volume ratio of 1:5 facilitated development of high-quality bonds with low void concentration.

- A methodology for compact modeling co-design optimization framework is developed for improving the thermal-mechanical performance of EV power modules. FEA simulations for thermal and structural analysis are performed in Workbench. DOE techniques are implemented to create a design space, which was used to create the response surface. The main conclusion drawn from the co-optimization analysis is that layer thicknesses have the most significant role in bettering thermal-mechanical performance.

- Embedded cooling was shown as a viable solution to the high heat fluxes that can be seen in wide bandgap power devices. A silicon test vehicle, which could be integrated at the bottom side into the die attach, showed power dissipation capabilities exceeding 1 kW/cm2 with single phase highly subcooled dielectric HFE 7200 while maintaining temperatures lower than 90°C.
- Dedicated end-winding cooling of the Nissan Leaf was shown to improve the end-winding temperatures by up to nominally 15°C. The LPTN network was also calibrated and compared against experimental measurements, which showed a maximum error of ~1°C.

Key Publications

1. Broughton, J. and Y. K. Joshi (2021). "Flow boiling in geometrically modified microchannels." Physics of Fluids **33**(10): 103308.
2. S. Sequeira, K. Bennion, J. E. Cousineau, S. Narumanchi, G. Moreno, S. Kumar, Y. Joshi (2021) "Validation and Parametric Investigations of an Internal Permanent Magnet Motor Using a Lumped Parameter Thermal Model." ASME J. Electronic Packaging (accepted for publication)

References

1. Harirchian, Garimella. 2010. "A comprehensive flow regime map for microchannel flow boiling with quantitative transition criteria." International Journal of Heat and Mass Transfer 2694–2702.
2. Pahinkar, D. G., W. Puckett, S. Graham, L. Boteler, D. Ibitayo, S. Narumanchi, P. Paret, D. DeVoto and J. Majo. 2018. "Transient Liquid Phase Bonding of AlN to AlSiC for Durable Power Electronic Packages." Advanced Engineering Materials 9.

Acknowledgements

The principal investigators would like to thank Gilbert Moreno, Paul Paret, Kevin Bennion, Emily Cousineau, and Sreekant Narumanchi from NREL for their help and contribution to this project. We would like to acknowledge our collaborators at NREL for conducting C-SAM imaging and providing thin Al coupons, as well as the Georgia Tech Machine shop for their help in cutting AlSiC plates using electrical discharge machining.

I.1.24 Heterogeneous Integration Technologies for High-temperature, High-density, Low-profile Power Modules of Wide Bandgap Devices in Electric Drive Applications (Virginia Tech)

Guo-Quan Lu, Principal Investigator
Virginia Tech
Department of MSE and ECE - 0111
Blacksburg, VA 24060
Email: gqlu@vt.edu

Rolando Burgos, Co-Principal Investigator
Virginia Tech
Department of ECE, CPES - 0179
Blacksburg, VA 24060
Email: rolando@vt.edu

Khai D.T. Ngo, Co-Principal Investigator
Virginia Tech
Department of ECE, CPES - 0179
Blacksburg, VA 24060
Email: kdtn@vt.edu

Susan Rogers, DOE Technology Development Manager
U.S. Department of Energy
Email: susan.rogers@ee.doe.gov

Start Date: October 1, 2020 End Date: September 30, 2021
Project Funding: $300,000 DOE share: $300,000 Non-DOE share: $0

Project Introduction

The goal of this project is to develop packaging technologies for making high-temperature, high-density, and low-profile wide-bandgap (WBG) power electronics modules. These modules are aimed at enabling the DOE VTO Electrification Technologies' University Consortium to reach its 2025 targets (listed below) for the cost, power density, and system peak power rating of automotive electric drive systems.

Table I.1.24.1 Power Electronics Requirements

Parameters	Measure
Cost ($/Kw)	≤ 2.7
Power Density (kW/L)	≥ 100
System Peak Power Rating (kW)	100

The objectives of this project are to:

- Develop a low-cost sintered-silver interconnect technology for packaging power modules and gate drivers capable of working over 200°C.
- Develop designs and fabrication processes of double-side cooled power modules with parasitic inductances < 5 nH, heat flux density > 400 W/cm^2, and working junction temperature > 200°C; and

- Design and prototype intelligent gate drivers with integrated current sensors and protection for the 200°C module.

A schematic of the hardware to be developed in this project is shown below in Figure I.1.24.1. Planar, double-side cooled phase-leg modules capable of working at 200°C ambient will be designed and fabricated. Multiple phase-leg modules will be assembled on cooling plates (with or without double-side cooling) and interfaced to a bus bar and gate-driver boards. The gate driver boards will have integrated current sensors, power supplies, and other components that are capable of working at 200°C ambient.

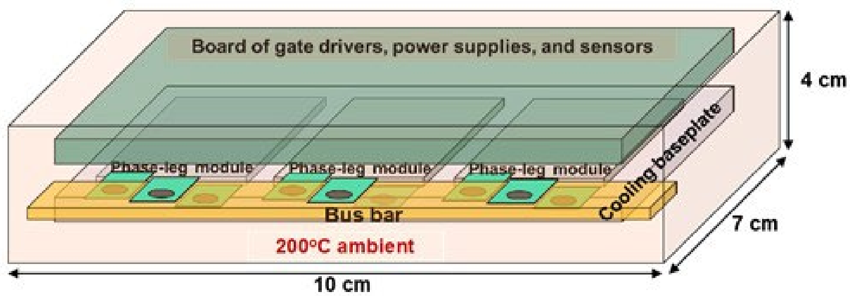

Figure I.1.24.1 Schematic of the hardware to be developed in this project.

For this reporting period, we focused on achieving the following specific objectives:

- SiC phase-leg module layout design and fabrication process development.
- Fabrication, test, and analysis of double-side cooled SiC phase-leg modules for delivery to ORNL.
- Design and test of a gate-driver board for delivery to ORNL.
- Delivery to ORNL an inverter subassembly consisting of six phase-leg SiC power modules and a gate-driver board.
- Design, analysis, and test of a current sensor with dynamic feedback compensation to mitigate the impact of the temperature on the output of the current sensor.
- Characterization of the efficiency of a single-output class-e power supply and analysis of the loss breakdown.
- Design and test of air-core transformer winding structures for a gate power supply with six secondary windings.

Approach

In the second year of this project, we designed two layouts of a double-side cooled SiC phase-leg module and conducted electrical and thermal simulations to analyze the package parasitic inductances and thermal resistances. In this year, we selected one of the two layouts, the one with better thermal performance and lower parasitic inductances, for fabrication and delivery to ORNL for assembling an inverter. The inverter requires six phase-leg modules of each rated at 1200 V and 100 A (RMS). Anticipating the yield issue, fabrication schedule was planned for making at least twelve modules.

As the phase-leg modules require gate-driving circuits for testing and for operation in the inverter, an effort was devoted to the design and fabrication of a gate-driver board for all six phase-leg modules. Since the goal for building the inverter is to demonstrate the integration of all the component technologies for achieving DOE's power density target, the required maximum junction temperature for the first batch of modules is less than 150°C. Consequently, the maximum operating temperature of all the driver components was selected to be below $125^{o}C$. A protection method based on the parasitic inductance of the power module was also incorporated in the design to protect the power modules from the short-circuit event. Double-pulse test (DPT) and continuous tests under 800V DC-bus voltage were developed to evaluate the gate driver. In the continued effort for current sensor development, a feedback loop of the current sensor circuit was modified such that a correction factor is continuously updated to mitigate the temperature effect. The performance of the updated current sensor was compared to that of the sensor with fixed compensation under different operating temperatures of the power module.

In the continued effort for high-temperature gate driver development, the efficiency of last year's single output class-e gate power supply was characterized. A key feature of the power supply is the use of an air-core transformer to avoid finding a high-temperature magnetic core with low core loss. From analyses of the converter efficiency and loss breakdown, the transformer loss takes most of the total loss. To minimize the transformer loss, effort was focused on improving its winding configuration. Designs consisting of multiple primary and multiple secondary windings were analyzed and compared with the aim of minimizing the size and/or maximizing the efficiency of the transformer.

Results

1. Phase-Leg Module Layout Selection and Fabrication Process Development

Last year we reported the electrical and thermal analyses of two phase-leg layouts shown in Figure I.1.24.2. We selected Layout #2 for fabrication because of its improved thermal performance and lower parasitic inductance. A thermistor was added in the module for temperature measurement. Figure I.1.24.3 shows the key processing steps developed for fabrication. The SiC device chips are Cree's 3rd generation SiC MOSFET rated at 1200 V, 149 A, and 13 mΩ. One SiC MOSFET is placed on the bottom substrate and the other on the top substrate. So, the top and bottom pieces were processed separately as shown in Figure I.1.24.3 (a)-(g). The die-attach as shown in Figure I.1.24.3 (c) was achieved by pressure-assisted silver-sintering of a silver preform (nanoTach-Pf from NBE Tech) to DBC substrate at 250°C for 30 minutes and under 3 MPa. Two silver posts were then attached to the dice's silver coated surface by pressure-less sintering of a silver paste at 245°C for 15 minutes. The thermistor was soldered on the substrate shown in Figure I.1.24.3 (d). The gate pad and Kelvin source were connected to the DBC substrate by wire bonding with 10-mil Aluminum wires, shown in Figure I.1.24.3 (e). Afterward, silicone rubber (Nusil 2188) was used to encapsulate the device area for protection in the subsequent fabrication step in Figure I.1.24.3 (f). In Figure I.1.24.3 (g), the copper terminals and pins for gate and Kelvin source connection were soldered on the DBC substrates. After that, the two half-pieces were joined by sintering of a silver paste at 245°C for 15 min under 2 MPa as shown in Figure I.1.24.3 (h). Lastly, the gap between the two DBC substrates was filled by an underfill material (ME-531 epoxy from LORD). Figure I.1.24.3 (j) shows the fabricated phase-leg module measured at 3 cm × 2 cm × 0.4 cm.

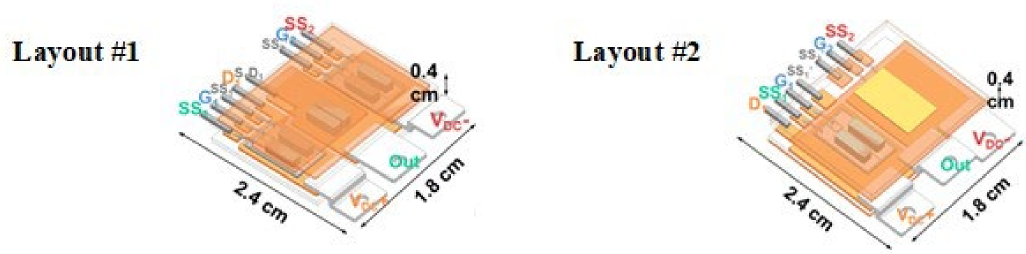

Figure I.1.24.2 Two layout designs of a double-side cooled phase-leg SiC module.

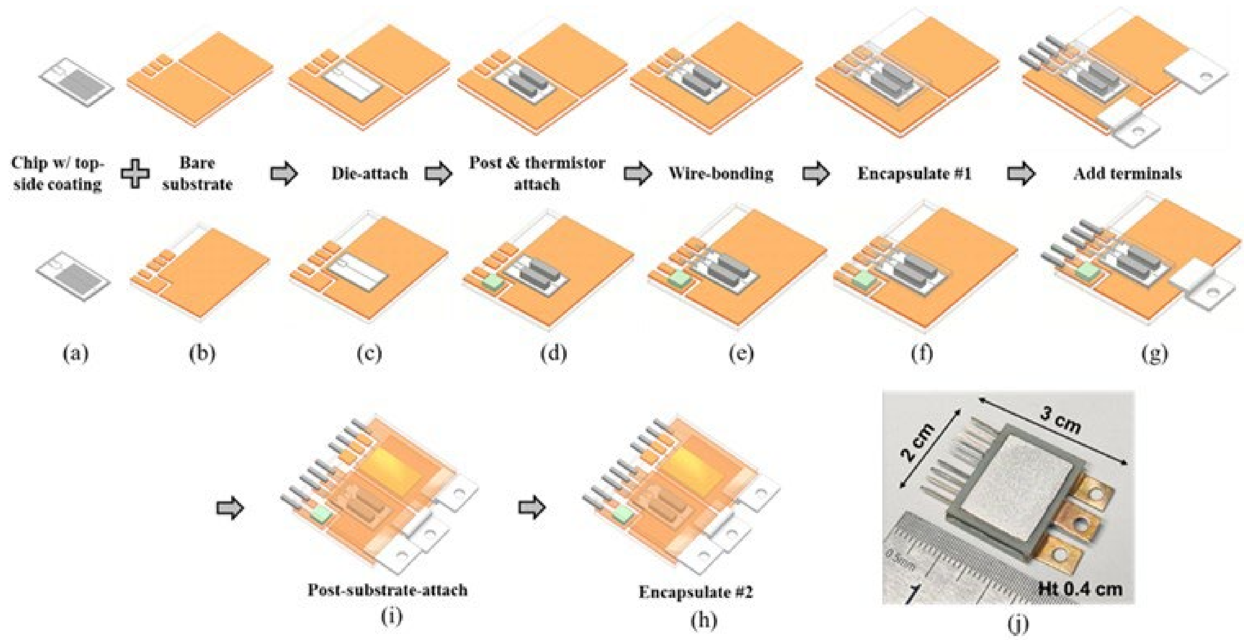

Figure I.1.24.3 Fabrication steps for making the phase-leg SiC modules.

2. Electrical Testing of the Fabricated SiC Phase-Leg Modules

A total of fourteen SiC phase-leg modules were fabricated. Six of the twelve were assembled with the gate-driver board for delivery to ORNL. Before shipping, the six modules were tested on a curve tracer. Table I.1.24.2 lists the measured static characteristics of each of the SiC MOSFETs in the six modules. They all showed acceptable R_{on} and leakage current at 1200 V.

Table I.1.24.2 Static Test Results of the Six SiC Phase-leg Modules

		Drain-to-source on-resistance (R_{on}/mΩ) @ V_{GS} = 15 V, I_D = 20 A		Drain-to-source leakage current (I_D/μA) @ V_{GS} = - 4 V, V_{DS} = 1200 V	
		13 (bare die - typical)	17 (bare die - max)	1 (bare die - typ)	40 (bare die - max)
# 1	upper	13.1		0.17	
	lower	12.9		0.34	
# 2	upper	12.8		0.17	
	lower	13.7		0.24	
# 3	upper	15.9		0.22	
	lower	15.2		0.17	
# 4	upper	16.1		0.20	
	lower	22.1		0.35	
# 5	upper	15.5		0.67	
	lower	15.1		0.51	
# 6	upper	18.1		0.30	
	lower	14.1		0.34	

3. inverter Subassembly Delivered to ORNL

Figure I.1.24.4 is the completed subassembly delivered to ORNL. It consists of six SiC phase-leg modules connected to a gate-driver board custom-designed and built for ORNL's segmented inverter. Alignment of the modules to the board was achieved using a 3D printed fixture supplied by ORNL. It helped aligning the six modules to the input/output terminals on the driver board. The control pins of the modules were soldered to the driver board using a lead-tin solder.

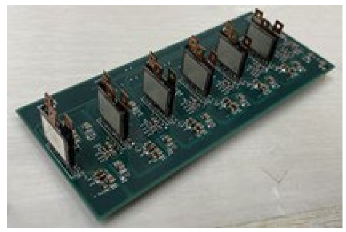

Figure I.1.24.4 The delivered inverter subassembly with six SiC phase-leg modules mounted on a gate-driver board.

4. Gate-Driver Board for the Six SiC Phase-Leg Modules

Figure I.1.24.5 is a close-up picture of the gate-driver board with the dimensions. After the board passed the funtionality test, it was used to test the switching performance of the SiC phase-leg power modules. Figure I.1.24.6 (a) shows the double-pulse test results on the switching waveforms of the current and voltage of the lower device in a power module. It is seen that the ringing in the switching voltage is only around 10% of the DC-bus voltage. The ringing on the switching current is also small. The zoom-in waveforms of the switching transients shown in Figure I.1.24.6 (b) and Figure I.1.24.6 (c) were used to estimate the turn-on and turn-off switching loss, respectively. A turn-on loss of 4.3 mJ and turn-off loss of 3.25 mJ were obtained by applying the average function in the oscilloscope to the switching loss waveform during the corresponding transients.

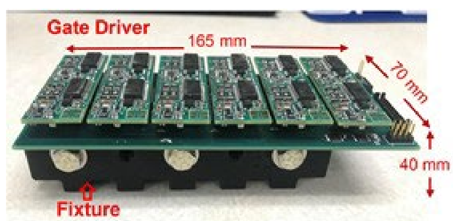

Figure I.1.24.5 Close-up view of the gate-driver board built for the six SiC phase-leg modules.

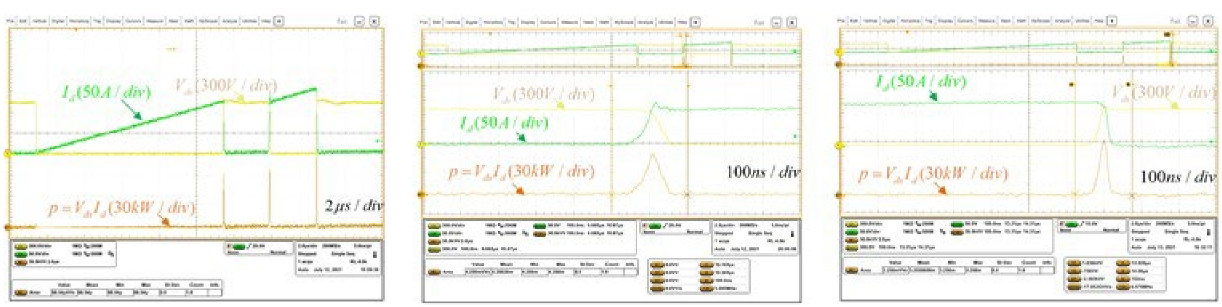

(a) Switching current, switching voltage, and switching loss

(b) turn-on loss measurement (4.3mJ)

(c) turn-off loss measurement (3.25 mJ)

Figure I.1.24.6 (a) Switching waveforms from a DPT test under 800 VDC; (b) zoom-in waveform of the turn-on transient for estimating the turn-on loss; and (c) zoom-in waveform of the turn-off transient for estimating the turn-off loss.

5. Current Sensor with Temperature Compensation

Figure I.1.24.7 (a) shows an implementaiton scheme for the current sensor based on package parasitic inductance. It features a dynamic feedback for temperature compensation. The current sensor was evaluated by the DPT test on a commercial power module in an experiment setup shown in Figure I.1.24.7 (b). The power module was heated on a hot plate, and the performance of the current sensor was compared to that with a fixed feedback under the same conditions.

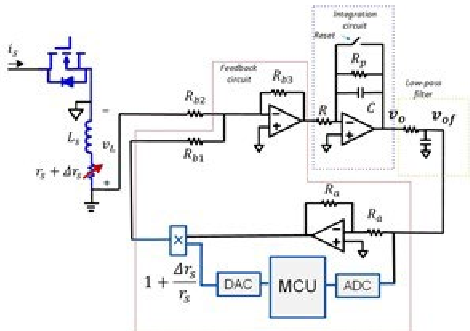

(a) Proposed current sensor scheme

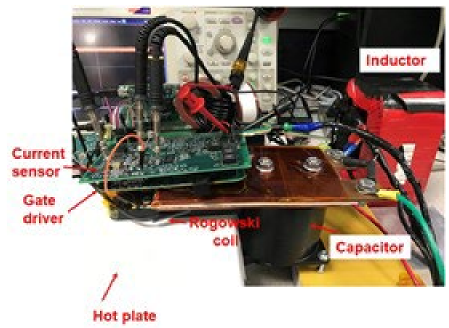

(b) Experiment setup of the DPT test

Figure I.1.24.7 Proposed current sensor scheme and the experimental setup to verify its performance

Shown in Figure I.1.24.8 (a) – (c) are the experimental waveforms of the switching current measured by the current sensor with dyanmic feedback, the sensor with fixed feedback, and a Rogowski coil. At room temperature, the current sensor with fixed feedback parameters designed for $150^{o}C$, recorded current with 11% deviation from the current recorded by the Rogowski coil, as shown in Figure I.1.24.8(a). By implementing the dynamic compensation, as shown in Figure I.1.24.8(b), the deviation was significantly reduced by the updates in the correction factor values. It is seen that, after two updates, the switching current with the dynamic-feedbacked current sensor is nearly the same as by the Rogowski coil. The magnified area in Figure I.1.24.8(c) shows a good response of the current sensor during both transient and conduction time intervals.

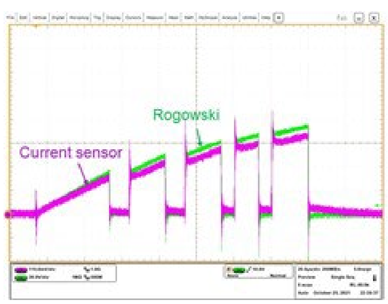

(a) Fixed compensation (designed for 150°C)

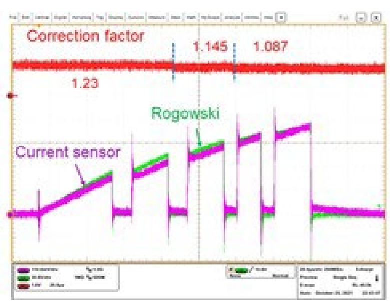

(b) Dynamic compensation

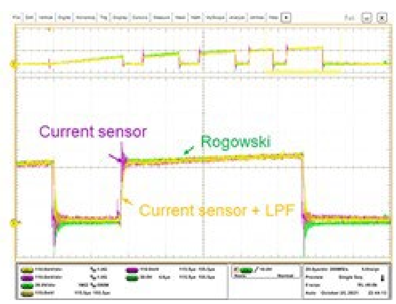

(c) Zoom-in area of Figure4(b)

Figure I.1.24.8 Waveforms of design current sensor compared to Rogowski coil under room temperature

6. Improved Design of the Air-Core Transformer with PCB Winding

6.1 Characterization of the Single-Output Class-E Gate Power Supply

A single-output class-e dc-dc converter was fabricated last year, and preliminary testing results were obtained. A loss analysis was conducted. Figure I.1.24.9 shows the converter hardware. Figure I.1.24.10 shows the efficiency curve and loss breakdown of the converter.

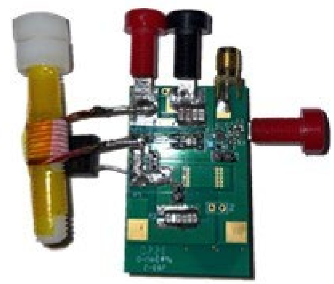

Figure I.1.24.9 The hardware of the single-output class-e gate power supply.

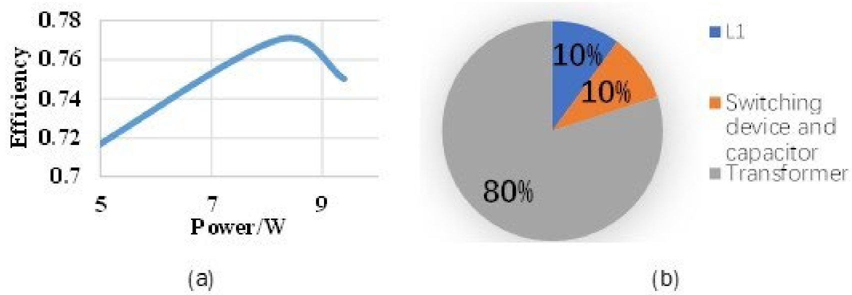

Figure I.1.24.10 (a) Efficiency curve of the power supply, and (b) loss breakdown of the power supply.

6.2 Impact of Air-Core Transformer Geometric Parameters

The goal for designing the air-core transformer is to maximize the quality factor (Q). Figure I.1.24.12 shows the geometric parameters of the transformer, including outer radius, inner radius, winding width, winding thickness, and spacing. The hardware in Figure I.1.24.9 used only 1 oz. copper. If 2 oz. copper is used, Q can be increased by 20%. Figure I.1.24.11 shows Q variation with the radius ratio. The outer radius was kept at 5 mm. Maximum Q is reached at the radius ratio between 0.55 and 0.65.

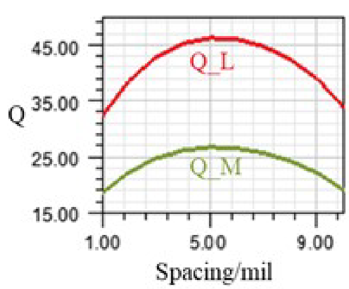

Figure I.1.24.11 Q variation with spacing.

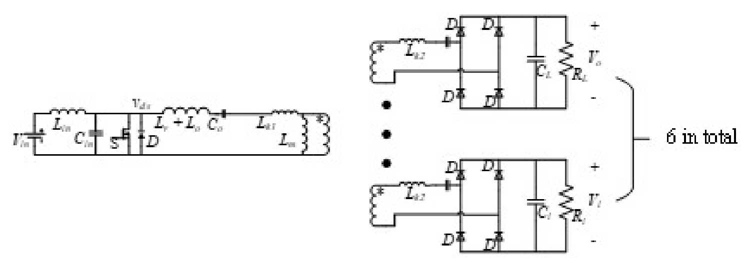

Figure I.1.24.12 Schematics of the class-e power supply with multiple secondary windings.

Figure I.1.24.11 shows Q variation with the spacing at a fixed radius ratio of 0.55. The winding width changes with the spacing accordingly. The maximum Q reaches 46 at 5 mil spacing. If the spacing has to be higher than 6 mil due to manufacturer's requirements, Q can still be 45.

Table I.1.24.3 summarizes an alternative design of the transformer parameters compared with the one in Figure I.1.24.9. The Q value of the new transformer is 85% higher than that in the earlier design.

Table I.1.24.3 Parameters of the original and improved transformer

	Inner radius ratio	Copper Thickness	Trace width	L, M	ESR	Q_L, Q_M
Original	0.2	1 oz.	12 mil	564 nH, 334 nH	0.97 Ω	24.8, 14.7
Improved	0.55	2 oz.	8 mil	676 nH, 392 nH	0.62 Ω	46, 27

6.3 Design of the Air-Core Transformer with Multiple Secondary windings

Since a typical electric drive system is a three-phase inverter consisting of six switching cells, the driver board has to have six isolated outputs at the same output voltage. One solution is to use six power supplies, each with a single output. This requires a large footprint and six times the number of components. A better solution would be a single power supply with six isolated outputs by using an air-core transformer made of one primary winding and six secondary windings. Figure I.1.24.12 is a schematic of this approach. Proceeding with this approach, two configurations for the primary winding were compared. Figure I.1.24.13 shows the lay-up scheme of the proposed transformer structure. Figure I.1.24.14 shows the transformer structures with the different primary winding configurations. Two transformers were designed with 300-nH mutual inductance. The split-winding structure achieved 45% less winding loss and a 70% reduction of the voltage stress on the primary windings.

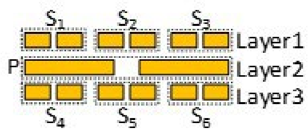

Figure I.1.24.13 Lay-up of the proposed transformer structure.

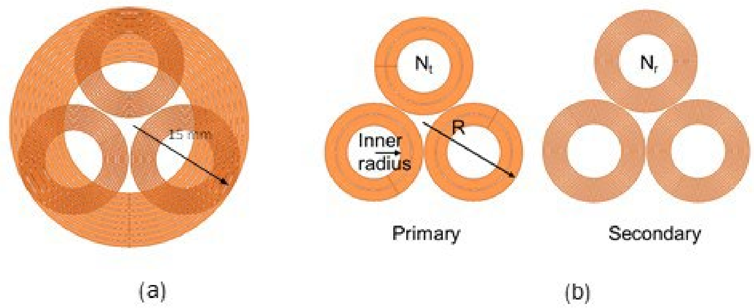

Figure I.1.24.14 Two primary winding configurations. (a) Single primary winding with large size. (b) Three small primary windings in series. Structure (b) achieved 45% less winding loss and a 70% reduction of the voltage stress on the primary windings.

6.4 Sweeping the Transformer Parameters for Minimum Loss

The transformer design in Figure I.1.24.14(b) was further improved by applying two-layer windings for the primary and secondary. The double-layer winding structure enables wider windings for the secondary at a 10% loss reduction. A smaller transformer size can be used under the minimum trace-width requirement from the manufacture. Transformer size was then swept to study the loss variation. Figure I.1.24.15 shows the loss and heat flux variation with different transformer outer radius. For each transformer size, parameters in Figure I.1.24.14(b) were swept to get the minimum loss. The isolation capacitance decreases by 32% from 15 mm to 12 mm but at a 25% loss increase.

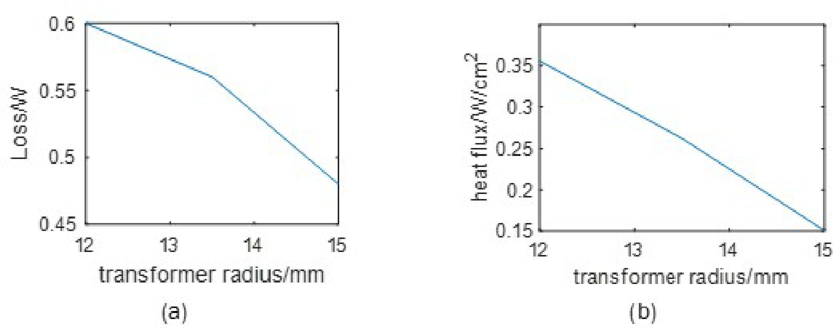

Figure I.1.24.15 Loss and heat flux variation with transformer size. (a) Loss variation. (b) heat flux variation.

Summary

A module packaging process was developed for fabricating planar, double-side cooled SiC phase-leg modules. Fourteen modules were produced. A gate-driver board was designed and fabricated for driving six modules required in a segmented inverter. Six of the fourteen modules were connected to the gate-driver board and characterized by double-pulse test and continuous test under 800 VDC. All of modules had acceptable R_{on} and low leakage current at 1200 V. The switching waveforms had small overshoots, and the switching losses were low. The subasembly was delivered to ORNL for assembly into an inverter for technology demonstration.

Continued the research effort for developing current sensors based on package paratsitic inductance. Emphasis was placed on compensating the temperature effect. Experimental results on a dynamic feedback scheme showed reduced temperature effect and improved output performance. In the future, experiments on the current sensor will be extended to converters under continuous operation such as buck, full-bridge inverters. After that, the current sensor will be modified for operation at $200^{o}C$.

Air-core transformer structures with six secondary windings were designed for a single power supply with six outputs. It was found that the split-winding structure of the primary side achieved a 45% reduction in transformer loss and a 70% reduction on the primary winding voltage stress. The transformer was optimized at different sizes and the optimal results for each transformer size were studied. The isolation capacitance decreases by 32% from 15 mm to 12 mm with a 25% loss increase.

Key Publications

1. C. Ding, H. Liu, K. D. T. Ngo, R. Burgos and G. -Q. Lu, “A Double-Side Cooled SiC MOSFET Power Module With Sintered-Silver Interposers: I-Design, Simulation, Fabrication, and Performance Characterization,” *IEEE Trans. Power Electron.*, vol. 36, no. 10, pp. 11672–11680, Oct. 2021.

2. Tam K.T. Nguyen, Slavko Mocevic, Keyao Sun, and Rolando Burgos, “Switching Current Measurement Based on Power Module Parasitics”, 2021 IEEE 12th Energy Conversion Congress & Exposition – Asia (ECCE-Asia), pp.1903–1908.

Acknowledgments

We are grateful to Dr. Burak Ozpineci, Dr. Gui-Jia Su, and Dr. Emre Gurpinar of Oak Ridge National Laboratory (ORNL) for working with us to better design our SiC power modules to fit in their segmented three-phase inverter. They will also support us with the testing of our power modules in the testbed at ORNL.

I.1.25 Integration Methods for High-Density Integrated Electric Drives (University of Arkansas)

H. Alan Mantooth, Principal Investigator
Department of Electrical Engineering
University of Arkansas
1475 West Cato Springs Road, Room 211
Fayetteville, AR 72701
Email: mantooth@uark.edu

Fang Luo, Principal Investigator
Department of Electrical and Computer Engineering,
Stony Brook University (SUNY at Stony Brook),
259 Light Engineering Building, Stony Brook, NY 11794
Email: fang.luo@stonybrook.edu

Susan Rogers, DOE Technology Development Manager
U.S. Department of Energy
Email: susan.rogers@ee.doe.gov

Start Date: October 1, 2020 End Date: September 30, 2021
Project Funding (FY21): $300,000 DOE share: $300,000 Non-DOE share: $0

Project Introduction

This project focuses on two key aspects of advancing electric drive technologies: integrated circuits and power electronic packaging. As part of the team's electronics portion, this project seeks to provide technologies that enable new power density advances. The first technology effort is integrating gate driving, sensing, and protection functions into the various packaging platforms that will be pursued by the team. Several technologies are possible, but the most advanced is high-temperature SiC / SOI based integrated circuitry that can be co-packaged with the SiC power devices. The team will pursue designs that serve the target electric drive train's specifications but can survive at junction temperatures expected to enhance power density while maintaining robustness and resiliency. The second technology effort is in advancing electronic packaging for electric drive train applications. Getting the most out of the advances in wide bandgap power semiconductor devices requires attention to careful packaging to minimize parasitic electrical influences on circuit performance and generated electromagnetic interference. Thermal management of the power devices and the surrounding circuit components must also be carefully managed. This leads to tradeoffs in the layout, arrangement, and interconnection of electronic components to balance these items. This effort will be performed in collaboration with several other organizations to achieve power density improvements for electric drives.

Objectives

The objective of the project is to research, develop, and test a heterogeneously integrated power module platform that will insert into a traction inverter system for power electronics modules capable of the following:

Table I.1.25.1: Power Electronics Requirements

Power Electronics Requirements	
Parameter	**Measure**
Cost ($/kW)	≤2.7
Power Density (kW/L)	≥100
System Peak Power Rating (kW)	100

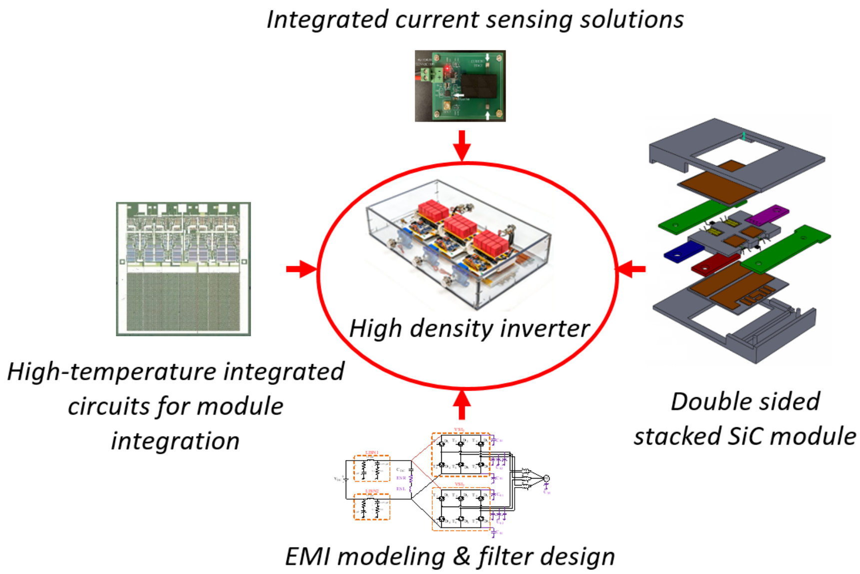

Figure I.1.25.1. Integration methods for high-density inverter.

Approach

The combined Arkansas and Stony Brook team broke down its activities across three major areas. The packaging research approach is to develop a detailed power module fabrication procedure and to fabricate the necessary parts of the power module, such as interposers, housing, and direct bond copper (DBC) substrates. Later parts come as assembly and testing of the integrated components such as gate driver and signal conditioning circuits for the sensors. The IC design group focuses on designing and testing the high-temperature integrated circuits for module integration. For the power electronic group, the focus is to come up with current measurement methods having features such as small size, high accuracy, lightweight, low cost, and easy integration. In the following section, some key results from budget period 3 are inserted.

Results

On the packaging side of the project, a stacked half-bridge power module was designed with integrated gate driver boards. The power module was validated through ANSYS^{TM} and SolidWorks simulations. The proposed power modules' fabrication procedure was planned in detail, and necessary modifications were applied to the substrates, fixtures, and housings. Different fabrication approaches were developed and tested for comparison. Then, the most preferred approaches were selected for fabricating each part of the power module. The integrated gate driver boards and the differential boards were assembled and tested to switch discrete devices in a half-bridge configuration in a double pulse test (DPT) setup at 800 V, 100 A. This verified the gate driver board's functionality. The fabrication process flow was finalized, and a dummy module and a functional power module were fabricated, as shown in Figure I.1.25.2.

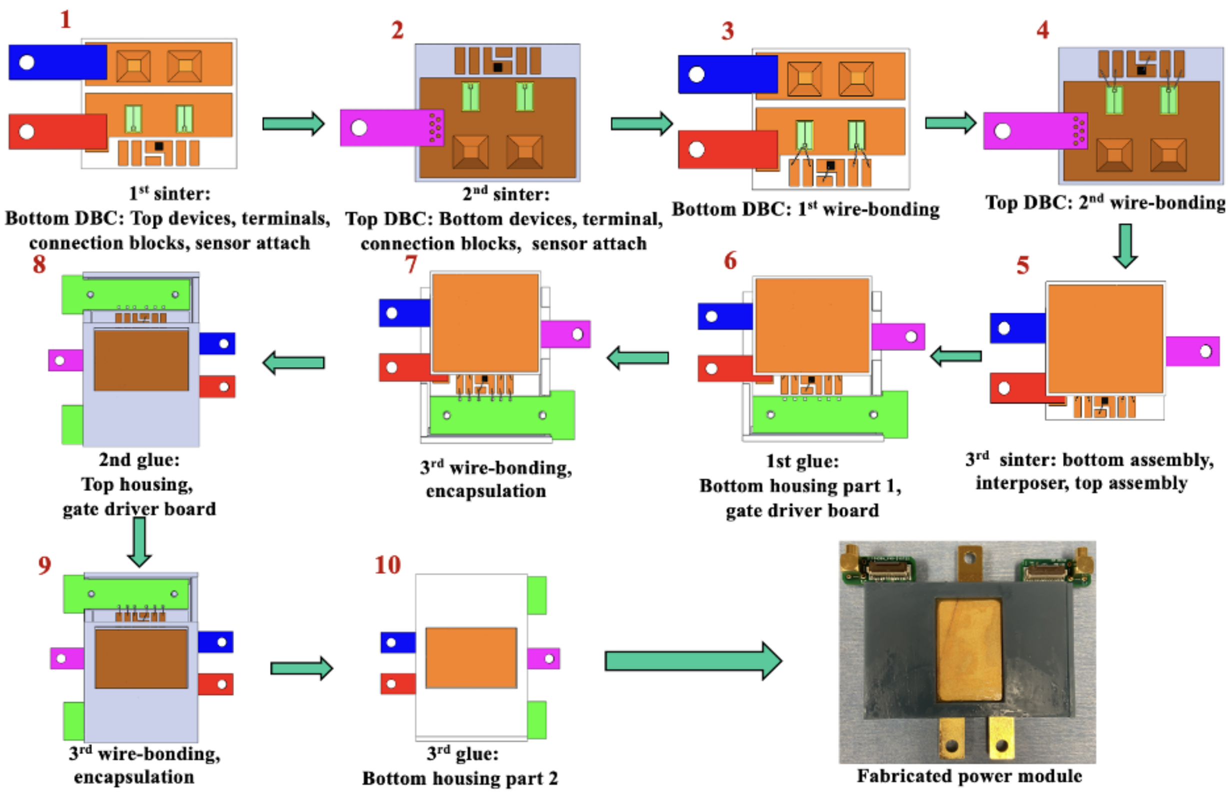

Figure I.1.25.2 Fabrication flow and fabricated power module.

A DPT printed circuit board (PCB) to test the fabricated power module was designed in Cadence's Allegro tool. The necessary voltage and current measurements were made using differential probes and Rogowski coils, as shown in Figure I.1.25.3.

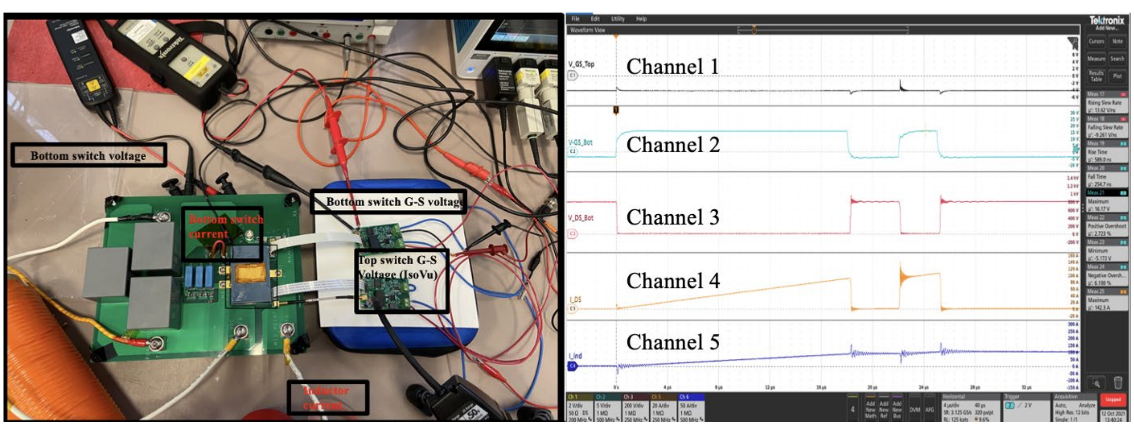

Figure I.1.25.3 DPT setup and resulting waveforms at 800 V, 108 A.

The DPT result at 800 V is also shown in Figure I.1.25.3. Channel 1 shows the -4V output of the top switch gate driver ICs, to always keep the top switch off during the DPT. Channel 2 shows the output of the gate driver ICs to switch on and off for the bottom switch. Channel 3 shows the drain-source voltage for the bottom switch, whose overshoot is only 20%. Channel 4 shows the drain-source current for the bottom switch, which has an overshoot of 27%. Channel 5 shows the inductor current. The experimental values of the turn-on and turn-off losses (considering devices switching at 30 kHz) are evaluated and shown in Table I.1.25.2.

Table I.1.25.2 Experimental Power Loss Calculation

Total turn-on loss (mJ/s))	2.4*30000
Total turn-off loss (mJ/s)	3.4*30000
Total power loss (per switch) (switching + conduction) (W)	(170+110) = 280
Total power loss (per device) (W)	140

Table I.1.25.3 gives the simulated power loss capability per device and the experimentally calculated power loss per device, which matches the simulation results closely.

Table I.1.25.3 Power Loss per Device from Simulation and Experiment

Module design	Convection co-efficient (W/m^2K)	Power dissipation capability per die (W) (Simulation)	Power dissipation per die (W) (Experiment)
Two paralleled CPM312000013A	10,000	145	140

The IC design team worked on designing the next version of high-temperature integrated circuits for module integration. The team had to transfer their designs from a silicon carbide (SiC) to a silicon-on-insulator (SOI) process because of the immature status of the SiC process and excessively high turn-around times. The team is using XFAB's 180 nm SOI process that can safely operate up to 175ºC, but most likely even beyond this figure. Figure I.1.25.4 shows the layout view of the full gate driver along with protection features such as active Miller clamping, UVLO, and desaturation detection circuits. The die area is approximately 3.14 mm x 3.14 mm with a high voltage (18 V) pad area of 100 µm x 100 µm and a low voltage (3 V) pad area of 50 µm x 50 µm.

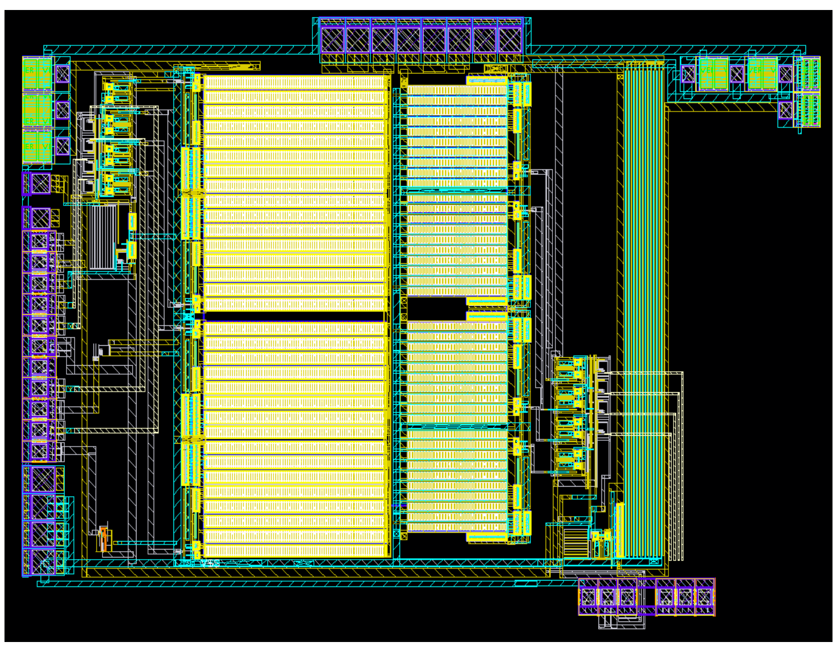

Figure I.1.25.4 Full-system gate driver layout view.

Table I.1.25.4 shows the simulation results for the gate driver's full-strength peak source-sink current after parasitic extraction at the TM (typical mean) corner.

Table I.1.25.4 Full Strength Peak Sink-source Current after Parasitic Extraction for TM (Typical Mean) Corner

27 °C		175 °C	
Peak source current (A)	Peak sink current (A)	Peak source current (A)	Peak sink current (A)
5.58	5.03	4.09	4.01

The other major design block of the IC is the sensing circuitry. This design aims to acquire and process the data from the current sensor and reject the noise. It consists of three instrumentation amplifiers taking input from two sensors and processing it to remove noise and amplify the required signal. Another amplifier is used as the output stage to drive the load and provide gain variability. The block diagram is shown in Figure I.1.25.5.

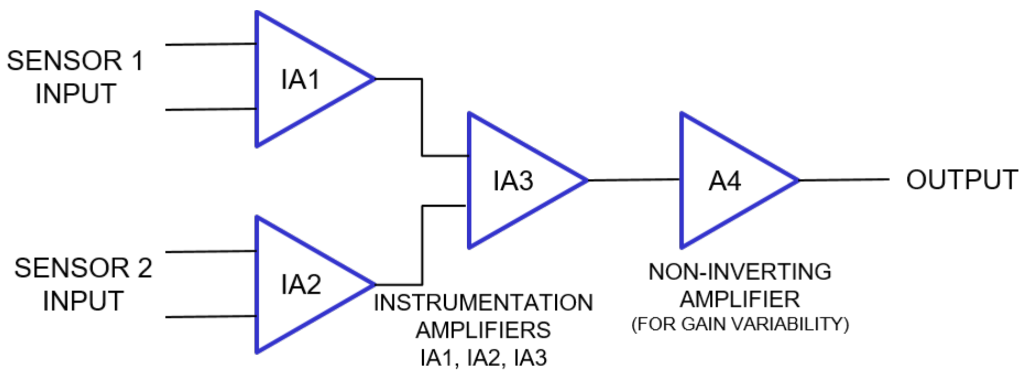

Figure I.1.25.5 Block diagram of the sensor interface circuit.

Figure I.1.25.6 shows the layout of this design. It has 13 I/O pins, including supply pins, input pins for the two sensors, output pins, and 3 bits for gain setting.

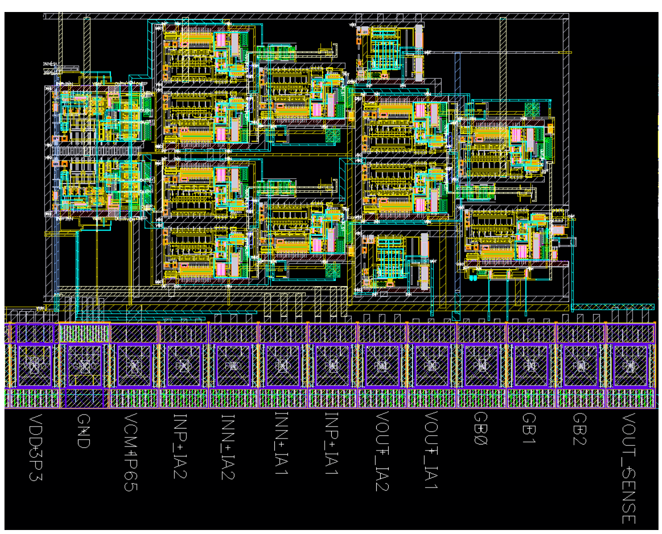

Figure I.1.25.6 The layout of the sensor interface circuit.

Figure I.1.25.7 shows the Monte Carlo plot of gain for the entire system after parasitic extraction. The gain bits are set for the system gain of 28 V/V. This plot shows that the gain remains constant across temperature and process corners with minor deviation.

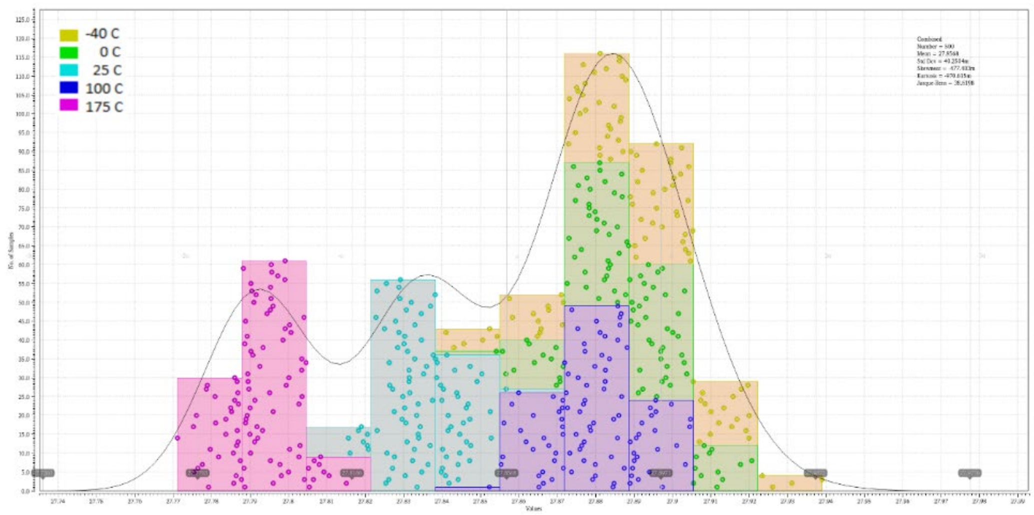

Figure I.1.25.7 Gain of the sensor interface circuit across temperature and process corners.

The team sent the GDSII files of these designs to the foundry for physical fabrication on Aug 16, 2021. The expected return date for those chips is mid-February 2022.

Among various methods, Rogowski coils and GMR current sensors are two accurate current measurement methods suitable for power module integration. GMR current sensors can measure both AC and DC currents, while Rogowski coils can only measure AC currents. Hence, the goal of the power electronic team is to use GMR current sensors and methods to increase the accuracy of the measurement and improve the performance of the sensors when exposed to external magnetic fields under different temperatures. One of the approaches with this goal is using two GMR sensors (TGS) method [1]. In this method, two similar current sensors are placed on a U shape current trace. For this configuration, the magnetic field that sensors are sensing is equal but in the reverse direction. Therefore, subtracting the output voltage of the sensors can help increase the resolution of the measurement compared to a single sensor. Furthermore, this method can eliminate or alleviate the effect of external magnetic fields and temperature fluctuation. Combining the TGS method with a properly designed signal conditioning circuitry can help to have a high bandwidth precise current measurement. Figure I.1.25.8 shows the schematic for LTspice simulation of the designed signal conditioning board. As shown in Figure I.1.25.8, two stages of instrumentation amplifier are used to alleviate the noise problem further and implement high gain. As for each instrumentation amplifier, gain bandwidth is a fixed value, selecting a lower gain for the device leads to higher bandwidth.

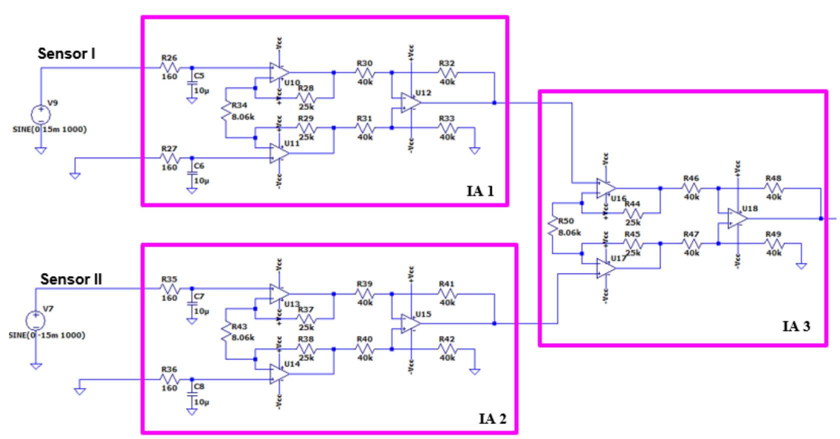

Figure I.1.25.8 Schematic for LTspice simulation of the signal conditioning circuit.

Figure I.1.25.9 shows the configuration of the TGS method implementation, and Figure I.1.25.10 presents the signal conditioning board mounted on the current trace board. Designing the signal conditioning board and the board including the current trace and sensors separately, allows testing various types of sensors and trace shapes without changing the signal conditioning board. Current sensors chosen for the preliminary tests are AA003-02E and AAL002-02E unipolar current sensors from NVE. This group of sensors is capable of generating a maximum of 60 mV/V output voltage, and if they are supplied with 5 V, the maximum output voltage is 0.3 V. As microcontrollers can interpret voltages between 0 V to 3 V, using two stages of instrumentation amplifiers, the output voltage of the sensors can be mapped to 0-3 V. Therefore, the gain of the instrumentation amplifier should be selected so that the sensor's output can be multiplied by ten. Because of having two stages of instrumentation amplifiers, the gain of each stage should be around 3.16.

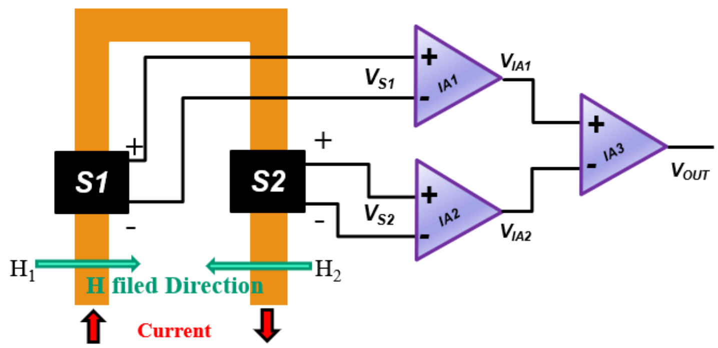

Figure I.1.25.9 Two GMR sensor (TGS) current measurement implementation.

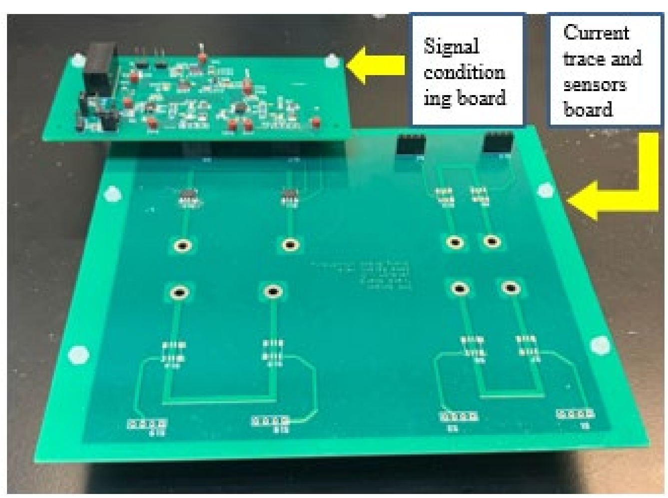

Figure I.1.25.10 Designed current trace and signal conditioning boards.

Because of the different behavior of the unidirectional and bidirectional GMR current sensors, the signal conditioning board is designed to test and evaluate the performance of the TGS method using both types of sensors. For debugging the TGS method, in which the outputs of signals are being subtracted, the signal conditioning circuitry can add the results alternatively. Figure I.1.25.11 shows the test result for subtracting the sensors' output after the first stage of instrumentation amplifiers (VIA1 – VIA2) and adding (VIA1 + VIA2) them. Additional tests to assess the performance of the method in case of fluctuating temperature will be implemented in the next step.

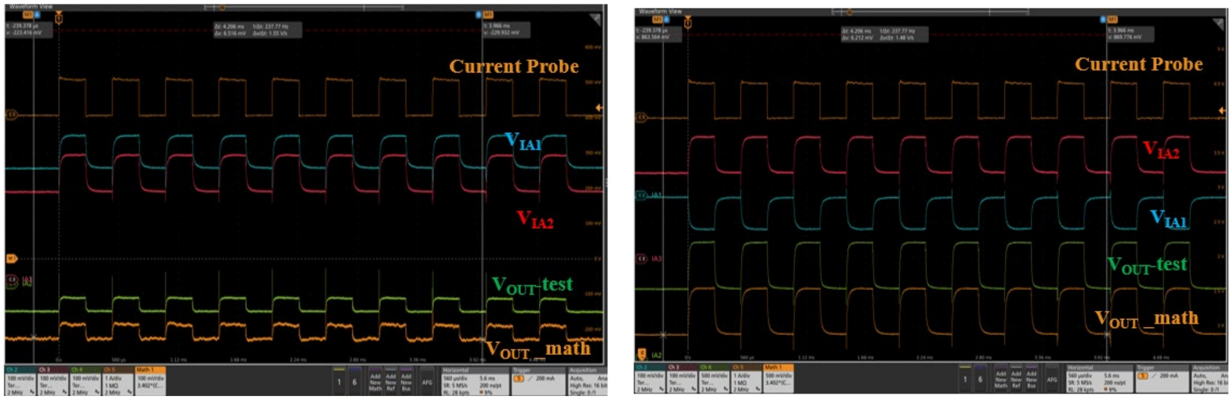

(a) (b)

Figure I.1.25.11 TGS method test results using unidirectional current sensors.

As shown from Figure I.1.25.11, the system's output ($V_{OUT\text{-}test}$) is similar to the expected results from the mathematical calculations (V_{OUT_math}), which validates the performance of the TGS method. More tests will be implemented to evaluate the different sensitivity or being exposed to different temperatures.

Conclusions

UA research is underway, with both packaging and IC design levels in full swing. Biweekly meetings are being held with the broader team, and UA-only meetings are being held in the intermediate weeks such that a project meeting is held each week. The UA team experienced delays in getting modules built and delivered to ORNL for their intended 100 kW inverter build. These delays were both technical and supply-chain oriented. At present, three (3) power modules have been successfully built and experimentally validated, while the final three (3) will be completed soon. In the grand scheme, overall project is on track technically, but just a few months behind on schedule. More publications are expected in the coming months as results are obtained from the sensing and module developments.

Key Publications

1. Rana Alizadeh, Kaoru Porter, Tom Cannon, and Simon Ang, "LTCC Interposers for Double-Sided Power Electronic Modules," accepted by IMAPS/ACerS 16th International Conference and Exhibition on Ceramic Interconnect and Ceramic Microsystems Technologies (CICMT 2020). Conference postponed due to coronavirus.

2. F. Luo et al., "Thermal Decoupling in Power Electronics Modules Using Thermal Pyrolytic Graphite," accepted by IMAPS/ACerS 16th International Conference and Exhibition on Ceramic Interconnect and Ceramic Microsystems Technologies (CICMT 2020). Conference postponed due to coronavirus.

3. A. Abbasi, A. Faruque, S. Roy, R. C. Murphree, T. Erlbacher, H. A. Mantooth, "Gate Driver Design in a 1um SiC CMOS Process for Heterogeneous Integration Inside SiC Power Module", 53rd International Symposium on Microelectronics: A Global Virtual Event.

References

1. C. Mușuroi *et al*, "High Sensitivity Differential Giant Magnetoresistance (GMR) Based Sensor for Non-Contacting DC/AC Current Measurement," *Sensors (Basel, Switzerland),* vol. 20, *(1),* pp. 323, 2020.

I.2 Electric Drive Technologies Development

I.2.1 Wound Field and Hybrid Synchronous Machines for EV Traction with Brushless Capacitive Rotor Field Excitation (Illinois Institute of Technology)

Ian P. Brown, Principal Investigator
Illinois Institute of Technology
3301 South Dearborn Street
Chicago, IL 60616
Email: ibrown1@iit.edu

Daniel C. Ludois, Principal Investigator
University of Wisconsin-Madison
1415 Engineering Drive
Madison, WI 53706
Email: ludois@wisc.edu

Steven Boyd, DOE Program Manager
U.S. Department of Energy
Email: steven.boyd@ee.doe.gov

Start Date: October 1, 2017 End Date: September 30, 21
Project Funding: $204,411 DOE share: $999,752 Non-DOE share: $112,995

Project Introduction

For mass adoption of electric vehicles (EVs), there is concern regarding the cost and materials in the supply chain for the vehicle's main traction motor. While Dept. of Energy programs have been successful at lowering the cost of traction inverters and wide bandgap power electronics, the cost of traction electric motors has been resistant to change. Today, interior permanent magnet synchronous machines (IPMSMs) and induction machines (IMs) are the commercially dominant traction motors.

The rare-earth permanent magnets (PMs) used in IPMSMs are subject to market volatility and are largely single sourced from a foreign power. The PMs are also a significant portion of the cost of IPMSMs and impose temperature limits. The PMs provide a fixed flux level which is always, "on", leading to safety concerns during inverter faults and requiring additional current to be injected into the machine during field weakening to buck the magnetic flux. This additional current lowers the power factor of the machine, requiring that the traction inverter be oversized to supply the reactive current, leading to increased ohmic losses in the stator and inverter. Induction machines (IMs) must also draw reactive current from the traction inverter to magnetize the machine leading to a lower power factor.

Wound field synchronous machines (WFSMs) and hybrid excitation synchronous machines (HESMs) are potentially advantageous alternatives to the commercially dominant IPMSMs and IMs. WFSMs are PM free, and because the DC field excitation is from the rotor side, the power factor of the machine is high, if not unity for most operating points. The complete control of the field excitation provides the potential for optimal field weakening and large constant power speed ranges with loss minimization. HESMs use a combination of PM and wound field excitation to combine the high efficiency of IPMSMs with the easy field weakening and high-power factor of WFSMs while using considerably less PM. They also reduce the field power requirements.

EV traction applications require extremely high reliability and power density inhibiting the use of brushes and other classical field power transfer technologies such as brushless exciters. Brushless capacitive power transfer offers an attractive means of providing power transfer to the rotor field windings of WFSMs and HESMs.

Objectives

The objective of this project is to design, develop, and demonstrate wound field and hybrid excitation (permanent magnet and wound field) synchronous machines, with brushless power transfer to the rotor field winding, that are capable of achieving the performance metrics in Table I.2.1.1. A focus of this project is the cost target of 4.7 $/kW. The brushless field power transfer will be accomplished using capacitive power transfer.

Table I.2.1.1 Prototype Wound Field and Hybrid Excitation Synchronous Machine Target Metrics

Parameter	Budget Period 2 Prototype	Final Prototype
Peak Power (kW)	≥55	≥55
Continuous Power (kW)	≥ 30	≥ 30
Specific Power Density (kW/kg)	1.5	1.6
Volumetric Power Density (kW/l)	5.0	5.7
Cost ($/kW)	-	4.7

Approach

To meet the cost and power conversion targets, a number of approaches are being developed simultaneously in the context of wound field and hybrid excitation synchronous machines though many of the technologies will also apply to other electric machine types and applications.

- High slot fill field and stator windings. Wound field synchronous machines are copper loss dominated. The efficiency and power density of WFSMs are directly related to the field winding slot fill. High slot fill winding technologies investigated include square/rectangular conductors, twisted square/rectangular conductors, and die compressed windings.
  - Target slot fill of ~70% to 80% compared to 40 to 45% for random/mush distributed windings.
- Brushless power transfer to the rotor field winding using electric fields in a capacitive power coupler (CPC) excited by high frequency power electronics.
  - Reduce the mechanical complexity of the rotating capacitors. Three simpler rotating capacitor designs have been investigated: journal bearings, integrated LC coupler, and printed circuit board (PCB) capacitive plates with a tank circuit.
  - Increase the frequency of excitation to the megahertz regime to allow the use of a smaller capacitance, e.g., PCB based capacitors with a relatively large airgap.
  - Develop a wide bandgap (GaN or SiC) power converter with high efficiency which minimizes losses by operating in resonant soft switching.
- Reduce the punching scrap from the construction of the lamination stack. Typically, 40% of the steel is scrapped when punching IPMSM laminations.
  - Segmented lamination structures allow for higher fill factors with needle or bobbin winding both rotor and stator windings and even higher slot fills, with die compressed windings with the added benefit of reduced end turn length. Bobbin winding of the field winding allows for high slot fills using square/rectangular conductors.
- Hybrid excitation synchronous machines to lower the field power requirements.
  - Bias the field flux for the most common operating point in a drive cycle with PMs.

- Extend the constant power speed range compared to pure permanent magnet machines.

- Develop high performance controls for WFSMs and HESMs.
- Develop WFSM design optimization techniques and software to optimally distribute and shape the active materials.

Results

The main activities of the past budget period have been the design, construction, and dynamometer testing of a final third generation WFSM prototype. Two potential WFSM topologies were designed. One version was with a die compressed 12 slot 10 pole fractional slot concentrated winding stator and die compressed field winding. The other topology was with a distributed hairpin stator with a general high slot fill field winding. Challenges were encountered in manufacturing die compressed stator windings with multiple parallel strands in hand, needed for the 12 slot 10 pole configuration, so it was decided to instead use the distributed hairpin stator. It is difficult and expensive to prototype a hairpin winding stator in an academic setting. For this reason, an off the shelf stator with hairpin windings was utilized, specifically the stator from a General Motors Chevy Volt Generation 1 Motor B, as shown in Figure I.2.1.1(a). The rotor was segmented to allow the use of bobbin wound square magnet wire, twisted square magnet wire where the magnet wire is laid in an interlocking 45-degree angle, and die compression for high slot fill field windings. The rotor segmentation also lowers the stamping electrical steel scrap. The field winding window in the rotor lamination is non-rectangular to maximize the field winding conductor cross-section area in the overall available rotor area.

Magnetic Design

The prototype WFSM was designed and optimized using a metamodel-based approach to maximize its efficiency over a custom set of five load points, Table I.2.1.2, while utilizing a fully per-unitized rotor geometric template, Figure I.2.1.1(b). The load points were selected and weighted to represent drive cycle operation. The optimization objectives and constraints are listed in Table I.2.1.3. The design that was prototyped was selected from a large set of designs generated during sensitivity studies and during optimizations. The predicted performance at the five load points of the design that was prototyped is listed in Table I.2.1.4. The peak terminal current, I_s, of operating point four is limited to that used in the original Chevy Volt powertrain. With the cooling implemented in this design it is anticipated that even higher peak powers are possible. The predicted peak volumetric power densities are listed in Table I.2.1.5 for active materials and the entire envelop of the machine including the end turns. The different base speeds depend on the available DC link voltage and desired constant power speed range. The maximum speed is structurally limited to 12 kRPM.

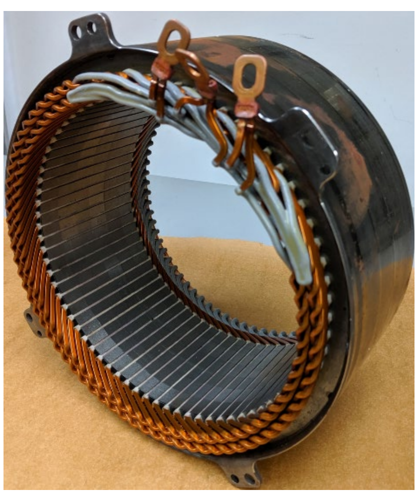

(a)

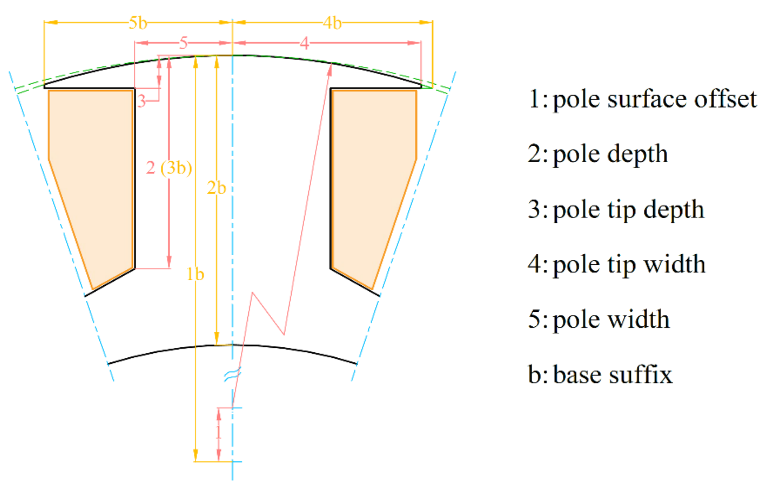

(b)

Figure I.2.1.1 (a) Chevy Volt Gen 1 Motor B with distributed hairpin winding used in the final prototype, (b) parametric rotor model used in the magnetic optimization.

Table I.2.1.2 Generation III Final WFSM Optimization Load Points

Operating Points	Speed (RPM)	Torque (Nm)	Output Power (kW)	DC Link Voltage (Vdc)
1	4,000	131.3	55	600
2	8,000	65.65	55	600
3	2,000	119.4	25	600
4	4,000	453.59	190	600
5	12,000	151.2	190	600

Table I.2.1.3 Optimization Objectives and Constraints

Quantity	Type	Expression
Weighted Efficiency	Objective	Maximize
Torque at all Load Points (p.u.)	Constraint	≥ 0.985
Peak Voltage at all Load Points (p.u.)	Constraint	≤ 0.94
Stator Current Density at all Load Points (A_{RMS_s}/mm^2)	Constraint	≤ 25
Field Current Density at all Load Points (A_{RMS}/mm^2)	Constraint	≤ 20

Table I.2.1.4 Predicted Performance of Generation III Final WFSM with Bobbin Wound Square Magnet Wire Field Winding

Load Point	Speed (RPM)	Torque (Nm)	Torque Ripple (pk2pk %)	Stator Current I_s (A_{peak})	Stator Current Density J_s (A_{RMS}/mm^2)	Field Current I_f (A_{dc})	Field Current Density J_f (A_{RMS}/mm^2)	Power Factor	Eff. (%) *, **, ***	Total Loss (W) *, **, ***
1	4000	131.65	6.83	205.48	8.26	6.07	7.62	0.97	95.26	2741
2	8000	65.38	5.08	144.27	5.80	4.00	5.02	1.00	95.59	2525
3	2000	119.68	6.72	190.28	7.65	5.66	7.10	0.95	93.85	1642
4	4000	454.34	0.55	608.00	24.44	13.00	15.67	0.98	93.59	13,035
5	12000	151.27	6.83	412.82	16.60	5.97	7.20	0.99	94.66	10,722

*Winding temperatures of 120 C° assumed; ATF spray cooling of end turns
**AC losses in stator conductors included through full FEA evaluation of conductors
*** 2 x iron loss build factor included
**** Stator with 6 or 8 conductors would significantly improve efficiency at high speed

Table I.2.1.5 Predicted Peak Volumetric Power Densities

	4,000 RPM Base Speed	6,000 RPM Base Speed
Active Material Volumetric Power Density (kW/l)	37.7	57.6
Volumetric Power Density Including End Turns (kW/l)	24.0	36.0

Final WFSM Prototype Construction

The final WFSM rotor was designed to potentially use three high slot fill field winding variants: square magnet wire, twisted square magnet wire, and die compressed field windings. Both the square magnet wire, Figure I.2.1.2, and twisted square magnet wire, Figure I.2.1.3, variants were constructed. A die was constructed, and trial coils wound for the die compressed winding, Figure I.2.1.4. Given time constraints and challenges with the reliable production of the die compressed field coils it was decided to only construct the square magnet wire and twisted square magnet wire variants. The three variants have different slot fills, structural properties, and ease of manufacturing. A common shaft system was used to interchange the rotors.

(a)

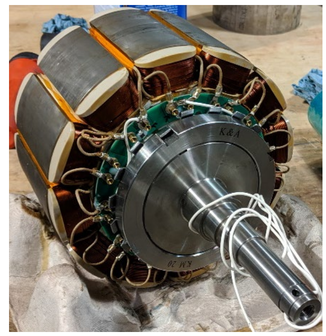

(b)

Figure I.2.1.2 (a) Square magnet wire rotor, (b) square magnet wire rotor on the shaft.

(a)

(b)

Figure I.2.1.3 Twisted square magnet wire, (a) pole, and (b) rotor.

(a)

(b)

Figure I.2.1.4 Trial die compressed field winding (a) before and (b) after compression.

Brushless Capacitive Power Transfer System

Over the course of this project, multiple brushless capacitive power transfer technologies and systems were developed including integrated magnetic and capacitive PCB couplers, capacitive coupling between journal bearings, three-phase large gap PCB capacitive couplers, and single-phase large gap PCB capacitive couplers. The single-phase large gap PCB capacitive coupler was used for bench and dynamometer testing with multiple generations of wound field synchronous machines. Multiple generations of GaN based inverters were developed along with ancillary circuitry for automatic resonance tracking, current sensing, compact low loss high frequency resonant tank inverters, and a rotating impedance matching buck converter. An overview of the developed single-phase PCB brushless capacitive power transfer system setup for bench testing with an earlier generation WFSM prototype is shown in Figure I.2.1.5. Final DC to DC performance tests for this system are listed in Table I.2.1.6. The setup in Figure I.2.1.5 is with a first generation GaN inverter. Using a 2nd generation GaN inverter over 1.1 kW of power transfer was achieved.

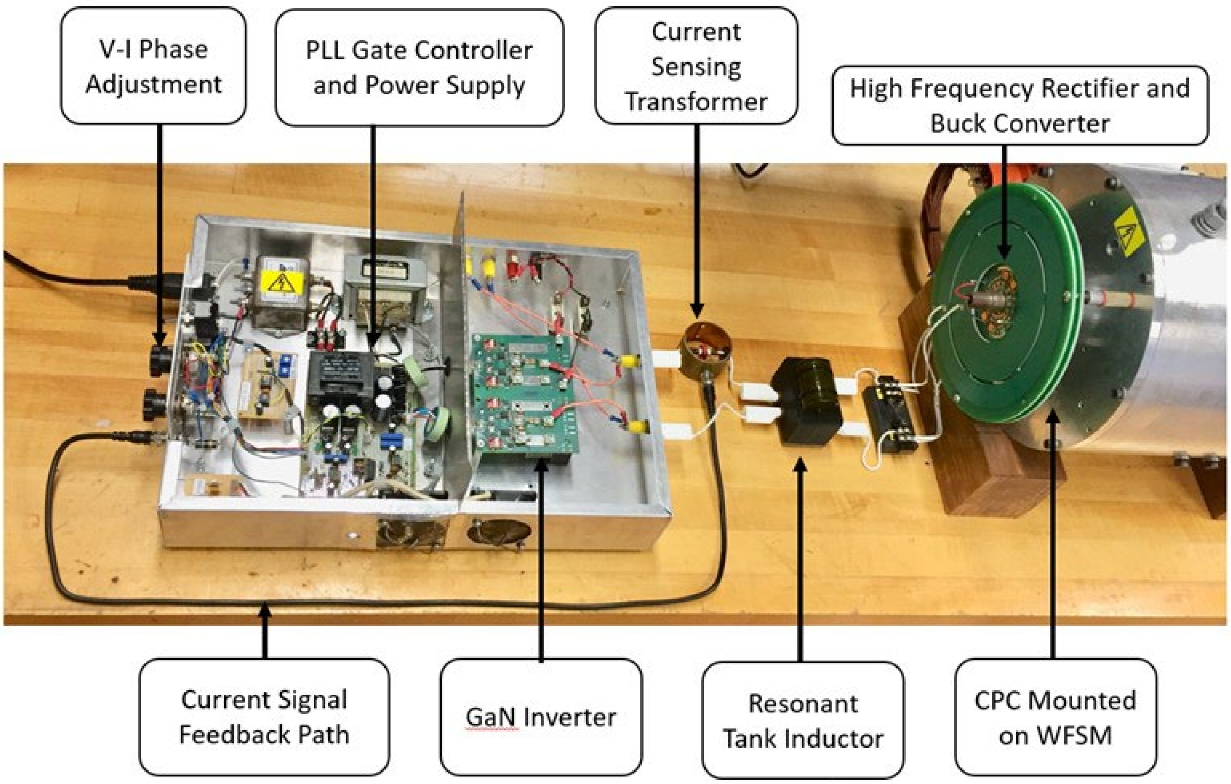

Figure I.2.1.5 Overview of brushless single-phase large gap PCB based capacitive power transfer system setup for bench testing with earlier generation WFSM

Table I.2.1.6 DC to DC Power Transfer to WFSM Field Winding During Bench Testing

V_{in} (V)	I_{in} (A)	V_{out} (V)	I_{out} (A)	P_{in} (W)	P_{out} (W)	Eff (%)	I_{ac} (A_{RMS})
150	3.74	139.8	3.61	561	504.96	90.01	5.69
160	3.98	148.9	3.84	636.8	572.37	89.88	6.02
170	3.85	150.7	3.90	654.5	587.73	89.80	6.33
170	4.17	157.1	4.05	708.9	636.41	89.77	6.13
180	4.35	169	4.16	783	702.20	89.68	6.48

Dynamometer Testing of Final WFSM Prototype

The final WFSM design with the square magnet wire field winding was dynamometer tested with the field excitation provided through brushes and slip rings and the single-phase PCB capacitive power coupler, Figure I.2.1.6(a) and Figure I.2.1.6(b). The Chevy Volt stator was rated for a peak current of 608 A_{peak} when installed in the Chevy Volt automobile. The inverter used to supply the stator during dynamometer testing was limited to a peak current of ~325 A_{peak}. Power analyzer test results near this current limit are shown in Figure I.2.1.7(a). The final WFSM was tested to the stator inverter current limit and also the load point 3 used in the optimization, Table I.2.1.7. The measured performance at load point three was very close to its predicted performance. During testing with the single-phase PCB capacitive coupler excitation was provided by two generations of GaN inverters with the first generation switching at ~1.6 MHz and the second at ~7.1 MHz. The inverter output voltage and field current for the 7.1 MHz switching is shown in Figure I.2.1.6(b).

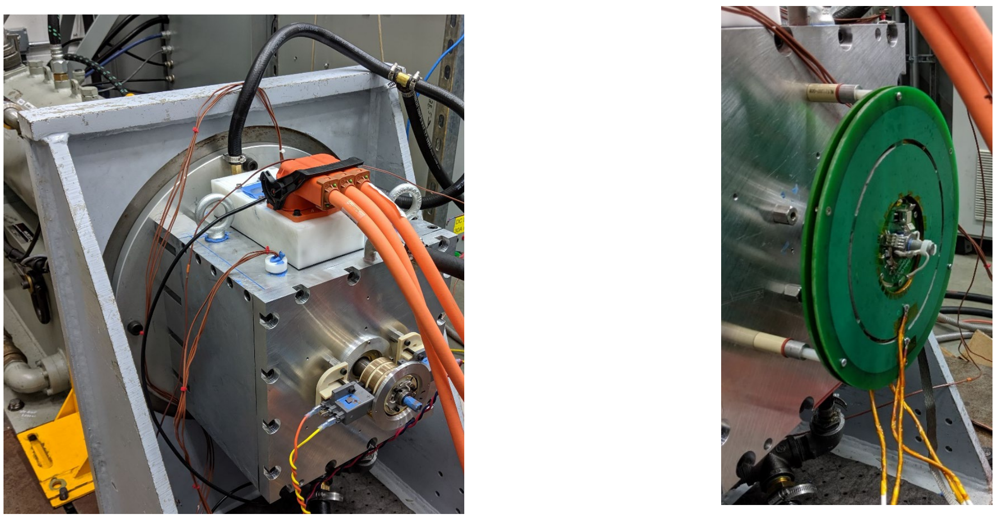

(a) (b)

Figure I.2.1.6 (a) Final WFSM prototype mounted on dynamometer with brushes and slip rings, and (b) brushless single-phase large gap PCB capacitive power coupler for field excitation

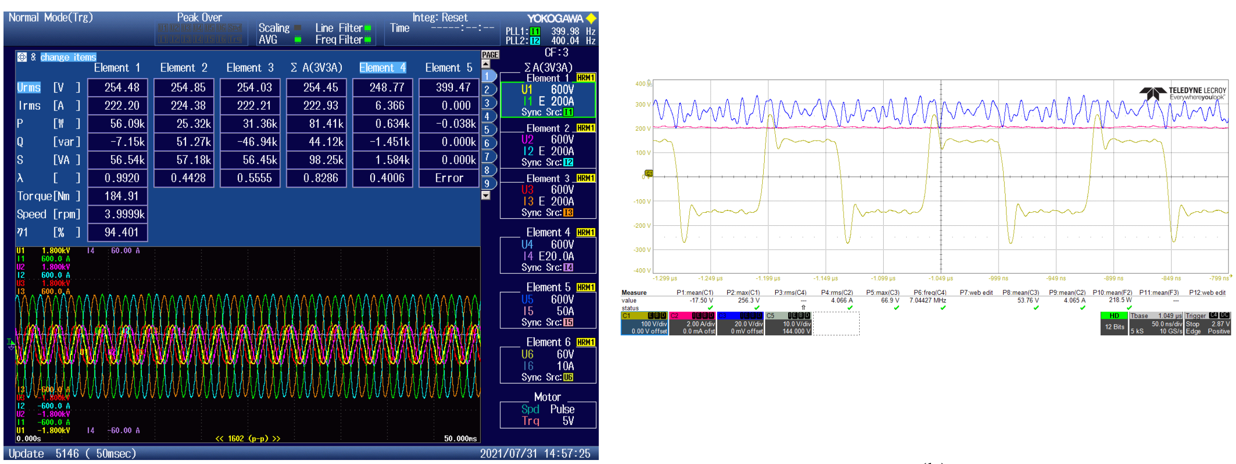

(a) (b)

Figure I.2.1.7 (a) Power analyzer results from operation near stator inverter current limit, and (b) single-phase CPC GaN inverter switching at ~7.1 MHz with 4 A field current.

Table I.2.1.7 Comparison of Predicted and Measured Performance at Load Point 3

	Speed (RPM)	Torque (Nm)	Is (A_{RMS})	If (A_{dc})	Power Factor	Efficiency (%)
Predicted	2,000	119.68	134.49	5.66	0.95	93.85
Measured	2,000	118.06	137.19	5.92	0.93	93.82

Conclusions

In this budget period a final wound field synchronous machine was designed, prototyped, and dynamometer tested. A metamodeling-based optimization technique was used to design wound field synchronous machines of two different stator winding topologies, a fractional slot concentrated winding and a hairpin distributed winding, for multiple load points. The hairpin distributed winding version was selected for prototyping. The rotor design was compatible with three high slot fill field winding technologies, square magnet wire, twisted square magnet wire, and die compressed. The square magnet wire and twisted square magnet wire variants were prototyped.

The final square magnet wire rotor variant of the wound field synchronous machine prototype was dynamometer tested with brushes and slip rings and brushless capacitive power transfer systems. For the brushless capacitive power transfer system, the capacitive coupler structure was a single-phase stack of two stator and one rotor printed circuit boards. The rotor printed circuit board contained the rotating rectifier. Two generations of high frequency inverters were tested switching at ~1.6 MHz and ~7.1 MHz.

The square magnet wire variant was dynamometer tested to the current limit of the available stator inverter. The measured performance matched very closely to the predicted performance. The predicted peak power output active volumetric power density is 37.7 kW/l and 57.6 kW/l for 4,000 RPM and 6,000 RPM base speeds respectively.

Wound field synchronous machines with brushless capacitive field excitation are a high power density electric traction motor topology that is free of permanent magnets. They also have the attractive properties of easy field weakening, high power factor, and reduced iron losses at high speed.

Key Publications

1. S. Hagen, M. Tisler, J.J. Dai, I.P. Brown, D.C. Ludois, “Use of the Rotating Rectifier Board as a Capacitive Power Coupler for Brushless Wound Field Synchronous Machines,” to appear in IEEE Journal of Emerging and Selected Topics in Power Electronics, 2021. DOI: 10.1109/JESTPE.2020.3039497.

I.2.2 Wound Field Synchronous Machine System Integration towards 8x Power Density and Commercialization (Magna Services of America, Inc.)

Lakshmi Varaha Iyer, Principal Investigator
Magna Services of America, Inc. (Magna R&D)
750 Tower Drive
Troy, MI 48098
Email: LakshmiVaraha.Iyer@magna.com

Susan Rogers, DOE Technology Development Manager
U.S. Department of Energy
Email: susan.rogers@ee.doe.gov

Start Date: October 1, 2019 End Date: December 31, 2022
Project Funding: $875,00 DOE share: $700,000 Non-DOE share: $175,000

Project Introduction

In support of VTO's Electric Drive R&D activity, the Electric Drive Technologies (EDT) Consortium, a multi-disciplinary team of national labs and universities, coordinates and conducts a portfolio of research to advance the state-of-the-art in electric drive technologies. The Consortium has established the following strategic goal listed below:

EDT Research Consortium Strategic Goal (compared to 2015 baseline)

A 125 kW electric traction drive system:

- 8X power density improvement, or 1/10 the volume (33 kW/L)
- ½ the cost ($3.3/kW)
- 2X useful life (300,000 miles)
- 1000 kW/L inverter and a <20,000 rpm, 50 kW/L electric motor.

Objective

The objective of this project is to design a Wound Field Synchronous Machine (WFSM) with 8X power density improvement and cost below $3.3/kW.

Approach

The approach includes design and development of wound field synchronous machine, cooling system and capacitive power coupling (CPC) technology. The project is divided into three budget periods outlined below:

- BP 1 – Simulation to determine feasibility of achieving goal and concept design
- BP 2 – Design motor for build and prototype rotor excitation system
- BP 3 – Build and test motor relative to project goals.

This report presents tasks pursued and results obtained in Budget Period (BP) 2. Budget period 2 includes tasks such as:

- Design and optimization of the electric motor and cooling system for
- Automotive reliability and manufacturing

- Prototyping and integration of the field excitation system.

Results

1. WFSM design and optimization

To maximize the wound field synchronous machine efficiency over a drive-cycle, a metamodeling optimization approach was developed using a flexible software architecture. The overall drive cycle efficiency is approximated by a weighted average efficiency calculated at a number of operating or load points. Load points at the peak power, continuous power, and maximum constant power speed outputs are included to ensure all desired operational points can be reached, Figure I.2.2.1.

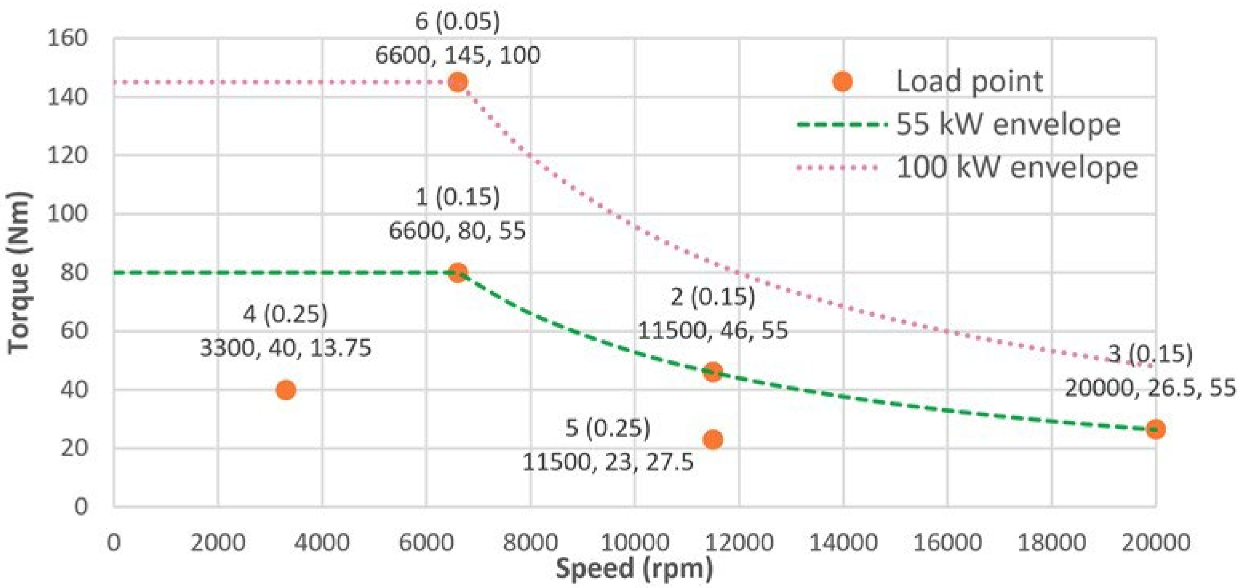

Figure I.2.2.1 Representative load points for weighted efficiency calculation. Load points are labeled: Number (weight), speed [RPM], torque [Nm], power output [kW]

Direct optimization of wound field synchronous machines for drive cycle efficiency is extremely computationally expensive. The computational expense of evaluating a wound field synchronous machine design is higher than a permanent magnet synchronous machine because of the variable field excitation. For this reason, a metamodeling optimization approach which forms the metamodel from a reduced number of samples compared to a direct optimization has been adopted. Once the meta-model is created it also allows the optimization to be rerun with different input parameters, constraints, or objectives without having to repeat the entire direct optimization. A representative metamodel for the average weighted efficiency is shown in Figure I.2.2.2. To further reduce the computational time the finite element evaluation of the wound field synchronous machine designs has been parallelized.

For each design evaluated during the metamodel creation, a full electromagnetic analysis is carried out at each load point. Included in the electromagnetic analysis is a simulation of the skin and proximity losses of the stator conductors. A stress analysis is also carried out for a 20% overspeed condition. The flexibility of the created software allows for the load points and desired simulated outputs to be easily changed. The designs can either use a fully parameterized stator geometry or one in which the conductor size is fixed to a discrete value. A number of custom rotor geometric templates have also been created which include small features critical for stress reduction. The custom rotor geometries are programmatically created as DXFs and imported for evaluation.

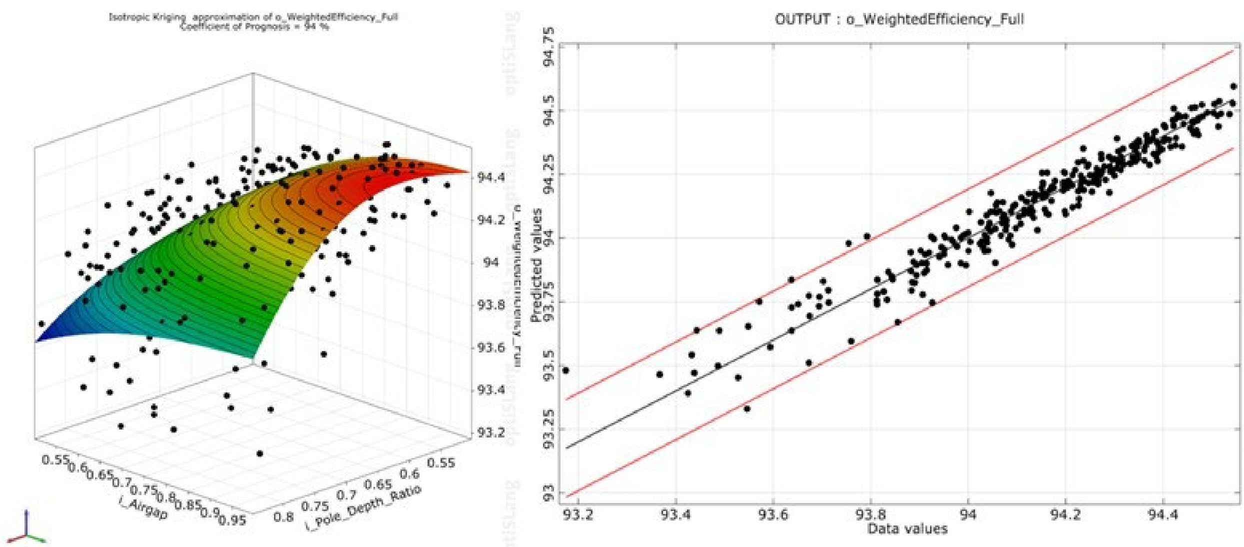

Figure I.2.2.2 Representative weighted efficiency metamodel surface for sampled designs indicated by black dots for two input parameters and comparison between actual and predicted values.

The metamodeling optimization approach and flexible software architecture has allowed the evaluation of a large number of machines of different power and speed ranges, slot pole combinations, and winding technologies.

Several potential prototype wound field synchronous machine designs have been optimized for a peak power density of 50 kW per liter. The design optimization process includes constraints on the maximum stress, peak current densities, torque ripple, and voltage limitations. Some designs include reuse of existing hairpin winding stators already in serial production for lower production equipment capital expenditure. Other fully custom designs with lower power outputs (100 kW target) have also been designed. A representative cross-section of an optimized wound field synchronous machine design is shown in Figure I.2.2.3.

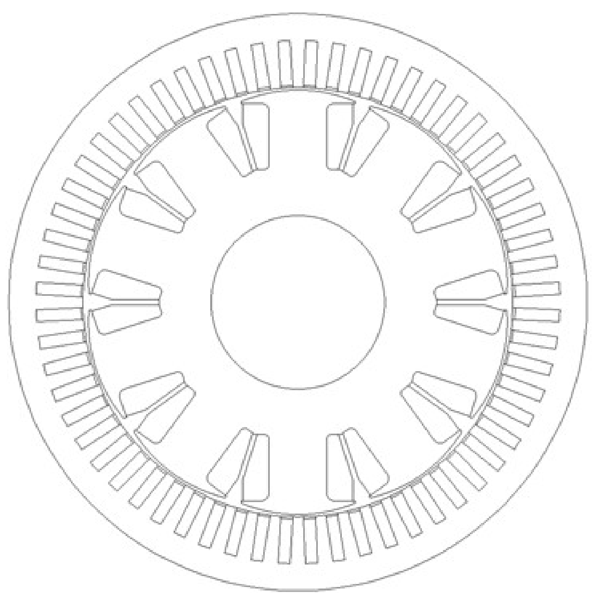

Figure I.2.2.3 Representative cross-section of optimized wound field synchronous machine

2. Stator and Rotor Cooling

Multiple cooling system architectures were investigated for the rotor and stator. Multiple stator cooling techniques based on water/glycol in stator jacket and stator jets with oil were investigated. Stator jacket is used as the baseline design. Stator jets could be optimized to arrive at a tradeoff between temperature rise, cost, flow rate, and heat exchanger size. Given the type of transmission, axial jet impingement technique was chosen for rotor cooling. Investigations were conducted on nozzle placement and number of jets impinging on the end winding and core on both axial ends of rotor. Effects of coil carrier were also included as it adds to thermal resistance. Channels were designed in the coil carrier to conduct oil to inner side of the coil carrier to cool the end-windings. This may affect drag losses. Oil temperatures between 75°C and 100°C were also investigated as it affects the cost and size of the water/glycol to oil heat exchanger. Flow rate of the oil was also investigated between 1L/min and 8 L/min as it affects the jet velocity, temperatures, cost, size and type of pump. Moving mesh versus moving reference frame simulations were also carried out to understand the difference in results. Although, moving mesh simulation is computationally expensive, it provides lower temperatures. Oil outlet design at the base of the motor was also investigated as it influences the reverse flow and heat transfer.

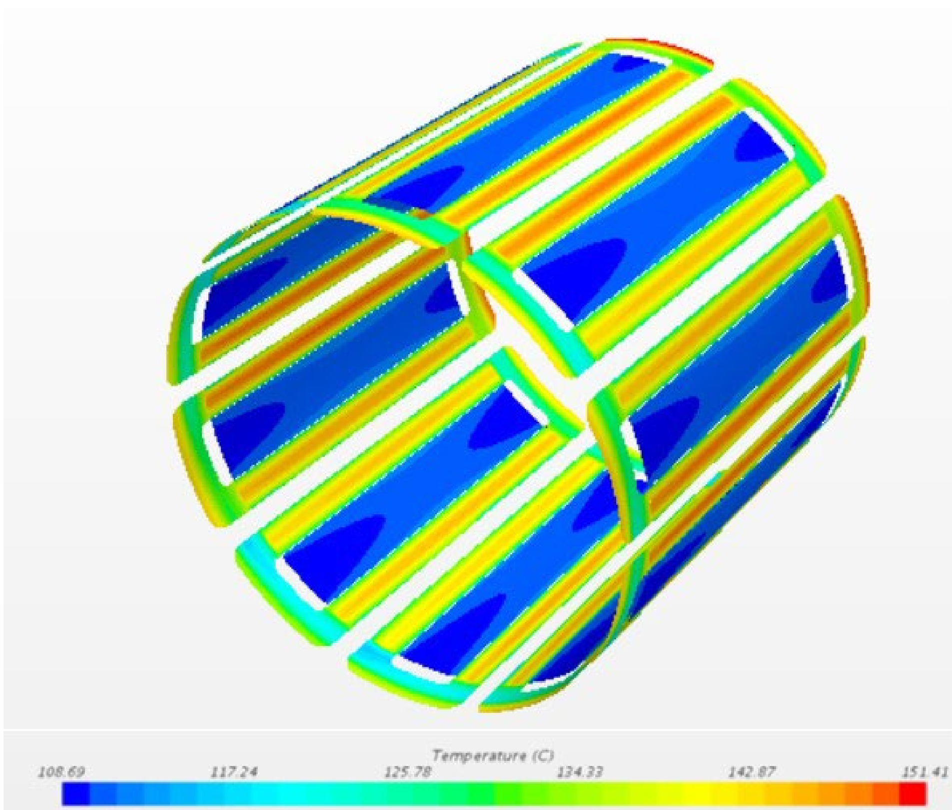

Figure I.2.2.4 Sample result from CFD simulations on the rotor. Maximum rotor temperature did not exceed 160°C using rotor jet cooling design.

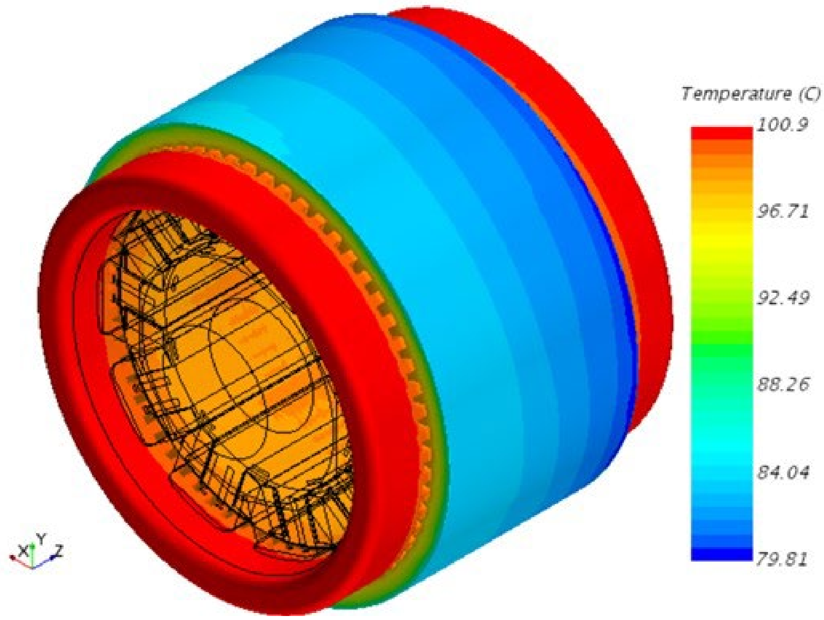

Figure I.2.2.5 Sample result from CFD simulations on the stator. Maximum stator temperature did not exceed 100°C using stator jacket cooling design.

3. Design of a Brushless Capacitive Excitation System

Motivation: All brushless wound field synchronous machines (WFSMs) utilize a diode rectifier on the rotor, no matter the form of AC coupling. A capacitive approach seeks to make the rectifier's printed circuit board the coupling structure, thereby eliminating rotating transformers or auxiliary rotor windings, potentially lowering the cost of brushless WFSM construction.

A capacitive excitation system was designed and iterated to achieve stable performance in the Industrial Scientific and Medical (ISM) frequency band and scale towards a peak powers > 1 kW. The current incarnation of the excitation system is described by the following circuit diagram. This architecture was chosen because the placement of C_{in} and L_{DC} naturally overcome the influence of the parasitic elements C_{diode} / C_p and L_p in the rectifier circuit. The primary challenge of the architecture is achieving > 90% efficiency (measured DC into DC out) at ISM frequencies as the parasitic elements can cause excessive ringing/overshoot in the circuit. The AC power source is a custom inverter, using a 650 VAC power source.

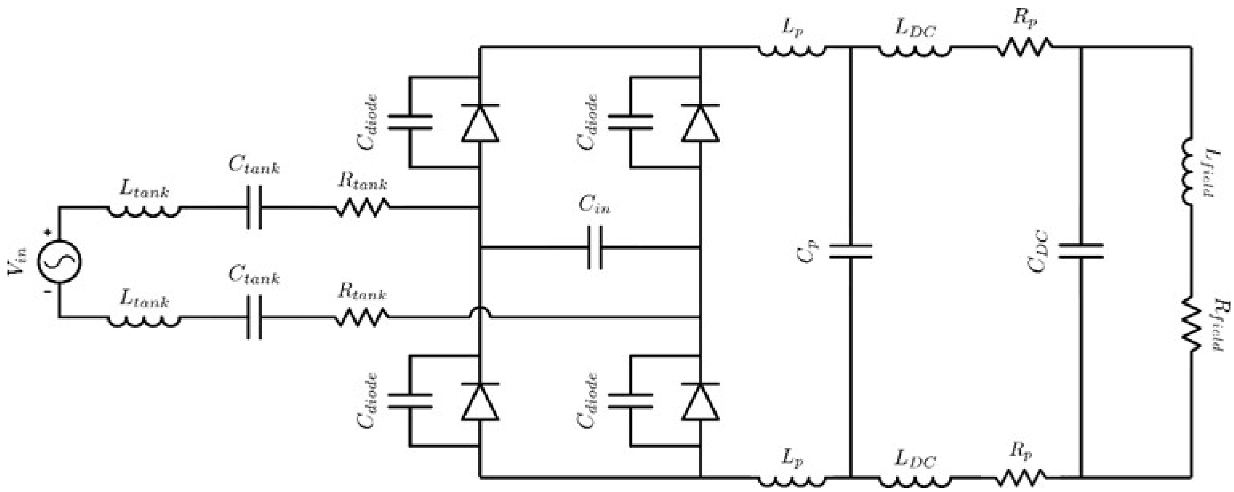

Figure I.2.2.6 Schematic design of brushless capacitive excitation system.

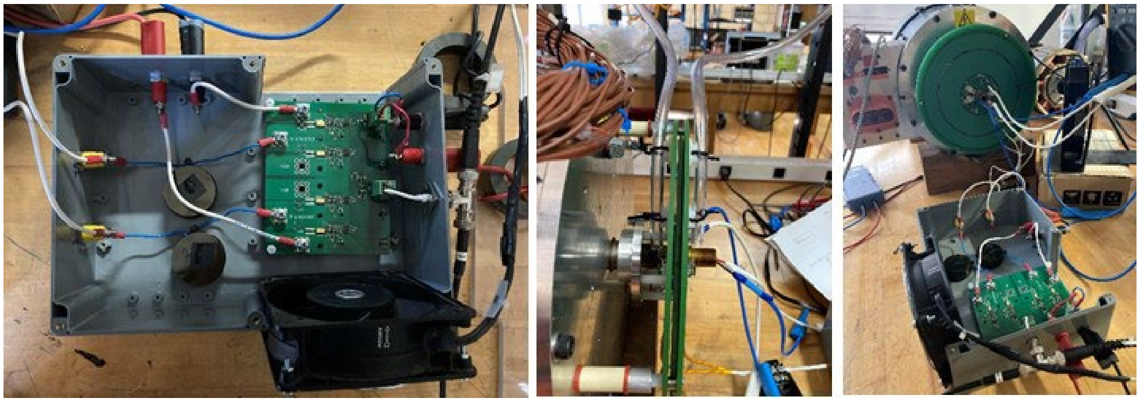

Figure I.2.2.7 Inverter and tank inductors (left) tank coupling capacitor disks and rotating rectifier (center) and whole system (right).

Initial test results are shown below via oscilloscope screen capture and plotted data. The system efficiency at this operating point is 91%. The high efficiency was achieved by eliminating the majority of the ringing rectifier waveforms and minimizing harmonic content in the tank circuit.

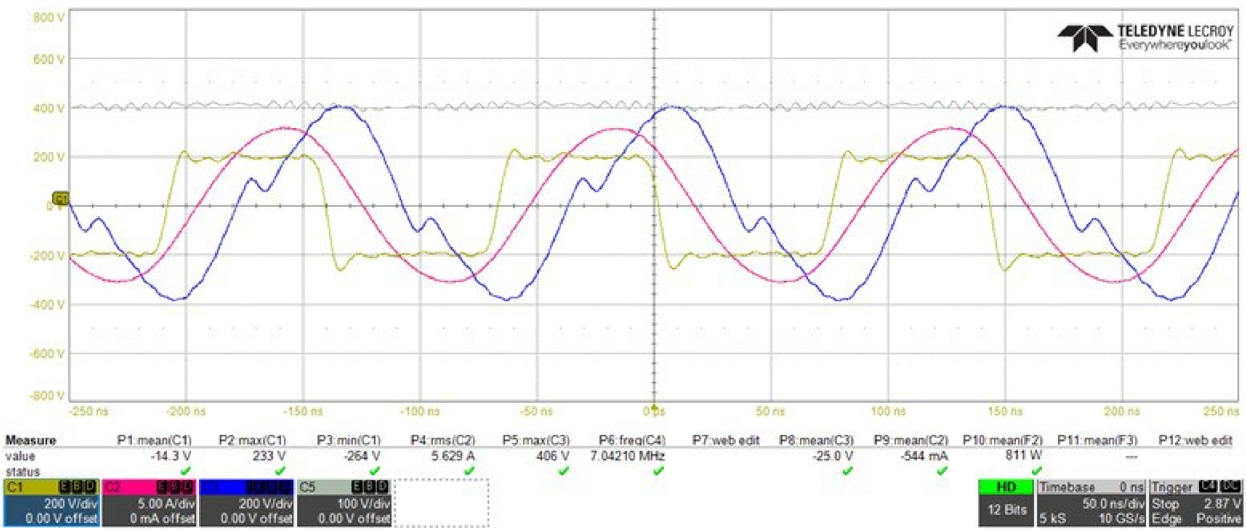

Figure I.2.2.8 Oscilloscope trace of ISM frequency output of the inverter (yellow), the tank current (red), rectifier input voltage (blue) and rotor field voltage (grey) during 650W output to the rotor field winding.

Further testing at other operating points resulted in the measured efficiency vs output power plot below. The red points on the curve represent tuning of the inverter for the highest efficiency.

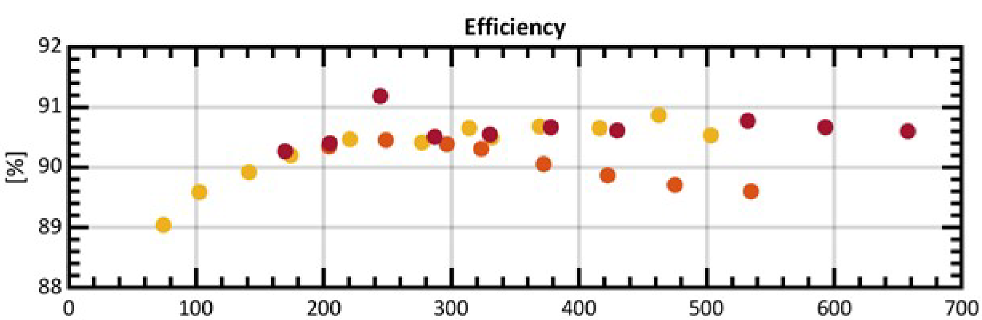

Figure I.2.2.9 Measured efficiency as a result of inverter tuning at various power levels

Next steps on the testing of the capacitive power coupler (CPC) excitation system include scaling output power to >1 kW. In parallel to this, a rotating transformer version of the excitation system will be designed / simulated as a backup plan in the event the CPC approach cannot provide power in the multi-kW range.

Conclusions

Multiple wound field synchronous machines with a power density of 50 kW/l have been designed. Fin down-selection of the design for prototyping is in process. A capacitive excitation system was developed and tested.

I.2.3 Low-Cost Rare-Earth Free Electric Drivetrain Enabled by Novel Permanent Magnets, Inverter, Integrated Design and Advanced Thermal Management (Marquette University)

Principal Investigator
Ayman El-Refaie
Marquette University
1637 West Wisconsin Avenue
Milwaukee, WI 53233
Email: ayman.el-refaie@marquette.edu

Steven Boyd, DOE Program Manager
U.S. Department of Energy
Email: steven.boyd@ee.doe.gov

Start Date: October 1, 2020 End Date: December 31, 2023
Project Funding: $6,250,000 DOE share: $5,000,000 Non-DOE share: $1,250,000

Project Introduction

This project presents a comprehensive approach to develop low-cost state-of-the art electric drivetrain system enabled by a comprehensive list of novel technologies which will lead to a rare-earth-free system at high DC bus voltage (700–800V) while meeting or exceeding the DOE targets of $7/kW and 12 kW/L and leapfrogging the state-of-the art. At the end of the project a full system will be designed, built, integrated and fully tested.

Objectives

The project brings together a group of organizations and experts with proven track record of technology developed and continuous research in the area of transportation electrification with special focus on electric and hybrid drivetrains for light-duty vehicle. The project team includes Marquette University (MU), Niron Magnetics Inc., Virginia Tech (VT), National Renewable Energy Lab (NREL), and General Motors (GM). MU will lead the overall effort as well as the development of the rare-earth free traction motor. Niron Magnetics will lead the development of the rare-earth free Iron Nitride (FeN) permanent magnets. VT will lead the development of the low-cost inverter. NREL will lead the development of the thermal management system (TMS) including system integration concepts. GM will lead the system integration and testing as well as oversee the overall effort to ensure that the developed technologies can feed into their future electric drivetrains. The baseline system that will be used in the project is the Chevy Bolt

Approach

- Budget Period (BP) 1: [Concepts development and tradeoff studies]:
    - Develop concepts, performing tradeoff studies of the various concepts and down-selecting concepts.
- Budget Period 2: [Detailed design, sub-component/component testing and risk retirement]:
    - Develop a detailed design, conduct design optimization, and conduct sub-component/component testing.
- Budget Period 3: [System integration and verification testing]:
    - Procure components, conduct system integration, and perform verification testing.

Results

Traction Motor Development

Developed a finite element analysis (FEA) model for the Chevy Bolt traction motor and performed electromagnetic analysis to quantify the torque-speed curve (Figure I.2.3.1) and efficiency map (Figure I.2.3.2) among other performance parameters. Refined the loss analysis for the Bolt motor. The results shown in Figure I.2.3.1 and Figure I.2.3.2 were performed in MotorCAD. An ANSYS FEA model has been also developed and the effect of end windings is taken into consideration and a comparison between the MotorCAD and ANSYS results is being performed to finalize the baseline performance in ANSYS which will be used for the optimization of the newly developed hybrid designs.

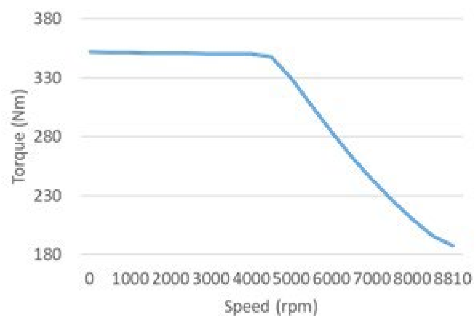

Figure I.2.3.1 Chevy Bolt traction motor torque-speed curve

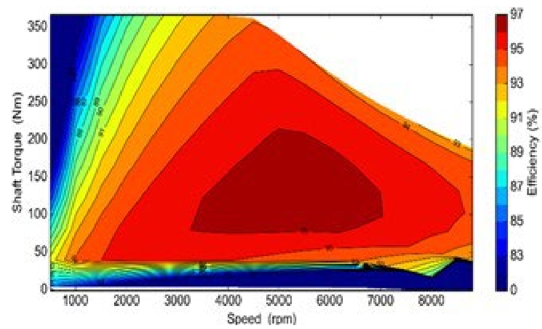

Figure I.2.3.2 Chevy Bolt traction motor efficiency map

Modified an optimization tool to develop new hybrid designs that reduce rare-earth content by combining ferrites and NdFeB permanent magnets.

Developed preliminary hybrid traction motor design. Figure I.2.3.3 shoes a sample of the differential evolution optimization results as well as the cross section of the optimum design that combines ferrites and NdFeB permanent magnets. Figure I.2.3.4 shows the demagnetization check of the optimum design at -20°C and 150°C. The optimum design produces the same average torque as the baseline Chevy Bolt motor while achieving ~40% reduction in NdFeB content with almost no risk of permanent demagnetization. Figure I.2.3.5 shows mechanical FEA results of the optimum design. All stresses are below the 350 MPa yield strength of the rotor lamination material.

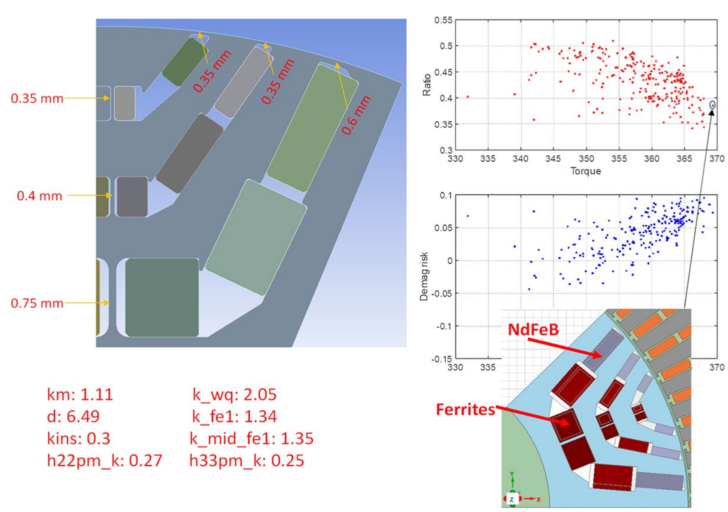

Figure I.2.3.3 Sample of optimization results and cross section of the optimum design that combines ferrites and NdFeB permanent magnets

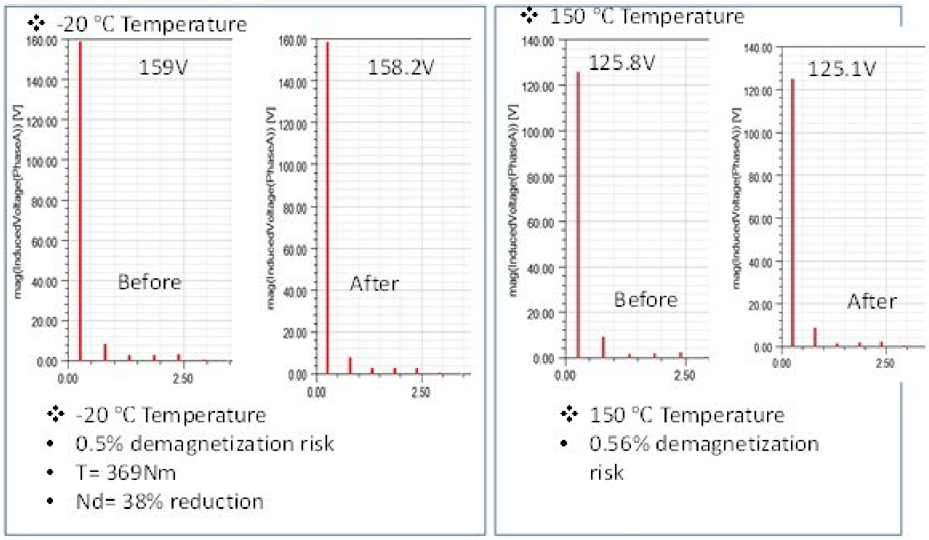

Figure I.2.3.4 Demagnetization check of optimum design at -20°C and 150°C

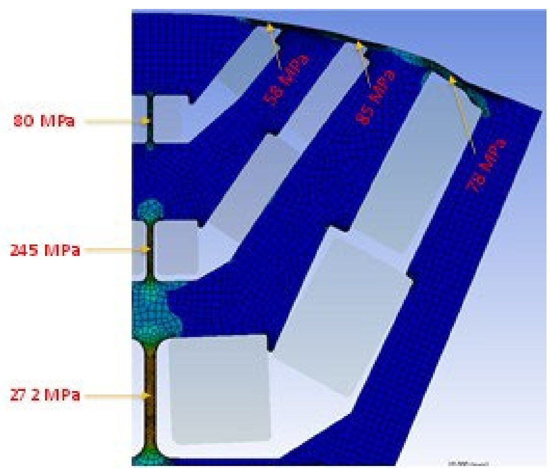

Figure I.2.3.5 Mechanical FEA results of the optimum design

Low-Cost Inverter Development

Powertrain Specifications

In this project, CPES is mainly focusing on traction inverter in the entire powertrain system. By taking the Chevy BOLT as our benchmark, the basic specifications of both benchmark and proposed traction inverter are presented in Table I.2.3.1.

Table I.2.3.1 Specifications of Traction Inverters

System	Chevy BOLT	Proposed Inverter
Maximum Power Rating (kW)	150	200
DC Bus Nominal Voltage (V)	360	800
Phase Current (Arms)	184 (Continuous)	≈300 (Continuous)
Efficiency (%)	98	≥98.5
Inverter Cost ($)	≈$4.667/kW	≤ $3.5/kW
Switching Frequency (kHz)	≈8~15	≥ 20

Inverter Topology Selection

Based on the specifications from Table I.2.3.1, several topology candidates have been considered and analyzed, including conventional two-level inverter, soft-switching inverter (both topologies and current control techniques), and three-level inverter (T-type, ANPC, Flying capacitor), as show in Figure I.2.3.6. Based on the efficiency map of all topology candidates, the soft-switching inverters only have 0.1%~0.3% higher efficiency than 3L T-type and conventional 2L. Moreover, the losses from auxiliary components in soft-switching topologies and stability issue haven't considered yet which may lead to an even lower efficiency. Comparing 3L-T-type and conventional 2L, 3L-T-type requires 12 more power devices in order to have a 0.1% higher efficiency than 2L. Also, when operating under 20kHz, the required DC capacitor for T-type is much higher than that for 2L. Eventually, from the aspect of efficiency, stability, number of power devices, and DC capacitor size, the conventional two-level (2L) hard-switching inverter is selected as inverter topology.

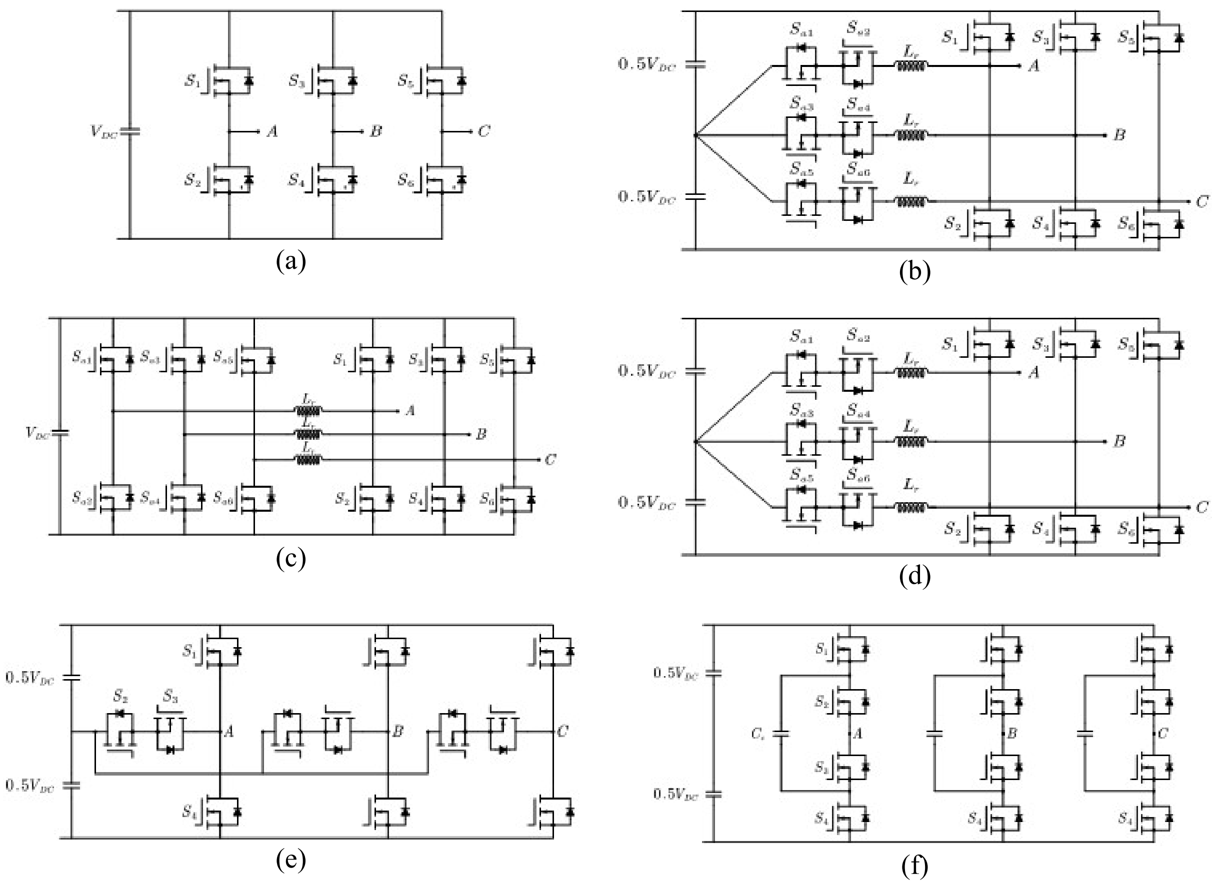

Figure I.2.3.6 The considered topology candidates of (a) conventional 2-level, (b) ARCP soft-switching, (c) ARCP variant soft-switching, (d) 3-level NPC, (e) 3-level T-type, and (f) 3-level Flying Capacitor.

Current Progress of Designed Inverter – Through-hole Device design (Version1)

The traction inverter will be designed into two versions, which are (Version 1) using discrete through-hole SiC MOSFET and (Version 2) using advanced embedded PCB technology. The purpose is to compare the performance and analyze tradeoff between two different versions. For the Version 1, power devices will be paralleled to handle the high phase current. The power device candidates are compared from original 50+ commercial products and final candidates with their key specs are listed in Table I.2.3.2.

Table I.2.3.2 Power Device Candidates

	NTH4L020N120SC1	UF3SC120009K4S	MSC017SMA120B4
Candidates			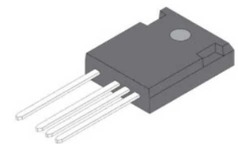
Manufacturer	ON Semiconductor	UnitedSiC	Microsemi
Package	TO-247-4L	TO-247-4L	TO-247-4L
Rated Voltage (*V*)	1200	1200	1200
Rated Current (*A*)	102	120	113
$R_{DS,on}$ $(m\Omega)$	20	9	17
$R_{\theta,JC}(^{\circ}\mathrm{C}/_{W})$	0.3	0.15	0.22

In order to design an inverter with better performances for paralleled discrete devices, the PCB layout comparison is important and necessary to understand the tradeoff between different layout design. The comparison will include the aspect of parasitic components, current sharing, transient performance, thermal, and footprint area. The PCB layout comparison is still ongoing, and the conclusion will be provided soon.

On the other hand, the overall architecture of gate driver design for Version 1 is completed. The selected gate driver IC is *UCC21750-Q1* from *Texas Instruments*. The gate driver board will include the power supply, gate driver, current booster, current sensor, and auxiliary circuits for above-mentioned components. The gate driver will integrate with power stage once the PCB comparison is completed.

Embedded PCB design (Version2)

To achieve a higher inverter efficiency, we propose the usage of 900V SiC MOSFETs for 800V automotive traction inverter applications. The usage of 900V SiC MOSFETs requires a low inductance current commutation loop design, to not surpass the MOSFET's breakdown voltage during switching transients. The proposed phase leg design combines discrete power semiconductors and the DC-link capacitor on one printed circuit board (PCB). This design approach enables a small current commutation loop.

Three PCB technologies: copper inlay PCB, ceramic inlay PCB and embedded dies within the PCB were considered for the inverter buildup. Finite element simulations were conducted. The copper inlay PCB and the ceramic inlay PCB technology were found not suited for the inverter buildup due to poor thermal conductivity and insufficient high current capabilities respectively. The embedded PCB enables a low inductance design with a current commutation loop inductance of approx. 0.7nH. Additionally, the technology enables double sided cooling. Resulting in a junction to heatsink thermal resistance smaller than $0.5\frac{K}{W}$. This allows for higher losses per device. Thus, decreasing the number of required paralleled MOSFETs for the given power rating.

The first version of the embedded PCB design is currently in development. The idea is to design an inverter phase design, with paralleled individual half bridges. This design approach allows for an inverter design that is scalable to the required power rating. Figure I.2.3.7 depicts the modular half bridge with adjacent DC-link capacitor. Figure I.2.3.8 shows the PCB cross-section with the embedded die sintered to a copper lead frame.

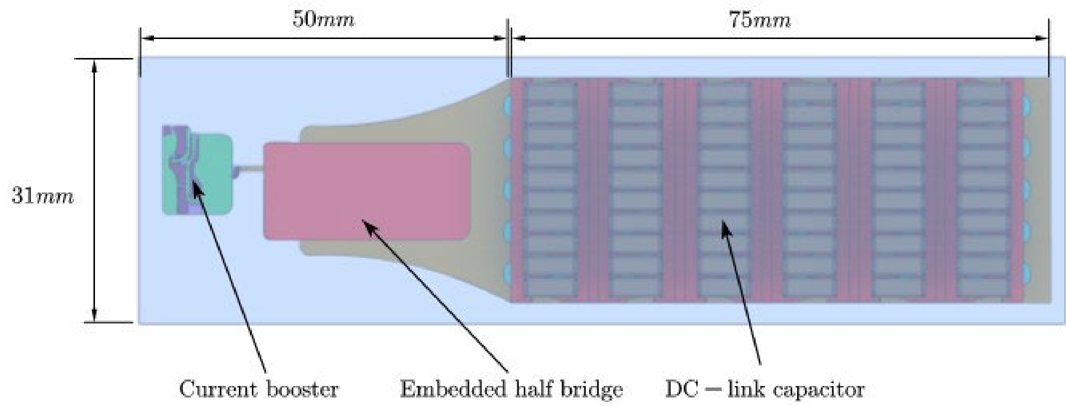

Figure I.2.3.7 Top view of half bridge design with embedded 900V SiC. MOSFETs

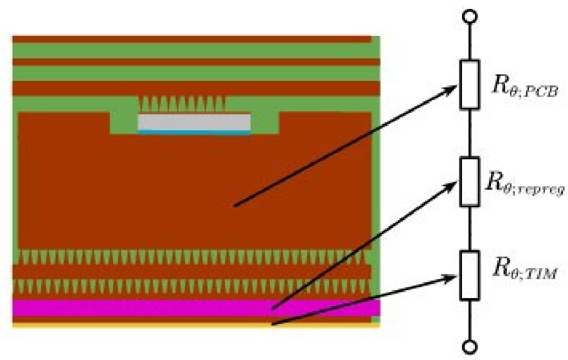

Figure I.2.3.8 Cross-section of embedded die with resulting thermal resistance path

Iron Nitride Magnet Development

The first technical achievement was selection of a candidate material for the ductile coating needed to enable high shear consolidation of iron nitride nanoparticles. After a literature review, appropriate precursor chemicals were identified for the desired coating. Processing parameters were developed for deposition of the coating on the iron nitride nanoparticles.

The coated nanoparticle production method was demonstrated by producing three samples of coated iron nitride nanoparticles. Each sample consisted of approximately 1.3 gram of nanoparticles. The iron nitride samples were made by reducing, nitriding, and coating iron oxide nanoparticle starting materials. Each of the three runs had slightly different deposition conditions. This was done to tune the deposition to deposit a uniform, stable coating on the surface of the nanoparticles.

ICP-OES analysis (Inductively-Coupled-Plasma Optical Emission Spectroscopy) analyses were performed on two of the three samples to verify the deposition of the coating. Additionally, the coating was directly observed using TEM (Transmission Electron Microscopy). TEM is able to measure both the thickness and uniformity of the coating. Figure I.2.3.9 is a high magnification images of the coated iron nitride nanoparticles. The images show a change in contrast near the surface of the nanoparticles. Elemental maps show that the cores of the nanoparticles contain Fe, and that the nanoparticle surface have a uniform layer that contains the desired coating composition. These images confirm that the nanoparticles are coated with a uniform layer that is approximately 3 nm thick. In the latest quarter, a larger-scale (70 gram) batch of coated iron nitride nanoparticle was produced for planned extrusion consolidation experiments.

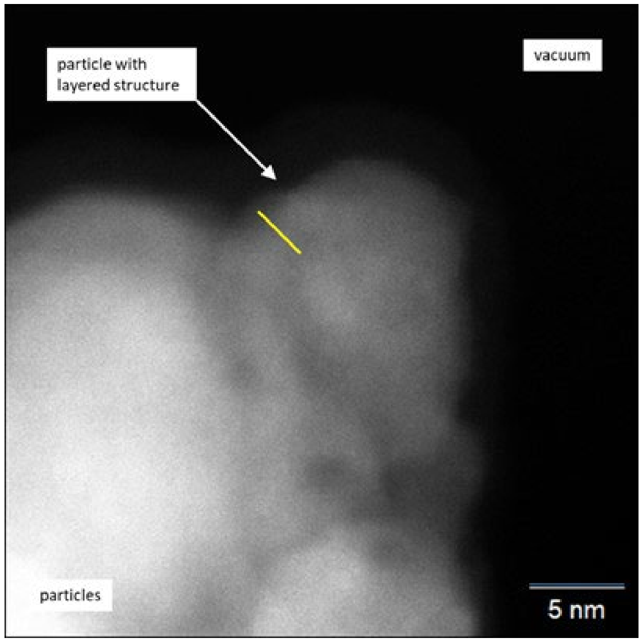

Figure I.2.3.9 High magnification STEM ADF image of conglomeration of coated iron nitride nanoparticles.

Planned consolidation experiments were delayed pending a reassessment of the magnetic alignment method to be used to magnetically align the nanoparticles prior to consolidation. Plans have been developed to use stress in addition to magnetic field to align the magnetic nanoparticles prior to consolidation. Demonstration samples with low nanoparticle volume fraction are currently being made. Once the alignment method has been demonstrated work will resume on producing consolidated samples with high volume fraction.

Thermal Management Development

During FY 2021, NREL efforts focused on developing baseline thermal models for the selected electric machine and inverter. Technical progress included preparing the 3D computer aided design (CAD) geometry of the electric machine (Figure I.2.3.10 and Figure I.2.3.11) and inverter (Figure I.2.3.12). The developed CAD models were integrated into finite element analysis (FEA) thermal modeling tools using reference material information and thermal interface property estimates. For the electric machine, NREL performed parameter sensitivity studies on boundary conditions to improve confidence in the FEA thermal model and validate the model to the extent possible with available literature data. For the inverter, NREL completed initial thermal simulations of the inverter power module using loss estimates (heat loads) from Virginia Tech at two operating switching frequencies (10kHz and 15 kHz). The performance data and learnings from the baseline electric machine and inverter simulations will be used in future work for evaluating the thermal performance of the new component designs developed by project team members.

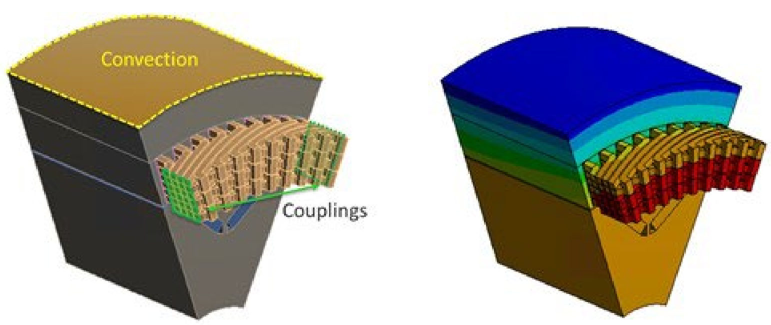

Figure I.2.3.10 Preliminary baseline thermal model comparing impact of sample boundary conditions (left) with case cooling and coupled end winding for accurate heat flow and resulting temperature profile (right).

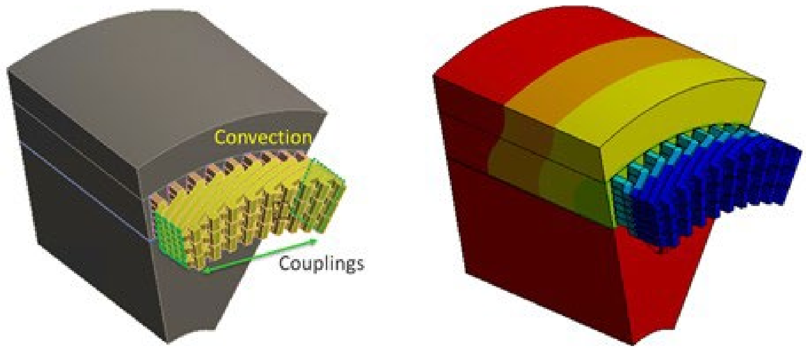

Figure I.2.3.11 Preliminary baseline thermal model comparing impact of sample boundary conditions (left) with end-winding cooling and coupled end winding for accurate heat flow and resulting temperature profile (right).

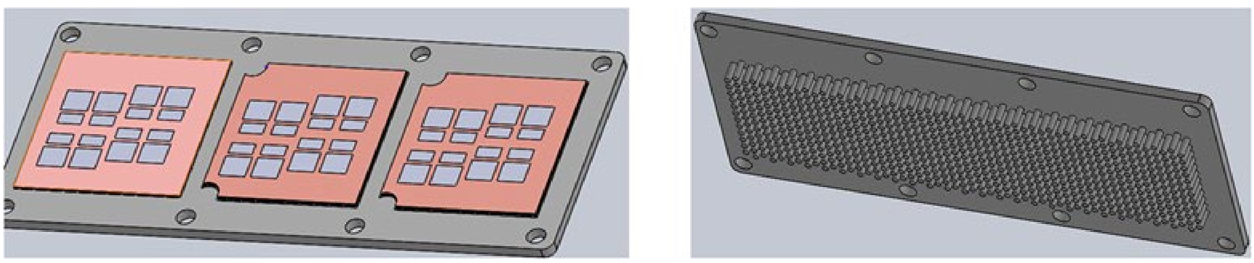

Figure I.2.3.12 Preliminary model for baseline power module thermal analysis (left). Preliminary model for baseline heat exchanger performance comparisons (right).

Conclusions

Technical achievements by Marquette University (MU) include the following:

- Benchmarking the baseline Chevy Bolt traction motor.
- Developed preliminary hybrid designs including NdFeB and ferrite permanent magnets. Preliminary results indicate that the hybrid designs can produce the same average torque as the Chevy Bolt motor with ~40% reduction in NdfeB magnets and with almost no risk of permanent demagnetization either at the minimum operating temperature of -20°C or at the maximum operating temperature of 150°C.
- Developed mechanical FEA models to assess the rotor integrity of the hybrid designs rotor integrity.

Technical achievements by Virginia Tech (VT) include the following:

- A total of 42 discrete SiC. MOSFETs. were selected as potential candidates as the inverter's main power switch. Further analysis was performed and a group of 6 devices have been down-selected for further investigation.
- PCB technologies were compared based on their capability to allow the integration of busbars, power devices, and logic into one PCB. The first PCB manufacturer contacted only offers embedded PCBs for low voltage applications. Talks are started with a second supplier regarding the feasibility of embedding SiC. MOSFET dies into the PCB.
- The study for DC-Link capacitors is conducted. Based on the previous survey of traction inverters it is obvious that the DC-link capacitor occupies a large portion of the total volume of the inverter. Therefore, the purpose of this study is to assess the required capacitance and commercial options in order to shrink the size of the DC-link capacitor. Two potential capacitors have been identified and compared.

- Different soft-switching techniques for two-level inverter are studied and compared. The studied techniques include auxiliary resonant circuits and current control techniques. The purpose of this study is to understand is it worth using soft-switching techniques for SiC-based inverter since SiC device can be operated at high switching frequency and has lower loss when compared to conventional-used IGBT devices
- The topology of the traction drive inverter is selected. Since the topologies of two-level voltage source inverters (2LVSI).ARCP inverters with soft-switching techniques, and the three-level inverter topologies have been evaluated. The comparison of topologies is provided from different aspects of performance. Based on the selected topology, the hardware design of the inverter is also provided.

Technical achievements by Niron Magnetics include the following:

- Selection of ZnO as the candidate material for the ductile coating needed to enable high shear consolidation of iron nitride nanoparticles
- Synthesis of iron nitride nanoparticles coated with ZnO.
- Verification of Zinc deposition via chemical analysis.
- Imaging of Zinc oxide coated nanoparticles by TEM
- Verification of air stability of ZnO coated nanoparticles through air exposure tests
- Production of uniaxially compacted samples of ZnO-coated nanoparticles
- Processing of a large (70 gram) batch of ZnO-coated iron nitride nanoparticles.
- Imaging of the ZnO coating on the surface of an iron nitride nanoparticle by Transmission Electron Microscopy
- Refocus of consolidation effort to avoid potential issue with pre-alignment of nanoparticles by development of stress-assisted magnetic alignment.

Technical achievements by NREL include the following:

- NREL developed 3D CAD and thermal finite element analysis (FEA) model for the baseline electric machine.
    - Developed CAD model with fully resolved hairpin end windings.
    - Developed steady-state thermal model to compare alternative boundary conditions.
    - Evaluated FEA model using refined losses
    - Performed parameter sensitivity study
- Identified representative inverter power module for baseline comparison.
    - Gathered representative power module information for 3D CAD model and material information.
    - Initiated work to develop FEA thermal models and baseline heat loads.
- NREL developed 3D CAD model and developed FEA thermal model for Infineon IGBT power module for baseline comparison.

- Developed models and performed initial simulations with loss estimates provided by Virginia Tech at two operating switching frequencies.

Acknowledgements

The project team would like to acknowledge the help and support from Mr. John Tabacchi, the NETL program manager.

I.2.4 Motor with Advanced Concepts for High Power Density and Integrated Cooling for Efficiency (Raytheon Technologies Research Center)

Dr. Jagadeesh Tangudu, Principal Investigator
Raytheon Technologies Research Center
411 Silver Lane
East Hartford, CT 06108
Email: jagadeesh.tangudu@rtx.com

Susan Rogers, DOE Technology Development Manager
U.S. Department of Energy
Email: susan.rogers@ee.doe.gov

Start Date: October 1, 2019 End Date: June 30, 2022
Project Funding (FY21): $599,611 DOE share: $479,689 Non-DOE share: $119,922

Project Introduction

Raytheon Technologies Research Center (RTRC) is the central research and development (R&D) organization for Raytheon Technologies Corporation (RTX), and has extensive expertise in the design, modeling and analysis of high-performance electrical machines and thermal management for all its business units. The proposing team consists of researchers from RTRC and John Deere (JD), will be referred as "Team". Each organization a has long track record of successful R&D of materials, manufacturing, components, and systems for energy efficiency applications. Motor power density and efficiency are limited by fundamental physical trade-offs between electromagnetics, thermal management, and structural design considerations. The team is proposing to utilize novel technologies and multi-physics design methods to develop a Motor with Advanced Concepts for High power density and INtegrated cooling for Efficiency (MACHINE), demonstrating an 8X improvement in power density.

Objectives

The objective of the project is to demonstrate a high speed (>20,000 RPM) electrical machine using non-heavy rare earth hard magnets, high Silicon soft magnetic steel, and embedded in-slot cooling. To achieve this goal, as part of this seedling effort, the proposed plan to address three key aspects with specific objectives towards meeting the target requirements, a) *Motor design:* Preliminary electromagnetic design meeting target performance metrics. This includes motor design studies to identify key machine parameters such as machine topology, operating speeds, material selection, number of poles, and current density. These parameters are optimized based on optimal magnetic loading, electric loading, airgap shear stress, and heat removal capacity of the select cooling mechanism; b) *Thermal Management:* The thermal management task includes identifying the appropriate materials, manufacturing methods and quantifies effective heat removal capacity for a select flow rate and pressure drop. This shall provide inputs to the motor design tasks in terms of maximum heat loads and achievable current density, and thereby contribute to the target power density; and c) *Build a sectional prototype:* Since this is a seedling effort, the team proposes to build a sectional prototype (3-4 slots) with concentrated winding and in-slot cooling. Heat load is generated by exciting the coils with current at a given current density and quantify the heat removal capacity of the thermal management solution by measuring the inlet and outlet temperatures.

Approach

Permanent magnet machines are proven to have high power density and efficiency. There mainly two types of permanent magnet machines: concentrated windings and distributed, which will both be explored. State-of-the-art motor drives impose a frequency limit, which sets the allowable maximum speed the motor can possibly achieve. Thus, the maximum frequency limit of the drive is proposed to use here. The main difference between the two topologies is that the windings are wound around a tooth for concentrated windings while the other spans a certain number of teeth to make a return. The cooling channels are placed in the slot with the windings to effectively cool the copper in a slot. The two design approaches will be optimized so that their best achievable performance can be compared, and a final design will be down-selected from the optimization results.

Direct cooling of the stator windings provides temperature and power density benefits over conventional cooling with an outer jacket. To accomplish direct winding cooling, ceramic channels are inserted into slim rectangular openings between adjacent windings. These channels have multiple small openings for flowing cooling fluid. A conformal header distributes flow to the cooling channels and collects the flow at the opposite end of the stack. The header is designed using topology optimization to be low loss and achieve uniform distribution of the flow to each channel in a compact space.

Results

The team has performed detailed modeling and analyses to verify the volumetric power density and efficiency of the final selected design. The simulated flux density, flux linkage, and the resulting torque production of the machine is shown in Figure I.2.4.1. The team also verified the magnet operating points under various fault current conditions and concluded that the magnets are safe to use without experiencing any permanent demagnetization. This verification is important since the chosen low dysprosium (< 0.5 Dy) magnets can be easily demagnetized at elevated operating temperature and the team has thickened the magnets deliberately to prevent this to happen. The team also computed the losses including the windage loss. The motor design still achieves 96.3% and 95.9% efficiency at the rated and the peak load condition, respectively. The overall performance metrics are given in Figure I.2.4.2. The cost was estimated to be $6.3/kW if a mass production can be considered. The operating temperature is not so high, and it can improve the reliability/life of the machine. In summary, the final design meets all the design metrics.

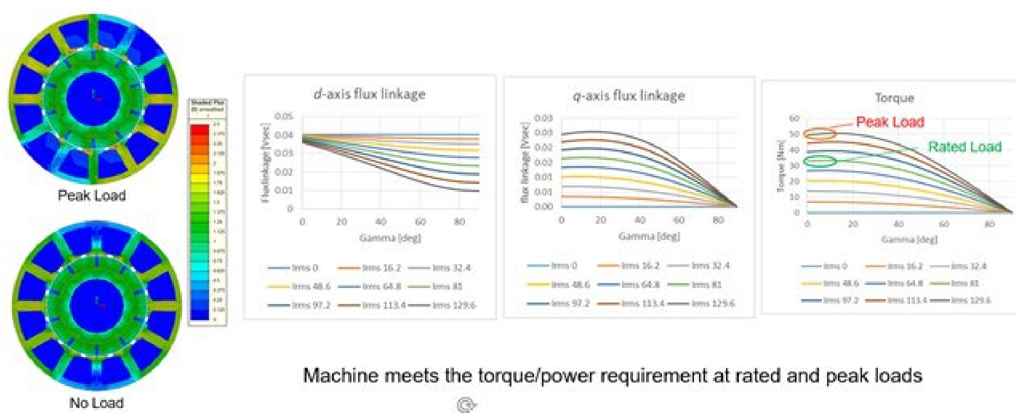

Figure I.2.4.1 Flux density distribution, flux linkage of the coil, and torque per amp characteristics (gamma is the current angle with zero degree aligned to *q*-axis and 90 degrees aligned to *d*-axis.

Specifications	SOA	Target Metrics	Current Design
Power Density (kW/L)	5.7	≥ 50	50.3
Cost ($/kW)	4.7	≤ 6	~6.3*
Life (-)	1X	≥ 2X	TBD
Peak Power (kW)	55	125	125
Max Speed (RPM)	2,800	≥ 20,000	20,000
DC Bus Voltage (V)	325	700	700
Volume (L)	25-35	≤ 2.5	2.485

Figure I.2.4.2 Summary of design metrics achieved in the final design against SOA

Stator and rotor cooling designs

Direct winding cooling in the stator can provide temperature and power density benefits over jacket cooling. The in-slot cooling concept has been refined to provide further benefit. An enhancement on the slot cooling is the "t" channel shown for section of the stator in Figure I.2.4.3. The cooling channels are feasible to be printed in aluminum nitride, which provides electrical insulation to the coolant while having high thermal conductivity for heat dissipation. The heat generated in the rotor is significantly less than that in the stator, but the maximum allowable temperature is also much lower, as is limited by the de-magnetization limit of the magnets. Due to the relative temperatures, convection though the air gap from the rotor to the stator is not a viable path for cooling. A conceptual cooling scheme using forced air has been developed. The temperature plot shown in Figure I.2.4.3(c) is the result of a model with air directed over the rotor top, through the rotor-stator gap, and over the bottom end. The air would be driven using a centrifugal impeller mounted to the top of the rotor below the profile of the windings. The axial air flow through the gap will also provide some cooling benefit to the stator.

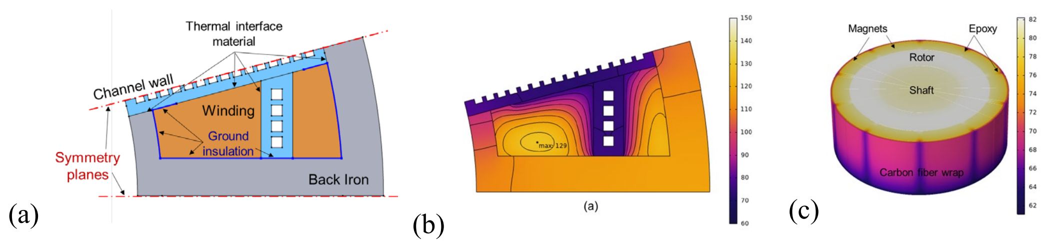

Figure I.2.4.3 (a) Domain used for the thermal model with t-shaped channel section. (b) Temperatures (°C) in the stator. (c) Temperatures (°C) in the rotor.

Assembly and header design

As strategies to route the flow, the team explored two approaches: (1) a topology optimized conformal flow header and (2) individual connector inlets to each channel. While both options are viable, the team down-selected to move forward with path (2) to take advantage of the available space between the windings created by the t-shaped cooling channels. The team considered a flow configuration with tubing and individual connectors between the tubing and flow channels, such as that shown in Figure I.2.4.4. The purpose was to balance the factors of power density and ease of manufacturability compared with the more advanced customized header concept. The configuration with two parallel flow paths emerged as the ideal configuration for this motor thermal management strategy.

	All parallel tube paths	**Two parallel tube paths**	**All series tube paths**
Pressure drop	0.09 psi	3.23 psi	24.6 psi
Pumping power	0.09 W	1.80 W	14.2 W
Total power density	51.6 kW/L	53.2 kW/L	53.3 kW/L
Note	--	Selected	--

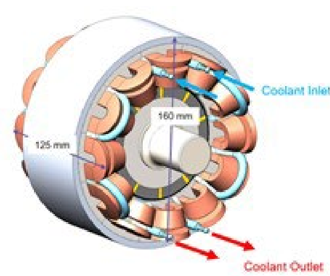

Figure I.2.4.4 Various configurations of flow supply to the cooling channels.

Sectional prototype

A sectional test prototype was designed for testing, as shown in Figure I.2.4.5, which includes two winding slots and three cooling channels. Four heaters will be embedded into the stator to mimic the heating occurring in the stator and the windings. During testing, the middle channel will be the primary area to gather data. The two outer channels serve the purpose of applying the proper boundary conditions around the windings. Water/glycol coolant will be pumped in a fluid loop evenly to the three channels. In the fluid, both temperature and pressure will be measured at the inlet and outlet of the middle channels. In the sectional prototype, temperatures will be measured at various locations within the windings and on the outside of the middle cooling channel. A fixture holds the test piece was designed, along with the main steps in the assembly process. The assembly process includes the following steps: (1) Insert 2 coil assemblies and stator laminations into the frame, (2) insert the cooling channels, and (3) clamp the plenum/headers to the end of the cores. The flow headers will be connected to fluid ports, leading a chiller and a flow meter, as well as temperature and pressure measurement instrumentation for the coolant.

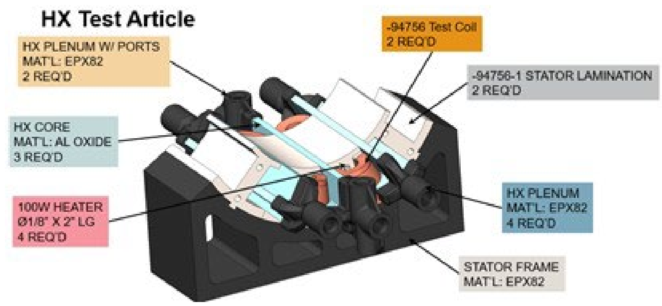

Figure I.2.4.5 Sectional prototype test assembly with integrated fixture.

Structural Analysis

Structural analysis was carried out on the final design that was down-selected from a set of deigns satisfying electromagnetic, thermal, and structural constraints. The magnet is bonded only to the carbon fiber (CF) wrap which is a conservative approach to design the CF wrap. At 20% overspeed, the maximum hoop stress in the CF wrap is ~1000 MPa which is below the design stress of 1226 MPa (considering a factor of safety of 2.25), see Figure I.2.4.6. This analysis suggests that an initial pretension of >1000 MPa in CF wrap can help overcome the effect of centrifugal forces and keep magnets in contact with the rotor-wheel throughout their operation.

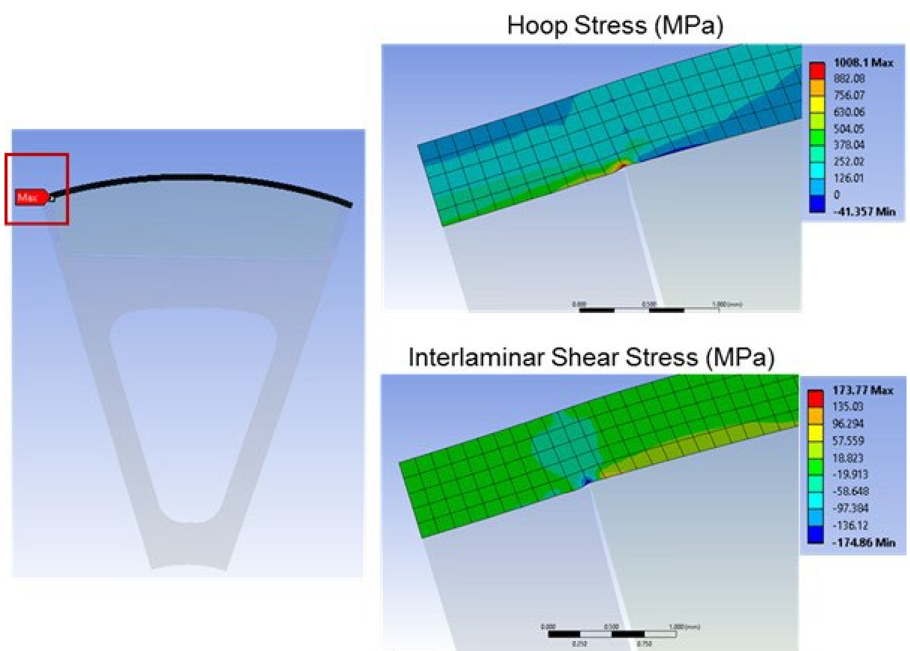

Figure I.2.4.6 FE analysis results showing areas of maximum hoop and inter laminar shear stress

Rotor Dynamic Analysis

Apart from making sure that the CF wrap meets functional requirements with enough factor of safety, it is important to look at the rotor dynamics of the shaft to make sure that the operating speed of the motor and the critical speed of the shaft do not interfere. Critical speed obtained from the rotor dynamic analysis of the shaft (see Figure I.2.4.7) for typical ball bearing stiffness values are presented in Table I.2.4.1. The first 3 critical speeds associated with the shaft are far away from the operating speed of the motor of 8000 RPM.

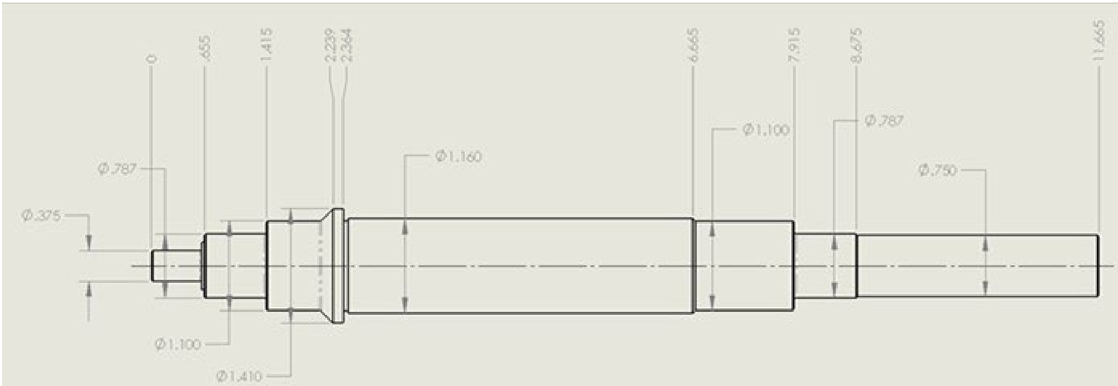

Figure I.2.4.7 Cross section of the shaft

Table I.2.4.1 Critical Speed of the shaft for various ball bearing stiffness

	Bearing Stiffness (lb-f/in)		Critical Speeds (RMP)		
	BRG1	BRG2	1st	2nd	3rd
Typical Ball Bearing Stiffness	2000	2000	2816	6802	66990
	100000	100000	16760	44090	74700
	250000	250000	21870	60530	85500
	500000	500000	24880	69900	99590
	100000	100000	26880	75750	114900
	5000000	5000000	28810	81510	136000
	10000000	10000000	29070	82340	139500

Conclusions

This project has completed preliminary design during phase-1 and currently meets proposed target metrics. MACHINE preliminary design currently meets the power density of 50.3 kW/L (goal of > 50 kW/l), slightly lower than the target cost and is currently at 6.3 $/kW (goal < 6 $/kW), along with a life of 1.95X (Target = 2X).

Key Publications

1. Z. S. Du and J. Tangudu, "High Speed Permanent Magnet Machine Design for Optimum Volumetric Power Density," 2021 IEEE Energy Conversion Congress and Exposition (ECCE), 2021, pp. 4546–4553, doi: 10.1109/ECCE47101.2021.9595044.

References

1. T. A. Lipo, Introduction to AC Machine Design, Wisconsin Power Electronics Research Center, Wisconsin, 2004

Acknowledgements

Acknowledgment: "This material is based upon work supported by the U.S. Department of Energy's Office of Energy Efficiency and Renewable Energy (EERE) under the Vehicle Technologies Program Office Award Number DE-EE0008867."

RTRC Team: Stephen Du, Kenji Homma, Kimberly Saviers, Joe Turney, Bob Dold, Brij Singh (John Deere), Jagadeesh Tangudu (PI)

NETL Manager: Jonathan Kung, Carla Winaught

I.2.5 Low Cost High-Performance HRE-Free 3-in-1 Electric Drive Unit (American Axle & Manufacturing)

Mr. David Crecelius, Principal Investigator
American Axle & Manufacturing
One Dauch Drive
Detroit, MI 48211
Email: David.Crecelius@aam.com

Steven Boyd, DOE Program Manager
U.S. Department of Energy
Email: steven.boyd@ee.doe.gov

Start Date: October 1, 2020 End Date: December 31, 2023
Project Funding: $6,250,000 DOE share: $5,000,000 Non-DOE share: $1,250,000

Project Introduction

The project team will expand upon American Axle & Manufacturing's (AAM) baseline technology and develop a high-speed, AC induction electric drive unit (EDU) with total direct-oil-cooling and integrated power electronics. The project will accelerate advancements in EDU technology by allowing AAM to build upon the progress made in developing the underlying baseline technologies. AAM proposes the following seven improvements to its baseline technology to be implemented in this research and development program: 1) Increased speed (30k RPM) AC induction motor, 2) Silver-sintering of discrete silicon carbide (SiC) metal-oxide-semiconductor field-effect transistors (MOSFET) to heat sinks, 3) Electrically insulated rotor bars, 4) Optimized lamination steel, 5) EDU-integrated 650VDC inverter package, 6) Over-molded stator with molded liners, and 7) 650VDC power-dense stator design.

Successful development of the technology will result in a substantial cost reduction for EDU systems in the market. Coupled with falling battery system costs, this will accelerate the market acceptance and related production scaling of battery electric vehicles.

Objectives

The objective of this project is to research, develop, and test a Heavy Rare Earth (HRE)-free 3-In-1 electric drive unit that has class leading power density and cost. The key technologies to be developed will meet or exceed the Department of Energy (DOE) targets of a cost ≤ $7/kilowatt, power density ≥ 12 kW/liter, and operating voltage ≥ 600 VDC.

Approach

Technology development within the project will build upon and reference against the AAM baseline Gen 5.0 EDU.

The project is being conducted in three (3) phases:

Design Development and Technology Research (Budget Period 1)

- Design, investigate, and develop core technologies
- Investigate stator lamination and over molding development, high speed motor development, and silicon carbide MOSFET packaging development
- Investigate, analyze, and assess costs of the developed technologies
- Select an optimized configuration for prototype build in budget period 2.

Prototype Component Fabrication and Unit Build (Budget Period 2)

- Fabricate over molded stators, high speed motors, and MOSFET silver sintered attachments
- Assemble motor-only units and full EDUs for subsequent dyno testing
- Test the motor-only units on the dyno with the test results being compared to the baseline.

Prototype Testing and Commercialization Planning (Budget Period 3)

- Test the full EDU on the dyno, with the results being compared to the baseline technology
- Document the EDU Bill of Materials (BOM) for comparison to benchmarked EDUs and cost targets
- Prepare a manufacturing and commercialization plan to produce the developed technology in high volume.

Results

Task 1.1 – High Efficiency Stator Development

The baseline electric traction drive system to be used for comparison purposes, and additional benchmarked systems including the Jaguar I-PACE and Tesla Model 3 EDUs, were reviewed. The summarized performance and high-level design cost data is shown in Table I.2.5.1. In addition to the baseline and benchmark units a specification for the HRE-free 3-In-1 EDU, based on the initial design of the high-speed motor, is included.

Table I.2.5.1 EDU Performance Summary and Comparison

PERFORMANCE SUMMARY					
MANUFACTURER	AAM	AAM	AAM	TESLA	
MODEL	I-PACE	Gen 5 Baseline	DOE Target	Model 3	
EDU INTEGRATION	2-in-1	3-in-1	3-in-1	3-in-1	
INVERTER TYPE	Si IGBT	SiC MOSFET	SiC MOSFET	SiC MOSFET	
MOTOR TOPOLOGY	PM	AC Induction	AC Induction	PM	
NOMINAL DC BUS VOLTAGE	350	350	650*	350	Vdc
EDU PEAK POWER	147	155	225	211	kW
MAX OUTPUT TORQUE	3146	3150	4563	3669	Nm (Axle)
EDU MASS	93.4	72	63	91	kg
EDU VOLUME	30.8	23.3	21.6	37.8	L
MOTOR-INVERTER VOLUME	17.1	11.8	10.1	18.8	Estimate
POWER DENSITY (Motor & Inverter)	8.6	13.1	22.3*	11.2	kW/liter
ESTIMATED COST/kW	[redacted]	[redacted]	$6.50*	[redacted]	Target

*These metrics meet the DOE goals

Note that in Table I.2.5.1 the blue highlighted cells in the DOE targeted design column show performance numbers that exceed the DOE program goals.

In developing the preliminary specification for the HRE-free 3-In-1 EDU, the Tesla Model 3 was selected as a donor vehicle platform. By having a vehicle platform identified, the EDU specifications could be developed at the vehicle level and will subsequently allow for vehicle level drive cycle simulations as the new EDU is designed. During the specification development a determination was made to study two different motor types during the budget period 1 analysis phase. One of the motors will be a high-power version and the second motor will be a high torque version. At the end of budget period 1 it will be decided which version will be built and tested during the budget period 2 build and test phase. Table I.2.5.2 shows the summary information for the preliminary HRE-free 3-In-1 EDU specification.

Table I.2.5.2 Vehicle Level EDU Specification

Vehicle Level Specification - HRE Free 3N1 EDU			
Platform/PROGRAM	AAM DOE Design A	AAM DOE Design B	
EDU purpose	Standare Torque, High Pwr	High Torque, Medium Pwr	
Vehicle Donor Application	Model 3	Model 3	
EDU Placement	Front Axle	Rear Axle	
Vehicle Parameters			
TWC	4500	4500	lbs
GVWR	5400	5400	lbs
Max vehicle speed - forward	160.9	160.9	kph
Max vehicle speed - forward	100.0	100.0	mph
Tire	785	785	rev/mi
Radius of tire	0.326	0.326	m
Max grade at GVW (includes Park function)	> 30	> 30	%
Axle type and suspension layout	Independent	Independent	
Drive Unit mechanical parameters			
Peak Torque	144	192	Nm
Max wheel speed	1308	1308	rpm
Max rotor speed	30000	30000	rpm
gear reduction	22.93	22.93	
peak power	180	160	kW
Vmax power	108	96	kW
Peak Torque at axle	3269	4359	Nm
Thrust	2252	3003	lbs
System Design Parameters			
Minimum Operating Voltage @ max discharge	470	470	V DC
Nominal Operating Voltage @ OC	650	650	V DC
Maximum Operating Voltage @ max charge	750	750	V DC
motor winding turns per coil	TBD	TBD	TPC
Max Current	TBD	TBD	A rms
Power requirement at axle vs time			
10 sec	180	160	kW
30 sec	90	80	kW
1800 sec	80	80	kW
3600 sec	80	80	kW
Interfaces			
Coolant Flow	12	12	l/min
Coolant Media	ATF ULV	ATF ULV	
Max Media Temperature	83	83	C
Inverter Integration	Integral	Integral	
Environmental			
Operating Temperature min	-40	-40	deg C
Operating Temperature max	85	85	deg C
Tmax (Soak Back: 30 min)	120	120	deg C
Paint Booth Temperature During Vehicle Repair	95	95	deg C
Altitude for Operation	4572	4572	meter
Altitude Maximum for Transport	13700	13700	meter
Sealing	IP67	IP67	

Stator Over Molding Development

As a summary of the stator over molding tasks, the stator over molding strategy was to investigate and develop over molding for stator slots to replace traditional slot liner paper in one over molding step, and to also investigate and develop stator winding over molding to encapsulate the winding end turns in a second over molding process. Design of the over molded stator winding end turns looks to be favorable and feasible, while the over molding of the stator slot to replace the slot liner paper is proving to be challenging.

Figure I.2.5.1 below shows the intended design of the over molded stator slot liners in a stator stack that is 7" in length. Over molding material is shown to cover the interior of the stator slots with a thickness of .25mm. The molding material replaces the traditional paper slot liner and provides improved thermal characteristics and heat transfer from the copper wire to the lamination steel while maintaining a good dielectric barrier. Although initial studies of material flow showed favorable results the study did not model actual slot fill capability. Subsequent flow simulations began to study the slot fill capability with the mold tool design taken into account. The more accurate mold flow simulation results are showing that the slot fill can only achieve a length of 2" to 3" of the total 7" stator height. The material gating was changed to determine if flow could be improved but minimal additional gains in slot fill length were achieved.

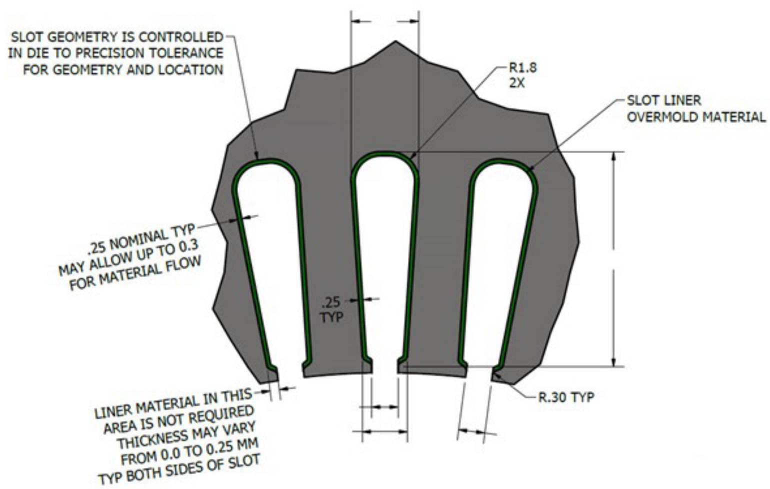

Figure I.2.5.1 Stator slot over mold concept

The full stator and winding over molding design activity has been started, working with the molding supplier. An initial over molding design was created and reviewed for practical implementation into a mold design. Figure I.2.5.2 shows the initial concept that was reviewed. Changes were made to the design to accommodate mold and gating requirements.

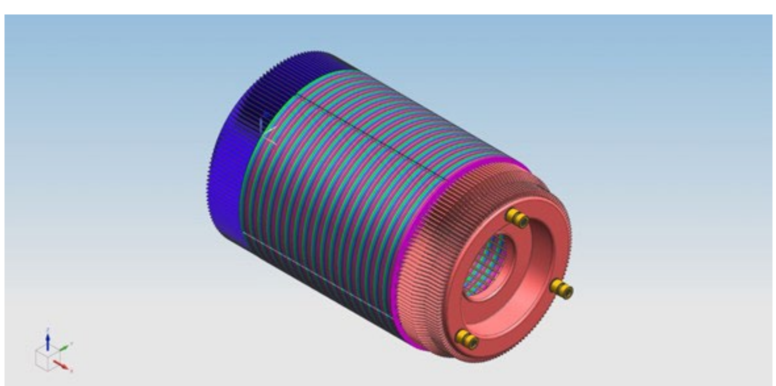

Figure I.2.5.2 Stator winding over mold concept

Task 1.2 – High Speed Induction Motor Development

High Speed Electromagnetic (EM) Design

Many EM designs have been completed during the project, with a total of 47 different designs being reviewed in a final analysis to compare power density, torque density, peak torque, and peak power. The torque and power requirements that were defined in the EDU specification for this project included both the high torque design option and the high-power design option. Table I.2.5.2 has the specification details for the Design A (high power) and Design B (high torque) options.

Based on the comparison analysis of the 47 different motor designs, one motor was selected as the design to move forward with into future builds for the project. Subsequent analysis of thermal performance to identify the continuous and peak areas of operation was started using finite element analysis (FEA). The selected motor, designated motor #12, provided the highest power density while still meeting the EDU specification requirements. Both the high torque and high-power design options were met with this single motor option.

When compared to the baseline design, the selected motor #12 design provides higher power and torque, reduces the phase current requirement, reduces the stator stack length, and has an increased voltage of 650VDC.

With the selection of motor design #12, project milestone 1.2, finishing the EM design of the high-speed induction motor has been completed.

Table I.2.5.3 provides a summary of the baseline design, EDU specifications for Designs A and B, and the selected EM design for motor #12.

Table I.2.5.3 Comparison of Selected Motor Design to Baseline and Specification

Parameter	Units	Baseline Design	Specification Design A	Specification Design B	Selected EM Design
Peak Torque (motor)	Nm	175	144	192	199
Peak Power (motor)	kW	155	180	160	225
Max Motor Speed	RPM	24,000	30,000	30,000	30,000
Gear Reduction Ratio	-	18.00	22.93	22.93	22.93
Vmax Power	kW	140	108	96	132
Peak Torque at Axle	Nm	3150	3302	4403	4563
Peak Phase Current	Arms	450	-	-	350
DC link Voltage	V	350	650	650	650
Power Density (motor only)	kW/L	40.9			67.3
Motor Stack Length	mm	177	-	-	152
Motor Diameter	mm	154	154	154	154
Turns Per Coil	-	3	-	-	5
Parallel Connections	-	4	-	-	4

The selected motor #12 torque – speed – efficiency curve is shown in Figure I.2.5.3.

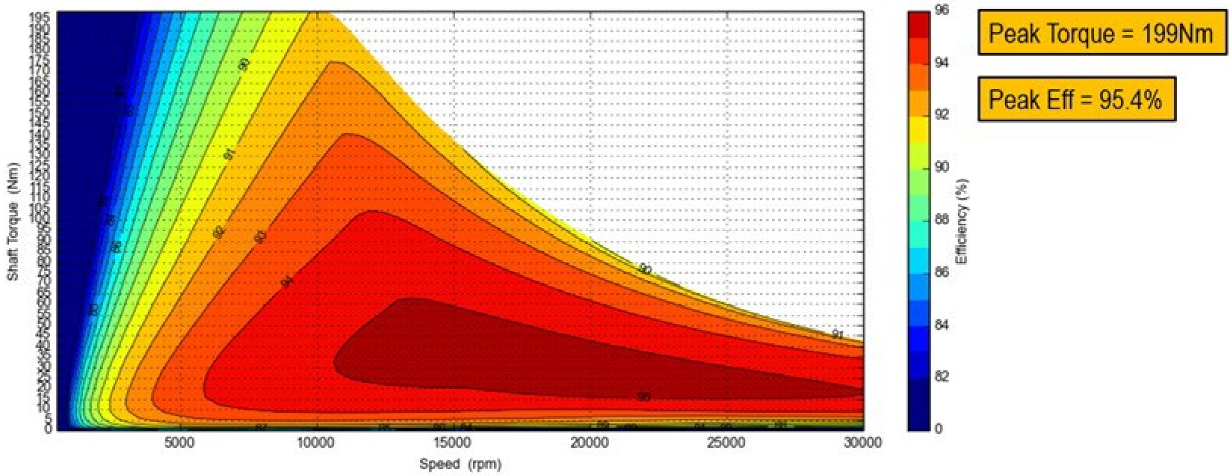

Figure I.2.5.3 Torque/Speed/Efficiency curve for motor #12 design

Task 1.3 – Advanced Packaging & Attachment Development of Discrete SiC MOSFETs

Silver Sintering Discrete Power Devices

Silver sintering of discrete power devices to a copper plate has been initially completed. Sample discrete MOSFETs in a TO-247 package were provided to the silver sintering supplier for initial process investigation and trial sintering of the device onto a copper plate. The MOSFETs were provided to the supplier with the standard tin plating on the backplane removed. Due to the backside metallization on the component, a decision was made to print and bond a small area of the package in order to show feasibility of the process.

The sample parts were assembled in the following manner:

- Sintering paste was printed on the backside of the package
- Package was then located on the copper plate
- The assembly was dried in an inert atmosphere
- The sintering process was accomplished using a Carver press
- A sheet of silicone rubber was placed over the location of the sinter paste to apply pressure only on the joint area
- The press was cycled using initial setting.

A successful sintering attachment appeared to occur, although additional testing and verification of the sintered joint is in process. Figure I.2.5.4 is an image of the TO-247 MOSFET sintered to the copper plate.

Figure I.2.5.4 TO-247 MOSFET Silver Sintered to Copper Plate

Conclusions

During the initial budget period, the project team has expanded upon AAM's baseline technology by designing a high-speed (30k RPM) induction motor (rotor and stator) operating with a 650VDC supply, successfully demonstrating a discrete MOSFET silver sintering attachment process, and developing a stator over molding design for improved thermal performance. It is believed that with the current trajectory of efforts to research, develop, and test a Heavy Rare Earth (HRE)-free 3-In-1 electric drive unit (EDU) that has class leading power density and cost, the project will meet or exceed the Department of Energy (DOE) targets of a cost less than $7/kilowatt, power density of less than 12 kW/liter, and an operating voltage of greater than 600 VDC.

II Grid and Infrastructure

II.1 Industry Awards

II.1.1 Development and Commercialization of Heavy-Duty Battery Electric Trucks Under Diverse Climate Conditions (Daimler Trucks North America LLC)

Marcus Malinosky, Principal Investigator
Daimler Trucks North America LLC
4555 N Channel Avenue
Portland, OR 97217
Email: marcus.malinosky@daimler.com

Lee Slezak, DOE Technology Manager
U.S. Department of Energy
Email: lee.slezak@ee.doe.gov

Start Date: October 1, 2019 End Date: December 31, 2022
Project Funding: $3,520,443 DOE share: $1,629,808 Non-DOE share: $1,890,635

Project Introduction

Daimler Trucks North America LLC (DTNA) is in the process of developing and demonstrating electric Innovation Fleet eCascadia 2.0 to improve cost, reliability, and performance over DTNA's completed heavy-duty electric truck. Improving cost and performance characteristics will address immediate barriers to adoption and support growth for zero-emission truck technologies in freight applications. Range and performance factors can prevent heavy-duty fleets from adopting zero-emission technologies. Support from the Department of Energy (DOE) will allow DTNA to overcome this barrier developing and demonstrating a more fully integrated and capable, commercialized 116" day-cab electric tractor to serve freight and goods movement sectors having a daily travel profile of up to 250 miles.

Meijer and United Parcel Service (UPS) are participating as co-creation fleet partners and South Coast Air Quality Management District (SCAQMD) is providing guidance and expertise on incentives, regulations, and policies as they relate to the market potential for heavy-duty electric trucks. This project will advance state-of-the-art heavy-duty electric truck technologies to full commercialization, and in doing so, provide a platform for the market to reduce fleet operating costs, diesel consumption, and energy costs, as well as significant NOx, PM, and carbon emissions.

Objectives

The objective of the DTNA E-Mobility Group (EMG) Innovation eCascadia 2.0 project is to research, develop, and demonstrate, a fully commercialized Class 7/8 electric tractor with range and durability sufficient to meet the needs of 70% of freight movement in the United States. DTNA completed the design of the prototype eCascadia 1.0 test units in 2019, which were operated by Penske Truck Leasing and NFI Industries throughout Southern California in 2019 and 2020.

This project aims to improve performance over the baseline prototype eCascadia by increasing the range up to 250 miles, increasing the fuel efficiency of 2.0 kWh/mile, increasing the battery capacity up to 550 kWh, reducing the curb weight down to approximately 20,000 lbs., lighter battery packaging, and enhancing the motor design, software, telematics, weatherization, and diagnostic systems customer-designed for electric trucks.

Leveraging the significant investment, experience, and learning from eCascadia 1.0, this proposed project will develop the next generation of this electric truck technology: the eCascadia 2.0, a commercialized electric truck product with significantly improved cost and operational performance capabilities.

Overall Technical Targets

- Develop and bring to market a fully commercialized, all-electric Class 7/8-day cab tractor.
- Increase range capabilities to 250 miles per charge and improve efficiency to achieve 2.0 kWh/mile through a redesigned 500-550 kWh battery back system and ultra-efficient integrated e-Axles.
- Provide a life-cycle cost-effective and zero-emission freight movement solution for more than 70% of use cases.

Approach

The project involves three (3) phases. During Phase 1, the vehicles were developed for real world conditions expected of a Class 7/8 tractor. Vehicle designs were approved by co-creation fleet partners and the B-Sample vehicle assembly was completed during this phase. Performance tests were conducted to validate vehicle design and operational capabilities. These tests will conclude with a ‘market readiness’ demonstration event. In Phase 2, the finalized vehicles will be delivered to fleets for initial deployment and the customer trials will begin. Performance data and records will be continuously captured to assess vehicle performance and durability. Upon receiving certification demonstrating vehicle readiness, DTNA EMG will work with co-creation fleets to develop case study and other promotional materials.

Project Phases

- Phase 1a: Research, Design Building, and Commissioning: Vehicle Design and Specification
- Phase 1b: Research, Design Building, and Commissioning: Commercial Scale Production Model
- Phase 2: Deployment and Demonstration.

DTNA EMG is leveraging global design, engineering, sourcing, and vertically integrated production capabilities to quickly achieve economies of scale and reduce product costs. Through a ‘co-creation’ approach with fleet partners, DTNA EMG will collect operator feedback and determine best practices for continuous improvement. To ensure a successful program, we will review and track the status of the program at the end of each phase. Based on the go/no-go decision points, we will evaluate the progress using the success criteria as shown in the table below. These are general success criteria that are associated with the Milestones as listed in the Milestone Log. Additionally, the Technology Readiness Level (TRL) status of the overall program will be reviewed for progressing from one TRL to the next level.

Technical Strategies

- Reengineer battery structure and develop proprietary design.
- Develop proprietary e-Axle integration.
- Simplify vehicle components and reduce the number of electric motors.
- Consolidate vehicle components and maximize assembly efficiency
- Develop proprietary control software to improve overall power and enable peak performance.
- Vertically integrate design, development, and in-house production of batteries, transmission, and telematics systems.

Results

DTNA EMG completed all Phase 1a and 1b milestones and technical targets during Budget Period 1 and Budget Period 2, respectively. Final assembly of the C-Sample was completed, and both target vehicle metrics and vehicle range targets for the C-Sample build were completed. Both the data list to be collected and analyzed (DVP) and design elements were finalized. The procurement of D-Sample vehicle components was completed, and the D-Sample development supplier selection and tooling supplier selection are in process

The following technical accomplishments and progress have been made:

Daily Software Testing (B and C-Samples)

- Daily testing on-going with B-Sample and C-Sample trucks.
- 'Bugs' being identified and resolved for future software builds.
- Global team works in unison to remove bugs and improve software for next release.

Front Box Shaker (C-Sample design)

- Completed B10 lifetime – 10 years of service mileage.
- Minor structural failures (brackets breaking at welds, incorrect torque, and increased bolt size)
- Components sent back to suppliers for evaluation.
- Changes being implemented for C-Sample durability.

Battery Shaker (C-Sample design)

- Completed B10 lifetime – 10 years of service mileage
- Buck of battery and frame rail installation for component shaker.
- Accelerated testing of higher risk components using RDLA inputs.
- This amount of weight (batteries) has not been supported by our frame rails before.

Summer Test (C-Sample design)

- Completed high temperature testing in Laughlin, Nevada.
- Validated thermal testing conducted in the tunnel.
- Vehicle drove Baker Grade and confirmed regenerative braking (900ft to 4,000ft and back).
- No de-rating occurred due to battery or e-Axle thermal circuits.

Crash Test (C-Sample design)

- Physical crash test conducted on real C-Sample vehicle for high voltage (HV) Shutdown calibration.
- Side impact test conducted.
- Front underrun test conducted.

Phase 2: Deployment and Demonstration is underway and on track to be completed by the end of Budget Period 3.

Table II.1.1.1 Project Milestones

PHASE	DESCRIPTION	STATUS/COMPLETION DATE*
Phase 1a (Budget Period 1)	100% Finalization of Component Specifications	COMPLETE (July 2019)
	Feasibility Analysis of Series Development Confirmed *(Go/No-Go)*	COMPLETE (April 2020)
	Project Implementation Specifications Confirmed	COMPLETE (April 2020)
	Supplier Pre-Selection Confirmed	COMPLETE (June 2020)
	B-Sample Vehicle Specification Targets Achieved *(Go/No-Go)*	COMPLETE (September 2020)
Phase 1b (Budget Period 2)	Target Vehicle Metrics Achieved	COMPLETE (September 2020)
	Final Assembly of Test Vehicles Complete	COMPELTE (June 2021)
	Finalization of Data List to be Completed and Analyzed	COMPLETE (June 2021)
	Finalization of Design Elements	COMPLETE (June 2021)
	C-Sample Vehicle Specification Targets Achieved *(Go/No-Go)*	COMPLETE (June 2021)
Phase 2 (Budget Period 3)	Start of Production Tests / 100% of Parts are Customer Ready	In Progress (November 2021)
	Start of Commercial Series Production	In Progress (January 2022)
	Vehicle Delivery and Demonstration Initiation	June 2022
	Data Evaluation, Measurement, and Verification	December 2022

**Please note that this table reflects completion dates that may be impacted by the ongoing COVID-19 public health crisis.*

The DTNA EMG initiated this project at TRL 4 and will progress to TRL 8 by the end of the project period. The project team characterized the initial technology readiness at TRL 4 because the prototype vehicle was currently on the test bench undergoing validation of high-voltage components on both the battery and e-Axle. The project team also conducted functionality testing in a prototype environment with early B-Sample supplier parts as well as validity and concept design testing of vehicle systems. The project team has advanced to TRL 7 upon the successful build of a C-Sample truck with knowledge of functionality in a real-world environment.

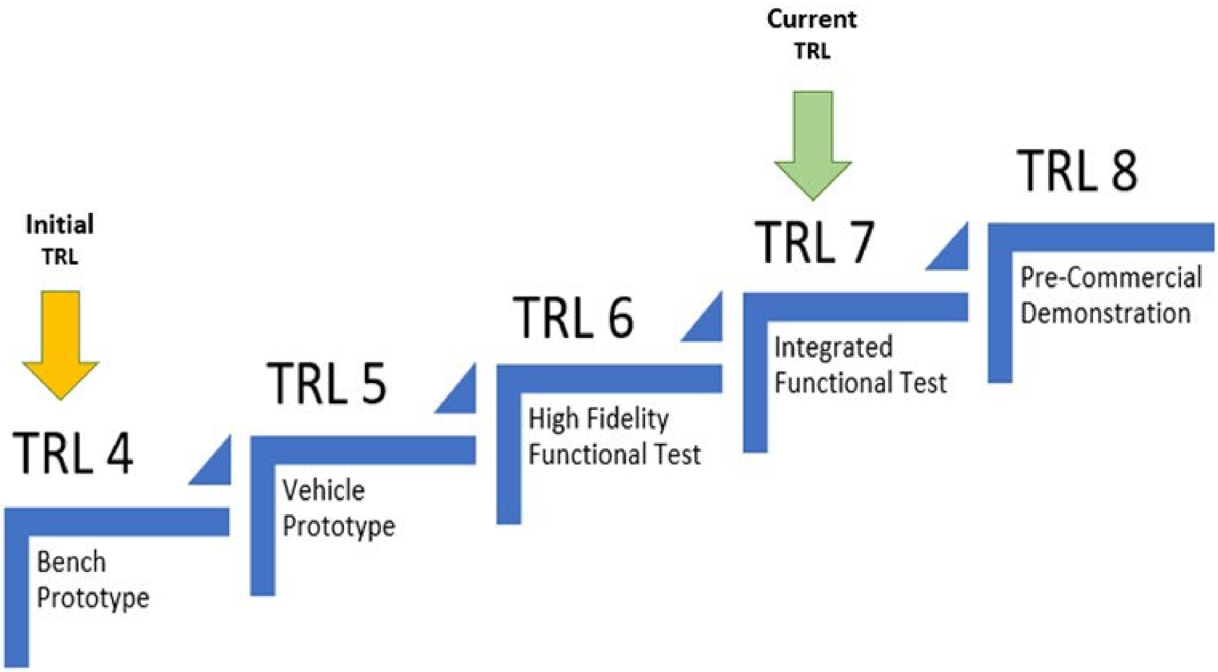

Figure II.1.1.1 Technology Readiness Level Advancement

The primary issue for the DTNA EMG project team is the uncertainty related to the ongoing COVID-19 public health crisis. Supply chain disruptions and mandatory changes to standard vehicle assembly procedures have slowed production. However, DTNA has been able to leverage its extensive resources as a leading global vehicle manufacturer to resolve supply issues and continue with a modified production schedule to achieve critical project milestones.

Social distancing is in effect in DTNA EMG facilities in accordance with public health guidelines regarding COVID-19 which recommend six feet of distance between individuals. This has slightly delayed production of the B- and C-Sample builds, however, the project team has still made significant progress and remain on track to complete vehicle assembly within the original timeline.

The COVID-19 public health crisis impacted the project team's ability to travel and meet with fleet partners to assess their infrastructure needs. Infrastructure evaluation for UPS and Meijer are planned for 2022 under the assumption that travel restrictions will be eased.

A compressed vehicle testing schedule was adopted to accommodate supply chain delays without revising the project schedule and timeline. The compressed schedule led to increased wear and tear on sample build vehicles which required additional maintenance to complete tests. Vehicle testing was ultimately successful, and the final phase of production is in progress.

Due to proprietary control of software and in-house production of key components, DTNA was able to adapt problems with sourcing and supply. The use of 'dummy' battery packs and other temporary components were made in-house when key shipments were delayed or damaged during the compressed testing schedule.

Conclusions

The project team has made significant progress and achieved critical project milestones for Phase 1a: Research, Design Building, and Commissioning: Vehicle Design and Specification and Phase 1b: Research, Design Building, and Commissioning: Commercial Scale Production Model, including completing the C-

Sample build and achieving critical go/no-go milestones including demonstrating an average efficiency of 2.1kWh/mile to realize 250-mile daily range capabilities.

The advanced heavy-duty transportation technologies supplied by DTNA through this project will result in a heavy-duty vehicle platform that provides added flexibility, operational performance, efficiency, and maintenance cost savings to the end user. The most direct outcome will be a commercial production capable of zero-emission heavy-duty option with a 250-mile range and sufficient payload for regional haul duty cycles (Table II.1.1.1). The larger outcome will be an acceleration of the market transformation away from petroleum-based fuels. DTNA's comprehensive sales team, dealer network, customer network, and maintenance and support teams will ensure that this is not a standalone zero-emission truck, but rather one that can be produced, marketed, and operated at scale to realize vast greenhouse gas and criteria pollutant emissions reductions, while also bringing zero-emission vehicles closer to cost parity. Through DTNA's 'co-creation' approach with its fleet partners, DTNA will continue to collect operator feedback and best practice information for continuous improvement activities and the development of best practice case studies for other future commercial vehicle operators.

II.1.2 Improving the Freight Productivity of a Heavy-Duty, Battery Electric Truck by Intelligent Energy Management

Teresa Taylor, Principal Investigator
Volvo Technology of America, LLC
7900 National Service Road
Greensboro, NC 27409
Email: teresa.taylor@volvo.com

William F. Northrop, Principal Investigator
University of Minnesota
200 Oak Street SE
Minneapolis, MN 55455
Email: wnorthro@umn.edu

Lee Slezak, DOE Technology Manager
U.S. Department of Energy
Email: lee.slezak@ee.doe.gov

Start Date: October 1, 2019 End Date: December 31, 2022
Project Funding: $4,869,889 DOE share: $3,799,536 Non-DOE share: $1,070,353

Project Introduction

Battery electric Class 8 trucks, including those from Volvo, have made significant advancements in the past five years; however, high battery cost and vehicle weight restricts their ability to match the range and productivity of conventional diesel trucks. Although an electric tractor can be equipped with a larger battery to last for a large portion of a 250-mile daily route, vehicle cost increases non-linearly with increased battery energy and must be sized to last 8 to 10 years to provide a proper return on investment. Therefore, on-route fast charging is necessary to balance economics, functionality, and longevity. The objective of the proposed project is to use vehicle and operations data to increase the vehicle range and lower the operating cost of battery electric Class 8 trucks that drive more than 250 miles per day using physics-based adaptive learning algorithms.

Objectives

The objective of the project is to use vehicle and operations data to increase the vehicle range and lower the operating cost of battery electric class 8 trucks that operate more than 250 miles per day using physics-based adaptive learning algorithms. The Project Team will develop and implement an intelligent-Energy Management System (i-EMS) with vehicle-to-cloud (V2C) connectivity integrated with physics-aware spatial data analytics (PSDA). The i-EMS rule-based methods will use collected vehicle and operations data and calculated parameters from fleet operator partners Murphy and HEB as inputs into physics-based adaptive learning algorithms developed in the project to predict and reduce future energy consumption of the vehicle. The resulting i-EMS will increase the vehicle driving range and lower the operating cost of BEV Class 8 freight movement trucks that drive ≥250 miles per day.

Approach

Our approach is to understand our fleet partners (HEB Companies and Murphy Logistics), baseline operations to be able to establish project duty cycles. In addition, we will combine physics-based truck model, battery information, utility demand charges and database parameters as inputs to a machine learning algorithm that will predict energy use, operational energy cost, and battery performance. The resulting i-EMS will be implemented on 2 Volvo VNR Battery Electric Vehicles, (BEVs), using a low-distraction screen to display charging and routing recommendations to the operators. Charging stations will be installed at HEB Companies and Murphy Logistics. Finally, we will demonstrate i-EMS in daily operations with HEB Companies in hot weather and Murphy Logistics in cold-weather conditions.

Results

The project has experienced some delays due to several factors; two main issues have been the Semi-Conductor shortage which led to a delay of the charger delivery and installation, and the other is due to the strike at our New River Valley facility where the VNR-electric is being built and assembled. Even with the delay the team has continued to make progress on all tasks.

Task 2: TECHNOLOGY & ALGORITHM DEVELOPMENT

Subtask 2.4 – Define on-route charging locations for demonstration

Define on-route charging locations for demonstration. The established routes at each operator, and other information from Task 1.2 will be analyzed to determine demonstration phase charging locations.

The Gilbarco Veeder-Root RTM75 charger has been delivered and installed at Murphy Logistics. Preliminary electrical work was completed at Murphy to prepare for charger delivery, including installing a 200-amp fused disconnect and a 125-amp copper feeder to the EV charger location. Figure II.1.2.1 shows the previously planned charger location at the warehouse. This location may change slightly to facilitate the simultaneous charging of both Volvo VNR electric trucks while both trucks are driving in Minnesota, which may require slight rerouting of the electrical cables put in place ahead of delivery.

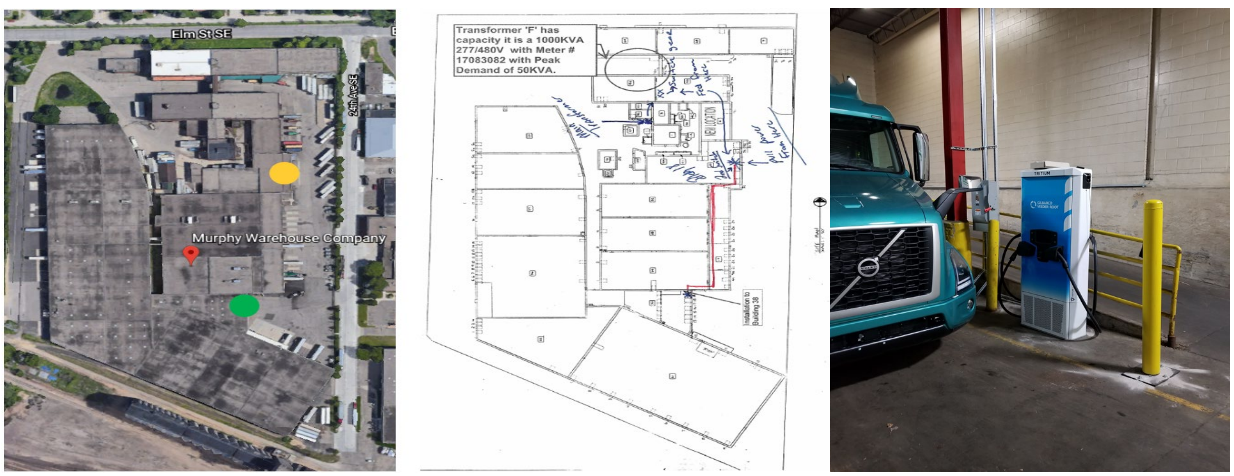

Figure II.1.2.1 Demonstration charger placement at Murphy Logistics. The yellow dot marks the location of the power source, a 1000 KVA transformer with 50 KVA peak demand and 277/480 V supplied voltage. The green dot marks the planned location of the RTM75 charger. The VNR-Electric Truck and Charger have arrived, and commissioning of the charger has begun.

HEB plans to install a high-powered charger, the Gilbarco Veeder-Root RT175s, to allow for faster charge times that better suit its more ambitious route scheduling.

Subtask 2.5 – Determine optimal on-route charging locations for fleets

Determine optimal locations for on-route charging for the two participating fleet operators.

The UMN team is currently awaiting information necessary to determine on-route charging locations. The scalable mixed-integer programming (MIP) technique described in Task 2.4 is currently planned to be used for Task 2.3 as well. For individual vehicles, a theoretical method for determining optimal charging locations along predetermined routes was proposed by the UMN team before the start of this project in a conference paper *Formal methods approach to the charging facility location problem for battery electric vehicles* published in the 2020 IEEE Intelligent Vehicles Symposium conference proceedings. Extending this work, the UMN team has explored using k-means clustering as well as genetic algorithm optimization to optimize charger locations along common trucking corridors before deciding to use a MIP formulation to optimize charging locations. Using MIP, the UMN team has developed a much more efficient algorithm for choosing charger stations along simple out-and-back routes as shown in Figure II.1.2.2. As with the GA optimization, the MIP formulation is constrained by charger placement cost, historical traffic data, and expected demand service.

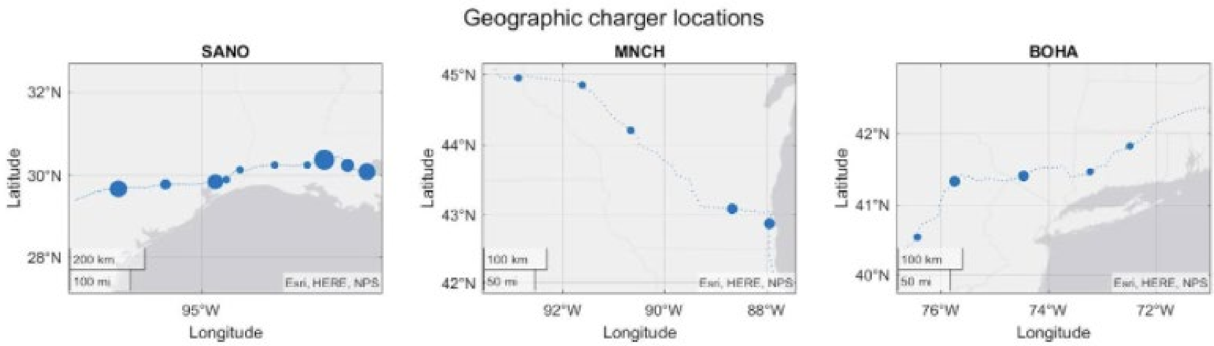

Figure II.1.2.2 Example optimal charger station placement output from genetic algorithm optimization. Locations and number of chargers were chosen along three common trucking corridors: (1) San Antonio, TX to/from New Orleans, LA, (2) Minneapolis, MN to/from Chicago, IL, (3) Boston, MA to/from Harrisburg, PA. The objective function considered local property costs, inter-charger distance, corridor trucking traffic, and expected charging wait times.

To optimize charger station locations for fleets of vehicles, the UMN team has developed a plan for simulating trucks on the road network according to driving data from the baseline vehicles. The formulation for optimization is as follows: Given the vehicle GPS data, the road network is discretized into a directed graph structure with edges denoting parts of road segments. Road segments are assigned time and state of charge weights according to the driving data and charging stations can be placed at a constrainable subset of nodes. In the simulation step, trucks are generated as agents on the road network according to historical driving data and navigate the same road segments according to the Volvo BEV model developed in Task 2.1. As the simulated trucks navigate the road network graph according to their routes, their states of charge are updated and the nodes in the road network at which trucks need to charge are monitored. When a truck needs to charge in the initial “relaxed” simulation, it is assumed that charging stations could be placed at any available node. The initial simulation then outputs the expected charging demand serviced by charger stations at each node on the road network, and the choice of charging stations is then formulated as a MIP optimization problem as written below where c is the vector of expected charging demand for each road network node, x is the number of chargers placed at each node, A is a block-diagonal matrix constraining the number of chargers near one another to be less than or equal to b.

$$\max_{\boldsymbol{x}} \boldsymbol{c}^T \boldsymbol{x} \text{ subject to } \boldsymbol{Ax} \leq \boldsymbol{b} \text{ and } x \geq 0, x \in \mathbb{Z}^{\boldsymbol{n}}$$

The number of chargers to place is iteratively increased until all vehicles are expected to be able to complete their routes with minimal expected delays waiting for other trucks to charge. The optimization is also subject to budgetary constraints, and inter-charger distance is constrained since no infrastructure is currently in place to allow the final charger placements to service a wider geographical area. The proposed process is summarized in Figure II.1.2.3.

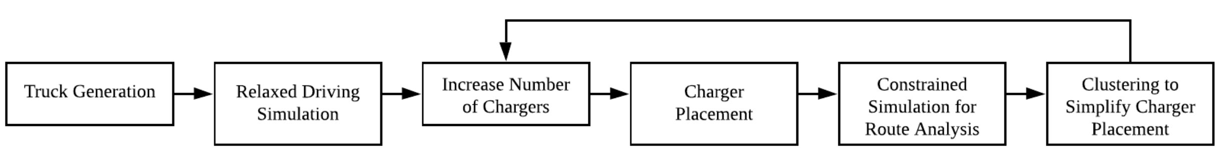

Figure II.1.2.3 Framework for the charger station optimization algorithm, which investigates the effect of iteratively increasing the number of chargers placed.

The UMN team is in the process of applying this method to both simulated example routes and to the practical baseline routes driven by Murphy and HEB trucks. This work is planned for completion after the DVI is successfully installed and fully operational in the first electric truck.

Subtask 2.6 – Develop Driver Vehicle Interface

A Driver-Vehicle Interface program application ("app") will be developed to send vehicle information to the team and to receive information from cloud-connected adaptive learning algorithms.

The initial interface development has begun and is currently being tested on a Samsung Galaxy Tab A7 tablet. The interface includes a map with routing information that covers about 3/5 of the screen from the left edge (possibly including a frequent destinations menu for pre-analyzed routes). The predicted remaining range (distance-to-empty or DTE), and the current state of charge are displayed in the top right. Notifications are displayed at the bottom right to show any possible routing changes or other alerts. At the middle right of the screen are two main buttons. The top button, when pressed, changes the screen to display charging information while the vehicle is at a charging station. The intention is for there to be a separate charging station menu when the vehicle is charging, showing the charge rate, state of charge, and the recommended charge level to complete the trip. The second button allows the driver to provide feedback on the DVI via a voice recording that is translated to English and auto transcribed. Additional interface updates will be implemented to submit the feedback to a cloud server.

Figure II.1.2.4 shows a data flow diagram with real time data transfers that will facilitate DVI operation.

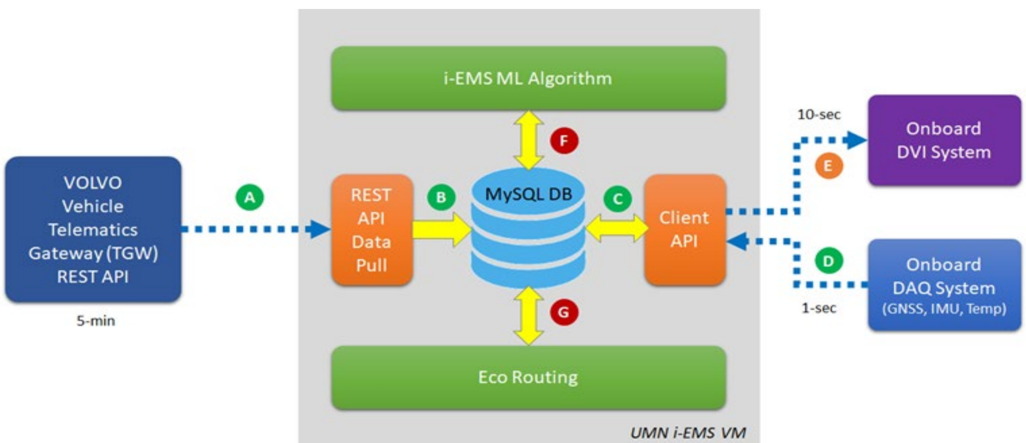

Figure II.1.2.4 DVI data flow diagram. A virtual server hosts the UMN models and algorithms, and stores recent driving data and algorithm outputs in a MySQL DB. The Volvo TGW sends five-minute updates of certain vehicle parameters, while the onboard DAQ system installed by UMN collects key parameters at a frequency of 1Hz.

A documentation on the connected vehicle data services API was received by the UMN and the UMN team has developed software to acquire vehicle data (such as, vehicle ID, timestamp, latitude, longitude, heading, speed, odometer, battery level, and others) from Volvo's quality assurance (QA) server. The API access to the QA server has been tested and working properly, and UMN now has access to real time vehicle data to begin testing the DVI before the first vehicle is delivered to Minnesota.

To help the fleet partners schedule their route ahead of time, a route builder interface has been developed, as shown in Figure II.1.2.5. This allows the user to submit routes to the eco-routing algorithm for early processing, which will help the DVI run more smoothly.

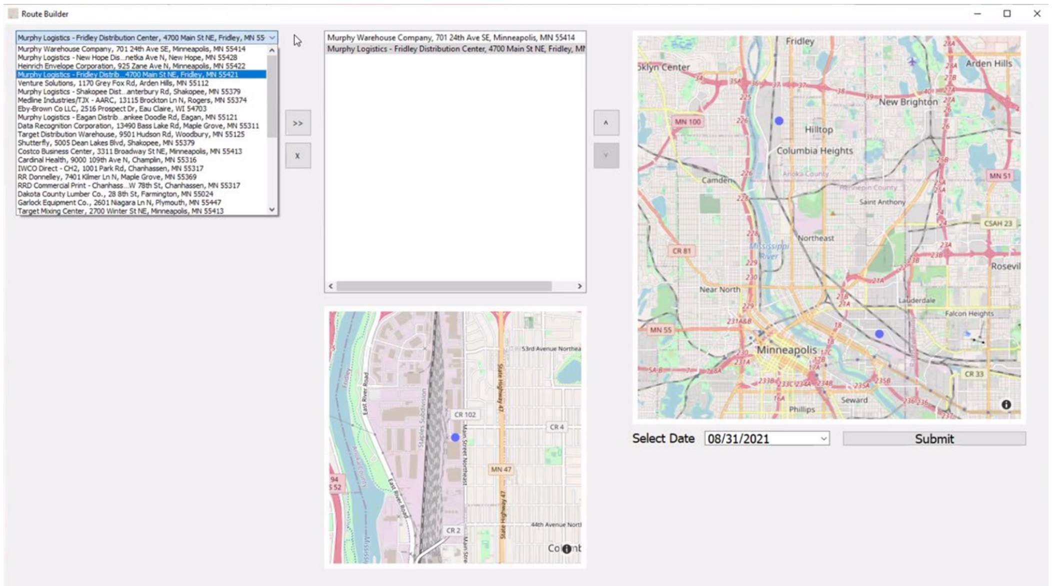

Figure II.1.2.5 Route builder application. A dropdown menu of previous destinations is given in the top left of the screen. Destinations can be put into the route sequence and ordered appropriately at the middle top of the interface. Each selected destination is displayed at the middle bottom, and a full view of all stops is given in the top right. The route can then be scheduled for a given date and time and submitted for processing by the eco-routing algorithm.

Task 3.0: Technology Verification and Vehicle Charging

Subtask 3.3 – Complete an operational cost model

Cost simulations will be developed to determine optimal charge scheduling, duration, and rate during a route.

The cost of electricity is the primary consideration in determining optimal charge scheduling. Thus far, the cost model has been simplified to approximate electricity costs at a fixed rate of $0.14 per kWh, with the charge rate limited by the chosen charger station model. If charging is done on-route, the optimal charge level (i.e., minimum SOC required to complete the trip) is fully determined by the machine learning range prediction algorithm from Task 2.2. Ideally, the charge rate can be maximized to limit driving delays as much as possible. However, dynamic electricity pricing can clearly impact the time at which it is most cost-effective to charge. Man-hours, the maximum safe charge rate, and dynamic electricity pricing should be considered in the final cost model. Smart overnight charge scheduling could also be beneficial for minimizing costs.

Further discussions will be required with Volvo and Gilbarco to fully develop an appropriate cost model before running simulations to estimate operating costs over a significant time period using the available driving data. Prior to determining final cost estimates, the current cost model is written and explained below in theoretical terms.

$$O(T,C,e) = M(T,C) + L(T,C) + F(T,C) + E(T,e)$$

The operating cost O is a mix of fixed costs, primarily including materials M, and variable costs including those for labor and maintenance L, fees (i.e., taxes and permits) F, and energy E. These components of the operating cost model are functions of, among other things, the number of trucks T, number of chargers C, and the price of electricity e. The operating costs of the two electric trucks may be compared to those of similar diesel trucks to perform a financial analysis of how long it would take to amortize the higher upfront costs of these new electric vehicles. The increased energy efficiency of the electric trucks and the differences in cost between diesel fuel and electricity is expected to significantly impact the relative value of the electric trucks over time.

Conclusions

The project team has made significant progress, while working mainly from home due to COVID regulations. Progress will increase now that the Truck has arrived in Minnesota. Murphy Logistics will be driving the Truck once the Charger is fully commissioned. Volvo‘s Battery Electric Service Manger was on-site to review the truck in detail with the UMN project team and the Fleet Customer. We have learned that the installation of a charger and the infrastructure is a complex task and requires upfront planning and expert guidance. Another consideration is the maintenance and support structure for the BEV once it is in operation. We are working with our Dealership Network to accommodate the service of the (2) VNR’s commissioned for this project.

II.1.3 Long-Range, Heavy-Duty Battery-Electric Vehicle with Megawatt Wireless Charging

Stan DeLizo, Principal Investigator
Kenworth Truck Company
485 Houser Way North
Renton, WA 98057
Email: stan.delizo@paccar.com

Lee Slezak, DOE Technology Manager
U.S. Department of Energy
Email: lee.slezak@ee.doe.gov

Start Date: October 1, 2019 End Date: December 31, 2022
Project Funding: $8,620,126 DOE share: $4,989,299 Non-DOE share: $3,630,838

Project Introduction

Most heavy-duty battery-electric trucks in operation today are designed for one shift per day and 100 miles or less operation, such as port drayage, due to the existing technology barriers of battery energy density and charging power capability. However, most truck operators prefer trucks that can achieve longer range without interrupting the daily delivery schedule to cover both intercity and regional hauling routes and to facilitate their dispatch efforts. For fleets where the diesel-powered trucks typically have a range of 350 to 500 miles, introducing trucks with shorter range presents a significant impact on operating cost, productivity, and schedule planning.

This project aims to demonstrate that 400 miles or more per day across two shifts can be achieved with little impact on a fleet's operations by developing a megawatt wireless charging technology that is capable of fully charging the battery pack during a driver's 30-minute required break. By applying the megawatt wireless charging technology, the daily operating range of the battery-electric truck-tractor can be extended without disrupting the delivery schedule and while keeping the required battery pack mass to a minimum.

Objectives

- Design and build a Class 8 Battery Electric Truck-Tractor with sufficient range to run from Seattle to Portland at 80,000 lbs. Gross Combination Weight.
- Design and build a wireless charging system capable of megawatt power transfer rate.
- Demonstrate the vehicle and charging system in commercial operations of at least 400 miles per day with a major shipping company.
- Collect and analyze data from commercial use over a period of up to three months, which will provide real-world feedback on how a large, electrified tractor-trailer might be used in freight operations.

Approach

During the project, Kenworth will leverage previously tested electric powertrain technology, and will design and build a Long-Range Battery-Electric Tractor (LRBET) specifically tailored for this application. Technical challenges that will be overcome during this project include mounting this quantity of battery capacity without adversely impacting the tractor's durability or vehicle dynamics, selecting appropriate battery chemistry and pack design to achieve high C-rate charging, providing adequate cooling for the batteries and power electronics during vehicle operations and the extreme fast charging, and developing the controls code to manage the vehicle during vehicle operations and during charging.

Utah State University (USU) will leverage its core expertise in high C-rate battery charging, high power density grid-tied power electronics and wireless charging systems to design the megawatt inductive charging equipment circuitry and topology. The planned inductive wireless charging system will allow power to be transferred wirelessly between a primary (charging) pad embedded in the ground and a secondary (receiving) pad mounted on the bottom of the vehicle by using high frequency AC magnetic fields. Inductive charging is a mature and proven technology. However, it is seeing wider adoption today due to the availability of high-performance semiconductor devices, capacitors, and cables. The technology can operate in varying environmental conditions, including rain and snow, requires no operator interaction, and maximizes effective use of land with no above ground obstacles or components.

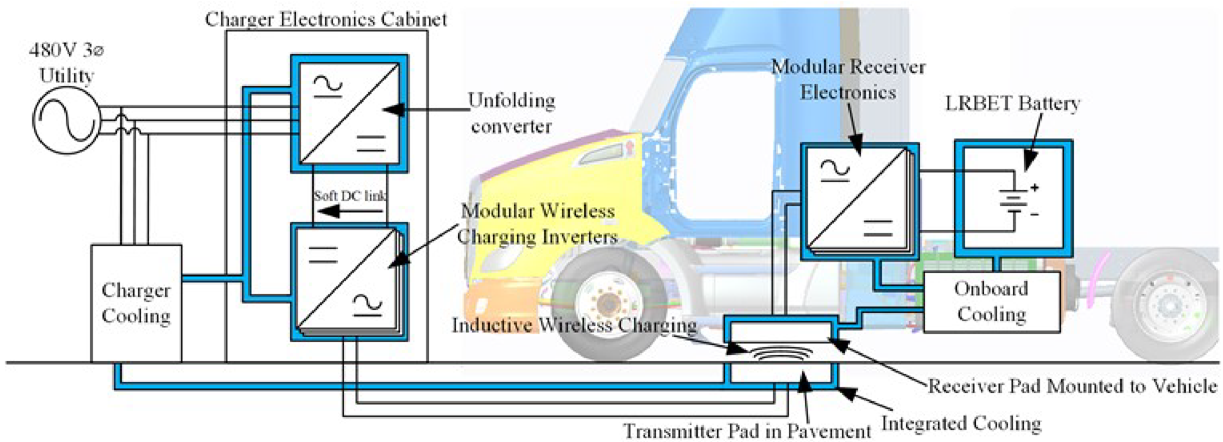

Figure II.1.3.1 System block diagram

WAVE has commercialized wireless charging systems capable of transferring up to 250 kW over an air gap of 10 inch and has obtained UL Field Certification. The maximum power that can be transferred with a wireless charging system is typically limited by the leakage magnetic fields that are generated since international standard bodies such as the International Commission on Non-Ionizing Radiation Protection (ICNIRP) regulate the maximum allowable leakage fields. USU has developed a charging pad configuration that utilizes multiple field shaping strategies as well as newly developed techniques to facilitate charging at power levels of one megawatt while maintaining leakage fields below ICNIRP regulations. USU's system has also considered other aspects of the system such as the power electronics design, thermal management, and tolerances.

Local electric utilities Seattle City Light and Portland General Electric will participate by providing installations of electrical grid connections and transformers to power the ground-based vehicle chargers at each location.

Results

Fourth Quarter 2020

The host chassis (#359051) was built on the production line and released to the R&D center for disassembly and preparation to receive the hybrid specific components.

The project team completed a site review of the UPS terminal facilities and have targeted several charger installation locations.

USU released and submitted the M1.3 report on the Design Parameters of the Single Stage AC-AC converter. The parameter design of the AC-AC conversion stage is presented in this report. Simulation results are presented to validate the operation of the AC-AC conversion stage design. The next step is to demonstrate a single module of the AC-AC converter working in conjunction with the WPT system. Also, the number of modules and the resolution of power control within each module will be further optimized through collaboration with the project team

Portland General Electric (PGE) and Seattle City Light (SCL) have submitted utility development proposals for project consideration. UPS hosted team tours and has target installation sites for the charging stations at their Portland and Seattle facilities.

Kenworth completed simulation models based on the route data and identified high voltage battery chemistries and thermal cooling requirements. Information was shared with USU for charging simulation.

MS#	Milestone	Type	Date Planned	Date Achieved
1.3	Design of AC-AC Converter Parameters	Technical	09/30/2020	10/28/2020

First Quarter 2021

Kenworth completed component and system designs for hybrid specific parts. Completed design and stress analysis for custom brackets required to mount major components. Manage receipt of incoming material and equipment, test received components and provide feedback to suppliers based on component performance. Manage component updates and modifications required when performance does not match specifications.

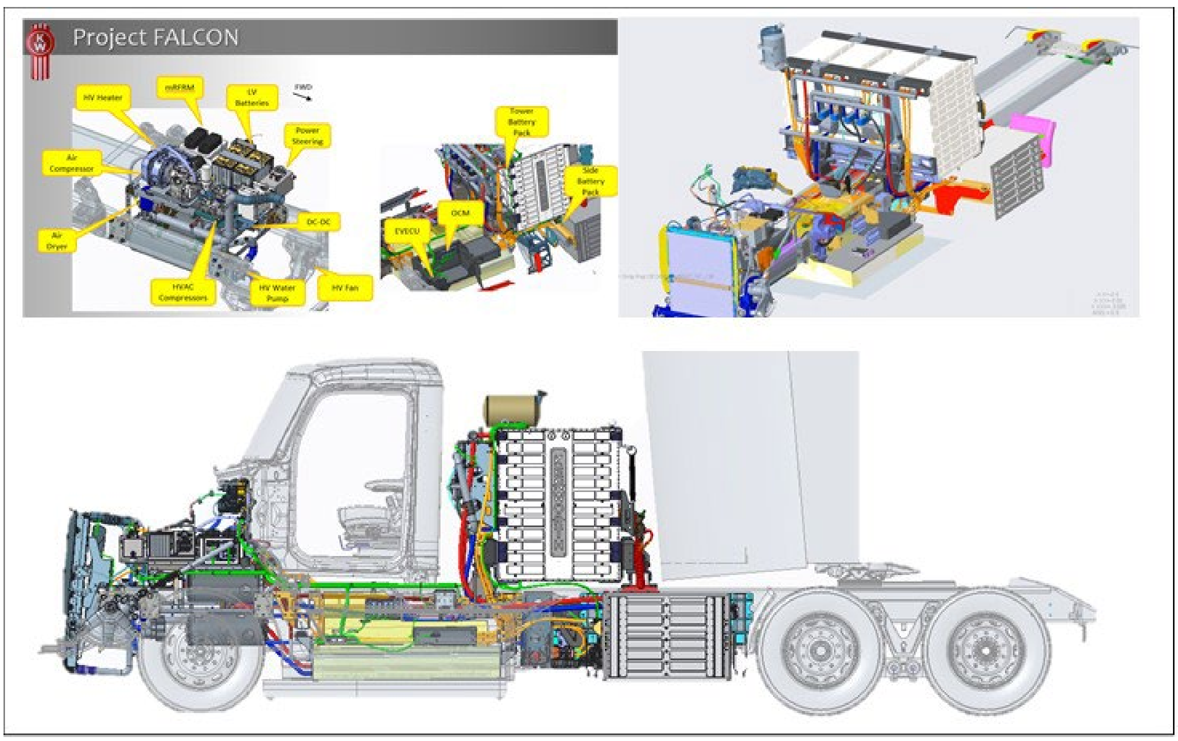

Figure II.1.3.2 Details of designed vehicle and major components

The USU team accomplished the full construction of the MW sized wireless pad and single 125 kW inverter module this quarter. All necessary parts for this build including the fabrication of bus bars, mounting plates, ceramic parts for electrical isolation, thermal management, and component housings were completed. Also completed was the soldering of Litz wire connections and the assembly of the pad power electronics and inverter required for the 125-kW testing (single module level). The Figure II.1.3.3 below provides a summarized photo recording of this build process.

The hardware result at 125 kW power and 573 V DC voltage. The inverter current lags the inverter voltage, resulting in high efficiency due to the soft-switching of the H-bridge inverter. The measured DC-DC efficiency was 93%.

Figure II.1.3.3 Physical Test Setup

SCL is proposing to intercept the existing duct-bank, decommission the existing transformer and install a new single transformer. The new transformer will be fed from the SCL pad mounted switch. All equipment will either be installed above ground or leverage space from existing installations (Figure II.1.3.4).

Figure II.1.3.4 SCL utility proposal to UPS Seattle for charge site

PGE proposed a similar system but would require all new construction from the local sub-station (Figure II.1.3.5). The site equipment is like the Seattle proposal, but with a below ground vault to hold some of the utility equipment and an overall smaller footprint in a low use corner of the Portland UPS facility.

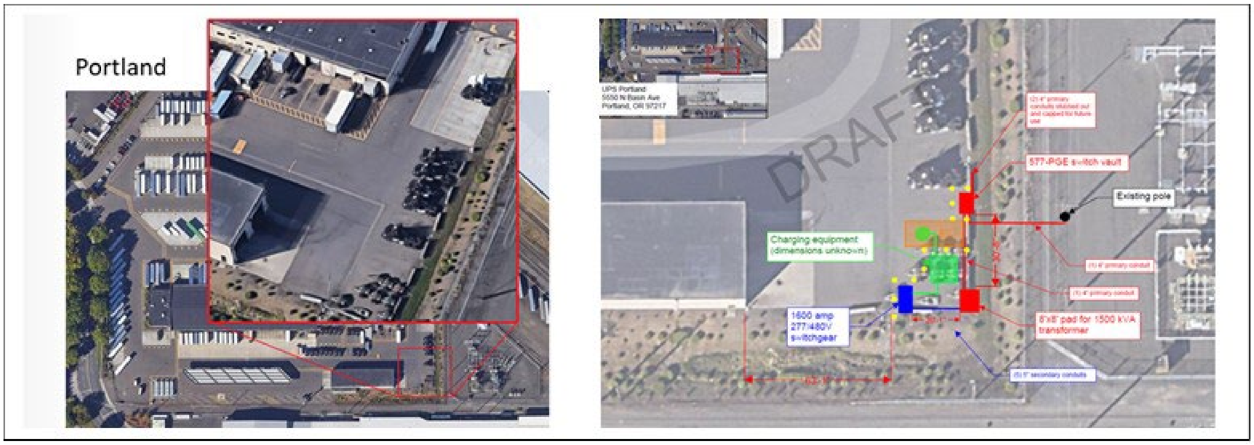

Figure II.1.3.5 PGE utility proposal to UPS Portland for charge site

UPS has identified resources and is working through internal process to determine how best to support the project timeline.

MS#	Milestone	Type	Date Planned	Date Achieved
1.4	Infrastructure Site Plans Complete	Administration	12/21/2020	01/12/2021
1.5	Proof of Concept Charger in Operation	Technical	12/31/2020	03/23/2021
2.1	Chassis Layout Design is Complete	Technical	03/30/2021	03/23/2021

Second Quarter 2021

Submit documentation for continuation and budget reallocation request

Chassis assembly begins (Figure II.1.3.6). Custom mounting brackets arrive from the fabricators, are test fit on the chassis and measured against design prints before application of the finish coat. The front auxiliary carriage brackets and electrified components were received, assembled, and installed on the chassis.

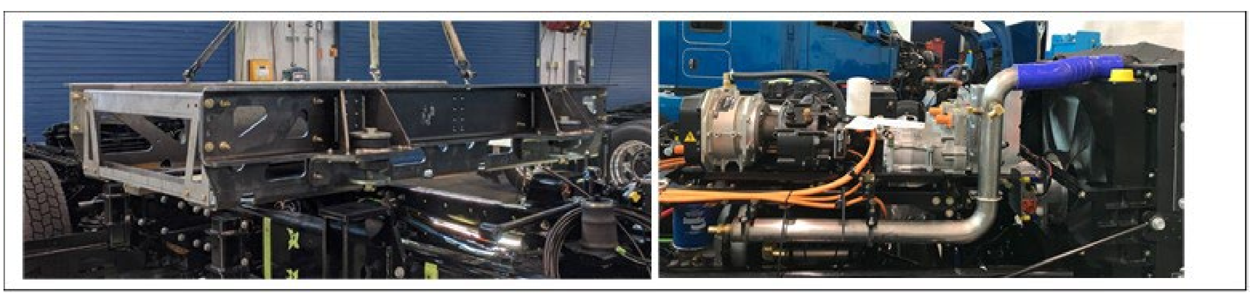

Figure II.1.3.6 Base chassis assembly with battery cradle and auxiliary components installed.

Cooling, electrical, communication and air system routings will be custom built and routed in place on the chassis to minimize connector stress. The prebuild is required to clock the connectors at each end of cable assembly and relieve installation stresses.

The custom side mounted HV battery modules are on site and are being assembled in an isolated area of the building (Figure II.1.3.7).

Figure II.1.3.7 HV battery tower assembly back of cab and alongside rail. Side rail pack showing battery module.

A parking stall charger layout package was developed and submitted to Kenworth for the Seattle and Portland UPS sites (Figure II.1.3.8). This package included drawings and dimensions of the site space claim, the chiller units, electronics cabinets, the primary charging pad, and the truck bump stop. A spreadsheet with information on the cable and conduit size and routing was also included in the transmittal. Included was the electrical specification sheet with all the necessary system requirements. The site plan was completed with input from USU, WAVE and Kenworth.

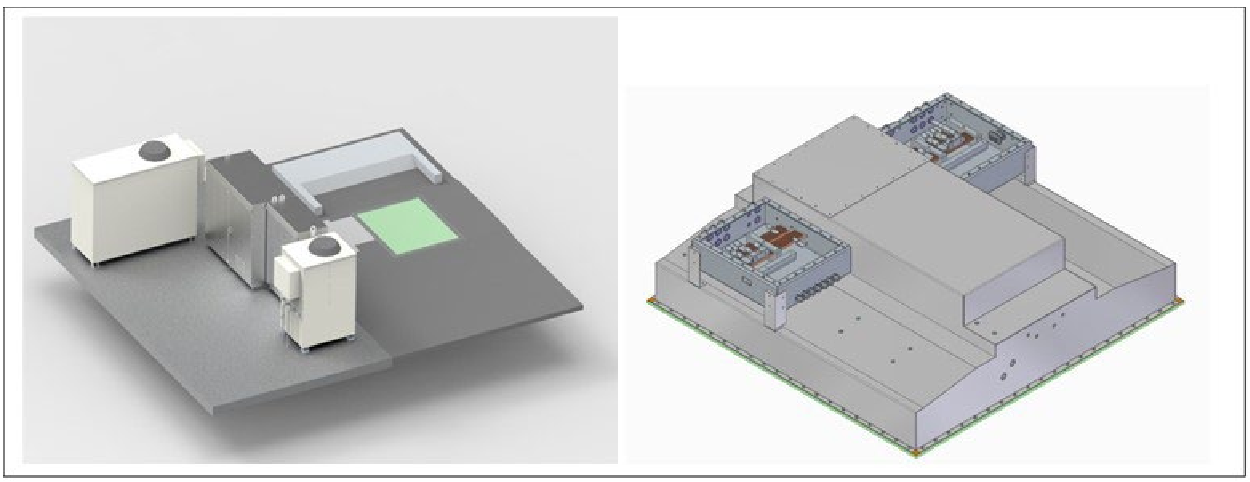

Figure II.1.3.8 Parking stall charge pad and supporting electrical equipment. Chassis mounted charge receiver.

USU completed structural design for the secondary side charging pad. USU designed a waterproof aluminum case and fiberglass cover for the secondary side pad. USU determined mounting locations and methods for the high-voltage connection junction boxes. USU and WAVE collaborated to determine a process for transitioning the models to WAVE's CAD system. Following this process, USU created CAD models and technical drawings for the parts and assemblies in the secondary side pad.

USU fabricated at small-scale test setup to validate the thermal management of the ceramics and potting of components (Figure II.1.3.9). The potting emphasis was on the Litz wire of the pad, with USU developing a test setup to prove out these processes. Epoxy potting efforts include creating a vacuum bagging process that can encompass the large pads and adequately pull the epoxy into the Litz. There have also been several small setups where different methods of blocking the epoxy were used to facilitate directing the epoxy to the desired location. These small setups have allowed for lessons learned like methods to apply adhesive to seal the epoxy forming walls and withstand the vacuum pressures. The image below is from the test setup and shows the use of thermocouples to measure the effectiveness of the design.

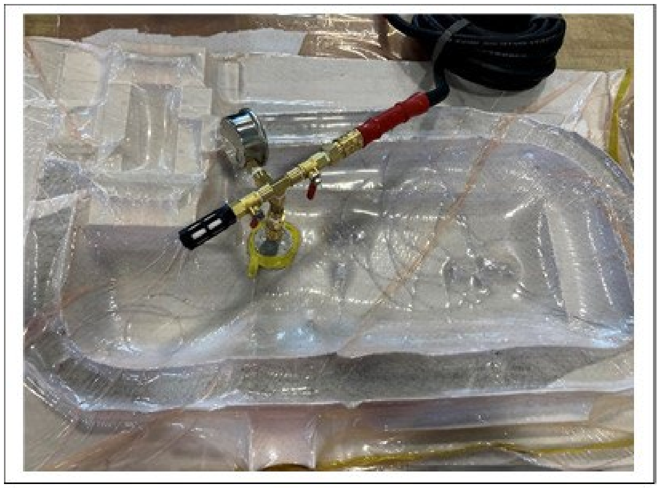

Figure II.1.3.9 Component potting test apparatus.

The 1 MW 3-phase unfolder design continues with the selection of the Diode and IGBT modules done. Thermal analysis is being carried out. In efforts to reduce the loop inductance and improve the system performance at 85 kHz switching, a 16-kW modular T-type inverter using discrete devices instead of power modules was developed. The power testing and the control implementation is ongoing. Following this testing, the modular T-type inverters will be scaled to 1 MW.

Due to the high current, special consideration had to be taken for the wiring from the cabinet to the primary pad. To meet the compliance requirements for the cables and connections, a junction box will be placed between the cabinet and the primary pad. The cables from the primary pad and the cabinet will be connected and the whole box potted. For all other wire routing, USU plans to use WAVE's conduit specifications.

SCL and PGE suggests that the switchgear is a major part of the ground-side equipment. The switchgear consists of a contactor, fuses, surge suppressor and EMI filter. The selection of the tentative switchgear equipment was completed. The discussions with vendors about the availability of the switchgear and the cabinet are ongoing. The electrical interconnections between different ground-side cabinets have been investigated.

UPS has completed work packages for the Architecture and Engineering (A&E) firms to quote. Plan is to use a single A&E firm to develop and manage the facility modifications. They will then source and contract local construction companies to focus on facility work.

MS#	Milestone	Type	Date Planned	Date Achieved
2.2	Charging site equipment design is complete	Technical	06/30/2021	06/30/2021

Third Quarter 2021

DOE approved the continuation request and revised budget to reflect the approved calculations for fringe and overhead and its impact on the overall cost share percentage and acknowledged and accepted the Kenworth recommendation for Stan DeLizo as principal investigator.

Kenworth completed component drawings and fabrication. The team is redirecting to building, integrating, and commissioning individual components into systems that are wired, plumbed, and routed to their respective sub-systems (Figure II.1.3.10).

Figure II.1.3.10 July chassis build status

The HV battery assembly stopped when the supplier reported they had failed their end of line tests (Figure II.1.3.11). Received material was returned and the team redirected to investigate and identify the root cause for the failed test. The preliminary results from their raw data suggest they can produce product to their specifications, but the process variation exceeded their control limits. Their engineering group identified machinery that would provide higher resolution data at a reasonable reliability. This machinery was added to their process and the team will start producing data for kW to review and analyze. The results from this analysis will allow KW to decide when battery assembly can proceed.

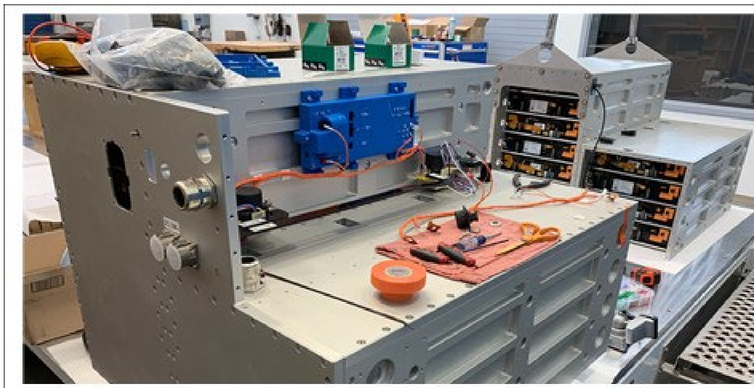

Figure II.1.3.11 Side pack HV battery assembly

The wireless charger is another at risk product (Figure II.1.3.12), but the risk appears to be primarily related to schedule and the transition from a university project to an industrial product. The two companies working this product have met and agreed to a transition plan that was shared with the rest of the team. An initial review by KW suggested that the transition plan did not develop many of the industrial components in parallel with the university plan. This issue was pointed out to the two teams, and they are working to resolve this deficiency and improve their delivery schedule.

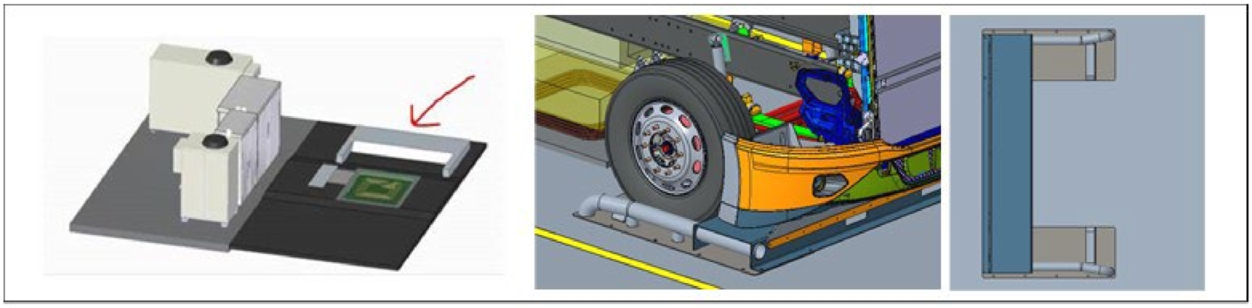

Figure II.1.3.12 Charge Equipment and PAD layout, Docking Station with Chassis, and Docking Station Detail

KW was also informed that the WAVE team wants the chassis shipped to Utah for a preliminary charge test of two ground based electrical systems. The intent is not clear to KW regarding this requested step as they are comfortable with the hardware designs, this suggests that the commissioning is for power and electrical tuning. KW has challenged WAVE to justify this added task. A Mockup wireless charger was built with a wired charger integrated to be used as a place holder until the final wireless charger is available from Wave and USU. This allows for charging of the HV batteries and driving of the vehicle, as well as be used to route and secure wires and cooling lines until the final unit is installed (Figure II.1.3.13).

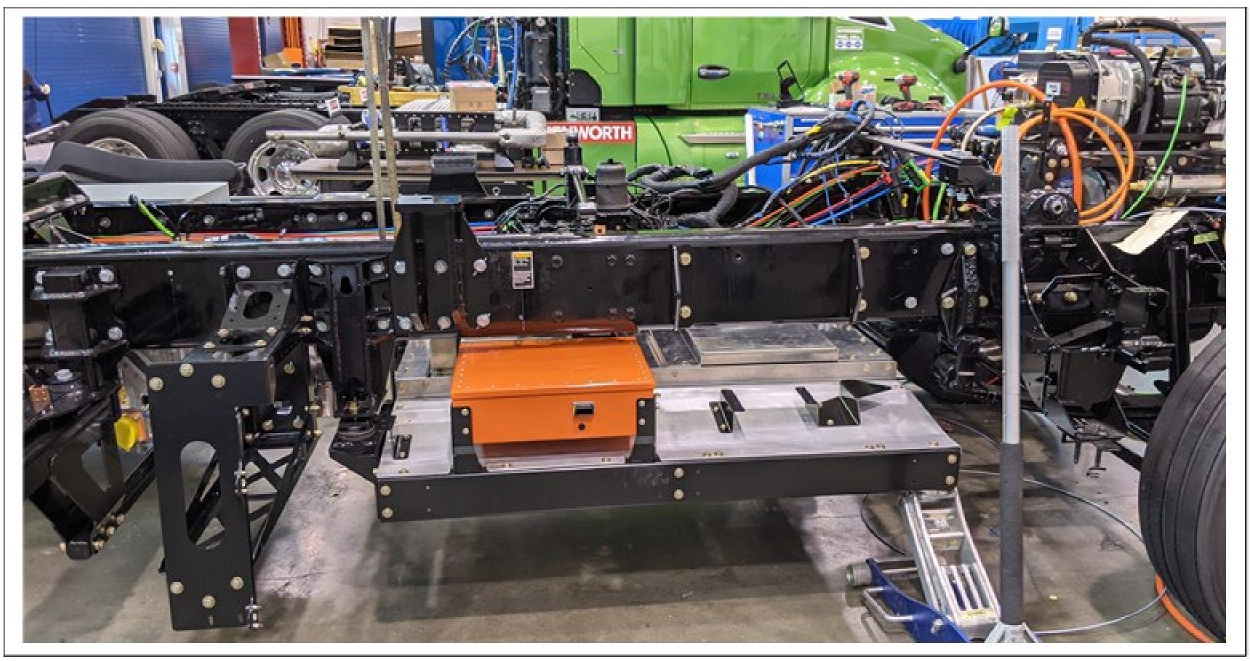

Figure II.1.3.13 Mock-Up of wireless charger installed on chassis

The motor/transmission assembly was installed without issue and the team is now focused on integrating the system and preparing it for an initial LV and communication wakeup (Figure II.1.3.14).

Figure II.1.3.14 Motor-Transmission Assembly installed in chassis

MS#	Milestone	Type	Date Planned	Date Achieved
2.3	Key components characterized and validated	Technical	9/30/2021	

Milestones for this quarter are at risk and will not meet the targeted completion date. The latest information from Utah State University responsible for the milestone noted suggest the revised targets for completion will be MS#2.3 12/31/2021

The proposed date for MS#2.3 may impact Kenworth's schedule to complete MS#3.1.

Conclusions

At the end of FY2021, the conclusions of this program to date are:

- Vehicle design and procurement is complete. Assembly of the hybrid components depends on availability. System integration is as challenging as predicted.
- The extreme charge conditions will test the limits of the HV battery chemistry. The supplier assembly processes required improvements to stabilize output reliability. Added quality checks were added to the assembly process to ensure product used in this application would perform within project parameters.
- The charge equipment designs are complete. Assembly challenges and progress to date suggest that the time between milestones will drive overall project progress (critical path). However, schedule is not completely tied to the assembly processes as material shortages are creating additional opportunities.
- Facility designs and plans although new to the end user and utility companies, are not creating unrealistic challenges. Progress is proceeding well to overall project schedule.
- Covid isolation mandates impacted project schedule.

II.1.4 High-Efficiency, Medium-Voltage-Input, Solid-State-Transformer-Based 400-kW/1000-V/400-A Extreme Fast Charger for Electric Vehicles (Delta Electronics (Americas) Ltd)

Charles Zhu, Principal Investigator
Delta Electronics (Americas) Ltd
46101 Fremont Boulevard
Fremont, CA 94538
Email: charles.zhu@deltaww.com

Steven Boyd, DOE Technology Development Manager
U.S. Department of Energy
Email: steven.boyd@ee.doe.gov

Start Date: July 20, 2018 End Date: May 30, 2022
Project Funding: $1,656,665 DOE share: $828,252 Non-DOE share: $828,413

Project Introduction

Range anxiety and long battery charging time continue to be critical challenges to mass adaptation of EVs. A major identified gap to wider adoption of BEVs is the ability and availability to refuel quickly or to fast charge. Studies have shown that in areas where drivers have access to 50-kW or 120-kW fast charge stations, annual electric vehicle (EV) miles traveled (i.e., eVMT) increased by over 25%, even in cases where fast charging was used for 1% to 5% of total charging events [1]. Charge stations of higher power not only alleviate the "range anxiety" and reduce the driver's waiting time, but also requires less investment. Michigan Energy Office completed a study in early 2019 titled "Electric Vehicle Charger Placement Optimization in Michigan: Phase I – Highways". This study finds a system with 150 kW chargers, though more expensive individually, actually has lower total system cost when compared to a 50 kW charging system when serving the same battery size EV [2]. To be truly competitive to the ICEV refueling experience, even higher power stations are necessary. However, high power charge stations would create large power draws from the grid. If this occurs during peak demand periods, grid capacity could be overloaded. This problem needs to be addressed to reduce the impact on the electric utility infrastructure.

The main goal of this project is to develop a 400-kW/400-A XFC system targeting total efficiency of 96.5 percent from the MVAC grid to a vehicle. The novel SST power cell topology, combined with a new silicon carbide (SiC) MOSFET device, enables a 3.5 percent improvement in system efficiency, a 50-percent smaller equipment footprint, and four times less weight than today's DCFC systems. The SST technology would directly utilize MVAC at 4.8-kV or 13.2-kV. This would eliminate the line frequency transformer (LFT), which steps down medium-voltage AC to 3-Phase 480-V line-to-line voltage in current DCFC systems. Activities in this fiscal year includes specification development, advanced circuit development and 1-phase series SST and Buck cell Integrated test.

Objectives

The objectives of the program are:

To design and test a high-efficiency, medium-voltage-input, solid-state-transformer-based 400-kW Extreme Fast Charger (XFC) for electric vehicles, achieving better than 96.5 percent efficiency.

To demonstrate extreme fast charging with a retrofitted General Motors' light-duty battery electric vehicle at 3C or higher charging rate for at least 50 percent increase of SOC.

To achieve a 180-mile charge within 10 minutes.

Approach

The XFC system consists of a Solid-State Transformer (SST), a Charge Controller (in power cabinet), a Charge Dispenser (A.K.A. User Unit) and an optional Energy Storage System (ESS). The system block diagram is illustrated in Figure II.1.4.1.

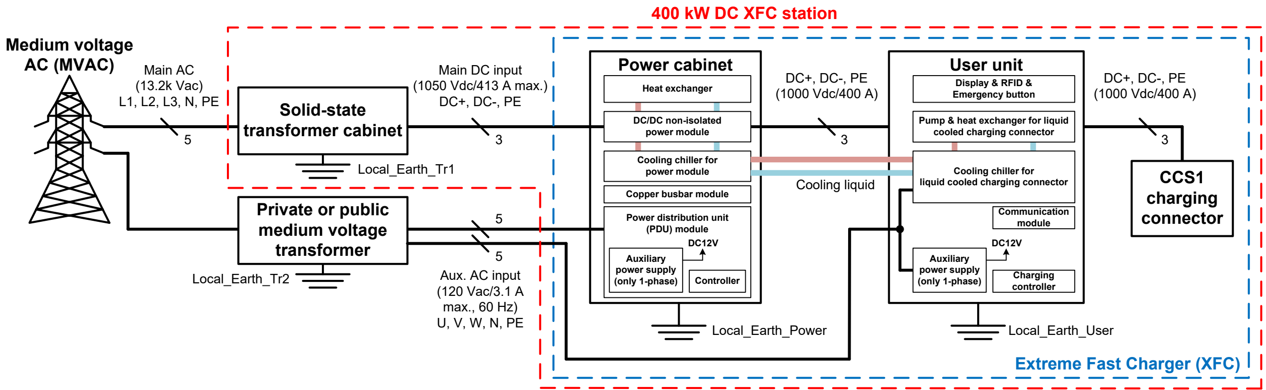

Figure II.1.4.1 XFC System Architecture

The SST is the key component in the whole system because it has multiple functions such as voltage step-down, AC/DC conversion, MV insulation, and grid interface. The team selected modularized architecture to accommodate the various voltages. Each SST module is rated at 15-kW, which is optimized for the transformer thermal dissipation. Cascaded H-bridge (CHB) topology is used in system level, which lowers the voltage stress on semiconductor devices, reduces the filter size with more voltage level, and improves the power quality and electromagnetic interference (EMI) performance on grid side. The power module's circuit diagram is illustrated in Figure II.1.4.2.

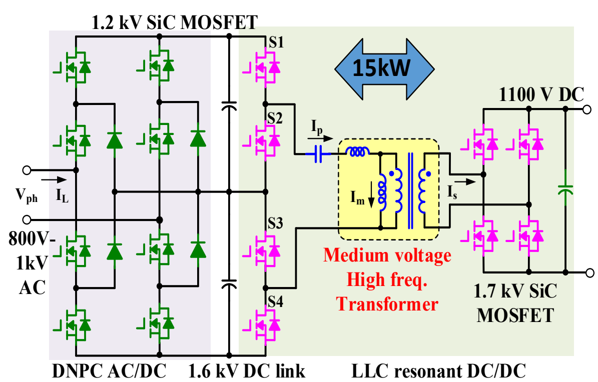

Figure II.1.4.2 Circuit Diagram of Power Module

The charging controller has a modularized design as well. Each power module is capable of outputting 200-A 135 kW, are connected in parallel. The charging controller module is based on Buck topology, thus also called Buck module. The buck converter runs at continuous conduction mode (CCM) with 50-kHz switching frequency. A full-bridge SiC MOSFET module with 1.2-kV, 50-A rating is used as the switching device. The picture of charging controller module is shown in the right half of Figure II.1.4.3.

Figure II.1.4.3 Picture of an SST Module at left, and Charging Controller (Buck) Module at right

For a 13.2-kV medium-voltage application, nine SST power cells in each phase are connected in series for the higher voltage. The outputs of all the power cells in three phases are connected in parallel to provide total 400-kW power to the 1050-V intermediate DC bus. Total 27 cells are installed in three cabinets. The SST also includes an AC input cabinet and a control/DC cabinet. The dimensions of the SST are 3100x1300x2100mm. The weight is approximately 3000 -kG. It is cooled by forced air. The cabinet is rated for NEMA 3R outdoor usage. Figure II.1.4.4 shows the complete 13.2-kV 400-kW SST.

Figure II.1.4.4 Front View of 13.2kV/400 kW SST Design

Three Buck power modules are connected in parallel to handle 500-A 400-kW charging power. The supporting plant includes a control module and a chiller. The dimensions of the power cabinet are 1318 x 1280 x 1432 mm. The weight is 800-kG. It is cooled by forced air with an internal chiller. Figure II.1.4.5 shows the complete 400-kW charger power cabinet.

Figure II.1.4.5 3-D View of the 400-kW Charger Power Cabinet

The dispenser features a 500A CCS1 vehicle charging interface, an LCD user interface and a charging cable chiller. The dimensions of the power cabinet are 600 x 400 x 2400 mm. The weight is 800-kG. It is cooled by forced air with an internal chiller. Figure II.1.4.6 shows the dispenser design.

Figure II.1.4.6 3-D View of the Charging Dispenser

The 400 kW power system and supporting infrastructure has been installed at NextEnergy's Microgrid Power Pavilion. This includes a step-up transformer, a 15kV switch, power distribution panels, contactor, surge suppression equipment, and all cabling. Final inspection of the XFC test setup was conducted on September 28, 2020. Figure II.1.4.7 and Figure II.1.4.8 are the pictures of the 400 kW XFC setup at NextEnergy.

Figure II.1.4.7 400 kW XFC Setup Front View (SST, Charger Power Cabinet, Dispenser, and DCE from left to right)

Figure II.1.4.8 400 kW XFC Setup Rear View (DCE Cooling System, Buck charger, SST from Left to Right)

In parallel to the XFC development, General Motor has been developing the vehicle Rechargeable Energy Storage System (RESS), Charge Inlet, and Vehicle Integration Control Module (VICM).

Build of the junction box was completed at General Motors in September 2021. Functional test is estimated at 50% complete, to be completed in October. Figure II.1.4.9 shows the assembled junction box.

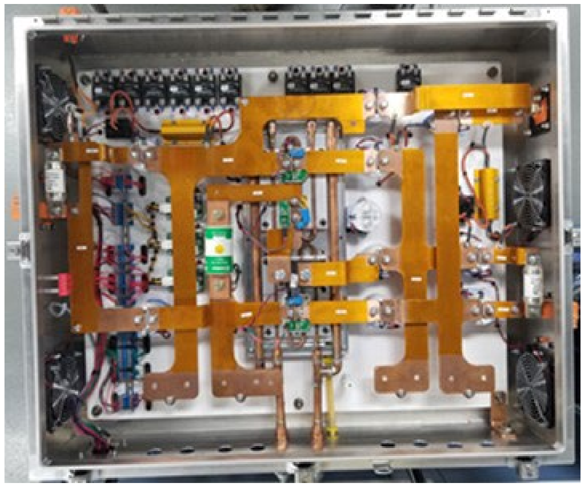

Figure II.1.4.9 Assembled Junction Box for Retrofit Vehicle

Testing of the four battery subpacks was completed in order to verify temperature rise is within thermal limits after occurrence of the current profile based on fast charging event. Since the test is primarily intended to evaluate joule heating induced temperature rise in cables, busbars, and contactors (not heat generated internally in the cells), a discharge current vs. time profile was used with current equal in magnitude to the charging current profile as determined from simulation with 500A total current.

Vehicle retrofit is 85% complete. The preparation of rear compartment is completed to make room for the battery pack. Cables and coolant lines have been routed. A bracketry has been fabricated to support the front part of RESS frame. Emergency shutdown mechanization and circuit interfaces has been developed. The vehicle body has been modified and the DC charge inlet has been installed on the right side of vehicle to the rear of the rear passenger door. Liquid cooling circuit for charge inlet and coolant fill bottle have been Installed. Quad RESS has been loaded into vehicle and attached to frame. Figure II.1.4.10 shows the retrofit vehicle with partially assembled RESS tray loaded.

Figure II.1.4.10 Retrofit Vehicle with Partially Assembled RESS Tray Loaded

To verify the interoperability charging power, vehicle charging tests were conducted with Chevy Bolt EV, Cadillac Lyriq EV, Volkswagen ID.4, and Ford Mach-E EVs. Figure II.1.4.11 and Figure II.1.4.12 show the pictures of testing with Chevy Bolt and Ford Mach-E, respectively.

Figure II.1.4.11 Charging Test with Chevy Bolt

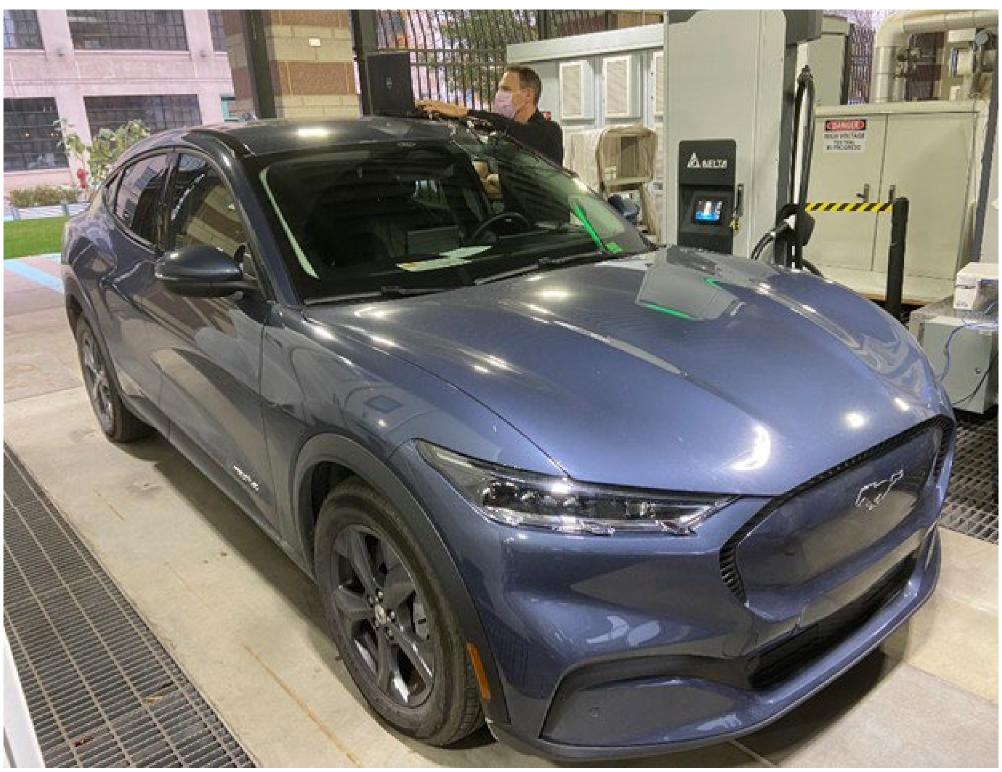

Figure II.1.4.12 Charging Test with Ford Mach-E

The SST's input power is 60Hz AC while its output power is DC. The 120Hz AC component in the power flow can be seen as power fluctuation. It is absorbed in the SST cell, either at the DC-link between AC/DC and DC/DC or at the output of the DC/DC. If the 120Hz power fluctuation is completely absorbed at the DC-link between AC/DC and DC/DC, the DC/DC stage has constant power flow control. This is the most commonly used strategy. The disadvantage of this strategy is it requires large capacitor at the DC link. If the 120Hz power fluctuation completely passes through the DC link and the DC/DC stage, the DC/DC stage has fluctuating power control and thus has higher power loss in return for smaller DC link capacitor. It is also possible to make a tradeoff and allow partial power fluctuation pass through the DC/DC stage. The power loss of the three methods are analyzed and compared to support the selection of the overall best solution for future designs.

Results

XFC Full System Efficiency Test Result

The function and efficiency of 400 kW XFC system was tested at full voltage and power range at total 44 points. The test result matches the design calculation very well. It meets and exceeds the specification. The peak efficiency is 97.6%. The efficiency curves have been reported in last year's report.

The AC input waveforms looks clean. Figure II.1.4.13 shows the typical AC input waveforms.

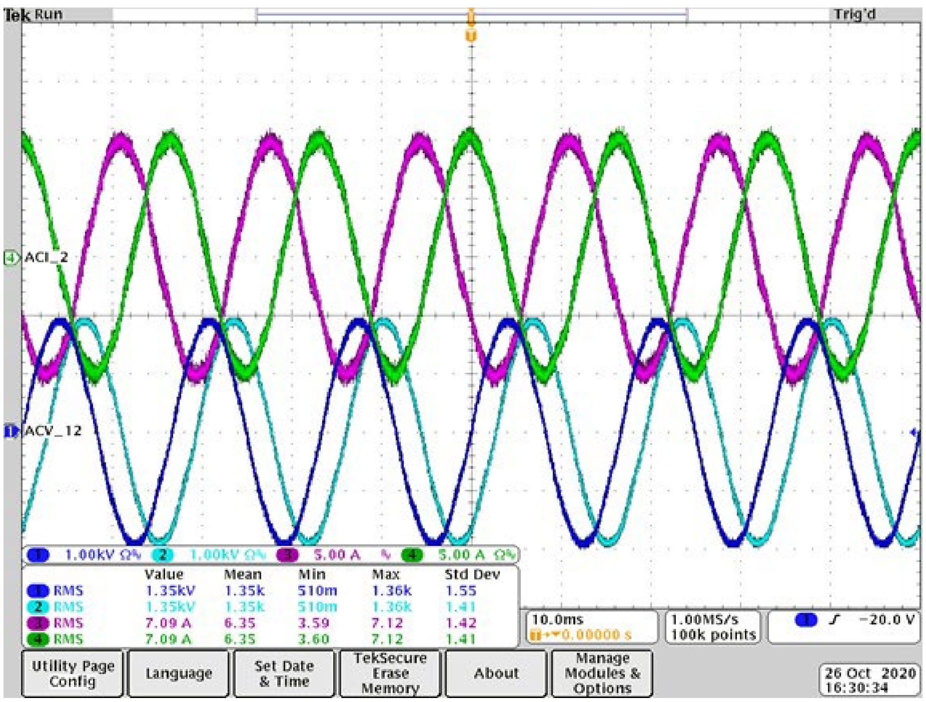

Figure II.1.4.13 AC Input Waveforms (CH1: VAB, CH2: VBC, CH3: IA, CH4: IB)

The power factor is above 95% when input power is above 50 kW, and above 99% when the input power is above 100 kW. Figure II.1.4.14 shows the power factor vs. input power.

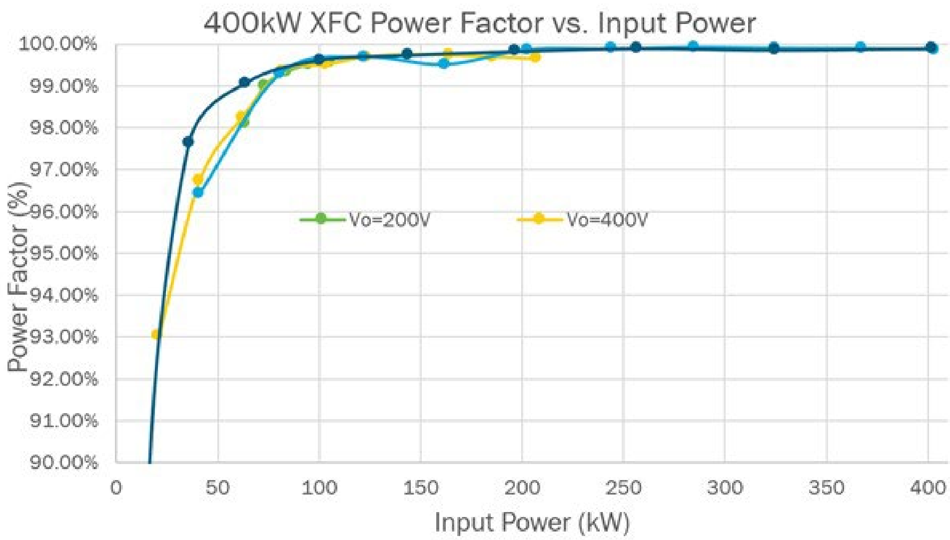

Figure II.1.4.14 Power Factor vs. Input Power

Power Loss Analysis Result for three SST Control Methods

The power loss of the SST power stage is analyzed for constant power flow control, fluctuating power flow control and partial fluctuating power flow control. The result are shows in Figure II.1.4.15, Figure II.1.4.16 and Figure II.1.4.17, respectively. The conventional constant power flow control has the lowest total power loss as well as the lowest transformer power loss. Extracting heat from transformer is more difficult than from other devices. Therefore, the transformer power loss has a high priority in design tradeoff. The analysis confirms that the constant power flow is the overall best control method among the three, even it requires more DC link capacitors.

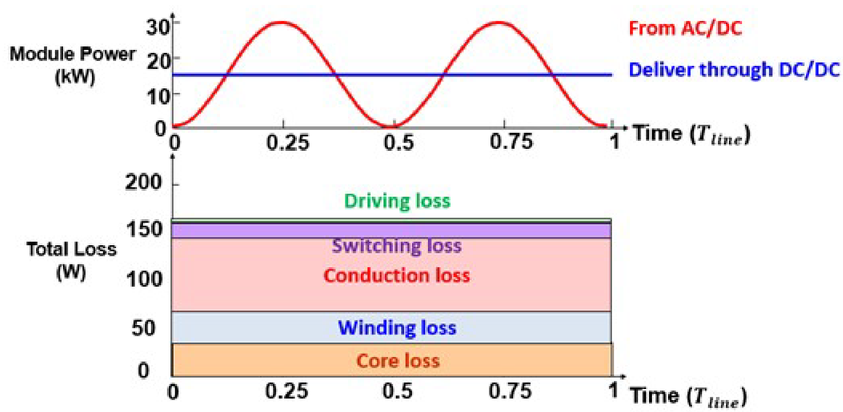

Figure II.1.4.15 Power loss breakdown for the constant power flow control

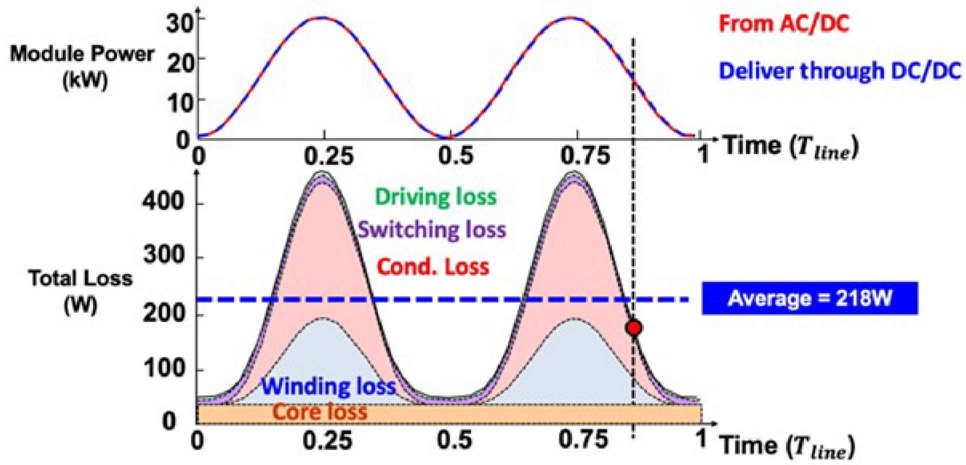

Figure II.1.4.16 Power loss breakdown for the fluctuating power flow control

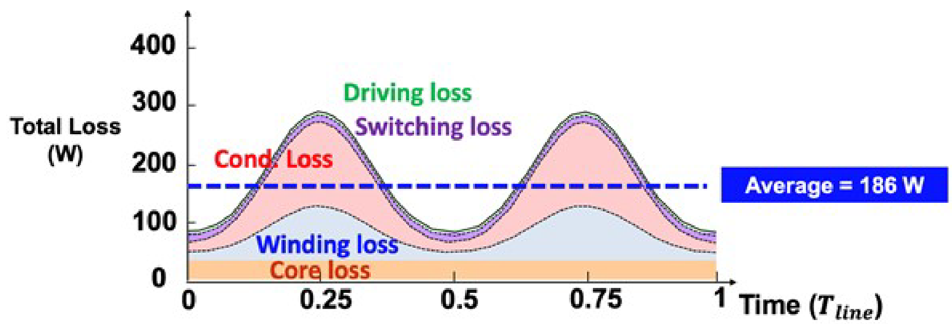

Figure II.1.4.17 Power loss breakdown for the partial fluctuating power flow control

Vehicle Charging Test Result

Vehicle charging tests were conducted with Chevy Bolt EV, Cadillac Lyriq EV, Volkswagen ID.4, and Ford Mach-E EVs. When charging Cadillac Lyriq EV, the maximum charging current of 500A lasted for approximately 10 minutes, accumulated in 5 sections. This shows that the XFC's maximum charging current exceeds the original objectives.

Program Delay

The development of the retrofit test vehicle and the construction of the final test and demonstration site were delayed due to the COVID-19 pandemic. Delta submitted a request for a six-month extension to this DOE program DE-EE0008361 from Nov 30, 2021, to May 30, 2022.

Conclusions

The test result shows that the 13.2kV 400 kW SST, the 400 kW Buck charger power cabinet and the dispenser meet the specification. The integration of the 13.2kV 400 kWXFC system is successful and the performance of simulated load meets and exceeds the target specification. The program objects of FY 2020 is completely met. The next step is to install an XFC system at DTE site and test full power charging with GM's retrofit vehicle.

Key Publications

1. Chi Zhang, Peter Barbosa, Zhiyu Shen, and Rudy Wang, "A Novel Three-level Phase-Shift Modulation for Serial Half Bridge LLC Resonant Converter," APEC 2021, June 2021.

2. Chunyang Zhao, Yi-Hsun Hsieh, Fred C. Lee, and Qing Li, "Design and Analysis of a High-frequency CLLC Resonant Converter with Medium Voltage insulation for Solid-State-Transformer," APEC 2021, June 2021.

3. Zheqing Li, Yi-Hsun Hsieh, Qiang Li, Fred C. Lee, and Chunyang Zhao, “Evaluation of Double-Line-Frequency Power Flow in Solid-State Transformers,” ICDCM 2021, July 2021.

References

1. D. Howel, S. Body, B. Cunningham, S. Gillard, and L. Slezak, “Enabling Fast Charging: A Technology Gap Assessment,” U.S. Department of Energy, October 2017. [Online]. Available: https://energy.gov/sites/prod/files/2017/10/f38/XFCn%20Technologyn%20Gapn%20Assessmentn%20Reportn FINALn 10202017.pdf

2. Mehrnaz Ghamami, Ali Zockaie, Joy Wang, Steven Miller, “Electric Vehicle Charger Placement Optimization in Michigan: Phase I – Highways”, Michigan Energy Office, February 2019. [Online]. Available: https://www.michigan.gov/documents/energy/EV-Charger-Placement-Opt-PhaseI-Final-Report-021319_646220_7.pdf

3. L. D. Stevanovic, K. S. Matocha, P. A. Losee, J. S. Glaser, J. J. Nasadoski, and S. D. Arthur, “Recent Advances in Silicon Carbide MOSFET Power Devices,” 2010 Twenty-Fifth Annual IEEE Applied Power Electronics Conference and Exposition (APEC), Palm Springs, CA, 2010, pp. 401–407.

4. J. S. Glaser, J. J. Nasadoski, P. A. Losee, A. S. Kashyap, K. S. Matocha, J. L. Garrett, and L. D. Stevanovic, “Direct Comparison of Silicon and Silicon Carbide Power Transistors in High-frequency Hard-switched Applications,” 2011 Twenty-Sixth Annual IEEE Applied Power Electronics Conference and Exposition (APEC), Fort Worth, TX, 2011, pp. 1049–1056.

5. T. Daranagama, N. Udugampola, R. McMahon, and F. Udrea, “Comparative Analysis of Static and Switching Performance of 1.2 kV Commercial SiC Transistors for High Power Density Applications,” The 1st IEEE Workshop on Wide Bandgap Power Devices and Applications, Columbus, OH, 2013, pp. 48–51.

Acknowledgements

This work is supported by the DOE Office of Energy Efficiency and Renewable Energy, Vehicle Technologies Office, and administrated by National Energy Technology Laboratory, under contract number DE-EE0008361. The author wishes to thank project team members:

Steven Boyd and Lee Slezak of VTO and Michael Ursic and John Jason Conley of NETL for their contributions.

II.1.5 Bidirectional Wireless Power Flow for Medium-Duty Vehicle-to-Grid Connectivity

Steven Sokolsky, Principal Investigator
CALSTART
1509 Wendy Lane
Madison, WI 53716
Email: ssokolsky@calstart.org

Omer C. Onar, Technical Lead
Oak Ridge National Laboratory, Vehicle Power Electronics Research Group,
National Transportation Research Center, 2360 Cherahala Boulevard
Knoxville, TN 37932
Email: onaroc@ornl.gov

Burak Ozpineci, Section Head and ORNL Program Manager
Oak Ridge National Laboratory, Vehicle and Mobility Systems Research Section
National Transportation Research Center, 2360 Cherahala Boulevard
Knoxville, TN 37932
Email: burak@ornl.gov

Lee Slezak, DOE Technology Manager
U.S. Department of Energy
Email: lee.slezak@ee.doe.gov

Start Date: October 2016 End Date: September 2022
Project Funding: $2,631,321 DOE share: $1,949,007 Non-DOE share: $712,314

Project Introduction

Wireless power transfer (WPT) is a paradigm shift in electric-vehicle (EV) charging that offers the consumer an autonomous, safe, and convenient option to conductive charging and its attendant need for cables. With WPT, charging process can be fully automated due to the vehicle and grid-side wireless communication systems, and is non-contacting and inherently isolated; therefore, issues with leakage currents, ground faults, and touch potentials do not exist. It also eliminates the need for touching the heavy, bulky, dirty cables and plugs. It eliminates the fear of forgetting to plug-in and running out of charge the following day and eliminates the tripping hazards in public parking lots and in highly populated areas such as shopping malls, warehouse loading areas, recreational areas, parking buildings, etc. Furthermore, the high-frequency (HF) magnetic fields employed in power transfer across a large air gap are focused and shielded, so that fringe fields (i.e., magnetic leakage/stray fields) attenuate rapidly over a transition region to levels well below limits set by international guidelines for the public zone. With the bidirectional wireless power transfer, not only vehicles can be wirelessly charged, but also the vehicles can wirelessly provide power back to the grid or the facility. With bidirectional power flow, vehicles can be enabled to provide microgrid or grid support or ancillary services. Grid support may include peak shaving, renewable energy firming/integration, time of use energy management, power quality improvement, voltage regulation, reactive power compensation, etc. Grid ancillary services to be provided might include spinning and non-spinning reserves, area/frequency regulation, load following, scheduling and dispatch, etc. if a number of vehicles are aggregated to provide such services. In the case of an outage, vehicle batteries can also serve as an emergency backup power for a period of time.

In this project, CALSTART, ORNL, UPS, Workhorse Group, and Cisco Systems proposed to model, research, analyze, design, develop, integrate, and demonstrate a bi-directional wireless power transfer system (BWPT) suitable for Class 5 and Class 6 medium-duty plug-in hybrid delivery trucks. The project team designs, develops, integrates, and tests a bi-directional wireless charging system capable of meeting the 11-inch ground clearance needed for UPS delivery trucks. After integrating to a Workhorse manufactured plug-in hybrid electric vehicle (PHEV), the system performance will be demonstrated at the deployment site. Within the first budget period of the project (May 2017-May 2018), team has completed the modeling, simulations, design, and analysis of the system power conversion stages including the 3-phase active front-end rectifier with power factor correction (also grid interface inverter), primary-side HF inverter (also primary-side rectifier), primary and secondary-side resonant tuning components, primary and secondary-side electromagnetic coupling coils, vehicle-side HF rectifier (also the vehicle-side HF inverter). As of submission time of this report, hardware both the primary and secondary sides have been completed and the power conversions stages have been successfully tested. All of the subsystems and components have been validated based on their parameters and performance metrics. Now the team is starting the vehicle integrations and system will be deployed with full vehicle integrations for the testing, demonstrations, and data collection purposes.

Objectives

The overall project objectives can be summarized as follows:

1. Provide an automated, high power, interoperable, high-efficiency wireless charging for a plug-in hybrid electric medium duty delivery truck with a nominal ground clearance of approximately eleven (11) inches.

2. Optimize the add-on vehicle-side wireless charging components through integration and utilization of already existing vehicle-side components while implementing grid-side controls and regulations to reduce the vehicle-side cost, size, volume, and complexity.

3. Utilize bi-directional wireless charging systems when trucks are parked in the yard for staging to provide grid support applications or ancillary or grid support services such as frequency regulation, load leveling/peak shaving/load factor improvement/reactive power support/demand charge management and spinning/non-spinning reserves.

4. Provide an integrated > 20 kW wireless charging system (grid to vehicle) with high efficiency (85%) while meeting the international guidelines on electromagnetic and electric field emissions during charging and include all other appropriate safety features.

5. In vehicle-to-grid mode, achieve 6.6kW wireless power transfer to building or grid loads.

Approach

Starting from the AC grid to the vehicle battery terminals, the system power converters must be well-designed and operated in order to achieve high efficiency. In addition, power flow control to the pick-up system should be resolved where the control parameters (DC link voltage, frequency, duty cycle, phase-shift, etc.) are actively controlled to improve efficiency while meeting the vehicle-side target voltage, current, and/or power. Simultaneously, vehicle-side DC link or battery voltage, current, temperature, and the state-of-charge (SOC) should be carefully monitored and fed-back to the primary side for controls. Moreover, the battery management system (BMS) or other vehicle-side functions (i.e., contactors and liquid cooling system) should be monitored for safety. The bidirectional wireless charging system that will be used in this project is shown in Figure II.1.5.1. This is the overall system architecture that is determined and agreed upon by the technical team. For this architecture, the baseline performance metrics have been defined, system specifications have been determined, and the hardware including the power stages and passive components have been designed and developed in ORNL PEEM laboratory. As shown in Figure II.1.5.1, system utilizes a three-phase rectifier/inverter system that interfaces the wireless charging system to the grid. During charging, the active-front end rectifier with power factor correction (PFC), delivers power from the grid with high power factor to the HF power inverter’s input. The input (grid) current is controlled in order to regulate the inverter input voltage, depending on the amount of power to be transferred to the vehicle-side battery. The HF power inverter generates the HF current for the primary coupling coil. On both primary and secondary, LCC type resonant tuning configuration was utilized for operational symmetry since the bidirectional power flow is needed.

Additionally, LCC type resonant tuning circuitry provides load and coupling factor independent constant current on primary coil which simplifies the communication requirements and the control systems. On the vehicle side, there is a receive coil with a rectifier/inverter, and a filter capacitor. During discharging or vehicle battery powering the AC grid/building loads, the vehicle-side converter is operated in an inverter mode and delivers HF current to the vehicle coil. The vehicle-side coil generates a magnetic field that is linked to the ground coil. The ground coil induces a high frequency voltage that is rectified and inverted to 60Hz to power the building loads or to the AC grid.

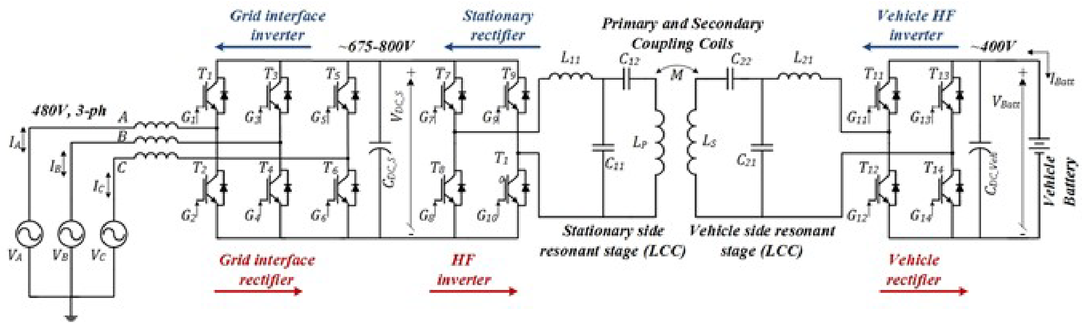

Figure II.1.5.1 System level diagram of the proposed architecture for the bidirectional wireless charging system.

This FY team continued the benchtop laboratory tests of the system for verifying the design parameters and the functionalities. This included testing and validating the parameters of each power conversion stage both at component and subsystem levels using grid and battery emulators. Later, the whole system integrated together, and the operation of the entire system is validated in both power flow directions including the communications link for the closed loop operation. Finally, the vehicle integrations are completed and the whole system is validated on the vehicle. The vehicle integration efforts are visualized in Figure II.1.5.2.

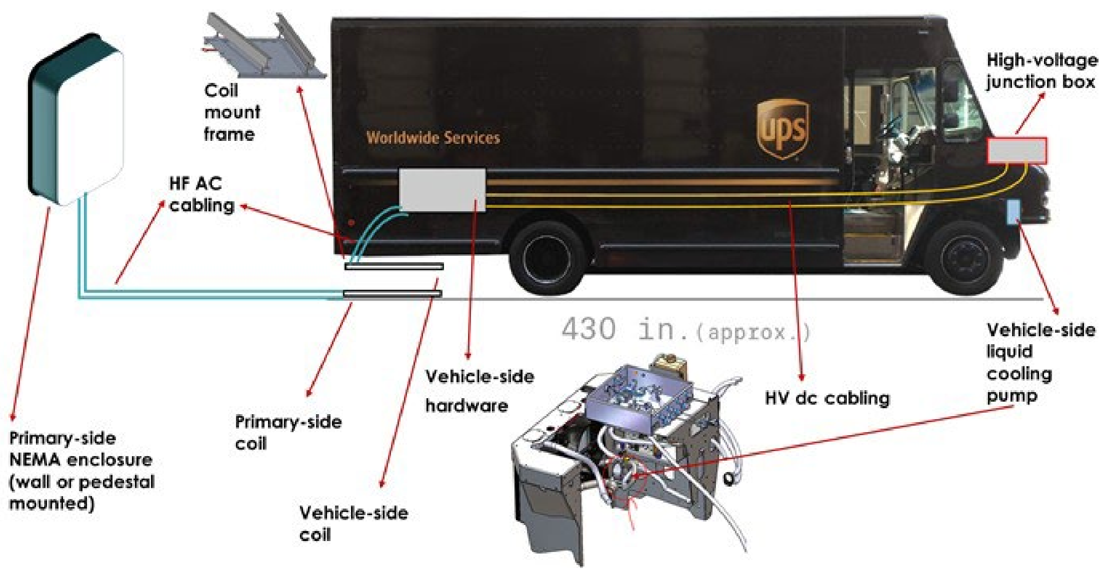

Figure II.1.5.2 System level diagram of the proposed architecture for the bidirectional wireless charging system.

The back of the vehicle is used for the vehicle-side coupler installation for two main reasons. The first reason is that these trucks back up at the docks; and the coil at the front of the vehicle would have larger misalignments if the vehicle was parked even with a small angle when backing up. The other reason is that a receiver coil at the front of the vehicle would require much longer high-frequency AC cabling from primary-side unit to the transmit pad. Similarly, a decision had to be made for the location of the vehicle side unit which could be either at the back closer to the receiver coil or at the front closer to the high-voltage junction box that houses the battery connection terminals. Team decided to mount the vehicle side unit closer to the vehicle-side coil in order to minimize the high-frequency cabling length from coil to the vehicle side unit. If mounted at the front, the high-frequency cabling around 30 feet would cause a considerable amount of losses in addition the stray fields generated along the cabling. High-voltage dc cabling on the other hand, is a lot more efficient than high-frequency ac cabling with no issues on field emissions. For the vehicle side coupler, ORNL developed a custom design coil mount frame that was installed on truck's crossmember rails. For the cooling of the vehicle-side power electronics, the initial wish was to utilize the existing liquid cooling system of the on-board charger. However, the 12V pump of the liquid cooling system was tightly surrounded by other engine related components and it was very difficult to access to the output hoses as well as to the pump 12V input to activate it when charging. In addition, since this pump is at the front of the vehicle while the vehicle-side unit is at the back, that 30 feet of length would cause considerable drop of the pressure in the cooling lines. Therefore, team decided to use a separate dedicated thermal management system for the vehicle-side unit of the wireless charging system.

In Figure II.1.5.3 (a), the primary-side hardware is shown which includes the input LC filter stage, 480V 3-phase connection to the front-end rectifier/inverter, high-frequency inverter/rectifier, and the inverter output LCC resonant tuning tank before the primary coupler. Primary-side also includes a main 3-phase contactor that connects and disconnects the system from/to grid which is followed by a pre-charge circuitry that uses a series resistor to charge the dc bus capacitors without a surge current which bypassed by another 3-phase contactor during normal operation. The input connection is also fused. Primary side also utilizes a DSP based controller and gate driver boards. 3-phase phase-to-neutral voltage sensors and 3-phase line current sensors at the input to properly control the input current. There is also a dc bus voltage sensor which is a direct indication of power transfer level. There is also a 480V 3-phase ac to 24V dc converter which is then converted to +/- 15V and 5V levels for low power controls, fans, sensors, DSP, gate drivers, and other electronics. Figure II.1.5.3 (b) shows the vehicle-side unit that consists of connection to the secondary coil, vehicle-side LCC resonant tank, high-frequency rectifier/inverter, power modules with gate drivers, DSP board, a main contactor to the battery along with a pre-charge circuitry with pre-charge resistor and bypass contactor, an output fuse, and an output filter inductor to reduce battery current ripples. This unit also includes 12V to +/- 15V and 5V converters for the operation of controllers, sensors, contactors, gate drivers, fans, and all other low power electronics etc.

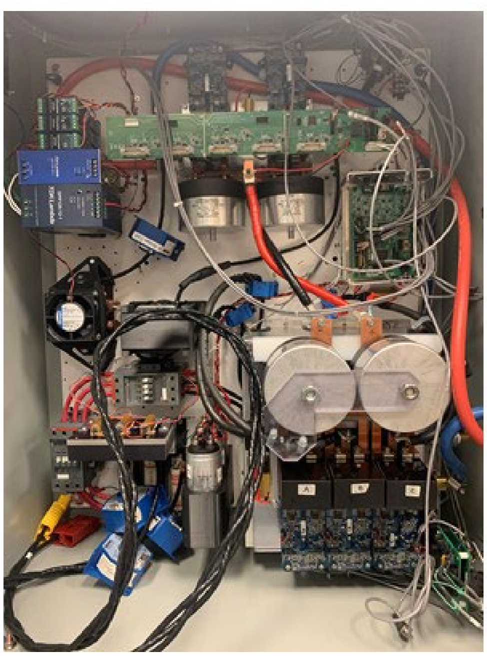

(a)

(b)

Figure II.1.5.3 Primary-side (a), and the secondary-side (b) hardware of the system.

Figure II.1.5.4 (a), the coil mounting rail frames are shown that are bolted to the vertically running vehicle crossmember rails with adjustable height. While the average vehicle ground clearance is about 11 inches, the lowest point under the vehicle is 8 inches above the ground which is the frontal subframe and the coupling rod or differential between the rear wheels. As required by the project, 11 inches magnetic airgap is used from the surface of the secondary coil to the ground level as shown in Figure II.1.5.4 (b).

.

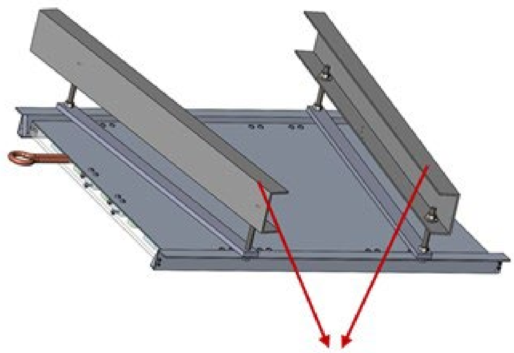

(a)

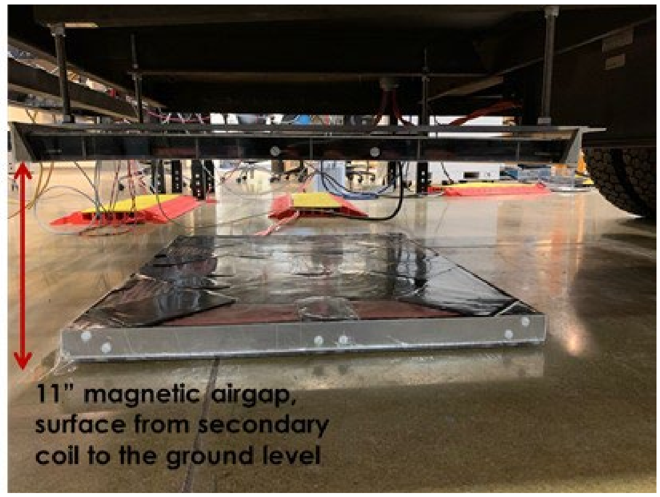

(b)

Figure II.1.5.4 Vehicle-side coil mount assembly (a) and the primary and secondary couplers with 11 inches magnetic airgap (b).

During this FY, UPS completed their site preparations with the installation of a 480V 3-phase disconnect switch at their Roswell, GA facility. ORNL added an additional user control mechanism to start charging, stop, and start discharging to provide controllability to the UPS staff to operate the wireless charging system. This is in addition to the computer-based control system that can be used to communicate the operational commands to the bidirectional wireless power transfer system through CAN bus or an Ethernet network. The other addition was to add high voltage to 12V dc/dc converters. During the earlier demonstration, 12V truck battery was used to supply all the auxiliary and thermal management system loads on the vehicle-side hardware. While this is still a viable approach if the truck is driven and charged every day, there is an increased risk of draining the 12V battery during charging. Therefore, the 12V truck battery is only used during the first minute of the wireless charging system. Once the wireless charging system starts and ramps up, the high voltage battery provides the auxiliary power demand through a high voltage to 12V dc/dc converter that takes over the 12V loads from the 12V truck battery. On the 12V bus of the vehicle-side electronics, ORNL uses 3 other dc/dc converters for 12V to +/-15V and 5V conversions to power the digital signal processor, interface boards, gate drivers, sensors, contactors, radio unit, and the liquid cooled chiller. This approach ensures the 12V battery is not drained while charging and its normal lifetime is not reduced.

Results

After extensive laboratory testing, the UPS truck and the wireless charging hardware are deployed at the Grid Research Integration and Deployment Center (GRID-C) of ORN as shown in Figure II.1.5.5 for the project demonstration event that was hold on February 27, 2020. The instrumentation setup for the demonstration is shown in Figure II.1.5.6 where a power analyzer was set to read the voltage, current, power, and efficiency of all the power conversion stages, an oscilloscope was used to capture some of the selected input and output voltage and current waveforms of the system. Finally, a laptop PC was connected to the vehicle battery management system (BMS) to display the battery voltage, current, and state-of-charge to the users.

Figure II.1.5.5 Resonant voltage gain of the system using the analytical model (a) and the experimental validation (b).

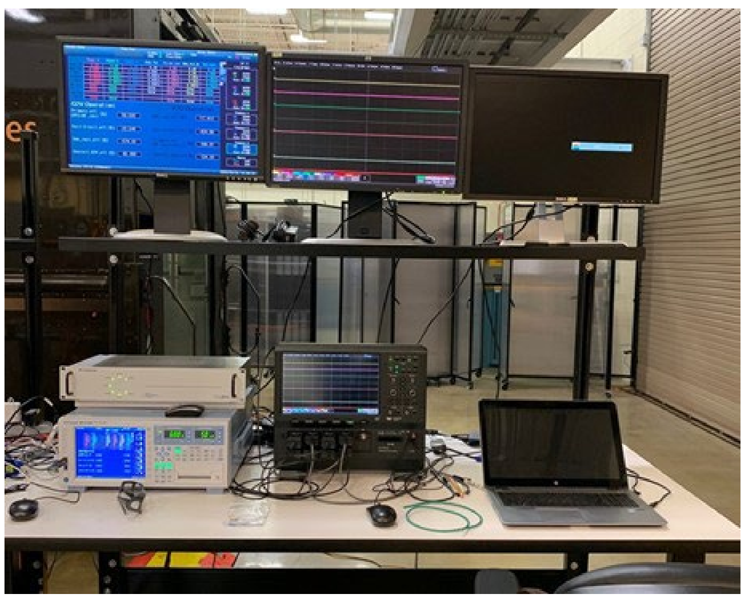

Figure II.1.5.6 Instrumentation setup for the project demonstration.

Demonstration of the system included displaying and recording the system performance in both power flow directions where G2V indicates power flow from grid-to-vehicle (charging or drawing power from the grid) and V2G indicates power flow from vehicle-to-grid (discharging or injecting power back to the grid). In Figure II.1.5.7, the power analyzer test results are displayed where the vehicle battery receives 20.36 kW of power. The combined efficiency of the grid interface converter (rectifier) and the high-frequency inverter is recoded 97.30%, coil-to-coil efficiency is 96.96% which includes the efficiency of the primary and secondary-side LCC resonant tuning components, and the vehicle-side rectifier efficiency is 98.59%. This results in an overall end-to-end efficiency of 93% for G2V (charge mode) operation (>85% was the project requirement). Also as shown in Figure 6, input power factor on the grid side was 0.999 (0.95 was the project requirement) for all the input phases while the total harmonic distortion on the input current was <0.8-0.95 on all phases (<5% was the project requirement). These performance results indicate that the system operation exceeds all the project requirements in terms of overall efficiency, power level, power factor, and total harmonic distortions.

Figure II.1.5.7 G2V operation test results.

Similar test results for the V2G (discharge mode) are displayed in Figure II.1.5.8 where 12.8 kW (>6.6 kW was the project requirement) was transferred from vehicle battery to the 480V 3-phase power grid. In this operating mode, vehicle-side inverter's efficiency was 99.38%, coil-to-coil efficiency was 92.8% including the losses across the resonant tuning components, and primary-side high-frequency rectifier and grid interface inverter's combined efficiency was recorded 96.61%. This results in an overall end-to-end efficiency of 89.09% (>85% was the project requirement) from vehicle battery to the power grid. In this mode of operation, the power factor was maintained >0.99 (0.95 was the project target) across all the grid phases while the total harmonic distortion on grid current was about 1–1.5% (<5% was the project target) across the grid phase currents. This mode of operation also met all the project requirements in terms of power level, power transfer efficiency, grid power factor, and the grid current total harmonic distortions. The main reason for less efficient operation in V2G mode is that most power converters and coupling coils are less efficient in light load operations, i.e., with some margin added, the overall system is designed for 30–35 kW; therefore, 12 kW is about 30% of the power rating. 20 kW power transfer to the grid would be a lot more efficient and comparable to the G2V efficiency.

Figure II.1.5.8 V2G operation test results.

Conclusions

During the first budget period of the project, the team worked on modeling, simulations, analysis, and design of the system power conversion stages and control systems. Upon the successful design review meeting in May 2018 which concluded the first budget period of the project, team started building the hardware of all the system power conversion stages along with the control systems. During the second budget period, team built all the power electronic converter hardware and fabricated all the passive components including the 3-phase grid-connected inductors, capacitor systems, resonant tuning circuit components, coupling coils, and the vehicle-side filter components. Team also designed and developed two DSP interface boards for the primary and secondary sides. Team has successfully tested the operation of the power conversion stages. Then the whole system tested together with the vehicle integrations. According to the results, G2V operation was 20.36 kW with 93% end-to-end efficiency over 11 inches of magnetic airgap with asymmetric voltage gain (~0.5) on the resonant stage with high power quality on the grid side. Similarly, V2G operation was demonstrated with 12.8 kW power transfer, 11 inches of airgap, 89.1% end-to-end efficiency, and asymmetric voltage gain (~2) on the resonant stage with high power quality on the grid side.

The second budget period work focused on final systems testing and validation along with the final fabrication of system components. The system components were packaged and final tests on the completed system were conducted. Budget Period 3 work will focus on the real-world demonstration of the fully-equipped vehicle and secondary-side capabilities at the UPS facility in Roswell, Georgia. The vehicle will be placed in normal operations at that facility and UPS will use the system for 6 months. Data will be collected during this period to demonstrate the repeatability of the performance and analysis of the use cases. At the same time the team will complete the business case and economic analyses using different use scenarios and electric rate options obtained from several utilities, typical of those that have seen PHEVs and BEVs introduced in their service territories.

Key Publications

1. "Secondary Active Rectifier Control Scheme for a Wireless Power Transfer System with Double-Sided LCC Compensation Topology," in Proc., 44th Annual Conference of the IEEE Industrial Electronics Society (IECON), October 2018, Washington, D.C.

2. "Sensitivity of an LCC-LCC Compensated 20-kW Bidirectional Wireless Charging System for Medium-Duty Vehicles," in Proc., IEEE Transportation Electrification Conference and Expo (ITEC), June 2019, Novi, MI.

3. "Bidirectional LCC-LCC Compensated 20-kW Wireless Power Transfer System for Medium-Duty Vehicle Applications," IEEE Transactions on Transportation Electrification, vol. 7, no. 3, pp. 1205–1218, September 2021.

Acknowledgements

Project team would like to thank Jason Conley of the National Energy Technology Laboratory for his continued guidance and support on this project.

II.1.6 Intelligent, Grid-Friendly, Modular Extreme Fast Charging System with Solid-State DC Protection (North Carolina State University)

Srdjan Lukic, Principal Investigator
North Carolina State University
1791 Varsity Drive
Raleigh, NC 27695
Email: smlukic@ncsu.edu

Steven Boyd, DOE Program Manager
U.S. Department of Energy
Email: steven.boyd@ee.doe.gov

Start Date: October 1, 2018 End Date: December 31, 2022
Project Funding: $2,435,511 DOE share: $1,099,164 Non-DOE share: $1,336,347

Project Introduction

With the wider adoption of electric vehicles, there is an urgent need for an electric vehicle (EV) charging infrastructure that will parallel the refueling capabilities of existing gasoline stations, particularly in regions where long-distance trips are common. However, designing and deploying such an EV charging infrastructure is complex, and must consider space constraints, industry standards, available technologies, grid capacity and impacts, and other technical and policy issues. This project aims to develop a framework for designing compact and efficient medium voltage (MV) extreme fast charging (XFC) stations for electric vehicles that minimize the negative effect on the power grid, while also minimizing installation and operating costs of the system and providing design flexibility for the installers and system integrators. By connecting directly to the MV distribution network, the proposed approach eliminates the need for a step-down transformer to provide low voltage service. Elimination of the low frequency transformer reduces the system footprint and system losses and eliminates inrush currents during grid black-start; in addition, placing power electronics directly on the distribution system, allows for high-bandwidth filtering and power factor connection. We will also demonstrate a DC distribution network protected using novel, intelligent solid-state (SS) dc circuit breakers (DCCB) that can isolate the smallest faulted circuit much faster than the state-of-the-art mechanical solutions.

Objectives

The team will design and deploy a 1MVA XFC station that connects directly to the power distribution system, operating at 13.2kV. The XFC station will consist of a solid-state transformer (SST) that delivers power to a shared DC bus, to which multiple vehicle charging dispensers and dc storage/generation units connect (see Figure II.1.6.1). The proposed **SST** connects directly to the 13.2kV supply, without the use of a step-down transformer; this approach significantly reduces the system footprint and power conversion losses compared to the state of the art (see Figure II.1.6.2). The smaller footprint allows system installation in space-constrained areas, while considerably reducing installation costs. Higher power conversion efficiency reduces operating costs by delivering more of the input power to the vehicle. The XFC system will connect to multiple EV charging dispensers and generators/storage units using a DC distribution network protected using novel intelligent **SS DCCB**. The shared DC bus naturally allows power sharing between all generators/loads, with minimum number of conversion stages. Each vehicle will interface to the DC bus through an **EV charging dispenser**, which is an isolated DC/DC converter rated to allow charging in the 50 kW to 350 kW range at the vehicle battery voltage. **The integrated energy management platform** will allow the utility to take control actions including curtailing power delivered to the station; controlling the power ramp rates; and controlling the XFC reactive power injection or providing other ancillary services.

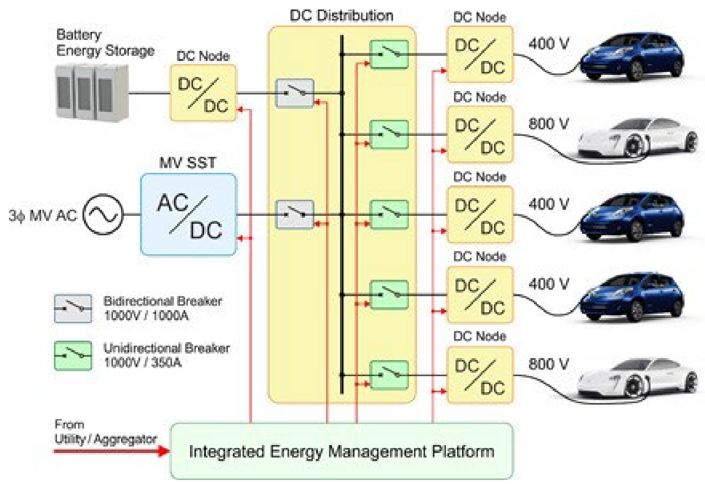

Figure II.1.6.1 Key components of the proposed XFC Station: MV SST, DC distribution network, and dispenser (dc node) that contains the dc/dc converter and vehicle interface

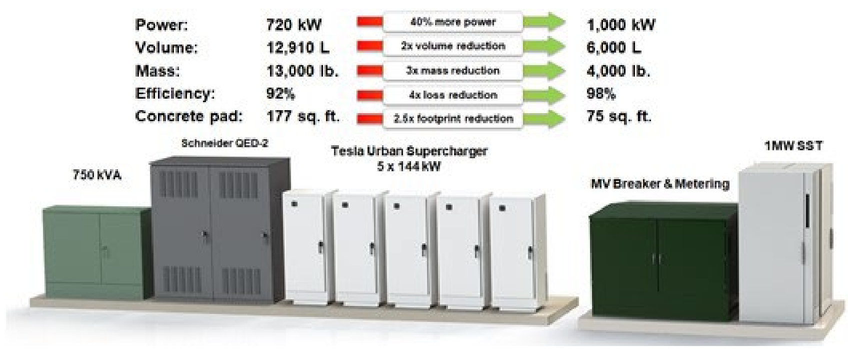

Figure II.1.6.2 Comparison of the proposed SST-based power conversion to the state-of-the art approach. The diagram shows the infrastructure required to convert power from an ac distribution voltage to a dc voltage and includes the power conversion, protection, isolation and metering considerations.

Approach

The scope of this project is to design, build, test and deploy the proposed MV XFC station in the field. The project will be conducted in three budget periods:

Budget Period 1 – Sub-system Development: This effort focused on designing, prototyping and testing the SST, SS DCCB, EV charging dispensers and the energy management platform. The team selected the demonstration site and completed the engineering drawings for the system deployment. The team also developed a detailed use case and fault case test plan.

Budget Period 2 – System Integration: The team finalized, packaged, and tested the SST, dispensers, SS DCCB, distribution network protection, and integrated energy management system. The systems will be fully tested in the lab prior to deployment to ensure that the system operates as expected. The site preparations will be completed to prepare the site for system deployment.

Budget Period 3 – System Deployment and Demonstration: The integrated 1MVA XFC will be shipped to the site and commissioned. The team will demonstrate the use case scenarios and fault scenarios outlined in the test plan and will develop a comprehensive operations and maintenance manual.

Results

The focus in FY2021 has been on the design, development and prototyping of the SSTs and the SS DCCBs and the testing of the integrated system. In addition, the team completed the deployment site preparation. The team faced significant setbacks due to the Covid-19 outbreak, subsequent shutdowns of facilities, and, more recently, supply chain delays that have made getting many components challenging. The team is working around these restrictions to keep the project timeline on track, and current projections are that no additional time delays will occur.

Solid-state transformer (SST) design, development, construction and system integration

The team has made significant progress towards demonstrating the MV SST proposed in the project plan. Our approach was to develop two versions of the SST, one for lab testing and validation (see Figure II.1.6.3, left) and the other for the final system deployment in the field (see Figure II.1.6.3, right). The final prototype will have optimized packaging and about 10 times the power density of the laboratory prototype.

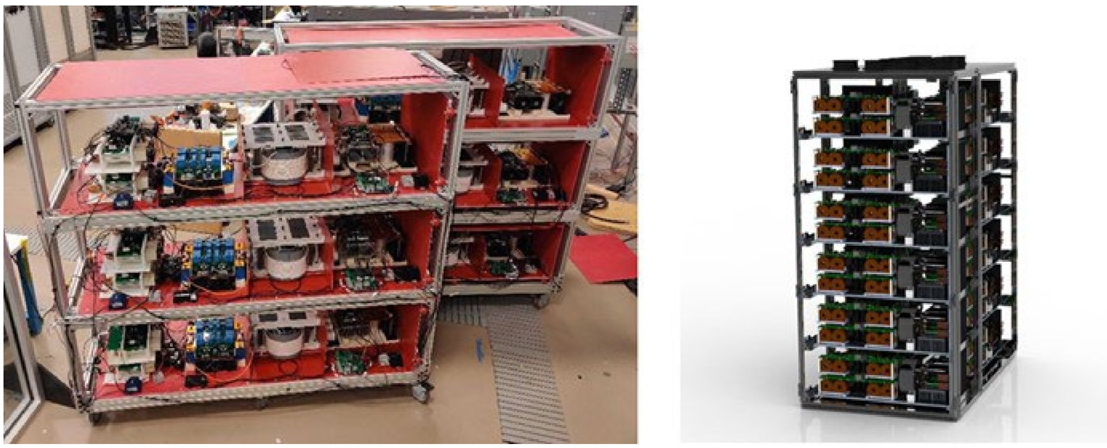

Figure II.1.6.3 Laboratory and field SST designs. Left: laboratory prototype of the SST used for hardware validation/optimization Right: SST prototype designed for field deployment.

The laboratory prototype of the SST was built for (1) hardware validation/optimization (2) as a controls testbed and (3) for system integration and protection validation; it was designed to deliver 500kVA at 4.2kVac input to a DC load at 750V. The system consists of six modules, each rated at 95 kW. Each module is made up of an active front end (AFE) and a dual active bridge (DAB) DC/DC converter. The AFE uses a full bridge topology, with each full-bridge switch using a series connection of three 1.2kV/16mOhm devices. Voltage sharing among the series-connected devices is achieved using the hybrid active and passive clamping circuit. Compared to the passive solution, the proposed hybrid solution has no requirement to fully charge and discharge the flying capacitors resulting in reduced power loss and capacitor size. The DAB topology uses an all SiC solution with 1700V modules on MV and 1200V modules on the low voltage (LV) sides. The switching frequency is 20kHz, and the module outputs are interleaved to minimize the storage requirements. A proportional-integral-resonant compensator eliminates second harmonic power oscillations on the MV DC bus. A bidirectional phase-shift modulator with capacitor voltage balancing generates the gate pulses for the primary and secondary bridges of the DAB. The transformer relies on winding separation in air to meet isolation requirements, and reinforced isolation between windings and core. The transformer design is compatible with insertion in oil.

We tested the interaction between the SST and the DC SSCB's to ensure safe operation of the entire system. The test setup, shown in Figure II.1.6.4(c), consists of the SST connected to the grid via a 3-phase 480V supply, a variac and a step-up transformer; it also includes AC breakers for protection. The DC SSCB interfaces the load to the SST; in addition, a pre-charge circuit connects to the DC bus of the SST. Two tests are shown in Figure II.1.6.4 to demonstrate the operation of the system: the startup procedure (Figure II.1.6.4(a)-(c)) and the loss of load (Figure II.1.6.4(e)-(f)).

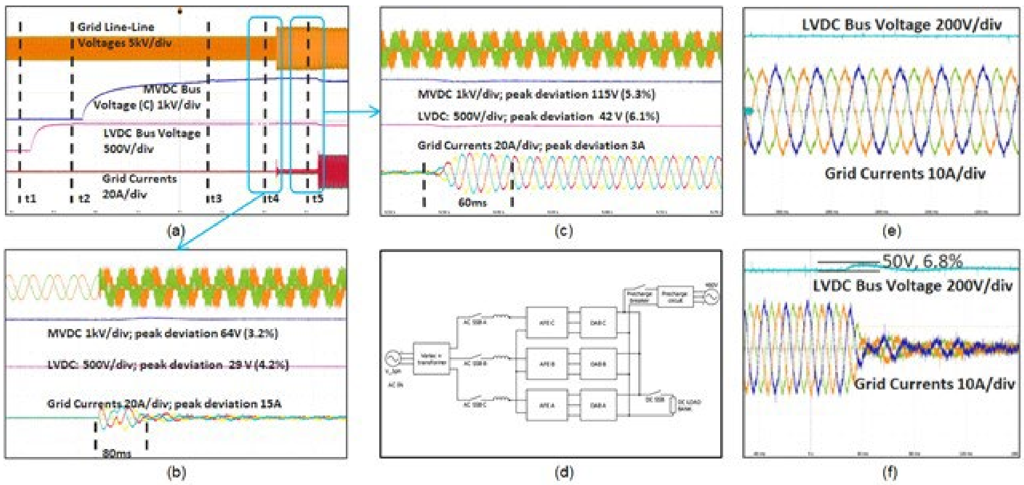

Figure II.1.6.4 Experimental test results and setup. (a) SST startup sequence; (b) zoom-in on period t4 of the startup sequence, showing the SST connecting to the grid; (c) zoom-in on period t5 of the startup sequence, showing a step change in load from zero to 32kW; (d) Setup used for testing the startup and loss of load tests; (e) steady state operation delivering 100 kW to the load; (f) zoom-in of the moment when the load is disconnected showing the load step change from 100 kW to zero and the resulting voltage dynamics.

The startup process, is defined by five time points shown in the Figure II.1.6.4(a), and described below:

- t1: Pre-charge circuit breaker closes, charging LV DC bus to 678 V from the 480 V, three phase power supply.
- t2: DAB switches begin operating in open loop and charge the MV DC bus.
- t3: DAB control loop closes and regulates the MV DC bus to 1.95 kV
- t4: AC SS breaker closes, making the SST grid connected. The DC breaker remains open, and the pre-charge circuit disconnects. At this point the AFE closed-loop control is initiated, and it regulates the LV DC bus voltage. Since the load is not connected, the current is near-zero.
- t5: The breaker closes and the load increases from zero to 32kW.

The loss of load test is shown in Figure II.1.6.4(e)-(f). Initially, the system is delivering 100 kW to a resistive load (see Figure II.1.6.4(e)), when a trip command is sent to the SSB, the SSB opens, causing an instantaneous loss of load. Two fiber optic lines control each SSB—one for the command signals and the second one for the status feedback. As seen in Figure II.1.6.4(f), the SST DC bus voltage increases by 50V or about 7% before settling back to the nominal value of 750V. This is well within the specifications of the system.

Development of solid-state circuit breakers

The team is developing the DC switchgear and two SS DCCB's. The 1500A class SS DCCB will be used as main circuit breakers, one connecting the power from the main power source (SST) and another connecting the battery energy storage system (CB 1 and CB2 in Figure II.1.6.5). The 500A class SS DCCB is a unidirectional breaker that will be used as branch circuit breaker for the protection of the cables transferring power from the SST to the DC/DC converters and to protect against short circuit and grounding faults (CB 3, 4 and 5 in Figure II.1.6.5).

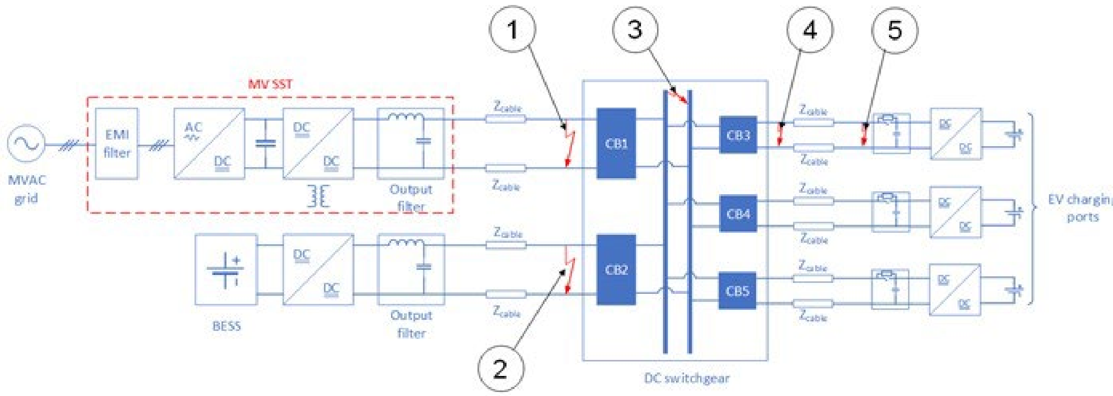

Figure II.1.6.5 Five fault scenarios considered for experimental validation.

The team has tested the protection coordination between the assembled prototypes (1500A and 500A SS DCCB). This is important, to validate that in the case of a fault event, only the breaker in the fault branch is selectively tripped and the rest of the system can continue operation, ensuring a high system availability. The five fault scenarios of interest are shown in Figure II.1.6.5. The test scenarios were tested in simulations and in hardware. The system has passed all tested scenarios for fault locations 3, 4, and 5 under different system impedances. Namely, the faults at locations 3, 4 and 5 (from Figure II.1.6.5) have been emulated in the lab with higher levels of system inductances ($L_{sys} \sim 300\mu H$), and breaker coordination has been successfully verified. The system inductances were then progressively lowered to validate the settings and performance of the control electronics.

The team is also completing assembly and testing the finalized designs of the individual breakers (1500A and 500A), and has finished assembling the key components, namely, the semiconductor stacks. Key components in the stack assemblies have been delivered and certified by experimental tests for both electrical and thermal performance. The final beta breakers are being completed based on lessons learned from the alpha prototypes. The switchgear cabinet, which hosts the six SS DC circuit breakers, has been designed and assembled and all 6 breakers will be connected after final thermal and electrical performance verification of each individual breaker (see Figure II.1.6.6). The switchgear has forced ventilation for cooling and a compact bus structure for power distribution.

Figure II.1.6.6 Solid-state dc switchgear assembly and testing.

Site selection and site preparation for deployment

NYPA has utilized approved value contracting to secure Engineering & Construction Management Services from Wendel Engineering. They in turn have established a sub-contract with an electrical firm familiar and on-site at the Clark Energy Center (CEC) facility. At NYPA CEC demonstration site, trenching, conduit and cable for entrance & exit between the anticipated R&D shipping container and the 15 kV transformer, were completed. Bonding, and grounding procedures were all followed, in accordance with NYPA requirements.

The excavated ‘spoils’ from digging were evaluated for any contamination and will be trucked off site for proper disposal. Supply chains of some vital site equipment continue to delay schedules. The area to stage the R&D project will be ‘winterized’ shortly, where the completion work will resume in Spring 2022.

Conclusions

In the current budget period, the team finalized, packaged, and tested the SST, the DC distribution network and protection, and integrated the energy management system. The systems will be fully tested in the lab prior to deployment to ensure that the system operates as expected. The site preparations will be completed prior to system deployment. The team has met its key milestones including the go/no-go milestone, having demonstrated the integration of the SST and the DC SSB. The outstanding tasks will be completed in the coming BP, including the completion of site preparation and complete system integration and testing, prior to shipping and commissioning the system in the first half of 2022.

Key Publications

1. H. Tu, H. Feng, S. Srdic and S. Lukic, “Extreme Fast Charging of Electric Vehicles: A Technology Overview,” in *IEEE Transactions on Transportation Electrification*, vol. 5, no. 4, pp. 861–878, Dec. 2019, doi: 10.1109/TTE.2019.2958709.

2. D. Wang and W. Yu, “Series Connection of SiC MOSFETs with Hybrid Active and Passive Clamping for Solid State Transformer Applications,” *2019 IEEE 7th Workshop on Wide Bandgap Power Devices and Applications (WiPDA)*, 2019, pp. 12–19, doi: 10.1109/WiPDA46397.2019.8998791.

3. M.A. Awal, I Husain, Md R. H. Bipu, O. Montes, F. Teng, H. Feng, M. Khan and S. Lukic, “Modular Medium Voltage AC to Low Voltage DC Converter for Extreme Fast Charging Applications”, arXiv preprint, submitted June 2020, arXiv:2007.04369

4. M.A. Awal, Md. Bipu, O. Montes, H. Feng, I. Husain, W. Yu and S. M. Lukic, “Capacitor Voltage Balancing for Neutral Point Clamped Dual Active Bridge Converters,” in *IEEE Transactions on Power Electronics*, vol. 35, no. 10, pp. 11267–11276, Oct. 2020, doi: 10.1109/TPEL.2020.2988272.

5. L. Qi, P. Cairoli, Z. Pan, C. Tschida, Z. Wang, V. R. Ramanan, L. Raciti, A. Antoniazzi, “Solid-State Circuit Breaker Protection for DC Shipboard Power Systems: Breaker Design, Protection Scheme, Validation Testing,” in *IEEE Transactions on Industry Applications*, vol. 56, no. 2, pp. 952–960, March-April 2020, doi: 10.1109/TIA.2019.2962762.

6. S. Chen, R. Hassan Bipu, D. Wang and W. Yu, “Analysis and solution of the unbalanced device voltage issue for SiC MOSFET based diode neutral point clamped converter,” *2020 IEEE Applied Power Electronics Conference and Exposition (APEC)*, 2020, pp. 2048–2055, doi: 10.1109/APEC39645.2020.9124451.

7. P. Cairoli, R. Rodrigues, U. Raheja, Y. Zhang, L. Raciti and A. Antoniazzi, “High Current Solid-State Circuit Breaker for safe, high efficiency DC systems in marine applications,” *2020 IEEE Transportation Electrification Conference & Expo (ITEC)*, 2020, pp. 936–941, doi: 10.1109/ITEC48692.2020.9161515.

8. R. Rodrigues, U. Raheja, P. Cairoli, L. Raciti and A. Antoniazzi, “Accelerated aging test of Solid-State DC Circuit Breaker based on 2.5 kV Reverse Blocking IGCT,” *2020 IEEE Energy Conversion Congress and Exposition (ECCE)*, 2020, pp. 6024–6029, doi: 10.1109/ECCE44975.2020.9235953.

9. Y. Zhang, U. Raheja, R. Rodrigues, P. Cairoli, L. Raciti and A. Antoniazzi, “Experimental Validation of Parallel Connection of RB-IGCTs for High Efficiency Solid State Circuit Breaker,” *2020 IEEE Energy Conversion Congress and Exposition (ECCE)*, 2020, pp. 6036–6042, doi: 10.1109/ECCE44975.2020.9235967.

10. R. Rodrigues, U. Raheja, Y. Zhang, P. Cairoli and A. Antoniazzi, “Power Loop Busbars Design and Experimental Validation of 1 kV, 5 kA Solid-State Circuit Breaker Using Parallel Connected RB-IGCTs,” in *IEEE Transactions on Industry Applications*, vol. 57, no. 3, pp. 1920–1927, May-June 2021, doi: 10.1109/TIA.2021.3062591.

11. R. Rodrigues, Y. Du, A. Antoniazzi and P. Cairoli, “A Review of Solid-State Circuit Breakers,” in *IEEE Transactions on Power Electronics*, vol. 36, no. 1, pp. 364–377, Jan. 2021, doi: 10.1109/TPEL.2020.3003358.

12. X. Song, Y. Du and P. Cairoli, “Survey and Experimental Evaluation of Voltage Clamping Components for Solid State Circuit Breakers,” *2021 IEEE Applied Power Electronics Conference and Exposition (APEC)*, 2021, pp. 401-406, doi: 10.1109/APEC42165.2021.9487424.

13. R. Rodrigues, Y. Zhang, U. Raheja, P. Cairoli, L. Raciti and A. Antoniazzi, “Robust 5 kA, 1 kV Solid-State DC Circuit Breaker for Next Generation Marine Power Systems,” *2021 IEEE Electric Ship Technologies Symposium (ESTS)*, 2021, pp. 1–7, doi: 10.1109/ESTS49166.2021.9512345.

14. Feng, Hao, Fei Teng, Oscar Andres Montes, M. A. Awal, Md Rashed Hassan Bipu, Iqbal Husain, and Srdjan Lukic, “Passive Capacitor Voltage Balancing of SiC-based Three-level Dual-Active-Bridge Converter Using Hybrid NPC-Flying Capacitor Structure,” in *IEEE Transactions on Power Electronics*, doi: 10.1109/TPEL.2021.3119210.

II.1.7 Development and Demonstration of Medium-Heavy Duty PHEV Work Trucks (Odyne Systems)

John R. Petras, Principle Investigator
Odyne Systems LLC
W237 N2878 Woodgate Road, Suite 2
Pewaukee, WI 53072
Email: John.Petras@Odyne.com

Ken Kelly, Principal Investigator
National Renewable Energy Laboratory (NREL)
15013 Denver West Parkway
Golden, CO 80401
Email: Kennith.Kelly@nrel.gov

David Smith, Principal Investigator
Oak Ridge National Laboratory (ORNL)
2370 Cherahala Boulevard
Knoxville, TN 37932
Email: Smithde@ornl.gov

Steven Boyd, DOE Program Manager
U.S. Department of Energy
Email: steven.boyd@ee.doe.gov

Start Date: January 19, 2017 End Date: January 31, 2021
Project Funding: $5,108,655 DOE share: $2,149,644 Non-DOE share: $2,959,013

Project Introduction

The heavy-duty vehicle market (Class 6-8) has been a difficult segment for the introduction of plug-in vehicles due to the large energy storage requirement (with corresponding cost), challenging duty cycles, and the diversity of vehicle configurations. The Work Truck market represents a significant opportunity for Heavy-Duty PHEV adoption. Odyne proposes development of a new class of PHEV Work Truck which will be modularized and customized to provide optimal ROI across multiple customers and applications. The proposed project will first demonstrate this technology as a Utility Work Truck variant:

- The usage cycle includes driving and stationary/worksite power requirements, ensuring full daily usage of the grid-charged battery (battery size: 15-30 kWhr). Though daily driving can often be short (an average of 26 miles per day), worksite power includes substantial demand (hydraulics, exportable 110/220V power, 12V support, HVAC).
- Worksite power demands for conventional vehicles require continuous loaded engine operation, resulting in significant emissions, fuel consumption and noise impacts.
- These trucks serve an industry that is strongly incentivized to promote vehicle electrification, and which has publicly committed to spending a portion of their annual vehicle purchase budget on electrified vehicles (EEI press release of 11/18/14).

This project will develop and demonstrate a medium/heavy duty plug-in hybrid solution capable of meeting the needs of the work truck market while delivering fuel and emissions reductions of 50% when evaluated against the full-day work truck duty cycle.

Objectives

The project goal is to design, develop, and demonstrate a new generation of medium/heavy-duty plug-in hybrid electric work truck that achieves a 50% reduction in fuel consumption versus a conventional vehicle baseline when evaluated across a full day work cycle representative of the vocational work truck. The primary objectives are:

- To simulate, design and develop unique and innovative integrated powertrain, software, and calibrations which will optimize the complete diesel/transmission/hybrid powertrain and demonstrate the potential for driving fuel efficiency improvements greater than 40% with commensurate reductions in GHG emissions.
- To develop and validate a modular Lithium-Ion battery system based on high volume lower cost cells and modules that are utilized in the light-duty sector which will meet the power, energy, and duty cycle requirements of the MD-HD vocational truck market at a cost approaching half that of currently available low volume solutions.
- To integrate fully electrified worksite functions and a daily duty cycle optimization function with the powertrain and battery solutions on an OEM class 6-7 chassis and demonstrate the capability of 50% reduction in total fuel used when measured against a full day duty cycle's and real-world performance.
- To demonstrate ten optimized PHEV work trucks and validate the vehicle's operating performance, emissions, and full work cycle fuel reduction capability in excess of 50%.

Approach

The proposed solution incorporates a simple, parallel hybrid system that allows the torque of the electric motor to augment the torque output of the diesel engine, thus saving fuel. The motor speed is synchronized with the engine speed through the existing power take-off (PTO) unit. The traction motor drives the PTO, adding torque to the rear axle, or converts torque from the PTO into power to charge the PHEV batteries (see Figure II.1.7.1). Six patents have been granted, and other patents are pending prior to initiation of this project.

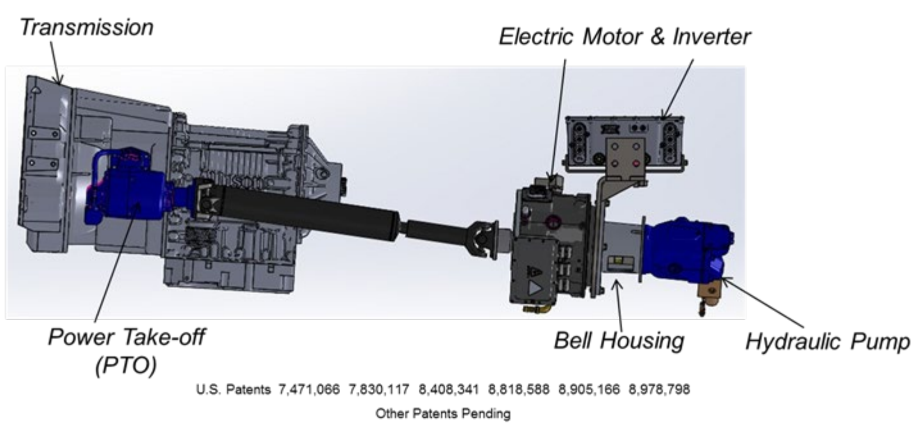

Figure II.1.7.1 Odyne powertrain configuration

The system is also designed to provide full jobsite engine off electrification utilizing power from the lithium-ion battery system to provide 120/240 V exportable power, 12V chassis systems support, high efficiency electric heating and air conditioning along with the power to drive the primary work equipment (Figure II.1.7.2).

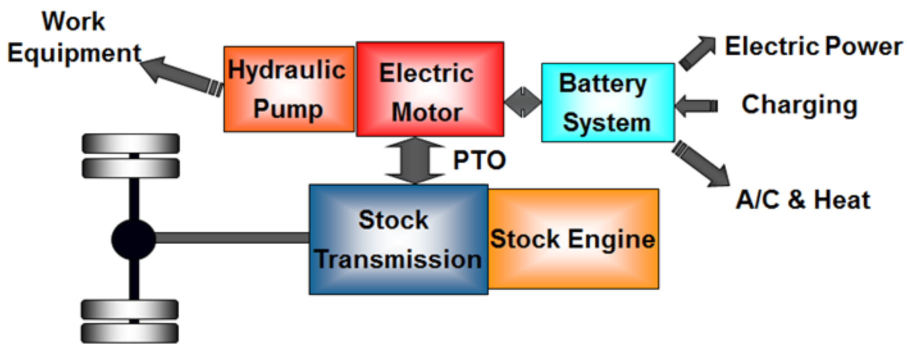

Figure II.1.7.2 Odyne hybrid architecture

The project will be conducted in three periods:

Period 1: System Design and Analysis

Analysis of existing fleet data will be performed and will be used for the establishment of baseline driving and full day usages cycles and current vehicle performance for system simulation, development and test. The project will create designs and systems which, when integrated, will produce a Medium-Heavy duty work truck capable of achieving requirements under real world conditions. The period will conclude with an analytical simulation verifying this performance improvement.

Period 2: System and Vehicle Verification

The subsystems will be verified and refined using prototype hardware and the full vehicle will undergo final development, functional and performance test. The prototype phase will conclude with test results confirming that the final design will provide a ≥50% reduction in fuel use under real world conditions. Approximately ten vehicles will be built to support field test and evaluation.

Period 3: Prototype Vehicle Demonstration

Ten vehicles will be put in regular service with telematics to measure performance. The Recipient will analyze the data along with customer feedback and will report the calculated real-world reduction in fuel use and customer acceptance of the technology.

The project will integrate three development streams into a final Prototype vehicle solution and 10 vehicle field demonstrations:

Powertrain Development and Optimization

- Odyne – Lead, Hybrid Powertrain development and design, Hybrid optimization and control strategies
- NREL – Duty cycle analysis, Dynamometer test, Full-year fuel use simulation and analysis
- Oak Ridge National Laboratory – Powertrain simulation and optimization, HIL Test
- Allison Transmission – Transmission control and optimization strategies.

Battery Development

- Odyne – System Specifications and integration requirements, system integration test
- Odyne, Ricardo Strategic Consulting – Battery System supply chain evaluation
- Enerdel – Lithium-Ion Module and BMS Supplier, Component System integration requirements.

Chassis Development & Integration

- Odyne – System design, control, cost, and integration lead, Systems Efficiency & Sizing, System build
- Freightliner – OEM Chassis Integration improvements, Prototype chassis supplier.

Results

In FY21, the project completed baseline and hybrid fuel and emissions testing on the National Renewable Energies Lab ReFUEL Chassis dynamometer, integration, and validation of the primary path battery system, and released final designs for the system to be integrated into the demonstration vehicles.

Powertrain Development and Optimization

The full vehicle dynamometer testing, planned for early 2020, was delayed by facility closures due to Covid-19. Driving performance results were delivered and analyzed in early FY21 (Table II.1.7.1). Under all three duty cycles, Odyne achieved the program goal of achieving greater than 50% improvement in driving fuel economy. NREL also provided stationary test results from the Stationary duty cycle created during Budget Period 1. The NREL calculation considers the energy utilized by electric PTO (ePTO) to be replenished by a field recharge (as opposed to Plug-in charge). This is a worst-case scenario; telematics data indicates 80-100% of ePTO energy is derived from Plug-in charge during a typical day. Under the NREL assumptions, the Odyne ePTO system utilized 80% less fuel and produced 98% less NOx when compared to a conventional Diesel PTO system (Table II.1.7.2).

Table II.1.7.1 NREL ReFUEL Chassis Dynamometer Results

Strategy	Duty Cycle	Distance (mi)	Fuel Used (Gal)	MPG	MPG Improvement (%)	Energy Used per Mile (kWh)
Conventional	UDDS	5.503	0.892	6.174		0.000
Hybrid Mild	UDDS	5.498	0.813	6.762	9.5%	0.060
Hybrid Aggressive	UDDS	5.514	0.528	10.456	69.4%	0.971
Conventional	Odyne Low	3.782	0.809	4.678		0.000
Hybrid Mild	Odyne Low	3.780	0.656	5.758	23.1%	0.508
Hybrid Aggressive	Odyne Low	3.788	0.476	7.954	70.0%	1.675
Conventional	Odyne Med	8.911	1.431	6.226		0.000
Hybrid Mild	Odyne Med	8.907	1.226	7.266	16.7%	0.197
Hybrid Aggressive	Odyne Med	8.897	0.815	10.918	75.4%	1.220

Table II.1.7.2 NREL ReFUEL Chassis Dynamometer Stationary Results

Strategy	Duty Cycle	Condition	Shaft Energy (kw-hr)	Fuel Used (Gal)	Efficiency (gal/kW-hr)	Gal/kW-hr Improvement (%)
Conventional PTO	NREL Stationary	Cold Start	1.450	0.6153	0.4243	
Hybrid ePTO Charge	Field Recharge	Cold Start	4.774	0.5328	0.0893	78.5%
Conventional PTO	NREL Stationary	Hot Start	1.451	0.6184	0.4261	
Hybrid ePTO Charge	Field Recharge	Hot Start	5.299	0.4580	0.0692	82.8%

Battery and Chassis System Development

During FY21, the design team completed the packaging, subsystem and component layouts and drawings to efficiently install the hybrid electrification system on a wide range of work trucks and updated the test truck to the new configuration. Because of the compact size of the Enerdel battery, most of the freestanding power and control components were able to be attached within the footprint of the previous battery bracket, greatly reducing the system package space, number of sub-assemblies, and wiring complexity. Figure II.1.7.3 represents the new configuration with the hybrid components represented in green and Figure II.1.7.4 is the updated test vehicle

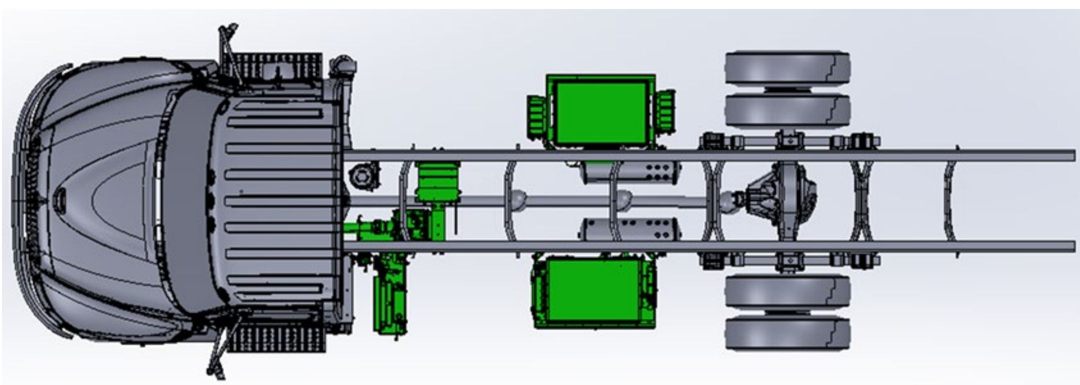

Figure II.1.7.3 Odyne Project System Layout

Figure II.1.7.4 Odyne Updated Test Vehicle

Conclusions

In FY21, the project completed the test of the hybrid drive strategies and completed the system integration, layout and design to be utilized for the demonstration vehicles as well as future Odyne production. The drive testing demonstrated that the system is capable of delivering up to 75% fuel economy improvement, depending on duty cycle, although a lessor driving strategy will ultimately be utilized when considering battery cost and size, stationary energy needs, and the real-world duty cycle of the Medium/Heavy Duty work truck. The final goal of the project is to demonstrate the capability to reduce the full day fuel use of a Medium/Heavy Duty work truck by over 50% in field demonstration.

Key Publications

1. SAE Journal Article 03-14-04-0030, SAE International Journal of Engines was released on 29-MAR-21. ORNL has published in OSTI under this project number.

Acknowledgements

Odyne wishes to acknowledge the substantial contributions of Michael Ursic (NETL), Eric Miller, Peter Sindler, Jonathan Burton, Matt Thornton, (NREL), Adian Cook, Dean Deter (Oak Ridge National Laboratory), Greg Mann, Brent Maurer (Allison Transmission), Dan Purdy (Freightliner Trucks), and Mark Kuhn, Alan Munday (Ricardo Strategic Consulting)

II.1.8 SCAQMD ZECT-SanPedro FCCEV and HEV Demo (South Coast Air Quality Management District)

Seungbum Ha, Program Supervisor
South Coast Air Quality Management District
21865 Copley Drive
Diamond Bar, CA 91765
Email: sha@aqmd.gov

Lee Slezak, DOE Technology Manager
U.S. Department of Energy
Email: lee.slezak@ee.doe.gov

Start Date: October 1, 2014 End Date: February 28, 2024
Project Funding: $20,410,075 DOE share: $9,725,000 Non-DOE share: $10,685,075

Project Introduction

The proposed project area is known as the Los Angeles Goods Movement and Industrial Corridor. This area is adjacent to the Ports of Long Beach and Los Angeles, the busiest port complex in North America. The area is in an industrial setting with diesel truck activity mingled with a variety of uses including residences, schools, daycares, and senior centers. The area is also a known Environmental Justice Community made up of predominantly low-income and minority populations that are adversely impacted by vehicle emissions.

The proposed technologies, fuel cell range extenders and hybrid electric trucks, face many challenges in the process of commercialization: proper sizing of the fuel cell stack, battery and fueling system; system integration and packaging of power train components and systems for safe, efficient, and economical deployment of the technologies are just a few of the challenges. Many options exist in sizing the energy systems for these type of vehicle architectures—making the battery, engine or fuel cell dominate in size; plug in charging versus operation in charge sustaining mode and sizing of the energy storage system. Considerations for the power requirements of vehicle under load and providing enough onboard energy to attain the range requirements for the drayage operation and duty cycles all come into play in the design of the energy storage and power systems. Another challenge is to design the energy and power train systems described above and then integrate them into a vehicle for safe and efficient operation that can be made economical in volume and series production.

Objectives

- Reduce criteria pollutants and GHG's in South Coast Air Basin by reducing diesel emissions from transportation and movement of goods
- Accelerate introduction and penetration of zero and near-zero emission fuel cell and hybrid technologies in cargo transport sector
- Execute a joint project with the Port of Los Angeles and Long Beach consisting of demonstration, data collection and analysis of seven fuel cell and hybrid trucks on five different vehicle architectures.

Approach

ZECT 2 Projects

Figure II.1.8.1 CTE/Kenworth Fuel Cell Truck

CTE/BAE Systems and Kenworth have developed a battery electric truck with a hydrogen fuel cell range extender. The vehicle will operate in electric mode at all times and all speeds until the battery energy system reaches a lower operating state of charge level, at which point the hydrogen range extender would be activated to supplement power.

TransPower has developed two battery electric trucks with hydrogen fuel cell range extenders. These trucks will employ a small fuel cell and stored hydrogen. One truck will be equipped with a 30-kW fuel cell and one with a 60-kW fuel cell, enabling a direct comparison of both variants.

Figure II.1.8.2 TransPower Fuel Cell Truck in Foreground & CNG Truck in Background

U.S. Hybrid has developed two equivalent battery electric trucks with an on-board hydrogen fuel cell generator. Each truck is estimated to have 20 kg of hydrogen storage at 350 BAR with an estimated fueling time under 10 minutes.

Figure II.1.8.3 U.S. Hybrid Truck: Design to Fabrication

Figure II.1.8.4 Kenworth/BAE - CNG Hybrid System Architecture

GTI/BAE Systems and Kenworth have developed one hybrid battery electric truck with CNG range extender. The proposed technical concept provides an all-electric mode, and in a conventional hybrid mode using CNG. The truck will have an on-board battery charger to fully charge the batteries in daily use.

Cummins (formerly Hydrogenics which was acquired by Cummins) will be developing and demonstrating a fuel cell range extended Class 8 truck. Hydrogenics working with Daimler's VVG dealership group developing a fuel cell range extended truck under a California Energy Commission (CEC) project.

- Two Hydrogenics HD90 fuel cell modules for a peak fuel cell power of 180 kW and a 53-kWh high-power battery pack
- Cummins 4-speed automated manual transmission
- 150-200mi range

Results

TransPower

Fourth Quarter 2020

- Recommissioning of the prototype truck, FC1 has been completed.
    - The truck has done simulated drayage service, completing tows at full 80,000 lbs. gross as well as tows of a less than fully loaded trailer. There is extensive data which will be included in the final report.
    - The periodic flashing of the amber engine light, mentioned in last month's report, was resolved with changes implemented in SCM software 824 and PCM_HD_604. This software is being tested in other fuel cell trucks as well, addressing most of the dashboard issues
    - The commissioning and validation has been initiated, the truck drives well but for the aforementioned power issues which are the current focus. The truck was driven 79 miles the past month, current mileage is 3305 miles.
- FC2
    - The truck was returned to service availability at TTSI following replacing a hydrogen recirculation pump. Further improvements in the cooling system power control were implemented late in the month, these improvements had first been implemented and tested with FC1 during its commissioning process. We have observed these changes allow smoother continuous operation of the fuel cell APU and should improve drivability.

First Quarter 2021

The team has completed the truck demonstration in Q4 2020 and provided a draft of final report.

The draft of final report includes details of demonstration including the data collected from the truck.

Meritor, which has acquired TransPower is negotiating to continue the operation with TTSI beyond ZECT II project.

In the meantime, these two fuel cell trucks are seeking for the opportunity of operating by other fleets that are interested in fuel cell drayage trucks.

Second and Third Quarter 2021

The team has completed the truck demonstration in Q4 2020 and provided a draft of final report.

The draft of final report includes details of demonstration including the data collected from the truck.

Meritor, which has acquired TransPower is negotiating to continue the operation with TTSI beyond ZECT II project.

In the meantime, these two fuel cell trucks are seeking for the opportunity of operating by other fleets that are interested in fuel cell drayage trucks.

US Hybrid

Fourth Quarter 2020

- US Hybrid FC#1 has completed the 24months demonstration at TTSI and is seeking an opportunity to expand the demonstration. US Hybrid and TTSI are discussing the contract terms and conditions for extending the demonstration. Otherwise, US Hybrid will find alternative fleet to use the FC#1.

- FC#2 has been upgraded for hydrogen tank from 25 to 35kg and can perform over 200mils range. TTSI is operating the truck actively and will test this vehicle from the port to Moreno valley warehouse.

First Quarter 2021

US Hybrid FC#1 has completed the 24months demonstration at TTSI and is seeking an opportunity to expand the demonstration. US Hybrid and TTSI are discussing the contract terms and conditions for extending the demonstration. Otherwise, US Hybrid will find alternative fleet to use the FC#1.

FC#2 has been upgraded for hydrogen tank from 25 to 35kg and can perform over 200miles range. TTSI is operating the truck actively and will test this vehicle from the port to Moreno valley warehouse.

Due to an extended range up to 200miles, Amazon and other fleet are interested in this truck for their service route including drayage from the Port to inland empire warehouses or between the warehouses in inland empire.

Once the service route and operation details are confirmed, FC#2 will be used for testing by other fleets.

Second and Third Quarter 2021

US Hybrid FC#1 has completed the 24months demonstration at TTSI and is seeking an opportunity to expand the demonstration. US Hybrid and TTSI are discussing the contract terms and conditions for extending the demonstration. Otherwise, US Hybrid will find alternative fleet to use the FC#1.

FC#2 has been upgraded for hydrogen tank from 25 to 35kg and can perform over 200miles range. TTSI is operating the truck actively and will test this vehicle from the port to Moreno valley warehouse.

Due to an extended range up to 200miles, Amazon and other fleet are interested in this truck for their service route including drayage from the Port to inland empire warehouses or between the warehouses in inland empire.

Both FC #1 and #2 have completed the demonstration and the final report will be provided.

CTE/BAE and Kenworth Fuel Cell Truck

Fourth Quarter 2020

Early in the reporting period, following issues have been addressed and resolved.

- The truck blew a LV fuse causing failures of the window and mirror controls.
- This was quickly replaced and did not result in any downtime.
- TTSI had to tow the truck due to overheating.

Upon review, TTSI discovered the driver had neglected to fuel the truck before taking it out.

For the rest of the reporting period, the truck ran most days of the week with no further issues reported and operated approximately 30miles/day. TTSI is currently training additional drivers due to increases in weekly freight, and this will allow the truck to be used every day of the week with the potential for two shifts a day. The truck's consistent performance has led the team to evaluate longer routes such as Fontana (50 miles one way). This led to a detailed discussion regarding the truck's performance capabilities, potential refueling issues, and risk to the truck's total service hours if there is a failure. NREL provided a preliminary analysis of the data collected up to this point to help determine the limitations of the truck and establish where the highest potential for failure is during a longer route. The Project Team will continue to work to minimize these risks and develop a plan to test the truck on a longer, more strenuous route.

First Quarter 2021

During the previous reporting period, the Amazon pilot ended roughly a week and a half early due to two power steering faults causing the operator to lose confidence in the vehicle. Kenworth engineering team provided a separate diagnosis for the two faults. The first fault was due to the operator cycling through the restart process too quickly and blowing a HV fuse. Currently, the truck requires a minimum of 3-5 minutes in standby after powering down. The second fault was due to a drop in CAN communication in the power steering pump controller that exceeded dwell time and resulted in steering control being shut down. After ending the pilot, the truck was returned to San Pedro operations and experienced a fault similar to the second fault in the Amazon demonstration. This resulted in TTSI's safety team grounding the vehicle until Kenworth can provide a guarantee that the issue is fully resolved. Kenworth sent a technician to attempt to further diagnose the issue, but the intermittent nature of the failure meant there were no abnormalities in the data thereby making the root cause difficult to pinpoint. Additionally, Kenworth cannot guarantee any fault resolution for a demonstration project as power steering issues can occur on commercial trucks.

Kenworth attempted to diagnose the recurring power steering issue and pinpoint a root cause.

Second and Third Quarter 2021

The demonstration has been completed and the final report was submitted.

This CTE fuel cell truck project had its ups and downs, but it represents a major step forward for electrification of class 8 trucks. Further, many of the project team members are trying to find ways to continue collaborating and working toward commercialization.

Since six trucks have completed the demonstration, the mobile refueler has been removed from the TTSI site.

GTI/BAE and Kenworth CNG Hybrid Truck

Fourth Quarter 2020

The team expected to finalize all project tasks and will continue working on the final report draft.

The HECT (KWCNG01) Chassis had the HV fuses for the air compressor replaced and the chassis returned to commercial service. Operators noted that window and mirror control occasionally faulted. However, a key cycle would resolve the fault. KW engineers are reviewing data to determine root cause and find a solution.

The truck completed 227 miles of near fault free operation in October. The total accumulated miles of commercial service in SoCal increased to 7,968 miles.

CALSTART continued working on Task 9 (Data Collection and Vehicle Performance Evaluation) and Task 10 (Commercialization Roadmap and Scenario Analysis). GTI continued to work on the final report draft.

The team has demonstrated 15 months of representative captive testing at PACCAR R&D facility and 11 months of revenue-service operation at TTSI.

First, Second, and Third Quarter 2021

The team has completed the truck demonstration in Q4 2020 and provided a draft of final report.

The draft of final report includes details of demonstration including the data collected from the truck and commercialization pathway for near and zero emission drayage trucks.

The team decided to take the truck back to KW R&D center and KW engineering team will investigate the root cause of issues that have taken place during the demonstration. The lessons-learned from this investigation will be used improve the design for next generation CNG hybrid trucks.

Cummins

Fourth Quarter 2020

- Cummins is requesting a revision to the scope of work, budget and schedule to pursue this project using Cummins' most up-to-date heavy-duty fuel cell powertrain architecture and design.
- Continued negotiations with the U.S. DOE and SCAQMD to pursue this project using Cummins' most up-to-date heavy-duty fuel cell powertrain architecture and design with extending project schedule up to end of 2023.

First Quarter 2021

- SCAQMD submitted a request for extension of project schedule and change of powertrain design of Cummins fuel cell truck.
- Continued negotiations with the U.S. DOE and SCAQMD to pursue this project using Cummins' most up-to-date heavy-duty fuel cell powertrain architecture and design.
- Continued negotiations with the U.S. DOE and SCAQMD to pursue this project using Cummins' most up-to-date heavy-duty fuel cell powertrain architecture and design with extending project schedule up to end of 2023.
- Longer supplier lead time for major components, Cummins companywide reduction in working hours (80% in Q2 & Q3).

Second Quarter 2021

- DOE approved a request for extension of project schedule and change of powertrain design of Cummins fuel cell truck.
- Cummins resumed the project using Cummins' most up-to-date heavy-duty fuel cell powertrain architecture and design with extending project schedule up to end of 2023.

Third Quarter 2021

- Executed contract amendment from SCAQMD to extend project to 09/30/2021.
- Continued negotiations with the U.S. DOE and SCAQMD to pursue this project using Cummins' most up-to-date heavy-duty fuel cell powertrain architecture and design.
- Conducted internal project kick-off meeting in August.
- Created high-level engineering project schedule and refined resource allocation plan.
- Completed high-level architecture.
- Began identifying major components and long-lead items.

II.1.9 Cybersecurity Platform and Certification Framework Development for eXtreme Fast Charging (XFC): Electric Power Research Institute (EPRI)

Sunil Chhaya, PhD, Principal Investigator
Electric Power Research Institute (EPRI)
3420 Hillview Avenue
Palo Alto, CA 94304
Email: schhaya@epri.com

Lee Slezak, DOE Technology Manager
U.S. Department of Energy
Email: lee.slezak@ee.doe.gov

Start Date: October 1, 2018 End Date: September 30, 2022
Total Project Funding: $2,786,278 DOE share: $1,547,678 Non-DOE share: $1,238,600

Project Introduction

In support of this paradigm shift to electric transportation, the EV charging infrastructure including the charging stations (also known as Electric Vehicle Supply Equipment, or EVSE), DC Fast Charging (DCFC) equipment and eXtreme Fast Charging (XFC, with charge rates above 200 kW) is being deployed at a fast pace. Studies estimate that 12-million residential charging points and 1.2-million public charging points will be installed in North America by 2030. In 2020, the United States (U.S.) has 25,000 alternating current (AC) Level 2 (AC-L2) EVSEs and over 4,000 direct current (DC) fast chargers (DCFC) installed.[1] AC Level 2 EVSEs are limited to 119.2-kilowatt(kW) peak power levels, and typical DCFCs can charge at up to 350 kW peak power levels. To meet EV drivers' increasing desire for faster charging times than AC-L2 or typical DCFC XFCs with power levels of > 200 kW are being deployed at strategic locations such as along highways. For example, the Electrify America initiative in the U.S. has deployed high-powered charging stations at levels up to 350 kW.[2] These high peak power levels mean that a malicious actor can cause a fleet of XFCs to pose larger impact on the grid, especially when multiple EVs are made to charge simultaneously.[3] Furthermore, given that the EVs, the charging networks, the payment networks, utility back office and the smart metering systems, as well as the charging network aggregators are all connected, cyber-intrusion at any point in the ecosystem could create risks in the other parts of the system, if the system is not properly designed.

To address this challenge, the Electric Power Research Institute (EPRI), electric utility partners, EV original equipment manufacturers (OEMs), charging station manufacturers, charging network operators, and research partners, which included U.S. DOE national laboratories, National Renewable Energy Laboratory (NREL) and Argonne National Laboratory (ANL), conducted research, development, and demonstration (RD&D) project titled, "Cybersecurity Platform and Certification Framework Development for XFC-Integrated Charging Infrastructure Ecosystem (*Secure Grid-XEV*)." Deriving from an earlier EPRI study,[4] the *XFC ecosystem* can be defined as the network of all involved players (organizations), systems, and sub-systems that are responsible for monitoring the grid-impacting data with an ability to send or receive control signals to alter the power usage of an XFC, using a diversity of communication technologies, and standards and protocols. With an emphasis on addressing the grid impacts resulting from potential cybersecurity compromises, the goal of the *Secure Grid-XEV* project is to develop and test technologies and approaches that identify, minimize, or eliminate critical cybersecurity vulnerabilities that result from the transition of EV charging to power levels above 200 kW, i.e., the *XFC ecosystem*.

At the forefront of cybersecurity research, EPRI has held a prominent role in Smart Grid Cybersecurity[5] by addressing the emerging threats to an interconnected electric sector through multidisciplinary, collaborative research on Cyber-Physical Security technologies, standards and business processes with a broad focus on enabling technologies, standards, demonstrations and technology transfer. EPRI has one of the longest-running

Electric Transportation[6] research programs, spanning over 3 decades and representing a global footprint of stakeholders engaged in collaborative RD&D focusing on EV and infrastructure technologies, vehicle-grid integration into distributed energy resources (DER) ecosystems, techno-economic and environmental analysis, and technology transfer for utilities and practitioners. Likewise, EPRI leads the electric industry in Information and Communications Technologies (ICT)[7] for electric sector by defining, formulating and implementing communication technologies and open, interoperable standards and protocols. Figure II.1.9.1 shows the project's focus on XFC infrastructure with the goal of strengthening the cybersecurity of EVs, EV charging infrastructure and the electric grid that intersects the three EPRI research portfolios of cybersecurity, electric transportation and ICT. All the three research portfolios were leveraged to enable secure interoperability among the electric grid, markets, and operations, and its integration across the EVs, and charging infrastructure.

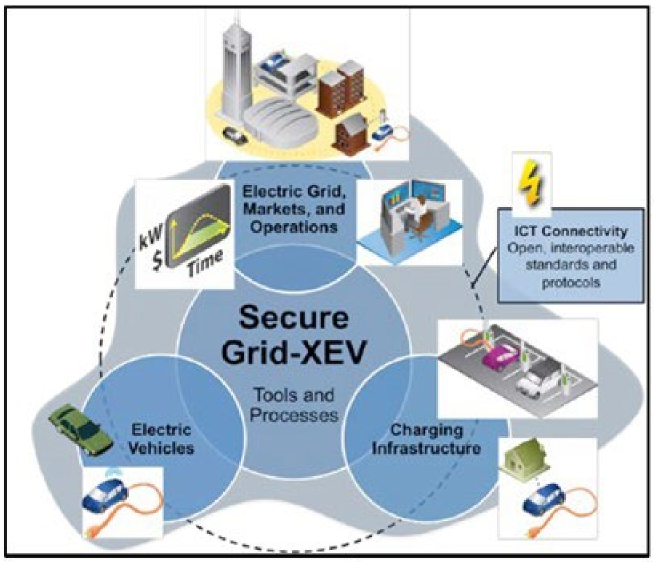

Figure II.1.9.1 Research scope of Cybersecurity Platform and Certification Framework Development for XFC-Integrated Charging Infrastructure Ecosystem (*Secure Grid-XEV*)

The EV ecosystem is extremely diverse, technologically advanced, and connected. This includes players such as EVSE and EV OEMs, grid operators, third-party network operators and service providers with each offering unique and diverse connected subsystem. Each subsystem and its component in the EV ecosystem are designed to operate standalone with direct interfaces to a connected subsystem. The study defines a subsystem, as any standalone system that an XFC interfaces with. A component is a functional part of a subsystem such as a payment module.

Goals and Objectives

The project goals are to: (1) Equip the EV and electric grid stakeholders with reference tools and processes that can be leveraged to support baseline security functional requirements; and (2) to accelerate the secure deployment and grid integration of EV charging infrastructure.

The core project objectives are to:

- Evaluate and assess cybersecurity risks to develop a reference network architecture of connected systems, sub-systems, and communications for an XFC ecosystem.
- Conduct cybersecurity threat and vulnerability assessment to identify and classify assets for XFC sub-systems.

- Recommend cybersecurity controls, system architecture, and a reference design for a *Secure Network Interface Card* (S-NIC) for XFCs.
- Assess and develop sub-system and component-level XFC ecosystem testing for verification of the requirements.
- Develop Integrated Grid Security Risk Management (IGSRM) tool for wider dissemination of research recommendations to the industry.
- Proactively engage diverse industry stakeholders for perform research analysis and conduct technology transfer through EV Infrastructure Cybersecurity Working Group (EVICWG).

Approach

Addressing cybersecurity for the XFC ecosystem requires a review of multifaceted technical and non-technical barriers, systems-centric requirements that involve all the EV ecosystem players, and engagement of the stakeholders to ensure that project findings are robust. Considering this approach, the project will be executed in two phases:

Phase 1 (October 2018—December 2019): Develop Reference Architecture. The study to assess cybersecurity risks, threats and vulnerabilities to analyze the functional cybersecurity requirements and a reference architecture for each of the subsystems and components within the XFC ecosystem.

Phase 2 (January 2021—September 2021): Combined Test Results and Assessment. Develop test plans, conduct laboratory tests to review the collated results to create a final set of cybersecurity requirements, and vulnerabilities and mitigation strategies.

The focus of this report is on the Phase 2 activities for the year 2021.

Phase 1 Summary

To summarize the Phase 1, the activities focused on the four core areas: 1) assess cybersecurity requirements; 2) conduct risk, threat, and vulnerability assessment; 3) mainstream the research; and 4) recommend cybersecurity controls, XFC ecosystem reference architecture, and S-NIC reference design. The Phase 2 final cybersecurity reference architecture and reference standards, test protocols and guiding principles for certification process will be developed based on the Phase 1 results so that stakeholders can effectively implement the architecture-specific modular security controls and standards for the XFC ecosystem.

As illustrated in Figure II.1.9.2, the Phase 1 research and approach included three core and interrelated activities for XFC components, systems, and sub-systems, and communication technologies: (1) develop framework for analyzing risks across the EV ecosystem; (2) assess threats and vulnerabilities based on functional requirements; and (3) recommendations with security controls and standards, and next steps. The project approach focused on identification of cybersecurity solutions.

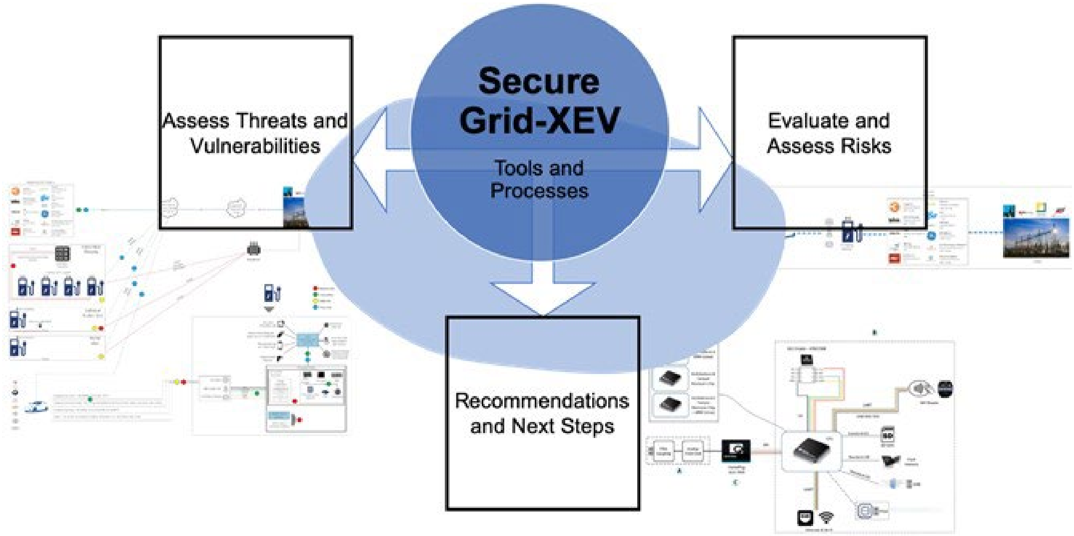

Figure II.1.9.2 Project Approach and Activities for Phase 1 Research

Each of these interrelated activities are reported in the 2019 report and include a classification and evaluation of cybersecurity risks for XFC infrastructure and its interrelated systems and sub-systems such as EVs, third-party operators, utilities, buildings, etc. This risk framework and XFC deployment architecture and communication technologies considerations were used for a comprehensive cybersecurity threat and vulnerability assessment. The risk mitigation techniques addressed the financial data, privacy of customer information and grid reliability controls. EV ecosystem-related communications standards based on open standards such as Level 2 AC, DCFC, XFC, and other EV charging standards will be assessed. As a result, recommended security controls and a reference design for secure network interface card (S-NIC) were proposed—all of which will become the basis for the Phase 2 research.

Phase 2 Summary

Phase 2 efforts focused on using Phase 1 findings and recommendations to:

Conduct Combined Test and Verify Results: The study conducted experiments and assessed results to create cybersecurity requirements, test protocols, results, vulnerabilities and mitigation schemes or strategies in close association with the cybersecurity reference architecture. An Integrated Grid Security Risk Management (IGSRM) tool was designed in support of the reference architecture.

Test and Verify Reference Architecture: The cybersecurity reference architecture, related technologies using various threat and vulnerability assessment techniques were tested and verified. These tests included network security for data-in-motion or transit, system and application-layer cybersecurity for interfaces and data-at-rest, physical security for components, and end-to-end security integration.

Develop an Integrated Grid Security Risk Management (IGSRM) Tool: The IGSRM design was used to develop a web evaluation tool prototype to help vendors, service providers and utilities to navigate through the various cybersecurity standards. All applicable network, system, application and physical security controls, communication standards were be included in the tool. The tool development shall be completed in 2021.

Mainstream and Standardize Interoperable Cyber Secure Ecosystem: Continuing from the Phase 1 efforts, the project engaged the EV Infrastructure Cybersecurity Working Group (EVICWG) to review project outcomes and obtain feedback to engage the industry in the market transformation of cybersecure XFC infrastructure. The final recommendations shall be transferred to a standard enforcement or interoperability certification process to ensure that the reference architecture is effectively applied to all XFC stakeholders and is industry-approved for implementation through deployments and regulatory framework.

To ensure adequate stakeholder coordination, and technology and knowledge transfer, the project leveraged the capabilities of partner U.S. DOE national laboratories: Argonne National Laboratory (ANL) and National Renewable Energy Laboratory (NREL) that comprise DOE's SMART Mobility Consortium [8]. This project also set up an "EV Infrastructure Cybersecurity Working Group (EVICWG)" to review project outcomes, obtain feedback, and to engage the industry in the market transformation of cybersecure XFC infrastructure.

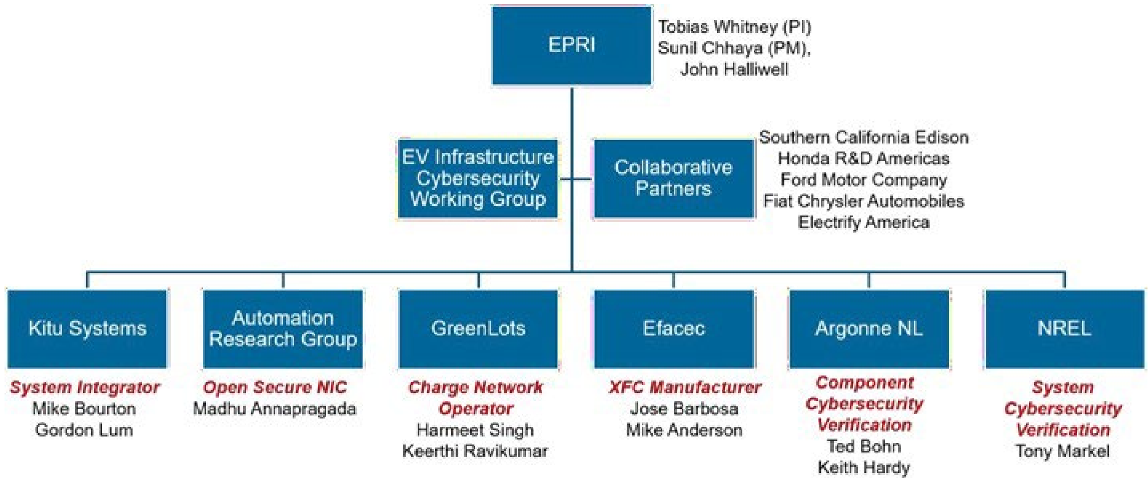

Figure II.1.9.3 Participants & Other Collaborating Organizations

Results

The following table summarizes the activities for 2020-2021 for which the results are described.

Table II.1.9.1 End-to-End Security Test Plan and Cybersecurity Testing Results

Milestone	Type	Description and Status	Delivery Date
End-to-End Security Test Plan	Technical	Cybersecurity testing plans.	Q1 2020 → **Draft submitted to DOE.**
Integrated Grid Security Risk Management (IGSRM) Tool Finalized	Technical	Tool prototype developed and updated based on testing results.	Q2-Q3 2020 → **completed by Q2 2020.**
Cybersecurity Testing and Results	Technical	Testing completed by EPRI and NREL with results documented. ANL testing and results are pending.	Q3 2020 Q1 2021 → **Due to COVID-19 Challenges, recommend completion by Q4 2021.**
Integrated Grid Security Risk Management Tool Published	Technical	Reference architecture is market-ready for implementation through industry deployments and regulatory framework.	Q3 2020 Q1 2021 → **Due to rescheduling of testing and process, scheduled completion by Q4 2021.**

The XFC infrastructure is large and has variety of actors in each subsystem. The labs have developed the test plans to best of their ability. The Cybersecurity Research Lab (CSRL) is primarily focused on the EVSE (Charge Station) and its interfaces. National Renewable Energy Lab (NREL) is focused on the communication link between EVSE and the backend/cloud. Lastly Argonne National Lab (ANL) is focused on communications between EVSE, Site Controller and Energy Storage. Overall test plans cover majority of areas in the XFC infrastructure needed to be tested. EPRI will continue to coordinate and prioritize areas to be tested with respect to key recommendations. The working group meetings have facilitated the laboratories to present their test plans and get valuable feedback on their approach and identify any potential gaps or missing areas. The table below summarizes the testing conducted by each of the laboratories.

Table II.1.9.2 Summary of the Test Cases by Partner Laboratories and Relation to Phase 1 Activities.

Laboratories and Test Cases	Relation to Key Recommendations
EPRI Cybersecurity Research Laboratory (CSRL) 1. Spoof Payment / Authentication System – SNIC 2. Evaluation of attack surface of UI 3. Evaluating functional behavior of EVSE in absence of network or un-responsive Charging service provider 4. EVSE Communications channel vulnerability assessment 5. Maliciously exploit EVSE API 6. Theft of Credentials or Keys	• PKI for end devices and their clouds. • Encryption of PII, data at rest and in motion • Secure NIC • 2-way communication between EVSE and cloud (Bi-directional) with defined alert stack.
National Renewable Energy Laboratory (NREL) 1. Man in the middle attack 2. Denial of Service attack 3. Communication chain EVSE to Cloud	• PKI for end devices and their clouds. • Encryption of PII, data at rest and in motion • Secure NIC
Argonne National Laboratory (ANL) 1. Network Level Site Controller: Evaluate dependencies of EVSE-EVSE interactions in clusters and the site controller. 2. Evaluate security of EVSE communications within a facility. 3. Test integrated energy storage, DC as a service with an EVSE. 4. Evaluate Confidentiality, Integrity and Availability (CIA) for communication between cloud/back-end and the EVSE.	• PKI for end devices and their clouds. • Encryption of PII, data at rest and in motion • Secure NIC • Load Smoothening by deploying power dense storage solutions.

The test plans and methodologies for sub-elements cybersecurity testing was done in the 2020, and bulk of the cybersecurity testing and analysis was executed during the last quarter of 2020 and the first quarter of 2021 with a few cybersecurity testing spilling into the second quarter of 2021. Below is a consolidated list of tests results that each of the laboratory has tested based on the cybersecurity recommendations. The key results for each test case considered is presented here.

Cybersecurity Testing Results from Cyber Security Research Lab, Electric Power Research Institute – Knoxville TN (CSRL)

For CSRL's testing, a 7.2 kW Level 2 charger was installed in the lab. The charger system was comprised of two primary components:

- EVSE Payment Module – payment processing, C&C, network routing
- EVSE Charging Module – power electronics for the charging system

An engineering workstation hosting a virtual instance of Kali Linux was used to facilitate the regular operation, profiling, and attempted exploitation of the charger. Logical and physical connections of the Test Environment are:

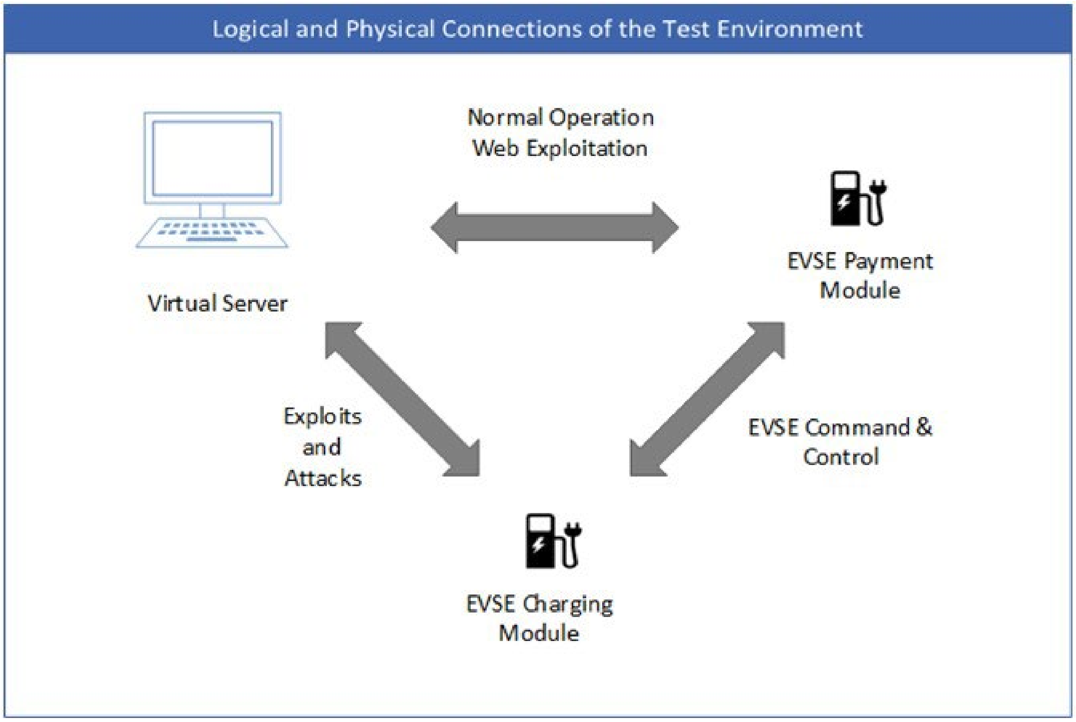

A. Evaluation of wireless interface (Charging Module, Payment module)

In this task, data is captured at the frequency of Zigbee transmissions and attempt to replay a "Start Chargee transmission"

The cybersecurity evaluation results are (system using Zigbee 2007 for wireless communication):

- The use of Zigbee 2007 or higher appears to have robust security controls
- While application layer encryption does not appear to be in use, default AES-128 network layer encryption, properly implemented provides robust security

The recommendations based on the analysis are:

- Ensure the implementation of appropriate cryptographic controls
- Implement logging for SEIM integration and analysis
- Mandatory whitelisting for network joins

B. Implement replay attack against serial EVSE

Monitor the serial communications going to the Charge controller and perform a replay attack using the captured data.

Finding based on the cybersecurity analysis are:

- Due to sequence number tags, handshake mechanisms, as well as timestamping, a replay attack is infeasible via this method.

The Cybersecurity Recommendations based on the analysis are:

- Implement intrusion alarms that will indicate opening of the EVSE enclosure to a SOC or similar security monitoring entity

C. Attempt to Crash UI interface on EVSE

This task consists of depressing all possible permutations of primary function buttons of the access panel to crash the UI (which would disable the EVSE functionality).

The cybersecurity analysis found that

- The system failed to respond at all unless triggered with one of the approved actions

The additional Cyber Recommendations based on the analysis:

- Require restricted access maintenance card or dongle for elevated UI privileges.

D. Evaluating functional behavior of EVSE in absence of network or un-responsive Charging service Provider

In consultation with EVSE manufacturer and CSP a determination was made that this pathway did not present a significant risk do to as loss of CSP would prevent the EVSE from initiating any further charge sessions until communications are restored. Future versions of the software would entail an immediate termination of charging with the loss of communications to the CSP.

Cybersecurity analysis findings:

- For the above listed reasons, no further testing or remediation

Recommendations based on cybersecurity analysis:

- In the event of loss of connectivity to CSP, allow for secondary or tertiary communications pathways for authorization
- Allow for fail open / fail close system state depending upon use case

E. Evaluating the SSH interface for vulnerability to exploitation

In this task the security of the SSH interface to the payment module is tested using Kali linus and associated SSH exploit tools it provides.

Cybersecurity findings are:

- EVSE uses OpenSSH 5.91p (protocol 2.0), and the SSH implementation appears to be secure and updated

Recommendations based on cybersecurity analysis are:

- Comply with recommendations of NISTR 7966 [2]
- Only enable SSH on systems that absolutely require it
- Keep SSH Client and Server implementations fully updated
- Harden SSH client / server implementations

F. Evaluate Web interface of payment module with a local workstation

This task involves the analysis of the web interface of payment module using web app exploitations originating from a Kali Linux workstation.

Cybersecurity analysis findings are listed below:

- While scans indicated that, it may be possible to exploit the system via the pushing of pulling of files to the web server, the Nmap exploit failed to work

Recommendations based on the analysis are listed below:

- Recommend implementing TLS for all webserver connections
- Recommend implementing IPsec betwixt the EVSE Gateway and any cellular connections.
- Implement a formal web application security framework (something akin to OWASP top ten) to protect against common web application exploits

G. Credential theft via external RFID scanner

This task considers the evaluation of system design to insert a RFID skimmer for capturing credentials.

The findings based on the analysis are:

- The payment module housing is constructed such that the RFID interface is underneath a narrow, sloped unibody construction with a prominent gradient adjacent to the sensor. As such, placing an RFID skimmer or similar interface on the payment module would be exceedingly obvious

The recommendation based on the cybersecurity analysis is:

- Implement a consumer verification method (CMV) to be used in conjunction with RFID use

Cybersecurity Testing Results from National renewable Energy Laboratory, Golden, CO. (NREL)

The EV ecosystem will include multiple components and entities that must communicate and coordinate securely. Within this testing project the primary components of interest were broken down into Vehicle, EVSE, and Systems Control/Backend. As shown in figure below, both the components and the interfaces between these systems present potential targets.

The tests performed included both physical and virtual components for replicating the environment with EVSE, communications, and the service provider/backend represented. The test strategy for this project focused on the communications between the charge network operator's server and the client (charger) to emulate vehicle charging infrastructure. Both local and remote server representations were used in addition to a virtual client and physical client to implement end-to-end OCPP communications. Outcomes of testing can characterize potential consequences of a malicious agent listening to the request/response sequences and injecting fake messages after capturing the details of the communication.

The OCPP server model originally provided by Argonne National Lab, developed using NodeRed and customized for the specific charging station, is being used to communicate with a 50 kW fast charger. The system currently implements OCPP v1.6. In addition, a virtual machine running Kali Linux is used for implementing malicious agent activities within the emulated charger network were utilized.

A. Replay attack scenario test

In this test scenario, a custom configure OCPP server was used to manage the EVSE, a 50 kW DCFC charging station that is authorized using the OCPP server.

Cybersecurity analysis findings:

- It was possible to intercept OCPP messages between the charger and server including the capture of the transaction id. Testing conducted did not successfully inject a replayed message.

Recommendations based on the cybersecurity testing:

- Use TLS for connections between client and server along with connections to certificate authority (CA)
- Use IPsec tunneling between point-to-point networking devices
- Require use of server and client authorization before session initiations.

B. Disruption of Services

In this scenario, disruption of EVSE charging services during a Denial of Service (DOS) attack is evaluated. The DOS attack occurred by flooding the network of the EVSE and the operator/server with ICMP messages and then initiating a new charge session.

Cybersecurity analysis findings:

- Overflow of sessions initiated causes the controller to decrease speed of operation

Recommendations based on cybersecurity recommendations:

- Employ application whitelisting with registered endpoints
- Configure client/server to limit session initiation attempts
- Practice network security fundamentals: 1) Sticky MAC addresses 2) Port security.

C. Simulate realistic scenario with charge network operation (CNO) instance

In this task virtual agents/ applications and simulated applications were setup to communicate with the backend network operation instance.

Cybersecurity analysis findings:

- The Greenlots Sky platform enabled seamless management of the chargers (clients) with the ability view additional information like energy consumed by individual units. From the backend perspective, Sky also enabled a live OCPP feed to monitor or debug messages. Additional recommendations such as the OCPP server request ChangeConfiguration through Sky provides better manageability of the server and connected clients.

Recommendations based on cybersecurity analysis:

- Implement an Intrusion Detection Systems (IDS) strategy to monitor rogue devices and malicious connection attempts
- Consider use of endpoint behavior analysis to flag untimely and abnormal activities.

D. Active comparison of OCPP2.0 and OCPP1.6 security functions

In this task, the security functions of OCPP 2.0 compared to 1.6 are being evaluated.

Cybersecurity analysis findings:

OCPP 2.0 heartbeat and BootNotifications messages were observed, and the virtual instance of OCPP 2.0 has limited functionality compared to a production system.

Recommendations based on cybersecurity analysis:

- OCPP 2.0 enhances security functions such as certificate management that can utilize public-private key pairs. When TLS is used, there is a "Charging Station Certificate" needed for authenticating against the central server. To leverage these enhancements it is recommended that,
    - The highest level of available security options be configured fully.
    - Similar levels of security are enacted across the EV charging ecosystem.
- Authentication functions can be used for preventing rogue EVSE operation and thus can be recommended that logging of admin/user activities along with role-based access restrictions are applied to certain EVSE operations.

Cybersecurity testing results from Argonne National Laboratory, Lemont IL (ANL)

The ANL testing and assessment areas for EV charging covered in this report include variations on communication pathways between EVSEs, local hosts, storage element controls, site level and cloud based back-office levels. These pathways span from local EVSE clusters to EVSE-facility to integrated storage to EVSE-cloud/backend interactions.

The current iteration of the EV-Smart Grid Interoperability Center at Argonne National lab is now at building 300, a facility solely dedicated to EV charging testing activities. The facility contains modern commercially produced testing tools include the Comemso ISO15118 protocol test tools (charging-analysis-test) as well as the Keysight/ScienLab 'Charging Discovery System' that both include secure communication 'man-in-the-middle' communication capabilities.

Use of these tools for EV-EVSE communication testing was in the initial FOA1919-1513 concept paper proposed testing of ANL vehicles and EVSEs. This scope was appropriately modified for the cybersecurity analysis execution in this project.

A. *EVSE-EVSE interactions in clusters and the site controller*

This task involved the setup and multiple EVSE clusters from off-the-shelf components, and a site controller to study the possible interactions between the multiple elements.

Cybersecurity analysis findings: Setting up the equipment on a transportable lab setting fixture facilitated side-by-side comparison of EVSE implementations and choice of hardware/software for communication, with obsolete systems unsupported leading to the need to replace instead of upgrade EVSE communication to keep systems secure to 2021 levels/recommendations.

Recommendation based on cybersecurity analysis: Follow best practices on setting up off-the-shelf interoperable EVSE connections, over-the-air upgrades on vulnerabilities is a necessity for secure and reliable EVSE-EVSE to site host connectivity

B. *Security of communications between EVSEs in a facility*

This task involves the security features of the various off-the-shelf EVSEs and the site controller communications.

Cybersecurity analysis findings: In general, very old generation EVSE with low feature set didn't rely on the cloud configured/approved operations. Medium recent generation EVSEs relied more on cloud connection to start/end sessions and set power levels. Newest generation EVSEs are most resilient to interruptions to host network connections. Only specially configured EVSEs/local gateways can switch to local control when network connection is lost.

Recommendations based on cybersecurity analysis: Local backup operation works best for resiliency of operations for manage loads/set access control to EVSE. WAN connected EVSEs don't usually have a backup, assuming high reliability of cell networks and near-real-time diagnostics.

C. *Integrated energy storage, DC as a service with DC EVSEs.*

This task is a communication between the energy storage system in the installation of clustered DC EVSEs. This configuration is very important in high density DC EVSE charger installations.

Cybersecurity analysis findings: This task is based on work-in-progress as new standards are being developed such as IEEE P2030.13 covering communication between DCaaS based DC distribution to EV charging nodes and storage elements for grid services. "P2030.13 – Guide for Electric Transportation Fast Charging Station Management System Functional Specification" https://standards.ieee.org/project/2030_13.html. As the standards are a work in progress- findings limited to observation that more development is needed for meaningful analysis.

Recommendations based on cybersecurity analysis: Support standards development that cover this under-specified use/test case.

D. *Communication between cloud/back-end and EVSEs.*

This task evaluates Confidentiality, Integrity and Availability (CIA) for communication between cloud/back-end and the EVSE. The Confidentiality-Integrity-Availability (CIA) triad applied to data exchange between EVSE nodes and cloud hosted services mainly apply to authorization, billing and dynamic control information that is part of the OCPP payload.

Cybersecurity analysis findings: The main path for confidential information for EV charging is via the ISO1511-20 based communication path for 'plug-and-charge' initiation, authentication and payment processes. The assessment is that information exchange between the EV and EVSE are secured via robust implementations of the ISO15118-20 stack and OCPP pass-through to the back-office applications.

Recommendations based on cybersecurity analysis: Support standards development that cover this under-specified use/test case

Part of the cybersecurity development included the development of Secure Network Interface Card (SNIC), which was designed and described in the Phase 1 report.

The SNIC was successfully moved from design phase to prototype development. The prototype is open source, and the schematics were made available to working group members and the laboratories participating in testing.

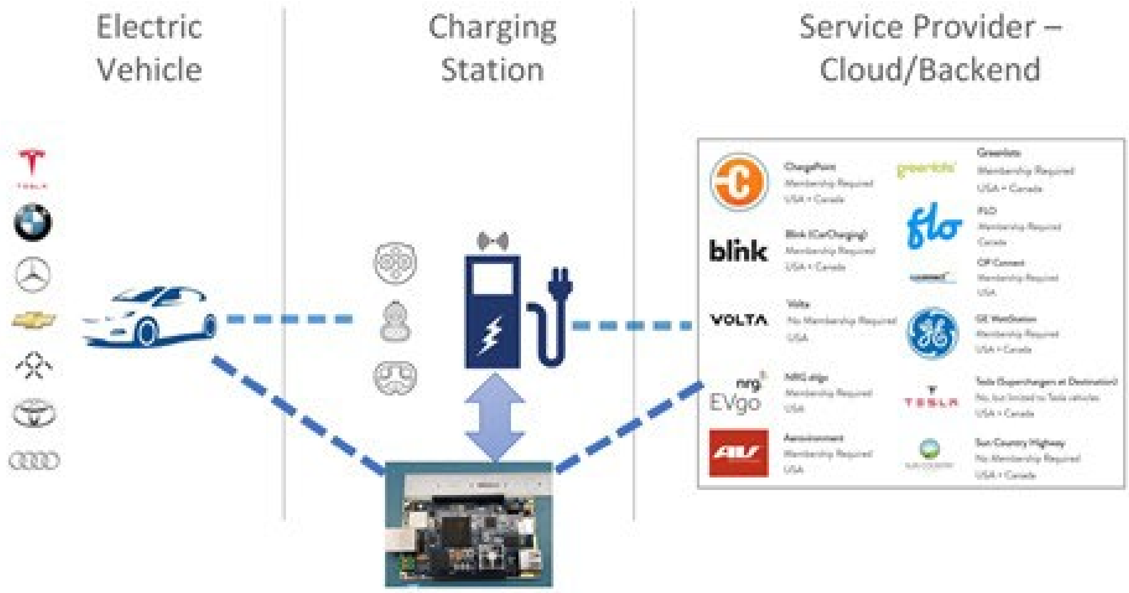

Figure II.1.9.4 Secure Network Interface Card Role in the XFC Infrastructure

The SNIC will play a key role in testing communication security and providing an opensource design to allow best practices and iterated improved security by design. Figure II.1.9.4 shows the position of SNIC in the XFC infrastructure. The SNIC will act as a wrapper to all communications originating from any of the subsystems shown below. Apart from securing the communications, it will provide protection to hardware from tampering and also verify changes to firmware and boot operations.

The major components of the system to support the requirements would fall into the following major categories:

- Central Processing Unit/System: This is the core of the system and the "brains" that will ensure proper elucidation of protocols and keep track of security issues. It also supports all required authentication mechanisms.
- Vehicle Communication: Capability of being able to communicate to the vehicle to support secure protocols for charge (and optionally discharge) in various deployment scenarios.
- Cloud Communication: Most of the current authentication methods require custom / open-source protocols travelling all the way to the cloud servers using the internet. So, to be able to utilize the benefits of these methods of authentication, the system(s) needs to have a way of communicating with the servers on the internet.
- Secure System: Support methodologies to ensure secure upgrades. Allow secure storage retrieval in HW. Support HW ECC to enhance security features for protocols and information handling.

The prototype for SNIC has arrived and will play a major role in testing activities conducted by the laboratories. Below is an image showing the prototype board with all the components in place.

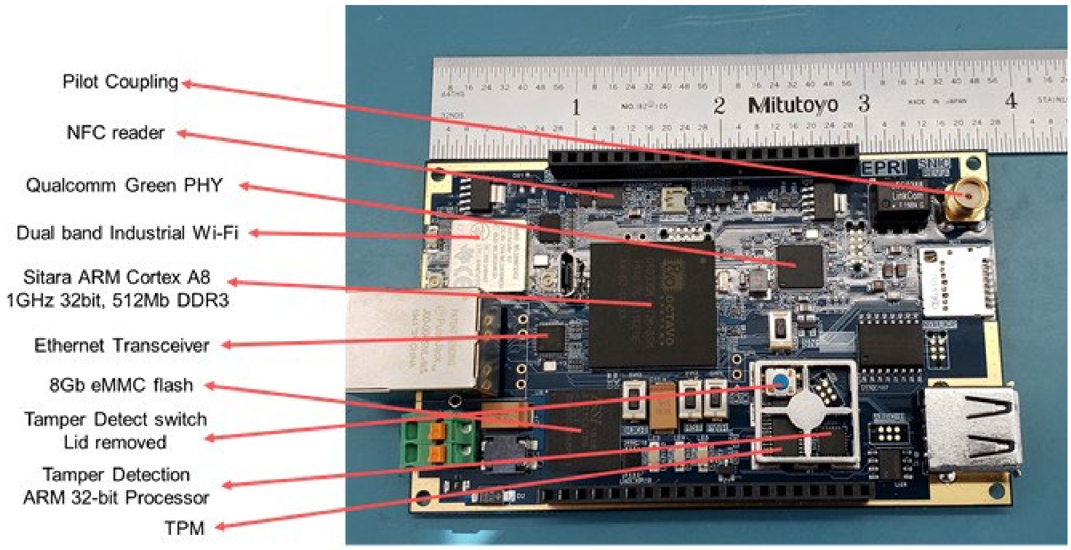

Figure II.1.9.5 Secure Network Interface Card prototype board

The different components of the Secure Network Interface Card (SNIC) and their setup or usage is presented in this section.

- Central Processing unit (CPU): The CPU consists of ARM Sitara processor running Debian Linux has been updated and tested on the board with required customizations. To leverage the latest updated kernel, as needed changes to the official IOT firmware produced. The latest firmware used in the board is obtained from the web page "https://beagleboard.org/latest-images"

- Hardware Interfaces: The SNIC is a multi-purpose board that could be used in an EVSE, EV or as an add-on to other existing hardware for example a non-networked EVSE and make the composite system a secure smart EVSE. Hence the SNIC has support for a variety of hardware interfaces. Drivers for I2C, SPI, UART, MMC going to different devices checked and tested. CAN interface is to be tested, support available in the kernel as a socket.

- Wi-Fi on-board support: The Wi-Fi chip chosen is based on TI WL1807 Wi-Fi connected to core CPU through MMC2 bus. Driver setup and working on prototype board. Configuration for Wi-Fi loaded from a file on the local filesystem. The

- NFC: The choice of NFC in this system is to have a methodology to authenticate and have a good cybersecure system. NFC is used in payment systems and has proven its security. Here, in this board, it is intended to be used for a number of non-payment purposes, admin authentication, Wi-Fi setup (not through ethernet/ remote), and add SSL layer security or encryption optionally. The NFC communication hardware is based on PN7120 NFC (NXP) connected to CPU through I2C #2 bus. The driver for this chip was setup and was working on prototype board.

- PLC Communications: The current state of protocols between EVSE and vehicle use the communications over pilot line. To enable support for such a system, a PLC communication chip based on QCA 7005 communicates that communicates to the CPU via SPI bus was used. An Open-Source driver for Linux was identified and used to setup the PLC for communications over the pilot line. Field testing the prototype board identified communication pin swapping, and hence in the next release that particular swapped pins would be modified which would enable proper PLC communications through the kernel as a socket.

- Trusted Platform Module: Trusted Platform Module (TPM, also known as ISO/IEC 11889) is an international standard for a secure cryptoprocessor and supports proper authentication of the platform which will occur at ever boot. The TPM module on board is the Microchip module AT97SC3205CT connected to CPU through I2C. Communication to chip through I2C channel was verified. Based on user application needs, it could be programmed to provide the necessary authentication primitives. However, recently, a new version of the TPM specification has upgraded the widely used 1.2 to 2.0 version. This chip only supports the TPM 1.2 specification, and hence in the next revision a new chip that supports TPM 2.0 specification will be included as a replacement to the current Atmel chip.

- Hardware Cryptographic Processor: The hardware cryptographic processor is based on ATECC508A and connected to the CPU through I2C. This device supports ECDH (Elliptic Curve Diffie-Hellman) key agreement, which makes it easy to add confidentiality (encryption/decryption) to digital systems. In addition, the chip supports built-in ECDSA sign-verify capabilities to provide highly secure asymmetric authentication. The combination of ECDH and ECDSA makes the device an ideal way to provide all three pillars of security such as confidentiality, data integrity, and authentication when used with MCU or MPUs running encryption/decryption algorithms (i.e., AES) in software. It also provides support for secure key storage to store device specific identifier PKI certificates and ECDSA provides methods of verification of device.

- Trust Zone Processor: Based on ATSAML11D16A connected to CPU through SPI bus. The Trust zone processor is a special purpose processor that provides a hardware sandbox for executing application and can update a corrupted or intentionally modified firmware executing in its zone. Thus, critical application functions requiring the highest level of security could be executed in this zone. This is achieved by a secure bootloader support which can detect modifications of the code that is executing in the trust zone and update the firmware appropriately. Some of the other benefits and application scenarios of using the Trust Zone processor on the SNIC include

    - Unique identifier for system. Cannot be modified or read by tapping onto the chip, but can only be verified (an alternative for physically un-cloneable functions)

    - Anonymize EVs/ user for backend authentication

    - Resilience: Authorize charging when backend not available (The EV must have charged at least once). Store PII anonymized in the TrustZone and allow verification in the absence of backend communications

    - Secure store of private keys for OTA for core processor. Update for device autogenerated, cannot be used by any other device

    - Enhance security by creating a secure IO channel to hardware ECC chip for small form factor (or embedded) device

    - Encrypt all communications with backend / EV / EVSE with pre-stored symmetric encryption keys or use PKI based system for authentication or authorization.

    - Secure log of access

    - Replace Vehicle ID with negotiated anonymized unique identifiers.

    - In combination with NFC for authenticating users at the device (for example an EVSE)

    - Include in EV or EVSE for the above benefits

    - Integrity check of firmware and components to make sure the system is matching the baseline

   - SNIC secure boot or verified application launch.

Additional details of the SAML11 trust zone processor for cybersecurity are:

- Encryption and decryption of data for communication or data storage
   - SAML11 includes AES128 Encryption and Decryption hardware acceleration
- Enhance security for sensitive data
   - SAML11 includes 256 byte of active shielded RAM with scrambling of Data- and Address bus
   - SAML11 includes 1KB of Data Flash with scrambling on Data bus
- Integrity – prevent modification of data
   - SAML11 includes SHA256 hardware acceleration to verify data and code
   - SAML11 includes CRC to verify data and code
- Secure boot – ensure your/the right software is running!
   - SAML11 can verify the code in the device before running the first line of the code
- Tamper Detect
   - SAML11 provides Tamper Detection and PCB Active Layer Protection. On Tamper detect signaled to the processor, the data flash can be deleted or scrambled based on the setting on the system. Tamper detection occurs when the metal shield in the TPM region is removed, and unit is powered up to probe the system. Alternatively, the TPM chip could be covered in heat sensitive material so that access to the chip is not available.
- TrustZone – secure tasks and protect your software IP
   - Allows to separate the MCU, memory, bus-system, and peripherals into trusted and non-trusted zones. All with minimum software overhead.
   - Allows to protect software/middleware: customers working with large/international developer teams or 3rd party and don´t want to share software IP.

Some sample use-case scenarios of using the Trust-Zone for cybersecurity systems are

A) Secure boot

The SAML11 creates a secure hardware sandbox by partitioning the available program and data space into "Trusted" and "Non-Trusted" regions as shown in the figure below.

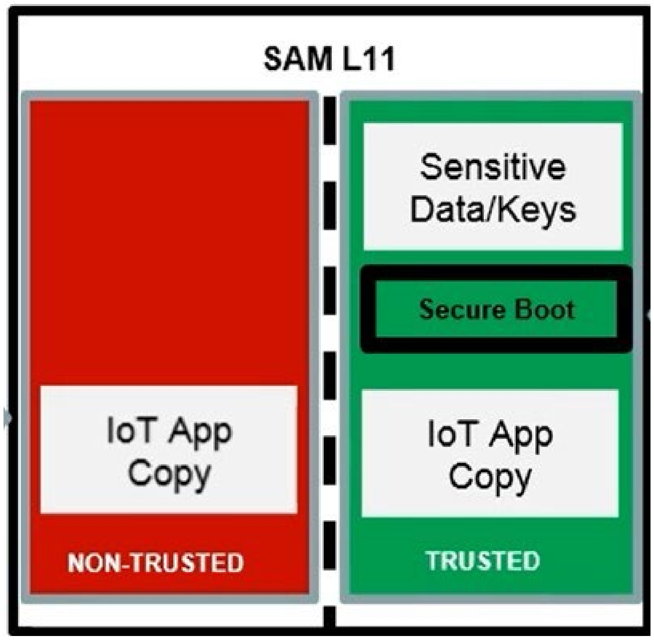

In the case of a modified app as shown in figure below, the secure boot could identify the modified app, erase it and put the original backup copy onto the non-trusted region and execute the original app.

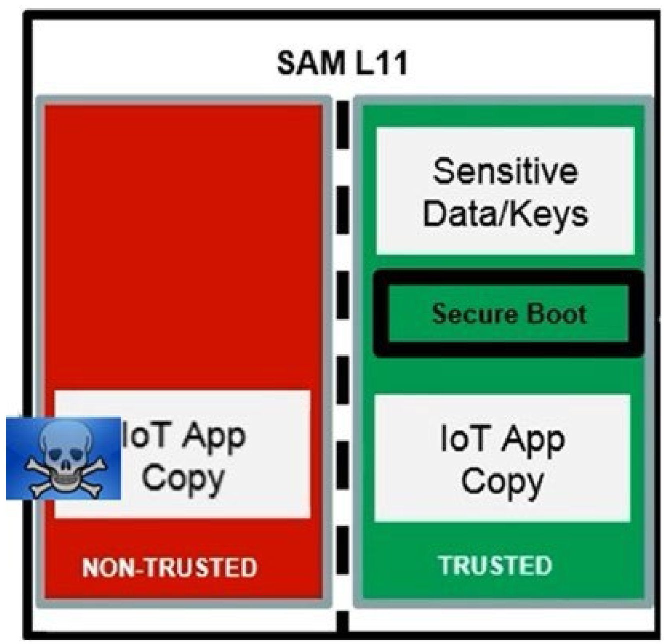

Such a process improves reliability of the SNIC to malware or intentional modifications in the field.

B) Secure on-board pathways for data communication from peripherals

In this use case, it creates a secure pathway between the keypad (where for example user is entering a pin) which goes directly to the trusted zone to be encrypted and send to the backend for verification. Data in the trusted zone cannot be read by any application executing in the non-trusted zone, and therefore an attacker will not be able to read the pin entered even if they are monitoring the memory in the chip.

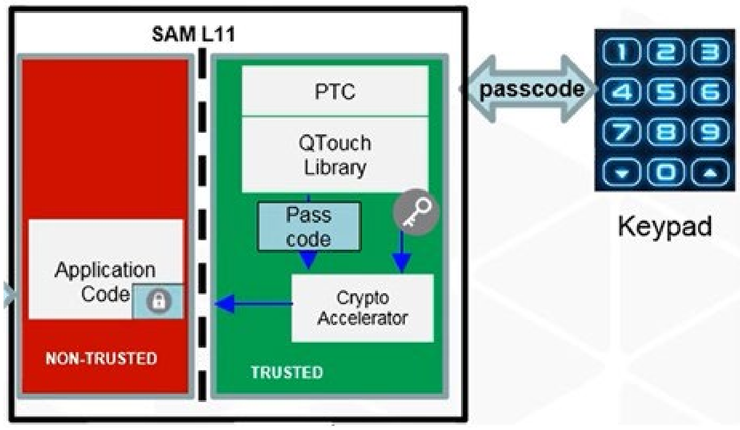

Integrated Grid Security Risk Management (IGSRM) Tool Finalized

To ensure modular development of the XFC ecosystem and assignment of cybersecurity risks and recommendations for the industry to use, the project team's activities resulted in the following:

a. Conducted design and development of the Integrated Grid Security Risk Management (IGSRM) tool. The tool is a security architecture tool (web-based) to help vendors, service providers and utilities navigate the various security considerations for the XFC ecosystem. The IGSRM tool provides a baseline for subsystem and end-to-end security controls. The team developed IGSRM functional specification and requirements and reviewed them with the EVICWG.

b. The team finalized the use of a well-known and industry-wide enterprise architecture modeling tool, Enterprise Architecture (EA). The EA tool provides scalable and modular features to develop the back-end library of XFC ecosystem and the related cybersecurity requirements or recommended controls.

c. The project team working on a scope for the subcontractor to develop the web-based tool that will provide the EV industry with the XFC subsystem-specific controls. The EVICWG members assisted in defining the requirements for the IGSRM tool. The web-based tool provides an easy to access tool across the industry stakeholders to motivate them to use the tool and cybersecurity practices.

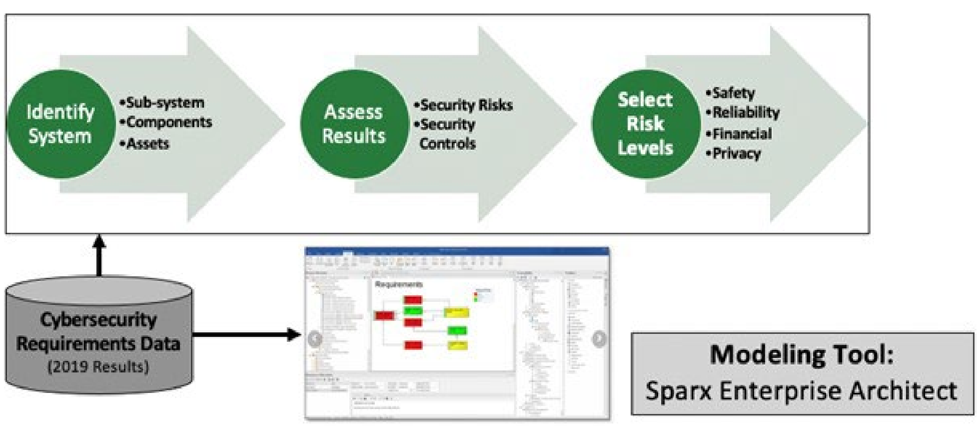

Figure II.1.9.6 Conceptual Representation of the IGSRM Tool

The guiding principles for the development of the tool included:

- Architectures should be recognizable representations of smart grid systems, sub-systems, and components (e.g., distribution, sub-station, grid-edge, DER).
- Tool* should be easy to navigate from high-level system architecture to define cybersecurity requirements for its sub-systems and components.
- Tool* should be easy to maintain and modular in design to include new architecture patterns and cybersecurity requirements.
- Tool* should be scalable and allow efficient design, reuse, and editing of architecture patterns and cybersecurity requirements for multiple architectures.
- Target audience:
  - Utility and industry members deploying grid systems, sub-systems, and components.
  - Cybersecurity practitioners familiar with the represented systems.

The IGSRM tool was developed and demonstrated to the EVICWG group members, and their feedback was implemented in the final version of the tool. Sample screenshots from the IGSRM tool are discussed below

The main login screen on starting the tool is shown in the figure below:

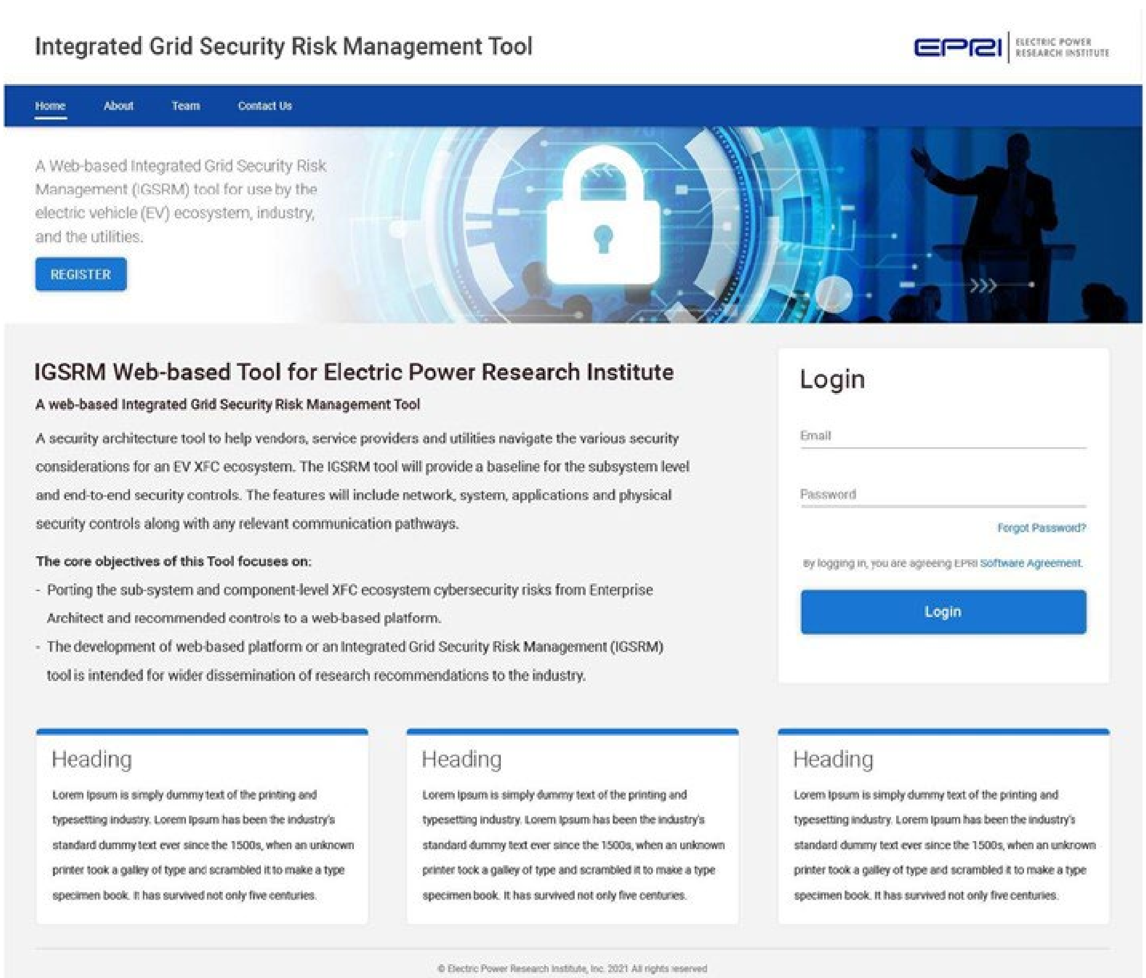

The tool allows user authenticated logins for cybersecurity reasons and allows users to sign up to use the tool on a regular basis. On logging in to the tool the main page showing the different subsystem is shown in the figure below.

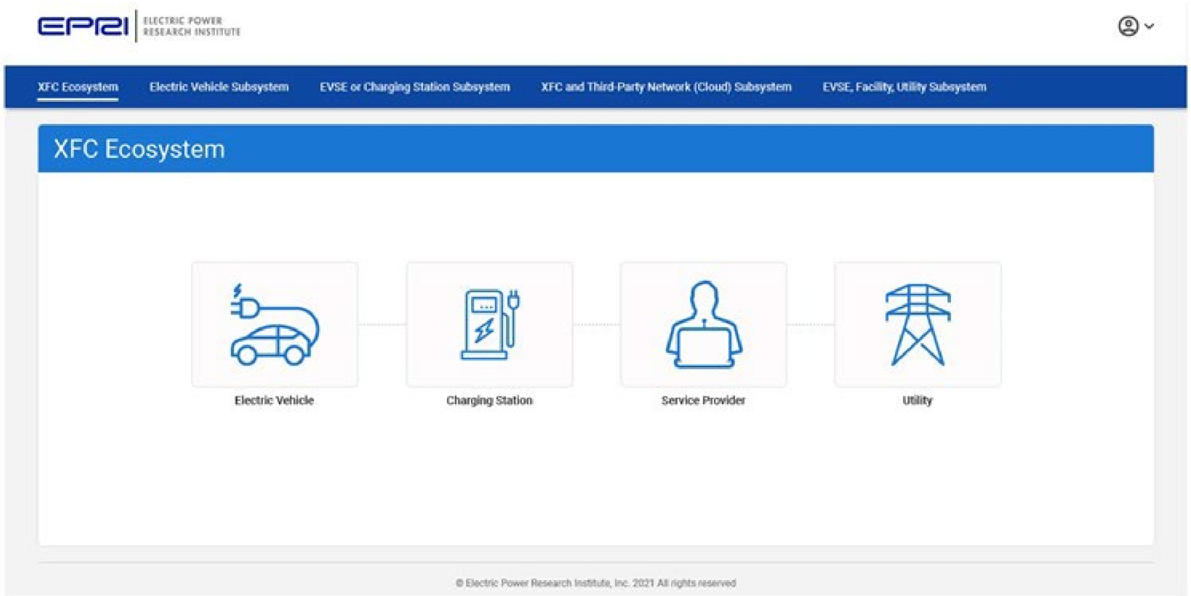

Drilling down to each subsystem provides more details about the different analysis and risks and indicates the type of risks involved and indicates on the screen the components that are affected.

Clicking on the Electric Vehicle will take you the specific cyber security, concern, analysis and recommendations as shown in the figure below.

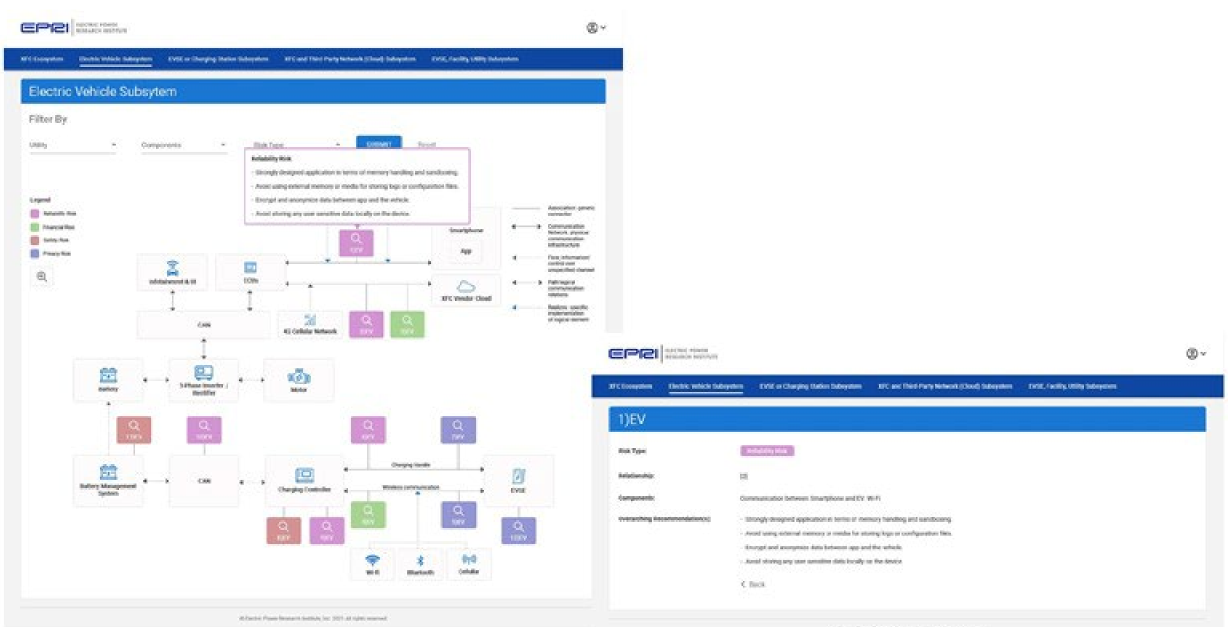

Clicking on the charging station in the main panel will show the cybersecurity analysis, risks as shown in the figure below.

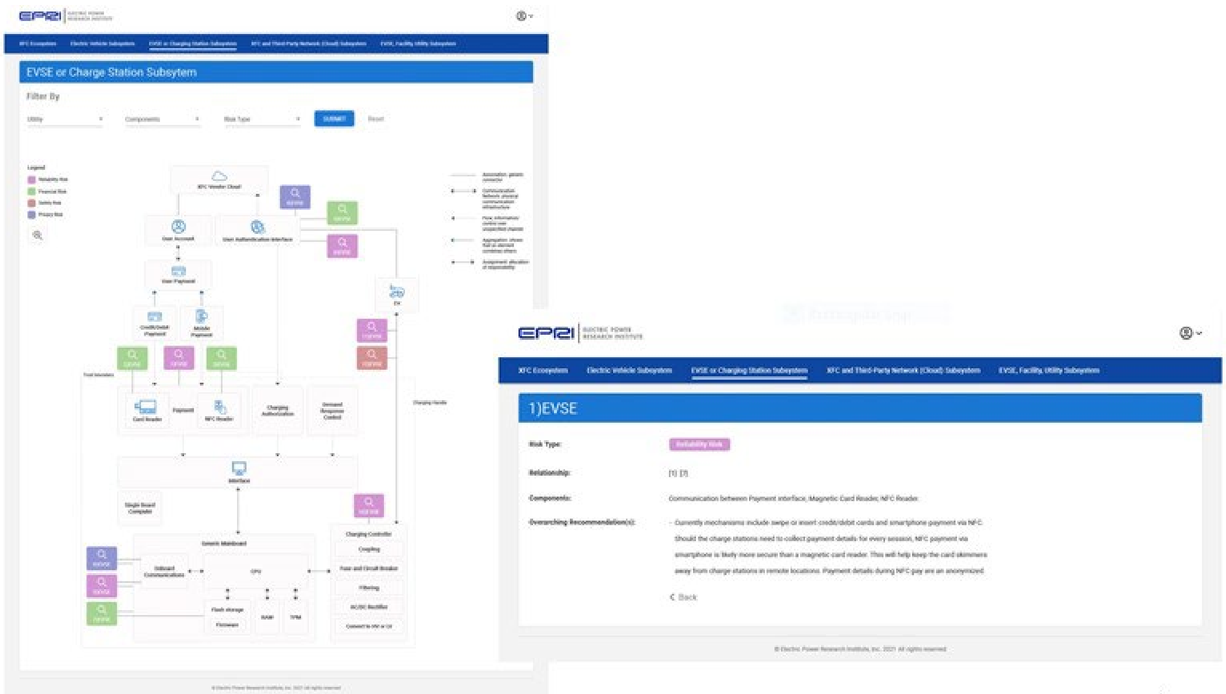

Clicking on the "service provider" in the main panel will display the screen as shown in the screenshot in the figure below.

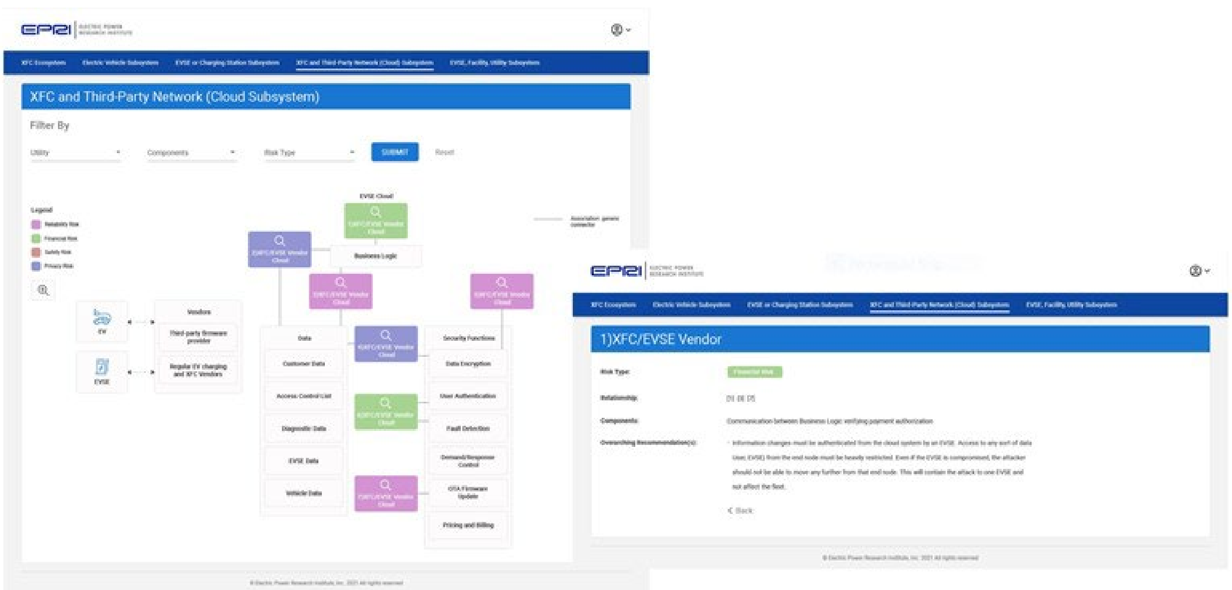

Clicking on the "Utility" in the main panel will display the risks, cybersecurity recommendations as shown in the screenshot in the figure below.

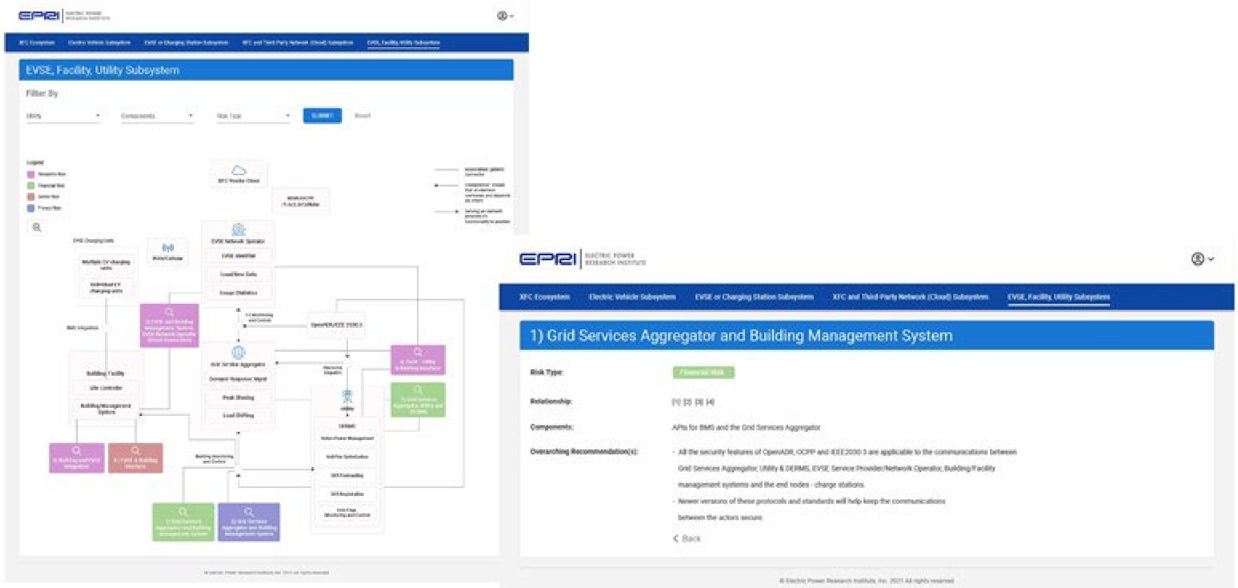

On any of the subsystem screens, clicking on a particular risk or analysis will pop up a dialog with more complete information of the cybersecurity analysis. Samples of the details are shown in right half of the relevant figures for the different subsystems.

Conclusions

In the development of the IGSRM tool, the EA tool and database provided a scalable architecture to develop new sub-systems, components, and cybersecurity risks and recommendations. The tool shall be used to develop a web-based IGSRM tool that reflect the reference cybersecurity architecture of a connected XFC ecosystem, recommended controls and their associated risk profiles.

For the cybersecurity testing at the laboratories, The EPRI CSRL team focused on the EVSE charging infrastructure in fulfilment of its evaluation objectives. That focus primarily being the data flows into and out of the EVSE that could be exploited for theft of theft of credentials, theft of service, or other malicious exploitation of the system via MITM, replay attacks or DOS. The utilization of standard cyber security controls to mitigate risk could provide great benefit in mitigating the risks associated with implementing this type of system. Encrypted channels for communication, message authentication methodologies, along with intrusion detection technologies would all aid in creating a secure, layered defense against a multitude of threats.

The NREL team completed laboratory testing of several cybersecurity aspects of the EV charging ecosystem using hardware, software emulation, and cloud interfaces. The tests performed focused on aspects of the OCPP communications between EVSE and a charge network operator server. The outcomes contribute to improving our understanding of the tools and test methods available for security testing of EVSE infrastructure in addition to identifying potential gaps and enhancements to the cybersecurity posture. The cyberattacks conducted through testing used MITM, replay, and denial of service methods toward the communications between the EVSE and the backend networks. The implementation options within the OCPP interoperability standards for EVSE allow for security configuration flexibility that can either provide more or less secure operating environments depending on network operator approach. Within a scenario with network access and un-encrypted communications, there is a clear ability to impact operations of the EV ecosystem. The use of encryption and authentication methods in current and future OCPP implementations is highly recommended based on these tests. The observations and recommendations provided from testing offer ways of improving the security and reliability of XFC infrastructure. These steps may be beneficial near-term actions while more overarching security solutions like a secure network interface card handling all communications with encryption can be developed and deployed broadly.

References

1. U.S. Department of Energy, Office of Energy Efficiency and Renewable Energy, Alternate Fuels Data Center Website, Accessible at https://afdc.energy.gov/stations/#/find/nearest?fuel=ELEC

2. Green Car Reports, Electrify America turns on first 350-kW fast charger in California. Accessible at https://www.greencarreports.com/news/1120372_electrify-america-turn-on-first-350-kw-fast-charger-in-california

3. Department of Energy (DOE), Office of Energy Efficiency and Renewable Energy (EERE). Fiscal Year 2018 Advanced Vehicle Technologies Research Funding Opportunity Announcement (FOA). 2018. DE-FOA-0001919.

4. Grid Security of Connected Devices: Final Report. EPRI, Palo Alto, CA: 2019. 3002016154.

5. EPRI's Cybersecurity Portfolio: https://www.epri.com/#/portfolio/2019/research_areas/2/072143

6. EPRI's ET Portfolio: https://www.epri.com/#/portfolio/2019/research_areas/2/053122

7. EPRI's ICT Portfolio: https://www.epri.com/#/portfolio/2019/research_areas/2/062333

8. The Systems and Modeling for Accelerated Research in Transportation (SMART) Mobility Consortium "aims to deliver new EEMS data, analysis, and modeling tools, and create new knowledge to support smarter mobility systems." https://www.energy.gov/eere/vehicles/energy-efficient-mobility-systems

Acknowledgements

The project team would like to recognize continued encouragement, support and understanding of DoE VTO program managers, John Conley and Lee Slezak.

The Principal Investigators would also like to express his profound gratitude to the entire team including EPRI staff, NREL and ANL scientists and engineers, industry partners comprising of automotive OEMs, utilities, vendors and integrators (Greenlots, EVSE, LLC, Kitu Systems, etc.), and the EVICWG members who formed the backbone of this project. The project success belongs to the team.

II.1.10 Wireless Extreme Fast Charging for Electric Trucks

Michael Masquelier, Principal Investigator
WAVE, Inc
4752 West California Avenue, Suite B400
Salt Lake City, UT 84104
Email: michael@waveipt.com

John J. Conley, DOE Project Manager
U.S. Department of Energy
National Energy Technology Laboratory
Email: john.conley@netl.doe.gov

Start Date: August 1, 2018 End Date: June 30, 2022
Project Funding: $9,838,241 DOE share: $4,292,137 Non-DOE share: $5,546,104

Project Introduction

The purpose of the wireless extreme fast charging (WXFC) truck project is to significantly accelerate electrification of heavy-duty trucks, starting with shipping ports and expanding to regional delivery operations across the US. Charging time and range anxiety are major barriers to electric vehicle adoption, particularly for truck applications. Therefore, the major goal of this project is to demonstrate high efficiency, WXFC as applied to Class-8 trucks that have a typically higher gap and lower available space than, for example, transit buses.

Objectives

The objective of this project is to develop and integrate a new 500 kW WXFC system developed by WAVE into a Class 8 electric drayage truck developed by Cummins so that it can automatically and wirelessly charge at a high charging rate (c-rate) during their dwell times. The proposed wireless charger features a direct connection to the Medium Voltage (MV) 3-phase grid developed by Utah State University and Schneider Electric and the final prototype will be deployed at Total Transportation Services Inc. (TTSI), which is a truck operator at the Port of Los Angeles (POLA).

Approach

WAVE has assembled a strong and diverse team to develop, deploy, and operate two all-electric Class-8 drayage trucks with WXFC at the Port of Los Angeles (POLA).

The WXFC truck project leverages active involvement of key partners on six major project tasks, as shown in Figure II.1.10.1. Project tasks include:

- Evaluation of a 250-kW wireless fast charging system in a Class 8 Truck field deployment.
- New development of 500 kW wireless power transmitter and receiver modules
- New battery pack and Class 8 truck powertrain development to support high C-rate charging
- New development of an MV grid-tied converter to improve safety and simplify grid integration of WXFC stations
- WXFC grid and vehicle side system integration
- WXFC system deployment and evaluation at POLA.

WXFC for electric trucks is a WAVE-led project with assistant from the following partners:

- The Port of Los Angeles – Deployment partner
- Los Angeles Department of Water and Power – Deployment partner
- Total Transportation Services Inc. – Port trucks partner
- Cummins – Truck integration and electric drivetrain partner
- Utah State University – Research partner
- Schneider Electric – Electrical supplier, industrialization partner.

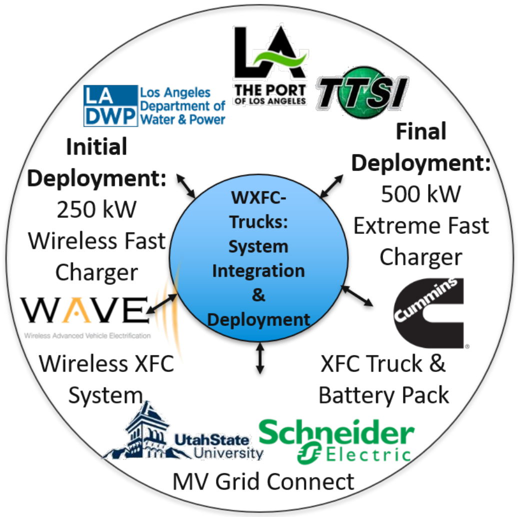

Figure II.1.10.1 WXFC project activities.

The general project approach for the MV AC-DC Converter, wireless charger, and the high c-rate Class 8 drayage truck development is outlined in Figure II.1.10.2.

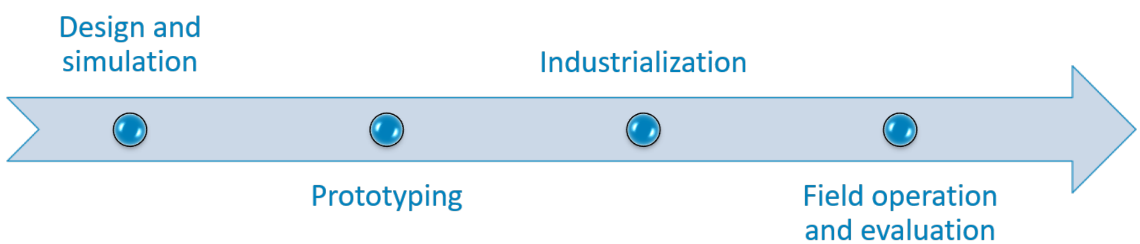

Figure II.1.10.2 Project design and implementation approach.

The USU approach to the MV, grid connected, AC/DC supply is:

- 3-phase unfolder with a soft DC bus two-level output
- Develop the 3-phase unfolder to achieve direct MV grid connection with switches commutating at the line frequency
- Design the series stacked isolated DC/DC converters to achieve the voltage step down function from MV naturally with near unity conversion ratio to obtain high efficiency.

The WAVE approach to the 500 kW wireless charger is:

- Deploy and simulate new magnetics design for the higher power density required at 500 kW.
- Build and categorize a 250 kW prototype pad set based on the new design.
- Leverage deployment experience with 250 kW charger to feed into design updates of the 500 kW charger.

The Cummins approach to the extreme fast charging capable electric truck is:

- Investigate appropriate battery chemistry (LTO cells or NMC cells)
- Design custom thermal management for the cell to facilitate charging at 3C
- Select appropriate battery pack capacity and cell chemistry to integrate with electric powertrain applicable to Class 8 drayage applications.

Results

The project team has worked together to define the requirements for the MV AC/DC supply, wireless charger, and Class 8 truck to deliver a solution that meets the needs of TTSI. A block diagram for the system is shown in Figure II.1.10.3.

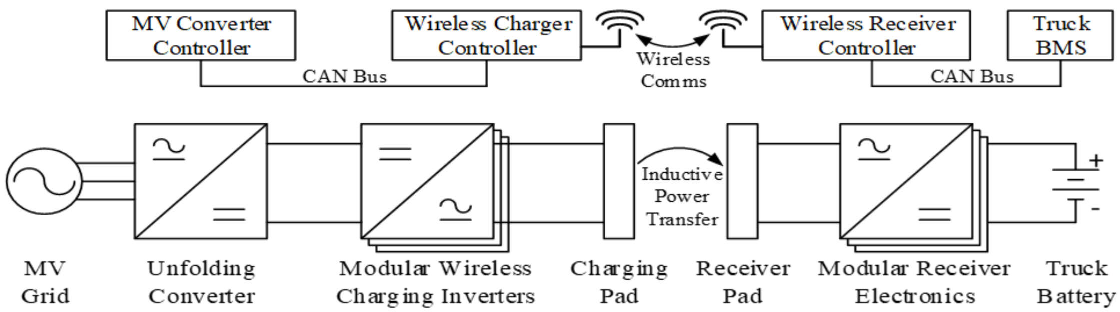

Figure II.1.10.3 System block diagram.

Key results and updates from each project partner are outlined below:

- WAVE-500 kW Wireless Charger Development and Build:
  - WAVE has achieved some major milestones during Budget Period 2 in 2021.
  - Completed construction of the wireless charging equipment including the primary pads, secondary pads, rectifier, and the primary cabinet.
  - Weight of the charging pads on an electric vehicle is one of the major concerns as it is a fixed load in addition to the battery weight that needs to be carried around along with the payload. WAVE team has developed the charging pad that is lighter than a current production pad of the same power level.
  - The major breakthrough was achieved by significantly reducing the size of the primary and secondary pads. This is key for achieving the higher charge levels in a limited space that is available for the charge pads on the truck.

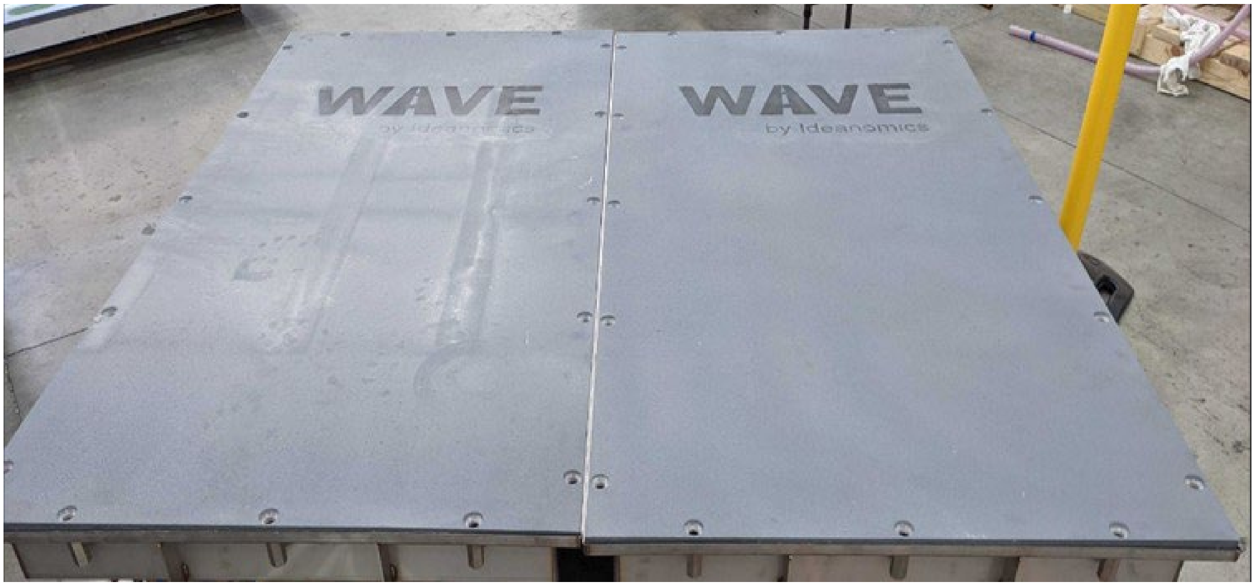

Figure II.1.10.4 Primary Charging Pads

- Cummins – Truck Activities:
    - Cummins completed building Truck 1 and Truck 2.
    - Thermal management validation, key to managing the temperatures of the WAVE components and battery under high power charging is complete.
    - Truck 1 was delivered to WAVE for charge testing.

Figure II.1.10.5 Cummins Truck

- USU – Unfolder and Module Industrialization:
    - USU and Schneider Electric have finalized the design for the unfolder, DC-DC module and connections have been finalized and released for fabrication.
    - The cabinet DC-DC modules and unfolder have completed UL Desk review for regulatory compliance. Field evaluation and testing will take place once modules are constructed.
    - Series stacking control testing was validated on 2 low power modules. The full 560 kW system control validation was finalized in simulation; considering such a significantly large input impedance.
    - The design of the 500 kW MV AC/DC system, sensing and protection was finalized, as shown in the figures below.

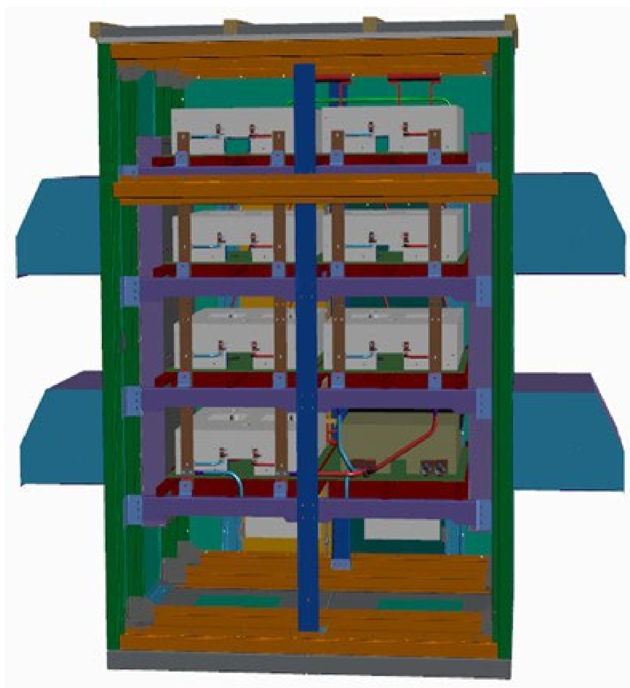

Figure II.1.10.6 Cabinet design for 500 kW MV AC/DC system

    - Cabinets for MV AC/DC system has been placed on order with Schneider Electric.
    - Motorpact and Custom 480V/120V AC Distribution Panel have also been ordered with Schneider Electric.
- WAVE – 500 kW Pads Integration w/ Truck 1:
    - The scope of the wireless charging system vehicle integration testing as pertaining to this integration is to verify all charger side and vehicle side components are functioning correctly.
    - WAVE and Cummins together @ WAVE have installed the vehicle charging pads, rectifier, and antenna on to the vehicle along with the coolant connections necessary to cool the pads while charging takes place.

Figure II.1.10.7 Vehicle Charge Pads installed to the truck

- WAVE & Cummins – 500 kW Charge Testing Results:

Figure II.1.10.8 Charge test setup

  - Physical quality check – Passed
  - Communications Testing – Passed
  - Contactor Operation /Shutdown Function – Passed
  - Charging of Individual Pad Sets at different power levels: 75 kW & 100 kW – Passed
  - Both individual pads were charged to full power with generator at 250 kW – Passed
  - **500 kW Charging** – The goal was to reach at least 500 kW at WAVE rectifier output. Both the charging pads were charged together to achieve the 500 kW – Passed.

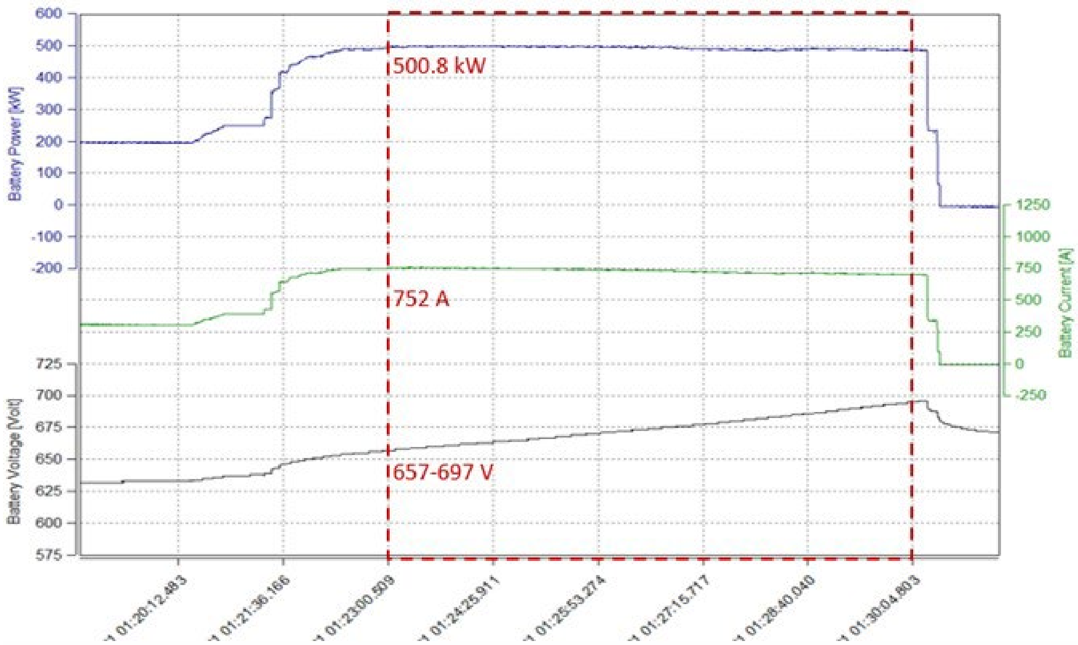

Figure II.1.10.9 500 kW Charging

- **3C Charge Rate**: Another milestone was to test 3C charging of the battery pack. The battery pack was temporarily reconfigured to demonstrate the 3C charging rate within the limits of the WAVE rectifier.

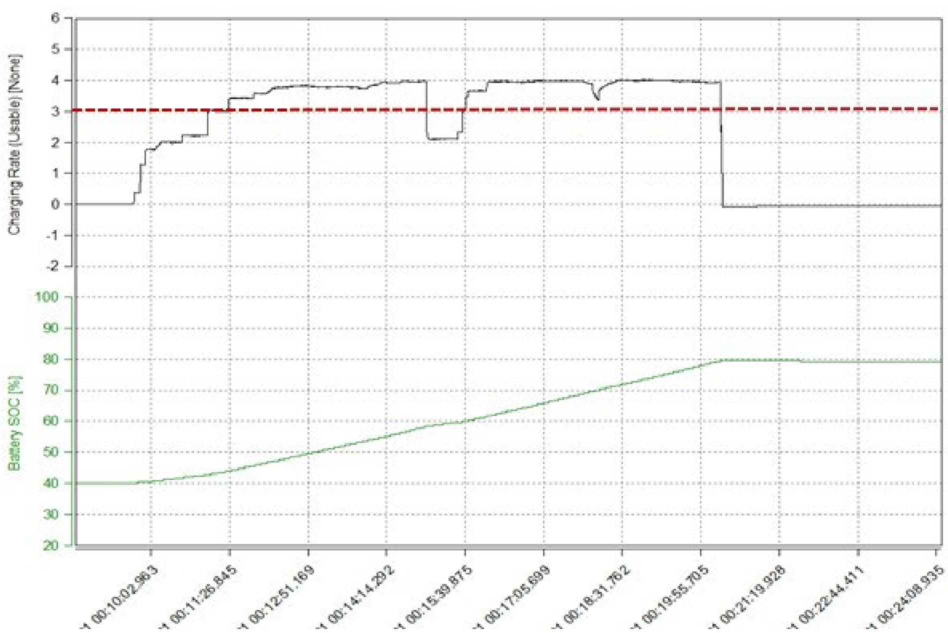

Figure II.1.10.10 3C Charging of the battery pack

- Thermal management is key to this project, as the charging pads transfers high power and at a higher C rate, the life of the batteries is adversely affected. Hence, for a longer than expected battery life, the batteries need to be cooled efficiently. The BMS during the charge testing has efficiently managed the temperatures of the battery system and kept them within the limits while charging at 500 kW and at 3C charge rate.

- Milestones achieved:
    - Battery pack validated – Battery pack testing demonstrates 3C charging capability
    - First truck constructed – with 3C charging capable battery pack
    - 500 kW wireless charging demonstrated
- GO/NO-GO Milestone achieved:
    - Demonstrated 500 kW wireless charging with truck at 3C charge rate.
- Site deployment activities:
    - Application for Port Permit has been submitted.
    - A circuit breaker retrofit has been placed on order with Schneider Electric along with the site engineering analysis needed to complete the installation of the breaker.
    - Cummins has completed and shared the deployment plan of the trucks at TTSI.

Challenges

COVID-19 has severely impacted the supply chain of the components needed to build the equipment and other assemblies at WAVE, USU & Cummins. Significant measures are being taken to address these issues like procuring alternate parts, changing current designs, and adding more resources to reduce the delays.

Conclusions

During this budget period, WAVE team has designed and built the wireless chargers that are smaller and lighter than a current production wireless charger of the same power level. Cummins completed the construction of the 2 trucks and Truck 1 was used for charge testing. The teams have successfully demonstrated the 500-kW power transfer and 3C charge rate with the charging pads installed on the Cummins truck in 2021. This is one of the crucial milestones that needs to be accomplished for an effective deployment of the wireless charging equipment and truck at TTSI.

This project is well positioned with the correct technical requirements to address the range anxiety and charging time restrictions, which are the key barriers to electric vehicle operation at the Port of Los Angeles. With all the partners involved in the final stages of the validation testing, we are on track to deploy and operate the systems at TTSI.

Key Publications

1. M. Masquelier, “Wireless Extreme Fast Charging for Electric Trucks.” 2019 DOE VTO Annual Merit Review, Washington, DC, June 2019.
2. M. Masquelier, “Wireless Extreme Fast Charging for Electric Trucks.” 2021 DOE VTO Annual Merit Review, Washington, DC, June 2021.

Acknowledgements

Project team would like to thank John J. Conley from National Energy Technology Laboratory and Lee Slezak from Department of Energy for their continued support and guidance on this project.

II.1.11 Direct Current Conversion Equipment Connected to the Medium-Voltage Grid for XFC Utilizing a Modular and Interoperable Architecture Performing Organization: Electric Power Research Institute (EPRI)

Principle Investigator: Watson Collins, Technical Executive
Electric Power Research Institute (EPRI)
3420 Hillview Avenue, Palo Alto, CA 943041338
Email: wcollins@epri.com

Lee Slezak, DOE Technology Manager
U.S. Department of Energy
Email: lee.slezak@ee.doe.gov

Start Date: October 1, 2018 End Date: October 31, 2022
Total Project Cost: $5,803,000 DOE share: $2,601,500 Non-DOE share: $3,201,500

Project Introduction

Preparation for vehicle charging at 150 kW and above is underway at multiple vehicle manufacturers, in the automotive, truck, and bus segments. The Society of Automotive Engineers (SAE) vehicle connector standards (SAE J-1772) have been evolving to accommodate these higher power levels. Connector standards also are being developed for conductive, automatic charging at power levels up to 1,200 kW (1,200 Amps at 1,000 Volts DC) by the SAE (SAE J-3105) to serve medium- and heavy-duty vehicles. In addition, the CharIN association is advocating for connector standards capable of delivering greater than 1MW power levels utilizing DC power supply. An industry consensus has emerged that DC power is the preferable means of delivering higher power to vehicles. The U.S. Department of Energy has recently coined the term Extreme Fast Charging (XFC) for 350 kW and above DC charging. For utilities, the current practice in serving DC fast charging sites involves the provision of a 480 Volt AC service fed from the medium voltage grid and converting to DC power for charging. For higher power levels and for simultaneous charging of many vehicles, this approach can create a large hardware footprint rendering it expensive to scale. To address this challenge, medium voltage Silicon Carbide (SiC) based AC to DC conversion solutions provide viable solutions. The SiC based conversion solutions eliminate the intermediate 480 Volt AC stage and convert utility's medium voltage to DC for vehicle charging. Additionally, such Direct Current technologies when integrated with a DC common bus could facilitate the integration of distributed energy resources (DER) to minimize the impact on the grid. This approach could help mitigate electric grid impacts, enable new integration approaches, reduce the impacts brought by demand charges, and reduce XFC related infrastructure costs. This DOE project addresses the design, development, implementation, and performance verification of a medium voltage SiC based conversion solution enabled for DER connectivity. Performance will be verified through laboratory testing and field installation to assess XFC with 350 kW capable vehicles. The project team will work with automakers, charging hardware manufacturers, utilities, and demonstration site hosts to address interoperability and commercialization pathways.

Objectives

The objective of the program is to develop and demonstrate prototype hardware for use in extreme fast charging (XFC) equipment capable of simultaneously charging multiple light duty plug-in electric vehicles (PEV)s at rates of ≥350 kW and a combined power level of ≥1 MW while minimizing the impact on the grid and operational costs. The hardware being developed includes medium voltage Silicone Carbide (SiC) -based AC to DC conversion equipment, DC Distribution bus and DC to DC head-end charging units.

The project goals are:

- Develop the design, performance guideline and specifications for the medium voltage (MV) connected Direct Current (DC) EV-charging architecture
- Test the MV-connected DC technology for Extreme Fast Charging (XFC) and document functional, performance characteristics
- Demonstrate the MV-connected DC technology at a viable field site available to charge XFC compatible vehicles, acquire performance data and document results.

Approach

To meet the project objectives, EPRI along with the project team will develop prototype hardware with upstream interfacing capabilities to the utility grid and downstream configuration for DC load distribution along with complete system engineering design. The overall system architecture is shown in Figure II.1.11.1. The system comprises of a medium-voltage AC-to-DC converter or the Solid-State Transformer, the DC distribution bus, and the head unit DC to DC converter units.

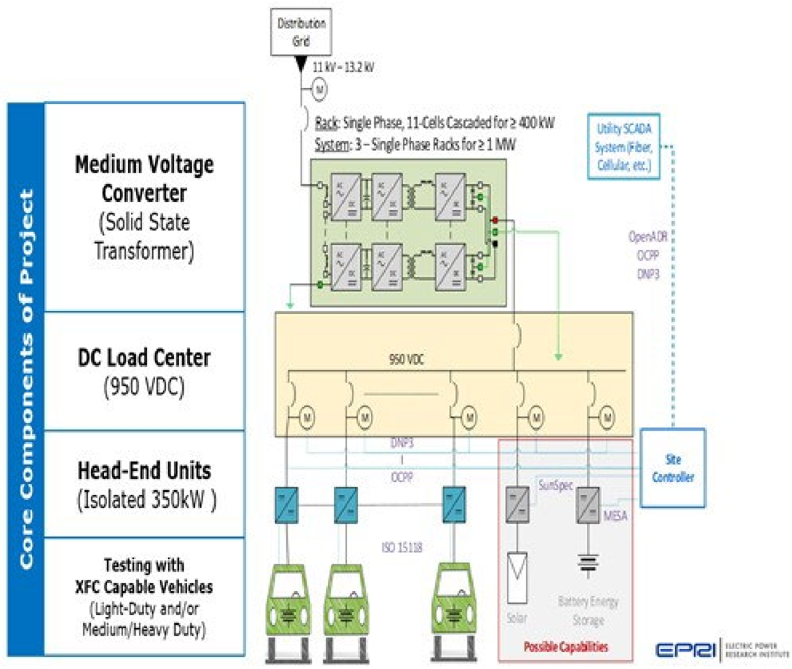

Figure II.1.11.1 Architecture and Core Components

A Utility interconnection interface (not shown in Figure 1) provides single point connectivity to the utility medium voltage Grid. The XFC hardware using DC technologies will serve to minimize adverse load impacts to the grid by facilitating EV Grid Integration and Services. DER such as PV, Energy Storage and microgrids can be connected to the hardware and maintain single point interconnectivity to the utility Grid. The Research effort could also serve to identify new opportunities for interoperability, flexible operation, and technical transfer activities. The project team will investigate potential impacts such as total cost of ownership including demand charges for XFC site hosts and utilities, efficiency improvements and reducing system losses, new capabilities for grid support (power factor correction, VAR compensation, disturbance isolation etc.) and optimization of equipment sizing for upstream Grid assets that serve the XFC equipment. The project will ultimately lead to a fully tested prototype system capable of charging multiple light-duty plug-in electric vehicles (EVs) at a combined power level of ≥1 MW. The system will be installed and demonstrated at a utility site to showcase extreme fast charging infrastructure.

Project Teaming Strategy

The project team is uniquely qualified to conduct research and demonstration tasks for the successful accomplishments of project objectives. EPRI is the project lead with equipment manufacturers, university and national lab partners supporting various tasks within the project.

- Power Electronics – System specifications determined collaboratively, while the development of the two major power electronics pieces designed by two leading manufacturers of power equipment:

  - Eaton is leading the work on the Medium Voltage AC to DC converters
  - Tritium is leading the work on the DC to DC head-end chargers
- Testing – Three levels of testing are included in the project:
  - Component level testing and end-of-line production testing performed by respective manufacturer
  - System testing at NREL with simulated and actual vehicle loads
  - Demonstration site testing in collaboration with host utility with actual vehicles
- Vehicles – Supporting automakers (Hyundai America Technical Center and Fiat Chrysler Automobiles) are included in the project to support testing. If vehicles capable of charging at 350 kW and above are unavailable for testing from supporting automakers, EPRI will identify and obtain vehicles from other vehicle manufacturers.
- Demonstration Site – EPRI has more the three supporting utilities interested in hosting the demonstration site. The decision on the actual demonstration site will be based on specific site characteristics identified by the utilities, anticipated vehicle charging to occur at site and the site development budget.

The project serves unique aspects which contribute to the accomplishment of project objectives:

- Pathway to Commercialization – Seeking to develop equipment, standards and techniques that exhibit possible pathways to commercialization.
- Interoperability – Seeking to develop a system capable of operating with power conversion equipment and head end units from multiple manufacturers.
- Technology Transfer – collaborating with industry participants throughout the project process.
- Diverse Project Team – including project partners from various perspectives (utilities, hardware manufactures, automotive manufacturers, national laboratories, and university)

EPRI is collaborating with multiple utilities and organizations as shown in Figure II.1.11.2. These efforts enable the project team improve industry engagement, assess interconnection and integration challenges, identify potential sites, and define demonstration requirements. The hardware design, manufacturing and testing of the XFC system is the first of its kind in many ways. Project partners and stakeholders have various perspectives based on use cases and their specific role and as a result the technical specifications to build a system versatile enough to accommodate various interconnection standards/best practices, protection requirements, loads and site requirements are quite broad.

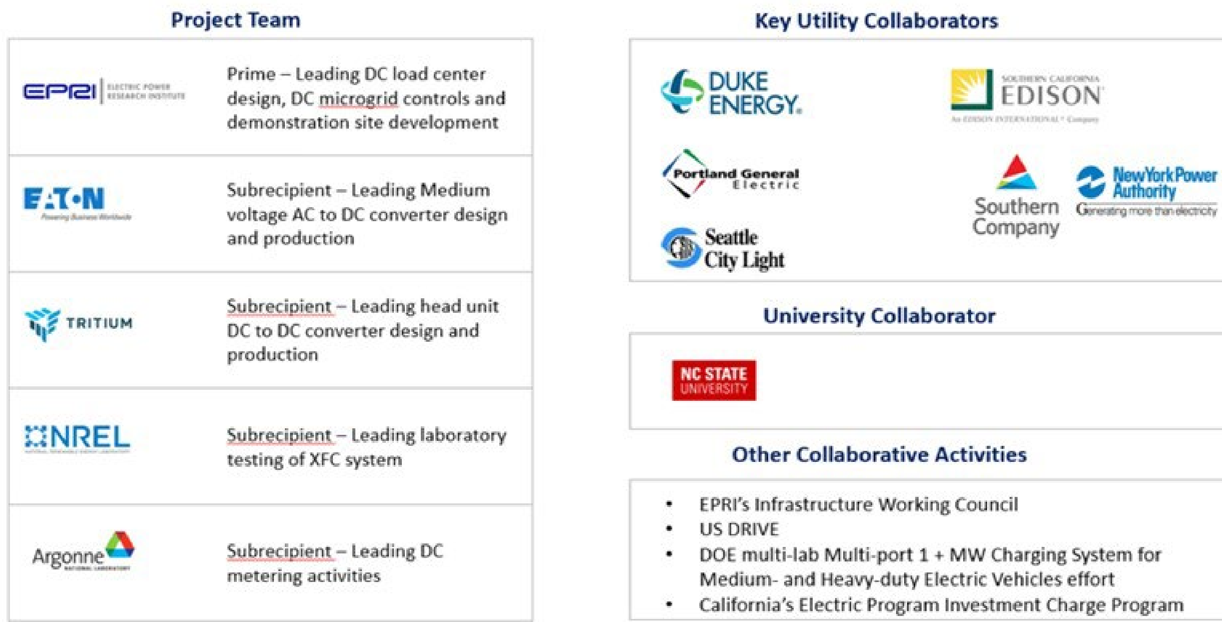

Figure II.1.11.2 Collaboration and Coordination

Challenges and Barriers

The project team has identified the following challenges and barriers that can potentially impact the project. Mitigation plans for some key ones have been identified to ensure project objectives are met in a timely manner and within budget.

- Covid-9 related impacts on supply chain, key resources, or organizations (Medium probability, Medium Impact).
- SST prototype development may not progress rapidly into commercialization pathways, unlike originally expected (High Probability, Medium Impact)
- Performance of the initial cell and module testing at Eaton's facility may not meet modeled results or desired site criteria (Low probability, Medium Impact)
- y-capacitance issues may be problematic for stable operations, protection, and safety of system (Low probability, Medium Impact)
- Unexpected problems may be discovered during testing at NREL's laboratory (Medium probability, Medium Impact)
- Lack of consensus of interoperability approaches, common understanding of DC topologies, equipment options and communications systems for the DC bus (Medium probability, Low Impact)
- Implementation of communication protocols. Which ones are appropriate, which ones are implemented vs standard being defined (Medium probability, Low Impact).

Key longer-term risks based on the current state of the industry are:

- Pathway to commercialization
- Lack of equipment and system standards

- Proprietary components and control/communications architecture
- Lack of standardized system design approaches
- Site-driven parametric dependencies that impact design.

The project team is seeking to develop equipment, standards and techniques that exhibit possible pathways to standardization and commercialization. The team is also exploring ways to develop design criterion focused on interoperability to support ways to operate with power conversion equipment and head end units from multiple manufacturers.

Project Status

Eaton Corporation is a multinational power management equipment manufacturing company with industry leading products for electric, aerospace, hydraulic and vehicle applications. Eaton has established expertise and knowledge in power electronics engineering and manufacturing. EPRI, Eaton, NREL and electric utilities have established the design for the XFC system and are collaborating on the design and fabrication of the Medium Voltage Converter System also known as the Solid-State Transformer (SST). The SST converts utility AC medium voltage at 11–13.2kV to 950–1000V DC. Eaton is manufacturing three (3) single-phase SST modules that constitutes the Medium Voltage Converter System. Each single-phase SST module consists of two (2) medium voltage converter racks, each rack composed of eleven (11) cells in cascaded H-bridge with dual-active-bridge configuration for a total power rating of ≥ 400 kW. The 11-cell single-phase cascade design bridges the 7.6/13.2kV utility medium voltage connection. Each cell has a power rating of 40 kW and are connected in parallel on the DC side of the converter.

Tritium are world leaders in DC-DC charging equipment with high power dispensing capabilities. Tritium has multiple commercially available EV chargers ranging from 75 kW to 350 kW. These chargers have been installed and operating in Europe and North America. This project will utilize Tritium's new, next generation 350 kW isolated DC to DC Head-End technology delivered in an IP65 sealed enclosure with liquid cooled technology. The 350 kW Tritium charger comprises of fourteen (14), 25 kW isolated DC to DC modules. The 25 kW modules have been fully factory-tested with multiple module combinations running synchronized and in parallel. Tritium delivered the first 150 kW isolated DC to DC Head-End Fast charger to NREL in October 2021 for testing and communication evaluation. The 350 kW DC to DC Head-End charger units that will be installed on site, will be delivered to NREL for comprehensive testing in 1Q 2022. A significant accomplishment for the project team was changing the DC to DC head-end unit from the originally scoped non-isolated design to isolated. This had to be done to accommodate the revised design of the DC distribution (DC Load Center), which Tritium took upon as a challenge and completed the design and initial testing. The originally planned Tritium's 350 kW non-isolated head unit had a switched matrix DC distribution.

Another significant accomplishment for the project is the design of the DC Load Center. EPRI with its internal experts developed the design specification for the DC Load Center (DC distribution Bus) along with protection, relaying and coordination functions managed by a PLC system. The design was based on hundreds of hours of engineering time and conversations between project partners (EPRI, Eaton, Tritium, NREL and ANL) for identifying interoperability aspects and specifying operational and safety definitions. The DC Load Center is being built by Peterson Electric Panel Manufacturing Company in Illinois and scheduled for factory acceptance testing in January 2022 prior to delivery to NREL for system integration and testing in 2022. The solid-state transformer (SST) feeds DC power to the DC Load Center, which then enables powering the galvanically isolated EV chargers to charge electric vehicles. Various UL and IEC standards require galvanic isolation between the grid and the vehicles, and from vehicle to vehicle. The use of a charging head with a 'buck' topology has been assessed. The Project Team selected a voltage of nominally 950V for the SST output to the DC distribution bus, as this gives adequate headroom above the 920V maximum required by the vehicle. The load on the DC distribution bus will come from the charging head units as planned within the project. Future enhancements to this project could be to add DER such as Photovoltaic (PV), Energy storage, and V2G vehicles, all of which can connect easily to the DC Bus. The team also decided on a mid-point grounded DC output from the SST to reduce the size of the DC gear and cable requirements.

Special facilities access and planned utilization:

- ANL: Argonne National Lab's efforts have been directed towards enabling harmonized EV charging device specifications and common test procedures. ANL has developed prototypes of accurate, stable, and easy to install low-cost compact DC submeters for high power EV charging
- (1000Vdc/500Adc). One of these prototypes has been commercialized by Riedon. The Riedon DC Smart Shunts are installed in the DC Load Center for DC metering. Meter functionality development, connection architecture, and testing of DC metering on this project was coordinated with ANL.
- NREL*:* Lab testing and verification of the XFC charging system with 3 installations of Tritium's DC to DC Head-End chargers, Eaton's Medium Voltage Converter System with three SST modules, the DC Load Center and 350 kW charge capable vehicles will be hosted and administered at NREL's Energy Systems Integration Facility (ESIF). The 182,500-square-foot (17,190-square-meter) facility is a first-of-its-kind design with a unique merging of three distinct and very specialized components: an ultra-green workplace, a high-performance computing data center, and a highly sophisticated high-bay laboratory. NREL is working with the project team to define the test procedures and acquire test equipment for system testing, operational and performance verification.

Results

The following results were accomplished during the second year (Y2021) of the project:

- **System Architecture and Specification**: Development of system architecture (Figure II.1.11.3) technical performance specification and interoperability parameter definitions for the medium-voltage AC to DC converter and the head unit DC to DC converter are finalized and complete. During 2021, there were refinements, reviews, and discussions on a few specifications mainly for the utility interface of the SST. Selection of a system topology, requirements and design trade-offs have been assessed. Converter design and control approach, input, and output ratings along with control functions haven't changed much from last years' definitions. Supply chain delays have impacted Eaton from realizing hardware and software configurations of the SST converter modules and the SST controller. A few changes in the controller design are still forthcoming, after component-level tests. Trade-off analyses between various commercially available SiC power modules is complete resulting in the most commercially ready devices selected for the project. Similarly, the high frequency transformer design was reviewed to understand impacts on AC harmonics and DC ripple due to the switching frequency and type of core material used in the transformer. Based on simulational performance analyses and efficiency targets the design was completed with off-the-shelf cores. Manufacturing of the high frequency transformers started in late fall 2021.

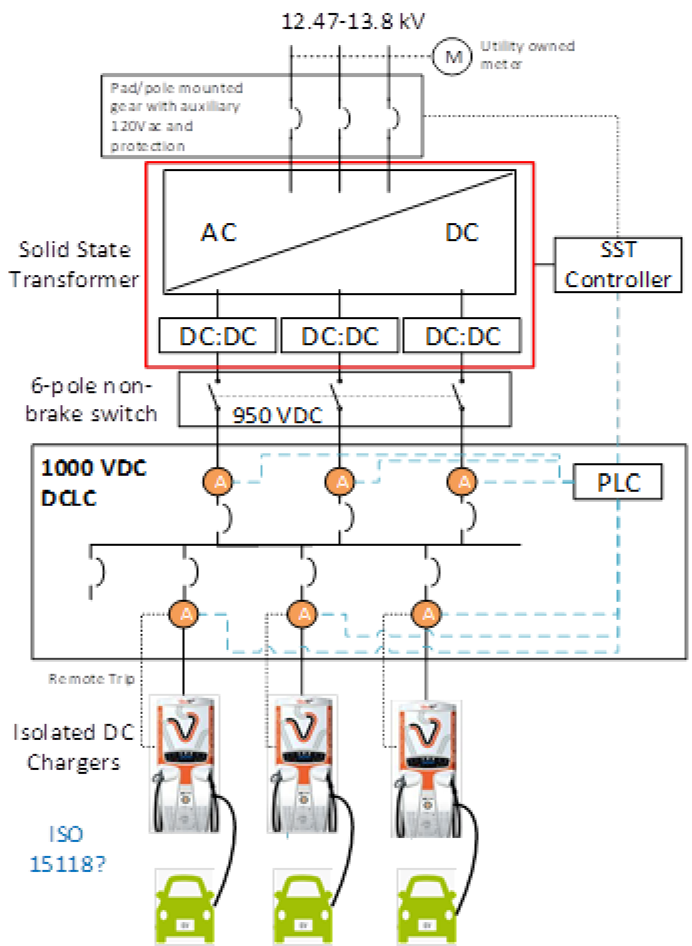

Figure II.1.11.3 Medium Voltage to DC Extreme Fast Charging (XFC) System Overview

- **DC Load Center design:** The specified design is shown in Figure II.1.11.4 and was finalized after review by AHJ for conducting the system testing at the test site (NREL). The DCLC is in the final stages of manufacturing by Peterson Electric Panel Manufacturing Company based in Berkeley, IL. The DCLC is custom equipment currently with a PLC incorporated for decision-making for protection and coordination. It is anticipated that the DCLC design will enable pathways for interoperable designs and commercialization. The Power components on the supply or input side of the DCLC include 3-500A 3P Eaton PV circuit breakers with 24VDC Shunt trip and 2-2A/2B aux contacts. The breakers have through door handle operator with padlock provisions. Hall effect current transducers shall supply analog breaker amperage information as well as ground fault amperage to PLC. The Power components on the load side or output side include, 3-500A 3P Eaton PV circuit breakers with 24VDC Shunt trip and 2-2A/2B aux contacts. Through door handle operator with padlock provisions are included. Hall effect current transducers shall supply analog breaker amperage information to PLC. Bender Ground fault sensor CTBC60P and control module RCMB301 provided for each load position. These are shown in Figure II.1.11.5.

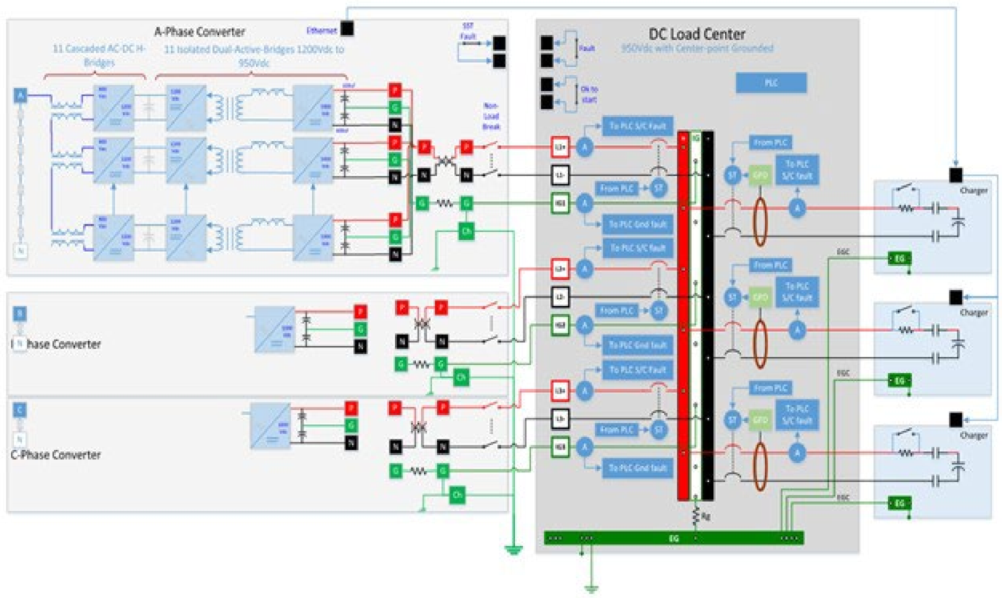

Figure II.1.11.4 Medium Voltage AC to DC Converter (SST) connection with DCLC and protection/relaying

Figure II.1.11.5 DCLC and power components – Eaton PV (DC) Breakers, Bender GF Sensor

- **DC Load Center PLC (Programmable Logic Controller):** DCLC Controller function specifications (using PLC) for fault coordination on the load side and to manage the timing of SST control have been determined and finalized. The PLC system for the DCLC (Figure II.1.11.6) has been finalized to Siemens S7-1500PLC with 2X16 DI Module, 2X8 DO Relay output, 4X4 Isolated Analog inputs. 24VDC with Emerson SolaHD S4KC DC UPS (1 kVA) and Heviduty SDU battery backup. The S4K2U is single-phase, industrial grade on-line (double conversion) UPS that takes 120 V ac input from the utility interface of the SST and converts it to 24 V DC for the PLC backup. PLC Scan time is estimated to be 1 ms at 30 ns/bit. Most of the design and configuration aspects are final. The key evaluation items for PLC that the team worked on are: PLC logic for braker fault handling operations—develop breaker alarm logic, response to e-stop conditions by alerting uses on an HMI and force breakers until e-stop is reset, System-level fault indicator logic and comms when PLC has detected a fault condition, comms to a SCADA system over Modbus—All I/O values, Alarm information, Mode (manual test mode vs. SCADA control) and the register mapping for bringing back status information to a remote database for monitoring and dashboarding application.

Figure II.1.11.6 DCLC Siemens PLC with Emerson SolaHD 1 kVA UPS back up

- **SST Medium-Voltage Converter Design and Manufacturing**: Module design, system topology determination and architecture development are complete. Prototype modules have been assembled and tested at low voltage at Eaton's lab. The three converter modules of the SST—A, B, C would be housed inside a standard 20 ft container (20x8x8 ft). The containerized package is shown in Figure II.1.11.7. The container is designed with air cooling ducting, exhaust fans for ventilation and cable trays for conductors with appropriate structural provisions for landing the MV feed and connections. A total of 6 racks are housed inside the SST, 2 racks per module (or phase). Each rack houses either 5 or 6 cells. In the 5-cell rack the controller for that phase is housed. The DC Load Center and the Utility Interconnection interface will be separate equipment packaged in panel enclosures. MV feed could be overhead or underground and the intermediate connections can be underground (trenched) but some of the details will be decided based on-site feasibility. A 400 A DC Disconnect switch feds the DCLC from the SST. Performance characteristics for an experimental 600V ac- 825V DC 43kW single-cell module implementation is complete. Rack design is complete with specifications updated for multiple components including multiple design iterations to improve thermal and magnetic performance of the DAB (Dual Active Bridge) High Frequency Transformer, DAB and AFE (Active Front End) inductors. Physical build of the converters is in progress. Controls and Protection design have been completed, but assembly and testing has been delayed due to Eaton's inability to secure components. Eaton has mentioned that they have tried but haven't been able to get parts due to the supply chain shortages in the semiconductor component space. Testing, simulation, and physical realization of advanced control systems for the converters hasn't advanced to where it should be per the schedule. This will delay system testing and deployment.

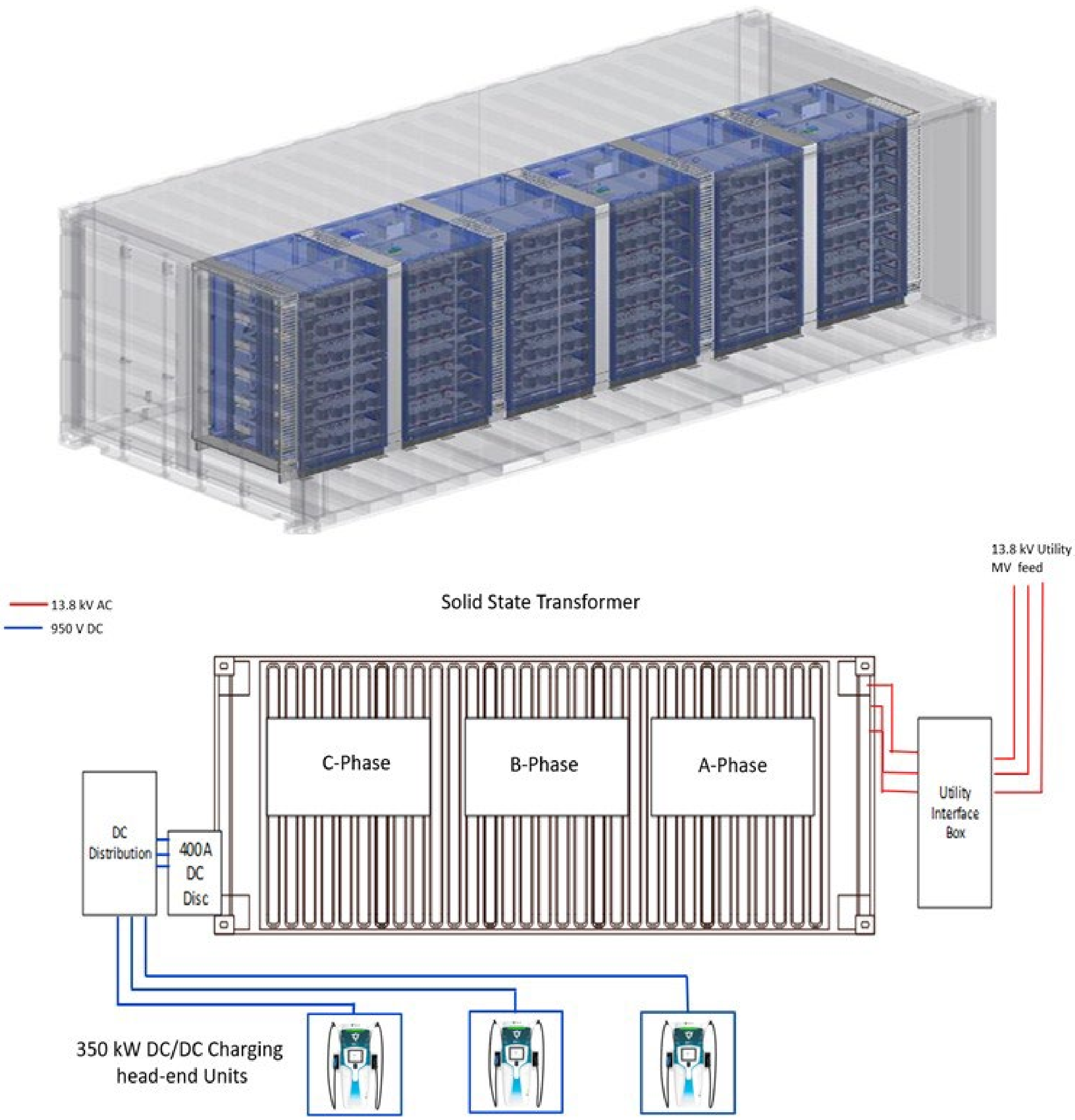

Figure II.1.11.7 Containerized SST and System Connections

- **Utility Interconnection Interface**: The SST requires a utility interconnection interface also referred to as the Utility Interconnection Box for Solid State Transformer (UIB-SST). The UIB-SST serves as the primary disconnect and protection interface between the medium voltage interconnection and the solid-state transformer (switched DC power supply) as a part of DC as a service customer supply. The UIB-SST contains pre-charging circuitry which helps control inrush current and mitigate voltage and power factor regulation issues for the utility. The anticipated packaging and component detail is shown in Figure II.1.11.8. The UIB-SST will have MV connections and neutral configurations that include Delta-Wye: Low voltage neutral fully insulated X0 bushing with removable ground strap and Grounded Wye-Wye high voltage neutral internally tied to the low voltage neutral and brought out as the H0X0 bushing in the secondary compartment with a removable ground strap. A Delta-Delta Transformer shall be provided without a neutral bushing. The MV bushings are anticipated to be of 600 A (15kV class) Integral bushings (dead-front), electrical-grade wet-process porcelain bushings (live-front). Several design discussions amongst the project team and with utilities revealed implementational challenges with the earlier design of the UIB-SST to meet Utility Electric Service Requirements.

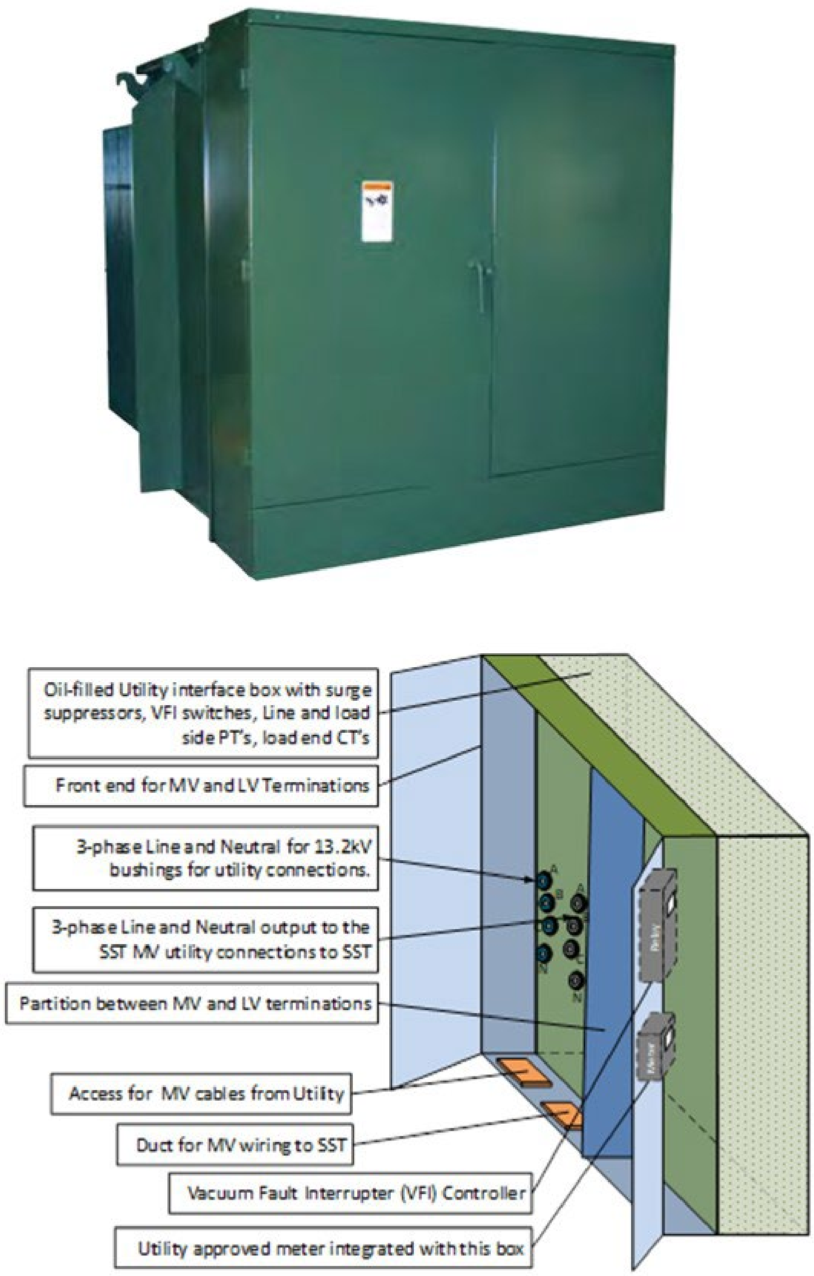

Figure II.1.11.8 UIB-SST: Utility Interface Box housing the Pre-Charge Circuit

- **XFC DC to DC Head End Unit Design and Manufacturing**: Tritium is on track in the design, manufacturing, and delivery schedule of the 350 kW DC to DC Head end units. A 150 kW DC to DC Head end unit designed and manufactured as a prototype has been shipped to NREL for testing. The 150-kW unit standalone testing at NREL is in progress with actual vehicles as well as with EV load banks. Tritium PKM platform 350 kW DC to DC Head end units (3 numbers) are under construction. The U.S compatible PKM platform Tritium DC to DC head units (Figure II.1.11.9) are being tested prior to full and final approvals for manufacturing. Components and parts have been procured and the units will be built according to the manufacturing plan. The 150 kW and 350 kW units are similar in design; hence the project team anticipates no major challenges in the manufacturing given that 150 kW charger has been manufactured successfully. Tritium has stated on project biweekly update calls that end-of-line production testing is an integral and standard part of their production process. This is followed by extensive EMC validation testing along with other performance measurements.

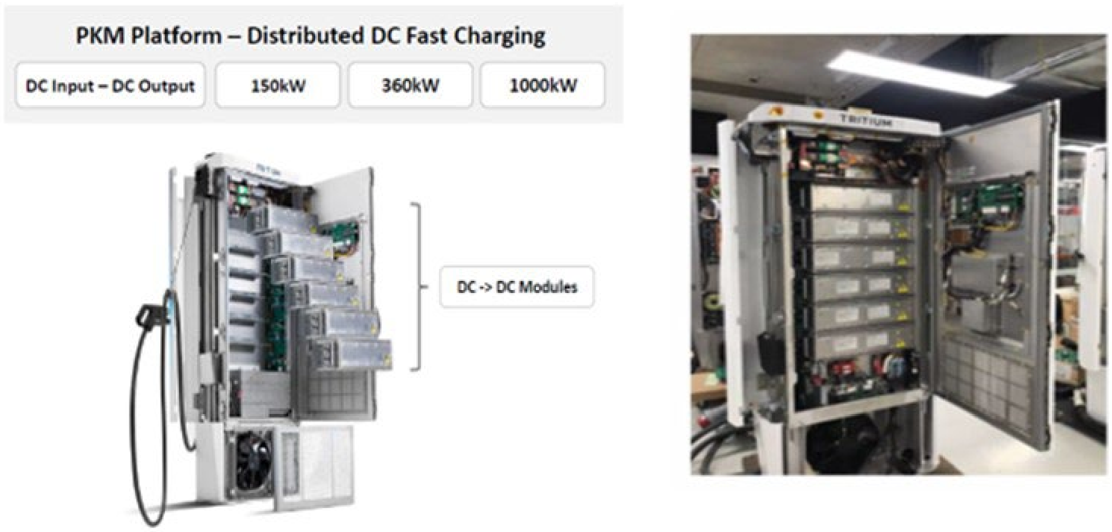

Figure II.1.11.9 Tritium DC to DC Head end Charging unit

- **Isolated Component and System Integrated Testing at NREL**: The project team is in the process of finalizing test requirements, test infrastructure and test procedures for component and full integrated system testing at NREL. The plan is to test individual components followed by complete system testing.

Key phases of testing include:

- Tritium 150 kW DC to DC head unit isolated testing. Test set up shown in Figure II.1.11.10
- DC Load Center isolated testing
- Tritium 350 kW DC to DC head unit charger isolated testing
- DC Load Center and Tritium 350 kW DC to DC head unit charger combined testing
- Single Phase SST isolated testing
- Single phase, DC Distribution, and Tritium (350 kW) combined testing
- Three phase Utility Interconnection box isolated testing
- Three phase, DC Distribution, and Tritium (350 kW) combined testing.

The schedule for testing is fluid due to delays in manufacturing of hardware and non-definitive equipment arrival dates at NREL. As equipment manufacturing timelines are firmed up, test plan and schedule will be updated based on definitive dates. Test plan will include multiple tests scenarios and tests to measure performance, efficiency, AC and DC interconnection and other interoperability metrics.

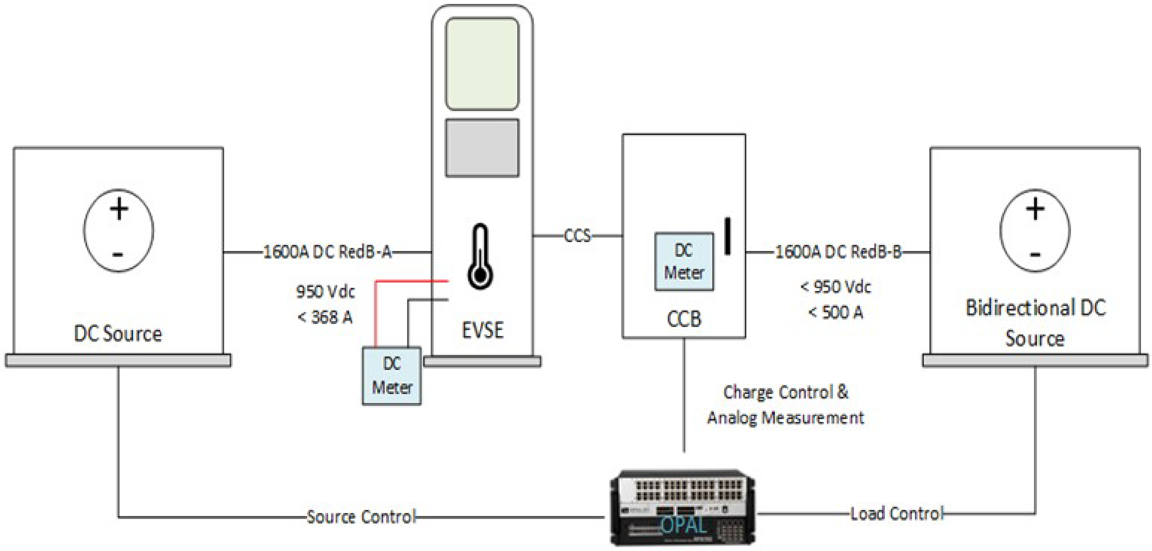

Figure II.1.11.10 Tritium Chargers Isolated testing

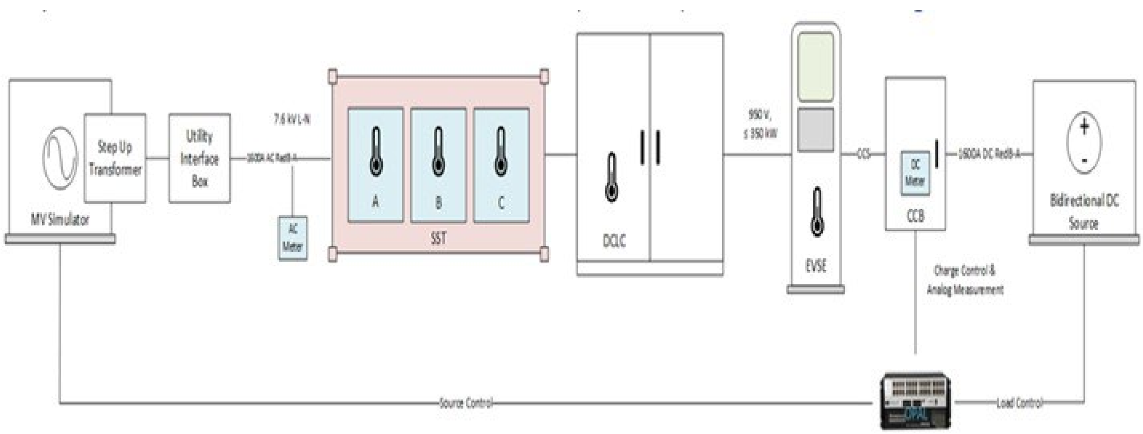

Figure II.1.11.11 Three-phase SST, DCLC and 350 kW Tritium Chargers Combined Testing

Conclusions

Prototypes of the DC to DC Head end charging units and the DC Load Center are at advanced stages of manufacturing. Several design and interoperability issues were discussed and resolved. The DC Load Center design and hardware realization is a significant success to the project as this has the potential for companies to create product lines, commercially available for DER and EV charging applications. Tritium has delivered the 150 kW DC to DC Head end charging unit to NREL for isolated testing, and tests are in progress to document full power performance. Eaton medium voltage connected SST module development has been slow and will likely result in delays deploying the system. Southern California Edison has been selected as the utility host site for deploying the XFC system. The deployment is anticipated to be at SCE's Research Center. Utilities continue to express interest in DC as a service models catered to fleet EV charging. There are several aspects related to utility practices, regulation, standards, and customer line of demarcation definitions that need discussion and support for market adoption of XFC type architectures. Market vendors are not making medium voltage connected charging equipment but are commercializing 480 V centralized power converters with an electromagnetic transformer on the front end. This solution will be challenging to scale up and is more expensive, with higher losses compared to the medium voltage connected power conversion with a solid-state device and a transformer-less active front end design.

Key Publications

Key publications developed are in the form of reports and presentations. The list is provided below. Copies of the publications are available upon request.

1. DOE DE-EE0008448 AMR 6-24-2021-final.ppt
2. DE-EE_ EE0008448_Quarterly Reports 2021
3. DOE DE-EE0008448 AMR 6-04-2020-final.ppt
4. DE-EE_ EE0008448_Quarterly Reports 2020
5. DE-EE_ EE0008448 Converter Design Parameters v15 Final
6. DE-EE_ EE0008448 Module Performance Characteristics Simulation Test Results v2
7. DE-EE_ EE0008448 Transformer Design Specifications v9
8. DE-EE_ EE0008448 DC Load Center Specification Design v15 Approved
9. DE-EE_ EE0008448 DC Load Center Operational Guidelines v4 Approved
10. DE-EE_ EE0008448 DC Load Center Power Diagrams & SST Details v2 Approved
11. DE-EE_ EE0008448 Comprehensive Grounding Schema v2 Final
12. DE-EE_ EE0008448 Utility Demonstration Site Selection Presentations
13. DE-EE_ EE0008448 DCLC Factory Acceptance Test Procedure v3 Final
14. DCaaS MVOTA Testing Plan NREL Version 4
15. DC Load Center Installation Considerations and Cabling Guidance
16. DCLC Isolated Testing Procedure for NREL v1
17. Utility Interconnection Box for Solid State Transformers Specification v1.0
18. Introduction to the Utility interconnection and DC interface for DCaaS
19. Medium Voltage Service Requirements & ESR Considerations for SST Interconnection version 4
20. Utility Medium Voltage Disconnect (VFI) Specification 1.0
21. Containerized Package Drawing.ppt v3
22. SST Specification version 12

II.2 High Power Charging (HPC) Enabling Technologies

II.2.1 High Power and Dynamic Wireless Charging of EVs (ORNL, INL, NREL)

Veda Prakash Galigekere, Principal Investigator
Oak Ridge National Laboratory
2360, Cherahala Boulevard
Knoxville, TN 37932
Email: galigekerevn@ornl.gov

Richard Carlson, Principal Investigator
Idaho National Laboratory
2525 North Fremont Avenue
Idaho Falls, ID 83415
Email: richard.carlson@inl.gov

Andrew Meintz, Principal Investigator
National Renewable Energy Laboratory
15013 Denver West Parkway
Golden, CO 80401
Email: andrew.meintz@nrel.gov

Burak Ozpineci, ORNL Program Manager
Oak Ridge National Laboratory
2360, Cherahala Boulevard
Knoxville, TN 37932
Email: burak@ornl.gov

Lee Slezak, DOE Technology Manager
U.S. Department of Energy
Email: Lee.slezak@ee.doe.gov

Start Date: October 1, 2019 End Date: March 31, 2022
Project Funding: $4,000,000 DOE share: $4,000,000 Non-DOE share: $0

Project Introduction

Dynamic charging of electric vehicles (EVs) has the potential to significantly alleviate range anxiety while concurrently reducing the required on-board battery capacity. Current state-of-the-art light duty dynamic wireless EV charging prototypes are limited in power level to approximately 20 kW. This necessitates a higher portion of the roadway infrastructure to be electrified, thereby increasing the infrastructure cost considerably.

It was previously determined that for light-duty (LD) vehicles to achieve charge balancing mode of operation on primary roadways with minimal infrastructure cost, power transfer levels in the range of 200 kW are required. The study was then extended to include the impact of dynamic wireless power transfer (DWPT) on intracity travel. A test platform for analyzing the large-scale deployment of DWPT was developed and a case study was conducted for Atlanta utilizing actual road network data. It was previously noted that with certain deployment scenario, 200 kW DWPT system would lead to up to 30.42 % vehicles experiencing more than 500-miles range and up to 21.06 % of vehicles realizing more than 1000-miles range as compared to an average 150-miles range without DWPT system.

For a nominal dynamic power transfer level of 200 kW, optimal system architecture including power electronics and power transfer couplers are identified to enable efficient transfer and accurate control of power for speeds indicative of real-world usage. The implications of embedding couplers in the roadway are analyzed and a suitable coupler system and power electronics are designed, developed, and laboratory characterization is carried out. Electromagnetic emissions and the required shielding solutions to ensure a safe high power dynamic wireless charging system are also developed. Necessary enabling technologies such as alignment, data acquisition, and communication systems are being developed to realize a practicable vehicle integrated 200 kW dynamic EV charging system.

Objectives

The overall goals and objectives are

1. Perform sensitivity analysis of the primary side LCC and secondary side series tuned 200 kW DWPT system to predict the power transfer profile as a function of vehicle coil position.

6. Conduct experimental validation of vehicle integrated 200 kW DWPT system in stationary mode, to serve as preliminary power transfer capability verification prior to validation in dynamic mode.

7. Conduct grid impact analysis of 200 kW DWPT system on distributed system and propose solutions based on renewable energy integration to reduce the grid impact of DWPT.

8. Explore the feasibility of using the 200 kW DWPT system which was developed for LD EVs to serve heavy-duty (HD) class 8 EVs and evaluate its impact on vehicle’s efficiency (kWh/mile) in Atlanta (case study), considering:

    - Long-haul class 8 vehicles, which use sleeper cab EV model
    - Regional class 8 vehicles, which use day cab EV model
    - Local class 8 vehicles, which use day cab EV model

9. Explore advanced shielding solutions to realize safe and reliable operation of 200 kW vehicle integrated dynamic wireless EV charging.

10. Develop data acquisition systems and methodologies for reliable and accurate characterization of 200 kW dynamic wireless EV charging system.

Approach

Sensitivity analysis of primary side LCC and secondary series tuned 200 kW dynamic wireless charging system

A mathematical model based on fundamental harmonic approximation (FHA) is developed to predict the variation or sensitivity of output power to variation in coil-to-coil misalignment [1]. A finite element analysis (FEA) electromagnetic simulation is conducted to determine the mutual inductance profile, equivalent transmitter, and receiver coil inductances for the variations in the misalignment in x and y-direction. Figure II.2.1.1 shows the transmitter and receiver coil dimensions, with the FEA simulation data-points. Figure II.2.1.2 shows the mutual inductance, transmitter coil inductance, L1, and receiver coil inductance, L2 acquired through FEA simulations over the range of x = -152 cm to x = 152 cm and y = -76 cm to y = 76 cm, where the origins of transmitter and receiver coils are aligned at x = y = 0. The air gap between the transmitter and receiver coil was 25.4 cm (per Hyundai Kona). A linear circuit model is derived using FHA, and circuit analysis is carried out to predict the various system parameters including the predicted input impedance and output power.

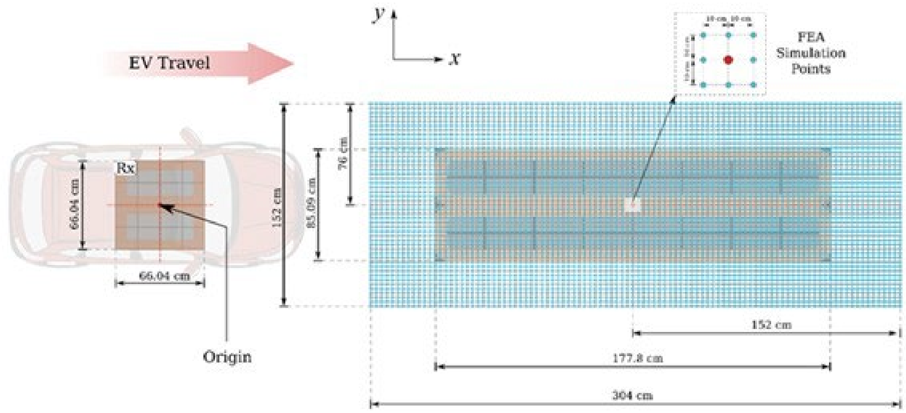

Figure II.2.1.1 200 kW WPT transmitter and receiver coil dimensions with FEA simulation points.

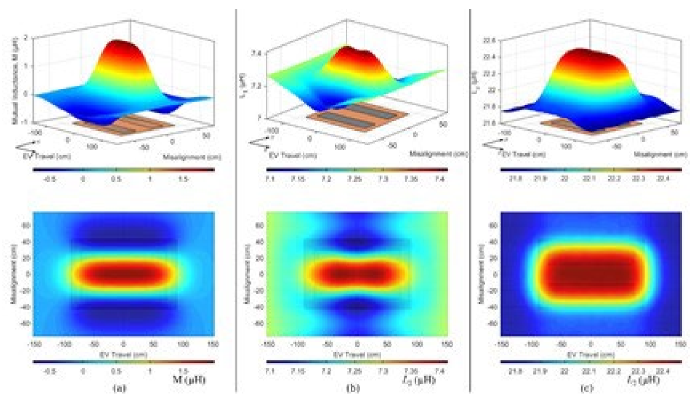

Figure II.2.1.2 (a) Mutual inductance, M, (b) transmitter inductance, L1, and (c) receiver inductance

Power transfer capability validation of 200 kW DWPT system

Optimized primary and secondary side high frequency (HF) SiC based power electronics, resonant network, and couplers were previously designed and prototyped in the laboratory. Primary and secondary side power electronics were individually validated up to the rated power in benchtop configuration. The secondary side dc-dc converter was observed to have phase current mismatch or imbalance which was attributed to insufficient resolution due to the DSP control board operating with a 10 ns resolution. To overcome this problem, a high-resolution control scheme was developed with a resolution of 200 ps.

To overcome this problem, a high-resolution control scheme was developed with a resolution of 200 ps. With the improved control resolution, DC-DC converter was validated up to 188 kW with 800 V input and regulated 400 V as the output. The satisfactory operation of secondary side DC-DC converter indicates that the required regulation to enable a smooth and safe dynamic wireless EV charging is functional.

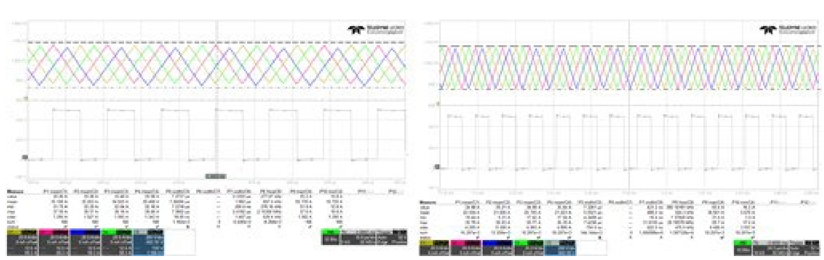

Figure II.2.1.3 High-resolution PWM improves current sharing among the secondary-side dc-dc converter phases. Left: Low-resolution PWM. Right: High-resolution PWM.

200 kW vehicle coupler and Aluminum shield which were previously validated using a benchtop setup were integrated into Hyundai Kona and is shown in Figure II.2.1.4. The Aluminum shield acts as a secondary shield in addition to the Ferrites in the receiver to ensure safe thermal operation. The vehicle integrated 200 kW DWPT system is shown in Figure II.2.1.5. Two NHR 9300 high voltage battery emulators are used each on the source side and load side respectively. The vehicle integrated 200 kW DWPT system was tested in stationary mode to evaluate the effect of vehicle body on power transfer and any possible interference or thermal hotspots.

Figure II.2.1.4 200 kW receiver coil and secondary Aluminum shield integrated to Hyundai Kona EV.

Figure II.2.1.5 Vehicle integrated 200 kW DWPT setup for validation of power transfer capability in stationary mode.

Grid Integration and Impact Analysis

A simulation study was conducted to quantitatively understand the impact of DWPT on the electric grid. The study focused on three aspects a) grid integration and control strategy, b) quantitative analysis of impact on the grid, c) optimal renewable energy integration to mitigate the impact on the grid.

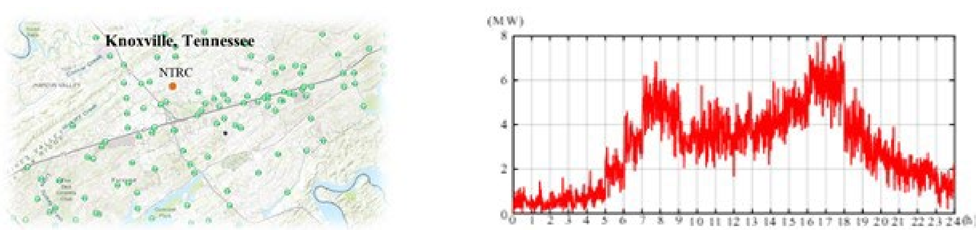

(a) (b)

Figure II.2.1.6 Location of AADT data and 24-h load profile.

To evaluate the grid impact of high-power DWPT system on distribution networks, a 24-h load profile was developed based on the load demand of a single vehicle and the 24-h traffic model. Considering that the charging power demand of DWPT system closely relates to traffic volume and vehicle speed, real annual average daily traffic (AADT) data and stochastic model were used to quantitatively analyze the vehicle distribution in 24 hours. As shown in Figure II.2.1.6 (a), the AADT data at Interstate 75 in the Knoxville, Tennessee section was derived from Department of Transportation's Federal Highway Administration. The traffic distribution data on weekdays and Poisson distribution process were used to generate the load profile on a minute time scale of 1-mile charging zone with 200 kW DWCS in 24 hours. The load profile matches the traffic distribution on weekdays. Two power peaks occurred at the morning and afternoon rush hour, and the maximum power demand is approximately 8 MW, as shown in Figure II.2.1.6 (b).

Figure II.2.1.7 shows the topology of grid integrated 200 kW DWPT system, including a step-down transformer, a grid interface, a full-bridge converter, and LCC-series resonant network. Considering the pulsating load profile of DWPT system, load transient response capability is critical for the grid interface converter for maintain the dc-bus voltage stable. Besides, the inherent unbalanced situation of distribution network would lead to 2nd order harmonics on the dc-bus voltage, which would further affect the stable operation of the entire system. To address these two issues, a control strategy was proposed to enhance the load transient response of the grid interface converter to meet the requirement of fast power change in DWPT system.

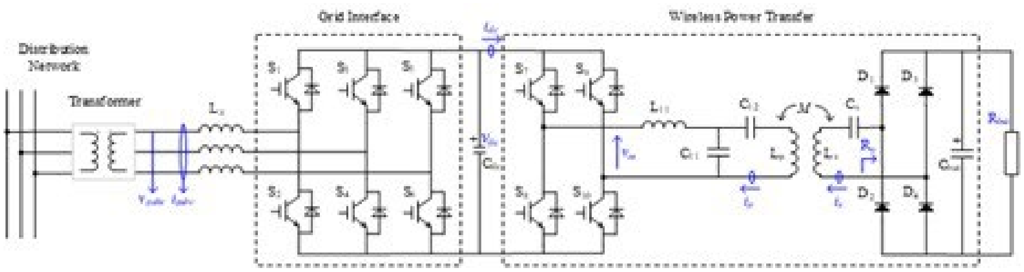

Figure II.2.1.7 Conventional three-phase grid interface as applied to interface 200 kW DWPT system.

Impact of Dynamic Wireless Charging on HD Class 8 Electric Vehicles Travel

The main objective is to leverage DWPT system that was sized and optimized for LD EVs to serve HD class 8 EV travels. Feasibility and impact of using DWPT system on primary roadways on the driving performance of HD class 8 travels, including local, regional, and long-haul in Atlanta metro area will be evaluated. EVI-InMotion tool that was developed in FY20 is considered for HD EV analysis after updating EV powertrain model with class 8 EV models. Representative high-resolution (1 sample/sec) class 8 vehicle travel data in Atlanta is developed and used as input for the analysis. Also, electric drivetrain models for class 8 sleeper- and day-cab EV are leveraged, and the associated DWPT system parameters are identified.

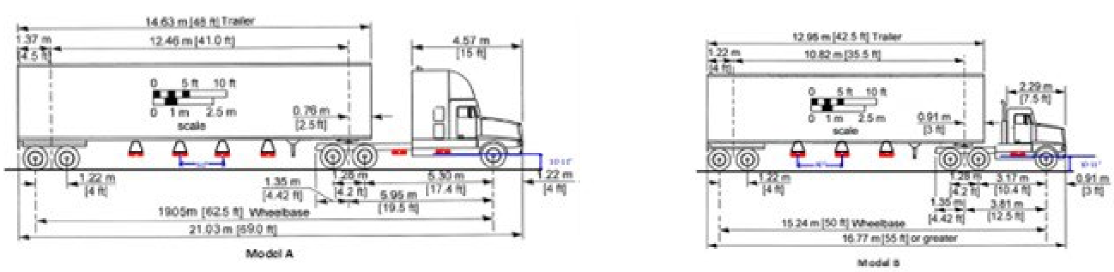

(a) (b)

Figure II.2.1.8 Class 8 HD EV model: (a) Sleeper cab and (b) Day cab.

Powertrain Class 8 EV Model: Two electric powertrain models for class 8 truck are leveraged from another NREL's project. These models are optimized for a maximum weight of 80,000 lbs. using the NREL's open access tool FASTSim [3]. A sleeper-cab EV model is optimized for 500-mile range (1.3-MWh battery) and used for long-haul vehicles, while a day-cab model is optimized for 300-mile range (721-kWh battery) and considered for regional and local vehicles. When they are used with DWPT system, smaller batteries are applied and multiple receivers are used in each vehicle based on the system design, as indicated in Figure II.2.1.8 and Table II.2.1.1. Smaller trailer/tractor of day-cab permits a maximum of four receivers to be installed in this vehicle.

Table II.2.1.1 Parameters of HD Class 8 EV with Different Designs of DWPT System.

		Low requirements for LD EVs	Medium requirements for LD EVs	High requirements for LD EVs
Approach based on LD vehicles		CS for intercity travels, min road coverage, (65 mph, 270 Wh/mile)	CS for intercity travels, min overall system cost, (74 mph, 310 Wh/mile)	CS for intercity travels, min overall system cost, (86 mph, 350 Wh/mile)
Roadway coverage (%)		8.2	14.56	16.6
Transmitter power (kW)		235	200	225
Sleeper Cab EV (baseline 1.3 MWh)	Battery size (kWh)	452.9	202.1	178.6
	# Receivers	6	5	5
	Max received power (kW)	~235 x 6 = 1,410	~200 x 5 = 1,000	~225 x 5 = 1,125
Day Cab EV (baseline 721 kWh)	Battery size (kWh)	447.6	199.8	176.6
	# Receivers	6→4	5→4	5→4
	Max received power (kW)	~235 x 6→4 = 1,410→940	~200 x 5→4 = 1,000→800	~225 x 5→4 = 1,125→900

High-resolution (1 Hz) travel data (speed, lat., and lon.,) was generated using real-world low-resolution waypoints (1 sample/h) for class 8 vehicle in Atlanta. The process to generate high-resolution data is: (1) Classification: classified into local, regional, and long-haul based on the radius of operation; (2) Subsampling: select a representative subset of the total dataset to reduce computational time; (3) Route generation: generate and validate route data using 1 sample/h waypoints; (4) Route discretization: develop 1 Hz route and speed profiles; and (5) Validation: the 1-Hz travel data subsample was validated in comparison with 1 sample/h waypoints subsample, and the original dataset.

EM Filed Shaping and Shielding Solutions

Through modeling and simulation, using advanced magnetics 3-D finite element modeling tools, new EM-field mitigation solutions and designs were designed and evaluated for performance and effectiveness. Additionally, laboratory hardware testing and evaluation is used to validate the modeling results therefore providing high levels of confidence in the effectiveness of future designs developed via modeling and simulation methods.

Data Acquisition System for DWPT System Characterization

Data acquisition requirements and methodologies are developed using the anticipated electrical parameters and performance design considerations. Due to the vehicle speed during power transfer for in-motion DWPT, i.e., 70mph vehicle speed, the data acquisition system must have very high sampling rate capabilities in order to accurately capture the electrical, magnetic, and power transfer performance of the DWPT system. The design approach in this task includes using commercially available sensors, meters, and data acquisition tools to minimize costs and accelerate development time.

Results

Sensitivity analysis of primary side LCC and secondary series tuned 200 kW dynamic wireless charging system

Figure II.2.1.9 (a) shows the input impedance of the primary side LCC and secondary side series tuned DWPT system. The magnitude of input impedance is minimal along the travel direction (x axis) and the phase angle is near zero. This indicates that the resonant system is predicted to operate as designed to facilitate 200 kW power transfer. This can be seen that the predicted output power in Figure II.2.1.9 (b) is 200 kW along the travel direction (x axis) for the horizontally aligned case (y = 0).

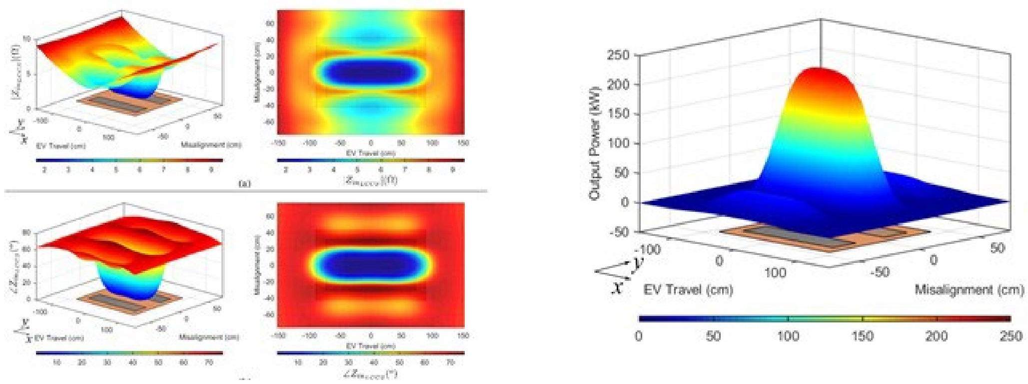

(a) (b)

Figure II.2.1.9 (a) Magnitude and phase of input impedance of 200 kW DWPT system (b) predicted output power as a function of vehicle coupler position with respect to the transmitter.

Power transfer capability validation of 200 kW DWPT system

The 200 kW DWPT system was validated in benchtop configuration up to 180 kW prior to integrating the receiver coupler to Hyundai Kona. The vehicle integrated 200 kW WPT output was connected to two HV Battery Emulator NHR 9300. The objective of the test was to validate that the vehicle body did not have a detrimental effect on safety or on the power transfer capability. Figure II.2.1.10 (a) shows the power analyzer results for the DWPT system being tested in stationary mode with the output power being 186.03 kW. The input voltage was 669.7 V, and the output voltage was 736 V. The secondary DC-DC converter was not included in the test as the objective was power transfer validation across the wireless couplers. The operating frequency was 83.9 KHz and it must be noted that the efficiency was 93.2 %. Figure II.2.1.10 (b) shows the thermal profile of the couplers after 10 minutes of power transfer, and it can be noted that the maximum observable temperature was 49.7 C.

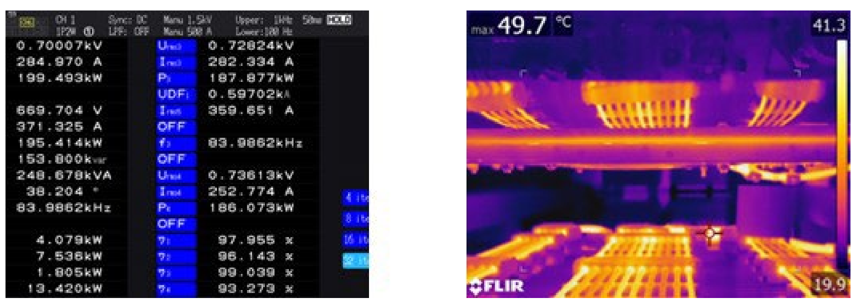

(a) (b)

Figure II.2.1.10 (a) Power analyzer results of the vehicle integrated 200 kW DWPT system test results in stationary mode with NHR9300 as the load (b) Thermal profile of the couplers after 10 minutes of operation at 186 kW.

Grid Integration and Impact Analysis

A novel control strategy to overcome the challenges of conventional control strategy which is hampered by 2nd order harmonics on the DC bus voltage when subjected to the pulsating dynamic wireless charging load profile. The proposed control strategy was verified by hardware-in-the-loop results developed in Opal-RT [2]. The HIL results demonstrate that the proposed control strategy not only enhances the load transient response capability, but also eliminates the 2nd-order oscillation on the dc-bus voltage caused by the imbalanced distribution network. It can also be noted that the 2nd harmonic is eliminated, and the power delivered to the EV battery is cleaner with the proposed control scheme.

The 24-Hour load profile developed and shown in Figure II.2.1.10 was fed to an IEE 13-bus distribution network simulation model. It was observed that the grid voltage dropped out of the safety bound of 0.95 p.u.

This indicates a significant challenge to distribution system operation in terms of voltage regulation, reserved transformer capacity, and load balance. To alleviate the impact of DWCS on the distribution network, a general dc-coupled configuration of a DWPT system with renewable energy integration as shown in Figure II.2.1.11 (a) was simulated. In Figure II.2.1.11 (b) From 0 am to 5 am, the ES absorbs power from utility grid, due to no power output from PV and wind turbine at this period. The peak power demand of DWCS and the peak power output from solar and wind energy are laid in the different time slot, that means ES unit is still required to shave the power peak of the DWCS. With the integration of solar and wind energy, the daily average power demand from utility grid decreases by 37%, and the required ES capacity decreases by 56.2%. This indicates that renewable energy integration and optimal control strategy can be used to overcome the impact on the gird and from 200 kW DWPT system.

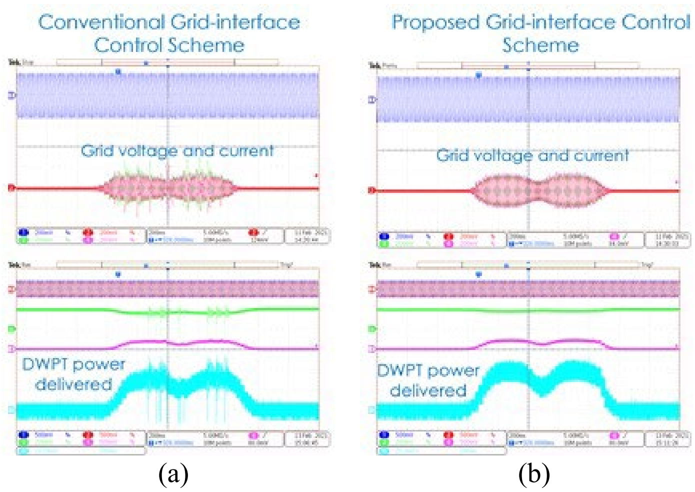

Figure II.2.1.11 Opal RT real-time simulation result showing the grid voltage and current and the DWPT power profile for the conventional and proposed control scheme.

Impact of Dynamic Wireless Charging on HD Class 8 Electric Vehicles Travel

The vehicle and system performance are measured by: (a) *vehicle efficiency (kWh/mile) per trip* and (b) *energy received from DWPT system per trip*. In addition, four modes of operation are used to identify a vehicle performance: *(1) No Charging (NC)*: vehicle never encounters charge from DWPT system; *Charge Depleting (CD)*: vehicle consumed energy > received energy from DWPT system (kWh/mile > 0); *Charge Gaining (CG)*: vehicle consumed energy < received energy from DWPT system (kWh/mile < 0); and *Charge Sustaining (CG)*: vehicle consumed energy ≈ received energy from DWPT system (kWh/mile ≈ 0).

Performance of long-haul vehicles with and without DWPT system is indicated in Figure II.2.1.12 (a) and (b), respectively. Considering DWPT system with EVs incorporate smaller batteries (453, 202.1, and 178.6 kWh) significantly reduces kWh/mile compared to the baseline EVs with 1.3 MWh. The best performance is realized with DWPT Hi that shows -0.28 kWh/mile in average, which means that EVs receive energy more than what they consume per trip. Performance of regional and local vehicles with and without DWPT system is indicated in Figure II.2.1.13 (a) and (b), respectively. The impact of DWPT system on local vehicles is less than regional and long-haul because significant part of the drive cycles for these vehicles happens on secondary and local (nonelectrified) roadways. It can be observed that, in most cases, DWPT system compensates vehicle consumption leading to CS and CG operation, especially with designs incorporate higher roadway coverage (e.g., DWPT Med and DWPT Hi). DWPT Hi shows the best performance among other designs with consistent negative kWh/mile in average.

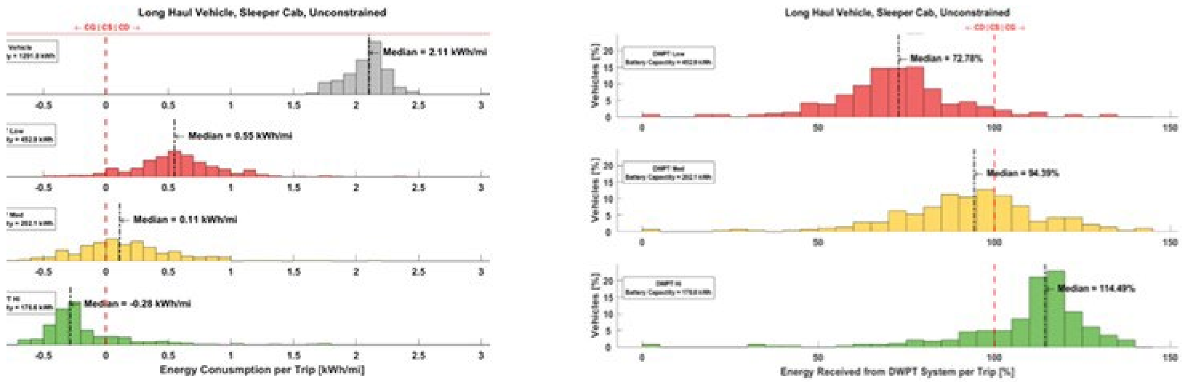

(a) (b)

Figure II.2.1.12 (a) Probability distribution of kWh/mile for long-haul vehicles in Atlanta without and with DWPT system, (b) Probability distribution of percentage energy from DWPT system for long-haul vehicles in Atlanta.

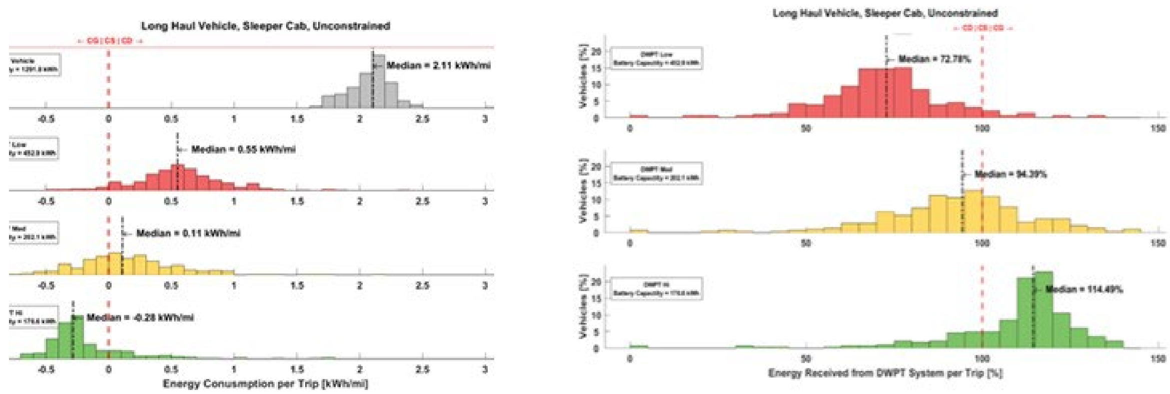

(a) (b)

Figure II.2.1.13 (a) Probability distribution of kWh/mile for regional vehicles in Atlanta without and with DWPT system, (b) Probability distribution of percentage energy from DWPT system for regional vehicles in Atlanta.

EM Filed Shaping and Shielding Solutions

In the driving direction, EV can be aligned with one ground-side coil, or positioned between two ground-side coils, as shown in Figure II.2.1.15. In the transverse direction, EV can run exactly along the charging pads' line, or with lateral misalignments, as shown in Figure II.2.1.15. To ensure EM safety under the worst case, all these typical scenarios need to be investigated. Figure II.2.1.15 (c) presents the simulated 2-D EM field distribution results when EV is positioned between 2 pads. Shielding solutions were proposed and validated by detailed FEA simulations for all the cases Figure II.2.1.14 [4]. Details about INL's shielding studies are given in [4] and [5].

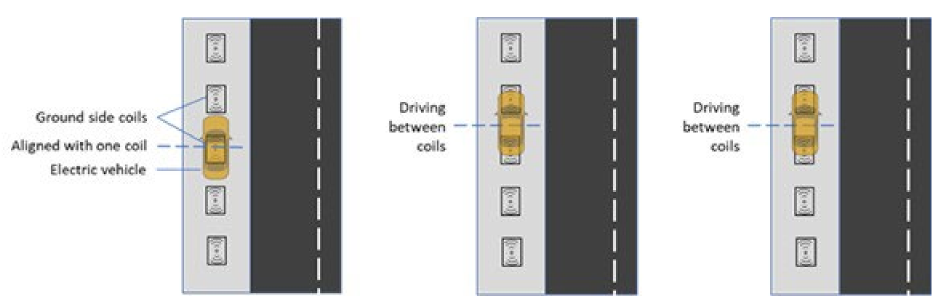

Figure II.2.1.14 DWPT scenarios for EM safety design.

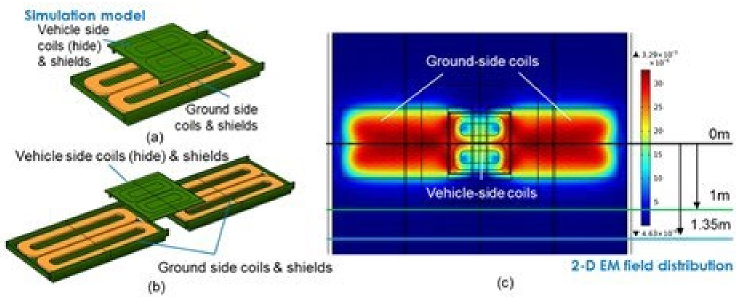

Figure II.2.1.15 Opal RT real-time simulation result showing the grid voltage and current and the DWPT power profile for the conventional and proposed control scheme.

Data Acquisition System for DWPT System Characterization

The non-power transfer measurements and data acquisition systems were evaluated using a production BEV and included the Y-alignment non-contact distance sensors, EM-field probe, wireless trigger synchronization system, LabVIEW wireless data transfer, and the data merge and analysis process. These efforts confirmed the proper functionality of the entire data acquisition system as well as highlight a few issues that need refinement prior to DWPT track testing including the repositioning of the wireless trigger synchronization receiver to ensure reception. Figure II.2.1.16 shows the DAQ evaluation in EVIL.

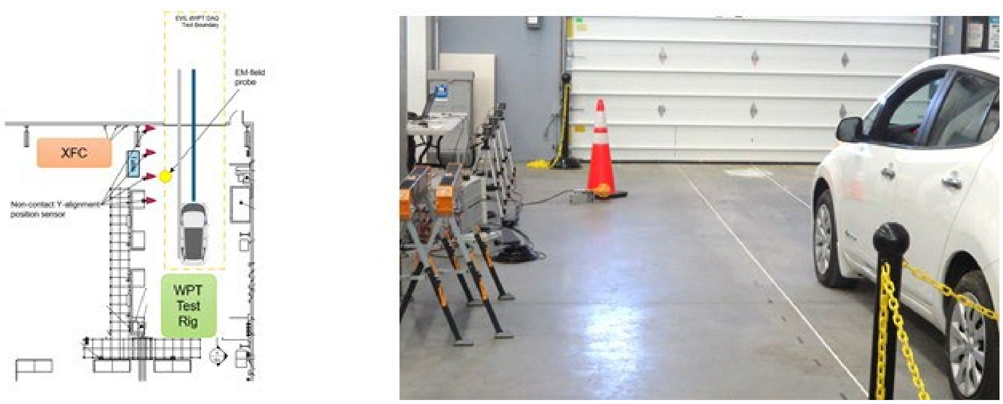

Figure II.2.1.16 Data Acquisition System validation conducted in INL's EVIL.

The DAQ evaluation involved the refinement and validation of the methods used to setup the sensors including the non-contact Y-alignment distance sensors, the power analyzer channel assignments, and the EM-field probe positioning and configuration. The setup up the non-contact distance sensors requires accurate placement of the sensor at a specified distance from the ground-side coil magnetic center. These four sensors must be parallel, level, and at the same height. To accomplish this, a 'position target' is positioned above each ground-side coil using a plumb-bob, in line with the magnetic center. Each non-contact distance sensors are then positioned with respect to each target at a specified distance.

Conclusions

- Linear circuit model of the 200 kW DWPT system was developed using fundamental harmonic approximation and the model was used to perform sensitivity analysis to variation in receiver coil position with respect to the transmitter. It was verified that resonant mode of operation and 200 kW output power will be feasible along the direction of the vehicle.

- 200 kW DWPT system was tested up to ~ 185 kW in both benchtop mode and with receiver coil integrated with Hyundai Kona. In both the cases, the recorded efficiency was over 93 %. The thermal profile of the transmitter and vehicle integrated receiver was recorded after 10 minutes of operation at

188 kW. The maximum observed temperature was 49.7 C, indicating thermal safety of the wireless power transfer system.

- Grid impact study was conducted using simulation to evaluate the impact of 200 kW DWPT system as applied to a real-world traffic model. IEEE 13-bus system and ORNL 200 kW DWPT system were used in OPAL RT based real-time simulation. It was observed that the grid voltage sagged below the stipulated 0.95 p.u. and had considerable second harmonics from the effect of DWPT. A novel control scheme was proposed and validated by simulation to eliminate the 2nd harmonic and to improve the transient capability. A renewable energy integrated DWPT system was proposed wherein the grid did not sag to 0.95 p.u. but stayed at or above 0.99 p.u. for the DWPT use case.

- Feasibility and impact of sing LD vehicle optimized 200 kW DWPT system on primary roadways on the driving performance of HD class 8 travels, including local, regional, and long-haul in Atlanta metro area were studied. The key take away are

    - Class 8 EV requires **5–6 receivers** to use the DWPT system that was optimized for LD EV (200–240 kW power and 8–20% roadway coverage) and compensate for vehicle energy depletion. DWPT system has the potential to significantly reduce the battery size with up to **65–85% reduction** in the sleeper-cab EV and **38–72% reduction** in the day-cab EV. Class 8 EVs with small-battery (200–450 kWh up to 72–85% reduction) and DWPT system can compensate for vehicle consumption leading to **negative/near-zero kWh/mile**. DWPT system is more effective for long-haul (CG: 77.8%) and regional (CG: 67%) than local (CG: 43.3%) travels.

    - **225-kW DWPT system with 16.6% roadway coverage** allows class 8 vehicles to realize consistent CS and CG operation with **5 receivers and 177-kWh battery**, leading to

        - 113% reduction in long-haul EVs energy consumption

        - 114% reduction in regional EVs energy consumption

        - 96% reduction in local EVs energy consumption

- Test plan and procedures for high-power DWPT evaluation were developed, including the design and validation of the data acquisition system.

- Active and passive shielding system were explored, and detailed simulation studies were carried out for the same. Shielding techniques developed indicated the emission were within the stipulated value when applied to the 200 kW DWPT system.

Key Publications

Oak Ridge National Laboratory

1. U. D. Kavimandan, V. P. Galigekere, B. Ozpineci, O. Onar and S. M. Mahajan, “The Impact of Inverter Dead-Time in Single-Phase Wireless Power Transfer Systems,” in IEEE Transactions on Power Electronics, vol. 37, no. 1, pp. 1074–1089, Jan. 2022, doi: 10.1109/TPEL.2021.3092400.

2. R. Zeng, V. P. Galigekere, O. C. Onar and B. Ozpineci, “Grid Integration and Impact Analysis of High-Power Dynamic Wireless Charging System in Distribution Network,” in IEEE Access, vol. 9, pp. 6746–6755, 2021, doi: 10.1109/ACCESS.2021.3049186.

3. L. Xue, V. Galigekere, E. Gurpinar, G. -j. Su and O. Onar, “Modular Design of Receiver Side Power Electronics for 200 kW High Power Dynamic Wireless Charging System,” 2021 IEEE Transportation Electrification Conference & Expo (ITEC), 2021, pp. 744–748, doi: 10.1109/ITEC51675.2021.9490095.

4. U. D. Kavimandan, V. P. Galigekere, O. Onar, M. Mohammad, B. Ozpineci and S. M. Mahajan, "The Sensitivity Analysis of Coil Misalignment for a 200-kW Dynamic Wireless Power Transfer System with an LCC-S and LCC-P Compensation," 2021 IEEE Transportation Electrification Conference & Expo (ITEC), 2021, pp. 1–8, doi: 10.1109/ITEC51675.2021.9490035.

5. R. Zeng, V. P. Galigekere, O. C. Onar and B. Ozpineci, "Improved Control Strategy of Grid Interface for EV High-Power Dynamic Wireless Charging," 2021 IEEE Applied Power Electronics Conference and Exposition (APEC), 2021, pp. 2574–2579, doi: 10.1109/APEC42165.2021.9487243.

6. R. Zeng, V. Galigekere, O. Onar and B. Ozpineci, "Optimized Renewable Energy Integration for EV High-Power Dynamic Wireless Charging Systems," 2021 IEEE Power & Energy Society Innovative Smart Grid Technologies Conference (ISGT), 2021, pp. 1–5, doi: 10.1109/ISGT49243.2021.9372265.

7. T. Saha, S. Mukherjee, V. P. Galigekere and O. C. Onar, "Design of Auxiliary Circuit Elements for Achieving Zero Voltage Switching in a Wireless Power Transfer System," 2020 IEEE Energy Conversion Congress and Exposition (ECCE), 2020, pp. 5537–5544, doi: 10.1109/ECCE44975.2020.9236138.

8. S. Mukherjee et al., "Control of Output Power in Primary Side LCC and Secondary Series Tuned Wireless Power Transfer System without Secondary Side Sensors," 2020 IEEE Energy Conversion Congress and Exposition (ECCE), 2020, pp. 5532–5536, doi: 10.1109/ECCE44975.2020.9236098.

9. U. D. Kavimandan, V. P. Galigekere, B. Ozpineci, J. Pries, O. Onar and S. M. Mahajan, "A Sensorless Coil Detection Scheme based on Dead-Time Effect in Dynamic Wireless Power Transfer Systems," 2020 IEEE Energy Conversion Congress and Exposition (ECCE), 2020, pp. 828–833, doi: 10.1109/ECCE44975.2020.9235368.

Idaho National Laboratory

1. B. Zhang et al., "Quasi-Dynamic Electromagnetic Field Safety Analysis and Mitigation for High-Power Dynamic Wireless Charging of Electric Vehicles," 2021 IEEE Transportation Electrification Conference & Expo (ITEC), 2021, pp. 1–7, doi: 10.1109/ITEC51675.2021.9490192.

National Renewable Energy Laboratory

1. Ahmed A. S. Mohamed, A. Meintz, and K. Walkowicz, "Planning of In-motion Electric Vehicle Charging on Freeways – IEEE Smart Grid." [Online]. Available: https://smartgrid.ieee.org/newsletters/february-2020/planning-of-in-motion-electric-vehicle-charging-on-freeways. [Accessed: 19-Mar-2020].

References

1. U. D. Kavimandan, V. P. Galigekere, O. Onar, M. Mohammad, B. Ozpineci and S. M. Mahajan, "The Sensitivity Analysis of Coil Misalignment for a 200-kW Dynamic Wireless Power Transfer System with an LCC-S and LCC-P Compensation," 2021 IEEE Transportation Electrification Conference & Expo (ITEC), 2021, pp. 1–8, doi: 10.1109/ITEC51675.2021.9490035.

2. R. Zeng, V. P. Galigekere, O. C. Onar and B. Ozpineci, "Grid Integration and Impact Analysis of High-Power Dynamic Wireless Charging System in Distribution Network," in IEEE Access, vol. 9, pp. 6746–6755, 2021, doi: 10.1109/ACCESS.2021.3049186.

3. A. Brooker, J. Gonder, L. Wang, E. Wood, S. Lopp, and L. Ramroth, "FASTSim: A Model to Estimate Vehicle Efficiency, Cost and Performance," presented at the SAE 2015 World Congress & Exhibition, Apr. 2015, doi: 10.4271/2015-01-0973.

4. Bo Zhang, Richard B. Carlson, Veda P. Galigekere, Omer C. Onar, Mostak Mohammad, Charles C. Dickerson, and Lee K. Walker, “Quasi-dynamic Electromagnetic Field Safety Analysis and Mitigation for High-Power Dynamic Wireless Charging of Electric Vehicle”, 2021 IEEE Transportation Electrification Conference and Exposition (ITEC), 21–25 June 2021.

5. Bo Zhang, Richard B. Carlson, Shawn D. Salisbury, Charles C. Dickerson, Timothy D. Pennington, Lee K. Walker and Eric J. Dufek, “Concept Design of Active Shielding for Dynamic Wireless Charging of Light-duty EV”, in 2020 IEEE Transportation Electrification Conference and Exposition (ITEC), pp. 844–850, 2020.

Acknowledgements

Project team would like to thank Lee Slezak from the U. S. Department of Energy for his continued guidance and support on this project.

II.2.2 Smart Electric Vehicle Charging for a Reliable and Resilient Grid (RECHARGE)

Jesse Bennett, Principal Investigator
National Renewable Energy Laboratory
5013 Denver West Parkway
Golden, CO 80401
Email: Jesse.Bennett@nrel.gov

Matthew Lave, Principal Investigator
Sandia National Laboratories
7011 East Avenue
Livermore, CA 94550
Email: mlave@sandia.gov

Don Scoffield, Principal Investigator
Idaho National Laboratory
775 MK Simpson Boulevard
Idaho Falls, ID 83415
Email: Don.Scoffield@inl.gov

Lee Slezak, DOE Technology Manager
U.S. Department of Energy
Email: lee.slezak@ee.doe.gov

Start Date: October 1, 2018 End Date: December 31, 2021
Project Funding: $2,000,000 DOE share: $2,000,000 Non-DOE share: $0

Project Introduction

Adoption of plug-in electric vehicles (EVs) has expanded over the last few years and the light duty market share of these vehicles will increase as the diversity of vehicle models continues to grow. On a national scale, the transportation sector was one of the largest consumers of energy in 2019, second only to electricity. The growing trend of electric transportation will shift this energy consumption to rely on the national electric grid more heavily. This project plans to assess the new load that will arise from EVs and electric vehicle supply equipment (EVSE) to determine possible challenges, as well as opportunities that may arise during this transition.

The National Renewable Energy Laboratory (NREL) is leading this three-year project, which also includes Sandia National Laboratories (SNL) and Idaho National Laboratory (INL). During the first year of this project The Recharge team analyzed EV adoption rates and real-world travel data for vehicles in the Minneapolis and Atlanta metro regions to assess possible charging needs using EVI-Pro. Using this technique, multiple charging scenarios were developed for varying adoption levels as well as charging preferences for home or workplace charging. The second year of this project, after developing and verifying grid models for each region, the team expanded on these efforts by assessing the grid impacts of EV charging under multiple scenarios in a co-simulation environment that included EVI-pro travel patterns, Caldera charging controls, and OpenDSS grid analysis [2]. These uncontrolled charging results were then compared to the grid performance using smart charge management (SCM) controls developed within the Caldera framework. Comparing the level of impact before and after the implementation of these control strategies helps to determine the value they offer: EV owners, building managers, charge network operators, grid services aggregators, and utilities.

The final year of this project involved the development of more sophisticated control strategies and a broader scope of grid impact analysis. This analysis was expanded to include the low-voltage secondary system in the Minneapolis region and the bulk electric supply within the Atlanta region. The new analysis in the Atlanta region also included resiliency impacts by considering the possible load growth as a result of hurricane evacuees traveling to or through the region. Supporting this new scope of grid analysis required additional details to expand the grid models in each of the regions of study, as well as an understanding of coastal evacuation patterns during hurricanes. Additionally, new control strategies were developed outside of Caldera, that accounted for DER predictions and inter-EVSE communications. Incorporating these new controls required a new simulation environment developed on the HELICS platform and the development of new DER adoption scenarios.

Objectives

Modeling SCM Strategies

The co-simulation environment established in project years one and two consists of EVI-Pro travel data, Caldera EV charging models, and OpenDSS grid analysis. There are five control strategies built within Caldera and this effort establishes a new co-simulation environment using HELICS, a platform which allows various transportation and power system related software modules to work together. Use of the HELICS platform enables the development of control strategies outside of Caldera to support new SCM control objectives.

Distribution Analysis

Uncontrolled charging of EVs may negatively impact the grid because of non-optimal distribution system operations. This effort leverages the new HELICS platform to assess the effectiveness of multiple control strategies to mitigate the impacts on distribution feeders due to EV charging in Minneapolis and Atlanta. The distribution analysis focuses on impacts to feeder primary conductor line loading and voltage concerns.

Secondary Analysis

The grid impacts of EV charging will not be isolated to feeder primary conductors. The secondary analysis investigates the impacts of uncontrolled and controlled EV charging on secondary networks, focusing on distribution transformer loading and voltage impacts at the customer service drop. This analysis provides a comparison of impacts between primary distribution feeders and secondary systems, as well as analysis on service transformer loading.

Bulk System Analysis

In addition to the distribution system, EV charging will have the potential to impact bulk electric systems as well. This effort assessed the impact of controlled and uncontrolled EV charging on the regional load of Atlanta through analysis of the peak demand time and magnitude, as well as three-hour ramp rates. These impacts were also considered with and without the addition of increased photovoltaic (PV) generation.

Resilience Analysis

The resilience analysis explored the EV charging impact to the electric power system during an emergency evacuation event. This emergency event involved coastal evacuees during a hurricane arriving at Atlanta feeders seeking various charging services over the course of a day. This effort included analysis of an increased regional demand for EV charging and SCM effectiveness under adverse conditions.

Approach

Modeling SCM Strategies

Caldera enables the modelling of EV charging and EV charging control strategies using a library of high-fidelity charging models derived from testing data that INL has collected over the past decade. Caldera contains 4 built in energy shifting strategies—TOU Immediate, Random Start, TOU Random and Centralized Aggregator—and 1 voltage support strategy—Volt/VAR. The INL team has developed a framework using

HELICS where the EV charging models in Caldera, the distribution feeder models in OpenDSS, and newly developed custom control strategies are each co-simulated in a HELICS federate as described in Figure II.2.2.1. The HELICS co-simulation framework facilitates communication and synchronization between the federates. In this effort, two custom external control strategies- ‘Consensus-based Volt/Watt’ and ‘Behind-the-Meter (BTM)” were developed which require the use of this HELICS co-simulation framework.

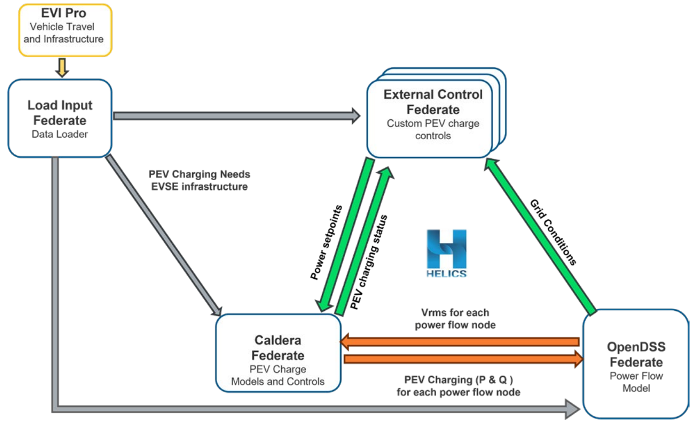

Figure II.2.2.1 HELICS Co-simulation Framework

Distribution Impact Analysis

Time-of-Use: EVs present a unique challenge to distribution system operations because of the potential magnitude and timing of load increases. Time-of-Use (TOU) electricity pricing is an established method to reduce peak system loads. To understand and quantify the potential impact of EV’s charging response to TOU pricing, this effort analyzed the grid impacts of EV charging with TOU controls. This analysis included Caldera’s TOU Immediate and TOU Random control strategies. The TOU Immediate begins charging at the start of each off-peak period, while the TOU random distributes the start of each charge session randomly throughout the off-peak periods. Both controls charge EVs during off-peak hours when it coincides with EV dwell. However, in the event a vehicle must charge during an on-peak period to finish a charge session, the vehicle’s energy needs receive a higher priority than TOU rates.

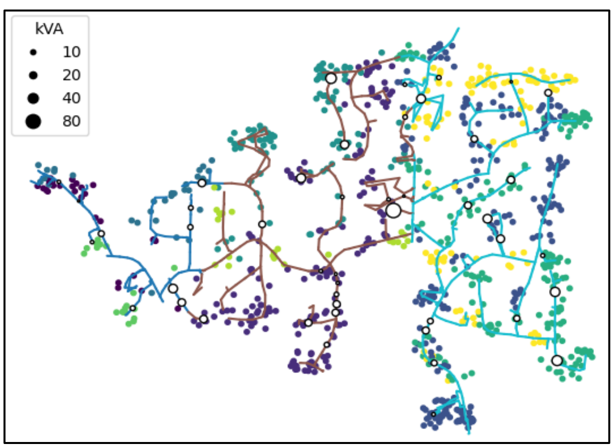

Figure II.2.2.2 Locations of PV systems, and EVSE groups on Feeder 1

Zone Volt/Watt Control: Beyond TOU rates, other developed controls, such as Volt/Watt are intended to provide voltage support. Implementation of the Volt/Watt control began by assigning each EVSE to one of nine groups based on the connected phase and its straight-line distance from the sub-station. Each EVSE group solves a distributed optimization problem to minimize the peak demand from the EVSE and mitigate voltage concerns with all EVSE in each group responding to voltage concerns in their territory. An example of the EVSE groups is shown in Figure II.2.2.2, where the different colors depict the groups.

BTM Control: To evaluate the combined impact of EV charging with distributed PV generation and behind-the-meter energy storage systems (ESS) this effort required the development of DER integration scenarios, including both PV and ESS. PV generation capacity was determined by the feeder peak with the total nameplate capacity of PV for each feeder set at 15% of the feeder’s maximum load—not to exceed the feeder minimum load—and distributed such that two-thirds of that capacity was at residential homes. Half of the locations where PV systems were distributed are co-located with ESS and the capacity of those systems was randomly distributed between 1.5 kW and the distribution service transform capacity rating. PV systems were simulated in OpenDSS and provided irradiance from a clear summer day. An example feeder with this DER deployment is presented in Figure II.1.2.2 where the size of a circle indicates DER capacity, filled-in circles are PV systems, and empty circles represent ESS.

Secondary Impact Analysis

In this effort, EVs were mapped down to the secondary network and assigned to residential locations. Time-series secondary load profiles were developed to conduct power flow simulations and assess the customer-level impacts due to the uncontrolled and controlled EV charging. A comparative study of the primary and secondary network analysis was conducted to evaluate the actual impacts that could occur at the secondary level before any issue was observed at the primary network. Further, detail analysis of the transformer loadings, time-series local level voltages and line loadings were studied.

Bulk Electric Impact Analysis

The impact of roughly 400,000 electric vehicles charging throughout the Atlanta metropolitan area was evaluated with and without the use of SCM. The assessment considered EV charging impacts on both the magnitude and time of the maximum and minimum load as well as the change in 3-hour ramps. The total load in the Atlanta area was estimated using the hourly net generation profile for the full Southern Company system and scaled proportionally to the fraction of Southern Company customers in the Atlanta region. This base load was combined with the Atlanta EV charging demand and PV generation from the DER scenarios to determine the net load profile for the region and assess controlled and uncontrolled EV charging impacts.

Resilience Analysis

To assess the effectiveness of SCM under an adverse event, a hurricane evacuation site assessment was performed for Atlanta. The assessment involved the collection and analysis of data such as local risk index, area populations, travel patterns, power system characteristics, available EVSE infrastructure, and historic evacuation information. This resulted in a hurricane evacuation scenario that consisted of inserting an additional 2,000 charge events on each test feeder over approximately 24 hours with initial states of charge ranging between 3% and 30%, which correspond to coastal evacuees traveling long distances. Most of the additional charge events were assigned to public charging nodes based on the expected behavior of evacuees.

The co-simulation routine was modified to: (a) accept new inputs defining the additional EV charge events (including state of charge and destination type); (b) allow for longer simulation times; and (c) generate new outputs for more detailed post-simulation analysis. In addition to evacuees, the feeders also had “normal” daily charging simulated under both home-dominant and work-dominant charging scenarios. These “normal” charging demands were simulated on the feeder peak day and assessed under various SCM strategies with no controls applied to public evacuee charging, as it was considered “essential” and could not be delayed.

Results

Modeling SCM Strategies

Each of the external SCM strategies—the Consensus-based Volt/Watt and BTM controls—are simulated using the new HELICS co-simulation platform to dispatch energy storage and/or shift EV charging within a vehicle’s dwell period to achieve their respective control objectives. These controls were developed by NREL and evaluated on the Minneapolis feeders in collaboration with Xcel Energy and on Atlanta feeders in collaboration with Southern Company. Each of these new SCM strategies are described below. For both strategies, vehicle energy demands are the top priority and in the event there will be insufficient dwell to deliver the vehicle energy needs or the battery has achieved a full state of charge, uncontrolled charging is resumed

Consensus-based Volt/Watt Control: The Volt/Watt control splits the smart charging problem across various computation nodes and then communicates with all the EVs under the same group, as outlined above, to arrive at the consensus via communication between residential EVs as established in this control. In the first layer of communication, EV energy needs and dwell periods within the same zone are shared to find the optimal charging profile to reduce the total peak demand. In the second layer of communication, the nodal voltage status is received from the distribution nodes and the charging peak is further reduced if an undervoltage (<0.975 p.u.) is reported anywhere within the group. The charging peak is further reduced through iterations within first layer of consensus until the node voltage is within acceptable limits. In the event of surplus PV generation and overvoltage scenario (>1.025 p.u.), this control allocates more power to each EV to create an additional charging demand and lowers the nodal voltage and brings it back within the limits.

BTM Control: The BTM strategy controls EV charging power and ESS charging/discharging power either to minimize peak facility load or to maximize utilization of local generation depending on facility types. For all commercial customers, the BTM strategy minimizes the facility net load to reduce demand charges and maximize utilization of local PV generation for residential customers to increase the value of generated electricity. For each control objective, the controller solves for an optimized EV and ESS profile for a 6-hour time horizon as informed by forecasts of facility load, PV generation, and EV energy needs.

Distribution Analysis

Behind-the-Meter Distributed Energy Resource: In the results for Minneapolis Feeder 8 (Figure II.2.2.3) for the home dominant scenario, as established in prior year's work [1], uncontrolled charging leads to increasing EVSE demand in the afternoon when PV generation is decreasing. However, the increased mid-day charging in the work dominant scenarios, shifts the uncontrolled loads to earlier in the day. Additionally, the BTM control is even more effective at increasing the use of PV in the work dominant scenario. Other controls, such as TOU random and Volt/Watt, shift loads to the morning hours when the feeder load is at a minimum and TOU rates are low.

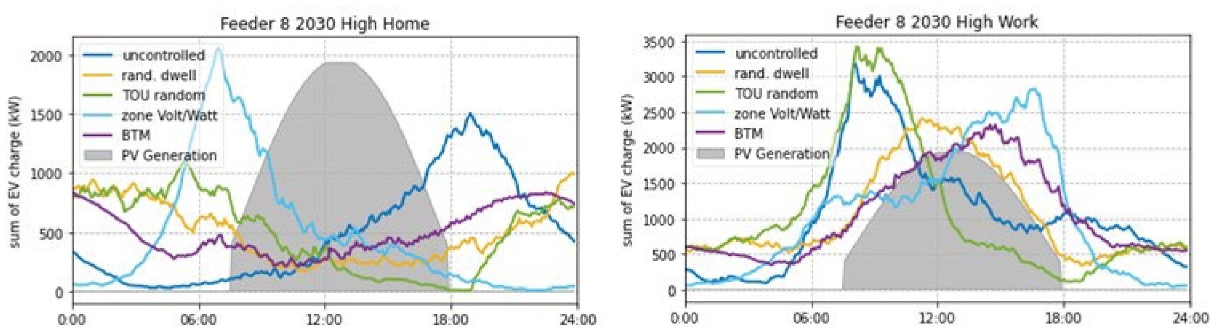

Figure II.2.2.3 Feeder 8 EV Charging Profiles with SCM and Uncontrolled Results

Secondary Impact Analysis

A comparative study of the primary and secondary network analysis revealed there could be more significant impacts on the secondary network. Figure II.2.2.4 depicts the maximum line loadings and minimum and maximum voltage range results of a feeder from Minneapolis for both primary network and secondary network analysis. The maximum line loading comparison shows that the secondary lines could be overburdened before primary lines due to the PEV charging on the network. Similarly, the voltages on the secondary network could drop below 0.95 per unit (ANSI limit) with the addition of PEV charging.

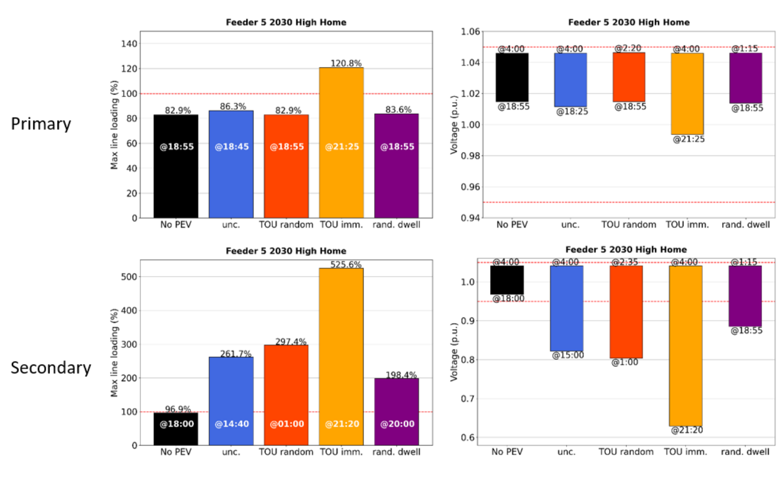

Figure II.2.2.4 A Comparison of Line Loading and Voltage Results for the Primary and Secondary System Analysis

Bulk Electric Impact Analysis

In the Atlanta region uncontrolled EV charging resulted in roughly a 4% increase in peak net load, compared to the peak net load with no EVs, and causes the peak to shift 0.5-1 hour later in the day. Three of the four control strategies (random, TOU random, and centralized) reduced the impact of EV charging on the peak load to a 1-2% increase. The TOU immediate strategy, however, results in a roughly 10% increase in peak load and causes the time of the peak load to shift several hours later to 7 PM, which is the beginning of the off-peak price period.

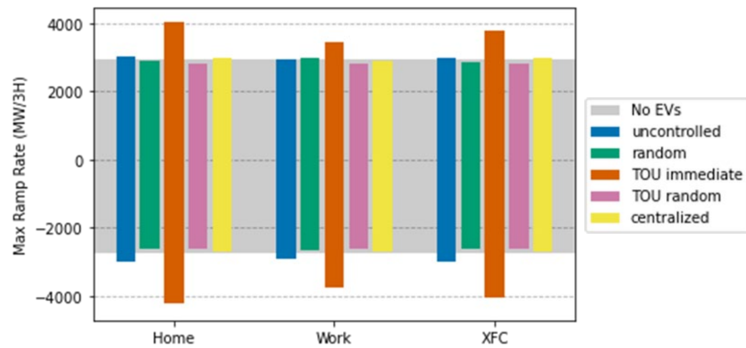

Figure II.2.2.5 Electric Vehicle Charging Impact on 3-hour Ramps

In addition to increased peak load from electric vehicles, the impact of EV charging on the maximum ramp rates was also evaluated. Figure II.2.2.5 shows the impact of EV charging on the maximum 3-hour ramps for each control strategy and integration scenario, where the shaded gray region shows the ramp for 2019 without EV charging. The upper and lower extents of each bar show the maximum up- and down-ramp respectively with EV charging under each control strategy. Uncontrolled EV charging results in a very slight increase to both the up and down ramps. The TOU immediate control strategy results in the most significant ramp, 4000 MW over 3 hours (roughly 28% of the maximum net load). The impact of the other three control strategies ranges from a small increase (centralized) to a small decrease (TOU random).

Resilience Analysis

For reference to “blue-sky” conditions, a typical day of “normal” charging was simulated between hours 0 and 24. The 2,000 additional charge events due to evacuees began when evacuees arrived starting at hour 31 and continued through hour 48. These additional evacuees were modeled as dwelling for up to 24 hours from arrival and led to an increase in simultaneous charging events as by much as 600 EVs, occurring around hour 48. The evacuee charging created a demand increase of about 4 MW between simulation hours 40 and 50. Uncontrolled peak PEV charging occurred during evening peak demand hours which further stressed the system. Most of the distribution feeders studied were able to accommodate the additional charging introduced by the simulated event. Figure II.2.2.6 presents uncontrolled system results during the simulated resilience event representing both a low voltage situation and a line overloading situation.

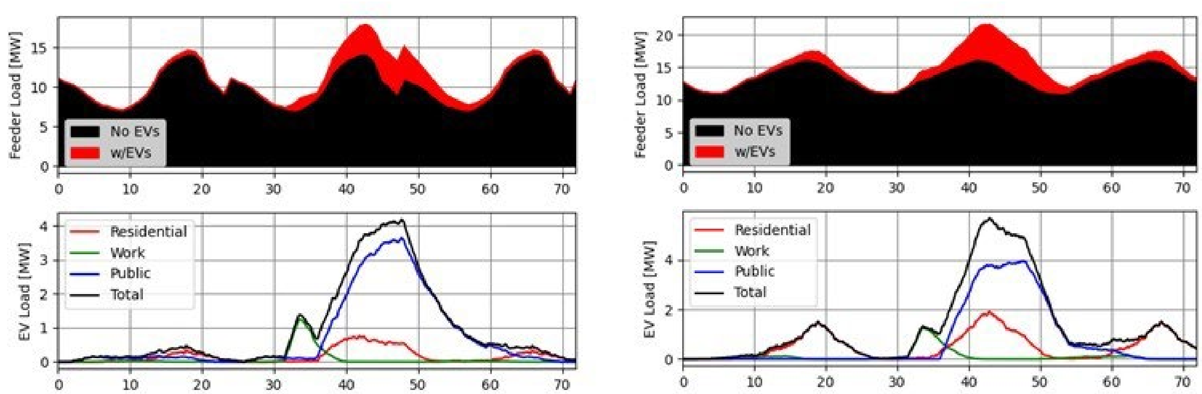

Figure II.2.2.6 Uncontrolled Results from a Feeder with Voltage Issues, Feeder 3 (a), and a Feeder with Line Overloading, Feeder 8 (b), During the Simulated Resilience Event.

These uncontrolled results present a worst-case scenario, without any grid impact mitigation from “normal” charging loads. The results in Figure II.2.2.7 show the analysis of EV charging loads where SCM strategies are applied. The two strategies dispersed (random dwell) or concentrated (TOU random) pre-existing residential and work charging events to allow slightly more capacity during peak demand hours. The alteration of pre-existing charge events also slightly affected the voltage profile of the system. In the case shown, both strategies reduced line overloading from approximately 120% to 110%, presenting how SCM strategies can still maintain effectiveness during emergency scenarios. These results show how, although evacuation load increases may cause greater impacts, SCM strategies applied to local EVs operating under “normal” charging loads, can still provide grid support and overcome the additional load impacts.

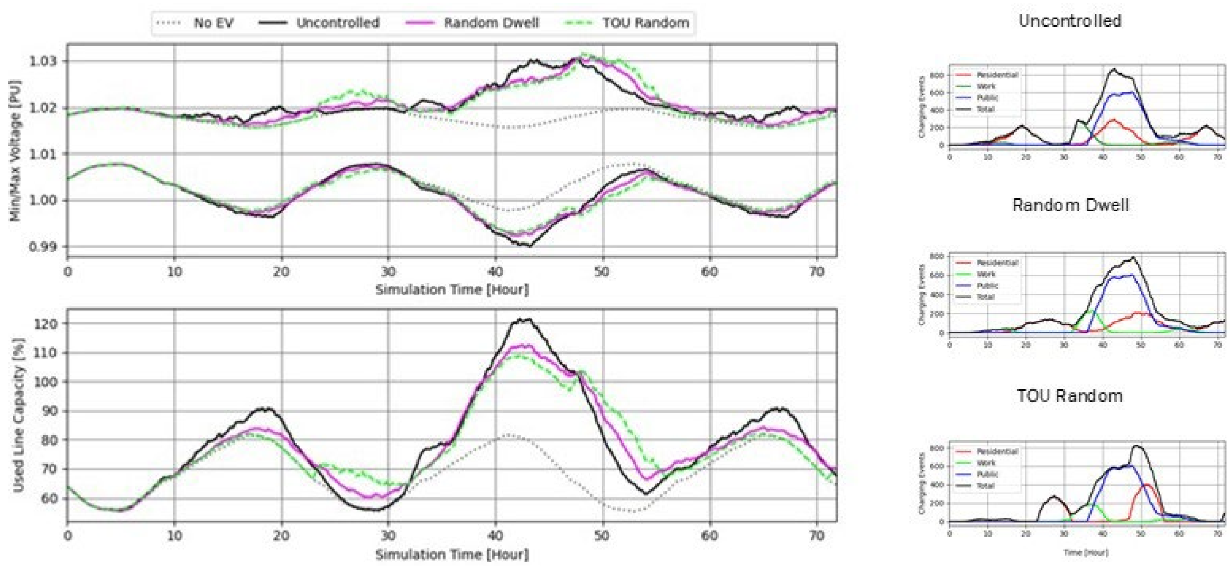

Figure II.2.2.7 Feeder 8 Energy Shifting Strategy Results (left) and Associated Simultaneous EV Charging Events for Uncontrolled, Random Dwell, and TOU Random Cases (right, from top to bottom).

Conclusions

The final year of this project has expanded both SCM control capabilities and grid impact analysis. Many different SCM strategies have been defined with a variety of control objectives. In addition, grid impacts including detailed secondary networks, bulk electric systems, and emergency evacuation scenarios have been considered. The results presented above display both the challenges and opportunities for EV adoption. These challenges and opportunities present themselves in different ways. Simple EV charging preferences such as work, or home dominant scenarios can increase peak loads when home charging coincides with a feeder peak or increase the use of renewable energy when workplace charging coincides with PV generation. Different applications of controls can create new timer-peaks (TOU Immediate), or more efficiently distribute loads (TOU Random, Random Start). In addition, some of the most complex controls such as BTM can provide different benefits for residential or workplace charging concerns, while still maximizing the use of PV generation. These new capabilities and scenarios reveal the opportunities for SCM, and the true value EV charge flexibility can offer the grid. While this just presents a few possible scenarios for SCM, it is clear there are significantly more opportunities that could be explored at higher adoptions and with larger vehicles.

Key Publications

1. T. Haines, B. M. Garcia, W. Vining, M. Lave, “A Co-Simulation Approach to Modeling Electric Vehicle Impacts on Distribution Feeders during Resilience Events,” 2021 Resilience Week (RWS), 2021

References

1. Bennett, J. et al. 2021. "Charging Infrastructure Technologies: Smart Electric Vehicle Charging for a Reliable and Resilient Grid (RECHARGE)." Presented at the *U.S. Department of Energy Vehicle Technologies Office Annual Merit Review*, June 23, 2021.

2. Open Distribution System Simulator™. Available: http://sourceforge.net/projects/electricdss/. Accessed October 11, 2019.

Acknowledgements

The RECHARGE Principal Investigators acknowledge the contributions of team members: Kalpesh Chaudhari, Brooke Garcia, Shibani Ghosh, Thad Haines, Birk Jones, Andrew Meintz, Myungsoo Jun, Chris Neuman, Priti Paudyal, Manoj Sundarrajan, Santosh Veda, and William Vining. The project team also acknowledges the support and guidance of Lee Slezak (DOE HQ) and Manish Mohanpurkar (INL).

II.2.3 High-Power Inductive Charging System Development and Integration for Mobility

Omer C. Onar, Principal Investigator
Oak Ridge National Laboratory, Power Electronics and Electric Machinery (PEEM) Group
National Transportation Research Center, 2360 Cherahala Boulevard
Knoxville, TN 37932
Email: onaroc@ornl.gov

Burak Ozpineci, Section Head and ORNL Program Manager
Oak Ridge National Laboratory, Vehicle and Mobility Systems Research Section
National Transportation Research Center, 2360 Cherahala Boulevard
Knoxville, TN 37932
Email: burak@ornl.gov

Lee Slezak, DOE Technology Manager
U.S. Department of Energy
Email: lee.slezak@ee.doe.gov

Start Date: October 2018 End Date: December 2022
Project Funding: $4,707,901 DOE share: $2,207,901 Non-DOE share: $2,500,000

Project Introduction

Extreme fast charging (XFC) is considered one of the most important research topics in the field of electromobility with the potential to significantly reduce charging times. With extreme fast charging, i.e., charge rates higher than or equal to 3C, it is possible to reduce EV charging times to 10 minutes for 50% increase in the battery state-of-charge (SOC). However, there are several challenges for establishing XFC systems, such as logistics and infrastructure requirements, design and deployment of the grid interface converters, grid power quality (power factor and harmonic distortions), availability of the power (integration with renewable energy or energy storage systems if needed), isolation requirements, distribution voltage level at the point of grid connection, hardware connectivity, power electronic semiconductor and architecture limitations, thermal management systems, and the vehicle side power delivery architectures.

High-power wireless power transfer (WPT) is an attractive option for fast charging because the user is not required to handle any heavy and bulky high-power equipment. WPT is also a key enabling technology for autonomous vehicles. However, power transfer capability of WPT systems is closely linked to the size and mass of the transmitter and receiver pads. The feasibility of high-power WPT systems greatly depend on the ability to improve the power density and specific power of wireless charging systems.

The difficulties of high-power wireless charging are exacerbated by the need to meet the same practical constraints associated with vehicle integration as lower power systems. Therefore, more advanced techniques are necessary to improve power density and specific power of wireless charging systems for high-power applications. This paper proposes three-phase inductive WPT systems with bipolar phase windings with significantly increased surface and volumetric power density of the couplers.

The primary objective of this project is to address the challenges of XFC charging systems for electric vehicles that increases their utilization factors, improves the total electric miles traveled, and improves their return on investment that results in industry and consumer acceptance. The project will also reduce the technology costs through a modular and reconfigurable power electronics architecture and by leveraging the current DOE research activities in power electronics, wide bandgap device-based power electronic converters, vehicle systems, wireless charging systems, and modernization of grid infrastructures in order to meet the project goals. This project will also generate DOE-owned intellectual property on high-frequency / high-power inverters, high-frequency ac links, novel integrated and polyphase magnetic structures, and thermal management systems to be used in extreme fast charging of EVs. Technology developed in this project will be transferable to other vehicle classes such as medium-duty and heavy-duty vehicles.

Objectives

This project is the first research effort that will showcase an inductive XFC charging system with all the outlined functionalities such as using a polyphase electromagnetic coupling coils and a modular, scalable, reconfigurable grid-interface power electronic converter architecture. The overall goals of the project to address the challenges of XFC charging systems are:

1. Provide a high-technology, fully automated, high-power, modular, scalable, interoperable, high-efficiency plug-less extreme fast charging system.
2. Design an inductive coupling system that supports a variety of vehicle ground clearances that is designed for 100-kW and 300-kW nominal power levels.
3. Have minimal grid level disruptions with <5% harmonic distortions on the grid current and >95% grid power factor.
4. Design and develop a polyphase electromagnetic coupling coils with optimal geometry for the highest utilization of the coupler surface area,
5. Achieve end-to-end high charging efficiencies greater than 90%,
6. Integrate vehicle to infrastructure charging communications, and
7. Understand and address vehicle integration issues of XFC technology, including energy storage impacts and thermal management considerations.

Approach

Starting from the ac grid to the vehicle battery terminals, the system power converters must be well-designed and operated in order to achieve high efficiency. In addition, power flow control to the secondary system should be resolved where the control parameters (dc link voltage, frequency, duty cycle, phase-shift, etc.) are actively controlled to improve efficiency while meeting the vehicle-side target voltage, current, and/or power. In this project, team used iterative design and utilized finite element analysis (FEA) based modeling for the design optimization of the electromagnetic coupling coils. Vehicle battery and grid voltage and power levels are used for the proper system design and cascaded down to the appropriate subsystems and components. Furthermore, research team modeled and simulated the grid interface (front-end) power blocks based on the dc link voltage requirements of the proposed system and the grid infrastructure parameters. Also, the system power conversion stages are designed in an integrated approach for an optimal system design in terms of complexity and compactness. Regarding the system tests, all the power conversion stages are being tested and validated individually before the full system integration (for functionality and performance) which is followed by the entire system tests using grid and battery emulators before vehicle integrations. Although it was not required, team also designed and developed a prototype for proof of concept before designing and developing the high power scaled couplers and converters. The system level circuit diagram of the proposed system is given in Figure II.2.3.1. Also shown in Figure II.2.3.1 is the double-sided LCC resonant tuning configuration implemented both for primary and secondary side with each phase having a dedicated compensation circuitry. In this extreme fast inductive charging system, primary-side power electronics, resonant tuning components, and the primary coupler are interoperable both with the 100-kW receiver and 300-kW receiver systems.

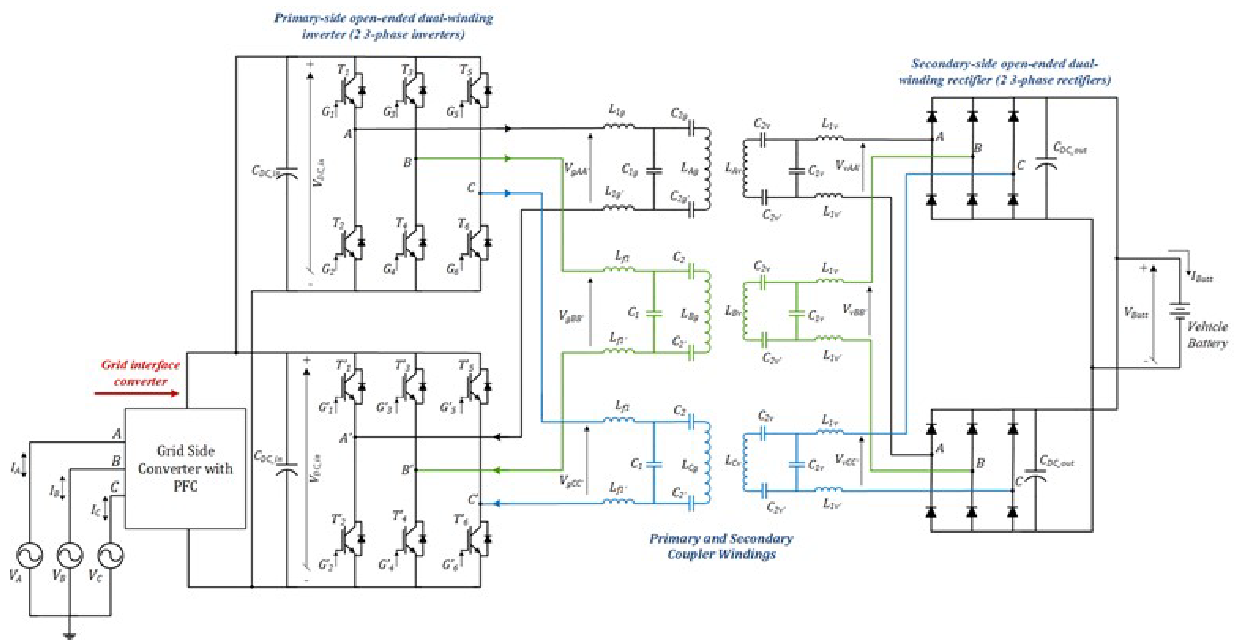

Figure II.2.3.1 System level diagram of the proposed XFC inductive charging system.

In order to achieve high-power at the high-frequency inverter level, the drive system uses open-ended winding dual-inverter design using two inverters sharing the same dc bus. This can also be interpreted as using 3 H-bridge inverters with each inverter feeding one phase of the primary coupler. Using a single three-phase inverter was not possible with ~300-kW output power due to current rating and thermal constraints of the semiconductor power devices. Although a second inverter increases number of components and the complexity, the total power rating and the power density of the drive system is significantly increased as this inverter assembly can provide up to 500-kW at the input. This approach doubles the effective output voltage while maintaining dc-link capacitor size reduction compared to a single 3-phase inverter.

Our earlier design studies determined to use the CREE SiC MOSFET power module CAS325M12HM2 (1200 V / 356 A, with an on-resistance of $R_{dson} = 3.7\ m\Omega$ and stray inductance of $L_{stray} = 5\ nH$) in the open-ended winding primary-side high-frequency inverter design as shown in Figure 2 including the engineering CAD drawing of the inverter system and its actual physical hardware development. Also shown in Figure 2 are differential line drivers and receivers and the digital signal processor (DSP) that controls the inverter. Differential line drivers and receivers are needed to convert the single-ended pulse width modulation (PWM) gate driver signals from DSP to differential ended signals that has the individual return lines on the gate driver.

Thermal performance is analyzed to evaluate the devices in a 3-phase inverter arrangement. Accordingly, each three-phase inverter shown in the primary-side in Figure II.2.3.2 is expected to operate up to 250-kW continuously which results in a total of 500-kW power capability of the primary-side power electronics. The other way to analyze and operate this inverter is that this structure is composed of 3 H-bridge inverters such that each H-bridge inverter powers one phase of the transmitter windings. The approximate dimensions of this development are 300 × 420 × 70 mm (W×L×H) which corresponds to 8.82 ℓ volume. This volume and 0.5-MW power rating provides a power density of 56.7 kW/ℓ.

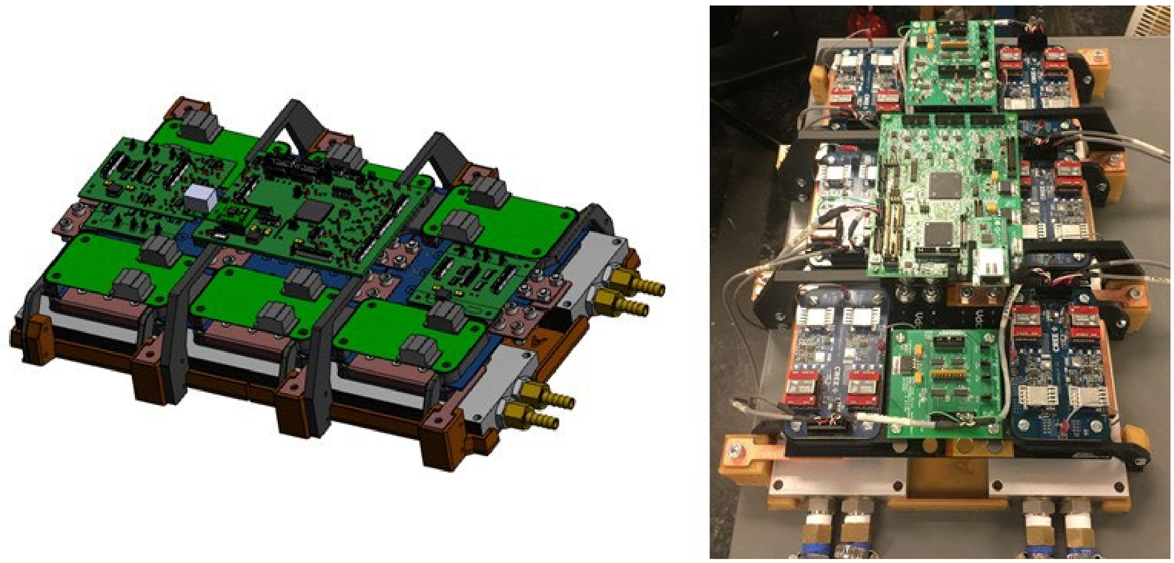

(a) (b)

Figure II.2.3.2 3D engineering CAD design of the 300-kW primary-side open-ended dual-winding high-frequency, high-power inverter (a) and the physical hardware development of the inverter (b).

For the vehicle-side, a 100-kW high-frequency rectifier design and development was completed using GeneSiC GB2X100MPS12-227silicon carbide Schottky diode modules. This rectifier unit has been tested to the rated power with a rectification efficiency of 99.3-99.4% while rectifying the 3-phase ~85 kHz input voltage. The 3D engineering drawing and the physical hardware development of the 100-kW rectifier unit is shown in Figure II.2.3.3. This rectifier is also designed as an open-ended dual winding rectifier and can be treated as a 2 of 3-phase rectifiers or 3 of H-bridge rectifiers.

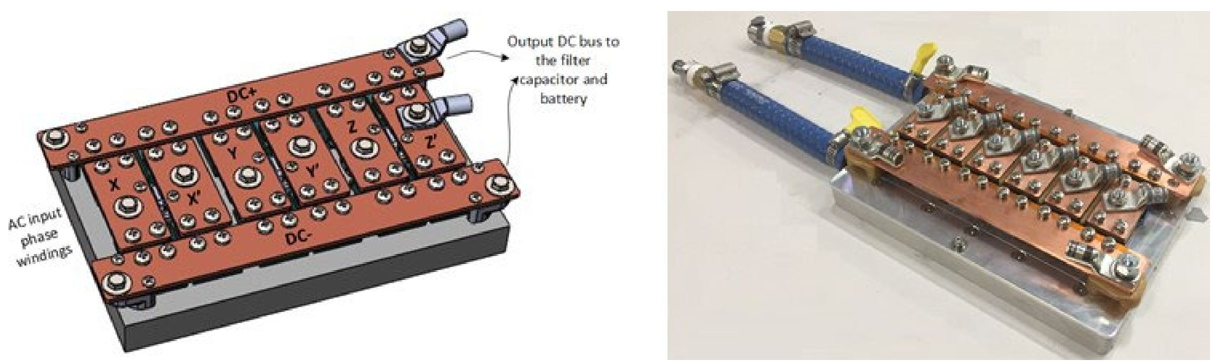

(a) (b)

Figure II.2.3.3 3D engineering CAD design of the 100-kW vehicle-side open-ended dual-winding high-frequency, high-power rectifier (a) and the physical hardware development of the rectifier (b).

The primary and secondary side couplers designed for this project are shown in Figure II.2.3.4 along with some of the key specifications. The transmitter is common and can perform both the 100- and 300-kW power transfer and it has a diameter of 750 mm which corresponds to 0.68 MW/m^2 surface power density. The 300-kW receiver has a diameter of 500 mm with a surface power density of 1.53 MW/m^2 while the 100-kW receiver has a diameter of 375 mm with 0.905 MW/m^2. The 300-kW rated receiver coupler has 8-10 times higher power density compared to other existing coupler technologies in the world.

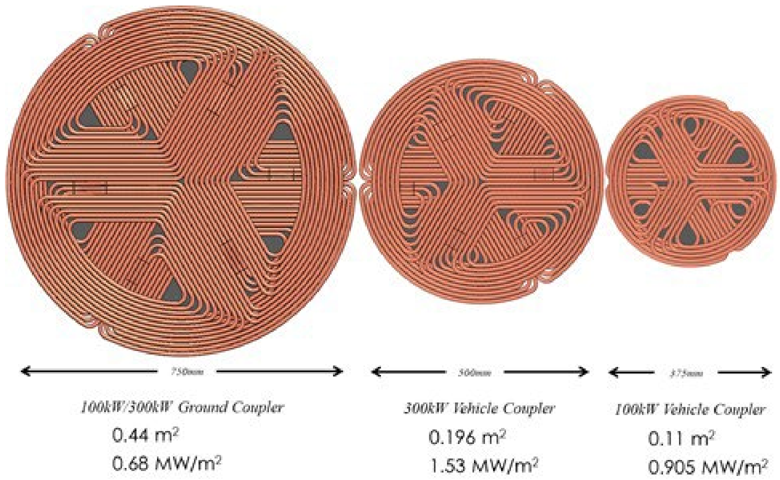

Figure II.2.3.4 Engineering CAD designs of the 100/300-kW transmitter and the 100 and 300-kW receiver pads.

Key parameters of the couplers are provided in Table II.2.3.1. It should also be noted that these couplers are designed for up to 125 mm misalignment tolerance in any direction. The completed laboratory development of 100/300-kW ground coupler and the 100-kW vehicle coupler are given in Figure II.2.3.5.

Table II.2.3.1 Primary and Secondary Side Coupler Specifications

	Interoperable Transmitter	100-kW Receiver	300-kW Receiver
Diameter	750 mm	375 mm	500 mm
Litz Wire / Wiring	3×4 AWG/phase	1×4 AWG/phase	3×4 AWG/phase
Litz + Ferrite Thickness	33.6 mm (18.6+15)	28.6 mm (18.6+10)	33.6 mm (18.6 + 15)
Litz + Wire Mass	42.2 kg (9.9+32.3)	8.8 kg (2.4+6.4)	19.4 kg (4.7+14.7)
Worst Case Losses	2362 W (697+1665)	596 W (169+311)	1343 W (331+1012)
Surface Area	0.44 m^2	0.196 m^2	0.11 m^2
Surface Power Density	0.68 MW/m^2	1.53 MW/m^2	0.905 MW/m^2
Coil-to-Coil Efficiency		97.4%	98.8%

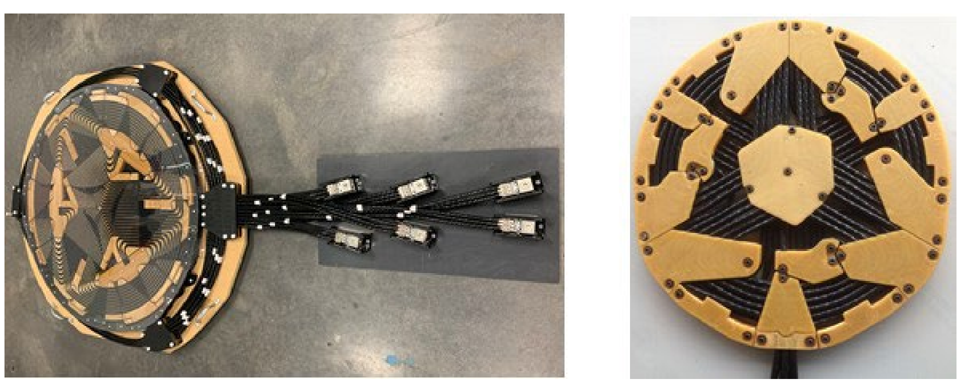

(a) (b)

Figure II.2.3.5 Hardware development of the 100/300-kW transmitter (a) and the 100-kW receiver pads.

For the 100-kW receiver coupler, ferrites added in simulations, only under the area covered by the coil. In order to the reduce the magnetic field emissions below ICNIRP 2010 requirements and to reduce the possible eddy current losses and temperature rise on the vehicle body, a vehicle-side shield was designed and developed. This shield design is shown in Figure II.2.3.6 (a) whereas the physical laboratory development is given in Figure II.2.3.6 (b).

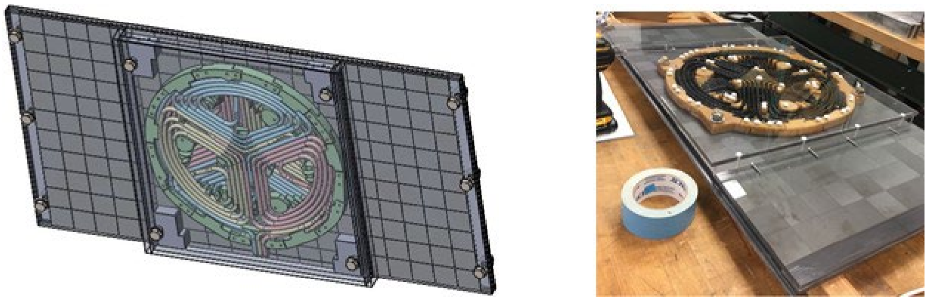

(a) (b)

Figure II.2.3.6 Engineering CAD design and the physical hardware development of the 100-kW receiver pad.

Team also received a Hyundai KONA EV from the Hyundai-Kia North America Technical Center (HATCI) as an in-kind cost share contribution to this project which is shown in Figure II.2.3.7 (a) at the parking lot of the National Transportation Research Center at ORNL and in Figure II.2.3.7 (b) on the vehicle lift. The structural design of the coil mount apparatus was also completed, and it is currently being fabricated at the ORNL machine shop as shown in Figure II.2.3.8. Upon the completion of the laboratory benchtop tests, vehicle integrations will be performed which will be followed by the vehicle tests.

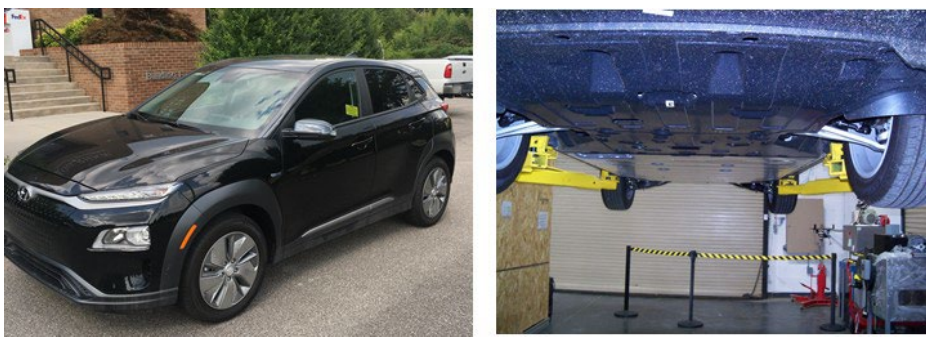

(a) (b)

Figure II.2.3.7 Hyundai KONA EV research vehicle at the parking lot (a) and on the vehicle lift (b).

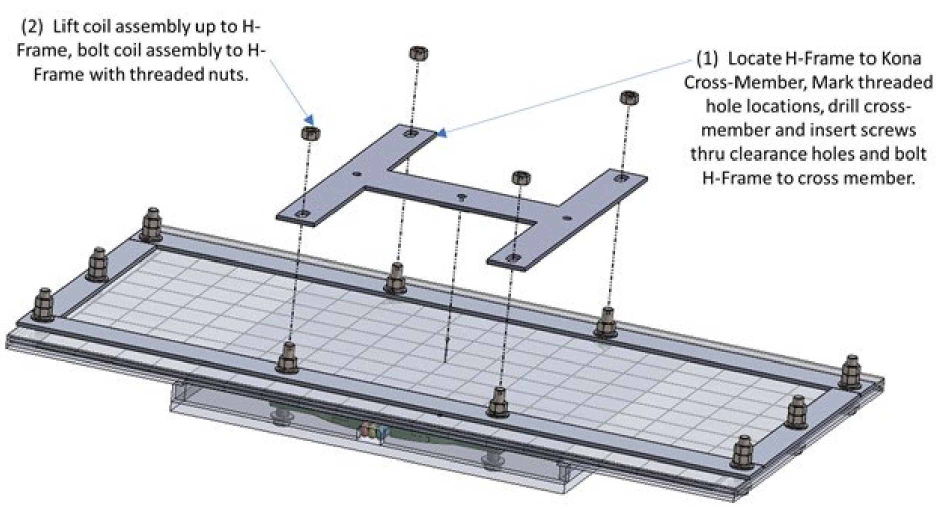

Figure II.2.3.8 100-kW receiver coil and the shielding system mounting platform designed for Hyundai KONA EV research vehicle integration.

Research team also received a Porsche Taycan research vehicle from VW Innovation Hub in Germany as their in-kind cost. The research vehicle arrived at ORNL's National Transportation Research Center as shown in Figure II.2.3.9. The research vehicle can take up to 2.8C charge rate that corresponds to 270 kW power that our design is capable of delivering. Due to the 800-V nominal battery voltage of this vehicle, the 300-kW rated receiver coupler design was slightly changed to accommodate to this change. Instead of three parallel wires per phase, due to the reduction in current with 800 V load voltage, number of parallel wires were reduced to 1 while increasing the number of turns by 2 additional turns to increase the voltage gain on the secondary side. The 300-kW receiver dimensions and the overall structure remains the same while maintaining the same designed surface power density.

Figure II.2.3.9 Porsche Taycan EV research vehicle at ORNL's Grid Research Integration and Deployment Center (GRIDC).

Results

The 100/300-kW interoperable transmitter coupler and the 100-kW receiver designed and developed for Hyundai Kona characterized in the laboratory with the self and mutual inductance measurements. Since there are 3 windings on primary-side and 3-windings on secondary side, the inductance matrix is a 6-by-6 matrix. The measurements revealed that for the given airgap of 6 inches, the inductance matrix of the actual hardware closely matched the inductance matrix of the coupler designs based on the finite element analysis (FEA) models. For these measurements on the hardware prototypes, team first used the open-circuit / short-circuit method. In order to validate the measurement results, we also used series / anti-series measurement method. Both methods resulted in the same values for the inductance matrix with very insignificant differences. The 6-by-6 inductance matrix elements obtained by the FEA-based model are given below.

$$L_{design} = \begin{bmatrix} L_a & M_{ab} & M_{ac} & M_{ax} & M_{ay} & M_{az} \\ M_{ba} & L_b & M_{bc} & M_{bx} & M_{by} & M_{bz} \\ M_{ca} & M_{cb} & L_c & M_{cx} & M_{cy} & M_{cz} \\ M_{xa} & M_{xb} & M_{xc} & L_x & M_{xy} & M_{xz} \\ M_{ya} & M_{yb} & M_{yc} & M_{yx} & L_y & M_{yz} \\ M_{za} & M_{zb} & M_{zc} & M_{zx} & M_{zy} & L_z \end{bmatrix} = \begin{bmatrix} 14.5 & -4 & -3.99 & -2.39 & 1.03 & 1.04 \\ -4 & 14.5 & -4 & 1.04 & -2.38 & 1.03 \\ -3.99 & -4 & 14.5 & 1.03 & 1.04 & -2.38 \\ -2.39 & 1.04 & 1.03 & 14.6 & -3.95 & -3.96 \\ 1.03 & -2.38 & 1.04 & -3.95 & 14.6 & -3.96 \\ 1.04 & 1.03 & -2.38 & -3.96 & -3.96 & 14.6 \end{bmatrix} \mu H$$

For comparisons, the inductance matrix obtained through measurements is provided below:

$$L_{measured} = \begin{bmatrix} 14.89 & -4.215 & -4.0725 & -1.665 & 1.0275 & 0.2325 \\ -4.215 & 15.08 & -4.1225 & 0.26 & -1.595 & 1.0625 \\ 4.0725 & 4.1225 & 14.8 & 1.13 & 0.2975 & -1.5225 \\ -1.665 & 0.26 & 1.13 & 15.82 & -3.93 & -3.56 \\ 1.0275 & -1.595 & 0.2975 & -3.93 & 15.62 & -3.4775 \\ 0.2325 & 1.0625 & -1.5225 & -3.56 & -3.4775 & 15.69 \end{bmatrix}$$

Additionally, ORNL team completed preliminary testing of the polyphase wireless charging system with 100/300 kW interoperable transmitter and primary side high-frequency inverter and 100-kW receiver coil and the rectifier for Hyundai Kona EV. The primary and secondary side polyphase couplers with some of the resonant tuning components are shown in Figure II.2.3.10.

Figure II.2.3.10 Polyphase transmitter and receiver couplers and resonant tuning components.

Experimental results with 99.75 kW input power and 90.60 kW output power were recorded with 90.83% dc-to-dc (input to output) efficiency at 727.55 V and 137.11 A input voltage and current and 363.54 V and 249.23 A output voltage and current. Total losses of 9.15 kW include the total losses of the inverter, rectifier, coupling coils, and the resonant tuning components. The results for dc-to-dc input and output readings are shown in Figure II.2.3.11 (a). High-frequency experimental results from polyphase inverter output to polyphase rectifier input are shown in Figure II.2.3.11 (b). In this figure A-A’, B-B’, and C-C’ indicate the inverter output phase and return lines while X-X’, Y-Y’, and Z-Z’ indicate the rectifier input phase and return lines for the open-ended winding configurations on both sides of the system. As seen from Figure II.2.3.11 (b), both inverter output and rectifier input voltages and currents have slight imbalances. While these imbalances would normally reduce inverter and rectifier efficiency in a delta (Δ) or star (Y) connected system, there is no impact of imbalances on system efficiency due to the due to the open-ended winding configuration on the inverter and rectifier since independent H-bridge inverters and rectifiers are used for each phase.

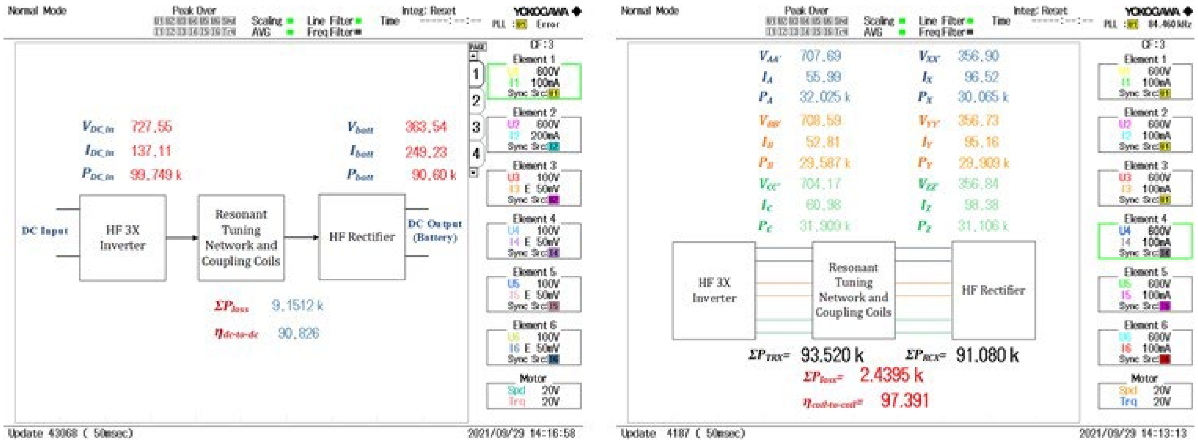

(a) (b)

Figure II.2.3.11 Power analyzer results for dc input and dc output and dc-to-dc efficiency (a) and inverter output and rectifier input (b).

At 90.60 kW output power, inverter input dc voltage and current and the inverter phase output voltages and currents are shown in Figure II.2.3.12. Overall, the dc input and inverter phase output voltage and current readings are in good agreement with the power analyzer results with slight differences due to the measurement equipment tolerance, accuracy, and bandwidth differences. On the secondary side, rectifier input phase voltages and currents as well as the dc output (load) voltage and current are shown in Figure II.2.3.13. While the RMS values are in overall good agreement with the power analyzer results, there are slight imbalances that do not affect the overall operation and the performance.

Figure II.2.3.12 Primary-side waveforms and RMS measurements including the inverter input voltage and current and the inverter output Phase-A, B, and C voltage and current measurements.

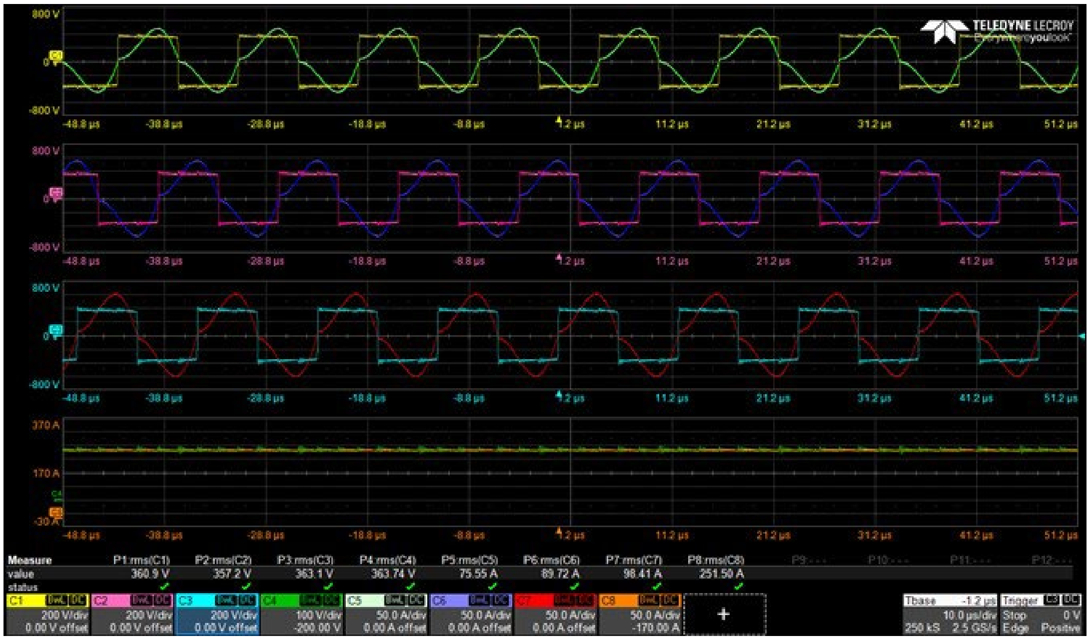

Figure II.2.3.13 Secondary-side waveforms and RMS measurements including the rectifier input Phase X, Y, and Z voltage and current and the rectifier output voltage and current.

Conclusions

During the first budget period of the project, the team worked on modeling, simulations, analysis, and design of the system power conversion stages and control systems and completed the design and simulations of the polyphase inductive charging system with a 300-kW interoperable transmitter and primary-side power electronics that can operate with 100- and 300-kW receiver systems. Since proposed concept is new, a relatively low-power, scaled-down version of the couplers was developed and tested to validate the concept and the operation. The prototype was tested with ~95% dc-to-dc efficiency with ~50-kW output. Simulation results agreed with the experimental results for improved confidence for the 100- and 300-kW systems. During the second budget period of the project, team worked on the hardware development and completed the development and fabrication of the high-frequency inverter, 100/300-kW interoperable transmitter, 100-kW polyphase receiver coupler for Hyundai Kona EV, and the 100-kW rectifier with all the resonant tuning components for the LCC-LCC tuning of the primary and secondary sides. The team also tested and validated the 100/300-kW interoperable transmitter and the 100-kW receiver including the coupling coils and the power electronics. So far, team achieved 99.75 kW input power and 90.60 kW output power with 90.83% dc-to-dc efficiency. Team is currently working towards increasing the overall efficiency with frequency modulation and updating some of the connection configurations and increased voltage gain of the resonant network. Completion of the benchtop 100-kW tests will be followed by the vehicle integration efforts for the Hyundai KONA EV. Successful testing of 100-kW power transfer to Hyundai KONA EV will be followed by demonstrations of the technology as well as the 270-kW demonstrations with Porsche Taycan EV.

Key Publications

1. "*Thermal Analysis of a 50 kW Three-Phase Wireless Charging System*," in Proc., IEEE Transportation Electrification Conference and Expo, June 2021, Chicago, IL.

2. "*Design and optimization of cancellation coil topologies for a ferrite-less wireless EV charging pad*," in Proc., IEEE Transportation Electrification Conference and Expo, June 2021, Chicago, IL.

3. "*Three-Phase LCC-LCC Compensated 50-kW Wireless Charging System with Non-Zero Interphase Coupling*," in Proc., IEEE Applied Power Electronics Conference and Exposition, June 2021, Phoenix, AZ.

4. "*Analysis of Magnetic Field Emissions and Shield Requirements for Interoperating High-Power EV Wireless Charging System*," in Proc., IEEE Applied Power Electronics Conference and Exposition, June 2021, Phoenix, AZ.

5. "*Phase Shift Control of a Three-Phase Inverter for Balanced Secondary Currents in Misaligned Three-Phase Inductive Power Transfer Systems*," in Proc., IEEE PELS Workshop on Emerging Technologies: Wireless Power Transfer (WoW), November 2020, Seoul, South Korea.

6. "*Shield Design for 50 kW Three-Phase Wireless Charging System*," in Proc., IEEE Energy Conversion Congress and Exposition, October 2020, Detroit, MI.

7. "*Control of Output Power in Primary Side LCC and Secondary Series Tuned Wireless Power Transfer System without Secondary Side Sensors*," in Proc., IEEE Energy Conversion Congress and Exposition, October 2020, Detroit, MI.

8. "*A Tradeoff Analysis of Series/Parallel Three-Phase Converter Topologies for Wireless Extreme Chargers*," in Proc., IEEE Transportation Electrification Conference and Expo (ITEC), June 2020, Chicago, IL.

9. "*Review of Safety and Exposure Limits of Electromagnetic Fields (EMF) in Wireless Electric Vehicle Charging (WEVC) Applications*," in Proc., IEEE Transportation Electrification Conference and Expo (ITEC), June 2020, Chicago, IL.

10. "*Comparison of Magnetic Field Emission from Unipolar and Bipolar Coil-Based Wireless Charging Systems*," in Proc., IEEE Transportation Electrification Conference and Expo (ITEC), June 2020, Chicago, IL.

11. "*Advances in High-Power Wireless Charging Systems: Overview and Design Considerations,*" *IEEE Transactions on Transportation Electrification*, vol. 6, no. 3, pp. 886–919, July 2020.

12. "*A 50 kW Three-Phase Wireless Power Transfer System Using Bipolar Windings and Series Resonant Networks for Rotating Magnetic Fields,*" IEEE Transactions on Power Electronics, vol. 35, no. 5, pp. 4500–4517, May 2020.

13. "*Comparison of Leakage Magnetic Field from Matched and Mismatched Double-D Coil based Wireless Charging System for Electric Vehicles*," in Proc., IEEE Energy Conversion Congress and Exposition (ECCE), Sept.–Oct. 2019, Baltimore, MD.

14. "*Variable Duty Control of Three-Phase Voltage Source Inverter for Wireless Power Transfer Systems*," in Proc., IEEE Energy Conversion Congress and Exposition (ECCE), Sept.–Oct. 2019, Baltimore, MD.

15. "*Design of an EMF Suppressing Magnetic Shield for a 100-kW DD-coil Wireless Charging System for Electric Vehicles,*" in Proc., IEEE Applied Power Electronics Conference and Exposition (APEC), March 2019, Anaheim, CA.

Acknowledgements

Project team would like to thank Jason Conley from National Energy Technology Laboratory for his continued guidance and support on this project.

II.2.4 Fast Charging: Interoperability and Integration Technologies (Argonne National Laboratory)

Daniel Dobrzynski, Principal Investigator
Argonne National Laboratory
9700 South Cass Avenue
Lemont, IL 60439
Email: ddobrzynski@anl.gov

Lee Slezak, DOE Technology Manager
U.S. Department of Energy
Email: lee.slezak@ee.doe.gov

Start Date: October 1, 2018 End Date: September 30, 2020 (Extended to March 31, 2022)
Project Funding: $800,000 DOE share: $800,000 Non-DOE share: $0

Project Introduction

This project addresses key enablers for fast charging, i.e., DC EVSE capable of delivering 150-350 kW, often referred to as extreme fast charging, or xFC. Argonne's areas of interest are testing and evaluation, focusing on EV-EVSE-network connectivity, interoperability, and backward compatibility (i.e., the requirement to charge vehicles with a lower battery voltage and 50 kW maximum charge rate).

This is a cooperative project with industry; participation ranges from providing technical support for purchased EVSE to providing complete EVSE system(s) and supporting the testing. Argonne provides infrastructure modifications, hardware installation and testing at the Smart Energy Plaza. The project will provide data and insight to support standards and technology development for xFC implementation in the public domain and enable studies related to grid impacts, energy management and mitigation of peak power demands.

As part of the cooperative agreement between DoE and the European Commission's Joint Research Center (JRC) xFC EVSE systems are being tested at JRC and Argonne, utilizing specific capabilities of each lab, e.g., electromagnetic compatibility and network connectivity/communication, respectively.

Objectives

The objective is to identify issues associated with EV-EVSE-network connectivity, interoperability, and backward compatibility. The project will also develop/verify interoperability test procedures for xFC in cooperation with JRC. Since xFC will be deployed in the public domain in support of DOE's objectives for vehicle fleet electrification, it is necessary to develop procedures to evaluate the functionality and interoperability of the systems.

The result of this effort was the development and production of interoperability test equipment by several manufacturers; this project uses some of that equipment and will develop any new procedures deemed necessary.

Approach

The primary issue is to understand the ramifications of implementing xFC, with peak charging rates of 5 to 50 times current Level 2 AC EVSE. Considerations include the requirements of and implications for the infrastructure, communication/control requirements and standards for the EV-EVSE connection as well as the grid interface. In addition, xFC must be incorporated in energy management strategies and integrated control schemes with other grid-connected devices (e.g., building energy management systems and battery storage).

The primary technical challenge is to assemble test hardware and implement a test program that covers the range of the vehicles that will utilize xFC systems, i.e., ranging from 50 kW @ ~400Vdc to 350 kW @~1000Vdc. And vehicles with 800–900-volt systems are becoming more available. Examples are the Tesla Model 3 and the Porsche Taycan; ANL has acquired both EVs for study and characterization.

ANL will utilize the fast charge capability in the VTO-sponsored NextGen Profiles project led by Argonne. The project's focus is the capture of EV charging profiles peaking above 200 kW while also characterizing the performance of EVSE during charging sessions. ANL will be able to leverage OEM relationships and EV access within NextGen Profiles project for interoperability studies.

Additional challenges in this project were the infrastructure modifications and installation of new charging equipment due to the failure of the previously installed system to function according to the specifications. This is the primary factor in the project extension by 18 months. But the delay was utilized effectively to upgrade the infrastructure (transformer and switchgear) to support charging power up to 1MW. This also provided the opportunity to install a battery energy storage system to be used in studies to minimize potential grid impacts of high-power charging.

ANL re-established collaboration with the European Commission's Joint Research Centre (JRC) that was interrupted by COVID-related restrictions at both labs. Regular bi-weekly meetings allow alignment of schedules, testing assets, and interoperability evaluation processes. The objective is to develop common test procedures and guidelines for evaluation of high power EVSE in the US and EU.

ANL and JRC directly contributed to the Global InterOP team (the precursor of the Global Grid Integration Program) for several years; ANL contributed the knowledge from leading the development of the SAE J2953 interoperability standard. The Global InterOP team produced a set of universal AC/DC requirements for interoperability verification testing in the US and Europe, which led to a series of testing requirements and procedures that were developed into testing libraries used by ScienLab and Keysight Technologies in the Keysight Charge Discovery System (CDS). ANL added the Keysight CDS system to its set of tools in FY 2021 and is currently exploring added capabilities offered by the CDS that include software and testing packages related to ISO 15118 Plug'n Charge (PnC). The PnC use cases focus on seamless charge scheduling and payment at public charging stations, which is likely to become an important interoperability issue for fast charging EVs.

Results

Infrastructure Buildout required for High Power Charging – The buildout for the infrastructure included installation of (2) 350 kW Fast Charging EVSE at the Energy Plaza, requiring considerable coordination internal and external to ANL. Prior to the COVID-19 pandemic ANL had proposed upgrading the infrastructure from 500 kW to 2.5MW, which would power the existing infrastructure at the plaza (building loads, AC EV charging loads, DC charging EV loads, and solar resources), the new 350 kW DC EVSE and 1MW battery storage system, as well as support future fast charging technology (up to 1MW).

The plan required coordination and funding from Laboratory Directorate along with outside council for professional construction engineering services. The design required efforts in electrical and power limit coordination and networking interface requirements provided by ABB (transformer and switchgear manufacture), BTCPower (EVSE OEM), Aggreko (Battery Energy Storage System manufacture), and Argonne Infrastructure and Facilities services (network and IT, and building alarm integration).

The site preparation, construction, installation, integration, and commissioning work occurred in FY 2021. The schedule was substantially impacted by COVID-related delays, including availability of equipment, contractor, and parts (e.g., fiber optic cabling and network switches). Other project delays were due to oversights by manufacturers and installers resulting in re-work, atypical requirements by the laboratory for hazard mitigation, and extended review periods.

Progress and final installation photos are shown below.

Figure II.2.4.1. Initial excavation

Figure II.2.4.2 Conduit routing

Figure II.2.4.3 Completed concrete pad

Figure II.2.4.4 Switchgear installation

Figure II.2.4.5 350 kW EVSE installation

Figure II.2.4.6 Battery Energy Storage System installation

Figure II.2.4.7 Completed Fast Charge and Battery Installation

Conclusions

The project team has made significant efforts in developing the capability for fast charging interoperability and grid impact studies by upgrading the Energy Plaza infrastructure, installing fast charging DC EVSE, and a battery energy storage system. Future work includes integration of the EVSE, grid switchgear metering, and the grid storage system into CIP.io, the ANL-developed energy management system at the Plaza. This capability will support development of control strategies to minimize the impact of fast charging on the grid as well as optimal use of battery energy storage in the overall energy management scheme of the Energy Plaza.

Acknowledgements

This work is sponsored by the Vehicle Technologies Office in the Office of Energy Efficiency and Renewable Energy Office, U.S. Department of Energy. The work in this report was conducted by researchers in the Advanced Mobility and Grid Integration Technology Section of the Energy Systems Division of Argonne National Laboratory.

II.2.5 Development of a Multiport 1+Megawatt Charging System for Medium and Heavy-Duty Electric Vehicles (NREL)

Andrew Meintz, Principal Investigator
National Renewable Energy Laboratory
15013 Denver West Parkway
Golden, CO 80401
Email: Andrew.Meintz@nrel.gov

Madhu Chinthavali, Principal Investigator
Oak Ridge National Laboratory
2360, Cherahala Boulevard
Knoxville, TN 37932
Email: chinthavalim@ornl.gov

Theodore Bohn, Principal Investigator
Argonne National Laboratory
9700 South Cass Avenue
Lemont, IL 60439
Email: tbohn@anl.gov

Lee Slezak, DOE Technology Manager
U.S. Department of Energy
Email: lee.slezak@ee.doe.gov

Start Date: October 1, 2018 End Date: December 31, 2021
Project Funding: $2,000,000 DOE share: $2,000,000 Non-DOE share: $0

Project Introduction

Medium-duty (MD) and heavy-duty (HD) electric vehicles (EVs) are being manufactured today and will soon necessitate the use of megawatt (MW)-scale charging systems that can quickly charge large capacity (~800 kWh) battery packs in less than ~30 minutes at an attractive charging cost ($/kWh). This fast charging time is needed to maximize the revenue-generating operations of commercial MD/HD vehicles. The integration of renewable energy and grid-tied energy storage, coupled with these large and semi-variable high-power vehicle charge events, will require an integrated system which has minimum impact on the grid. Many challenges must be met to realize this integrated system, including 1) optimizing power demand and management requirements, 2) configuring local infrastructure requirements, 3) designing grid interface converters, 4) managing impacts on grid power quality, 5) developing distribution voltage-level hardware for grid connection, 6) developing safe and robust hardware connections, 7) overcoming power electronics semiconductor and architecture limitations, 8) developing robust thermal management systems, and 9) developing vehicle-side power delivery architectures.

This project, led by the National Renewable Energy Laboratory (NREL) in coordination with Oak Ridge National Laboratory (ORNL) and Argonne National Laboratory (ANL), will create models of the system and components, control methods for power and charging, and hardware to address MW-scale charging infrastructure challenges for MD/HD EVs. The primary objective of this project is to develop solutions which enable 1+ MW charging systems for MD/HD EVs of various vocations to maximize utilization and the all-electric miles travelled and improve the return on investment, ensuring industry and consumer acceptance. The project will design and develop a cost-efficient, modular, and reconfigurable power electronics architecture, leveraging current DOE research activities and team members' world-class experience, wide bandgap device-based power electronic converters, vehicle charging and energy storage systems, and grid modernization. In

2021, the project made significant advancements toward these goals. These advancements include power electronic hardware design and control, industry engagement, power grid impact analysis, charging connectors, and system control simulation and hardware implementation.

This project will ensure that the United States remains a leader in innovative transportation systems by accelerating adoption of MD/HD EVs and assuring the convenient, flexible, and safe integration of 'beyond' extreme fast-charging (XFC) technology with our nation's grid infrastructure.

Objectives

Functional validation of single multiport MW charging system through HIL simulation

This task will verify the advanced functions of a single multiport MW charging system in a grid connected and/or HIL environment, including control and communication performance. We will model the DER, load, and power electronics interface of a single multiport MW charging system in a HIL real-time emulator, and then integrate the HIL model with developed power stage host controllers and a central controller for a complete HIL testing system. We will test the basic functions such as charging profile tracking, soft startup, and voltage/current regulation, as well as advanced grid-support functions such as volt/var functions.

Energy Management and Site Controller (NREL)

To integrate these multi-megawatt sites with the grid a smart control for overall site management is needed. This control system must incorporate grid constraints, minimizes charging time and cost, and support multiport charging stations with onsite distributed energy resources (DER).

Power Electronic Converter, Models, and Controllers (ORNL)

This work proposes the development of power electronic converter models and controllers to support a xFC DC multiport for charging HD-EVs and supporting grid, energy storage, and renewable integration as presented in Figure II.2.5.1. The multiport design is composed of cascaded h-bridge (CHB) converters and dual-active bridge (DAB) converters that couple on a 2kV DC link.

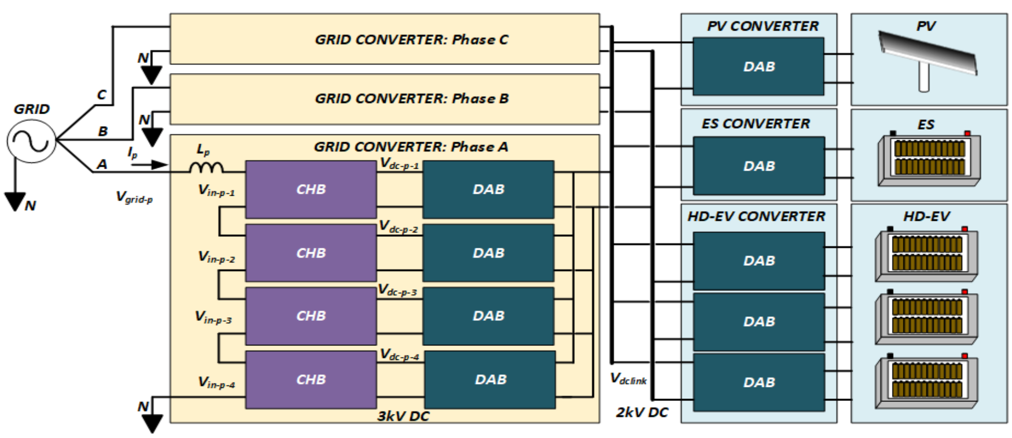

Figure II.2.5.1 Single Multi-port for Charging HD-EVs.

Connector Evaluation (NREL)

A new multi-megawatt charging standard is needed for the electrification of medium- and heavy-duty vehicles as existing charging standards are not capable at these power levels. This project is supporting the Charing Interface Initiative, CharIN, an association of specialists from various industries which promotes the standardization and interoperability of battery charging systems for electrified vehicles through the Megawatt Charging System (MCS) Task Force. NREL hosted a CharIN MCS evaluation event to evaluate prototype designs from multiple manufacturers with the objective of providing feedback that improves interoperability, reliability, efficiency, and cost-effectiveness of high-speed medium- and heavy-duty electric vehicle charging systems.

Industry Engagement (ANL)

Building an 'information nexus' on megawatt level charging system requirements which can be discussed with industry stakeholders. Address control/safety functions for MW+ multiport charging of 'commercial electric vehicles at scale'. The objectives for the industry engagement effort in year 1 established an industry work group to discuss and capture MW+ Multiport charging system requirements for MD and HD electric vehicles. Hosted monthly web based interactive meetings and several in person meetings to gather input and feedback for content of the charging requirements report.

In year 2 and 3, this effort leveraged year 1 requirements document to create a technology testbed capabilities matrix. Use matrix to specify capabilities allowing the goal of the testbed is to serve as a method to evaluate standards gap and collect data.

Approach

Functional validation of single multiport MW charging system through HIL simulation

In the previous years of this project, a set of optimal charging stations are identified to achieve different levels of electrification in MD/HD commercial trucks operating within a five-state exclusive region in western United States. The resultant station schedules are simulated using NREL's Electric Vehicle Infrastructure, Energy Estimation, and Site Optimization (EVI-EnSite) tool to identify station-wise charging infrastructure needs and corresponding charging loads. The station load profiles are post-processed using 14 different metrics to down select candidate stations for HIL simulation. These metrics include identifying temporal locations of charging peaks and valleys, synchronization of charging peaks and valleys with solar/system load peaks and valleys, peak to average charging load, peak durations, and number and amount of large charging ramps. The final down selection is carried out by selecting charging stations with three 1.2 MW charging ports that satisfy some of the metrics mentioned earlier. Vehicle schedules for these selected days and stations are converted into CSV files that the HIL setup can recognize and simulate corresponding vehicle arrival and charging behavior at the station.

Energy Management and Site Controller (NREL)

Site controller is a bi-level real-time energy management system, which monitors the entire system in real-time, including distributed energy resources (DERs), EV loads, and grid, and manages EV charging, power dispatch for ESSs, and PV operation. It incorporates (see Figure II.2.5.2):

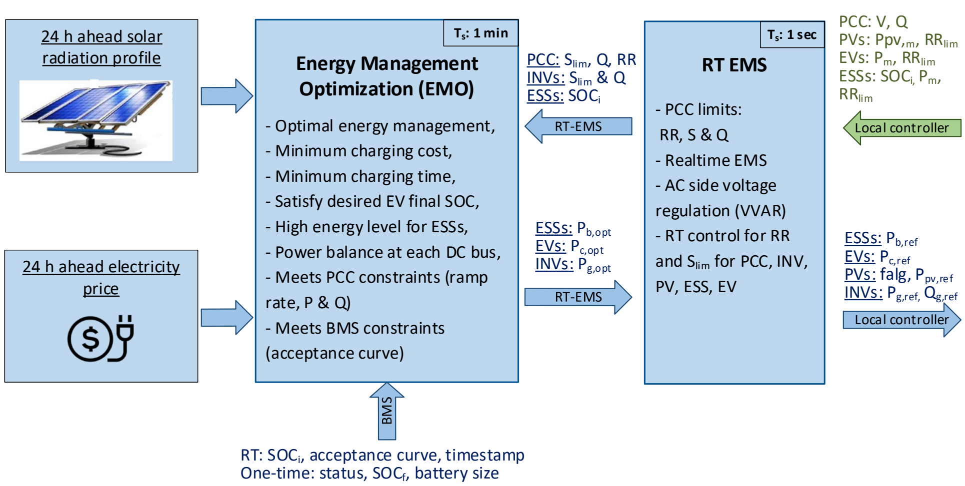

Figure II.2.5.2 Block diagram of the site controller (EMO and RT-EMS)

- Energy Management Optimization (EMO), which optimizes the overall station performance in real-time considering limitations for grid, EV, BMS, and converters.
- Real-time Energy Management System (RT-EMS), which coordinates between the optimal set point from EMO and real-time variability of EV load and DERs, and performs voltage regulation on the AC side using volt-var.

The EMO solves a multi-objective linear optimization problem every minute to estimate the charging power, and energy storage system dispatch, considering predicted solar radiation, real-time electricity price, real-time station schedule, real-time EV battery acceptance power, and real-time distribution feeder capacity. RT-EMS compares between optimum set point and real-time measurements and adjust the set point to compensate for fast disturbances in EV load and DERs.

Power Electronic Converter, Models, and Controllers (ORNL)

The converter and multi-port model are to be integrated into a real-time simulation platform with converter controls and integration performed in hardware as shown in Figure II.2.5.3. The converter modeling consists of non-switching-based models that represent the physical dynamic performance of the converters through mathematical representations of the inductance and capacitance implications on the voltage and current. This simplification is necessary to include the full number of converters represented in the converter topology within a single Opal-RT platform. Resource integration controllers (RIC) tie the converters to the modelled resources within the simulation platform. A central controller performs the integration of the different resources for integration with the real-time energy management system controller.

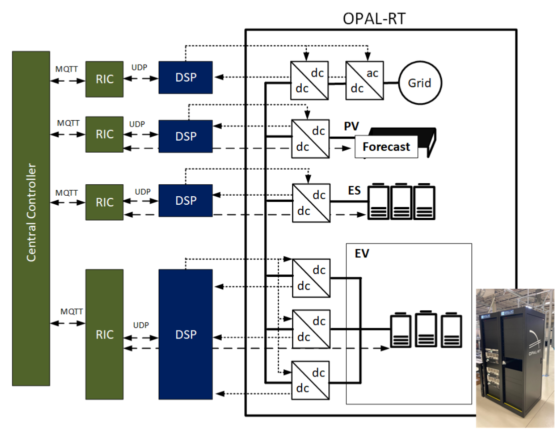

Figure II.2.5.3 Controller hardware in the loop setup for modeling and development.

Connector Evaluation (NREL)

The connector evaluation event supported manufacturer-provided equipment characterization in functional operation at three different current levels while considering implications of mechanical wear and misalignment. Manufacturers provided both new and aged—through repetitive insertion and contamination aging—components for evaluation. Level 1 tests used a test bench set up to record instrumentation of participant manufacturer's charging equipment thermal performance up to 350A with only passive cooling. Level 2 and 3 tests used a test bench set up to record instrumentation of participant manufacturer's charging equipment thermal performance up to 3000A with active cooling. At each level once the equipment reached steady-state thermal condition a misalignment force was applied to the end of the handle in the up, down, left, and right directions to apply a torque on the connector and inlet.

Results

Functional validation of single multiport MW charging system through HIL simulation

Six scenarios are selected for the CHIL experiments based on the methodology described in the previous section. Some example charging load profiles that are selected for the HIL simulation are shown in Figure II.2.5.4. Vehicle schedules, facility load, and PV generation for these selected days and stations are converted into CSV files that the HIL setup can recognize and simulate corresponding vehicle arrival and charging behavior at the station.

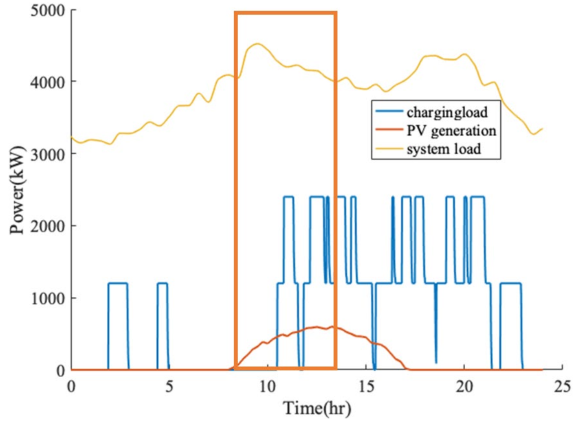

Figure II.2.5.4 Scenarios for CHIL simulation. (Left) Charging peak happens at the time when the system is not heavily loaded [scenario 1]. (Right) Charging load happens when the system load is heavy [scenario 2].

Energy Management and Site Controller (NREL)

The EMO, RT-EMS, and BMS have been implemented on single board computer embedded systems and the SW models (distribution feeder, DC bus, EV battery) have been integrated into a single OPAL-RT platform. They communicate with each other via CAN and analog interfaces as shown in Figure II.2.5.5. CHIL test results show that average voltage drops of all feeder nodes for controlled charging with ESS are about 3.5% in average less than for uncontrolled charging without ESS.

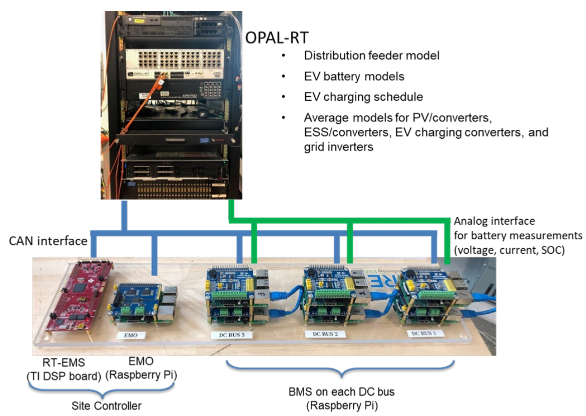

Figure II.2.5.5 Controller hardware in the loop setup

Power Electronic Converter, Models, and Controllers (ORNL)

The C-HIL testbed has been constructed and vetted as shown in Figure II.2.5.6. A demonstration of the stability and control of the individual power electronic converters and multi-port and communications network has been performed. The resources (energy storage (ES) and electric vehicle (EV) load) are dispatched manually with a target power setpoint dispatch. The test is run for approximately 10 minutes with the shared DC bus regulated by the CHB-DAB grid side converter during the entire interval. Ramp rates have been set to for both the EV and ES systems to ensure stability is maintained within the converter controls.

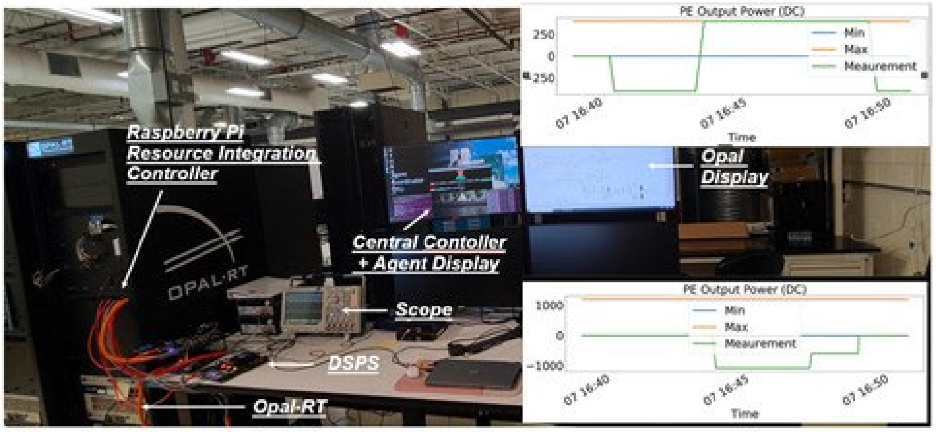

Figure II.2.5.6 Controller hardware in the loop setup and results of 10-minute simulation.

Connector Evaluation (NREL):

The event included thermal evaluation for Level 1, 2, and 3 with the misalignment forces applied. Figure II.2.5.7 captures the evaluation bench with a misalignment force applied to the connector under load. The event results were compiled for an anonymized report for the MCS Task Force and functional evaluation data of the thermal performance of the connectors and inlets were shared with the hardware developers.

Figure II.2.5.7 MCS connector and Inlet Misalignment Evaluation

Conclusions

The use of medium voltage silicon carbide devices and low inductance power modules provides a key enabler to minimize the number of series stack stages required for medium voltage grid connection and to increase the switching frequency for the DAB topologies. The interaction of the source and load DABs was simulated in conjunction with the PV and ESS on the 2kV bus to demonstrate the source side stability and simultaneous charging of EV and ESS battery. These controls were implemented in embedded controllers and implemented in the CHIL Architecture which has been coupled with the average and switching models developed in the power electronics hardware section.

A battery management system and site controller have been developed to allow for the CHIL evaluation of a site that can manage the charger rate of multiple vehicles with the distributed energy resources and grid constraints. These control systems have been implemented in embedded hardware for the demonstration and have generated results showing improvement of the integrated site relative to an uncontrolled charging case.

This project has undertaken a significant industry engagement and support effort. The interaction with the CharIN MCS task force to support the development of multi-megawatt connectors is providing key insights in thermal, fit and function, and communications. The monthly web meetings are ensuring that the results of this project are shared with industry for feedback and that the approaches undertaken are ground.

Key Publications

1. Xiangqi Zhu, Barry Mather, Partha Mishra, Mingzhi Zhang, and Andrew Meintz, "Grid Impact Analysis and Mitigation of En-Route Charging Stations for Heavy-Duty Electric Vehicles", under review in IEEE Transactions on Sustainable Energy.

2. Partha Mishra, Eric Miller, Shriram Santhanagopalan, Kevin Bennion, and Andrew Meintz, "A Framework To Analyze The Requirements Of A Multiport Megawatt-Level Charging Station For Heavy-Duty Electric Vehicles," under review in Applied Energy.

Acknowledgements

The 1+MW Charging System for MD/HD Principal Investigators acknowledge the contributions of team members: Aswad Adib, Rachit Agarwal, Kevin Bennion, Mike Coop, Keith Davidson, Myungsoo Jun, Rasel Mahmud, Shilpa Marti, Partha Mishra, Ahmed Mohamed, Brian Rowden, Darren Paschedag, Shriram Santhanagopalan, Michael Starke, Isaac Tolbert, and Xiangqi Zhu. The project team also acknowledges the support and guidance of Lee Slezak (DOE HQ).

II.2.6 Grid-Enhanced Mobility-Integrated Network Infrastructures for Extreme Fast Charging [GEMINI-xFC] (NREL, LBNL)

Andrew Meintz, Principal Investigator
National Renewable Energy Laboratory
15013 Denver West Parkway
Golden, CO 80401
Email: andrew.meintz@nel.gov

Timothy Lipman, Principal Investigator
Lawrence Berkeley National Laboratory
2150 Allston Way, #280
Berkeley, CA 94720
Email: tlipman@lbl.gov

Lee Slezak, DOE Technology Manager
U.S. Department of Energy
Email: lee.slezak@ee.doe.gov

Start Date: December 1, 2019 End Date: December 31, 2022
Project Funding: $1,000,000 DOE share: $1,000,000 Non-DOE share: $0

Project Introduction

The Grid Enhanced Mobility-Integrated Network Infrastructures – Extreme Fast Charging (GEMINI-XFC) project is exploring the grid impacts of future electric transportation scenarios and the ability of coordinated grid and mobility control to help manage resulting challenges. The project focuses on the demands of extreme fast charging (XFC) for the light duty fleet on the electric distribution system. GEMINI-XFC is creating a novel joint grid-transportation co-simulation framework that captures mobility and electric interactions at the individual level for millions of customer/agents covering an entire large metropolitan region to provide unprecedented resolution and scale for evaluating controllers and analyzing impacts and synergies across transportation and the power system.

Increasing vehicle electrification will significantly alter the transportation sector over the coming decades. These changes will likely require extensive use of extreme fast charging (XFC), especially for larger vehicles, to enable long-distance travel, and to support consumers that cannot reliably charge at home or work. Simultaneously, the continued growth of mobility-as-a-service will also require fast charging solutions to support greater vehicle utilization and avoid expensive downtime. Furthermore, self-driving vehicles will likely require high rates of utilization and XFC will be necessary to enable effective cost-recovery.

However, uncoordinated XFC can create grid challenges, particularly at the distribution level (Muratori 2018; Masoum et al. 2010). Two strategies can support widespread XFC: upgrade all systems to enable worst-case, fully coincident loads or use integrated planning to co-design a smart system based on advanced controls that leverage load flexibility and distributed energy resources (DERs). With the right design, operating practices, and control, XFC can simultaneously support both mobility and grid operations, but fully realizing the potential of XFC will require unprecedented coordination among the charging infrastructure, grid, and vehicles.

The future demand for XFC and the optimal control strategy to mitigate grid challenges will depend on the evolution of both the transportation and power systems. Transportation scenarios with varying levels of electric vehicle (EV) adoption and penetration of advanced mobility options (e.g., ride-hailing and automation) as well as grid scenarios differing in variable renewable energy generation and prevalence of DERs will be explored to assess the resulting impacts of XFC.

Objectives

The GEMINI-XFC project combines high-fidelity grid and transport modeling at an unprecedented level of resolution to both co-design and simulate operations of a smart system based on advanced controls that leverage load flexibility and DERs to optimize the integration of XFC across a full regional scale.[1] A key goal of the project is to conceive, develop, implement, and evaluate a smart controller to mitigate possible negative effects of EV XFC on electric distribution systems.

To do so, GEMINI-XFC uses first-of-a-kind integrated high-fidelity grid and transport modeling to identify effective pathways for widespread electrification by leveraging control to minimize the impact of XFC on distribution systems at a full regional scale with individual customer resolution. The focus of GEMINI-XFC is on-road passenger mobility in the entire San Francisco Bay Area looking at transportation options and grid systems in a long-term future (~2040) characterized by significant changes compared to today's systems.

Approach

Broadly, the project has three parallel and interacting efforts:

- Mobility-grid controller design for XFC integration
- Transportation scenario development, charging infrastructure, and demand-side modeling
- Large-scale transportation-grid co-simulation for performance evaluation and impact analysis.

Controller Design

The overall controller aims to co-optimize mobility and power systems operations: minimize outages, travel and charging times, voltage excursions, and excessive operation of legacy voltage control devices. The different control objectives are weighted such that critical objectives, like avoiding outages are prioritized first, while desirable outcomes that are not critical are weighted less. For the grid aspects, most of the considerations have three categories: 1) an absolute limit that should not be violated for reliable operations, 2) an acceptable operating range, where operation should be limited to shorter durations, and 3) a desired operating range where operations can be conducted indefinitely. For instance, above a certain power threshold (often well over the nominal rating) distribution line and transformer overloads, have a high likelihood of leading to outages.

The smart controller is structured and implemented in two distinct levels: planning and operation levels. The planning level determines charging station levels and locations as exogenous input to the operations simulation. The operational level uses inputs from the planning level and several transportation and grid scenarios to control EV charging and distributed storage assets and simulates responses of passenger vehicle movement and charging of EVs, and distribution system stability.

Co-simulation for evaluation and analysis

To reach these control evaluation goals, transportation and grid scenarios are being developed and run in a co-simulation that involves mobility and distribution grid models, as illustrated in Figure II.2.6.1. The Hierarchical Engine for Large-scale Infrastructure Co-Simulation (HELICS) will coordinate execution timing and data flows among all participating sub-models (Palmintier et al. 2017). The Behavior, Energy, Autonomy, and Mobility (BEAM) model is used to model mobility (Sheppard and Waraich 2019) and the PyDSS extensions (Latif 2020) to OpenDSS is used to model the electric distribution systems. Data for electric distribution system is taken from the Smart-DS project's synthetic San Francisco dataset (Palmintier et al. 2021).

---

[1] XFC in this project is defined with a grid perspective: any EV charge point (or station) with a charger (or plug) capable of charging at 250 kW or more, or at least 1 MW of total site load from several chargers of least 50 kW each.

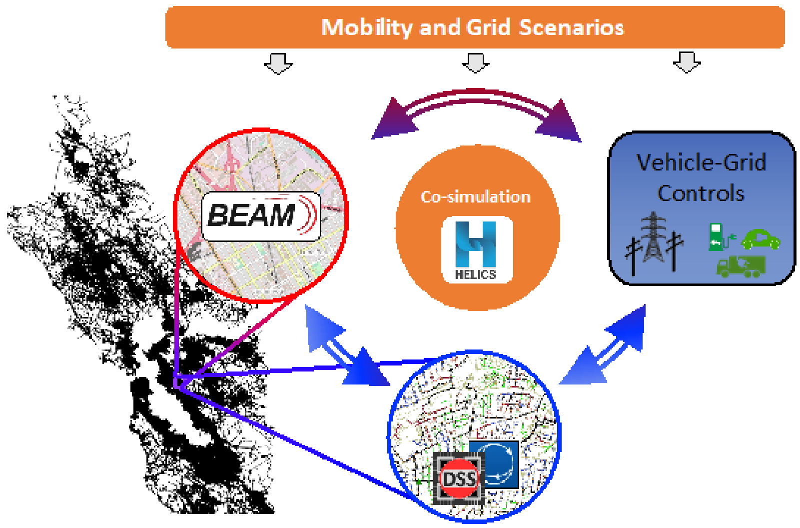

Figure II.2.6.1 HELICS co-simulation framework overview

Transportation Modeling

The BEAM model is used in the HELICS framework to simulate the transportation network and EV charging demands both geographically and temporally for a sample analysis day. BEAM is an agent-based transportation system model designed for analyzing future large-scale transportation network scenarios. Privately owned EVs charge at home (if residential charging is available) and at other locations, including workplace and public charging. Automated electric ride-hailing vehicles are assumed to charge at a set of charging depots that can be accessed only by automated ride-hailing vehicles. Human-driven electric ride-hailing vehicles compete with non-ride hail vehicles on the public charging network.

The optimal depot charging network is defined by FCSPlan (Zhang et al. 2020) and the open to the public charging network is defined by a High-Fidelity Siting Algorithm (HFSA), both with an iterative process. In the first iteration of this process, vehicles are simulated as having access to XFC or medium power direct current fast charging (DCFC) levels at all potential parking spots. Using initial outputs from BEAM, based on nodal demands in this scenario with unconstrained charging infrastructure, the FCSPlan model then chooses optimal locations for a limited amount of DCFC stations to support the operation of the automated electric ride-hailing vehicles.

Infrastructure Siting

The HFSA also takes an initial iteration from BEAM, this defines the charging needs for each of the 1454 TAZ in the Bay Area. The HFSA has knowledge of all parcel data and the number of parking spaces for all locations. Public and workplace chargers are optimized by only creating multiple EVSE when simultaneous charging needs to occur. Residential charging for SFDs are capped at 2 chargers per home and MUD are capped at the number of parking spaces onsite. Knowledge of the purpose of trips is integrated into the algorithm by forcing charging events to happen in the purpose location, for example if the purpose of a trip was to buy groceries the charge event would take place at a randomly selected grocery store within the area.

The constrained charging networks generated by FCSPlan, and EVI-Pro are used in BEAM for subsequent runs with the same vehicle fleet, and system performance metrics are produced using this more detailed fleet simulation.

Grid Analysis

BEAM, the distribution model, and the distribution controller, interface via the HELICS co-simulation platform. This co-simulation allows each simulation to maintain high fidelity modeling by avoiding the need for a single computationally demanding model that captures all assets and behaviors. The transportation system will be modeled down to individual vehicles at a 5-minute resolution and the distribution system down to individual customers at a 15-minute resolution loads and 5-minute solar generation profiles. These high-fidelity model interactions allow increased flexibility of control and better representation of charging effects on the grid. A hierarchy of brokers will manage the large number of metrics passed from the grid federates to the controller and transportation federate. Many federates will pass messages to a broker for each region and regional brokers will pass messages to a top tier broker for inter-regional communications.

Results

The Oakland Alameda region has been selected for demonstration and debugging before simulations are extended to the full Bay Area. This region is one of the larger, more complex regions and contains both urban and suburban areas as well as a mix of residential, commercial, and industrial sites.

Transport Modeling

The transportation model BEAM balances demand and supply in an evolutionary and iterative way to reach a pseudo-equilibrium that would represents the real-world observed speed and the average travel time. The demand is a set of activity plans (ActivitySim), synthetic population (SynthPop), households and workplaces (UrbanSim) that are generated and calibrated by the UrbanSim team. The current demand that is being used under this project is a TAZ-level San Francisco Bay Area from the 2010 census data. This demand incorporates not only commuters' trips but also schools, universities, and discretionary activities such shopping and socials. It also considers carpooling among same household members. In order to represent the 2035 GEMINI Baseline, so far, we only expand the population size without updating land use.

One critical point of connection between demand and supply in BEAM is the adoptions and vehicle types. To assign specific type of vehicles to different households we use a transportation demand model (TEMPO) that produces an income distribution of vehicle types, including battery and plugging hybrid electric vehicles. Once vehicles have been assigned to most households, we iterate BEAM for a dozen of iterations until the road network speeds reach relaxation. Afterwards we generate charging demand for the HFSA to site the infrastructure. The latter is then used to run a scenario and measure the impact of the infrastructure on the charging demand.

To evaluate the approach mentioned hereinabove we limited the study area to Oakland and Alameda cities due to their representation of bay area type of land use. The following plots depict the charging site power with an intensity lower than 1 MW per non-XFC site and greater than 1 MW for XFC sites along the study area. We expect that the actual load will be slightly larger than shown on these plots due to a modelling mismatch that prevents certain household from accessing their EVs, which will be fixed in the full bay area run.

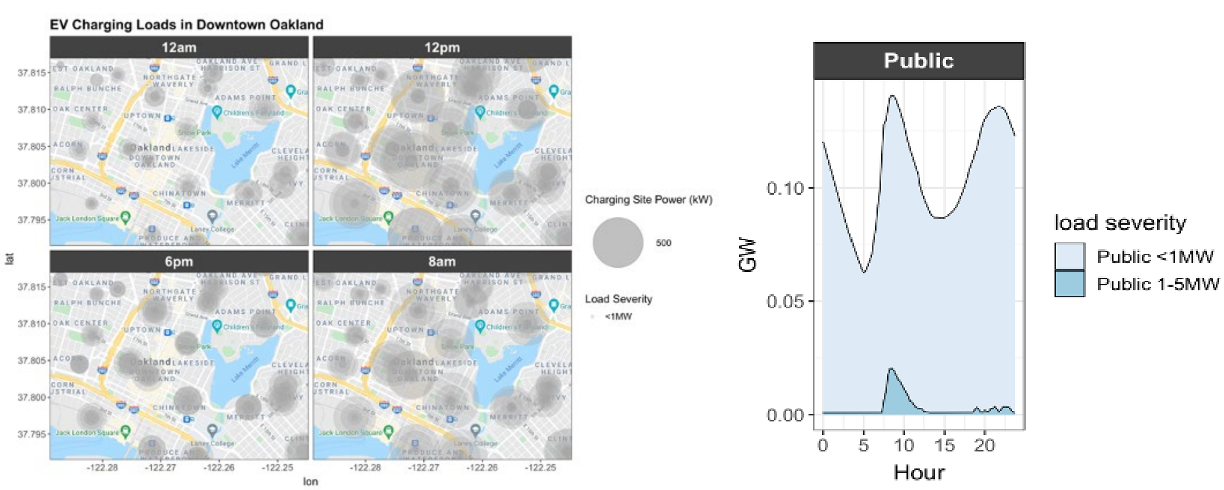

Figure II.2.6.2. Alameda simulated demand with 100% home charging availability

Scenario2 and Scenario3 with respectively 100% and 87.5% home charging availability in Figure II.2.6.3 shows a significant drop of the overall total energy charged in Scenario3 due to the limited access to home chargers. At the same time, we observe an increase in XFC as an alternative solution to whom who are unable to charge at home.

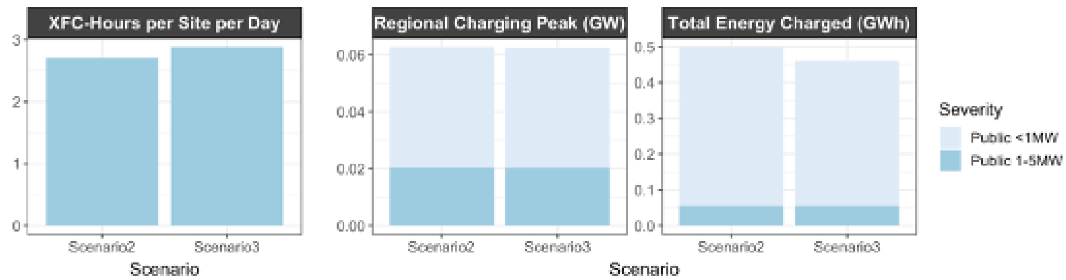

Figure II.2.6.3. Alameda simulated demand with 100% home charging availability

Infrastructure Siting

The HFSA was created for the placement of charging infrastructure in a way that is credible to possible real-world scenarios. The results for Alameda are shown in Figure II.2.6.4. Alameda was chosen as an initial run and is listed as transportation Scenario 3. The full Bay Area is still being worked and debugged; preliminary results show the assigning of all Bay Area chargers in under 5 minutes. The algorithm sited the charge locations based on the types of homes people live in and the reasons for travel.

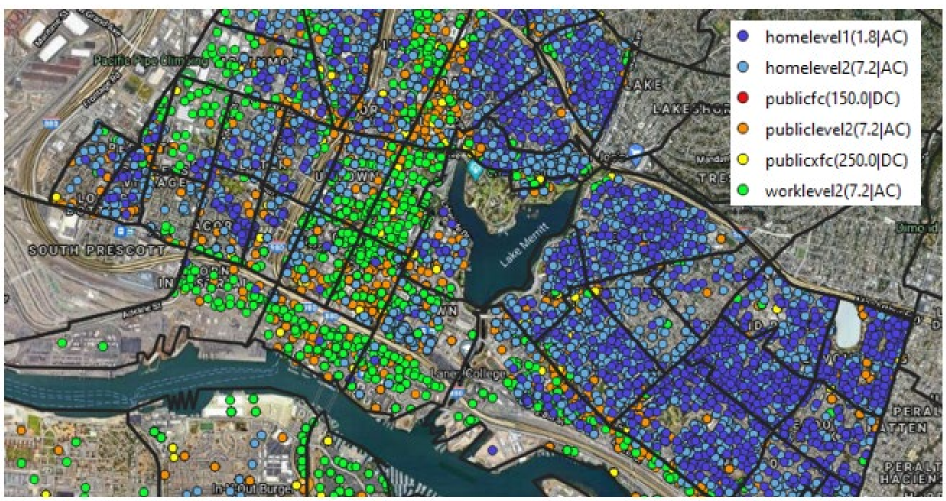

Figure II.2.6.4. Alameda infrastructure siting with 87.5% home charging availability

Grid Analysis

Through the infrastructure siting effort EV charging stations are identified and connected to the closest line with appropriate voltage and number of phases in the distribution model. This connection includes the addition of a new line and new load point. Given the specific parcel locations used for infrastructure siting, this nearest neighbor method results in connections with the correct load points.

The Oakland Alameda region with medium DER adoption case has been simulated using the HELICS broker framework with BEAM, the distribution model, and distribution controller. This area experiences voltages typically above nominal but not above ANSI limits when run without EV charging as seen in Figure II.2.6.5. These slightly higher voltages are likely due to the adoption of distributed solar and storage throughout the region. The high DER adoption grid scenario requires further tuning to include grid upgrades even without EV charging to allow for convergence of powerflow solutions for comparison to the case with EV charging.

A visualization method has been created to allow for more rapid analysis of results and identifying and tuning the distribution model to remedy convergence issues or voltage regulation controls.

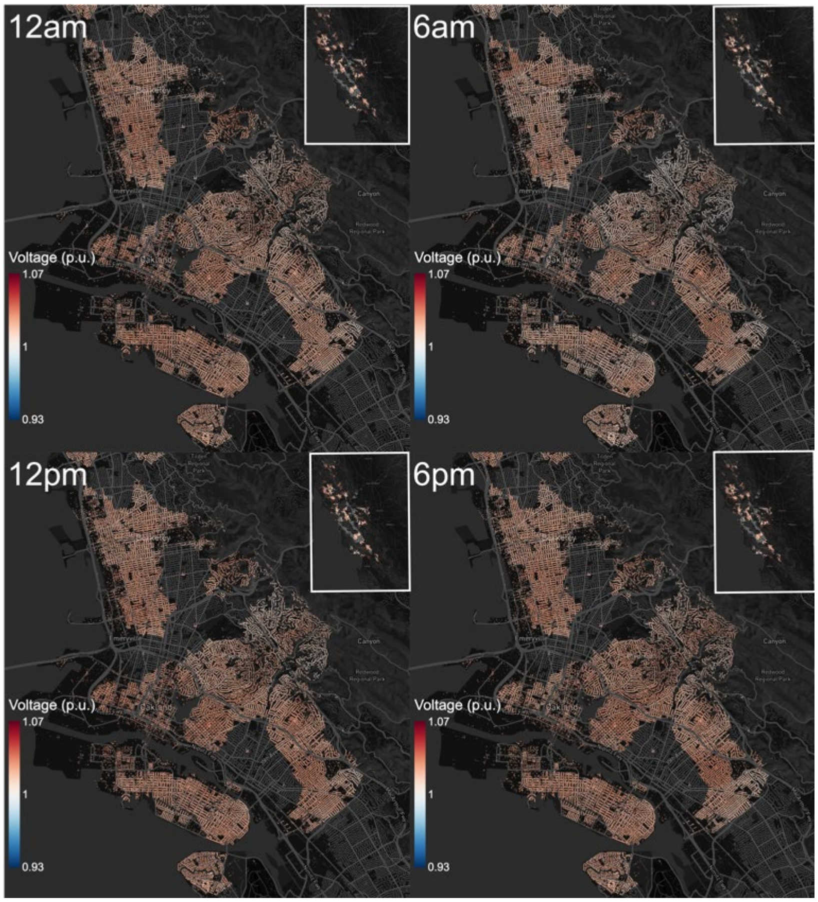

Figure II.2.6.5. Preliminary distribution system results for Alameda and Oakland's distribution system

Conclusions

In conclusion, the GEMINI project team has demonstrated the ability of BEAM to model XFC events in time and space across a modeling day of the SF Bay Area. The effort has focused on analysis within the Alameda and Oakland area for detailed evaluation of charger siting onto the distribution feeders in this region. This case has been simulated with differ infrastructure and travel constraints and the grid model has been developed. The project team will work next to further implement these control strategies into progressively larger co-simulation scenarios with BEAM and PyDSS to expand into the complete SF Bay area.

References

1. Masoum, Amir S., Sara Deilami, Paul S. Moses, and Ahmed Abu-Siada. 2010. "Impacts of Battery Charging Rates of Plug-in Electric Vehicle on Smart Grid Distribution Systems." In 2010 IEEE PES Innovative Smart Grid Technologies Conference Europe (ISGT Europe),.https://doi.org/10.1109/ISGTEUROPE.2010.5638981.

2. Muratori, Matteo. 2018. "Impact of Uncoordinated Plug-in Electric Vehicle Charging on Residential Power Demand." Nature Energy3 (3): 193–201. https://doi.org/10.1038/s41560-017-0074-z.

3. Palmintier, Bryan, Tarek Elgindy, Carlos Mateo, Fernando Postigo, Tomás Gómez, Fernando de Cuadra, and Pablo Duenas Martinez. 2021. "Experiences Developing Large-Scale Synthetic U.S.-

Style Distribution Test Systems." Electric Power Systems Research190 (January):106665. https://doi.org/10.1016/j.epsr.2020.106665.

4. Palmintier, Bryan, Dheepak Krishnamurthy, Philip Top, Steve Smith, Jeff Daily, and Jason Fuller. 2017. "Design of the HELICS High-Performance Transmission-Distribution-Communication-Market Co-Simulation Framework." In Proc. of the 2017 Workshop on Modeling and Simulation of Cyber-Physical Energy Systems. Pittsburgh, PA. https://doi.org/10.1109/MSCPES.2017.8064542.

5. C. Sheppard, R. Waraich, A. Campbell, A. Pozdnukov, A. R. Gopal, Modeling plug-in electric vehicle charging demand with BEAM: The framework for behavior energy autonomy mobility, Tech. Rep., Lawrence Berkeley National Lab. (LBNL), Berkeley, CA (United States) (2017).

6. Zhang, Hongcai, Colin J.R. Sheppard, Timothy E. Lipman, Teng Zeng, and Scott J. Moura (2020). Charging Infrastructure Demands of Shared-use Autonomous Electric Vehicles in Urban Areas. Transportation Research Part D: Transport and Environment 78: 102210. 10.1016/j.trd.2019.102210.

7. UrbanSim, https://urbansim.com/

8. ActivitySim, https://activitysim.github.io/

9. Synthpop, https://github.com/UDST/synthpop

10. TEMPO, https://www.nrel.gov/transportation/tempo-model.html

Acknowledgements

The GEMINI project Principal Investigators acknowledge the contributions of team members Bryan Palmintier, Nadia Panossian, Chris Neuman, Paige Jadun, Heather Chang, Ranjit Desai (NREL), Haitam Laarabi, Keith Moffat, Colin Sheppard, and Zachary Needell (LBNL), as well as those of project advisor Alexandra von Meier (UC Berkeley). The project team also acknowledges the support of Lee Slezak (DOE HQ), Matteo Muratori, John Farrell (NREL), and Tom Kirchstetter and Mike Mills (LBNL).

II.3 Smart Charge Management

II.3.1 Smart Vehicle-Grid Integration (Argonne National Laboratory)

Keith Hardy, Principal Investigator
Argonne National Laboratory
9700 South Cass Avenue
Lemont, IL 60439
Email: khardy@anl.gov

Lee Slezak, DOE Technology Manager
U.S. Department of Energy
Email: lee.slezak@ee.doe.gov

Start Date: October 1, 2018 End Date: September 30, 2021 (ext. to March 31, 2022)
Project Funding: $2,000,000 DOE share: $2,000,000 Non-DOE share: $0

Project Introduction

Problem Statement – The charging of grid connected vehicles must be managed and controlled or else the impacts of EVs at scale on the grid will be extremely disruptive, expensive, and will lead to the need for increased generating capacity. EVs at scale can contribute to grid resilience and reliability if charged intelligently. This will require controlled charge management that is coordinated with building and distribution network loads and requirements. Grid services previously identified in VTO-sponsored projects must be integrated into Smart Charge Management (SCM) schemes to maximize the potential benefit of EVs at scale to vehicle owners, building managers, charging network operators, grid services aggregators, and utilities.

Benefits of plug-in vehicles will be fully realized when the automotive, EVSE and utility industries cooperate, technically and programmatically, to ensure an integrated grid perspective and an implementation approach that supports sustainable business—the ultimate objective of vehicle-grid integration (VGI). This project takes a step in that direction by partnering with the Global Grid Integration Program, whose members are from U.S. and European automotive, utilities, energy companies and research organizations. The intent is to collaborate on use cases/requirements for vehicle-grid integration and interim technology demonstrations, leading to a 'public' demonstration of smart energy management, where vehicles, buildings, renewable energy sources and energy storage are linked to meet the needs of customers as well as the electric power grid. This project will result in a managed network of devices at Argonne's Smart Energy Plaza capable of demonstrating the use cases/grid services specified by the GMLC and our industry partners.

Objectives

Primary goals – Demonstrate how smart charge management can be integrated with a network of building systems, renewables, and energy storage, using an open-source approach to:

- Respond to grid conditions/signals with minimal impact on local operations
- Identify potential benefits/impacts of EVs @ scale (controlled v. uncontrolled charging)
- Maximize the benefits of VGI on the customer-side of the meter
- Develop monetization scenarios of VGI for owners, utilities, and aggregators.

Achieving this goal necessitates several technical achievements: incorporating protocols for High-Level Communication (HLC) to enable 'smart' charging; control strategies that balance the needs on the customer-side of the meter with grid conditions; and enabling technologies (i.e., digital communication, tools to verify interoperability and perform diagnostics). The first three goals can be addressed in a laboratory environment such as the Argonne Energy Plaza, however the fourth requires collaboration with stakeholders such as utilities or aggregators. This was not possible due to the restrictions in place over the last two years.

FY 2021 was intended to be the final year of a 3-year project, with the objective of demonstrating a fully integrated 'grid of things' concept to illustrate the benefits of controlled versus uncontrolled charging using the energy plaza and a simulated grid. Field testing, technology transfer and commercialization studies would be initiated for the enabling technologies. And public demonstration projects with industry partners would be pursued.

Limited access to Argonne in FY 2020 due to COVID restrictions, as well as delays at vendors/subcontractors, impacted the schedule substantially, resulting in extending the project through Q2 FY 2022. The objectives of the third year were adjusted to demonstrate as many of the use cases and develop the enabling technologies as much as possible. The final report was shifted to the end of Q2 FY 2022.

Approach

Argonne utilized the integrated network of devices at the Energy Plaza to develop integrated control strategies to accommodate EV charging, building power, solar PV and interacting with the Argonne grid. This included demonstrating the flexibility to manage loads and supply power from the customer side of the meter … considering conditions on the grid side of the meter as well as a simulated distribution network.

In addition, the plaza is used to demonstrate enabling technologies that support smart energy management, including the Common Integration Platform (CIP.io), Smart Charge Adapter (SCA), the Diagnostic Electric Vehicle Adapter (DEVA), SpEC communication control modules, sub-metering, test equipment to verify interoperability, and integrated solutions for vehicle connectivity and communication in a workplace.

The integration of real-time characteristics of the Plaza with distribution and transmission system models to assess grid impacts of EV charging (i.e., Task 3) is a joint effort with Idaho National Laboratory (INL).

Tasks 1 and 2: Quantify benefits of smart charging

Barriers

- Lack of consensus on 'smart' VGI communication protocols (i.e., ISO 15118 or SEP2.0)
- Use cases demonstrated in the GMLC 062 project were implemented without the 'smart' protocols due to lack of commercially available compliant hardware (EVs and EVSE)
- GMLC use cases were originally specified before the ISO 15118 standard communication protocol was developed.

Solution

Acquire EVs and EVSE with HLC, link to Argonne's common integration platform (CIP.io) and demonstrate the GMLC-defined use cases using 'smart' communication and control:

- Acquire ISO 15118-compliant EVs and EVSE and adapt ISO 15118 EVSE to CIP.io
- Demonstrate the GMLC uses cases utilizing the EVSE at the Energy Plaza (i.e., demand response, charge mitigation, frequency regulation, and distribution upgrade deferral) as well as cases suggested by utility partners referred to as 'GMLC+' (i.e., Plug'n Charge, or PnC, and transactive energy trading using cryptocurrency).

Argonne acquired a 2018 Smart ED EV that is ISO 15118-2-compliant, but the message sampling rate is inadequate to demonstrate V1G frequency regulation and it does not support PnC. An alternative solution was chosen; to lease a Porsche Taycan that is equipped with ISO 15118. Two compliant EVSE were acquired as well, but both used proprietary communication protocols that did not allow external EVSE control, despite efforts to collaborate with the manufacturers. The solution was to develop an ISO 15118-2-compliant EVSE internally (smart charging ecosystem described in Results section). When all the use case demonstrations are completed in FY 2022, the benefits of smart versus controlled charging will be discussed in the final report.

Regarding transactive energy trading, Argonne developed a transactive framework for EV charging capacity distribution (patent applied for) to prepare for this use case, but further effort has been suspended until the ramifications of the March 2021 announcement by MOBI regarding a new standard on blockchain for VGI (https://dlt.mobi/mobi-announces-the-first-electric-vehicle-grid-integration-standard-on-blockchain-in-collaboration-with-honda-pge-and-gm-among-others/) is understood and the need for further research is deemed necessary. This will not likely resume before the end of this project.

Task 3. Optimized control for grid resiliency/reliability; Impact of EVs @ scale

Barriers

- Unknown ability of multiple EVSE/workplace environment using SCM techniques to respond to grid conditions
- Lack of control strategies that consider the customer and the grid simultaneously
- Unknown impact of EVs @ scale.

Solution

Characterize the ability of the network of controlled devices on the customer side of the meter (at the Energy Plaza) to respond to grid conditions utilizing control strategies that support the customer and/or the grid. Translate the network response characteristics to node characteristics in the Argonne distributed network model (DNM) and link to the INL distribution and transmission models to identify potential impacts of controlled versus uncontrolled charging at a regional level.

Task 4. Early-stage R&D; Interoperability/grid integration components

Barriers

- Interoperability verification and diagnostics
- Compact sub-meters for multi-unit EVSE installations
- VGI solution for OEMs
- Integrated solutions for vehicle connectivity to local/workplace networks for energy management.

Solutions

- Develop and demonstrate the Diagnostic Electric Vehicle Adapter (DEVA) – Based on the refined SCA, this device enables digital communication for smart charge management, assesses EV-EVSE interoperability and identifies faults.
- Compact, low-cost sub-meters – The original plan was to focus on a power panel configuration to monitor and report from multiple EVSE as well as net load on the main feed to the load center. However, the sub-meter technology is now sponsored by the DOE Technology Commercialization Fund; the focus is component development for multiple applications and the status is reported separately.
- Develop the Smart Inlet for OEM applications – This device was proposed as a possible solution to VGI following discussions with an OEM in FY 2018, however the technology development was cancelled due to a lack of commitment by the OEM.

- Develop and demonstrate technologies to implement VGI in the workplace, e.g., smart interoperable AC L2 EVSE, containerized CIP.io, reservation system and charge scheduling based on smart communication (i.e., ISO 15118).

Results

Note that all the tasks in the Smart VGI project depend on access to the facilities and equipment at the Energy Plaza, though some of the prerequisite computer-based work (e.g., strategy/control algorithm development, grid modeling) can be performed remotely. Hence, the schedule to complete the tasks was substantially impacted by COVID-related restrictions at Argonne as well as delayed deliveries and support by vendors.

Quantifying the benefits of smart charging and developing control strategies for VGI depend on integrating EVs and EVSE with HLC capability. As mentioned previously, the limitations of available EV and EVSE necessitated acquiring an additional smart EV and developing a smart EVSE. These additional efforts and COVID-related delays resulted in a schedule slip into Q2 FY 2022.

Tasks 1 and 2: Quantify benefits of smart charging

The Argonne ISO 15118-2-compliant proof of concept (POC) EVSE was used with the Smart ED to demonstrate control strategies for several GMLC use case, including load shaping, demand response, demand charge mitigation, distribution upgrade deferral and charging coordinated with PV. Figure II.3.1.1 illustrates a demand response case. Frequency regulation will be addressed in FY 2022 with the Taycan. However, demonstration of PnC in the lab will require significant effort from Porsche and a PnC-compatible EVSE manufacturer in addition to our effort to set up a PKI ecosystem at the lab. Based on our previous experience, this would not occur by Q2 FY 2022; this is a candidate for further effort supporting the VGI/SCM or cyber activities under the recently announced VTO-sponsored EVs @ Scale consortium. The benefits of smart versus controlled/uncontrolled charging will be addressed in the final report.

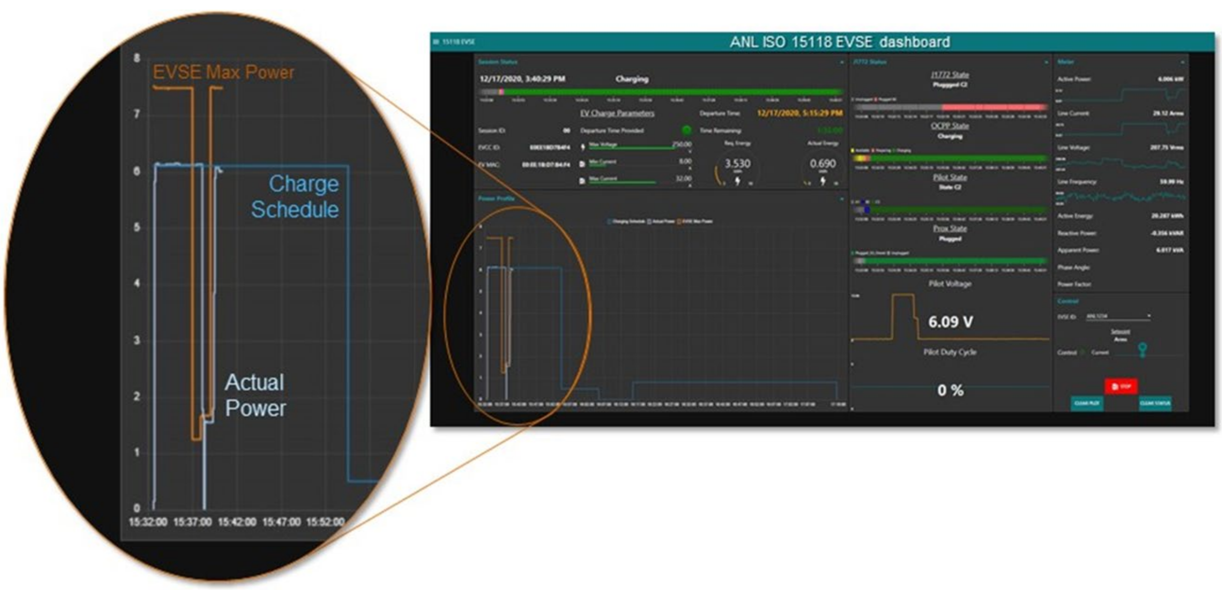

Figure II.3.1.1 Demand response use case example

Task 3. Optimized control for grid resiliency/reliability; Impact of EVs @ scale

Accomplishments this year included the linkage between Argonne and INL to simulate grid impacts due to charging large numbers of EVs (Figure II.3.1.2) and INL's development of a transmission model to provide real-time frequency signals for frequency regulation studies.

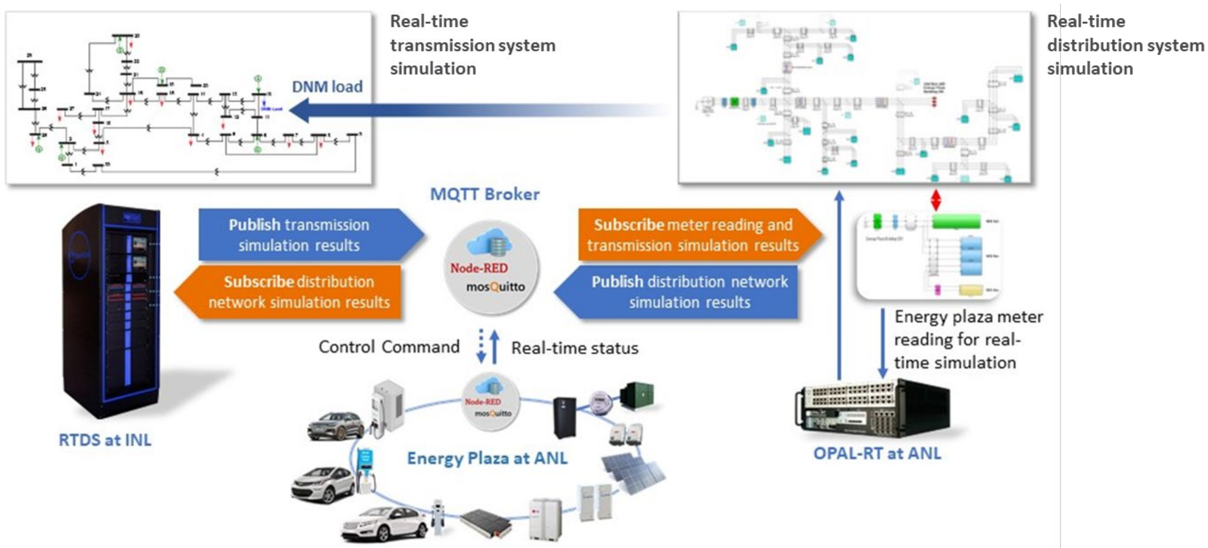

Figure II.3.1.2 INL and Argonne real-time simulation models linked for grid impacts analysis

Figure II.3.1.3 is an example of the grid frequency analysis, which was accomplished by INL scaling the loads from the distributed network model (DNM) in their transmission model. The results show the possible impact of controlled EV charging, i.e., without control the frequency dropped below 59.95 Hz (the green plot); with control, the frequency drop is recovered to the pre-determined acceptable range (59.95-60.05 Hz).

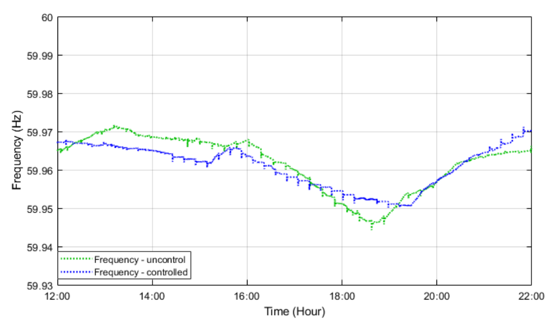

Figure II.3.1.3 Impact of EV charging on line frequency

Task 4. Early-stage R&D; Interoperability/grid integration components

Diagnostic Electric Vehicle Adapter (DEVA)

Designed to provide connectivity and communication diagnostics, the Mk III beta version of DEVA was completed in FY 2021. Based on the SCA Mk II hardware, it is being developed further to include an ISO 15118 AC EVSE emulator w/ sniffer and an oscilloscope mode to sample EVSE or PEV pilot/prox (real-time) w/ sampling of AC voltage/current waveform.

Figure II.3.1.4 Mk III beta version of DEVA

Communication Control Module (SpEC II)

An updated version of the SpEC I module, the beta version of SpEC II was completed in FY 2021. In addition to refining the board layout, features include sub-metering (AC/DC), an AC coupled HPGP circuit for power line communication (PLC), and SAE J2411 (CAN) communication. SpEC II can be utilized as an EVCC or SECC); it is used in Argonne's smart interoperable AC L2 proof-of-concept EVSE and can replace the SpEC I module currently being used by a U.S. DC EVSE manufacturer.

Figure II.3.1.5 Beta version SpEC II module

Smart Charging Ecosystem

Initiated out of necessity due to the lack of production smart EVSE, this effort has evolved to an integrated solution for smart charging and EV integration in local/workplace operations. The elements of the ecosystem include a smart interoperable AC L2 EVSE (i.e., with multiple communication protocols and connectivity options), an associated ISO 15118 dashboard, charge scheduler with user interface and containerized CIP.io. The system will be used to demonstrate smart use cases with the Porsche Taycan.

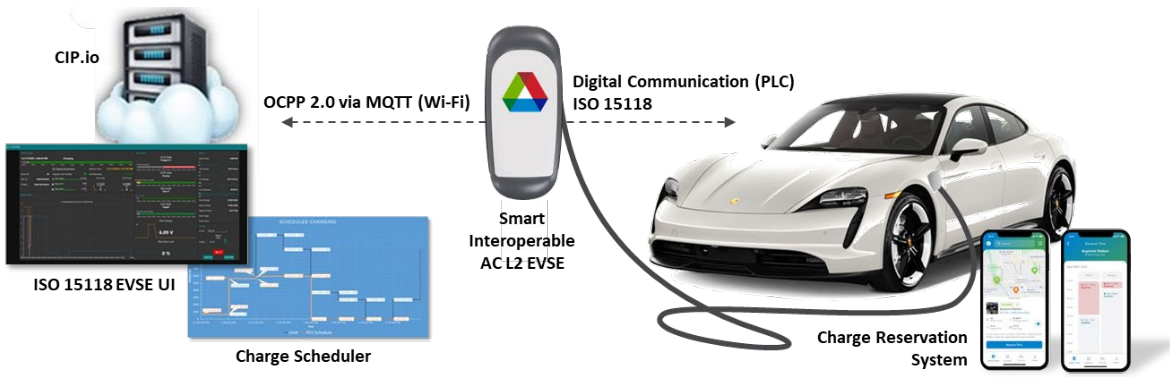

Figure II.3.1.6 Argonne-developed smart charging ecosystem

Development of a workplace EV charge reservation system began in FY 2021. Leveraging the cloud platform developed under the Smart Charge Adapter TCF project, the charge reservation system will allow EV drivers to utilize a mobile app to reserve a public/semi-public charge station. In addition to the added benefit of a mobile app for EV charge management, the ANL researchers will focus on implementing smart charge algorithms once the platform is up and running. These algorithms will leverage historical charging data to predict campus wide EV demand and individual energy needs and departure times. In addition to a machine learning approach, the platform will allow the researchers to implement and test a standards-based approach to EV charge scheduling.

Conclusions

The primary objective to demonstrate how smart charge management can be integrated with a network of building systems, renewables, and energy storage to respond to grid conditions and perform grid services/use cases has been demonstrated. The final assessment of the benefits of smart charging versus controlled and uncontrolled charging will be discussed in the final report after the use cases are completed in Q2 FY 2022.

The real-time performance of the network of devices at the Energy Plaza has been linked to Argonne's distributed network model and regional distribution and transmission models at Idaho National Laboratory to enable analysis of grid impacts. Preliminary results have been obtained to date; the final assessment of potential grid impacts will be in the final report in Q2 FY 2022.

Beta versions of both the Diagnostic Electric Vehicle Adaptor (DEVA) and the second generation of the communication control module (SpEC II) were accomplished in FY 2021. A proof-of-concept smart charging ecosystem was developed, including an ISO 15118 AC L2 EVSE (leveraging the SpEC II module) and an updated, dockerized CIP.io with EVSE user interface, charge scheduler and charge reservation system. The system will be utilized in the remaining smart use case demonstrations and the reservations system will be piloted on the Argonne campus in FY 2022.

Future Work – The project will be completed in the first two quarters of FY 2022. Remaining tasks include demonstration of the frequency regulation use case, quantification of the Energy Plaza's response time to grid conditions to complete the grid impact studies, further development of DEVA, SpEC II, and containerized CIP.io as well as delivery of the beta reservation system.

Key Publications/Presentations

1. Argonne National Laboratory. 2021. "New adapter enables monitoring and control of PEV charging stations." https://www.anl.gov/es/article/new-adapter-enables-monitoring-and- control-of-pev-charging-stations.

2. Hardy, K. 2021. "Charging Infrastructure Technologies: Smart Vehicle-Grid Integration – ANL." Presented at the U.S. Department of Energy Vehicle Technologies Office Annual Merit Review, June 23, 2021

3. J. D. Harper, "Smart Vehicle Grid Integration Project Overview." California Energy Commission Infrastructure Modeling Summit. September 15, 2021

4. D. Dobrzynski, J. D. Harper, US Patent Application Publication – Transactive Framework for Electric Vehicle Charging Capacity Distribution, Pub. No.: US 2021/0342958, Nov. 4, 2021

Acknowledgements

This project is sponsored by the Vehicle Technologies Office in the Office of Energy Efficiency and Renewable Energy Office, U.S. Department of Energy. The work was conducted by researchers in the Advanced Mobility and Grid Integration Technology Section of the Energy Systems Division of Argonne National Laboratory, including Jason Harper, Dan Dobrzynski, Bryan Nystrom, and Zhouquan Wu.

II.3.2 Adapter for Smart EV Charging TCF (Argonne National Laboratory)

Jason D. Harper, Principal Investigator
Argonne National Laboratory
9700 South Cass Avenue
Lemont, IL 60439
Email: jharper@anl.gov

Lee Slezak, DOE Technology Manager
U.S. Department of Energy
Email: lee.slezak@ee.doe.gov

Start Date: October 1, 2018 End Date: May 30, 2022
Project Funding: $1,180,698 DOE share: $590,349 Non-DOE share: $590,349

Project Introduction

Argonne National Laboratory (ANL) has invented and patented a universal smart charge adapter (SCA) that is connected between any AC charge station and plug-in electric vehicle. The smart charge adapter integrates legacy non-networked AC charge stations into a managed charging network that allows communication with grid operators. The smart charge adapter enables metering, monitoring and management control of charge sessions in response to local supply/demand levels. Qmulus, LLC (Chicago, IL) has an agreement with Argonne regarding the issued US patent and the EU patent application, with the intent to commercialize the technology.

The availability of the smart charge adapter will support the integration of EV charging as an additional grid resource, enabling grid operators to maintain supply/demand grid balance in part by controlling networked EV charging sessions as needed. As more EVs come under this level of control, it will support a reduction in the potential for brownouts, outages and voltage/frequency fluctuations that are caused by excess demand within a local or regional grid. Currently available charge stations (EVSE) are either not connected to the developing smart grid or are connected only through proprietary, insular platforms making it extremely difficult to interface charge sessions from large networks of diverse EVSE to monitor and control EV charging demand.

Figure II.3.2.1 The SCA is an in-line adapter for SAE J1772TM PEV charging (Mk III design)

Qmulus is the commercialization partner working with ANL. Final development of the Beta prototype and commercial smart charge adapter is underway on a contract basis with a contract-engineering firm. Zen Ecosystems (Newport Beach, CA) is providing access to its customer base for the full field trial. California Energy Commission (CEC) is providing advisory services for engagement with California utilities and for regional market and EV user information.

The primary goal of the project is to create a commercial SCA design that includes hardware, firmware, and software applications. The Beta prototypes will be tested at ANL in a controlled use setting and with end-users in Zen Ecosystems' coverage areas in California. Feedback from the current Beta device and our Beta pilot programs will lead to a commercial SCA design. Additional pilot(s) are targeted for California utilities (and/or another regional utility) in cooperation with Zen and the California Energy Commission (CEC).

Objectives

Qmulus' commercialization strategy initially focuses on public and semi-public owners of EVSE who are interested in a low cost, single interface for their networked and non-networked EVSE. These users will be able to network all their AC EVSE, regardless of brand, under a single interface via the SCA's Wi-Fi communications and cloud platform. Qmulus' longer-term strategy will target utilities to support their grid management needs. Residential users are also considered in their planning, particularly to support the various utility energy savings programs in which an EV driver may enroll. The initial markets are guiding the development plan, since larger scale users desire a more rigorously tested and certified solution. Ultimately, Qmulus hopes to support utility-sponsored energy programs for both home and workplace charging, enabling utilities to realize increased potential for smart grid management.

Development of the Beta version of the SCA was not complete by the start of the TCF award period thus the TCF funds were used, in part, towards final development and testing at ANL during Phase 1 of the TCF project. Conformance to the specifications is being substantiated in testing by ANL. The SCA will satisfy all design requirements and conformance tests before being deployed in pilot programs. A successful Phase 1 will result in beta HW and software ready for pilot program deployment as well as the design of the commercial SCA.

In Phase 2, the Beta prototypes will be field tested in two separate pilot programs. Phase 2 will provide critical data and feedback on the Beta SCA that will guide the development of the commercial version. User surveys will be conducted throughout the pilot programs to understand users' perceptions of the device, applications and controlling software. The surveys will be revised and updated as new information is obtained. Qmulus will work with CEC to understand and target the needs of California consumers and utilities for a smart grid enabled SCA. Root cause failure analysis (RCFA) will be used to examine any devices that have failed in the field to identify the causes behind the failure. These findings will support any changes to the design package for a commercial SCA.

In Phase 3, the partnership will continue its ongoing efforts with CEC to engage one or more utilities to plan an EV Smart Charging Pilot. In addition, further collaborations with Zen will be developed. This will parallel Qmulus' commercial roll-out for public and semi-public users. Working independently of the TCF project, Qmulus will have completed all business development and marketing steps required for the short-term launch goals. Engagement with a utility and planning for a demonstration pilot will be important for the intermediate and long-term business strategy. A successful Phase 3 will result in identifying proactive utilities looking to implement EV smart charging programs and engaging them.

Approach

Phase 1: Finalize SCA Development and Testing

This phase began prior to TCF funding; however, it has carried into the TCF period. This phase involves finalizing all hardware (mechanical/electrical), software, firmware, and cloud platform. Design will focus first on a Beta SCA and web platform that are as close to commercial products as possible. Twenty Beta SCAs will be built for testing in the Phase 2 field trial. A user friendly, secure, and reliable Beta web platform will be developed. Testing will be performed in the laboratory and at ANL's interoperability center.

Phase 2: Beta Pilot Program

Qmulus, Zen and ANL would implement two small-scale EV Demand Response pilot projects, utilizing Zen's OpenADR 2.0a/b certified cloud which would enable the SCA to act as a Virtual End Node (VEN), providing automated Demand Response dispatch from utility Demand Response Automation Servers (DRAS). The first pilot (Pilot A) would be performed at ANL. Pilot B would focus on the integration of the ZEN's OpenADR cloud interface into the Qmulus Cloud Platform to add EV charging into an OpenADR demand response program. Successful completion of Pilot B would result in the integration of the SCA/QCP into Zen's OpenADR system for 2 weeks with simulated DR events.

Phase 3: Utility Pilot Planning

Qmulus is partnering with Zen and the California Energy Commission (CEC) to identify California utilities willing to participate in an EV Smart Charging pilot. Prior to the TCF award, Qmulus and CEC will use their established contacts to engage partners and plan the pilot in California. Qmulus is also currently looking for potential partners in the Chicago, Denver, and Minneapolis metropolitan areas. Given the long planning periods of utilities, it is not expected that this Phase will be completed during the TCF project period, only that the engagement of partners, planning and development of the pilot will occur. If successful, the TCF project will lead to the EV Smart Charging pilot project, which will also support Qmulus' goal of identifying utilities that are potential customers for the SCA. Results of the EV Smart Charging Pilot may lead to further revisions to the design of the device, its software or firmware (if needed) or to a utility production package that ensures a reliable, rugged device and software that can be integrated into utility management systems or easily exchanged for utility-developed software.

Results

Progress was made in further developing the smart charge adapter hardware and firmware in FY21. Testing of the Mk III commercial alpha 3D printed prototypes were performed, and the results drove the redesign of mechanical components and electrical circuits. The Mk IV commercial beta will be the final tooled design (Figure II.3.2.2). Significant work was made on the Qmulus Cloud platform to add additional features and fix bugs. The ANL beta pilot program was conducted this fiscal year with the MK II prototypes and Zen Ecosystem's OpenADR 2.0a platform was integrated with the Qmulus cloud platform.

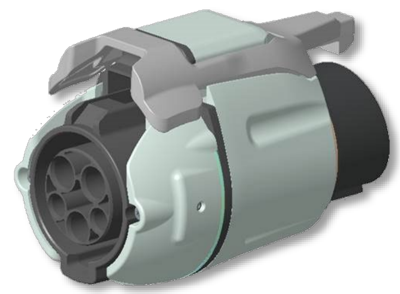

Figure II.3.2.2 Mk IV Commercial Beta Smart Charge Adapter: Portable, Robust and Easy to Use.

Smart Charge Adapter Hardware

Extensive testing was performed with multiple EVs and EVSE with the Mk III prototypes. Mechanically, the custom EVSE connector, PEV inlet with their respective custom sockets and pins were interoperable with all EVs and EVSE tested. There were some issues with the SCA latch and its ability to stay latched to a specific EV OEM inlet. This issue was identified and fixed in the redesign (Mk IV). The locking mechanism that locks the SCA to an EVSE connector had issues. This mechanism has been redesigned as well in the Mk IV. The LED light pipe was a new addition to the Mk III and did not fill entirely with light, using only 4 LEDs possibly due to the number and placement of the LEDs. This issue has been fixed in the Mk IV design.

From an electrical perspective, the SCA firmware was updated to account for the new electrical components/design of the MK III. The battery capacity was doubled and confirmed. The new wake-up circuits allow the SCA to stay in a deeper sleep state to conserve energy when an active charge session is not occurring. The MK IV design and tooled unit production was put on hold for the majority of FY 21 due to the pandemic and uncertainty regarding the cost share to be provided by the commercial partner.

Qmulus Cloud Platform and Mobile App Development

The first phase of the Qmulus Cloud Platform (QCP) was finished in FY20. Features of the cloud platform include management, monitoring and control of Smart Charge Adapters as well as Open Charge Point Protocol EVSE. The second phase of work was kicked off in Q4 of FY20 and continued through FY21. The development work focused on implementing a third-party API to integrate Qmulus devices into third party applications including the Zen HQ™ platform for demand response applications. Additional features implemented include charge scheduling, authorization/access control, group power management, and enhanced notifications. These features were fully tested and validated by Argonne.

Pilot Programs

The ANL pilot (Pilot A) began in Q1 of FY21 with deploying four Mk II beta SCA's at the ANL Smart Energy Plaza. The SCA's were locked onto a single port of four BTCP 40A L2 EVSE shown in Figure II.3.2.3. There are a total of 12 ports at the Smart Energy Plaza for employee EV charging. Argonne employees had the option to select a port with or without an SCA. Although there was limited charging at the Smart Energy Plaza due to the pandemic, 221 charge sessions occurred with SCA ports resulting in 3.125 MWh of energy being dispensed (Figure II.3.2.4). The Mk II prototypes held up well considering their exposure to the fall, winter, spring, and summer seasons. No mechanical failures occurred though the white prototype housings turned yellow due to the lack of UV resistance in the plastic. This will be taken into consideration when choosing the commercial housing material.

Figure II.3.2.3 Mk II SCA deployment at ANL Smart Energy Plaza.

Figure II.3.2.4 Smart Energy Plaza SCA Pilot Data for FY21.

Multiple adapters were utilized by Argonne employees at their place of residence. Feedback from the employees has been positive. Data collection is ongoing. In addition to Argonne employee deployment, Argonne has provided potential partners access to the MK II prototypes for testing in their own laboratories. The list of companies that have tested the MK II prototypes include BMW, Stellantis, Duke Energy, Ameren, Hilo Energie, and EVMatch.

Zen Ecosystems provided ANL access to their OpenADR 2.0a VTN for demand response integration with the Qmulus cloud platform. The two systems were integrated, and preliminary testing was accomplished with the four SCAs at the Smart Energy Plaza.

Conclusions

The four Mk II prototypes deployed in the pilot at the Smart Energy Plaza performed well and withstood the elements with minimal downtime; data analysis will be provided in the final report. In addition to the ANL pilot, adapters were provided to Argonne employees and partners for test and evaluation. The Zen Ecosystem's OpenADR 2.0a platform was integrated with the Qmulus cloud platform in preparation for the California pilots.

The fully tested SCA Mk III prototypes bring the design one step closer to a commercial design. The Mk IV commercial beta will be the final tooled design; it will be completed in FY22, leading to the production of tooled commercial smart charge adapters.

II.3.3 Scalable Electric Vehicle Smart Charging Using Collaborative Autonomy (LLNL)

Steve Chapin, Principal Investigator
Lawrence Livermore National Laboratory
7000 East Avenue
Livermore, CA 94550
Email: chapin8@llnl.gov

Jovana Helms, Principal Investigator
Lawrence Livermore National Laboratory
7000 East Avenue
Livermore, CA 94550
Email: helms7@llnl.gov

Lee Slezak, DOE Technology Manager
U.S. Department of Energy
Email: lee.slezak@ee.doe.gov

Start Date: October 1, 2018 End Date: September 30, 2021
Project Funding: $1,570,000 DOE share: $1,570,000 Non-DOE share: $0

Project Introduction

Since 2011 the number of plug-in electric vehicles (PEVs) has grown exponentially, both in the U.S. and across the world, and this number is expected to continue to grow [2]. Along with these new vehicles, coupled with increases in vehicle battery sizes, comes a large demand for electric vehicle charging stations. The expected increase in electricity demand from PEV charging presents a challenge to reliable power grid operation, as many PEV owners are likely to plug in their vehicles immediately after the morning and afternoon commutes, times of day that are already high-demand periods for the power grid. In this way, unregulated charging would lead to higher demand peaks, increasing the need for controllable generation and thus making reliable power grid operation more difficult.

To illustrate the scale of the problem imposed by widespread PEV adoption, consider the Riverside Public Utilities, which has approximately 110,000 metered customers spread across 14 distribution feeders. At the California average of 63 PEV per 1,000 households, RPU customers would own approximately 7,000 EVs, which is of a scale handled by traditional centralized mechanisms. EVs represented over 11% of light-duty vehicle sales in California during the first three quarters of 2021, putting them on pace to sell more than a 250,000 for the year. California had approximately 820,000 PEVs registered as of November 2021 [3], and is expected to grow above 8,000,000 EV by 2030[2], and also representing 33-50% of the total vehicles on the road in California. This means that RPU would be supplying charging for 45,000-97,000 vehicles in 2030.

In contrast, if properly managed, the widespread adoption of PEVs presents a mechanism for demand response (DR) through vehicle charging. While today most charging stations simply provide power to connected vehicles until the charge capacity is reached, there has been a great deal of interest in developing “smart charging” technology, that is, charging stations with the ability to respond to market signals to control vehicle charging. Smart charging stations have the potential to communicate with the power grid to implement demand response, i.e., intelligently charge PEVs in order to improve charging economics, and to improve the resilience and reliability of the power grid [4]-[9].With these methods, typically a PEV owner specifies some willingness

[2] Since 2012, California has averaged a 34% increase in sales each year. This obviously cannot continue indefinitely (at that rate, CA would sell 3.5 million EV in 2030; in 2021 *total* light duty vehicle sales in California will be between 2.1 and 2.3 million). A more modest 25% growth rate in sales yields about 8 million PEV in CA by 2030.

to have vehicle charging delayed in exchange for a lower price. Given that flexibility, smart charging can be used to shift demand from peak hours to off-peak hours.

Smart charging could also be used to improve power grid stability and protect equipment such as transformers from overloading. While Independent System/Regional Transmission Operators[3] (ISO/RTO) are responsible for managing bulk power transfer, Distribution System Operators (DSO) are responsible for lower-voltage power supply for consumers. A DSO could therefore take advantage of a smart charging system to provide flexibility in load management to preserve equipment health. In particular, the DSO could set limits on the power flow across certain components, with an eye to grid stability and reliability, and require that EV charge providers operate within those constraints.

Simultaneously, charge network operators (CNO) that operate many charging stations will wish to minimize the overall cost of supplying their customers' needs; in turn, the customers may receive preferable pricing from the CNO, which can act as an aggregator and resell DR services to the DSO as part of that cost minimization. Thus, there are three sets of constraints in tension when determining a charging schedule for a fleet of PEVs: the overall available power supplied by the DSO, the power demanded by PEV owners, and the cost minimization sought by CNO in supplying their customers.

Objectives

Our objectives for FY 21 (Year 3) of the project extend our results achieved during Years 1 and 2, to wit:

- Alternating direction method of multipliers (ADMM)-based algorithmic framework for computing feasible charging schedules for a fleet of PEVs. This algorithmic framework allowed us to compute a 24-hour schedule based on projected arrivals of PEVs with stated charging demands (Year 1).
- Support for node failure, either through malice or misfortune. This allowed us to test the ability of our system to remove compromised electric vehicle supply equipment (EVSE) from the network, both for charging and computational purposes.
- Support for demand response and multiple administrative authorities through a mechanism allowing multiple EVSE from a CNO to join in spinning reserve and provide DR services to the DSO.

We had 4 new objectives for Year 3:

- Generate realistic projected demand based on sampling from a set of real charge session data (in this case, a year's worth of charging data from commercial and residential charging stations across the San Francisco Bay area).
- Support a rolling horizon for computation of new charging schedules, so that every 5 minutes we computed new schedules based on the current state of the grid, charging equipment, and connected EVs.
- Incorporate a decentralized, resilient *allreduce* operation, allowing the charging stations to compute the sum of decentralized data, which is necessary to remove the aggregator from the distributed decomposition of the scheduling problem to yield a fully-decentralized composition. It is important to distinguish distributed computations, which may have a centralized aggregator or controlling node, from decentralized computations, which have no controlling node or central aggregation point.
- Incorporate a DSO module that, in addition to setting constraints for power flows across the system, can trigger DR events, and see those DR actions taken in our simulations.

[3] The equivalent in Europe is the Transmission System Operator.

Approach

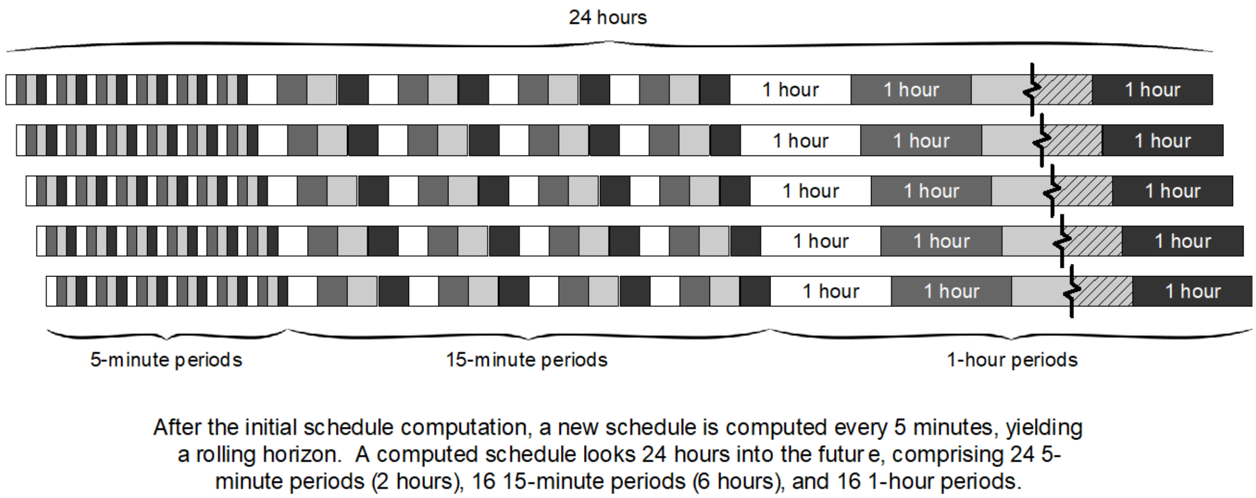

Figure II.3.3.1 Schedule Computation Yielding a Rolling Horizon

To reach our first two objectives, we start with a model for a sequence of 24-hour schedules shown in Figure II.3.3.1. The basic period in the schedule is a 5-minute interval. For the first two hours of a 24-hour schedule, we track each 5-minute interval in its own period. For the next six hours, we group the 5-minute intervals into twenty-four 15-minute periods, and then for the remaining sixteen hours, we group the intervals into sixteen 1-hour periods.

Table II.3.3.1 Attributes of a Charging Session

Field Name	Description
Session ID	A unique identifier for this charging session
Starting Period	Period within the 24-hour schedule when it starts
Ending Period	Period within the 24-hour schedule when it ends
Charging Station ID	Unique identifier for the charging station to which EV is connected
Port	Port number at the charging station
Max Charge Rate	Maximum power draw (in kW)
Efficiency	Efficiency factor for charging battery (.91 to .99)
Max Battery Capacity	Maximum usable battery capacity (in kWh)
State of Charge at Plugin	Battery level at start of seesion (in kWh)
Desired State of Charge	Desired battery level by end of session (in kWh)

Within the schedule, each charging session has the fields shown in Table II.3.3.1. The unique identifier is only used to distinguish sessions. The starting and ending periods refer to the variable-length period numbers as shown in Figure II.3.3.1—periods 0-23 are the 5-minute periods comprising the first two hours of the schedule; periods 24-47 are the 15-minute periods comprising the next six hours; and periods 48-63 are the 1-hour periods. Charging station IDs are unique, and commercial charging stations have two ports, while residential stations only have one. The remaining fields are self-explanatory.

The charging session data we use as the basis for generating our EV demand comprises approximately 455,000 charging sessions collected over one year on about 4,500 charging stations in the San Francisco Bay Area. The ratio of commercial/public to residential charging was approximately 10 to 1, with commercial charging stations having two charge ports and residential stations having 1. As we were simulating a 24-hour period during the work week, we restricted the data we used for schedule generation to only those session that started

Monday-Friday. Figure II.3.3.2 displays a graph summarizing the charging session statistics for all weekday sessions.

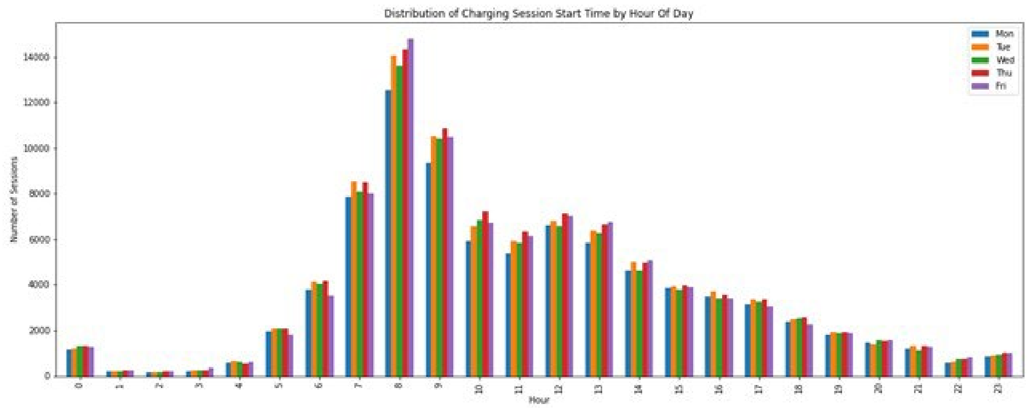

Figure II.3.3.2 Distribution of Charging Session Start Time by Hour of Day, Weekdays

This charging data is dominated by commercial charging, as can be seen by examining Figure II.3.3.3 and Figure II.3.3.4, which show residential and commercial charging (note the different scales on the two graphs; displaying the residential charging sessions on the commercial scale causes several of the lower entries to become nearly invisible; as with the number of chargers, the number of charging sessions is also approximately a 10:1 ratio for commercial to residential). Because we separate the data, we can tune our demand generation to reflect different hypothetical penetration levels for commercial and residential charging. Our current work maintains the 10:1 ratio seen in the original data.

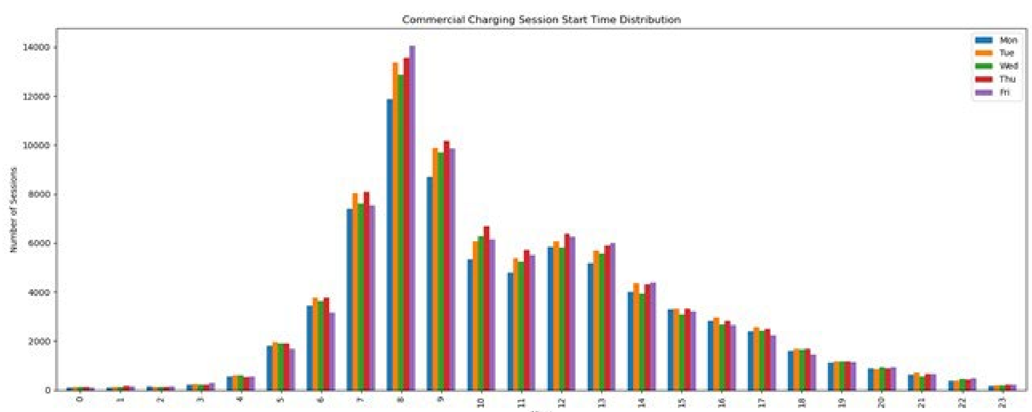

Figure II.3.3.3 Commercial Weekday Charging, by Starting Hour

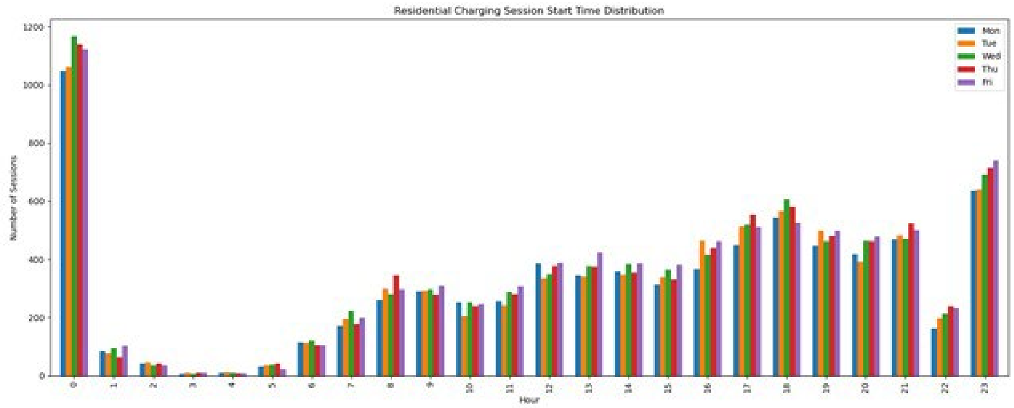

Figure II.3.3.4 Residential Weekday Charging, by Starting Hour

For our demand response mechanisms to have effect, the distribution grid must be loaded near its saturation point. To accomplish this, we started with a GridLAB-D model of a distribution grid at a nearby utility, and uniformly distributed additional charging stations (at the 10:1 ratio). We also measured the arrival frequency of new charging sessions at each type of station and incorporated that factor in our determining the number of additional stations necessary so that we are likely to see the distribution grid pushed to its limit during the peak afternoon hours. The schedule generator includes a scaling factor that can be applied to the arrival rate to increase the load on the grid without requiring the placement of additional charging stations (other parameters, such as the maximum power draw at a station, can also be adjusted to tune the stress on the grid).

Our decentralized formulation of the optimization problem for EV charging requires the use of a distributed sum operation to replace the aggregator that exsists in a distributed formulation. For some associative, commutative operation $\bigoplus$, and assuming every computing agent *i* in a group has data x_i, then *allreduce* has the group collectively compute $\overline{x} = \overset{\otimes}{\underset{i}{}} x_i$, which, in our case, is simply a decentralized sum operation (using + for $\otimes$). The *allreduce* operation is not new, but our decentralized implementation of it is.

Results

To generate the schedule for a day, it is necessary to "prefill" the hours leading up to the start of the day of interest with a realistic set of charging sessions. Generating demand starting at midnight omits charging sessions that would have started say, at 11pm, and last through the early morning hours. Therefore, we start generating from an empty schedule a day in advance of the first time period in the simulation. We then adjust any charging session that began on the previous day, chopping off the portion that came before the start of the simulated day, and adjusting its start time (and duration) so that only the "tail" of the session is represented. Similarly, we must allow a runout of charging sessions so that the simulator, when solving the decentralized ADMM problem, has 24 hours of projected future data.

The simulation schedule for a single day comprises projections for 288 24-hour periods of demand, each of them offset from the prior one by five minutes (cf. Figure II.3.3.1, with 288 rows). To compute a new row (S_{i+1}), we start with the current schedule (S_i),[4] and follow these steps:

1. Advance the clock by five minutes. This means that the period for future charging sessions may change; charging sessions that were scheduled to start in the first five minutes of period the first 15-minute period (period 24) move into the last 5-minute period (period 23), and sessions at the beginning of the first 1-hour period (period 48) move into the last 15-minute period (period 47).

[4] The initial schedule, S_0, is empty.

2. Find all sessions that terminated at the end of the prior time period, and perform postprocessing for them, marking their charging station/port as free and doing summary accounting.
3. For each of the *n_sess* sessions currently in the schedule, check whether it terminates early by performing a probability check against a tunable threshold. If it does terminate early, perform postprocessing for it. This represents EV owners ending sessions early for active sessions or changing their minds and canceling future sessions.
4. Check *n_sess* times for additions to the schedule by performing a probability check against a tunable parameter. Each time the value is below the threshold, sample the appropriate data set (commercial or residential) and attempt to find an open charging station that can accept that session.[5]
5. For the 5-minute window that just moved into view in the final 1-hour period, make a probability check once per charging port that is not already assigned a session in that window, using the appropriate arrival probability (commercial or residential).

After generating 72 hours' worth of charge session data, we write out the schedule starting at the beginning of hour 24. The rolling forward of time in the schedule has the desirable property that nearer events are more accurately predicted; sessions scheduled farther in the future have a higher aggregate chance of being canceled.

Our implementation of *allreduce* is shown in Figure II.3.3.5. The procedure takes as input the local data x_i, the operation to perform the reduce with (in our case, +), and the set of agents, p, over which to perform the reduction. As part of this project, this functionality was added to the Skynet collaborative autonomy system developed at Lawrence Livermore. The procedure builds a ring in the communication graph, where each agent sends the same information to $r \in \mathbb{N}\ (r > 0)$ neighbors, introducing redundancy in the computation, mitigating agent or communications channel failure during the *allreduce* operation. This introduces a bounded amount of noise when failures occur and is exact otherwise; this is a tradeoff of speed for accuracy, which is acceptable for our application. The system is resilient for up to $r - 1$ crash failures. Noise is introduced in this case because not all remaining agents will have received the data from the agent that failed. Our iterative method will reduce the noise in the next iteration. For increased scalability, agents can be structured into a tree rather than a ring, with each set of siblings performing an *allreduce*, starting at the leaves and combining results going up the tree, with the overall result communicated down, yielding logarithmic scaling.

procedure $\texttt{allreduce}_r(x_i, \otimes, p)$
  $\hat{x}_i \leftarrow x_i$.
  for $k = 1, \ldots, p$ **do**
    Send $\hat{x}_i$ to agents $(i + \ell)\%p$ for $\ell = 1, \ldots, r$.
    $\ell^* \leftarrow \min\{\ell \in \{1, \ldots, r\} | \text{received } \hat{x}_{i-\ell}\}$
    $\hat{x}_i \leftarrow \hat{x}_{i-\ell^*} \otimes x_i$.

Figure II.3.3.5 Implementation of *allreduce*

Conclusions

The Stargazer project at Lawrence Livermore National Lab investigated mechanisms for scalable, managed EV charging while improving grid reliability. As part of this work, we developed a model for model for EV charge optimization and tested it under synthetic load using a centralized simulation in year 1. In year 2 we developed a distributed formulation of the model based on the alternating direction method of multipliers, incorporating failure tolerance and initial provisions for demand response (via spinning reserve). We analyzed

[5] This may require iteration, and the number of attempts to do this is capped.

performance of the system through simulation on groups of up to 1,100 charging stations with uniformly random demands; details of this work are found in [1]. In year 3 we added realistic demand schedules based on a year's worth of charging for light-duty EV. We also extended the implementation to be completely decentralized and added a distribution systems agent to trigger demand response in the simulation.

Our future work will be to extend the model and formulation to accommodate vehicle-to-grid services, to incorporate systems running on Raspberry Pi single-board computers running the Skynet runtime system, with a demonstration prototype of a network of Raspberry Pis controlling OpenEVSE charging stations.

Key Publications

1. Ignacio Aravena, Steve J. Chapin, and Colin Ponce. "Decentralized Failure-Tolerant Optimization of Electrical Vehicle Charging." IEEE Transactions on the Smart Grid, Volume 12, Issue 5, pp. 4068–4078, Sept. 2021, doi: 10.1109/TSG.2021.3080583.

References

1. Agency, International Energy, "Global EV Outlook," 2017. [Online]. Available: https://www.iea.org/publications/freepublications/publication/GlobalEVOutlook2017.pdf.
2. J. Szczesny, "Sales of Electric Vehicles Growing Steadily in California," The Detroit Bureau, 11 Dec 2018. [Online]. Available: https://www.thedetroitbureau.com/2018/12/sales-of-electric-vehicles-growing-steadily-in-california/.
3. S. Deilami, A. S. Masoum, P. S. Moses and M. A. S. Masoum, "Real-Time Coordination of Plug-In Electric Vehicle Charging in Smart Grids to Minimize Power Losses and Improve Voltage Profile," Transactions on Smart Grid, vol. 2, no. 3, pp. 456–467, Sep 2011.
4. Z. Fan, "A Distributed Demand Response Algorithm and Its Application to PHEV Smart Charging in Smart Grids," Transactions on Smart Grids, vol. 3, no. 3, pp. 1280–1290, Sep 2012.
5. P. Zhang, K. Qian, C. Zhou, B. G. Stewart and D. M. Hepburn, "A Methodology for Optimization of Power Systems Demand Due to Electric Vehicle Charging Load," Transactions on Power Systems, vol. 27, no. 3, pp. 1628–1636, Aug 2012.
6. S. Shao, M. Pipattanasomporn and S. Rahman, "Demand Response as a Load Shaping Tool in an Intelligent Grid with Electric Vehicles," Transactions on Smart Grid, vol. 2, no. 4, pp. 624–631, Dec 2011.
7. P. Finn, C. Fitzpatrick and D. Conolly, "Demand-side Management of Electric Car Charging: Benefits for Consumer and Grid," Energy, vol. 42, no. 1, pp. 358–363, 2012.
8. R. Abousleiman and R. Scholer, "Smart Charging: System Design and Implementation for Interaction Between Plug-In Electric Vehicles and the Power Grid," Transactions on Transportation, vol. 1, no. 1, pp. 18–25, Jun 2015.
9. C. Wu, H. Mohsenian-Rad, J. Huang and J. Jatskevich, "PEV-Based Combined Frequency and Voltage Regulation for Smart Grid," in PES Innovative Smart Grid Technologies (ISGT), Washington, DC, 2012.
10. Y. S. Lam, K. C. Leung and V. O. K. Li, "Capacity Estimation for Vehicle-to-Grid Frequency Regulation Services with Smart Charging Mechanism," Transactions on Smart Trid, vol. 7, no. 1, pp. 156–166, Jan 2016.
11. Wachter and L. T. Biegler, "On the implementation of an interior-point filter line-search algorithm for large-scale nonlinear programming," Mathematical Prog., vol. 106, no. 1, pp. 25–57, 2006.

12. HSL, “A collection of fortran codes for large scale scientific computation,” 2015. [Online]. Available: http://www.hsl.rl.ac.uk/

13. Message Passing Interface Forum, “MPI: a message-passing interface standard,” June 2015, version 3.1. [Online]. Available: https://www.mpiforum.org/docs/mpi-3.1/mpi31-report.pdf

14. M. G. Vaya, G. Andersson, and S. Boyd, “Decentralized control of plug-´ in electric vehicles under driving uncertainty,” in IEEE PES Innovative Smart Grid Technologies, Europe, 2014, pp. 1–6.

Acknowledgements

Thanks to Jon Donadee and Amy Musselman for developing the original solution in Year 1, to Colin Ponce for continued development of the underlying Skynet ADMM platform and for his contributions to publication [1], and to Jovana Helms for assistance in project administration.

II.4 Cyber Security

II.4.1 Securing Vehicle Charging Infrastructure

Jay Johnson, Principal Investigator
Sandia National Laboratories
P.O. Box 5800 MS1033
Albuquerque, NM 87185
Email: jjohns2@sandia.gov

Lee Slezak, DOE Technology Manager
U.S. Department of Energy
Email: lee.slezak@ee.doe.gov

Start Date: October 1, 2018 End Date: December 31, 2021
Project Funding: $3,000,000 DOE share: $3,000,000 Non-DOE share: $0

Project Introduction

As the U.S. electrifies the transportation sector, cyberattacks targeting vehicle charging could impact several critical infrastructure sectors including power systems, manufacturing, medical services, and agriculture. This is a growing area of concern as charging stations increase power delivery capabilities and must communicate to authorize charging, sequence the charging process, and manage load (grid operators, vehicles, OEM vendors, charging network operators, etc.). The research challenges are numerous and complicated because there are many end users, stakeholders, and software and equipment vendors interests involved. Poorly implemented electric vehicle supply equipment (EVSE), electric vehicle (EV), or grid operator communication systems could be a significant risk to EV adoption because the political, social, and financial impact of cyberattacks—or public perception of such—would ripple across the industry and produce lasting effects. Unfortunately, there is currently no comprehensive EVSE cybersecurity approach and limited best practices have been adopted by the EV/EVSE industry. There is an incomplete industry understanding of the attack surface, interconnected assets, and unsecured interfaces. Thus, comprehensive cybersecurity recommendations founded on sound research are necessary to secure EV charging infrastructure. This project provided the power, security, and automotive industry with a strong technical basis for securing this infrastructure by developing threat models, determining technology gaps, and identifying or developing effective countermeasures. Specifically, the team created a cybersecurity threat model and performed a technical risk assessment of EVSE assets across multiple manufacturers and vendors, so that automotive, charging, and utility stakeholders could better protect customers, vehicles, and power systems in the face of new cyber threats.

Objectives

The goal of this project was to protect U.S. critical infrastructure and improve energy security through technical risk analysis under scenarios with massive deployment of interoperable EV chargers. To improve the vehicle industry's cybersecurity posture, this project:

- Conducted adversary-based assessments of EVSE and supporting systems,
- Created a threat model of EV charging, and
- Analyzed power system impacts for different attack scenarios.

This provided DOE and automotive, EVSE vendors, and utility stakeholders with:

- Clear documentation of gaps in EVSE cybersecurity and the path forward to address those weaknesses,
- A threat model for EVSEs and associated infrastructure and services,
- Recommendations for the automotive industry based on the adversary-based assessments, and
- Cyberattack impact analyses of the power system with remediation recommendations.

Approach

The team executed the following integrated cybersecurity R&D tasks:

1. Conduct threat modelling to understand what potential cyber hazards exist with EVSE interfaces
2. Assess the current state-of-the-art cybersecurity posture of EVSE equipment using authorized, adversary-based assessment techniques (penetration testing and red teaming)
3. Establish credible attack vectors based on the cybersecurity assessments and threat model
4. Determine the impact of current and potential vulnerabilities on distribution and transmission power systems
5. Create a risk matrix to prioritize mitigations that reduce the number of high-consequence/low-threat level attacks.

The task structure of this project is shown in Figure II.4.1.1, wherein the left side (blue) estimates the probability of different attack scenarios, and the right side (green) estimates the consequence of attack scenarios. The cybersecurity risk of a particular attack is the combination of the likelihood and impact of the attack. By studying a range of attack scenarios, mitigations could be determined to prevent attacks at specific points in the cyberattack kill chain [1].

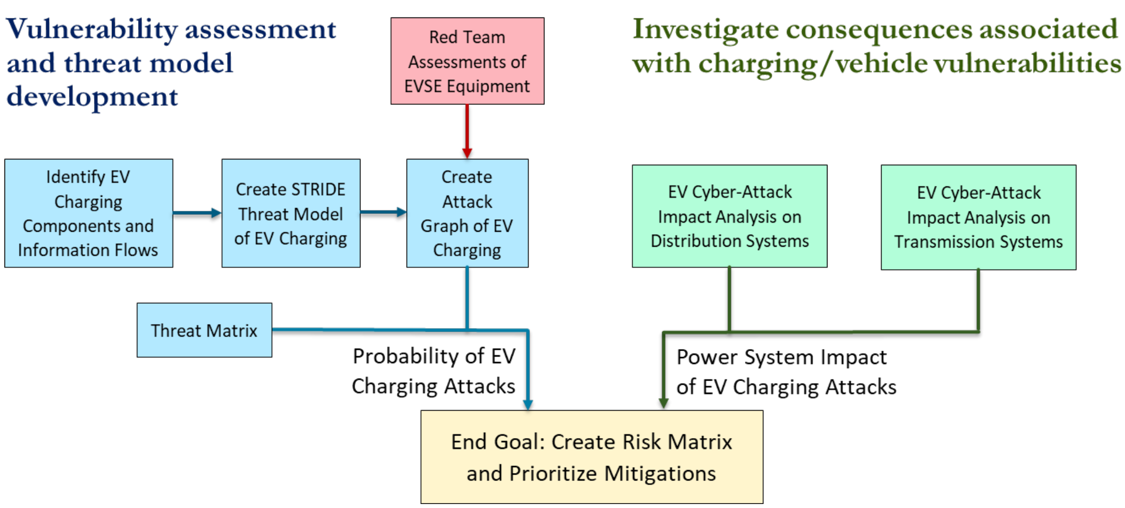

Figure II.4.1.1 Project tasking.

Results

The project team evaluated probable attacks based on hands-on cybersecurity assessments with partner organizations and evaluated the probability of success. A detailed threat model was created for EVSE with connections to external entities. Attack graphs were developed based on this model, and then revised based on real-world results from penetration testing of multiple EVSE. Transmission and distribution simulations of

EVSE charging were conducted to determine if malicious control of EVSE could cause inter-area oscillations, generator tripping, or high or low voltages on feeder circuits.

EVSE Penetration Testing

For three years, the team worked closely with multiple EVSE manufacturers, vendors, and owners to better understand the vulnerabilities presented by EVSE and their associated networks. In addition to the local interfaces, the team studied vulnerabilities that affected information and operational technology (IT/OT) systems such as remote access controls, insecure protocols, and the ability to fingerprint devices from their online presence. This involved working with the threat models, attack graphs, and validating attack vectors. Findings from network traffic analysis, forensic analysis, and open-source information gathering led to vulnerability enumeration in EVSE devices as well as their supporting infrastructure. Use of unencrypted protocols, such as OCPP 1.6 and MQTT, on the globally routable Internet have resulted in several findings that were disseminated back to EVSE manufacturers for remediation [2]. Additionally, the team was able to use their findings to create a generalized "fingerprint" for EVSE deployments, allowing the team to search for and enumerate similar systems that were Internet connected. From these similar systems, specific characteristics such as open ports, software versions, or reports of vulnerabilities were used to identify other instances of EVSE deployments. The hands-on assessments of EVSE equipment found many areas for improvement, e.g., failure to physically secure EVSE enclosures; default passwords for internal systems, or credentials posted inside enclosure; data not encrypted at rest and only financial data being encrypted in transit; unnecessary ports and services are enabled. A list of best practices was generated from these assessments [3], shown in Figure II.4.1.2. An anonymized set of findings is presented in the final project report [4]. The assessment team also provided EVSE partners with the findings and potential mitigations for identified vulnerabilities. Some recommendations are included in Figure II.4.1.3.

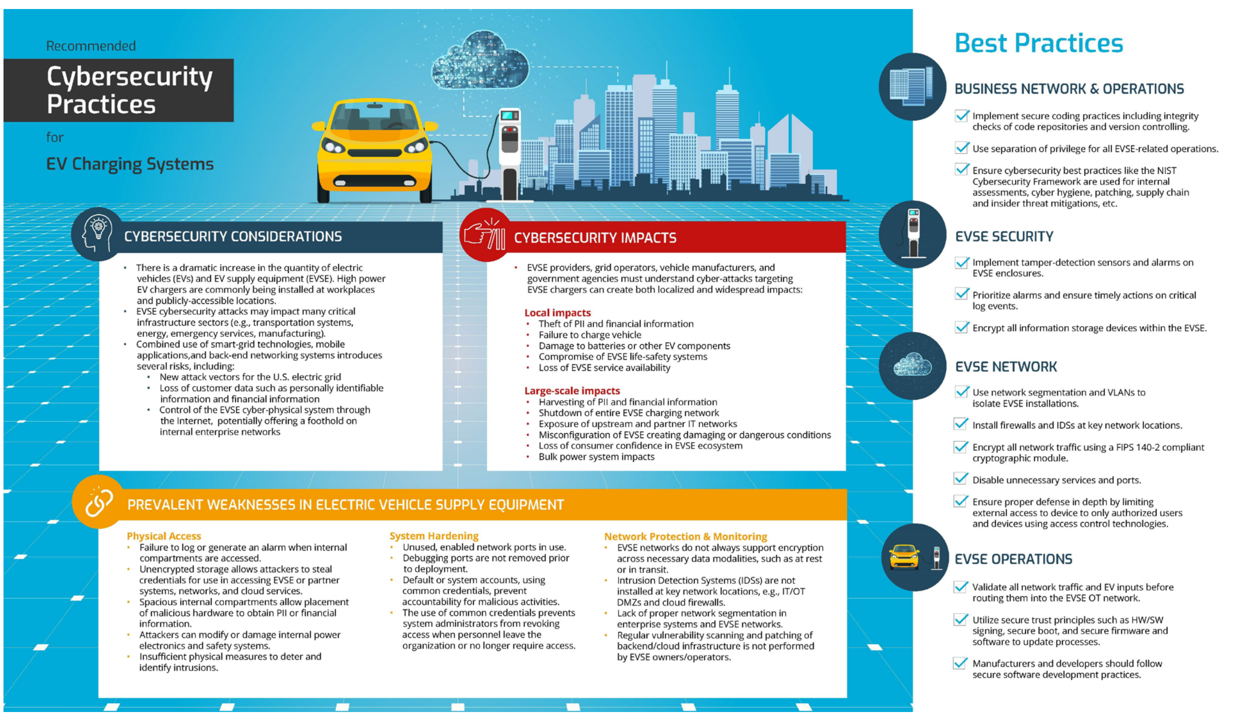

Figure II.4.1.2 EVSE Best Practices [3].

Attack Graphs

Attack graphs show the steps an attacker must take to move from a system/network access point to a consequence of concern or objective. The use of attack graphs simplifies the identification of key steps an attacker must take to achieve their objectives, allowing those actions to be detected or prevented. Figure

II.4.1.4 illustrates access points, staging areas, and consequences of concern related to a generic EV charger network. In this figure, one of the attack paths involves an attacker using an initial compromise of an EVSE provider's business network to impact the bulk power system. By analyzing the steps in this attack path, the attack may be detected or prevented by monitoring for unusual Network Time Protocol traffic or requiring code signing of EVSE updates. The team used the information gathered from their assessments, publicly available information regarding vulnerabilities, and knowledge regarding the tactics, techniques, and procedures used by attackers to advise the attack graph. In the case of coordinated EVSE attacks that disrupt the power system, there were two major questions:

- Can the attacker "pivot" between the components, systems, and networks in the EV/EVSE ecosystem to compromise the necessary information flows?
- Can an attacker synchronize their attack to affect large portions of the grid simultaneously?

From the assessment activities, it appears both are possible so an attacker *could* manipulate large networks of EVSE devices.

Figure II.4.1.3 EVSE vendor recommendations based on penetration tests of EVSE equipment and networks [3].

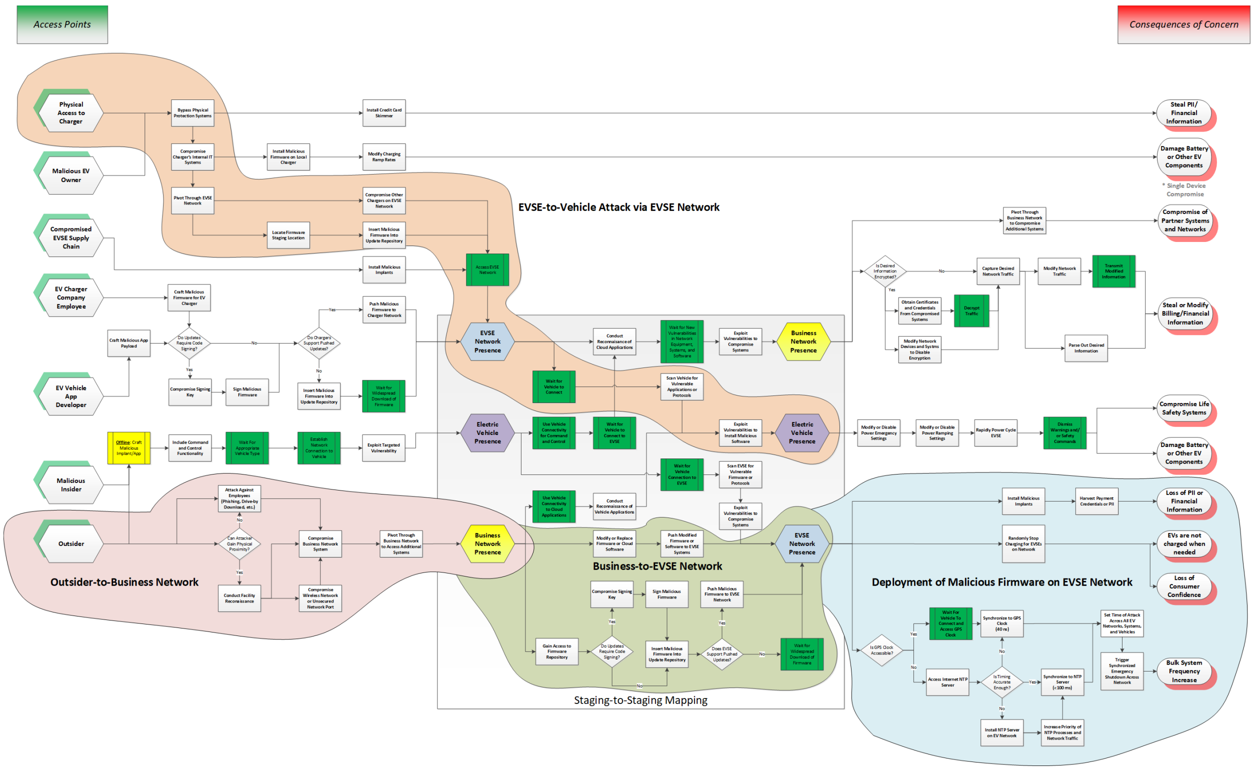

Figure II.4.1.4 Complete graph. Details presented in [2].

Threat Model Development

PNNL led the task to develop a threat model of high-power electric vehicle charging infrastructure and systemically analyze it for threats that have the potential to bring wide-ranging consequences to the electric grid and transportation systems. PNNL derived a novel consequence-centric variant of the STRIDE threat modeling methodology to: (i) discover consequences that potentially impact vehicles, the electric supply, and transportation; and (ii) focus subsequent modeling and analysis on threats that may precipitate the consequence. STRIDE is an industry-accepted approach to threat modeling, first made popular for its application at Microsoft. Examples of the system models used for the threat modeling are depicted in Figure II.4.1.5, which show decomposition of chargers and vehicle into components, how data flows between components, and the relationships of components to external entities. After the threats are enumerated, safeguards and countermeasures are identified to mitigate the vulnerabilities. By focusing on consequences, insights into the security and resiliency of the EV charging ecosystem are gained. Importantly, the threat model analysis suggests that no single entity (for example, charging station vendor or charging network operator) is ideally situated to secure the ecosystem, but instead, requires the concerted effort of the ecosystem. The threat model, analysis, and results are detailed in [7].

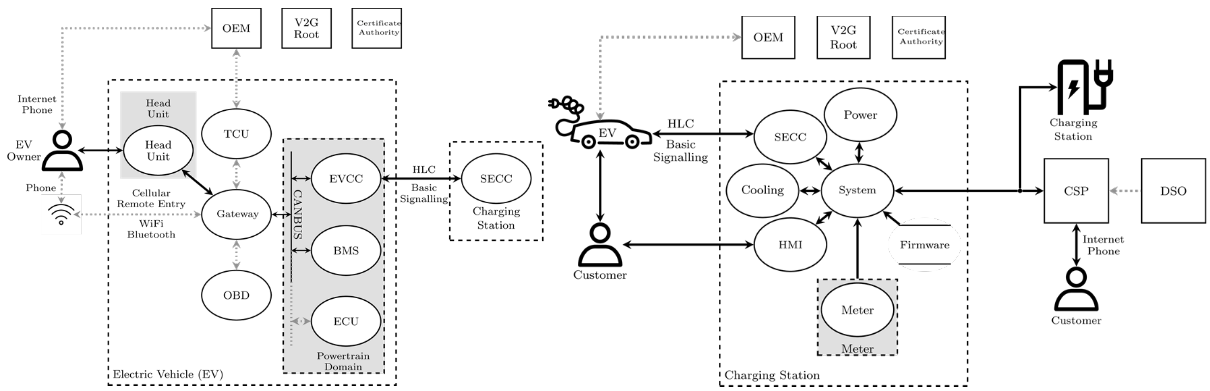

Figure II.4.1.5 The vehicle system model (left) depicts the components of the vehicle and their relationship to the charger. The charger system model (right) illustrates the relationship of the components and information flows.

Distribution and Transmission System Consequence Analysis Simulations

Transmission simulations of coordinated charging control was modeled for the Western Electricity Coordinating Council (WECC) were performed to understand bulk system impact from coordinated cyberattacks. PNNL's Consequence Analysis results indicated, that for the specific events studied in this work, the impact on the WECC system would be minimal [8]. Two different types of studies were simulated: a large discrete WECC-wide EV load drop across the region intended to raise frequency, and several smaller EV load modulation events intended to excite system inter-area oscillations along the California Oregon Intertie (COI). Conceptually, if loads in the north are high and loads in the south are low, this will create a flow north along the COI. Similarly, when loads are low in the north and high in the south, this will tend to generate flows south along the COI. No significant adverse effects were observed in either set of simulations, however, COI flows of up to 3 times the oscillating load size were observed in the load modulation studies. Inter-area oscillations are of concern in that they put the grid in elevated state of risk during system events as well as making it difficult to achieve ideal transfer capacities and optimal power flows.

It is also possible that EVSE operations at the distribution level could result in poor power quality. The largest risk is that voltages will be perturbed to levels that increase equipment wear, trip DER equipment, or decrease power delivery efficiency from low power factors. EVSE misoperation that causes voltages to reaching levels that cause pumps to stall, or other load failures is unlikely as utility planning will prevent these significant issues by installing appropriate voltage regulation equipment like on-load tap-changers in transformers and capacitor banks. Simulations were conducted on a rural 12 kV distribution feeder in a highly commercial load area. Nine 250 kW, 3-phase, 480 V stations were simulated at the end of the feeder. Scenarios included 2.25 MW charging sequences with and without V2G capabilities to generate high and low feeder voltages during peak and min load periods. The results for steady-state charging and discharging with different power factors showed that distribution voltage profile did exit ANSI C84.1 *American National Standard for Electric Power Systems and Equipment—Voltage Ratings (60 Hz)* voltage range A. In this extreme case, the utility would be in violation of the standard, but only if all chargers were in use at the same time and the station was located at the end of the feeder. And even if the stations were temporarily in this over or under-voltage state, there would be no impact on grid reliability or resilience from such an event.

Conclusions

This project helped identify potential EV charger vulnerabilities and quantify the risk to critical infrastructure when vehicle chargers are maliciously controlled. This risk assessment is only an initial step in a continuous process of hardening charging infrastructure against cyber-attacks. There is much more work to secure charging infrastructure from cyberattacks, including:

- Developing standardized policies for managing chargers and other assets in the charging ecosystem.

- Designing effective perimeter defenses to protect the assets including firewalls, access control mechanisms, data-in-flight requirements (encryption, authentication), etc.
- Creating situational awareness systems and intrusion detection/prevention systems in an ecosystem of diverse communication networks and systems.
- Researching response mechanisms to prevent further adversary actions on the system, nonrepudiation technologies, and dynamic responses.
- Creating hardware- and software-based fallback and contingency operating modes.

References

1. Lockheed Martin, The Cyber Kill Chain, accessed 10/26/2021, URL: https://www.lockheedmartin.com/en-us/capabilities/cyber/cyber-kill-chain.html
2. R. Varriale, R. Crawford, M. Jaynes, Risks of Electric Vehicle Supply Equipment Integration Within Building Energy Management System Environments: A Look at Remote Attack Surface and Implications. In: Choo KK.R., Morris T., Peterson G., Imsand E. (eds) National Cyber Summit (NCS) Research Track 2021. NCS 2021. Lecture Notes in Networks and Systems, vol 310. Springer, Cham., 2022. https://doi.org/10.1007/978-3-030-84614-5_13v
3. J. Johnson, B. Anderson, B. Wright, J. Daley, R. Varriale, "Recommended Cybersecurity Practices for EV Charging Systems," Sandia National Laboratories, SAND2020-11401 D, http://doi.org/10.13140/RG.2.2.11141.37602.
4. J. Johnson, et al., "Securing Electric Vehicle Charging Infrastructure – Final Report," Sandia Technical Report, 2022 (forthcoming). http://doi.org/10.13140/RG.2.2.28243.12329
5. B. Anderson, "Securing Vehicle Charging Infrastructure Against Cybersecurity Threats," 2020 SAE Hybrid and Electric Vehicle Symposium, Pasadena, CA, 28–30 Jan 2020.
6. R.M. Pratt, "Cybersecurity: Securing Vehicle Charging Infrastructure – Consequence Analysis and Threat Assessment," PNNL-SA-152801, 06/02/2020. https://www.energy.gov/sites/default/files/2020/06/f75/elt263_pratt_2020_p_4.24.20_1126AM_LR.pdf
7. T.E. Carroll, G.B. Dindlebeck, R.M. Pratt, L.R. O'Neil, "A Threat Model of High-Power Electric Vehicle Charging Infrastructure," Pacific Northwest National Laboratory Technical Report PNNL-SA-157336, 2021. Manuscript submitted for publication.
8. J.G. O'Brien, P.R. Maloney, U. Agrawal, T.E. Carroll, R.M. Pratt, "Electric vehicle infrastructure consequence assessment," Pacific Northwest National Laboratory Technical Report PNNL-29514, 2019. Manuscript awaiting DOE concurrence for submittal.

Acknowledgements

We wish to thank the multi-laboratory team for this work: SNL (Ben Anderson, Brian Wright, Josh Daley, Jimmy Quiroz), PNNL (Rick Pratt, Tom Carroll, Lori Ross O'Neil, Brian Dindlebeck, Patrick Maloney, James O'Brien) and ANL (Roland Varriale, Ted Bohn, and Keith Hardy).

Sandia National Laboratories is a multimission laboratory managed and operated by National Technology & Engineering Solutions of Sandia, LLC, a wholly owned subsidiary of Honeywell International Inc., for the U.S. Department of Energy's National Nuclear Security Administration under contract DE-NA0003525.

II.4.2 Consequence-Driven Cybersecurity for High Power EV Charging Infrastructure (Idaho National Lab, Oak Ridge National Lab, National Renewable Energy Lab)

Richard "Barney" Carlson and Kenneth Rohde, Principal Investigators
Idaho National Lab
2525 North Fremont Avenue
Idaho Falls, ID 83415
Email: richard.carlson@in.gov, kenneth.rohde@inl.gov

Tony Markel and Anuj Sanghvi, Principal Investigators
National Renewable Energy Laboratory
15013 Denver West Pkwy
Golden CO 80401
Email: tony.markel@nrel.gov; anuj.sanghvi@nrel.gov

Michael D. Iannacone and Omer Onar, Principal Investigators
Oak Ridge National Laboratory
1 Bethel Valley Rd
Oak Ridge, TN 37830
Email: Iannaconemd@ornl.gov; onaroc@ornl.gov

Lee Slezak, DOE Technology Manager
U.S. Department of Energy
Email: lee.slezak@ee.doe.gov

Start Date: October 1, 2020 End Date: September 30, 2021
Project Funding: $995,000 DOE share: $995,000 Non-DOE share: $0

Project Introduction

With the emergence of electrified transportation, there is a desire for faster recharge times and integrated smart energy management for charging infrastructure. The development and deployment of extreme fast charging (XFC) and wireless power transfer (WPT) emphasizes the need for cybersecurity of these high-power EV charging systems. The use of high voltage, high current, and magnetic fields for high power charging systems presents potential public safety hazards if not controlled and secured properly. Additionally, many advanced control systems and communication networks are utilized to maximize the efficiency of this high-power EV charging infrastructure. With these advanced hardware and controls systems, cybersecurity vulnerabilities are present and must be secured to ensure safe, reliable, and resilient operation.

This cybersecurity project includes the analysis and evaluation of cybersecurity of high-power conductive and wireless charging infrastructure. INL leads this project in collaboration with ORNL, NREL, ABB, Tritium, and Electrify America focused on prioritizing and securing cybersecurity vulnerabilities and threats for high-power EV charging infrastructure. This research project conceptualizes and prioritizes disruptive events caused by cyber means related to XFC and WPT systems, evaluates the impact severity potential of these events, and develops mitigation solutions to secure the infrastructure.

Charging infrastructure is designed to meet EV energy transfer requirements with safe, high efficiency operation at a low cost, but often cybersecurity is not at the forefront of the design process when engineering such systems. By identifying and prioritizing potential disruptive cybersecurity events into a list of HCEs, cybersecurity research efforts can be focused on the highest priority events. Using input from industry manufacturing, engineering, cybersecurity, and electric sector subject matter experts, a comprehensive list of HCEs has been developed for high-power EV charging infrastructure.

In addition to the XFC challenges discussed above, chargers using wireless power transfer (WPT) are also emerging from the research environment into the early stages of commercial products; pilot sites for these systems have already reached >250 kW. It is critically important to protect these devices and their supporting information networks, and to do this at the earliest stage possible as these products are being developed.

This project uses an approach to manage cybersecurity risks adapted from a proven process used by INL to secure power plants and other critical infrastructure. It goes beyond generic “good hygiene” cybersecurity recommendations and instead presents a consequence-driven approach to holistically assess, prioritize, and manage a broad range of risks, from privacy concerns and denial of service to destruction of property and disruption of the electric grid. The project team examines the impact and feasibility of these risks and makes specific recommendations to the industry for how these can be mitigated.

Objectives

Charging infrastructure is a system of systems, including physical, communication, and control layers. Physical systems include vehicles, charging equipment, supporting electrical equipment at the charging site (e.g., power converters, transformers, etc.), distributed energy resources (DERs) such as stationary energy storage and solar photovoltaic (PV) arrays that support XFC charging stations, and the distribution feeder electrical equipment that services charging sites. The objective of this project is to develop solutions and recommendation for the highest prioritized events to secure vulnerabilities, means to detect attacks, and methodologies to respond and restore from an HCE. The outcome of the project will be actionable information that industry can immediately apply to their WPT product development efforts, including recommendations on High Consequence Event (HCEs) mitigation strategies, allowing them to engineer cybersecurity into their products before market introduction. This project will identify the highest priority risks and recommend mitigation strategies, providing industry and government leaders the means to focus their finite resources.

Approach

The impact and consequence-based cybersecurity analysis framework used in this project first prioritizes high consequence events caused by cybersecurity manipulation that can cause physical adverse effects to the EV charging infrastructure. This prioritization is accomplished using an internally developed scoring matrix based on impact severity and cybersecurity manipulation complexity. Secondly, the impact severity and cybersecurity complexity of these potential events are evaluated using laboratory equipment to validate the prioritization and to investigate the vulnerabilities and attack pathways leading to the high consequence events. Third, mitigation solutions and strategies are developed to secure vulnerabilities and threats. Lastly, publication of recommendations, project findings, and a stakeholder action plan will be published to inform industry of the solutions developed to secure high power charging infrastructure.

Cybersecurity vulnerability and cyber-attack path assessment in this project will be focused on device-level and supervisory control systems and the sophisticated communication they require within and between vehicles, EVSE, DERs, building and other third-party controllers, utilities, and/or other entities. Assessment of the electric grid’s cybersecurity vulnerabilities is addressed by other programs and is therefore out of the scope of this project. However, this project will assess threats to the local distribution network and broader grid stability caused by compromised high power charging infrastructure.

The effort required for the success of this three-year project led by Idaho National Lab involves the collaboration of two other national labs (National Renewable Energy Lab, Oak Ridge National Lab) and three collaborative industry partners (ABB, Tritium, Electrify America). Together the expertise and capabilities of these partners will enable the successful outcome for this project.

Results

This third and final year of the project focused on revising the scoring and ranking of the high-consequence event based on laboratory results and findings, the development and recommendation of mitigation solutions, and publishing the results and findings of this project.

High-Consequence Events Revised Scoring and Ranking: Upon completion of the laboratory evaluations of the impact severity and cyber manipulation complexity of the highest-ranked HCEs, the scoring and prioritization ranking of these HCEs is revised based on these new results and insights. Several of the initial HCE scores remain unchanged, however a few HCE scores change due to revised impact-severity scores or cyber-complexity multiplier scores.

Of the few HCEs with increased scoring, HCE 1 which involves grid stability impacts due to concurrent XFC load shed, score increased because several methods were identified to enable XFC load shed via internal controls-communication or external-communications manipulation. Of note, a few methods were determined to enable the concurrent load shed of many XFCs via external communications, not just by individually manipulating XFCs. This ability to concurrently manipulate many XFC resulted in an increase of the cyber-complexity multiplier score to 4 because enacting this event is less difficult than hypothesized. Previously, the score was based on concurrently manipulating several individual XFCs, rather than manipulating the smart energy-management system to execute coordinated commands.

Another noteworthy change in scoring impacted HCEs 2 and 8, involving the manipulation of a liquid-cooled XFC cable thermal-management system. Through laboratory evaluation, the manipulation of this system is demonstrated to be possible via internal control-communication manipulation, resulting in no coolant flow in the cable system even during full current (500 A) operation. This confirms the initial impact-severity score and increases the cyber-complexity multiplier score to 4 for charge events when the vehicle does not monitor the temperature of the vehicle charging-inlet port. However, for charge events when the vehicle monitors the inlet-port temperature, the cyber-complexity multiplier score is much lower because the difficulty of successfully manipulating both XFC and EV thermal measurements is significantly more difficult.

The largest change in scoring involves HCE 12 which is the theft or alteration of data transmitted between the vehicle, EVSE, EV driver, network operator, etc. Laboratory evaluation verified a wireless-sniffing methodology of data or information theft from the liquid-cooled cable CCS communications (Baker, et. al.). Initial cyber-complexity scoring is based on assumptions that data theft or alteration is only possible with electrical connection to the communications wiring of the XFC or the CCS cable. However, with the proper tools and knowledge, this data theft can be accomplished without physically contacting any part of the XFC. Therefore, the HCE cyber-complexity multiplier score significantly increased, resulting in a significant change in the HCE prioritization ranking from twelfth to fourth.

Mitigation Solutions: Recommendations for mitigation solutions and strategies from this project can improve the security posture of high-power charging EV infrastructure. These recommendations are detailed in the following section and are grouped into two categories: general and specific mitigations.

General Mitigations: The following lists the general mitigations that can be applied to systems, including high-power vehicle-charging infrastructure. These mitigations are included in various industry standards or recommended best practices for secure systems.

- Implement secure boot methods: use chip-manufacturer features such as Secure Firmware Update (SFU) and Secure Boot
- Control network segmentation (isolate from Internet-connected devices)
- Implement secure code-signing of patches and firmware updates
- Use secure network-communication methods (e.g., SSH, Secure Socket Layer/Transport Layer Security (TLS), OCPP 2.0)
- Intrusion Detection and Prevention (Intrusion Detection System/Intrusion Prevention System) on remote-access servers

- Implement a zero-trust network architecture between charging stations and management servers.

Specific Mitigations: Recommendations for mitigations specifically focused on high-power charging infrastructure are listed below. Many of these solutions are derived from the HCE evaluations results and findings in an effort to reduce the impact severity and/or increase the difficulty of cyber-manipulation.

- Controlled shutdown during an end-charge session or load shed event thereby increasing the duration of the power-transfer ramp down, resulting in a less-severe rate of change of power draw therefore decreasing the load shed's potential negative impact
- Local energy storage adjacent to XFC site to buffer grid-feeder transients and improve voltage stability
- For prevention of wireless sniffing of data or information
    - Wire mesh shielding over CCS cable
    - Encryption of the CCS messages between the EV and the charge station, such as used in ISO 15118 standard which uses TLS
- Additional gate-driver logic to prevent short circuit of gate drivers (μm-technology complementary metal-oxide semiconductor transistors)
- Host Intrusion Detection (HIDS) to monitor critical system files
- Manage and filter internet connectivity (tunnel or virtual private network)
- Safety Instrumented System (SIS) monitoring XFC operation, electrical performance, temperatures, communications, etc.

Detailed Mitigation Description of a Safety Instrumented System for XFC

For industrial control systems with the potential for HCEs, SISs are used to monitor and respond to anomalies and adverse situations. An SIS intrusion and exploit detection system was developed and integrated into a 350 kW XFC as part of this project. The SIS monitors internal and external communications, measures critical operational parameters, and responds with a graded scale output correlating to the severity of identified event. This SIS is focused on detecting intrusion and anomalies as a result of cybersecurity manipulation, but the SIS is also able to detect a wide range of other anomalies caused by hardware malfunction, vandalism, or even natural environmental events. The main components and communication systems monitored by the SIS include the following measurements and communication networks.

- Communications messages: internal command and control network, external communications with the EV (CCS, CHAdeMO, etc.) and with smart energy-management systems (OCPP, Open Platform Communications Unified Architecture, etc.)
- Electrical measurements: AC input power and power quality, DC output power, and auxiliary system power, including the liquid-cooled cable thermal-management system power.
- Temperature measurements: CCS cable system (cable and connector), power-cabinet air temperature, and ambient air temperature
- Component states: AC input contactors, DC output contactors for each connector (CCS, CHAdeMO, etc.) and door switches for all accessible enclosures.

The SIS is a robust monitoring and detection system because of the numerous redundant inputs which enable high confidence in the identification of operational anomalies or cyber-manipulation. For example, during the manipulation of the XFC liquid-cooled cable thermal-management system, the SIS is able to determine anomalies associated with this thermal-management system by measuring the ambient temperature, liquid-cooled cable and connector temperature, chiller pump power, and the DC current delivered to the vehicle both from measured and communications values. Additionally, the door-switch states are used to determine whether previous unauthorized access occurred. Operational anomalies, including cyber-manipulation, can be detected if these signals or measurements do not correlate to one another or if any piece of information is out of expected bounds (example: reduced or no coolant flow, excessively high cable or connector temperature, measured DC transfer does not match delivered current). Development of SIS response and recovery actions to the various levels of identified anomaly severity will be determined in a future research project. Proper response to anomalies and minimization of false-positive responses, while still quickly and appropriately responding to detected anomalies, is a difficult challenge. The final HCE prioritization detailed in this publication is the basis for the future efforts of initial levels of response to detected anomalies.

In this project, numerous exploits focused on enacting one or more high-consequence events were launched in the laboratory on a 350 kW capable XFC equipped with the SIS to verify the SIS functionality, quantify the SIS performance, and identify gaps or any areas of needed improvement in the SIS. Figure II.4.2.1 shows the testing results from one exploit launched against the XFC liquid cable thermal management system during 350 kW operation. The exploit disables the thermal management system and the temperature monitoring by the XFC. This exploit successfully accomplishes 350 kW operation with no cooling of the liquid cooled cable which in turn results in the cable temperature and connector temperature exceeding the 55°C thermal safety limit within two minutes. The SIS immediately detected this malicious exploit by identifying the low current draw by the chiller system during high-power charging operation. Additionally, the SIS detected the cable and connector temperatures exceeding the thermal safety limits. This laboratory evaluation demonstrates the successful functionality and performance of the SIS integrated in the 350 kW XFC.

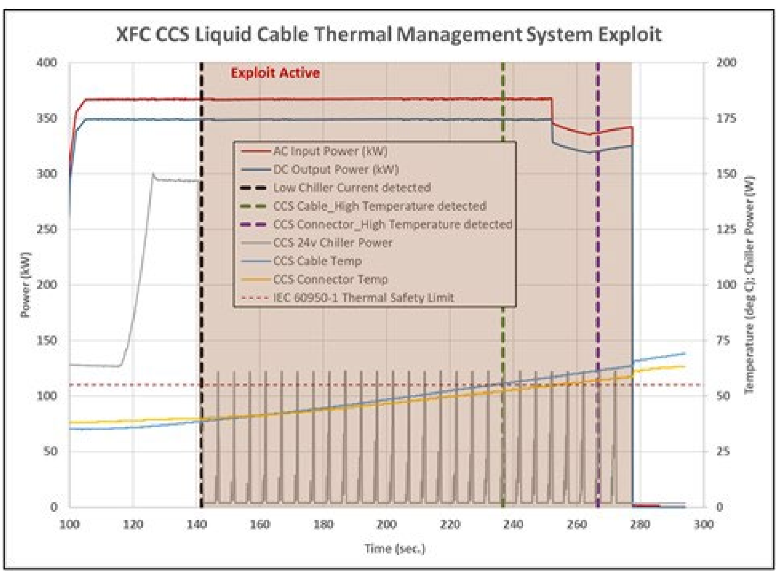

Figure II.4.2.1 SIS Detected Exploit of the XFC's Liquid-cooled Cable Thermal Management System

<u>Publication of Project Results and Findings</u>: Several venues for the dissemination and publication of the results and findings from this project are utilized. This includes presentations to technical organization including the IEEE CyberPELS conference, Auto-ISAC Summit 2021, and a journal publication still in the review process. The various publications methods detailed the analysis methods to score and prioritize the HCEs as well as the laboratory testing results used to verify or adjust the scoring therefore reprioritizing the HCEs. Also, the mitigation solutions and strategies are detailed as recommendations to industry to immediate solutions to improve the security posture of high-power EV charging infrastructure.

Conclusions

As high-power EV charging infrastructure deployment and use increases, the need for cybersecurity is vital for safe and reliable operation. Traditional cybersecurity efforts focus on keeping cyber-adversaries out of system networks. This project was conducted under the assumption that a determined and well-resourced adversary will eventually gain access to nearly any network. Research efforts for this project focus on trying to prevent catastrophic manipulation and misuse of high-power EV charging infrastructure. To effectively do so, researchers first conceptualized events that could be brought about by cyber-manipulation to create a physically adverse effect on high-powered EVSEs, EVs, and/or the electric grid-distribution feeder network. Researchers then quantitatively prioritize the events, using impact severity and cyber-manipulation-complexity scoring. Laboratory evaluation with high-power charging infrastructure is conducted on selected HCEs to verify or adjust the scoring of the impact severity and cyber-manipulation complexity, thereby enabling the reranking and reprioritization of the HCEs. The development and recommendation of mitigation solutions to prevent the HCEs is a main focus of this study. Several mitigation solutions are included in several standards and recommended practices; however, specific mitigation solutions are also needed for the unique aspects of high-power charging infrastructure, one of which is the integration of an SIS into high-power charging-infrastructure hardware.

Key Publications

1. Carlson, R.; Rohde, K.; Consequence-driven Cybersecurity for High-Power EV Charging Infrastructure; Auto-ISAC Summit 2021 presentation. https://automotiveisac.com/auto-isac-summit-2021/

2. Carlson, R.; Rohde, K.; Consequence-driven Cybersecurity for High-Power EV Charging Infrastructure; IEEE CyberPELS 2019 presentation. https://attend.ieee.org/cpsi-2019/tutorials/

3. Sanghvi, A., Markel, T., “Cybersecurity for Electric Vehicle Fast-Charging Infrastructure.” IEEE Innovative Smart Grid Technologies Conference. February 15–18, 2021.

4. Park, Yongwan, Omer C. Onar, and Burak Ozpineci. “Potential Cybersecurity Issues of Fast Charging Stations with Quantitative Severity Analysis.” In 2019 IEEE CyberPELS (CyberPELS), pp. 1–7. IEEE, 2019.

References

1. Richard Baker, Ivan Martinovic; “Losing the Car Keys: Wireless PHY-Layer Insecurity in EV Charging”, University of Oxford, 28th USENIX Security Symposium, 978-1-939133-06-9, 2019.

(This page intentionally left blank)

For more information, visit:
energy.gov/eere/vehicles

DOE/EE-2614 • August 2022